THEMATIC MAPPER CRITICAL ELEMENTS BREADBOARD PROGRAM

NASA CONTRACT NAS5-20589

HUGHES AIRCRAFT COMPANY
Space and Communications Group
P O Box 92919
Los Angeles, California 90009

APRIL 1976

FINAL REPORT

Prepared For
GODDARD SPACE FLIGHT CENTER
Greenbelt, Maryland 20771

SCG 60165

TECHNICAL REPORT STANDARD TITLE PAGE

1. Report No.	2. Government Accession No.	3. Recipient's Catalog No.

4. Title and Subtitle	5. Report Date
Final Report Thematic Mapper Critical Elements Breadboard Program	1 April 1976
	6. Performing Organization Code
7. Author(s) C.H. Dale, Jr., J.L. Engel, E. D. Harney	8. Performing Organization Report No. HS-236/D2241
9. Performing Organization Name and Address Hughes Aircraft Company Space and Communications Group P.O. Box 92919 Los Angeles, CA 90009	10. Work Unit No.
	11. Contract or Grant No. NAS 5-20589
	13. Type of Report and Period Covered Final-29 June 1974 through 31 Jan. 1976
12. Sponsoring Agency Name and Address National Aeronautics & Space Administration Goddard Space Flight Center Greenbelt, Maryland 20771	14. Sponsoring Agency Code

15. Supplementary Notes

16. Abstract

This development was undertaken to demonstrate the feasibility of the three principal features of the Hughes Thematic Mapper which had not been flight proven on either the Multispectral Scanner or the Visible Infrared Spin Scan Radiometer. These features include a 40.6 cm bidirectional scan mirror assembly, a scan line corrector and a silicon photodiode array with integral preamplifier input stages. These three assemblies were designed, fabricated, and tested to demonstrate performance consistent with requirements of the Thematic Mapper System. The measured performance met or exceeded the original design goals in all cases with the qualification that well defined and well understood deficiencies in the design of the photodiode array package will require the prescribed corrections before flight use.

17. Key Words (Selected by Author(s))	18. Distribution Statement
Object space scanner Beryllium eggcrate mirror Torque while turnaround scanning Optomechanical scan line corrector Silicon photodiode array	

19. Security Classif. (of this report)	20. Security Classif. (of this page)	21. No. of Pages	22. Price*
Unclassified	Unclassified	-	

*For sale by the Clearinghouse for Federal Scientific and Technical Information, Springfield, Virginia 22151.

CONTENTS

1.0 INTRODUCTION AND SUMMARY

This report presents the results of an 18 month breadboard development program to demonstrate the feasibility and performance of critical elements of the Hughes Thematic Mapper (TM). The work was performed under Contract NAS 5-20589 dated 29 June 1974 and subsequent modifications. The original contract was limited to development of a 40.6 cm version of the earlier 23 cm Multispectral Scanner (MSS) scan mirror assembly (SMA). Near the close of this original one year effort the contract was modified and extended to permit several new design improvements to be made to the torquing control and mirror reversal mechanism. At about the same time two additional modifications to the contract were made to permit development of a scan line corrector (SLC) and a silicon photodiode array (SiPDA). The work on the SMA, SLC, and SiPDA was carried on as separate projects which have culminated in demonstration of the desired performance at the close of the contract, though not in every detail for every parameter.

Figure 1-1 depicts the general concept of the Hughes Thematic Mapper. The three new elements are called out among the total complement of instrument assemblies which are already flight proven.

A general summary of the program requirements and results is presented in the following paragraphs. Subsequent sections are organized as essentially autonomous reports of the three projects, each containing its own detailed summary. Section 2 presents the details of the design, development, and test of the SLC. Section 3 presents similar data on the SiPDA and Section 4 presents the detailed coverage of the SMA effort. Formal test data logs are presented as appendices for each of the assemblies. Further details of development and diagnostic testing can be found in the engineering log books which are submitted separately from this report.

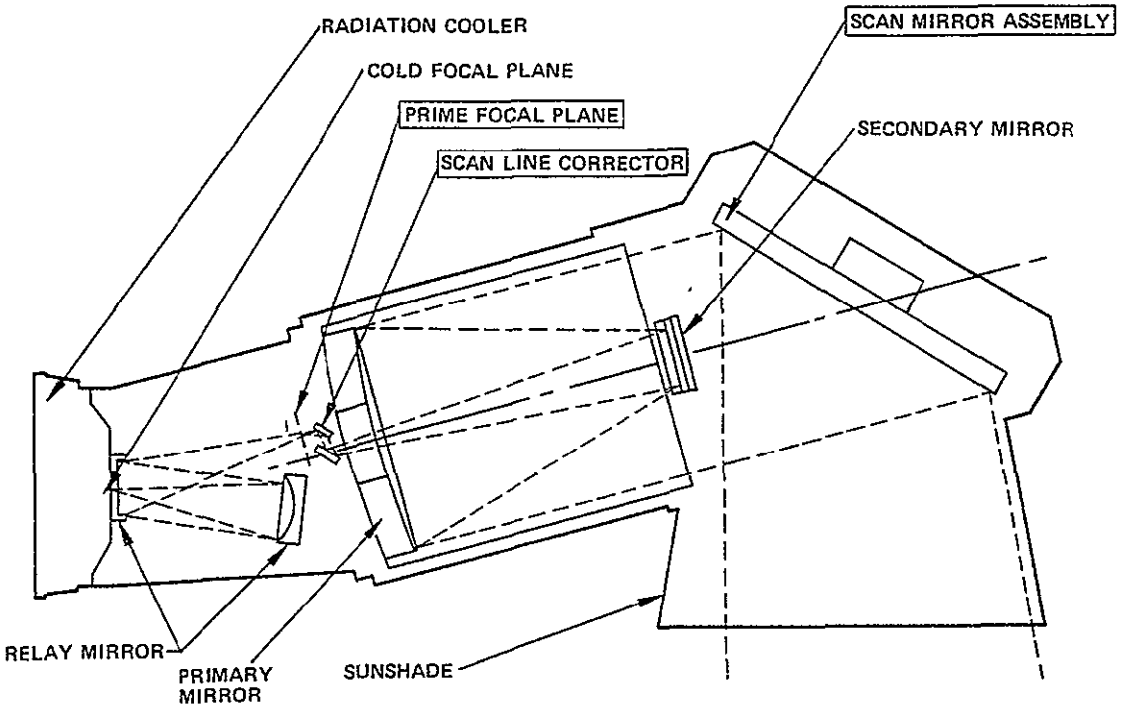

Figure 1-1. Hughes Thematic Mapper optical design concept

1.1 SCAN LINE CORRECTOR

The requirement for high scan efficiency in the TM makes it necessary to use both the forward and reverse scans of the scan mirror for taking data. The MSS sampled its detectors only during the forward scan, i.e., the east to west sweeps of the mapped strip and as such was able to achieve 45% scanning efficiency. Successive sweeps then are contiguous and collinear. Thematic Mapper is expected to achieve 80% or higher scan efficiency so as to minimize the peak data rates, hence the data handling difficulties. A large oscillating scan mirror, such as in MSS or larger, is limited by inertial forces to moving essentially at constant angular velocity, i.e., no fast flyback after scan. This then dictates the use of equal period data producing scans alternating in the forward and reverse directions and with minimal time spent during reversal. Scanning thus, the alternate sweeps are not collinear since the in track motion (north to south) of the spacecraft would cause the east-west and west-east sweeps to overlap each other at the edges of the swath. A solution to this is provided by a beam steering mirror which during scan mirror reversals, snaps forward along the spacecraft path by a distance equal to the width of a sweep and then slowly moves back to its original position during the scan period. In this way the crisscrossing scan mirror sweeps are corrected so that they become collinear as portrayed in Figure 2.1-1. The device which has been developed to perform this corrective motion is called a scan line corrector.

The SLC is composed of a two-mirror assembly which is rotated back and forth on a motor driven shaft. This assembly is mounted in the converging beam just ahead of the first focus of the telescope. Because the total along track deflection of the beam which the SLC performs is just the width of one scan of 16 scan lines, or approximately 16 instantaneous fields of view (IFOVs), while the scan mirror is sweeping over 6000 IFOVs across track, the control precision required of the SLC is several hundred times less than that required of the scan mirror assembly.

The performance of the SLC must be such that it causes less than 3 microradians of blurring in the image. This is accomplished by minimizing the flexibility of its structures, or its susceptibility to vibration,

and by maximizing the flatness of its mirrors. The mirror quality in both flatness and reflectivity was not a feasibility issue. Vibrational performance of this untried mechanism was at issue and during the early phases of testing structural stiffening was necessary. The final tests were conducted with a mechanism which demonstrated a good margin in structural stiffness.

The other performance requirements of the SLC related to geometric accuracy in the scanning process. Since the SLC moves the beam of focussed rays in a direction which is perpendicular to the scan lines, the precision of motion in the cross scan direction is critical. The design objective is to produce geometric errors of less than 0.05 IFOV. Motion errors in the other direction, i.e., along sweep, are not critical since errors greater than one part in 200 would be necessary to create 0.08 IFOV image error and simple analysis of the test data and structural analysis indicates that this magnitude of SLC cross scan error is not possible. The requirement in the SLC slong scan, or scanner cross sweep direction, is that the synchronization with the scan mirror, i.e., SLC repeatability, and the linearity of its angular rate be such that image errors of much less than 0.1 IFOV be maintained. These requirements and the measured values are tabulated in Table 1.1-1 as IFOV spatial error. The error budget, or performance requirement, is stated in one sigma values and the measured performance is given in worst case values. It is seen that very comfortable margins exist in the present design which itself has further room for refinement if necessary for instruments of higher precision than TM.

TABLE 1.1-1. SLC ROTATIONAL PERFORMANCE SUMMARY

Parameter	Geometric Requirement, 1σ IFOVs	Demonstrated in Test, Worst Case Peak, IFOVs
Deviation from linear scan		
Short term	0.035	0.033
Over 2 weeks	0.100	0.033
Repeatability		
Scan to scan	0.047	0.016
Over 30 seconds	0.100	0.022

The critical geometric requirements on the SLC precision were set so that errors would not significantly increase the total system geometric accuracy when combined with the scan mirror assembly errors. Short term one sigma errors were set at approximately one-third to one-half the values of like errors in the SMA.

Scan efficiency of 85% was designed into the device so that it would match the expected efficiency of the SMA. The test results showed that a linear portion of the SLC scan is available both before and after the active scan period to allow for timing errors.

The SLC was tested over a range of frequencies from 14 to 19 Hz to assure its compatibility with an operating range of 7 to 10 Hz for the SMA (SMA produces two scans per cycle).

1.2 SILICON PHOTODIODE ARRAY ASSEMBLY

The resolution and signal-to-noise performance being sought for the Thematic Mapper represents substantial improvements over the performance obtained in the MSS. When a reasonable increase is made in the size of the optics (aperture diameter of 23 cm for MSS to 41 cm for TM) a major increase in the number of detectors per spectral band is still required to meet the desired TM performance. MSS carried 6 photomultiplier tubes for each of its first three spectral bands. In TM, this number would have to increase 12 or more per band. Implementation of this would, in turn, impose a heavy technical and cost burden on TM. It was recognized by NASA, therefore, that an attempt should be made to simplify the detection scheme for TM by using photodiode arrays mounted directly on the focal plane. The development of low noise, high bandwidth silicon detector arrays and demonstration of their feasibility for meeting the TM requirements were set as the principal objectives of this breadboard development task.

The specific performance requirements for the arrays was established on the basis of results of earlier development of a single hybrid detector/preamplifier unit. The best performance achieved in this single hybrid detector channel became the design goal for the array. The most important performance parameters of the hybrid detector were the frequency response and wideband noise. The frequency response after treble boost

was flat over the required 50 kHz bandwidth except for a 1 dB peak at 5 kHz and produced 2.1 millivolts noise in the 10^9 ohm load resistor over this bandwidth.

Detector arrays were designed to specification and built by two vendors: E, G and G and United Detector Technology, Inc. (UDT). A layout assembly for the detector arrays and the source follower input stages of the preamplifiers was designed and built. On this assembly were mounted Texas Instruments (Great Briton affiliate) BF 805 J-FET chips and an array of 10^9 ohm load resistors. This hybrid array was then connected to the remainder of the preamplifier, located out of the focal plane, which included the treble boost circuits and presample filters. The detector arrays included 24 active elements and 2 inactive (opaque covered) elements for crosstalk measurements. The design goals and measured performance are listed in Table 1.2-1.

TABLE 1.2-1. SiPDA PERFORMANCE

Parameter	Design Goal	Demonstrated
Detector Array		
Dark Current, Amps	3.0×10^{-11} max	1.5×10^{-11}
Impedance, ohms	2.0×10^9 min	10^{10}
Capacitance, picofarads	1.0	1.0
Responsivity	Equal HP 4205	Less than spec
Stray Responsivity	<5% beyond active area	Excessive
Focal Plane Assembly		
Frequency Response (boosted)	Flat to 50 kHz	Flat to 50 kHz*
Wideband Noise, mV	2.1	2.3*

*Measurements taken with light source focussed inside active area. When array was flooded with light, response from stray capacitance produced uneven frequency response with substantial increase in noise at high frequency end of the band; wideband noise varied from 2.5 to 4.0 mV depending on geometry of circuits tested.

In summary, combined effects of excessive stray capacitance due to improper design of photomasks and stray capacitances from less than optimum circuit board layout produced undesirable noise performance. By extensive diagnostic testing, the sources of the problems have been identified. Improved designs and improved measurement methods learned from these results are being pursued further on Company funds. From improvements in board layout, photomask design and state of the art responsivity, the achievement of the desired signal-to-noise and crosstalk performance is highly probable.

1.3 SCAN MIRROR ASSEMBLY

The development of a large scale version of the SMA flown on the MSS was the initial objective of this contractual effort. The MSS employed an elliptical scan mirror 23 cm wide by 35 cm long. The TM mirror minimum size was expected to be 41 by 48 cm with a corresponding increase in inertial effects on both the instrument and the spacecraft. The goals of the development were to construct and demonstrate such a scan mirror which operates with sufficient precision to provide the geometric performance increase which the TM should provide over MSS, and also to do so without unacceptably distorting the scan mirror figure or other optical properties of the TM instrument or other instruments operating on the same spacecraft with TM.

Design, fabrication, and testing of the mirror itself was undertaken as the first order of business while development of the mechanical and electronic control assemblies was phased so as to be completed when the mirror was ready for integration and dynamic testing. This was expected to occur 10 months from go-ahead. Meanwhile, the checkout of the mechanical and electronic assemblies, as well as an improved MSS SMA test facility would be carried out by using a mass and inertial representation of the actual mirror. The cruciform "dummy" mirror and its fittings were also constructed to the same dimensional tolerances as the flight mirror. Its optical and mechanical properties were expected to differ slightly because of its lower stiffness to weight ratio compared with the flight mirror.

In the eleventh month of the program the simultaneous combination of a delay in receipt of the flight type mirror, the unexpected high values of jitter experienced with the dummy mirror and the availability of a newly proven, Company funded technique for torquing during turnaround with much less massive bumpers than the MSS type, presented an opportunity to reassess the design of the SMA. Incorporation of the new torquer and bumpers offered the possibility of demonstrating a near linear forward and reverse scan with very low jitter. NASA chose this course and the SMA development was extended six months to permit these performance improvements to be demonstrated.

1.3.1 Scan Mirror Development

A 23 cm MSS scan mirror scaled up to the 41 cm TM size would increase in inertia by somewhat greater than the increase in surface area (a factor of 4 in inertia versus 3.1 in area). The increase in spacecraft reaction to this oscillating inertia and the increase in vibration resulting from the turnaround impulses going into the support structure, suggested that some lighter weight construction should be considered. A brazed beryllium eggcrate mirror 51 cm in diameter had been constructed by Grant and Kamper of San Diego and had been polished successfully by Perkin Elmer. This approach would permit the size growth with only a 50% increase in inertia. This eggcrate construction would also be much stiffer than the MSS construction, thereby causing mirror surface vibrations to damp more quickly. For these reasons this design approach was selected over the earlier MSS and other analyzed mirror designs.

The progress in assembling and polishing the chosen eggcrate design was far less than ideal and required a substantial number of corrective operations before the mirror was ready for final testing. Although the resulting mirror quality was far from perfection at the completion of polishing as a result of the extensive rework during manufacturing operations, it has performed successfully both optically and mechanically. After exhaustive testing for almost a year, often under heavily overstressed conditions, it has shown no optical or structural degradation.

The principal measure of performance in the mirror is its resistance to optical degradation. This can be divided into throughput and image quality factors.

The main throughput factor is reflectivity. Demonstration of high reflectivity with low polarization differential had been demonstrated on the MSS and VISSR flight mirrors and was not a feasibility issue. A serviceable coating of aluminum with protective overcoating was applied to the polished beryllium both for protection and for improved throughput in the bench test setup. The aluminum can be removed if the customary silver coating would be needed for flight use or flight qualification.

Image quality factors were clearly at issue for this large oscillating mirror. These factors are identifiable as slope errors of various forms, each of which contribute to increased blur spot size, or MTF degradation, in the instrument. These slope errors can also be equated to errors created by an equivalent first mode bend in the mirror with an amplitude measured in wavelengths or micrometers. With MSS performance as a model, a goal was established for the TM mirror so as to limit this total amplitude from all sources to 0.91 micrometers. The conversion from the many irregular slope patterns which form on the mirror due to thermal and mechanical forces is inexact but does provide a reasonable estimate in common terms of how well the mirror performs. The low amplitude, high frequency pattern of the core on the surface is better treated as an MTF loss. The values in Table 1.3-1 are converted from the various test data found in Section 4.

When the manufacturing and polishing tolerances were established for the TM scan mirror, only the height variation and surface quality parameters were specified. This is typically adequate for mirrors with more massive surface thickness. A value of 0.5 fringe (0.14 micrometer) was imposed on the polisher. As can be seen in Table 1.2-1, it would have been impractical to hold to this value since, with the lightweight characteristics of the TM mirror, other errors have predominated. To achieve the most flexibility and economy, a better means would be to measure the surface in terms of system MTF degradation so that effort is applied on each feature of performance in proportion to its effect on total system performance. This is

TABLE 1.3-1. SCAN MIRROR SURFACE ERRORS
(Heights of Equivalent First Mode Shape in Micrometers)

Temperature	Polishing Temp	±2.8°C	±5.5°C	±11°C
Basic figure after polishing	0.226	0.262	0.294	0.307
Dynamics (worst case during active scan)	0.127	0.127	0.127	0.127
Total	0.353	0.389	0.421	0.434
Maximum allowable	0.910	0.910	0.910	0.910
(System MTF degradation due primarily to core print through on sample mirror, %)				
Core print through pattern	0	1.3	3.4	6.2

especially important if the demonstrated advantages of this new lightweight mirror technology are to be applied properly in mirrors of much larger size.

1.3.2 Scan Mirror Assembly Performance

In addition to the mirror contributions to image blur, the scanning performance of the SMA must be such as to minimize significant geometric errors such as loss of data due to overlap or underlap of scan lines; nonlinearities which produce mapping errors and misregistration between spectral bands; and repeatability errors which distort the image. Other precision features of less critical significance are scan efficiency and operational flexibility.

1.3.2.1 Operational Flexibility

The demonstrated SMA design is readily adjustable to permit scan frequencies between 5 and 15 Hz with probably a factor 2 greater range above and below these values with minor redesign. Scan amplitudes are also adjustable from small fractions of the current 185 km swath to values up to 3 times greater.

1.3.2.2 Scan Efficiency

An original objective of the program was to increase the scan efficiency of the MSS SMA design from 45% to 80%. The increase to 80% with the original breadboard design was marginal with the MSS torquing format in which the energy restoration was accomplished by torquing throughout most of the scan period. In this MSS control mode and with the lossy MSS type bumpers, the mirror is accelerated on the rescan to a velocity well above the average, thereby limiting scan efficiency. With the conversion to low loss bumpers and torque during turnaround, forward and reverse scans are permitted to run at nearly constant velocity and the efficiency is limited only by the turnaround duration. Since turnaround time is an adjustable parameter with leaf spring bumpers, SMA scanning efficiency up to 90% is possible with the current mission requirement for a 7 Hz scan frequency. The breadboard testing at 7 Hz was done at an efficiency of 85% to minimize structural resonance unique to the bench setup. This limitation is not expected to prevail with the flight support structure.

1.3.2.3 Cross Axis Jitter

Cross axis motion of the mirror which does not repeat on successive forward and reverse scans causes overlap or underlap in the imagery. This apparent jitter is typically caused by unequal bouncing of the mirror on each of its supporting flex pivots. A portion of the measured jitter is also created by test set electrical and optical noise which the detector in the laboratory test setup interprets as mirror angular motion.

Prior to the changeover in the torquer and bumper designs an extensive period of diagnostic testing was accomplished in an attempt to reduce the vibration-induced jitter. Minimum values obtained during this phase of the program were approximately 8 microradians in mirror coordinates. With the change to low mass bumpers, which provide a significant increase in the coefficient of restitution, much less energy was converted to vibration. The jitter was almost immediately reduced to within the measurement accuracy of the test setup which is on the order of 1 microradian. The bulk of the subsequent effort over the final five months of the program was devoted to reducing the along scan repeatability errors to a minimum.

1.3.2.4 Along Scan Repeatability

An objective to reduce repeatability errors to a point which would obviate the requirement for corrective ground processing was introduced along with the redesign for torque while turnaround. This requires that each scan line produce an equal number of data samples and, further, that equal numbered samples on adjacent lines be aligned within 0.1 IFOV, or 4.25 microradians. With IFOV dwell times on the order of 10 microseconds, this meant scan period repeatability errors should be held to 1 microsecond.

Absolute achievement of this value has not been demonstrated although it can be shown that when measurement errors are removed from the data, a 1 microsecond RMS error in scan to rescan repeatability has been achieved. This error results from the integration of the mirror velocity error at start of scan and, therefore, reaches this value of time or position error only at the end of scan. The average error across the swath is half this value.

The mechanical noise, which is the principal contributor to this error, has been measured independently of the control system noise and has been found to be essentially random with gaussian distribution. Its RMS value is less than 0.7 microsecond, or less than 3 microradians in scan angle coordinates (0.07 IFOV).

The current bumper design may be amenable to improvements which will reduce the mechanical noise. The control electronics are also amenable to more precise operation by conversion from analog to digital circuits. By these approaches, which are being pursued on Company funds, the random and some systematic noise sources hopefully will be reduced to peak values which are well within the 0.1 IFOV requirement.

The tendency of the scan period to drift over periods of minutes to weeks is suppressed by the crystal control reference, the phase lock loop and the velocity damping controls. Margins in these controls will maintain constant line length as mechanical wear and electrical changes occur over periods of months to years.

1.3.2.5 Scan Linearity

The scan mirror, during the active portion of the scanning cycle, is inertially free of all forces except the weak flex pivot torque. This torque

modifies an otherwise perfectly linear and repeatable scan motion with a slight sinusoidal velocity variation. This has been calculated and measured to be +1.3 and -2.0% from linear. The variation of the MSS mirror was somewhat larger and means for removing the error were provided in the ground processor. The TM sampling precision and band-to-band registration requirements are such that a means for removing the nonlinearity at the source would be desirable. Such means have been developed on an earlier IR&D program. The technique is simple, reliable, and uses no power or mechanical devices. A torque equal and opposite to the flex pivot torque is applied to the mirror by the interaction of permanent magnets mounted on both the mirror and the support structure. Using this technique residual nonlinearity in the mirror velocity is such as to produce less than 10 microradians mapping error. This is a factor of 50 less than the uncompensated nonlinearity measured on the contract.

1.3.2.6 Summary of SMA Performance

Table 1.3-2 summarizes the significant design objectives and measured performance values of the scan mechanism. These are oriented essentially to geometric accuracy since the optical characteristics are given in Table 1.3-1.

TABLE 1.3-2. SMA PERFORMANCE SUMMARY

Parameter	Design Goal	Demonstrated
Along Scan Repeatability, μrad, rms	4.2	4.1
Cross Scan Jitter, μrad, rms	3.0	2.8
Scan Linearity, μrad	±21	±10
Scan Frequency, Hz	7 to 10	5 to 11
Scan Efficiency, %	80	85

2.0 SCAN LINE CORRECTOR

2.1 TASK DESCRIPTION

2.1.1 Background

The data rate of the Thematic Mapper can be minimized by maximizing the scan efficiency of the sensor. The MSS used an oscillating scan mirror which takes data during the forward portion of the cycle only and has a scanning efficiency of approximately 45%. By taking data during both the forward and reverse scans the scanning efficiency of the Thematic Mapper can be increased to approximately 85%. This will simplify the design of the multiplexer and telemetry channels and will reduce the bandwidth requirements of sensor data channels.

However, when both the forward and reverse scans of an oscillating scan mirror are used to take data, traces contiguous at the nadir will underlap and overlap at mirror reversal due to spacecraft motion along the ground track. This effect, grossly exaggerated, is shown in Figure 2.1-1a.

2.1.2 SLC Concept

The underlap and overlap can be removed by the addition of another mirror system (a Scan Line Corrector) which produces the correcting motion shown in Figure 2.1-1b resulting in the corrected scan pattern shown in Figure 2.1-1c. The concept of adding a Scan Line Corrector (SLC) to produce an increase in scanning efficiency without underlap or overlap was introduced during the point design study phase of the Thematic Mapper program.

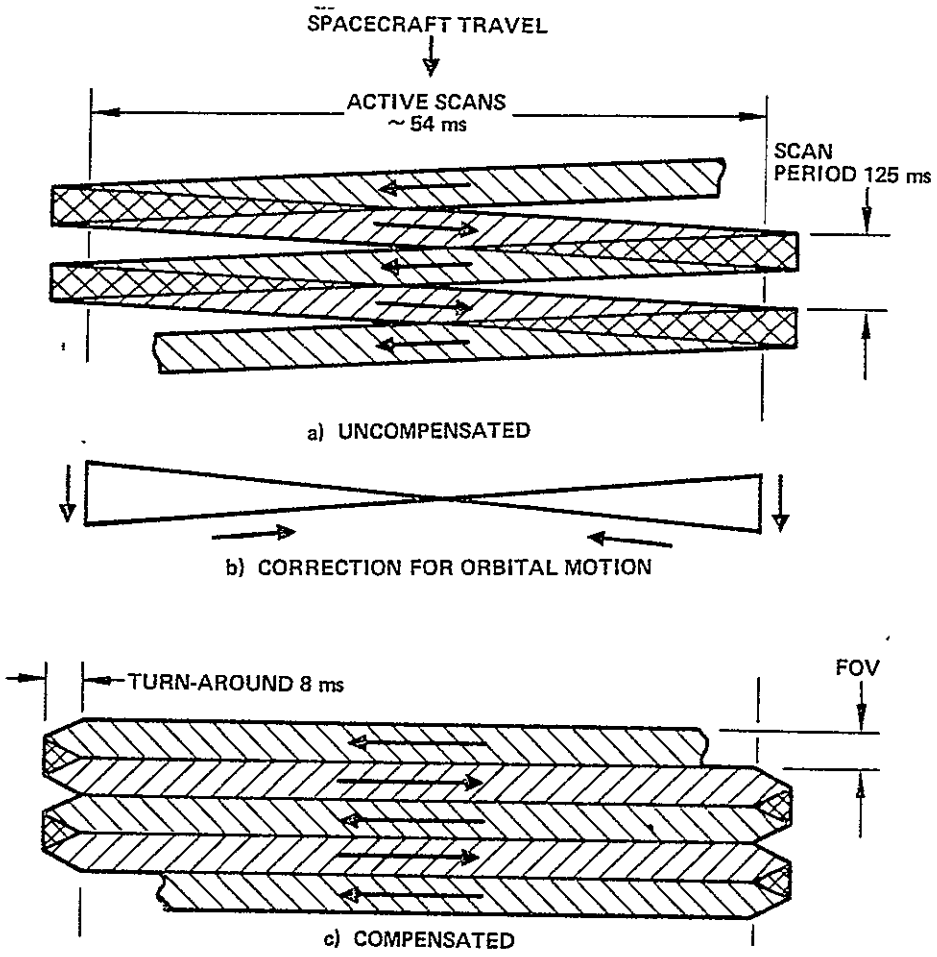

Figure 2.1-1. Scanner ground patterns

The SLC generates a sawtooth motion during the active portions of the scan mirror cycle (with a fast retrace during scan mirror turnarounds) to compensate for spacecraft motion along the ground track and produce contiguous, bidirectional scans. The SLC angle/time relationship is shown in Figure 2.1-2. The values of θ_{SLC} are generally less than 1 milliradian.

2.1.3 Development Task

Due to the untried SLC concept and the rather fast linear motion required, a developmental program was instituted. The purpose of this program was to demonstrate the feasibility of the SLC concept through analysis, design, fabrication and test of an engineering model SLC.

The SLC design parameters for this development task were chosen to cover an amplitude range for 16 to 24 detectors and a frequency range for scan mirror frequencies from 7 to 10 Hz. To show that the design frequency chosen was not critical, it was decided that it would be best to test the SLC over a range of frequencies which would bracket those anticipated for the Thematic Mapper applications. The task began in April 1975 and was completed in January 1976. Performance testing was completed in December 1975.

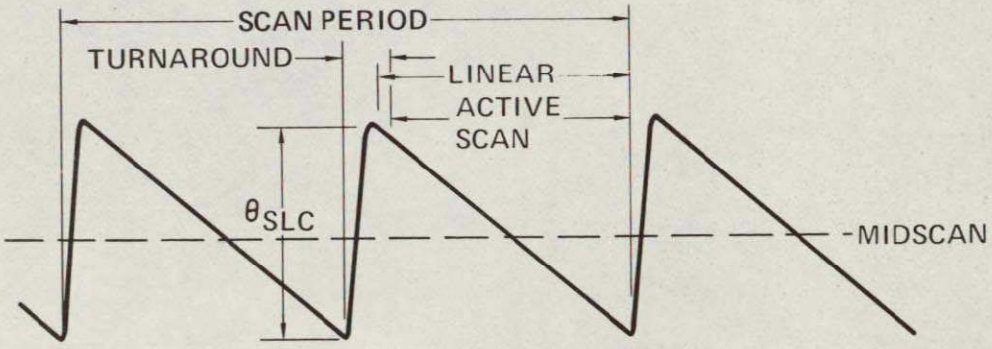

Figure 2.1-2. SLC motion.

2.2 RESULTS SUMMARY

An engineering model of the SLC with control electronics was fabricated and extensively tested. The tests results exceeded the design goals and indicate that an SLC can be fabricated which will meet its requirements with substantial margin. A photograph of the SLC is shown in Figure 2.2-1. Due to the high cost and long lead time required for the procurement of beryllium mirrors and mirror holders, the model SLC was

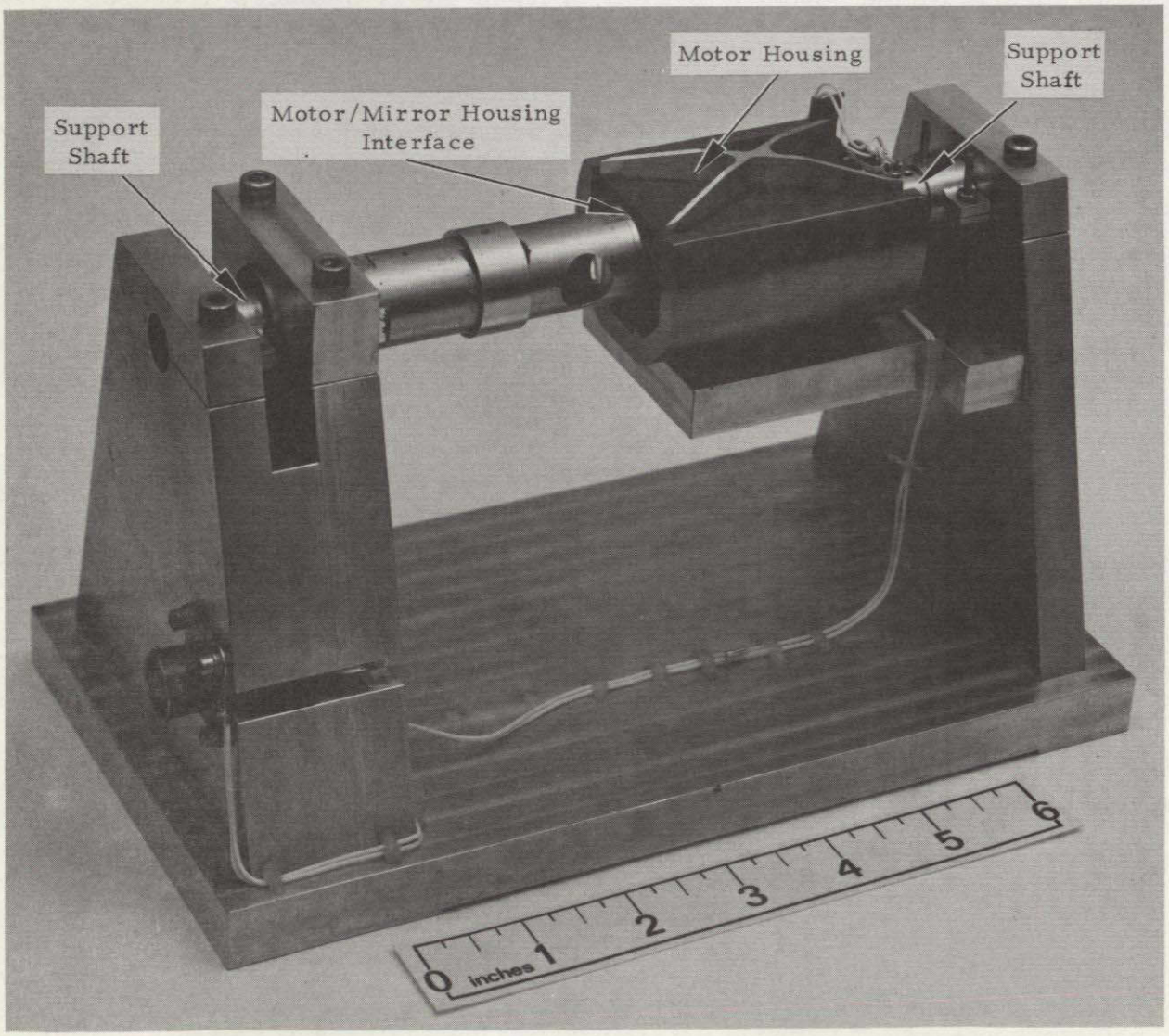

Figure 2.2-1. Breadboard model SLC (arrows indicate areas which required stiffening).

built using undersized mirrors mounted in a cylindrical aluminum housing. The housing was designed to simulate the inertia of the beryllium flight components. The mechanism consisted of an Aeroflex Model TMC20-1P moving coil dc torque motor; a cylindrical, mass simulating, aluminum mirror housing; and an Aeroflex Model TG10Y-59P tachometer, all supported by a pair of Bendix flex pivots. The scan mechanism inertia was measured and found to be 117 gm cm^2 as compared to a calculated flight design value of 91.7 gm cm^2. The torque constant of the flex pivots was measured and found to be 4.6×10^7 dyne cm/rad as compared to a nominal value of 5.0×10^7 dyne cm/rad. The natural frequency of the breadboard scan mechanism was found to be 100 Hz.

When the SLC was first integrated with the control electronics, four locations of torsional weakness were discovered in the mechanism which caused underdamped oscillations to be produced at scan turnaround. The areas of weakness are indicated by the arrows in Figure 2.2-1. One by one these areas were strengthened until acceptable performance of the SLC was obtained. The motor coil housing was stiffened by the addition of the cruciform rib, which can be seen in the photograph, but will be completely redesigned for the flight program to maximize stiffness. A sketch showing a possible configuration for the motor coil housing is shown in Figure 2.2-2.

After the integration of the SLC mechanism and control electronics was completed and the operation appeared to be as desired, the SLC was tested to determine scan deviation (from linear angular rate), repeatability, and jitter at frequencies of 13.0, 14.2, and 19.0 Hz. An SLC frequency of 14.2 Hz corresponds to the present baseline Thematic Mapper scan mirror frequency of 7.1 Hz.

An oscilloscope photograph of the SLC motion is shown in Figure 2.2-3. The photograph was made by projecting a HeNe laser beam through the SLC onto a United Detector Technology position sensitive detector located where the focal plane of the Thematic Mapper would be. The photograph was taken with the SLC operating at 14.2 Hz. The oscilloscope time base was adjusted such that two cycles of the SLC motion occupied 10 cm of the display. The photograph of Figure 2.2-4 shows one cycle of the SLC motion along with the

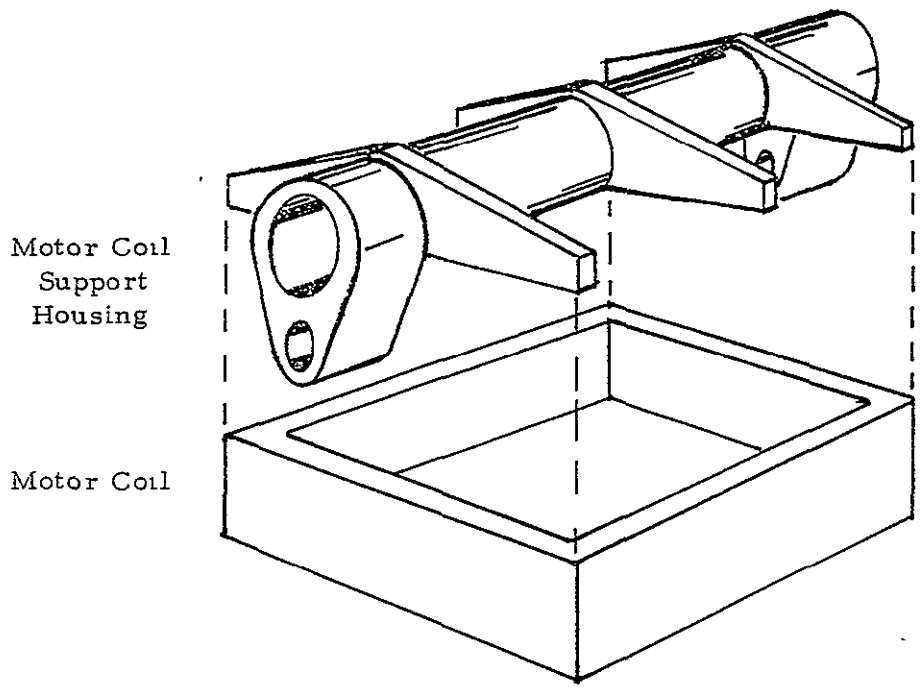

Figure 2.2-2. Improved motor coil housing design.

output of the tachometer. The vertical calibration of the tachometer trace is 50 mv/cm with zero volts corresponding to the dashed graticule line near the top of the photograph. The tachometer sensitivity is 60 mv/rad/sec which at 564 mrad/sec (the nominal SLC rate) corresponds to 33.84 mv. The variations in the tachometer output are caused primarily by an underdamped flexing of the motor coil housing during retrace and should be eliminated to provide an even greater margin of performance than demonstrated by a simple improvement in the motor housing design. The peak displacements caused by these rate variations are quite small because of the relatively high frequency at which they occur.

The scan rate, linearity, repeatability, and jitter results are tabulated in Table 2.2-1 along with the applicable Thematic Mapper requirements. The scan deviation indicates how the SLC performance deviates from a perfect nominal scan.

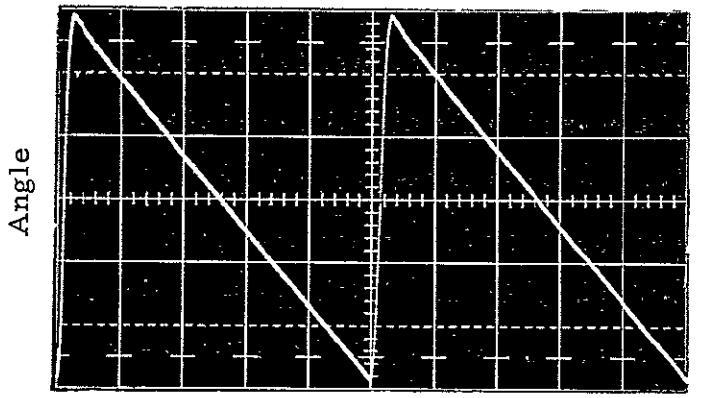

Figure 2.2-3. SLC motion

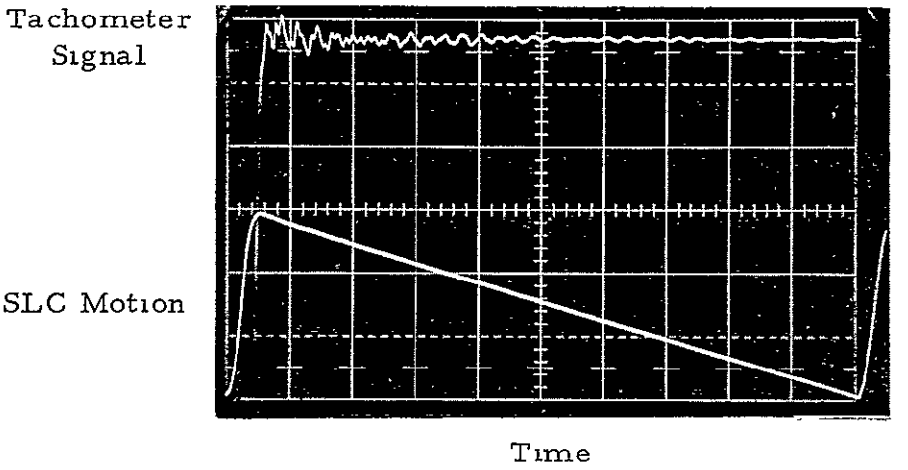

Figure 2.2-4. SLC motion and tachometer signal

The long term rate and position stability were monitored for a period of 14 days. The scan rate showed a peak-to-peak variation of 0.71% during that period which corresponds to a scan deviation of 4.4 μrad. During the same period the position of the SLC was monitored and the peak-to-peak variation of the image in the focal plane was found to be 0.0018 inch. This corresponds to a boresight error of only 18.7 μrad, which is negligible.

TABLE 2.2-1. RESULTS SUMMARY

Parameter	Values, μrad		
	At 13.0 Hz	At 19.0 Hz	Requirement
Scan Deviation			
Worst Case,	0.99	1.40	
1σ	0.45	0.67	1.5 (1σ)
Repeatability			
Scan to Scan			
Worst Case,	0.66	0.47	
1σ	0.15	0.12	2.0 (1σ)
Over 30 Seconds			
Worst Case	0.94	0.75	6.0 (3σ)

The cross-axis motion of the SLC was not measured during this program due to both the difficulty in making the measurement and the relative insensitivity of the optical system to this type of error. For example, to produce a cross-axis jitter in the image plane of 2 μrad would require a differential center shift between the two flex pivots of approximately 2.5 mm. The maximum specified center shift for the flex pivots at a rotation of 17.5 mrad is 0.003% of the diameter which in this case is 1.25 cm. This would produce a maximum center shift in each pivot of approximately 38 μm and a differential center shift of at least an order of magnitude less. The actual SLC amplitude is less than 1 mrad.

The results of this development program indicate that the SLC concept is sound and that the required motion can be produced with more than sufficient accuracy for the Thematic Mapper application. Prior to building an SLC for a flight program the mechanical design must be reviewed with particular attention given to the stiffness of the components, especially the motor coil housing.

2.3 BASELINE SLC DESCRIPTION

2.3.1 Principles of Operation

2.3.1.1 Fundamentals of SLC Mechanization

The exclusive purpose of the Scan Line Corrector (SLC) is to correct the scan pattern of a bidirectional object space scan system to compensate for spacecraft motion along the ground track during the active portion of the scan. This function is provided by the motion of a pair of plane parallel mirrors located slightly ahead of the telescope focal plane (see Figure 2.3-1) which rotate about a common axis in such a manner as to keep the sensor's detectors looking perpendicular to the ground track during each active scan. The required motion of the SLC is a sawtooth motion (see Figure 2.1-2) with a frequency of twice the scan mirror frequency.

A drawing showing a possible flight model configuration of the SLC is shown in Figure 2.3-2. The drive for the SLC is very similar to a galvanometer movement. A torque generating device, a moving-coil, brushless, dc torque motor, is suspended on a shaft by flexure pivots. On the same shaft is a tachometer generator to supply rate feedback to the control system and a beryllium housing which holds a pair of plane beryllium mirrors which deflect the optical rays from the telescope in such a manner as to produce an image in the focal plane which is corrected for spacecraft motion.

A block diagram of the SLC and control electronics is shown in Figure 2.3-3. A triggered function generator produces a waveform that defines the shape of the ramp to be followed by the mirror mechanism. The generator waveform is summed with the tachometer feedback signal and an offset control signal, and together drive a power amplifier which drives the torque motor.

The SLC is synchronized to the main scan mirror by the "end of scan" pulses which are generated by the scan monitor. The "end of scan" pulses are used to reset the function generator which in turn causes the SLC mirror mechanism to retrace. The "end of scan" pulses also initiate a precision delay function after which the next ramp function begins. The retrace time

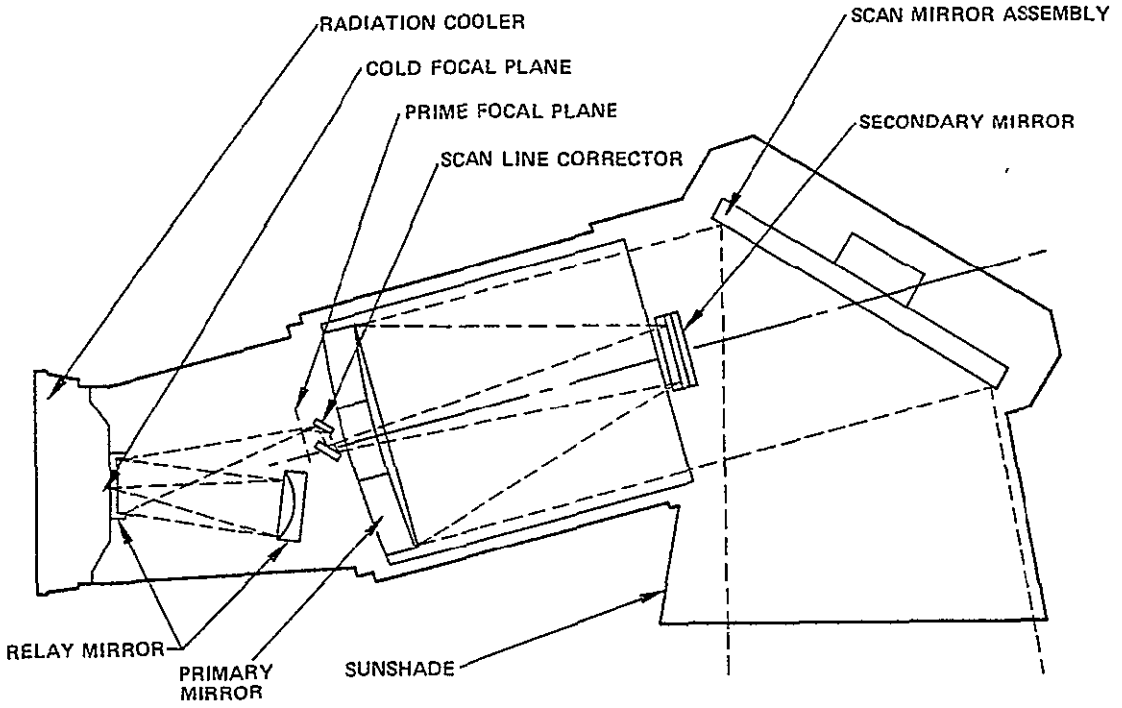

Figure 2.3-1. Thematic Mapper optical system

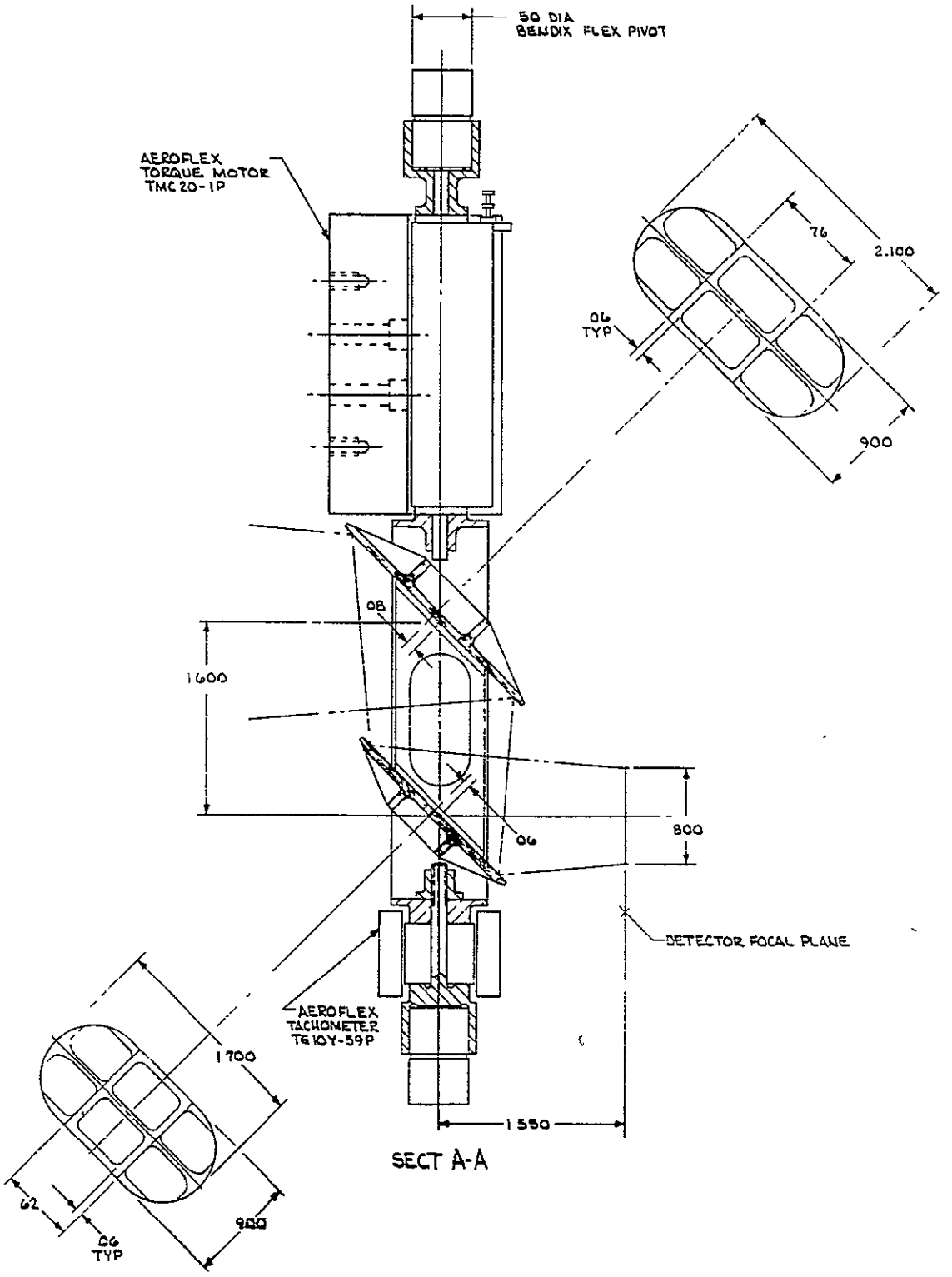

Figure 2.3-2. Possible SLC flight model

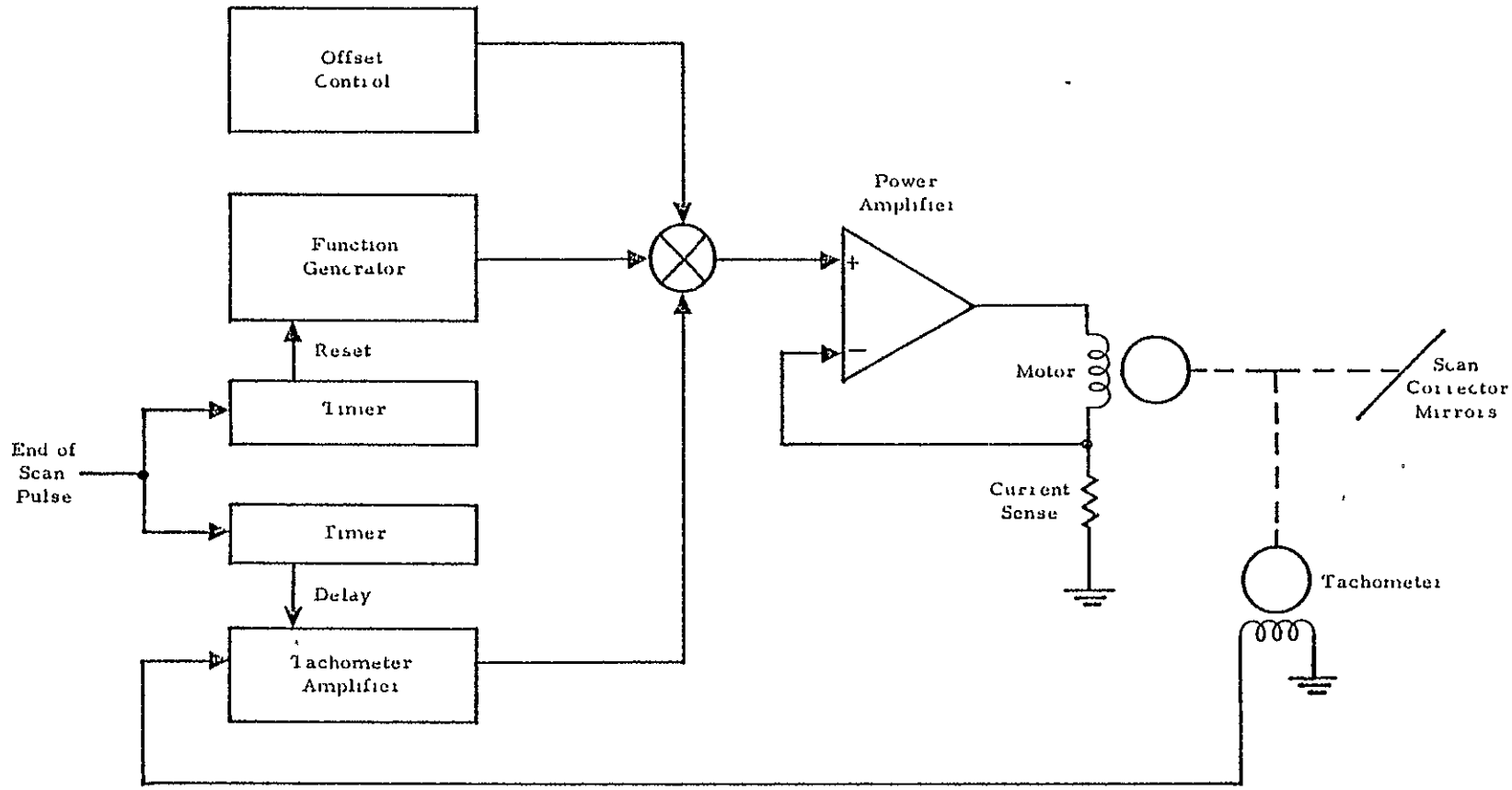

Figure 2.3-3. SLC functional block diagram

is determined primarily by the natural frequency of the SLC mechanism and can be minimized by keeping the inertia low and the torque constant of the flexure pivots as high as possible consistent with the torque capabilities of the motor. After turnaround, the delay function permits adequate shaft jitter settling time before start of scan occurs.

2.3.2 SLC Design Parameters

The relationship of the SLC motion to the orbital parameters and other instrument parameters is as follows: By knowing the orbital altitude, a parameter v/h can be calculated. The v/h has the dimensions of radians/second and is the apparent angular ground rate. This is the rate that the SLC is intended to compensate; i.e., the SLC must produce a rate which in object space is equal to v/h. In an instrument using bidirectional scanning, the frequency of oscillation of the scan mirror is connected to v/h through the relationship

$$\frac{v}{h} = f_s \, 2n\alpha \tag{1}$$

where

f_s = the scan frequency

n = the number of detectors per band along track

α = the instantaneous field of view

The scan frequency (f_s) is determined by selecting the number of detectors (of the specified field of view) required to meet the signal-to-noise requirements of the instrument and calculating the frequency from equation (1). The frequency of the SLC motion is equal to 2 f_s as the SLC must correct for the ground motion during both the forward and reverse portions of the scan mirror cycle. The amplitude of the SLC motion is determined from the following relationship

$$\beta = k_s \frac{T}{2}\left(\frac{v}{h}\right) \tag{2}$$

where

β = the SLC amplitude in radians in object space

k_s = the scanning efficiency

T = the scan mirror period ($1/f_s$)

It can be seen from equation (2) that the SLC amplitude is directly proportional to the scanning efficiency, i.e., the SLC must correct for the ground rate for only that portion of the scan cycle during which data are being taken. From equations (1) and (2), it can be seen that the amplitude of the SLC motion is related to $n\alpha$ in the following manner

$$\beta = k_s \, n\alpha$$

Since the SLC does not view object space directly but looks through the instrument telescope, the actual SLC rate and amplitude are a function of the telescope focal length and the SLC mirror separation, and can be found by using the following equations:

$$\dot{\theta}_{SLC} = \frac{v}{h} \cdot \frac{fl}{x}$$

$$\theta_{SLC} = k_s \, n\alpha \, \frac{fl}{x}$$

where

$\dot{\theta}_{SLC}$ = the actual SLC rotational rate

θ_{SLC} = the actual SLC rotational amplitude

fl = the telescope focal length

x = the SLC mirror separation

A list of parameters which were used to design the developmental model of the SLC is included in Table 2.3-1, and a sketch showing the mirror spacing and focal plane location is shown in Figure 2.3-2. A range of scan frequencies was chosen which would bracket the anticipated Thematic Mapper frequency. The SLC was designed with the ability to operate over this range

TABLE 2.3-1. SLC DESIGN PARAMETERS

Parameter	Symbol	Design Value
Telescope Aperture	D	41 cm
Effective Focal Length	EFL	244 cm
Relative Aperture	f/No.	6.0
Orbital Altitude	h	717 km
Apparent Angular Ground Rate	v/h	9.4 mr/sec
SLC Scan Rate	$\dot{\theta}_{SLC}$	564 mr/sec
Image Displacement Rate	v_d	2.29 cm/sec
Scan Efficiency (SMA)	k_s	0.85
Settling Time Before Scan	k_{sy}	0.06 scan
Scan Frequency (SMA)	f_s	6.5 to 9.5 Hz
SLC Frequency	$2 f_s$	13.0 to 19.0 Hz
SLC Duty Cycle	$k_s + k_{sy}$	≥0.90
Time for Active Scan	t_s	
19 Hz		≥47.4 msec
13 Hz		≥69.2 msec
SLC Rotational Amplitude	$\theta_{SLC} = t_s \dot{\theta}_{SLC}$	
19 Hz		≥26.7 mrad
13 Hz		≥39.0 mrad
Amplitude of Image Displacement	$d = t_s v_d$	
19 Hz		109 mm
13 Hz		157 mm

of frequencies. The settling time was established as a means of relating the SLC scan duration to the SMA scan. This ensures that the SLC is moving at the desired rate prior to the start of the SMA active scan.

2.3.3 Electronic Design

A breadboard scan driver was constructed which is similar to a computer model described in Section 2.4.3, Electronic Analysis. The system used a tachometer feedback for rate control of the mirror. A linear

ramp was generated by a capacitor integrator, and reset at the end of scan. The integrator initial condition determined mirror position after retrace. Tachometer feedback was separated into positive and negative components, amplified, then summed with the linear ramp. This signal was connected to a current mode power amplifier which drove the motor.

Initial testing of this system showed that the mechanical components had resonances which were not in phase with the tachometer signal, so that they were not controlled. The mechanical components were stiffened to eliminate the resonances and tests were made of scan position versus time. The testing showed that the system was working well, but had a scan-to-scan jitter. This jitter can be seen as variations in the SLC amplitude as shown in the photograph of Figure 2.3-4. The photograph was taken by reflecting a laser beam off of an external mirror mounted on the SLC onto a paper target and panning a camera across the target with its shutter open. The conical motion was generated by the camera. The source of this jitter was traced to the integrator which generated the linear ramp signal. A variation in the dc level of the integrator was caused by insertion of the initial condition at the integrator input.

The initial condition, or mirror position after retrace, was changed to a constant level at the amplifier which sums the ramp and tachometer feedback signals. This eliminated the jitter. A photograph showing the jitter-free SLC amplitude is shown in Figure 2.3-5. The difference between the start of scan time and a constant is on the order of a microsecond, or 0.0115 μrad in object space.

Further testing showed that the system was within specification, but that greater margin was desired. A delay was introduced into the tachometer feedback, so that no feedback was applied during a variable period starting from the end of scan signal. By adjusting the delay period and tachometer gain, it is possible to obtain a near ideal response. Figure 2.3-6 shows the breadboard scan drive in its present configuration. In a form suitable for flight use, the electronics would require an average power of approximately 4.5 watts.

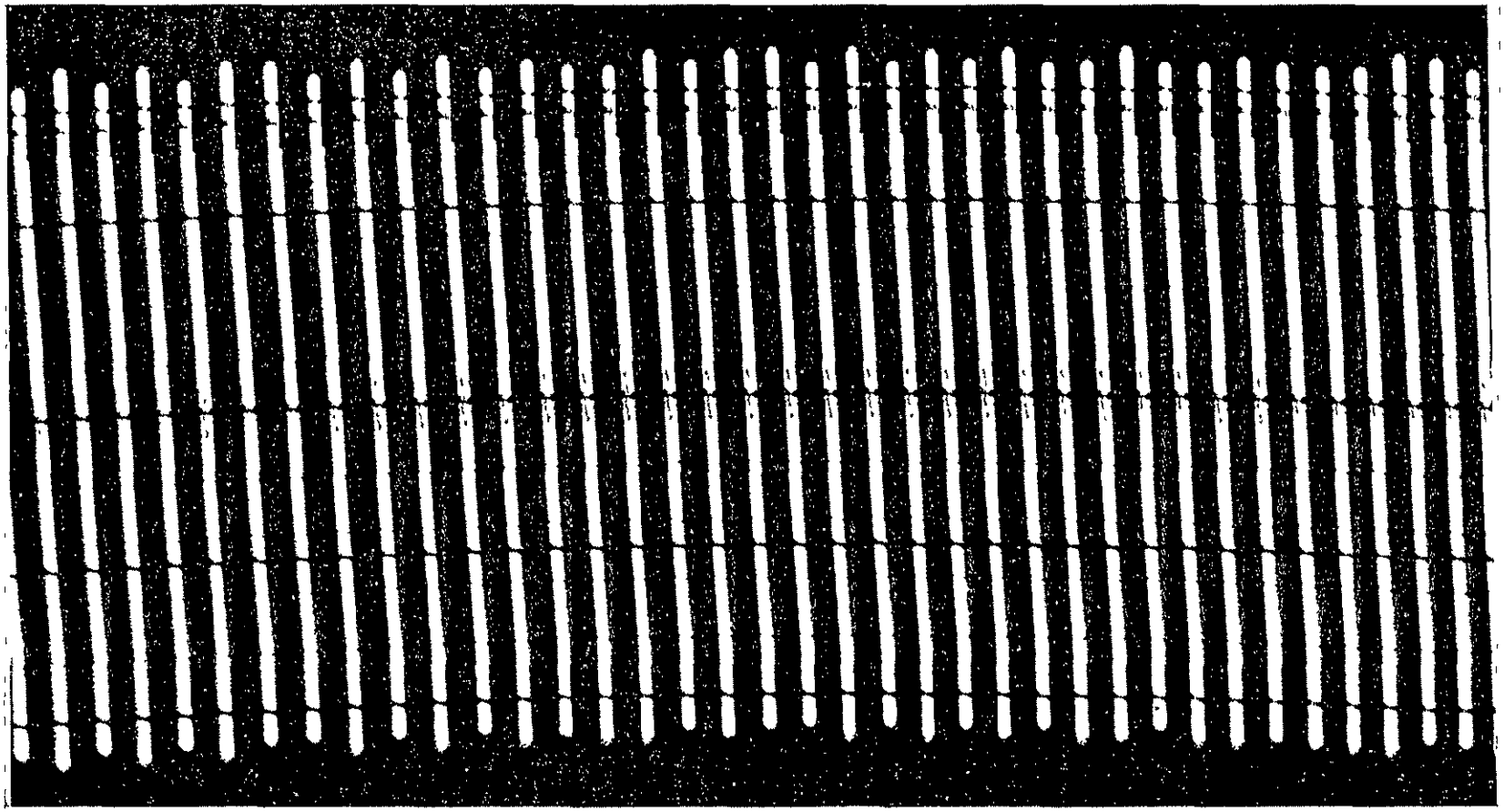

Figure 2.3-4. SLC scan jitter

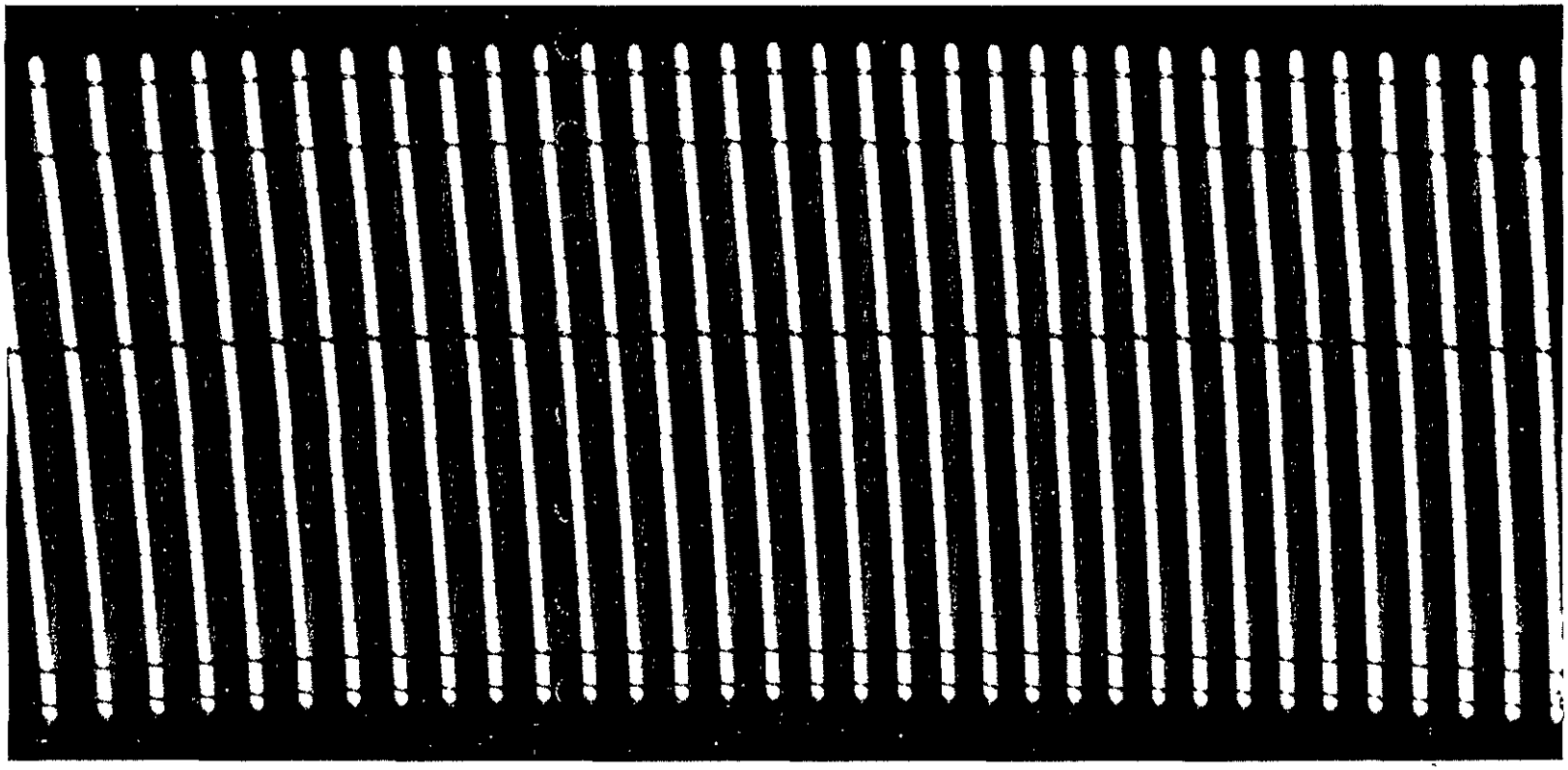

Figure 2.3-5. Jitter-free SLC motion

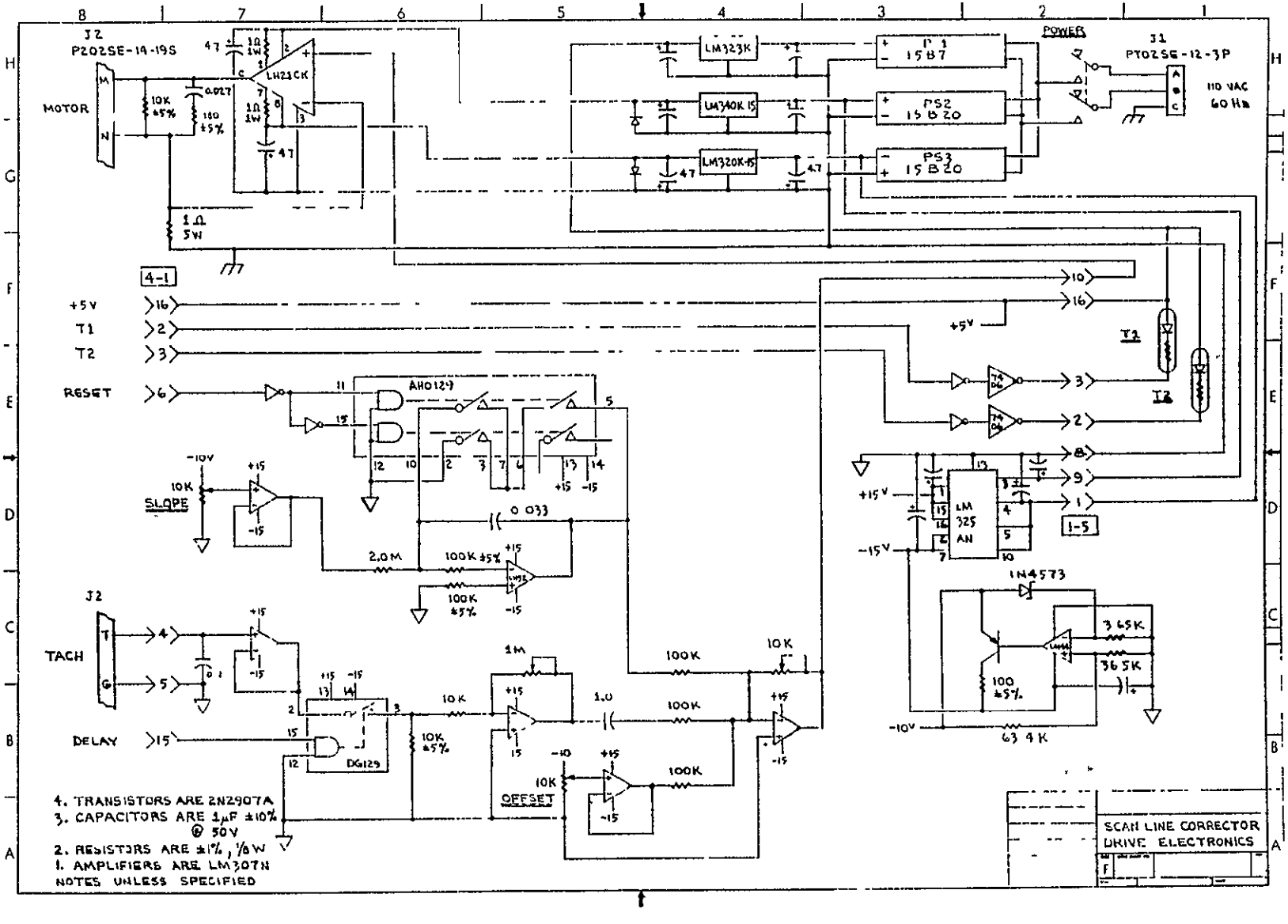

Figure 2.3-6. Scan line corrector breadboard drive electronics

2.4 SCAN LINE CORRECTOR ANALYSIS

2.4.1 Structural Analysis

2.4.1.1 Summary

The design for the SLC flight mirror assembly was analyzed to determine its structural integrity during retrace inertial loading. The analysis procedure was basically to: 1) determine the mass properties of the yoke, mirrors, and mirror assembly, 2) formulate a three-dimensional finite element model of the complete SLC, 3) find the lowest several vibration mode shapes and frequencies of the structure, 4) determine the maximum angular acceleration of the structure during retrace, 5) calculate the stresses and displacements in the structure assuming the maximum angular acceleration to be a steady-state acceleration.

The results of the analysis show that the maximum stress generated in the structure during retrace is less than 140 psi. Maximum rotation of the lower mirror relative to the upper mirror is 2 μrad about the rotation axis. The fundamental frequency of vibration is 6200 Hz in a torsional mode about the rotation axis.

The combination of low stress, small displacements, and high fundamental frequency (relative to its scan frequency) indicates the scan line corrector is a structurally sound design.

2.4.1.2 Analysis

The objectives of this analysis were basically twofold: 1) the capability of the scan line corrector (SLC) to withstand operational inertial loads needed to be determined; 2) the capability of the SLC to maintain mirror alignment during operation needed to be determined. The analysis procedure used to meet these objectives was basically to do the following.

1. Calculate the mass properties of the mirrors, yoke, and assembled structure.
2. Using these mass properties, make rough hand calculations of the torsional natural frequency.
3. Formulate a three-dimensional mathematical (finite element) model of the SLC.

4. Determine the lowest several vibration node shapes and corresponding frequencies of the model.
5. Find the maximum instantaneous acceleration of the SLC during retrace.
6. Calculate the displacements and stresses in the SLC model assuming the maximum angular acceleration to be steady state.
7. Evaluate the stress level relative to material strength, and evaluate the displacements in terms of mirror alignment and distortion.
8. Select and pair flex pivot supports from Bendix catalog.

The details of this procedure follow.

2.4.1.3 Mass Properties

The detailed mass properties calculations of the mirrors, yoke, and assembled SLC are shown in Appendix A. The mass moment of inertia calculations are summarized as follows:

	$lb\text{-}in.\text{-}sec^2 \times 10^{-6}$
Upper Mirror	10.3
Lower Mirror	6.9
Channel Selection	21.6
Mirror Support Plates	0.6
Bottom Flange	2.2
Top Flange	1.1
Flex Pivot Adapter, Nut	0.9
Flex Pivot Adapter	0.7
Total SLC	44.3
Tachometer	2.5
Motor	34.4
Total	81.2

2.4.1.4 Hand Calculations

Rough hand calculations were made of the torsional fundamental frequency. Using first conservatively flexible, then conservatively stiff estimates of the torsional stiffness, frequency values of 1700 and 7000 Hz

were obtained. A best estimate was made of about 5000 Hz. These calculations were made as a rough check on the finite element results, and did indeed bracket the final solution.

2.4.1.5 Mathematical Model of SLC

The mathematical approach used for the analysis was the finite element method. The computer program STARDYNE was utilized.

The finite element model of the SLC is shown in Figures 2.4-1 and 2.4-2. The model assumes linear elasticity and small displacements. The yoke is beryllium while the mirrors are nickel (0.005 inch thick Kanigen) plated beryllium. To account for density and modulus differences between the nickel and beryllium, cross-sectional area-weighted material properties were used for the mirrors. The material properties used for the yoke and mirrors were:

	Modulus (psi)	Poisson Ratio	Density ($lb/in.^3$)
Yoke (Be)	42.0E6	0.025	0.0670
Mirrors (Be + Ni)	40.4E6	0.062	0.0108

The yoke channel sections were modeled by assembling quadrilateral thin plate elements (for the web) and beam elements (for the flanges). The mirrors were modeled as an assembly of triangular and quadrilateral thin plate elements with beams between the rib stiffeners.

The top of the yoke was considered a fixed boundary since the control system prescribed the rotation of the top. Also, the axial stiffness of the flex pivots (SLC supports) is high relative to inertial loading in that direction. The bottom of the yoke was modeled with very stiff beams connecting the yoke channels to a center node (see Figure 2.4-2). Springs connected to this center node approximated the radial stiffness of the bottom flex pivot. Additional springs connected to the nodes at the bottom of the yoke channels represented the axial stiffness of the bottom flex pivot.

A listing of the STARDYNE input for the model is given in Table 2.4-1.

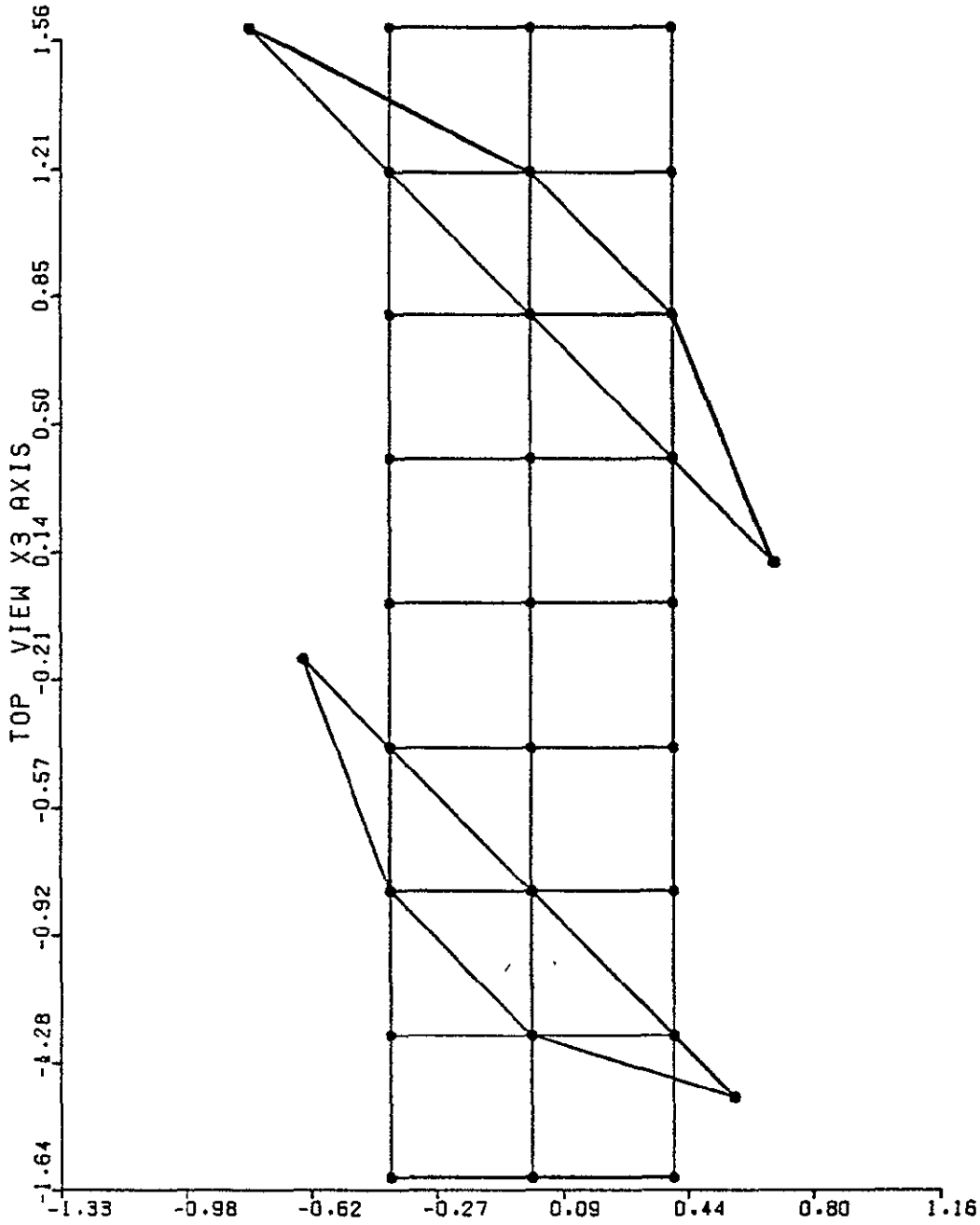

Figure 2.4-1. Finite element model of SLC (side view)

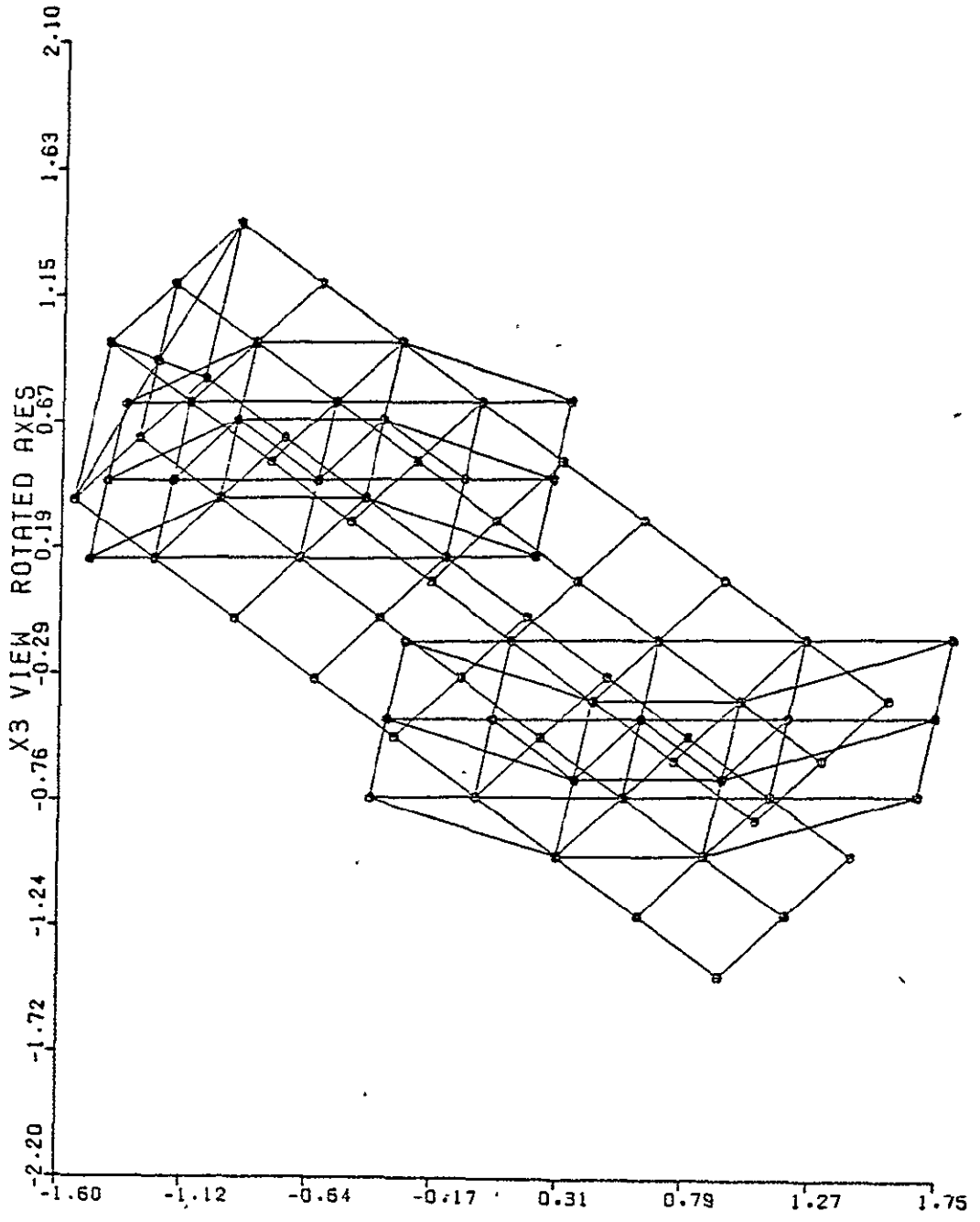

Figure 2 4-2. Finite element model of SLC (perspective view)

Table 2.4-1. Listing of STARDYNE input for SLC analysis

```
START                                                    2211   1
PLOTS          1w        SC428     --          -
 SCAN TYPE CORRECTOR ANALYSIS.     COMPLETE STRUCTURE.
MATLG      1 BERYLLIUM      42.E6      .025      .267
MATLG      2                 1.E8
MATLG      3 BE + NI        40.4E6       .062    .1r756
END
NODEG      1   25   3      -0.4      -1.6     8.492      -0.4      1.6     0.492
           2   26   3       0.0      -1.6     0.492       0.0      1.6     0.492
           3   27   3       0.4      -1.6     0.492       0.4      1.6     0.492
          28   52   3      -0.4      -1.6    -0.492      -0.4      1.6    -0.492
          29   53   3                -1.6    -0.492       0.0      1.6    -0.492
          30   54   3       0.4      -1.6    -0.492       0.4      1.6    -0.492
NODE      55                         -1.6
NODE      57          2.                                          0.492
NODE      58                         1.6
NODE      59          2.                                         -0.492
NODE      60      -0.643              -0.157          .492
          61       0.576              -1.376          .492
          62      -0.643              -0.157
          63      -0.4                -0.4
          64      -0.4                -0.8
          65                          -0.8
          66       0.4                -0.8
          67                          -1.2
          68      -0.4                -1.2
          69       0.576              -1.376
          70      -0.643              -0.157         -0.492
          71       0.576              -1.376         -0.492
          72      -0.797               1.597           .492
          73       0.69                0.11            .492
          74      -0.797               1.597
          75      -0.4                 0.2
          76                           1.2
          77                           0.8
          78       0.4                 0.8
          79       0.4                 0.4
          80       0.69                0.11
          81      -0.797               1.597          -.492
          82       0.69                0.11           -.492
END
RESTG      2                   1
RESTG     29                   1
RESTG      5                   1
RESTG     66                   1
RESTG     38                   1
RESTG     41                   1
RESTG     44                   1
RESTG     32                   1
RESTG     11                   1
RESTG     14                   1
RESTG     17                   1
RESTG     23                   1
RESTG     75                   1
RESTG     80                   1
RESTG     25              111111
RESTG     26              111111
RESTG     27              111111
RESTG     52              111111
RESTG     53              111111
RESTG     54              111111
END
BRECT      1    8    1    3    4    3   57    1    1
           9   16    3    3    6    3   57    1    1
          17   24   28    3   31    3   58    1    1
          25   32   30    3   33    3   58    1    1
BRECT     33        55         1              2    2
          34        55         2              2    2
          35        55         3              2    2
          36        55        28              2    2
          37        55        29              2    2
          38        55        30              2    2
          39        28         1              2    2
          40        30         3              2    2
BRECT     41         7        63              3    3
          42        63        34
          43         5        66
          44        66        32
```

Table 2 4-1. Listing of STARDYNE input for SLC analysis (Cont)

```
                45        50        75
                46        75        23
                47        48        77
                48        77        21
END
BPROP2           1       .06       .15                    1.5       1.5
BPROP2           2       .25       .25                     1.5       1.5
BPROP2           3       .06       .06                      1.5       1.5
END
TRIAB            1        59         7        10         3 1     .06
TRIAB            2         7         8        10
                 3         7         5         8
                 4         5         6         8
                 5         5        60         6
                 6        61        63        62
                 7        63        64        65
                 8        63        66        64
                 9        66        67        64
                10        66        68        67
                11        69        34        37
                12        34        35        37
                13        34        32        35
                14        32        33        35
                15        32        70        33
                16        71        22        23
                17        22        20        23
                18        20        21        23
                19        20        18        21
                20        18        72        21
                21        73        74        75
                22        74        76        75
                23        76        77        75
                24        76        78        77
                25        79        79        77
                26        80        49        50
                27        49        47        50
                28        47        48        50
                29        47        45        48
                30        45        91        48
END
QUADB            1   8     1   3     2   3     5   3     4   3     1     1   0.050          2
                 9  16     2   3     3   3     6   3     5   3     1     1
                17  24    28   3    29   3    32   3    31   3     1     1
                25  32    29   3    30   3    34   3    32   3     1     1
QUADB           33        10        62        61        59        3     1
                34         8        64        62        10
                35         6        67        64         8
                36        60        68        67         6
                37        62        37        69        61
                38        64        35        37        62
                39        67        33        35        64
                40        68        70        33        67
                41        49        74        73        80
                42        47        76        74        49
                43        45        78        76        47
                44        81        79        78        45
                45        74        22        71        72
                46        76        20        22        74
                47        78        18        20        76
                48        79        72        18        78
END
MADDEL          101
MADDX            1     2   200000.
                 2     2   200000.
                 3     2   200000.
                28     2   200000.
                29     2   200000.
                30     2   200000.
ENDEL
MADDEL          101
MADDX           55     1  1000000.                                        1000000.
ENDFL
END
ENDGEOM
 INVERSE ITERATION TO FIND FIRST THREE MODES.
INVITR                                -1                    3          1.   1.E6
OPTION           1        1
ENDMODEL
```

2.4.1.6 Fundamental Modes of Vibration

To determine the sensitivity of the SLC to the dynamic environment, the lowest three natural modes of vibration were first determined. Figures 2.4-3, 2.4-4, and 2.4-5 illustrate these mode shapes. The vibration frequencies for the flight mirror assembly were found to be 6300, 6900, and 8900 Hz.

2.4.1.7 Dynamic Environment

The dynamic environment seen by the SLC is illustrated by the angular position versus time plot shown in Figure 2.4-6. This plot was generated by the continuous systems modeling computer program with which the SLC control system was analyzed. The program also computes the SLC angular acceleration versus time. The maximum angular acceleration of the SLC (during retrace) was computed as 18700 rad/sec^2.

Since the fundamental period (0.158 msec) is much smaller than the period of the excitation during trace (2.0 msec), a constant angular acceleration solution for the SLC response was obtained. The SLC was assumed to be subject to inertial loads resulting from 20,000 rad/sec^2 angular acceleration, somewhat greater than the expected peak of 18700 rad/sec^2. This loading condition imposes conservatively high stresses and displacements relative to the actual dynamic case.

The deformed shape of the SLC under this loading condition is shown in Figure 2.4-7. The maximum calculated rotation of the lower mirror relative to the upper mirror is 4 μr. Peak stress occurs in the yoke and is less than 140 psi. Cross-axis jitter should be small since the maximum off-axis displacement of the mirror centers is less than 1 microinch.

2.4.1.8 Conclusions

The scan line corrector appears to be well designed. Its fundamental frequency is high, relative to its operational frequency and the maximum stress is low. Additionally, the maximum distortion of the structure is small, and occurs during retrace. It is therefore concluded that the scan line corrector is a structurally sound design.

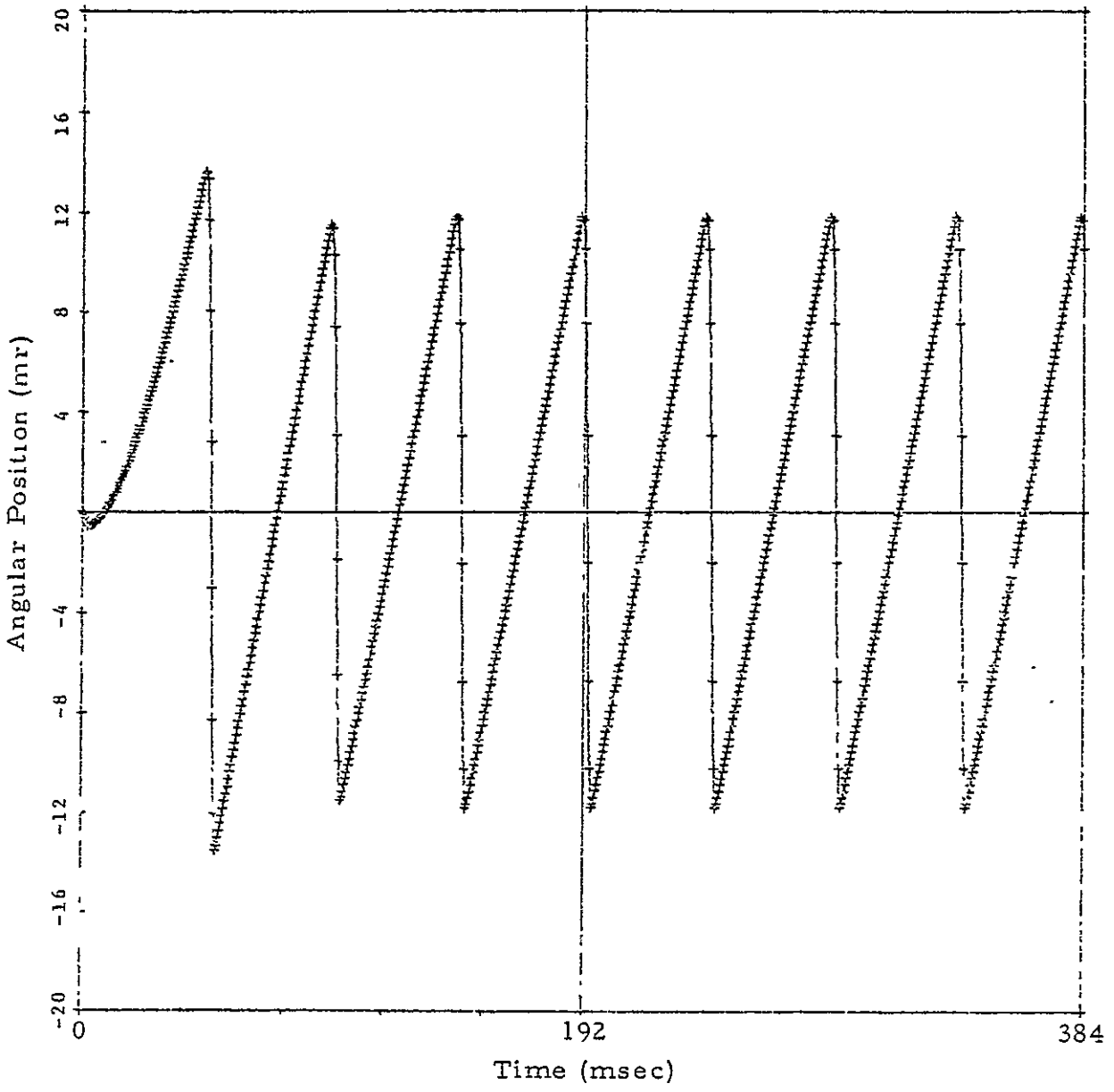

Figure 2.4-3. SLC angular position versus time

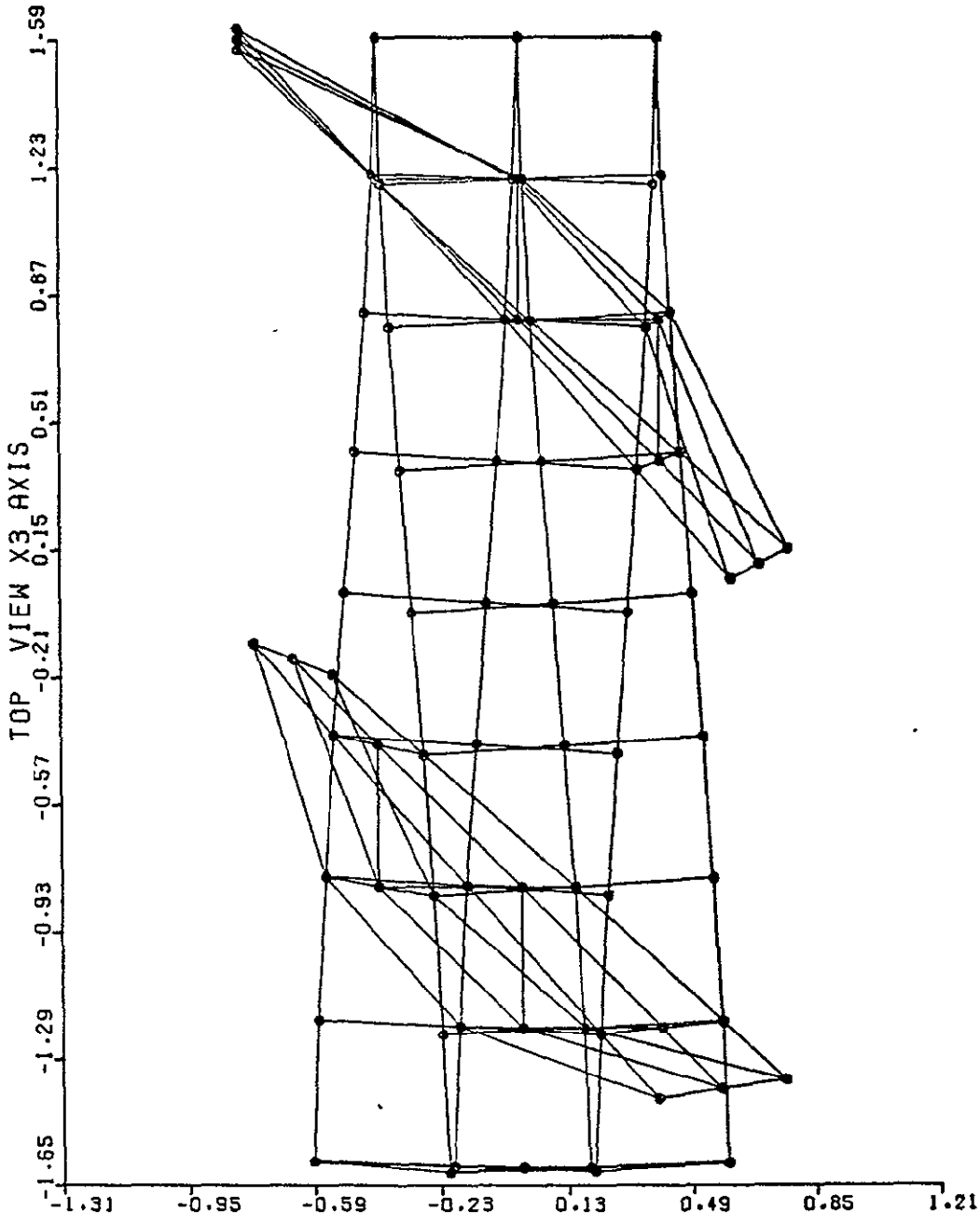

Figure 2.4-4. Fundamental mode shape, 6300 Hz

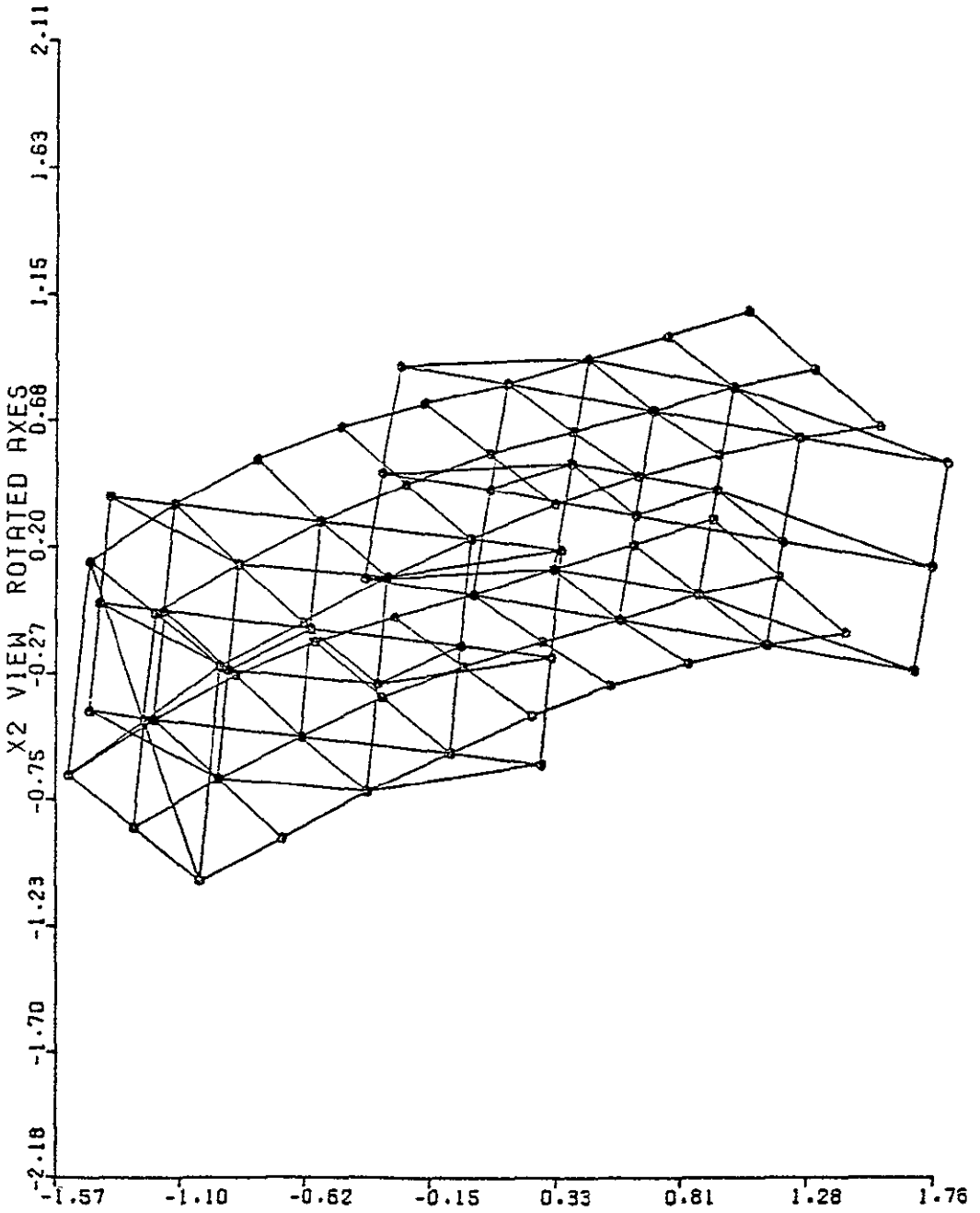

Figure 2.4-5. Second mode, 6900 Hz

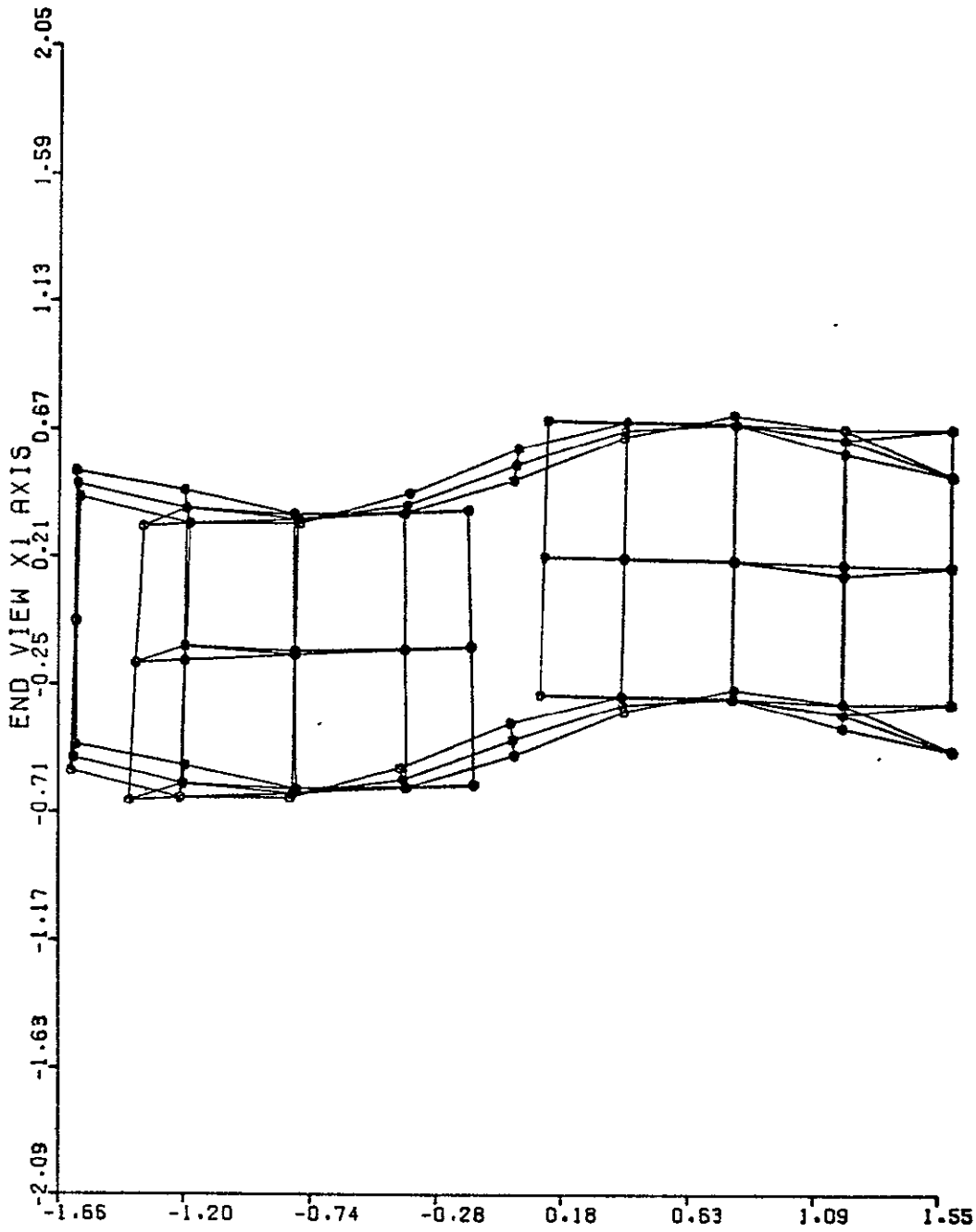

Figure 2.4-6. Third mode, 8900 Hz

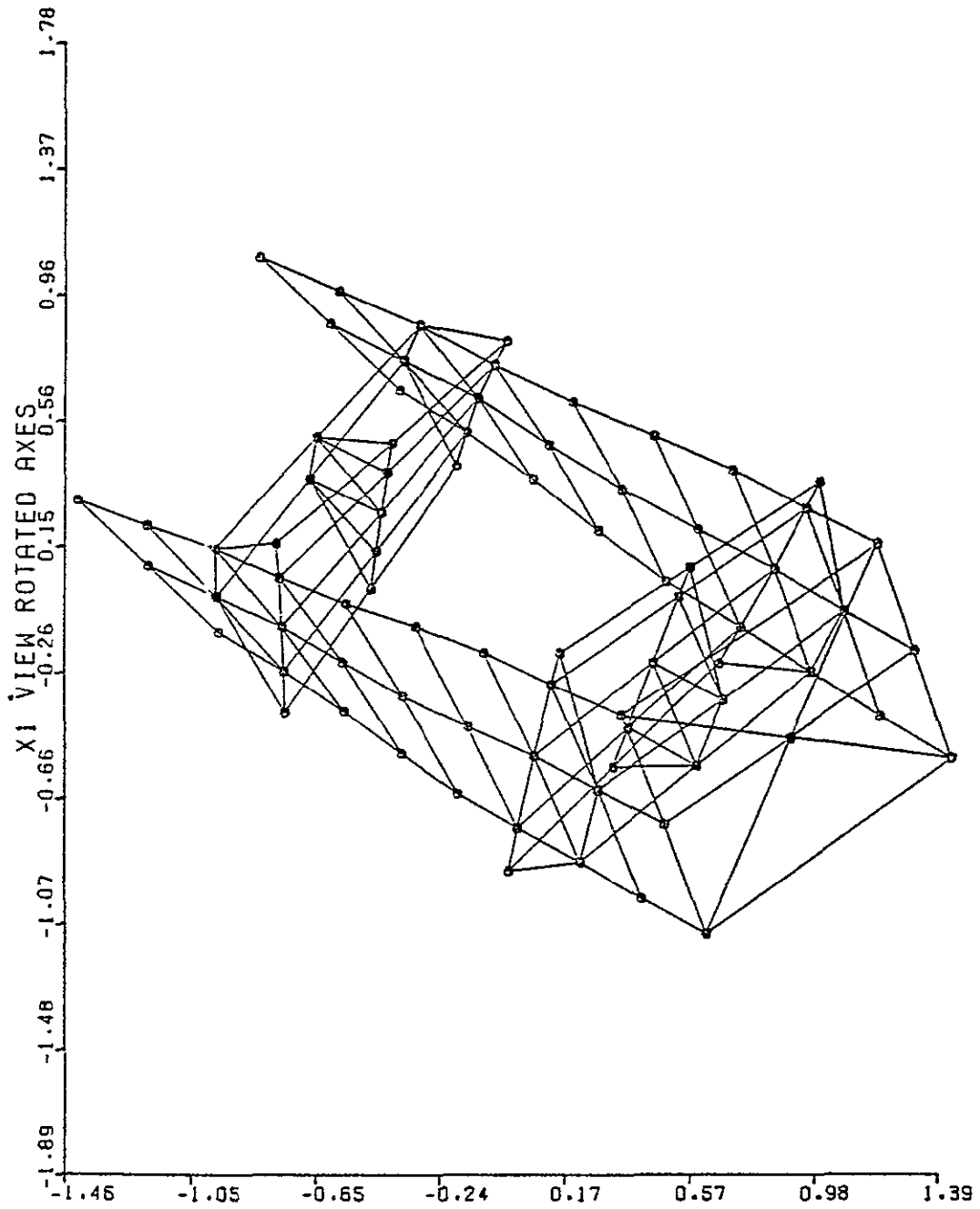

Figure 2 4-7. Perspective view of SLC under constant angular acceleration (distortion magnified)

2.4.2 Optical Analysis

2.4.2.1 Optical Considerations

The system shown in Figure 2.3-1 shows the Scan Line Corrector (SLC) and its function within an optical system. The concept chosen represents a good balance of mechanical simplicity and high optical performance.

Initial SLC design parameters were established as a baseline for design. For review, certain parameters critical to the optical analysis are stated here.

Telescope Aperture	40.6 cm
Telescope f/No.	6
IFOV	42.6 μr
Number of Detectors	16
Array Length	682 μrad (1.66 mm)

A model of the SLC system was entered into the POSD optical ray trace program for analysis. The model included Ritchey Chretien primary optics followed by two mirrors for the scan line corrector, and the image plane. Rotation of the SLC mirrors is accomplished by a simple angle change in the computer, with results printed for the same image plane. Edge rays are traced through the optical system and their crossing point is indicative of the focal point. Rays were traced at 0, 4.4, 8.8, 13, and 18 mrad rotation of the SLC and at object space field angles of 0, 0.5, and 1.0 mrad. From these rays, most of the optical effects as influenced by the SLC can be determined.

2.4.2.2 Amplitude of Motion

The SLC must create a maximum image motion equal to the array length, defined previously as 1.66 mm. Using the SLC dimensions shown in Figure 2.3-2 with a 4 cm mirror separation, the required 1.66 mm (±0.83 mm) motion is achieved by an SLC rotation of ±20.05 mr. There is a 60:1 ratio of SLC rotation to displacement in object space. This 60:1 ratio is also an indication of the amount that tolerances are less stringent on the SLC as compared to the object plane scan mirror.

2.4.2.3 Out of Focus

For the scan angle above, the SLC moves the image out of focus by 7.6 μm at the extreme end of scan. It would be normal to position a detector array midway in this focal range so that the defocus experienced would be ±3.8 μm. In terms of energy blur, this would create a spot 0.65 μm in diameter or 0.24 μrad in diameter. This blur is insignificant. If it were a full order of magnitude worse, it would be of little concern.

2.4.2.4 Line Straightness

The scan motion created by the SLC projected into object space shows no tendency to create curved lines. Using rays 1 mrad off axis, the projected line is straight to 0.008 μrad.

2.4.2.5 Scan Linearity

The scan motion is linear with SLC rotation. From the first increment of SLC rotation (4.4 mrad) there is an image displacement of 177 μm. At 8.8 mrad rotation exactly twice this displacement is desired; at 18 mrad rotation, four times the displacement is desired. Calculated values differed from the desired displacement by 0.02 μm. This corresponds to an object space displacement of 0.008 μrad.

2.4.2.6 Sensitivity of Mirror Alignment

It was necessary to determine if unusually tight assembly tolerances were necessary. The values used for the tilt angles in the computer program were altered to simulate a misaligned optical system. Initially an error of 18 mrad was put on both SLC mirrors such that they remained parallel to each other but with the optical axis incident at 0.8 rad. The resultant scan defects were small. In a second test, a tilt error of 18 mrad was imposed on two different axes of one SLC mirror. The results can be summarized to say:

1. Defocus by scanning is unaffected by as gross a value as 18 mrad misalignment of the mirrors.
2. Line straightness in object space is 0.24 μrad in the worst case.
3. Linearity of motion deviates by 0.016 μrad in the worst case.

These values would all seem acceptable for flight use. Alignment errors should never even approach 18 mrad.

2.4.2.7 Surface Flatness

Suitable operation of the SLC will require that the mirrors be flat. Preliminary tolerance check has started with the assumption that no ray be deviated from its ideal position by more than 1 μrad. This leads to the eventual conclusion that the SLC mirrors should have a slope error no greater than one fringe/inch on the surface.

2.4.2.8 Miscellaneous Comments

The SLC will be quite insensitivie toward introducing jitter in the image. Any translation of the SLC mechanism produced no change in image position. Internal scan modulation should not be a problèm as 1) the image motion is very small, and 2) the same optical elements are needed in all cases.

2.4.2.9 Image Rotation

Properly assembled SLC mirrors will produce no image rotation. If the mirrors have a relative displacement α in the direction of SLC rotation, the image will rotate by α. Misalignments in the other two axes do not produce image rotation.

2.4.3 Electronic Analysis

Prior to design of the electronics, the SLC system was modeled using the Continuous System Modeling Program. This program is useful for modeling servomechanisms with the capability of modifying system parameters as variables, and furnishes both variables printout and an X-Y plot. A block diagram of the SLC simulation is shown in Figure 2.4-8. A typical X-Y plot of mirror position versus time is shown in Figure 2.4-9. The variables printout corresponding to the X-Y plot is shown in Table 2.4-2 for a time interval between 150 msec and 162 msec from start. The frèquency for this example is 20 Hz. The total spring constant is 649 oz-in/rad with an assumed

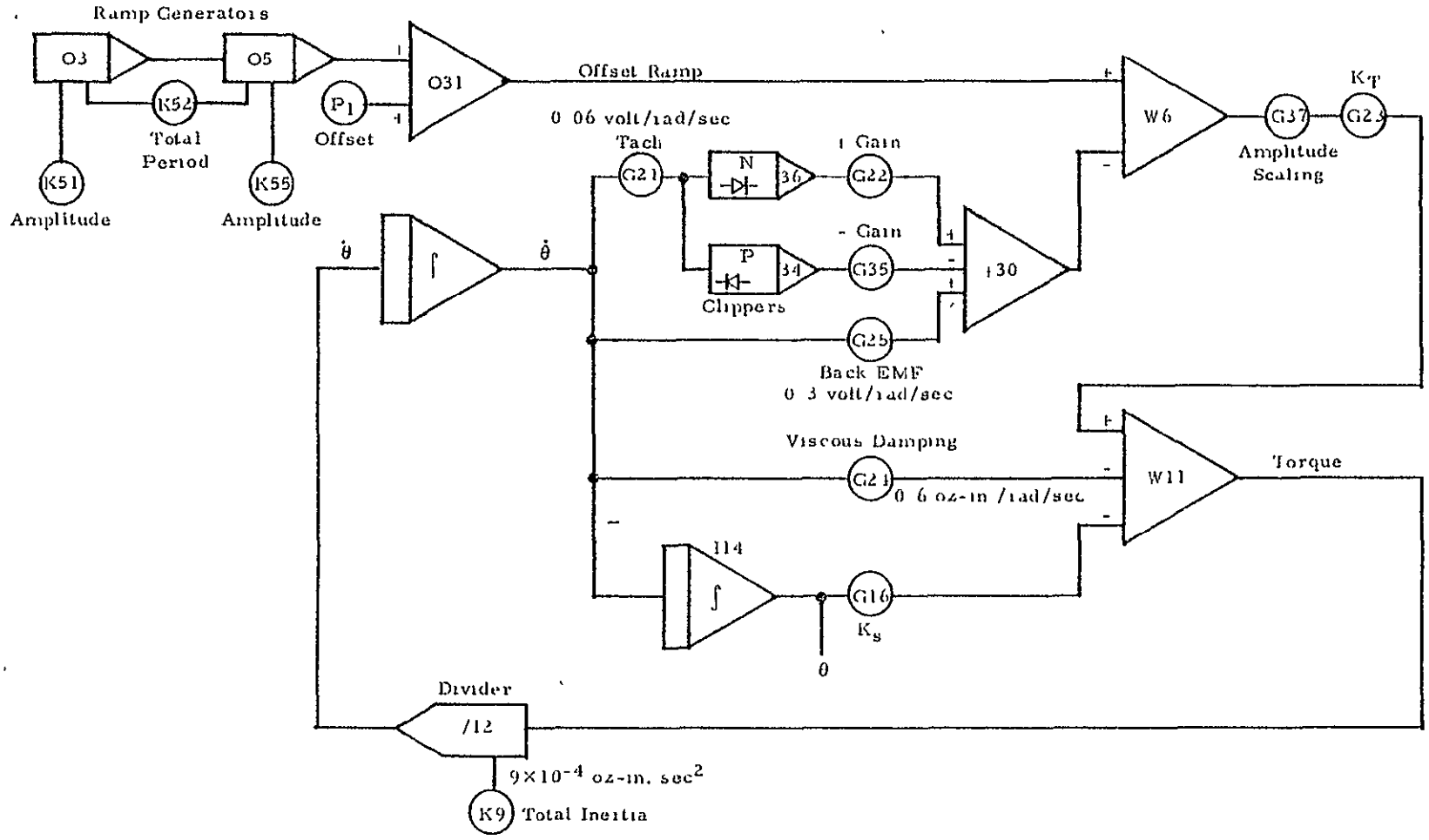

Figure 2.4-8. SLC simulation block diagram

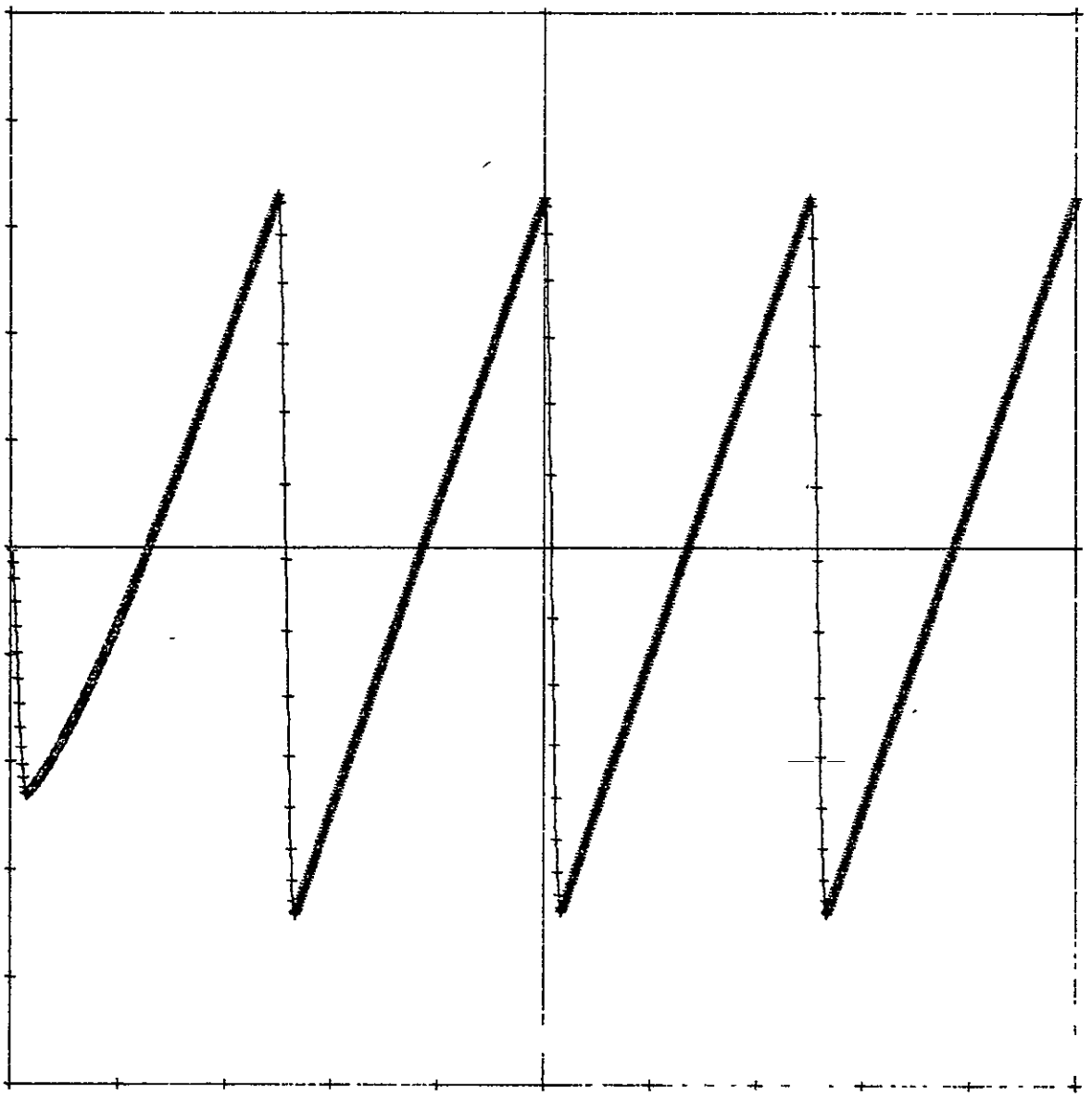

Figure 2.4-9. SLC angle versus time

Table 2.4-2. Computer output - SLC simulation

Time (sec)	Offset Ramp	Rate Feedback Signal	Torque (in-oz)	Velocity (rad/s)	Position (rad)
0.150	-2.7280	0.0000	-6.0622	-3.8710	0.0131
0.151	-2.6920	0.0000	-5.9822	-8.0722	0.0117
0.151	-2.6560	0.0000	-5.9022	-9.7635	0.0099
0.151	-2.6200	0.0000	-5.8222	-10.9631	0.0078
0.151	-2.5840	0.0000	-5.7422	-11.7000	0.0056
0.151	-2.5480	0.0000	-5.6622	-12.0124	0.0032
0.152	-2.5120	0.0000	-5.5822	-11.9449	0.0008
0.152	-2.4760	0.0000	-5.5022	-11.5470	-0.0016
0.152	-2.4400	0.0000	-5.4222	-10.8706	-0.0038
0.152	-2.4040	0.0000	-5.3422	-9.9689	-0.0059
0.152	-2.3680	0.0000	-5.2622	-8.8945	-0.0078
0.153	-2.3320	0.0000	-5.1822	-7.6979	-0.0095
0.153	-2.2960	0.0000	-5.1022	-6.4268	-0.0109
0.153	-2.2600	0.0000	-5.0222	-5.1247	-0.0120
0.153	-2.2240	0.0000	-4.9422	-3.8307	-0.0129
0.153	-2.1880	0.0000	-4.8622	-2.5786	-0.0136
0.154	-2.1520	0.0000	-4.7822	-1.3970	-0.0140
0.154	-2.1160	0.0000	-4.7022	-0.3090	-0.0141
0.154	-2.0800	1.2121	-7.3157	0.3978	-0.0141
0.154	-2.0440	1.7000	-8.3200	0.5580	-0.0140
0.154	-2.0080	1.8309	-8.5310	0.6009	-0.0139
0.155	-1.9720	1.8661	-8.5290	0.6125	-0.0138
0.155	-1.9360	1.8755	-8.4699	0.6156	-0.0136
0.155	-1.9000	1.8780	-8.3955	0.6164	-0.0135
0.155	-1.8640	1.8786	-8.3170	0.6166	-0.0134
0.155	-1.8280	1.8788	-8.2373	0.6166	-0.0133
0.156	-1.7920	1.8788	-8.1574	0.6167	-0.0131
0.156	-1.7560	1.8788	-8.0774	0.6167	-0.0130
0.156	-1.7200	1.8788	-7.9974	0.6167	-0.0129
0.156	-1.6840	1.8788	-7.9173	0.6166	-0.0128
0.156	-1.6480	1.8788	-7.8373	0.6166	-0.0126
0.157	-1.6120	1.8788	-7.7572	0.6166	-0.0125
0.157	-1.5760	1.8787	-7.6772	0.6166	-0.0124
0.157	-1.5400	1.8787	-7.5972	0.6166	-0.0123
0.157	-1.5040	1.8787	-7.5171	0.6166	-0.0122
0.157	-1.4680	1.8787	-7.4371	0.6166	-0.0120
0.158	-1.4320	1.8787	-7.3571	0.6166	-0.0119
0.158	-1.3960	1.8787	-7.2770	0.6166	-0.0118
0.158	-1.3600	1.8787	-7.1970	0.6166	-0.0117
0.158	-1.3240	1.8786	-7.1170	0.6166	-0.0115
0.158	-1.2880	1.8786	-7.0369	0.6166	-0.0114
0.159	-1.2520	1.8786	-6.9569	0.6166	-0.0113
0.159	-1.2160	1.8786	-6.8769	0.6166	-0.0112
0.159	-1.1800	1.8786	-6.7969	0.6166	-0.0110
0.159	-1.1440	1.8786	-6.7168	0.6166	-0.0109
0.159	-1.1080	1.8786	-6.6368	0.6166	-0.0108
0.160	-1.0720	1.8785	-6.5568	0.6166	-0.0107
0.160	-1.0360	1.8785	-6.4767	0.6166	-0.0105
0.160	-1.0000	1.8785	-6.3967	0.6166	-0.0104
0.160	-0.9640	1.8785	-6.3167	0.6166	-0.0103
0.160	-0.9280	1.8785	-6.2367	0.6165	-0.0102
0.161	-0.8920	1.8785	-6.1566	0.6165	-0.0101
0.161	-0.8560	1.8785	-6.0766	0.6165	-0.0099
0.161	-0.8200	1.8785	-5.9966	0.6165	-0.0098
0.161	-0.7840	1.8785	-5.9166	0.6165	-0.0097
0.161	-0.7480	1.8784	-5.8365	0.6165	-0.0096
0.162	-0.7120	1.8784	-5.7565	0.6165	-0.0094
0.162	-0.6760	1.8784	-5.6765	0.6165	-0.0093

inertia of 9×10^{-4} oz-in. sec^2. With a scan interval of 50 msec, the retrace started 0.8 msec before the first line of printout in this example. The velocity is 0.6167 rad/sec at 156 msec, indicating a small overshoot from the final value of 0.6165 rad/sec at 162 msec. To minimize retrace time, the tachometer feedback was separated into separate gain values for positive and negative amplitudes. This worked well for the computer simulation but was abandoned in favor of a delayed tachometer signal during breadboard development.

2.5 PERFORMANCE TESTING

Two types of tests were conducted to verify the performance of the SLC. When the mechanical assembly of the mechanism was completed, measurements were made to determine that the inertia, torque constant, and natural frequency were compatible with the calculated values of the anticipated flight model design. After integration with the control electronics, tests were conducted to verify that the dynamic performance (including scan rate, linearity, scan jitter, and repeatability) was consistent with the requirements of the Thematic Mapper instrument.

2.5.1 Mechanical Tests

The test setup for the mechanical tests is shown in Figure 2.5-1. The SLC was positioned on a rotary table in front of an autocollimator. The cross hairs from the focal plane of the autocollimator can be seen being projected through the mirrors of the SLC in Figure 2.5-2. Test mirrors were temporarily cemented to both sides of the mirror housing to allow for measurement of the angle of rotation of the SLC during these tests.

The torque constant of the flex pivots was determined by hanging known masses from a lever arm of known length, thereby producing a rotational torque on the system as shown in Figure 2.5-3.

The resultant angular displacement of the SLC was measured by the autocollimator. The torque constant was determined at four increments of torque in each direction about the rest position. The value of the torque

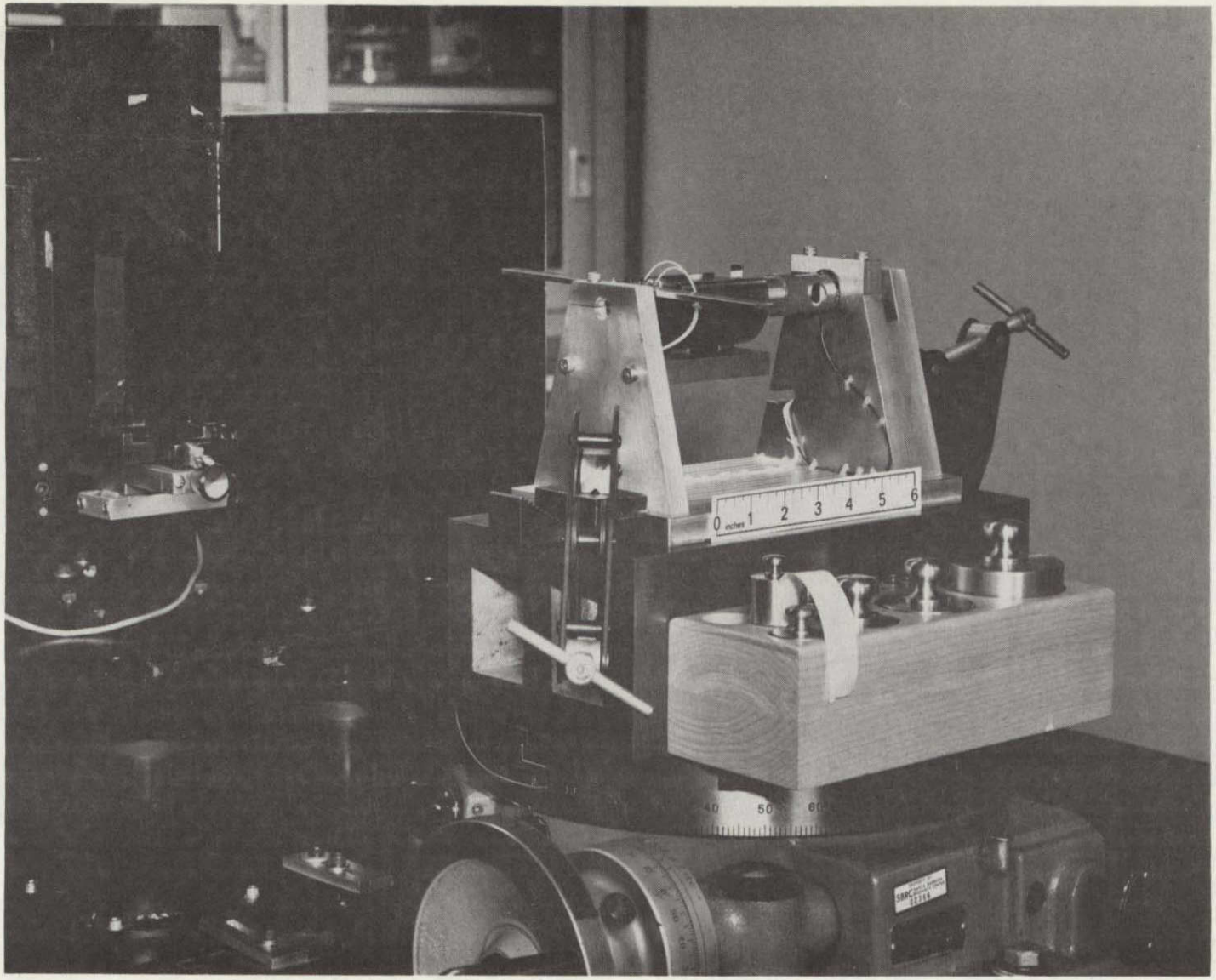

Figure 2.5-1. Test setup for mechanical tests

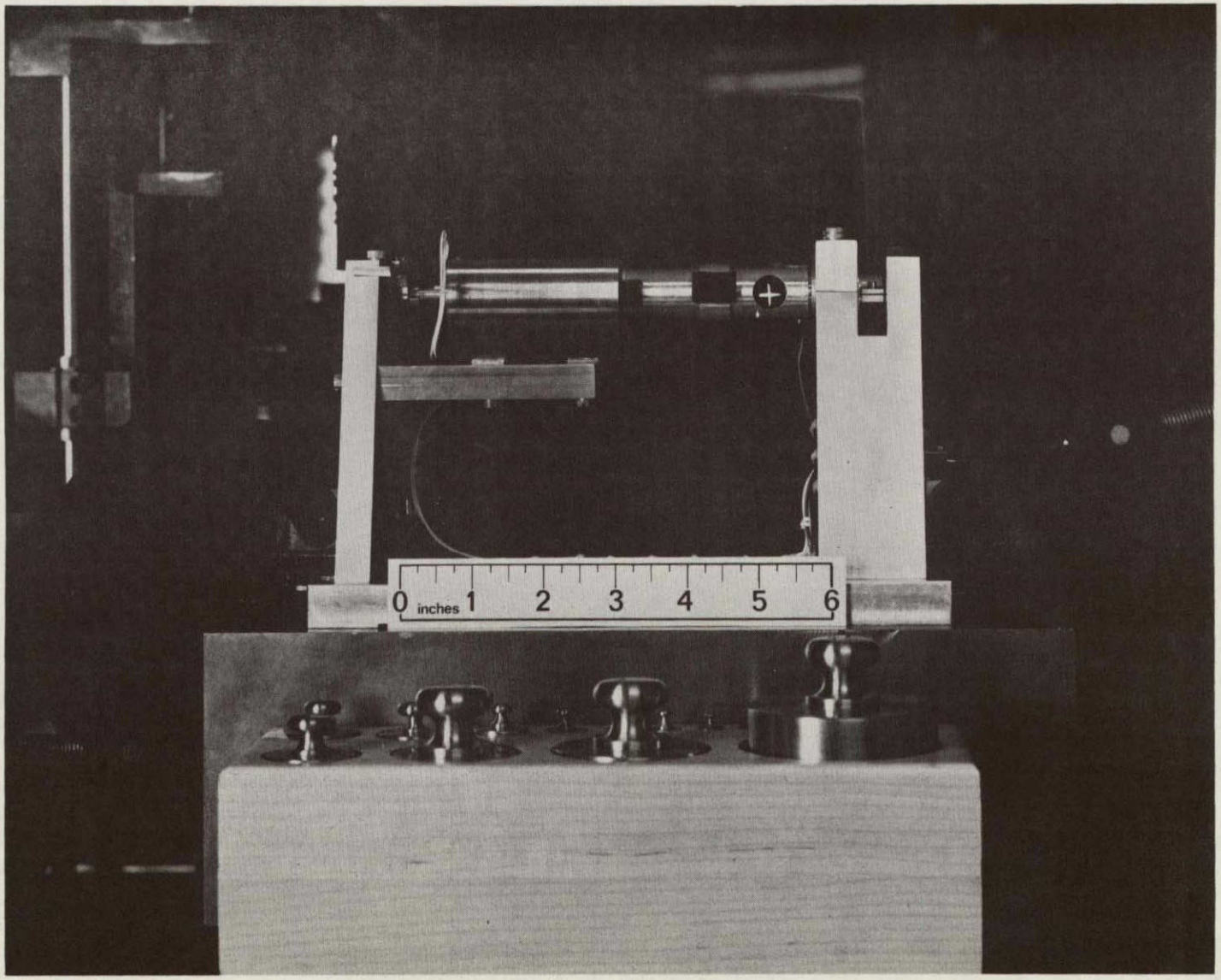

Figure 2.5-2. Test setup for mechanical tests

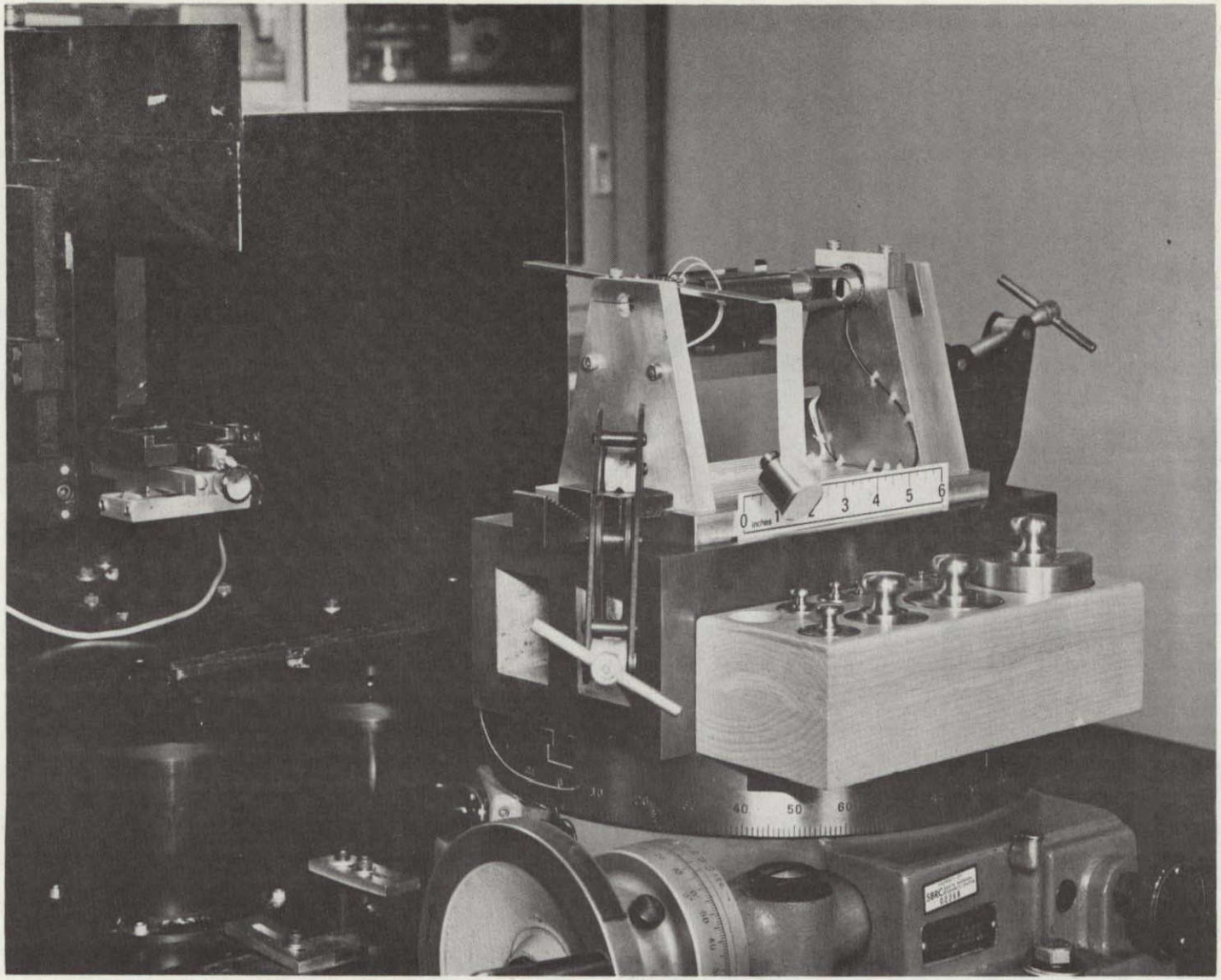

Figure 2.5-3. Determination of torque constant

constant was found to be 4.64×10^7 dyne cm/rad. The nominal value of the Bendix flex pivots was 4.97×10^7 dyne cm/rad ± 10%.

The inertia was determined by mechanically exciting the system and observing the natural frequency as indicated by the tachometer output on an oscilloscope. The natural frequency was found to be 100 Hz. The inertia was then calculated using the following equation:

$$I = \left(\frac{T}{2\pi}\right)^2 K = 117.5 \text{ gm cm}^2$$

where I = inertia (gm cm^2)

K = torque constant (dyne cm/rad)

T = period of oscillation (sec)

A photograph of the tachometer output which shows the natural frequency of the SLC mechanism is shown in Figure 2.5-4.

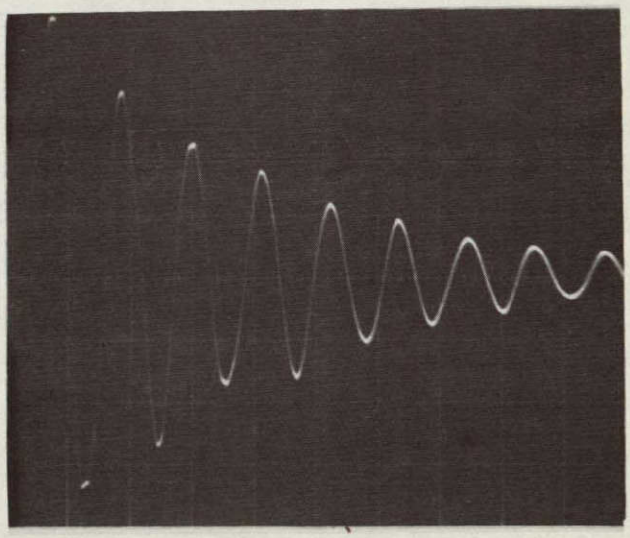

Figure 2.5-4. Determination of natural frequency

The value of the inertia anticipated for the flight version of the SLC using beryllium mirrors on a beryllium mirror holder was calculated to be 92 gm cm^2. The breadboard model therefore is a fairly good simulation of the flight SLC, and should be slightly more difficult to produce the desired motion than the flight model, due to its higher inertia.

The test data for these tests are contained in pages 1 to 13 of the log book.

2.5.2 Dynamic Performance Tests

2.5.2.1 Test Setup

The test setup for the dynamic performance tests is shown in Figure 2.5-5. From left to right along the front edge of the granite slab are the test electronics box, the control electronics box, an HeNe laser (which projected a beam of light into the SLC), the SLC, and a linear detector array (with amplifiers).

2.5.2.2 Test Method

The motion of the SLC mechanism was measured by positioning a linear array of regularly spaced silicon detectors behind the SLC in the location of the Thematic Mapper focal plane, and projecting a beam of light from an HeNe laser through the SLC and onto the detector array. A photograph showing a close-up of the laser, the SLC, and the detector array is shown in Figure 2.5-6. The detector array consists of 50, 0.2 x 0.16 mm detectors spaced 0.038 mm apart as shown in Figure 2.5-7. Since the maximum expected scan amplitude corresponds to a displacement of 1.57 mm in the focal plane, only ten adjacent detectors were connected. The detector array was mounted on an x, y, z micrometer stage so it could be accurately positioned. As the SLC rotated, the laser beam was scanned along the array illuminating the individual diodes sequentially. As the beam crossed the edge of each diode, a pulse was generated.

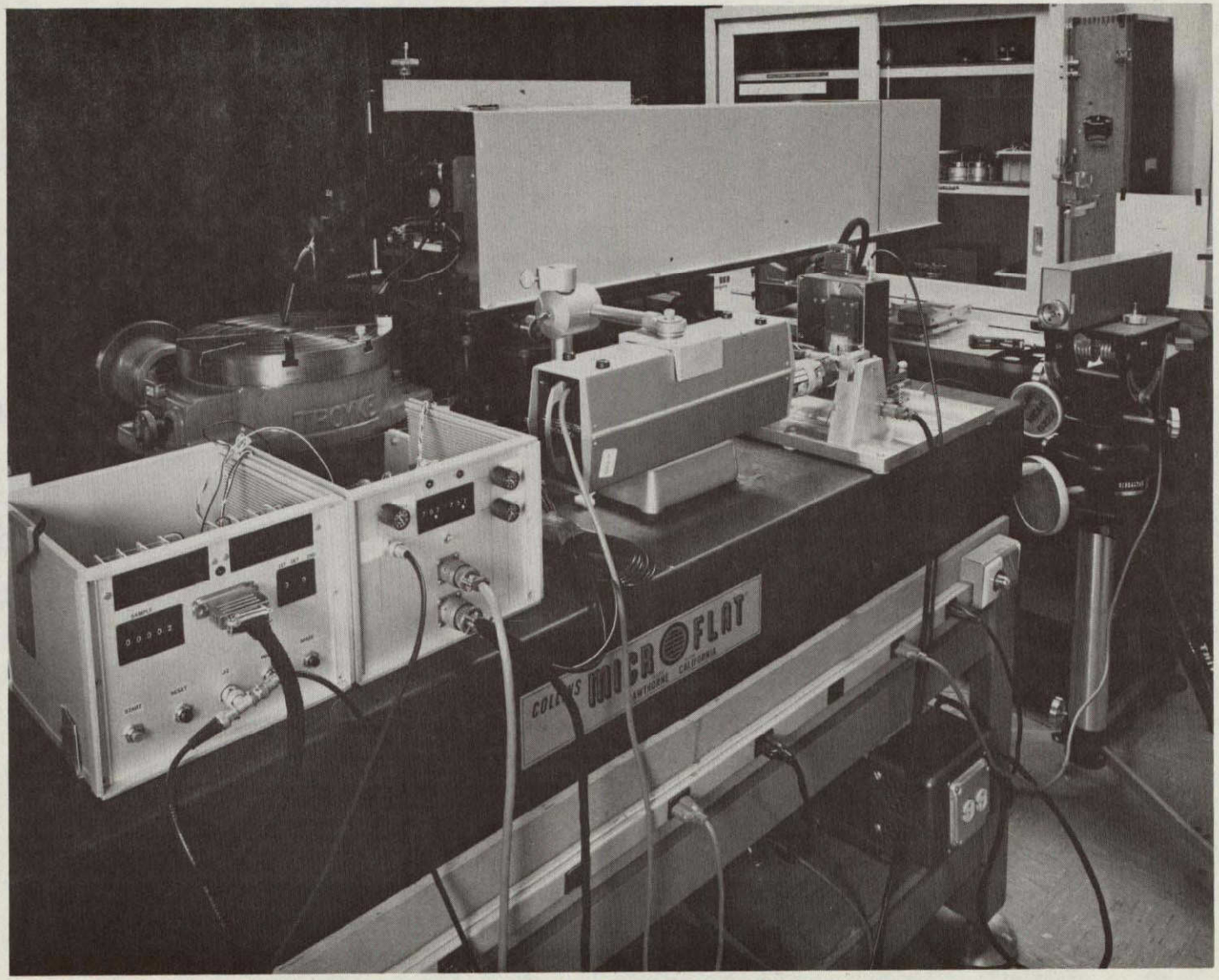

Figure 2.5-5. Test setup for dynamic tests

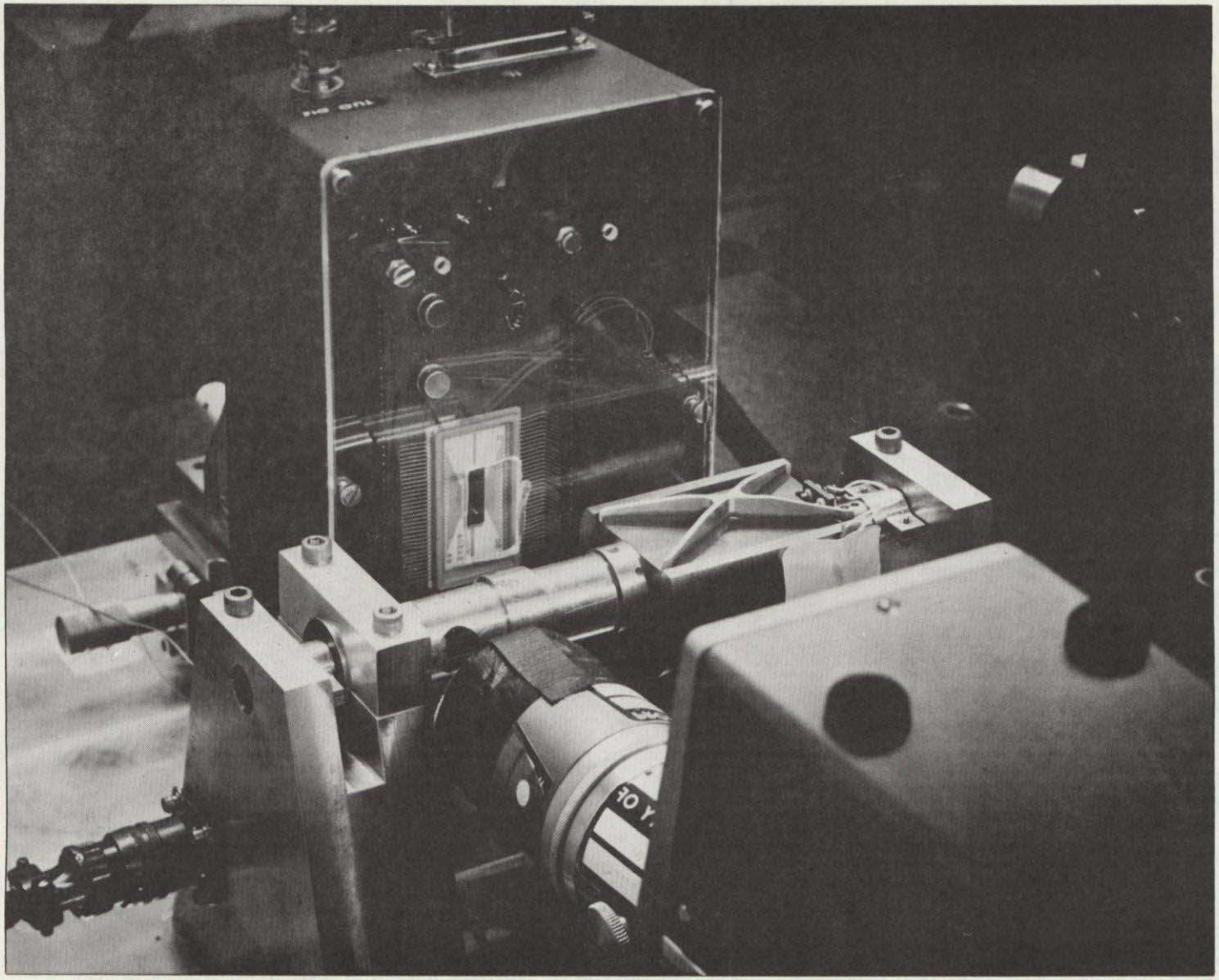

Figure 2.5-6. Laser, SLC, and detector array

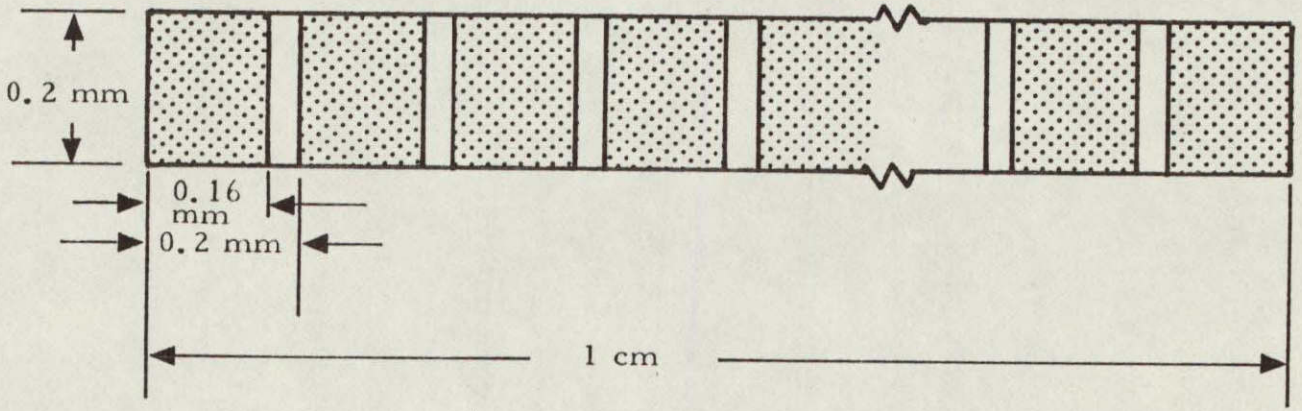

Figure 2.5-7. Silicon detector array

The test electronics box is shown in the left half of Figure 2.5-8. It has a pair of thumbwheel switches which enable the operator to select the pair of detectors between which the time interval is measured. Another set of five thumbwheel switches (labeled sample) allows the operator to select the number of SLC scans (from 1 to 99,999) over which the selected time interval is measured. The digital display shows the minimum and maximum time intervals measured for the selected pair of detectors for the selected number of scans.

The SLC was tested for scan rate, linearity, repeatability, and jitter at operating frequencies of 13.0, 14.2, and 19.0 Hz. Data sheets for all tests are contained in Appendix B.

2.5.2.3 Test Procedure. The tests were conducted in the following manner: The scan period was set up for the desired frequency using the thumbwheel switches on the control electronics box; the offset, gain, and slope controls were varied until the tachometer output indicated that the linearity was optimized. A pair of detectors was selected which spanned as much of the active scan as possible and the time interval was measured over five pairs of scan cycles to determine that the rate was very close to the desired rate. Figure 2.5-9 shows a photograph of the tachometer output along with the pulses from detectors 3 and 10. Detector No. 3 is positioned approximately 10% of the way into the scan period (the beginning of the active portion of the scan). Detector No. 10 is located at the end of the scan.

A confirmation of the scan amplitude was then made manually, positioning the detector array (using the micrometer adjustment) at varying positions from 10% to 90% throughout the scan and recording the micrometer reading. By using the intensified portion of the oscilloscope trace, a given detector was accurately positioned at any desired position in the scan. The photographs in Figure 2.5-10 show detector No. 7 at positions of 50% and 99% into the scan. The scan amplitude and a rough indication of scan linearity could be derived from this information.

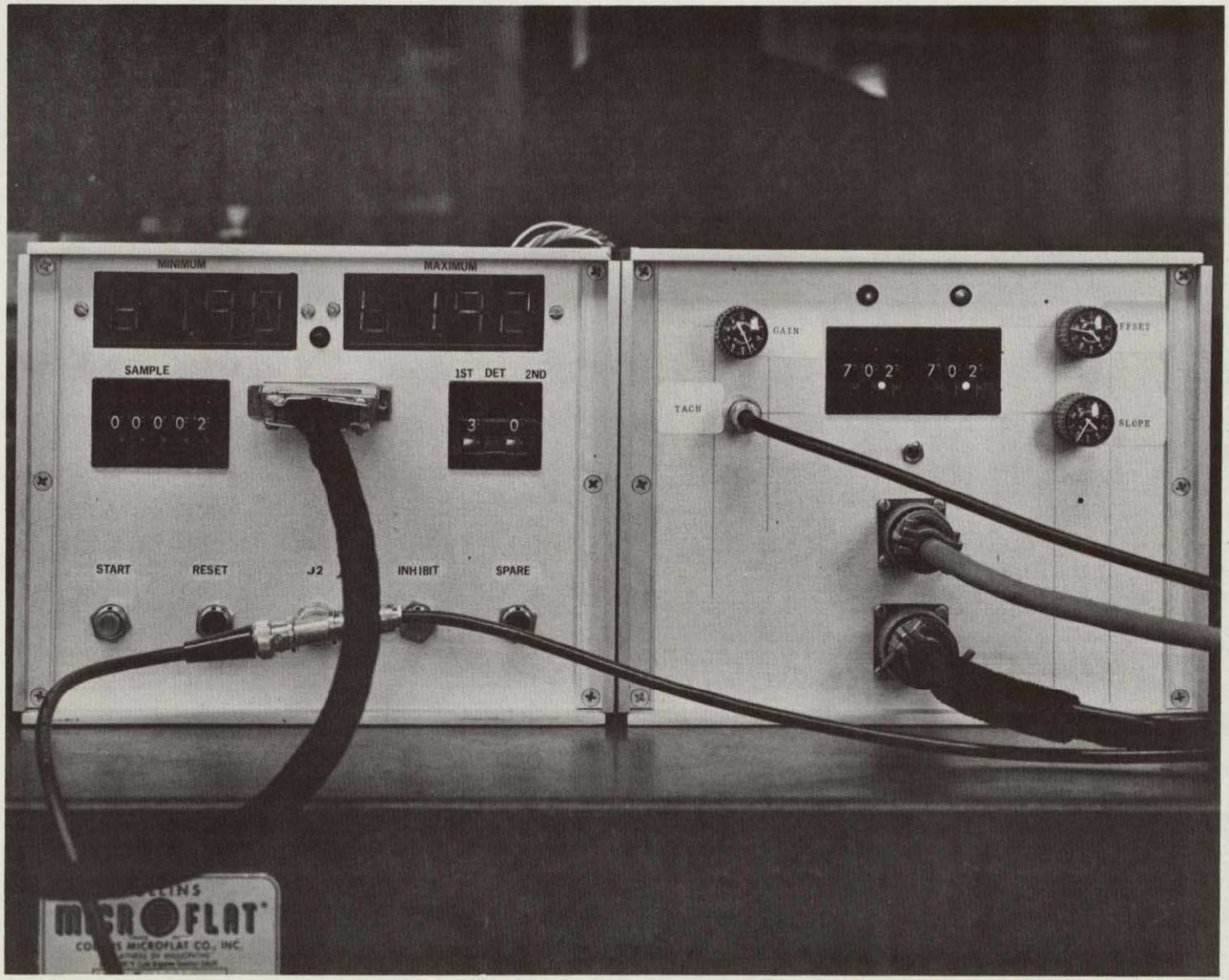

Figure 2.5-8. Test electronics and control electronics

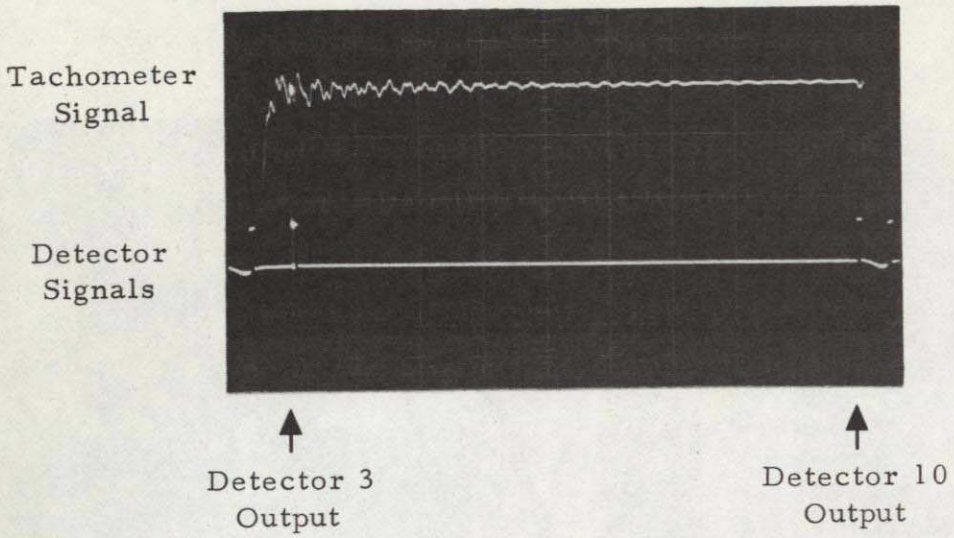

Figure 2.5-9. Detector signals

The scan linearity and scan-to-scan repeatability measurements were made by dividing the scan amplitude into an integral number of segments, with each segment being as close as possible to 0.2mm, and then positioning by micrometer an adjacent pair of detectors so that it spans one segment, and taking 20 pairs of minimum and maximum time interval measurements at each segment successively. The sample switch on the test box was set at 2 so that each data pair gave scan-to-scan repeatability information and the 20 data pairs were averaged to find the average scan rate over each segment.

By seeing how the rate varied, segment by segment, the displacement as a function of time was calculated and the deviation from a perfect scan at the nominal rate was determined. The photographs of Figure 2.5-11 show detectors 7 and 8 at three different positions in the scan.

The scan jitter was determined by measuring the time interval between the SLC reset pulse ("end of scan") and the start of scan. This was done by setting the first detector thumbwheel to 0 (the 0 on this thumbwheel is connected to the SLC reset pulse) and the second detector thumbwheel to 7 with detector No. 7 positioned at the start of scan (10% into the scan period).

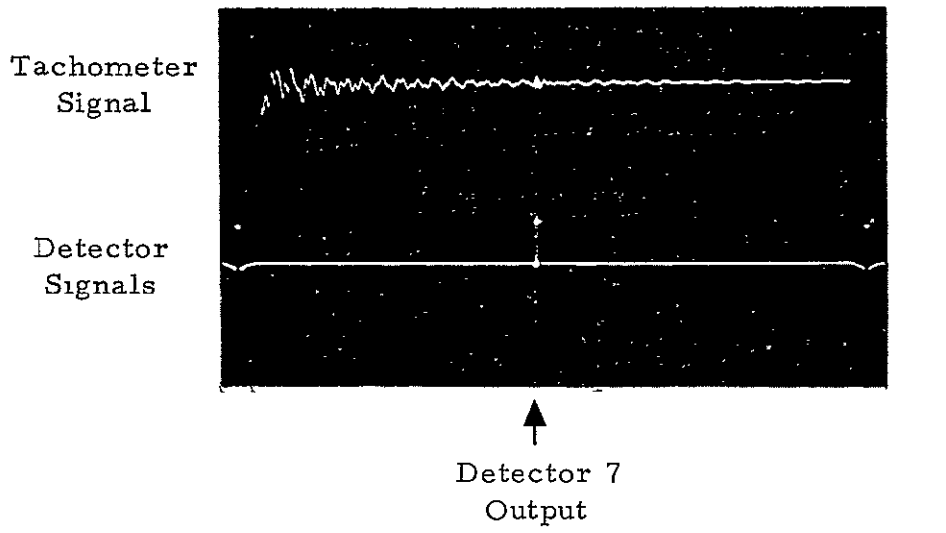

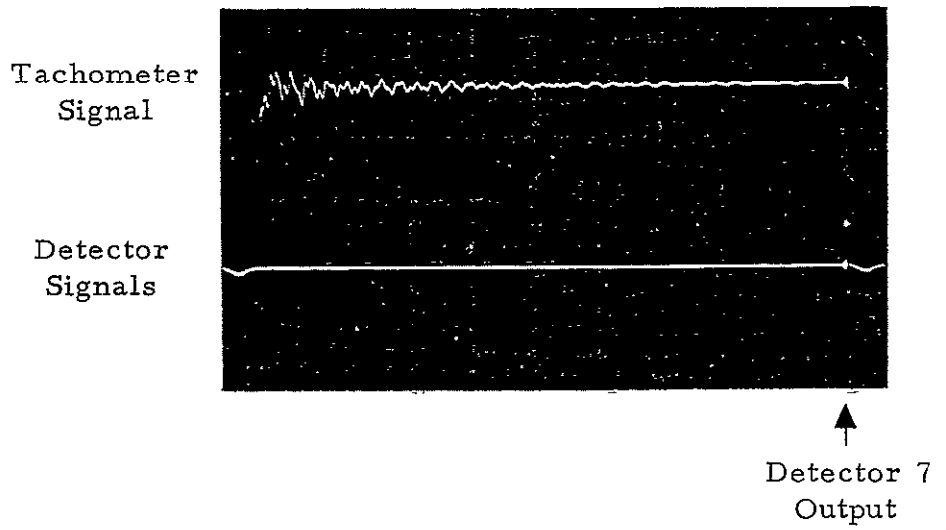

Figure 2.5-10. Detector 7 at 50% and 99% of scan

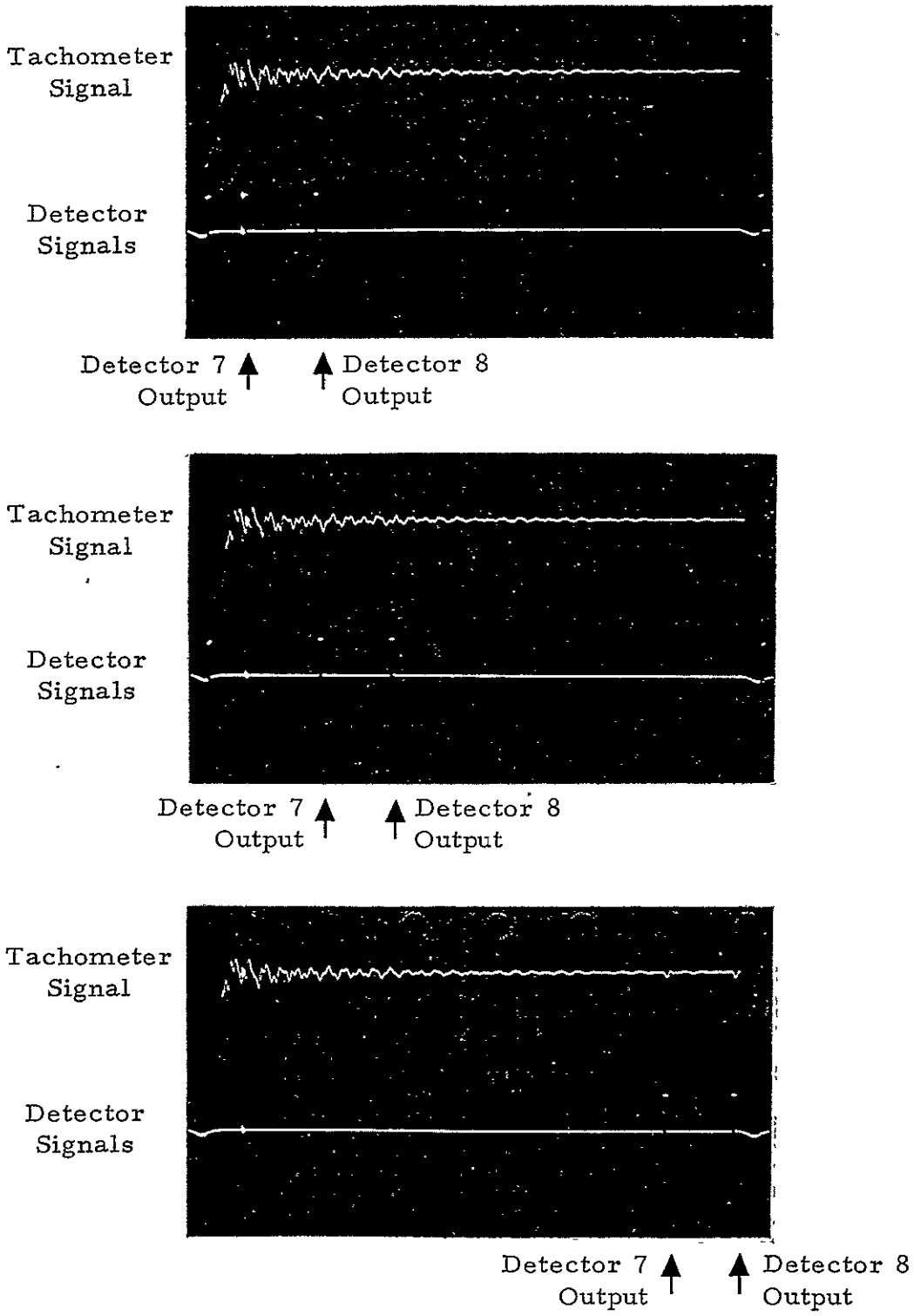

Figure 2.5-11. Detectors 7 and 8 at various positions in scan

The 30-second repeatability was measured by setting the "sample" thumbwheel switches on the test electronics box for the number of cycles which would occur in a 30-second period (at 14.2 Hz, the number of samples is 426) and noting the peak-to-peak variation in the time interval to cover the full scan amplitude. For the 14.2-Hz case, detectors 3 and 10 were used and positioned as shown in Figure 2.5-9.

Summaries of the test data taken at the three frequencies are shown in Tables 2.5-1 through 2.5-3 and Figures 2.5-12 through 2.5-14. (Each Table has a corresponding Figure.) The complete test data are included in Appendix B.

Table 2.5-1. 13 0-Hz data summary

$2f_s$ = 13.0 Hz

T = 0.0769 sec 0.9T = 0.0692 sec

0.9 T/7 = 0.009887 sec (seven equal increments)

Scan Deviation Data

Time (msec)	Rate (in./sec)	Displ (mils)	Cumulative Displ (mils)	Nominal Displ (mils)	Δ (mils)	Error % Full Scale
9.886	0.905	8.947	8.947	8.912	+0.035	0.056
19.771	0.902	8.917	17.864	17 834	+0.030	0.048
29.657	0.900	8 897	26 761	26.751	+0.010	0.016
39 543	0.898	8.877	35.638	35.668	-0.030	0.048
49.429	0 900	8.897	44.535	44.585	-0.050	0.080
59.314	0.901	8.907	53.442	53.501	-0.059	0.094
69.200	0.904	8.937	62.379	62.418	-0.039	0.062

displacement = 62.379 mils nominal displacement = 62.418 mils

average rate = 0.9014 in./sec nominal rate = 0.902 in./sec

Repeatability

Scan to Scan (data from all seven increments)

Worst Case = 0.07 msec = 0.66 μrad

σ = 0.016 msec = 0.15 μrad

30-Second Period (one frame)

Worst Case (from 10 runs) = 0.10 msec = 0.94 μrad

Worst Case Average (of 10) = 0.67 msec = 0.63 μrad

Scan Jitter (Scan to Scan)

Worst Case = 0.04 msec = 0.38 μrad

σ = 0.021 msec = 0.20 μrad

All angles referred to object space

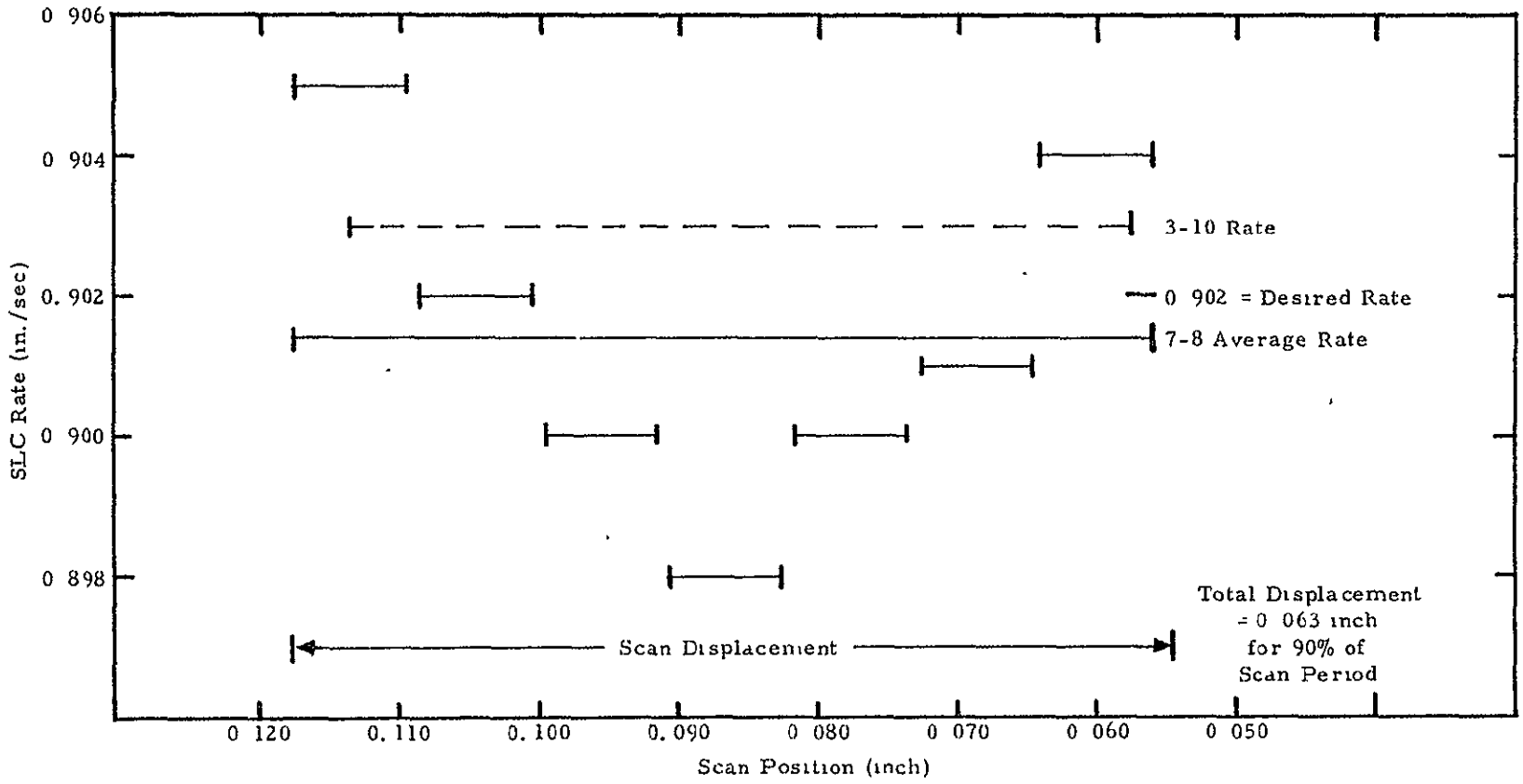

Figure 2 5-12. 13. 0-Hz test data, 8 December 1975

Table 2.5-2 14.2-Hz data summary

$2f_s$ = 14.236 Hz

T = 0.0702 sec 0.9T = 0 0632 sec

0.9 T/7 = 0.009026 sec (seven equal time increments)

Scan Deviation Data

Time (msec)	Rate (in./sec)	Displ (mils)	Cumulative Displ (mils)	Nominal Displ (mils)	Δ (mils)	Error % Full Scale
9.031	0.8891	8.030	8.030	8.146	-0.116	0.20
18.063	0.8922	8.058	16.088	16.293	-0.205	0.36
27 094	0.9004	8.132	24.220	24.439	-0.219	0.38
36.126	0.8995	8 124	32.344	32.585	-0.241	0.42
45.157	0.8995	8.124	40.468	40.732	-0.264	0.46
54.189	0 8997	8.126	48.594	48.878	-0.284	0.50
63.220	0 9016	8.143	56.737	57.024	-0.287	0.50

displacement = 56.737 mils nominal displacement = 57.024 mils

average rate = 0.8794 in./sec nominal rate = 0.902 in./sec

Repeatability

Scan to Scan (data from all seven increments)

Worst Case = 0.07 msec = 0.66 μrad

σ = 0.0114 msec = 0.11 μrad

30-Second Period (one frame)

Worst Case = 0.11 msec = 1.03 μrad

Average (of 10 Worst Cases) = 0.07 msec = 0.66 μrad

Scan Jitter (Scan to Scan)

Worst Case = 0.05 msec = 0.47 μrad

σ = 0.028 msec = 0.26 μrad

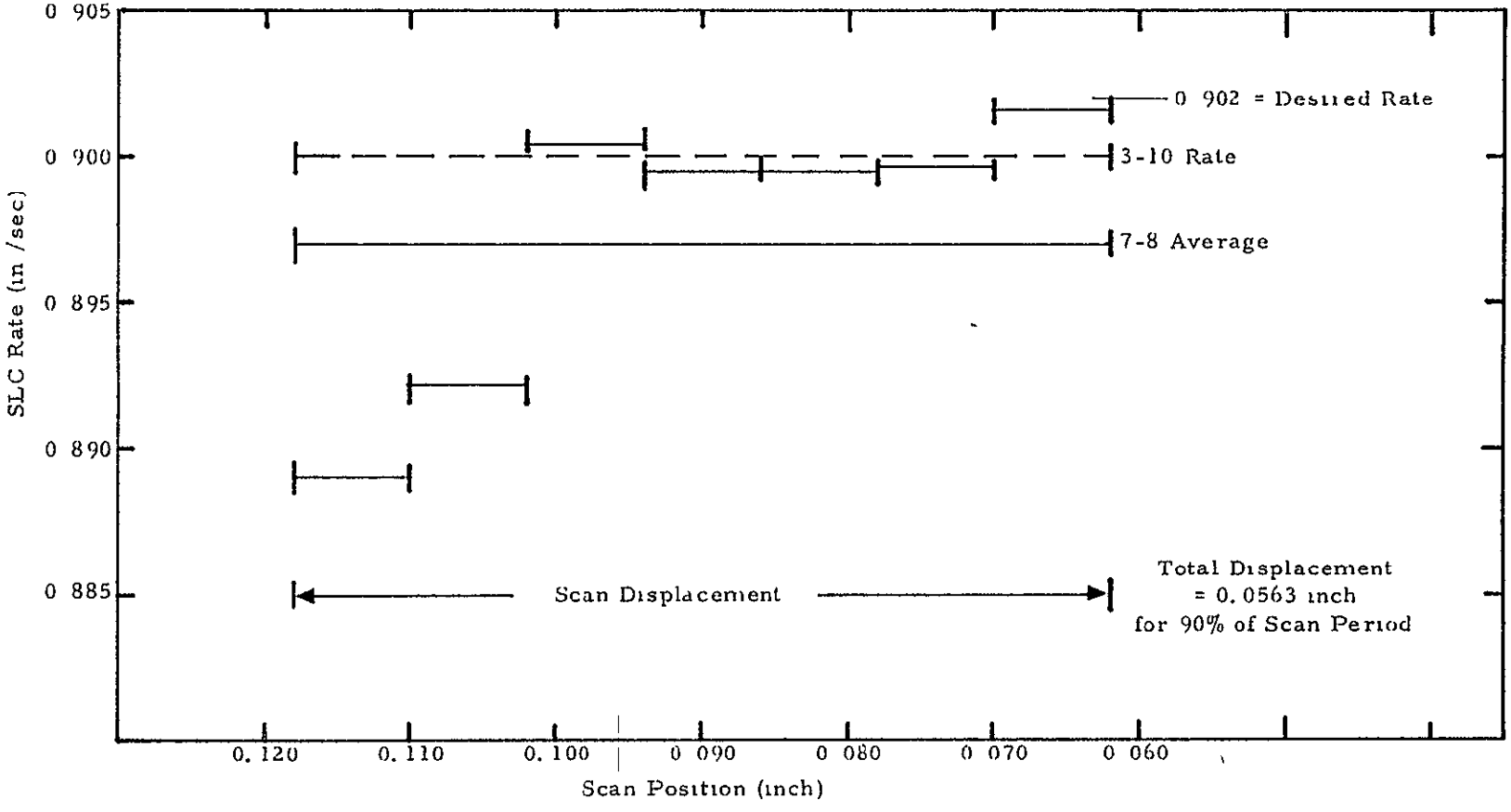

Figure 2.5-13. 14.2-Hz test data, 8 December 1975

Table 2.5-3. 19 0-Hz data summary

$2f_s$ = 19.0 Hz

T = 0.0526 sec 0.9T = 0.0474 sec

0.9 T/6 = 0.007895 sec (six equal increments)

Scan Deviation Data

Time (msec)	Rate (in./sec)	Displ (mils)	Cumulative Displ (mils)	Nominal Displ (mils)	Δ (mils)	Error % Full Scale
7.985	0.898	7.089	7.089	7.121	-0.032	0.075
15.789	0.898	7.089	14.178	14.242	-0.064	0.150
23.684	0.902	7.121	21.299	21.363	-0.064	0.150
31.579	0.9025	7.125	28.424	28.484	-0.060	0.140
39.474	0.9025	7.125	35.549	35.605	-0.056	0.131
47 368	0.900	7.105	42.654	42.726	-0.072	0.169

displacement = 42.654 mils nominal displacement = 42.726 mils

average rate = 0.9005 in./sec nominal rate = 0.902 in./sec

Repeatability

Scan to Scan (data from all six increments)

Worst Case = 0.05 msec = 0.47 μrad

σ = 0.013 msec = 0.12 μrad

30-Second Period (one frame)

Worst Case = 0.08 msec = 0.75 μrad

Average (of 10 Worst Cases) = 0.069 msec = 0.65 μrad

Scan Jitter (Scan to Scan)

Worst Case = 0 07 msec = 0.66 μrad

σ = 0.028 msec = 0.26 μrad

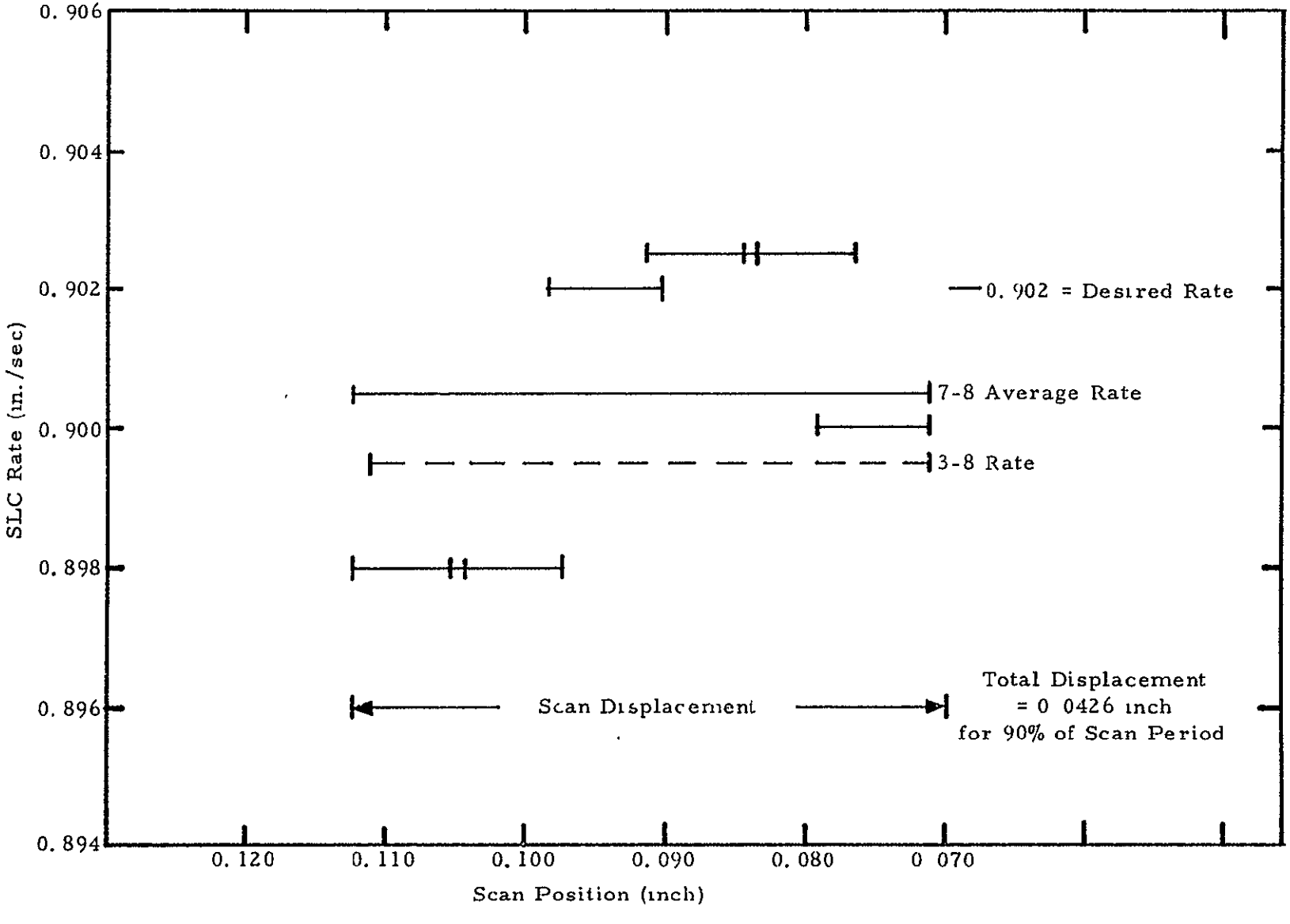

Figure 2. 5-14. 19. 0-Hz test data, 8 December 1975

3.0 SILICON PHOTODIODE ARRAY ASSEMBLY

3.1 TASK DESCRIPTION

3.1.1 Purpose

The purpose of this task was to demonstrate the feasibility of using monolithic silicon photodetector diode arrays for satisfying the performance requirements of the Thematic Mapper. The application of very low noise, high bandwidth silicon arrays in high resolution mechanical scanners had not been demonstrated and was therefore determined to be a critical element requiring breadboard development prior to a design commitment. It is the purpose of this report to briefly review the selected array/preamplifier configuration and to summarize all the test results.

3.1.2 Background

The Multispectral Scanner (MSS) which has successfully flown on Landsats 1 and 2 measures the reflected solar radiation from earth in four spectral bands covering the wavelength region from 0.5 μm to 1.1 μm. The first three bands employ six photomultiplier tubes each and the fourth band uses six discrete silicon photodiodes. The energy is collected by an array of optical fibers in the instrument focal plane and piped to the photomultipliers and silicon diodes which due to their large physical size were required to be packaged some distance away.

The goal of the Thematic Mapper is to provide improved spatial and spectral resolution as compared to the performance of the MSS, while preserving the signal to noise ratio (S/N). It was felt that this could best be accomplished by increasing the number of detectors per band (approximately 16 to 32) and by locating the detectors themselves in the focal plane to

eliminate the fiber optics losses and minimize the size and complexity of packaging between 64 and 128 discrete detectors. To mount the detectors in the telescope focal plane would require the development of monolithic detector arrays and their associated preamplifiers. In the Hughes Thematic Mapper baseline design 16 detectors per band have been estimated to meet the expected performance requirement. However, this would necessitate the development of low noise preamplifiers (approximately 3X better than the equivalent MSS performance) with bandwidths of approximately 50 kHz.

The first step in this development was the evaluation of the design, assembly and testing of a single channel hybrid detector/preamplifier which had been accomplished on an earlier contract, NAS 5-20528, which supported definition studies for an Earth Observation Satellite. This evaluation was accomplished during the first half of 1975 and reported in the final report of that contract in December 1975. The measured results of that development were very favorable with the detector responsivity being adequate and the preamplifier wideband noise (2.1 mv rms for a transimpedence amplifier with a 10^9 ohm feedback resistance, 50 kHz) in good agreement with that predicted by a computerized noise model. This performance was thereafter established as the criterion for the array. The next phase of the development was to procure a monolithic silicon detector array and test it with preamplifiers identical to the one above in a focal plane assembly (FPA). The balance of this report will describe the focal plane assembly and the measured test results.

3.2 RESULTS SUMMARY

Silicon detector arrays were purchased from EG&G and United Detector Technology (UDT) in accordance with SBRC Specification 15483 and SBRC Drawing 49788 which are included in Appendix C. Photographs of the EG&G and UDT arrays are shown in Figures 3.2-1 and 3.2-2, respectively. Each diode array contained 24 active elements and two opaque elements for the measurement of crosstalk.

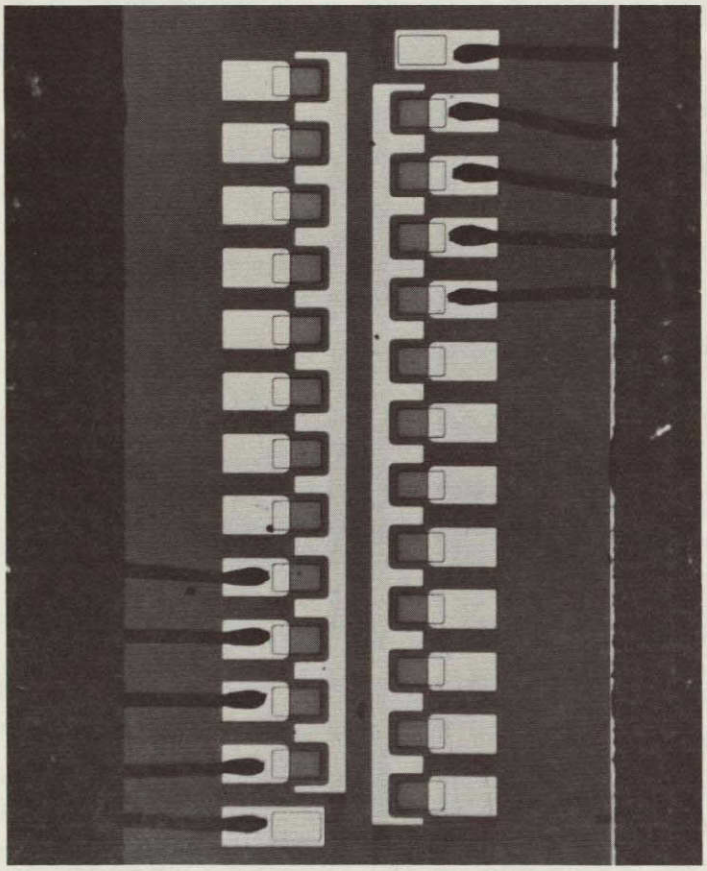

Figure 3.2-1. EG&G detector array

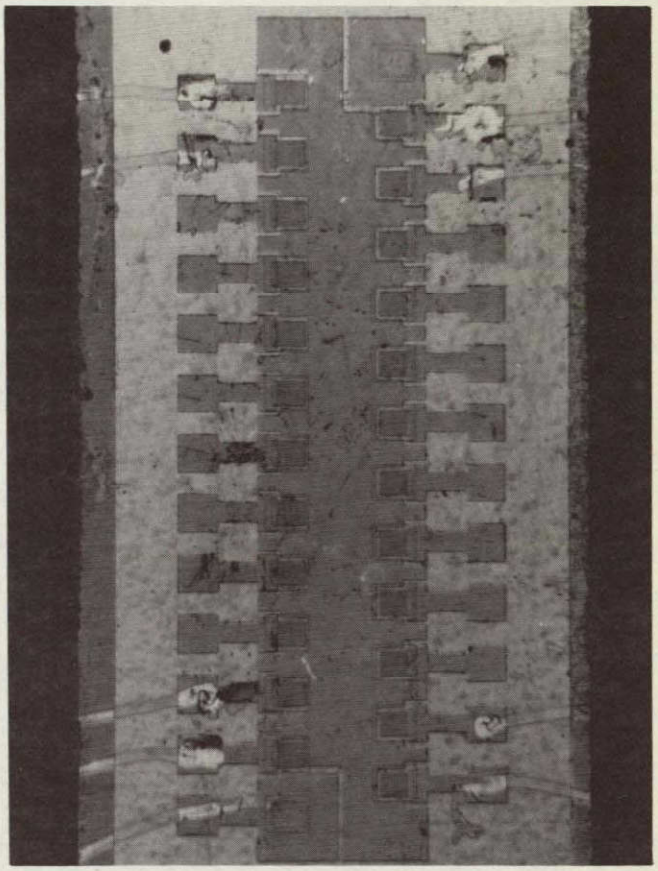

Figure 3.2-2. UDT detector array

3.2.1 Detector Tests

The diode arrays were tested for leakage current, impedance, capacitance, responsivity, and sensitivity contour prior to assembly into the FPA. The leakage current, impedance, and capacitance of both the EG&G and UDT arrays were well within the specification limits. The responsivities of each array were less than the minimum specified value. Attempts by UDT to bring up their responsivity with an antireflection (AR) coating were and continue to be unsuccessful. The EG&G device was uncoated, and it is believed that with a proper AR coating the EG&G device could easily meet the specification requirements. As an example of the potential of the EG&G array, the responsivity of a discrete EG&G device with a newly developed AR coating was measured at SBRC and is plotted in Figure 3.2-3. Both the EG&G and UDT arrays displayed an excessive amount of response to photocarriers generated in areas outside of the active area diffusion. The major cause of this stray response is due to inadequate masking. The solution to this problem appears to be the addition of an insulating layer over the complete array surface, except for the active areas, followed by an opaque metal mask or absorbing layer. Neither UDT nor EG&G have the capability to apply such a mask. Another source of stray response was due to the generation of carriers in adjacent active areas which diffused to the detector being measured. This was particularly evident in the tests of the EG&G array whose adjacent elements were left floating during the crosstalk tests. When performing this test on the UDT array, grounding the adjacent elements reduced this effect by an order of magnitude. These results are discussed later and portrayed in Figures 3.3-6 and 3.3-7. Biasing the adjacent elements would further reduce the effect to an acceptable level. Although time did not allow for the procurement of new devices with improved responsitivity patterns during this program it is believed that future array procurements can overcome these deficiencies.

3.2.2 Focal Plane Assembly Tests

The discussion that follows refers to the anticipated performance of the circuit shown in Section 3.5. Upon completion of the device related tests, the EG&G and UDT arrays were assembled into a focal plane concept which

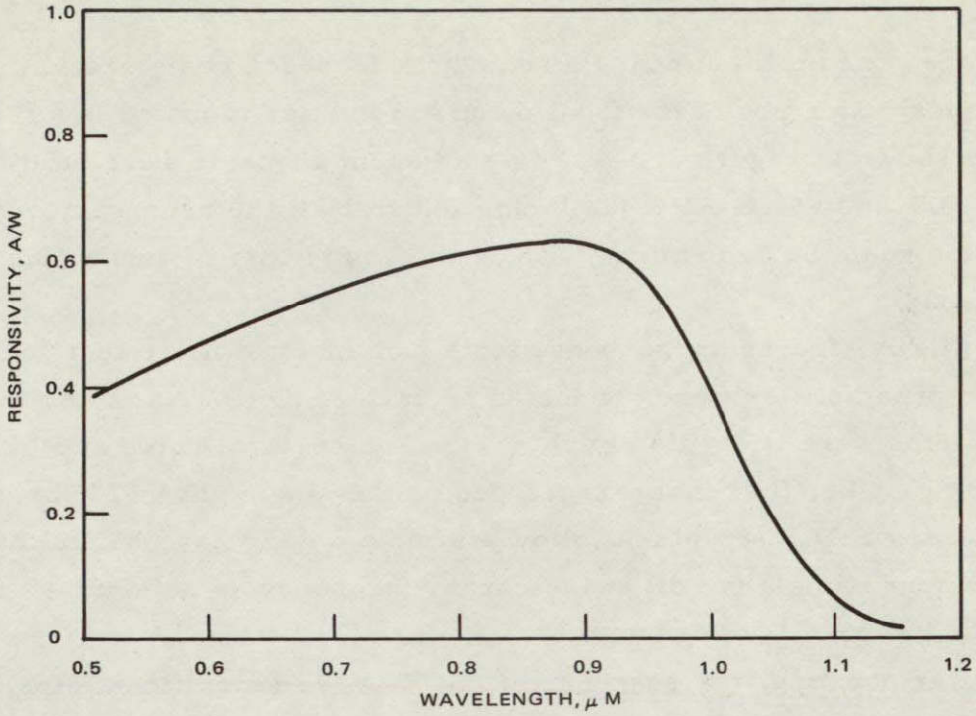

Figure 3.2-3. EG&G 0.020 inch diameter silicon detector chip responsibility Example of response from single discrete detector.

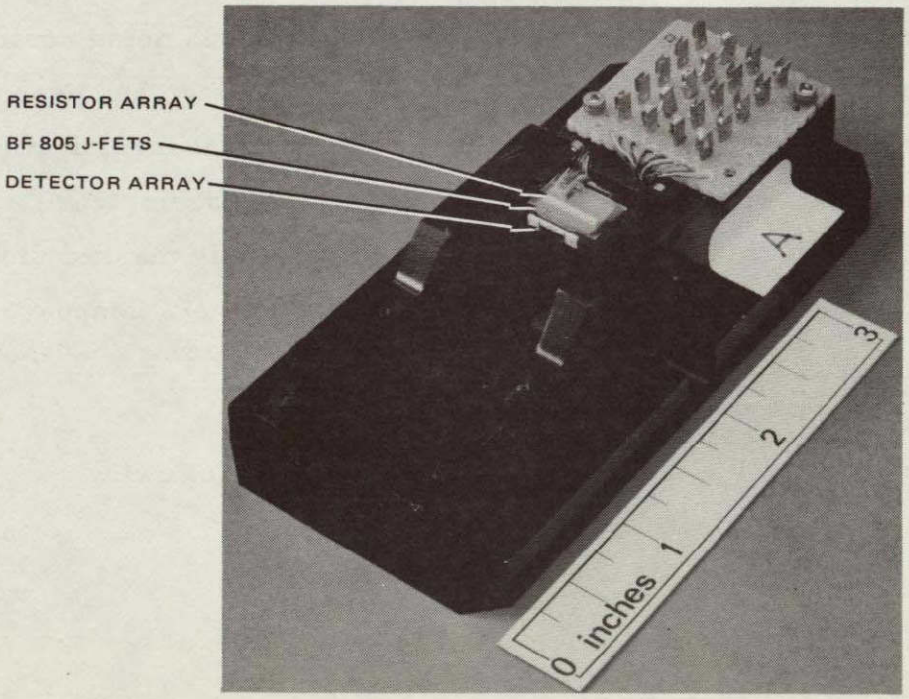

Figure 3.2-4. Focal plane assembly in test fixture

included the preamplifier input FETs and the feedback resistors. A photograph showing one of the focal plane assemblies mounted in a test fixture is shown in Figure 3.2-4. Five adjacent channels were built up in both the UDT and EG&G FPAs as it was felt that all the necessary operational information could be determined without the complexity of connecting up all of the channels.

Initially, frequency response tests and spectral noise tests of the unboosted preamplifier were conducted on each of the UDT and EG&G arrays. Two problems were immediately obvious. The spectral noise at 50 kHz was significantly higher than that experienced on the single channel hybrid device. The frequency response did not follow a simple 6 dB/octave RC rolloff, but was down approximately 8 dB at the corner frequency as determined from the eventual 6 dB/octave assymtote.

After boosting, the response of the FPAs had significant dips in the passband at the unboosted corner frequency and the wideband noise was significantly greater than the 2.1 mv predicted by the noise model and experienced by the single channel hybrid configuration. The increased noise and uneven frequency response were both attributed to the FPA layout. Attempts were made to separate the effects of the various noise contributors and layout restrictions but time did not allow for the design and assembly of a new, improved FPA configuration. From experimental investigations on this imperfect layout it is believed that by exercising extreme care a layout can be generated which, when accompanied by a properly masked diode array, will attain the performance desired for the Thematic Mapper application.

3.3 DETECTOR TESTS

The EGG and UDT arrays were checked for the following characteristics:

1) Leakage current
2) Impedance

3) Capacitance

4) Responsivity

5) Sensitivity contour

3.3.1 Leakage Current and Impedance

Leakage current and impedance were measured by making a V-I plot for each detector site. Plots were made under conditions of total darkness and sufficient illumination to produce the approximate Thematic Mapper full scale signal current (2.0×10^{-9} A). Results are shown in Figure 3.3-1 for dark and Figure 3.3-2 for illuminated detectors. Figure 3.3-1 shows the dark leakage to be well within the 30 pA allotted and the dark impedance to be about $2.5 \times 10^{11}\Omega$ for both devices. Figure 3.3-2 shows the illuminated impedance to be about $10^{10}\Omega$ for the UDT and slightly greater for EGG. The minimum specified impedance was $2.0 \times 10^{9}\Omega$.

Although Figures 3.3-1 and 3.3-2 are taken for single sites, both arrays were quite uniform from site to site.

3.3.2 Capacitance

Capacitance was measured using the circuit of Figure 3.3-3. The $1/2\pi Rf_{3dB}$ frequency was measured with and without the detector connected and an input capacitance calculated for each case according to the formula $C_{IN} = 1/2\pi Rf_{3dB}$. Results were similar for both arrays. The capacitance with the detector was 4.8 pF and without the detector was 3.8. This means the detector capacitance is about 1 pF which is the maximum specified value. This test was made for several values of V_r, the detector reverse bias voltage. No change in capacitance was observed. This is probably because the junction capacitance is quite small compared to the lead and mask capacitance.

3.3.3 Responsivity

Responsivity tests were made by comparing an array site to the response of a standard calibrated detector under the same conditions of illumination. The illuminating source was focused down to a spot

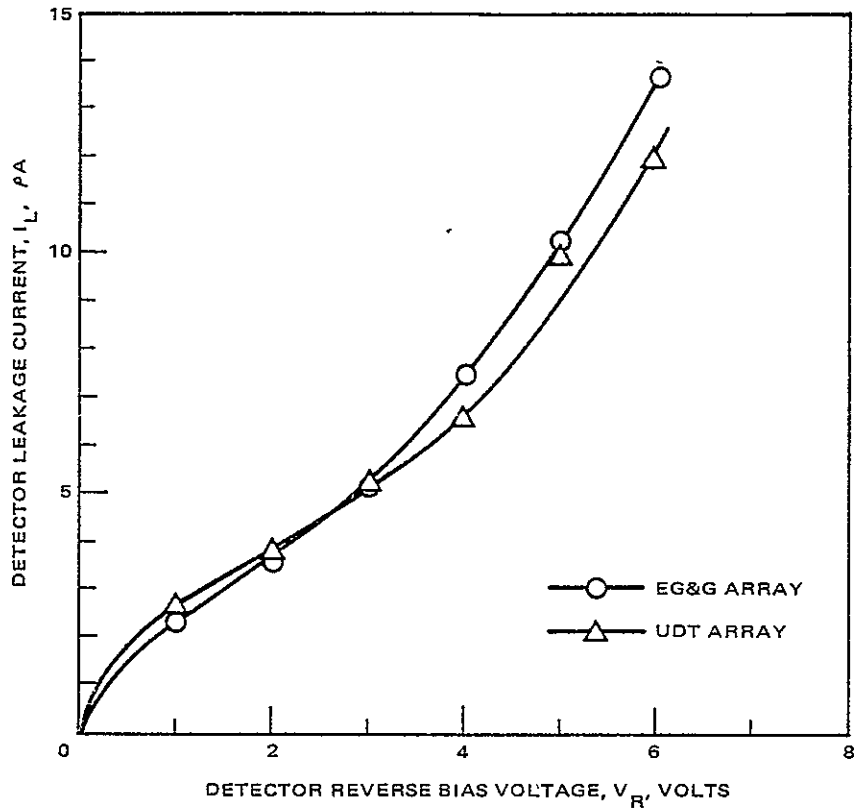

Figure 3.3-1. Dark leakage and impedance versus reverse bias

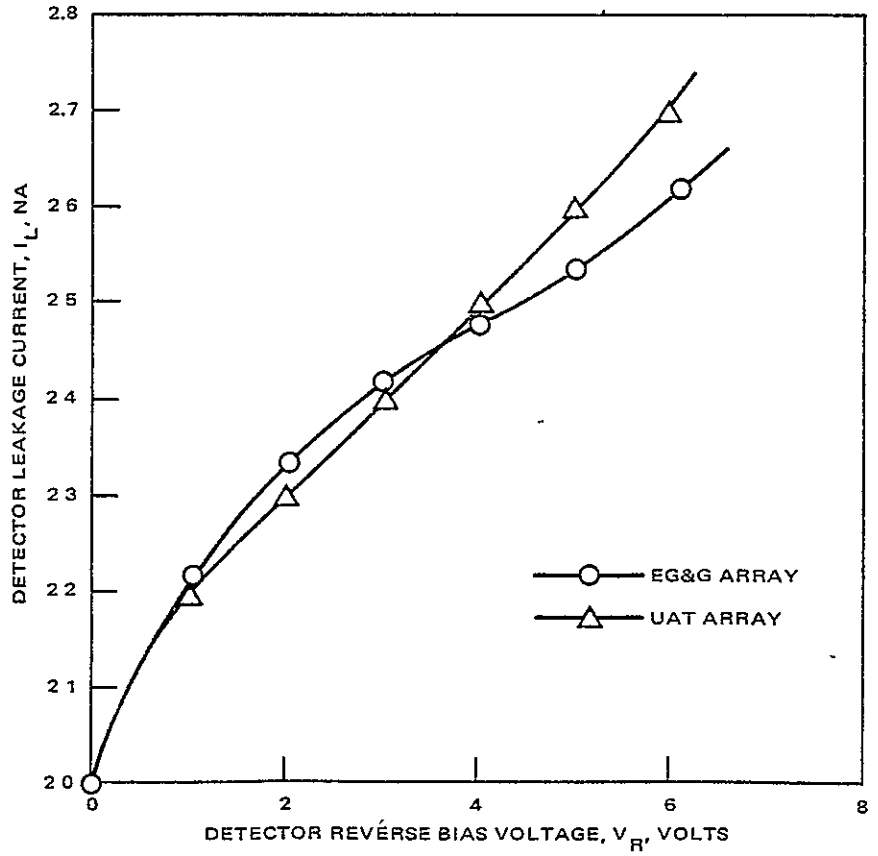

Figure 3.3-2. Illuminated current and impedance versus reverse bias

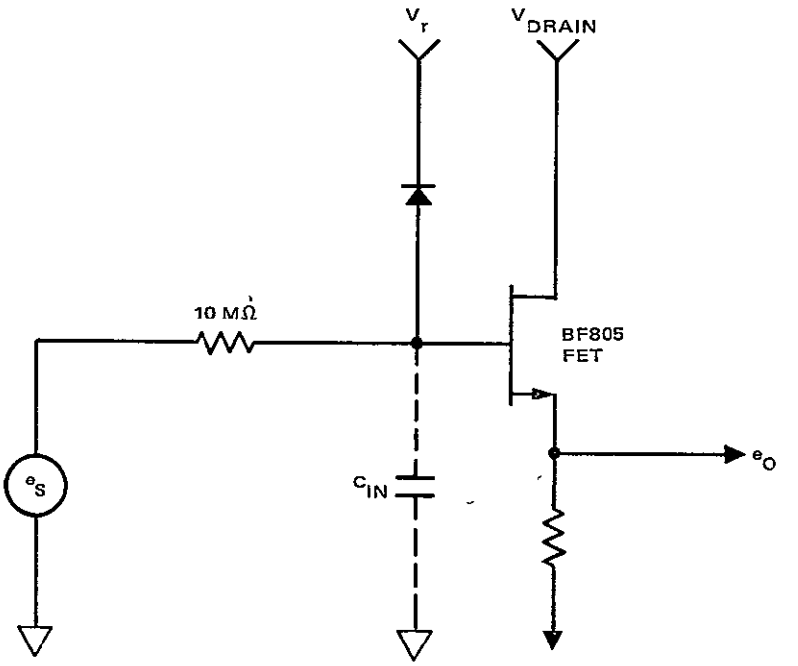

Figure 3.3-3. Capacitance measurement circuit

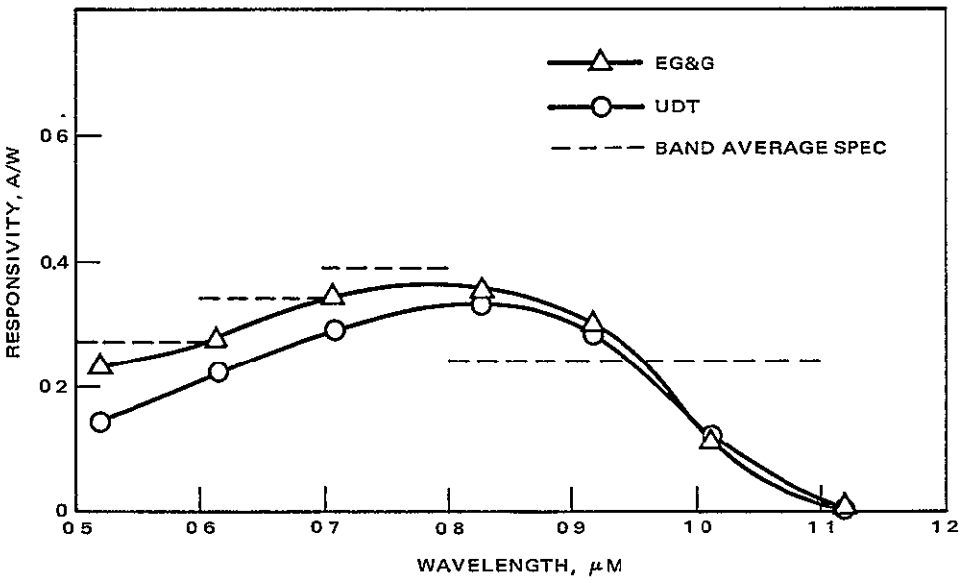

Figure 3.3-4. Detector array responsivity

approximately 0.001 inch in diameter. In this way all the energy from the illuminating source fell onto the detector surface for both the standard and test detectors. The spot size was verified by moving the array horizontally 0.001 inch at a time and recording the signal intensity. The distance between the half power points on the resulting curve of intensity versus displacement was about 0.0035 inch, indicating that the spot size was small compared to the 0.003 inch detector. Optical filters with 20 nm spectral bandwidths were used to measure the responsivity at approximately 100 nm intervals. Typical results are plotted in Figure 3.3-4. The dotted lines show the specified average responsivity within given spectral bands. Neither EG&G nor UDT met the requirement in any band, although both were confident at the start that they could. If the detectors had been masked better, it would have been easier to determine the responsivity, because the array could have been flooded with a calibrated light source and comparisons to a standard detector could have been made on the basis of area. As it is, so much light from outside the active area contributes to the signal current that it is necessary to use the focused spot which could produce errors due to scattering.

3.3.4 Sensitivity Contour

Sensitivity plots were made using the same focused spot of light. The detector array was mounted on an x-y table and intensity was plotted over the detector active area and its immediate neighborhood. The plots are shown in Figures 3.3-5 and 3.3-6. In these tests, the output current of the detector marked "lead" was monitored. The numbers on the plot are the values of current in nA produced when the light spot illuminated the locations of the number. Thus, at the beginning of the test, the light is focused onto the center of the detector being monitored. The value of the output current is written on the plot in the center of the monitored detector. Then the spot is moved to the edge or to a point outside the monitored detector and the current again recorded. The process is continued until a complete contour is obtained. Rough calculations based on these results indicate that if the

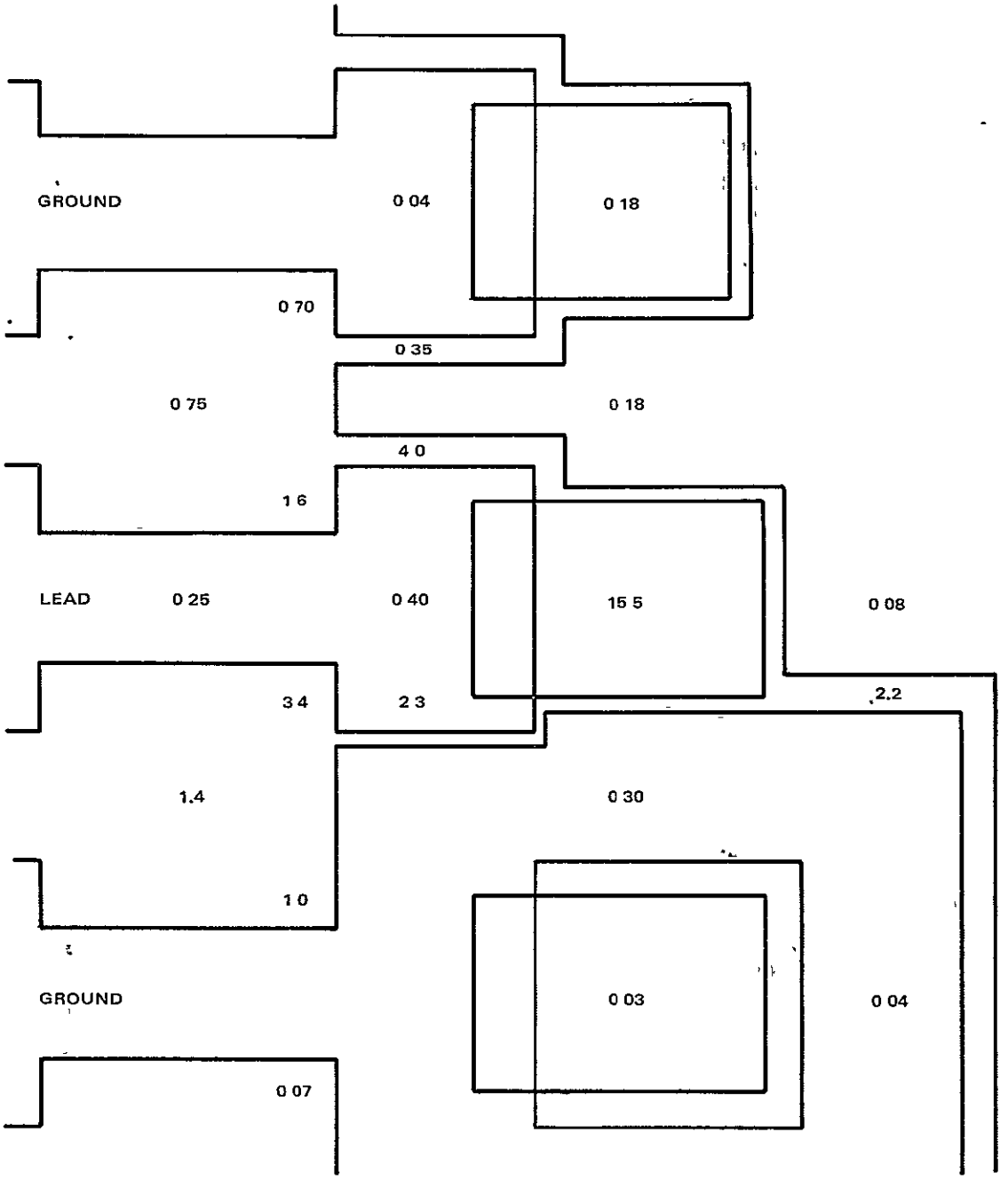

Figure 3.3-5. Relative signal output (nA) as function of position on UDT array

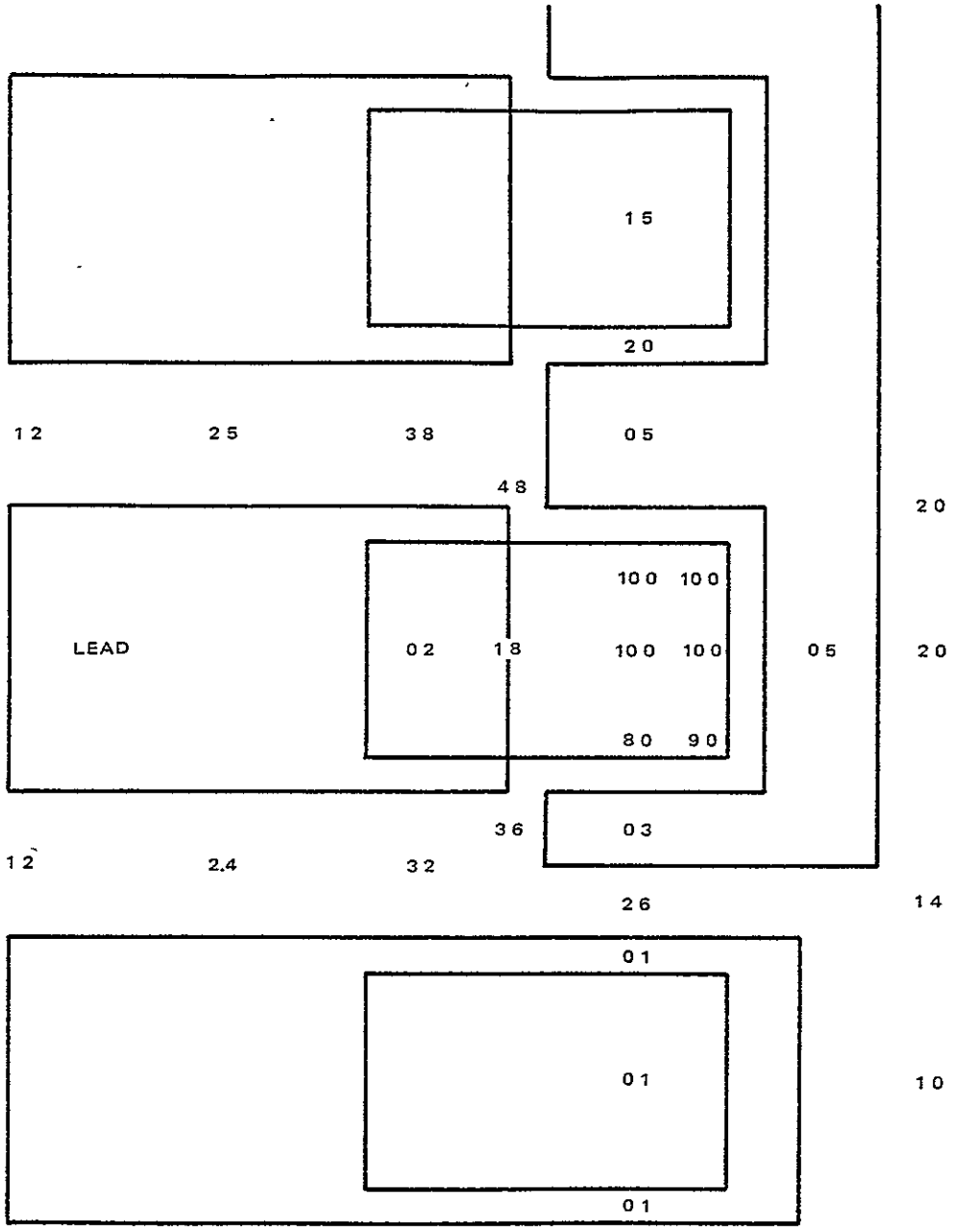

Figure 3.3-6. Relative signal output (nA) as function of position on EG&G array

array were flooded with light, about 20 percent of the signal current would be due to stray light falling outside the active area. This of course means a 1 percent crosstalk specification could not be met. The manufacturers now feel that adequate masking is not readily obtained using their available technology. The Carlsbad Division of Hughes Aircraft Company is currently under contract to SBRC to produce a detector array using multilayer processes of the type used in the manufacture of charge coupled devices. Excellent masking should be obtained with this device.

3.4 FOCAL PLANE ASSEMBLY CONFIGURATION

3.4.1 Design Requirements

The primary requirement of the FPA was to provide a means for mounting and interconnecting the detector arrays and their associated critical preamplifier components (input FET chips and $10^9\Omega$ feedback resistors) in an assembly which was a maximum of .10 inch wide in the along scan direction. This dimension was chosen as a reasonable value which if increased would make it more difficult to mount five arrays side by side in the telescope focal plane. An additional concern for the FPA design was the circuit layout and the choice of materials that would ensure a high impedance path between adjacent circuits and between all circuits and ground.

3.4.2 Major Components

The assembly consists of an aluminum frame which is used to support the electronic components and enable the mechanical attachment to an optical housing.

Sapphire amplifier boards with vacuum deposited gold circuitry are bonded to each side of the frame to provide the support and wiring for the transistor chip, resistor array, silicon diode array, and the output wiring.

A silver filled epoxy (Epoxy Technology PN EPO-TEK H20E) was used to bond the transistor chip to the amplifier board and provide the electrical connection between the gate of the FET and its circuit pad. All other parts of the assembly were bonded with an Epoxy Technology insulating material, PN EPO-TEK H54. Both materials showed excellent handling, bonding, conducting, and insulating properties.

Figure 3.4-1 shows the circuit layout, components, and wiring. Also, the released assembly and detail drawings are listed in Appendix C.

Figure 3.4-2 indicates a fixture that was designed for assembly and test of the SiPDA assembly.

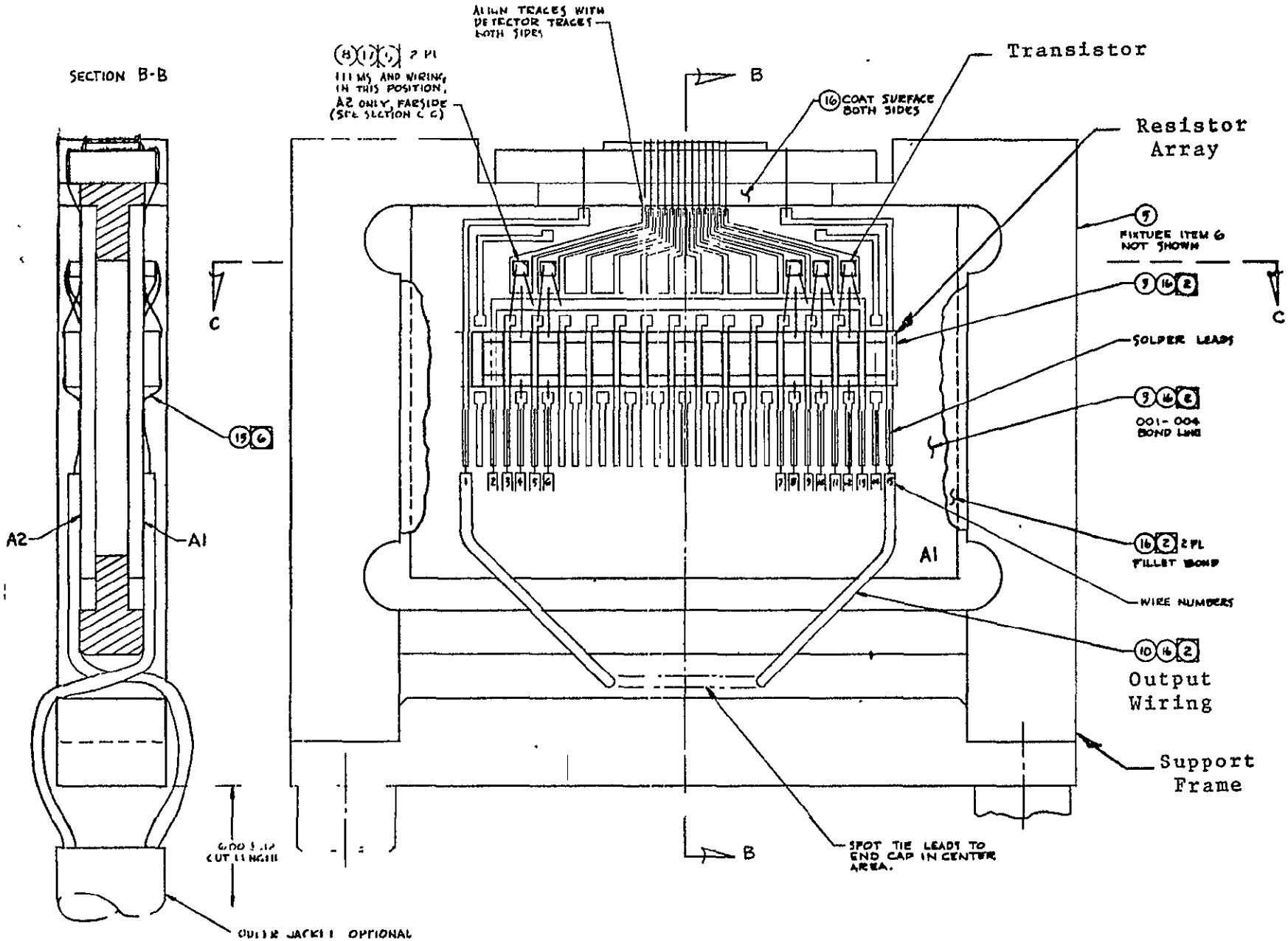
SECTION B-B
ALIGN TRACES WITH DETECTOR TRACES BOTH SIDES
(8)(17)(5) 2 PL
111 MS AND WIRING IN THIS POSITION, A2 ONLY, FARSIDE (SEE SECTION C C)
B
(16) COAT SURFACE BOTH SIDES
Transistor
Resistor Array
(9) FIXTURE ITEM 6 NOT SHOWN
(9)(16)(2)
SOLDER LEADS
(9)(16)(8) 001-004 BOND LINE
C
(19)(6)
A2
A1
(16)(2) 2 PL FILLET BOND
WIRE NUMBERS
(10)(16)(2) Output Wiring
Support Frame
SPOT TIE LEADS TO END CAP IN CENTER AREA.
OUTER JACKET OPTIONAL

Figure 3.4-1

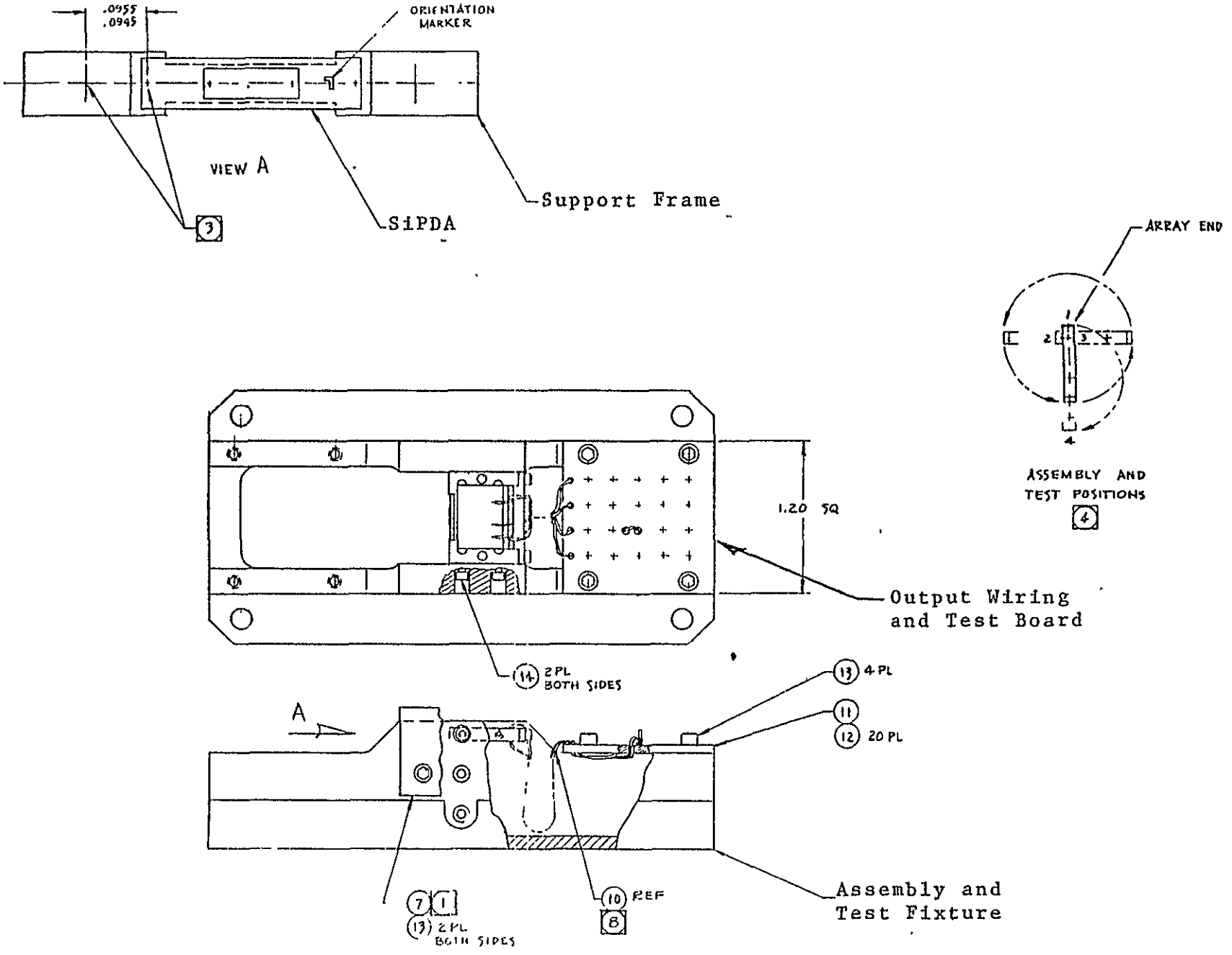
.0955
.0945
ORIENTATION MARKER
VIEW A
3
SiPDA
Support Frame
ARRAY END
1
2
3
4
ASSEMBLY AND TEST POSITIONS
4
1.20 SQ
Output Wiring and Test Board
14 2PL BOTH SIDES
13 4PL
11
12 20 PL
A
7
1
13 2PL BOTH SIDES
10 REF
8
Assembly and Test Fixture

Figure 3.4-2

3.4.3 Interconnect Wiring

The wiring between components was accomplished using a Hughes pulse bonding instrument, Model HPB 360, which is suitable for thermal compression (TC) bonding. One mil diameter gold wire was stitch bonded to each component pad to provide the connections. Weld schedules were established in all cases on samples supplied by the vendors for this purpose to ensure the integrity of each bond. The final weld schedules were such that the wire would break before the actual bond failed.

3.4.4 Output Wiring

The output wiring utilized a round multiconductor cable to facilitate the testing of the assembly.

The ultimate design would use a flat shielded cable that would allow several of the assemblies to be stacked side by side. Also, the flat cable provides better shielding and reduces crosstalk between adjacent signal channels.

3.4.5 Silicon Photodetector Diode Array

The array shown in Figure 3.4-3 contains 26 elements for this design of which two end elements are used for crosstalk measurements between adjacent channels. The detectors are layed out in a staggered geometry to provide contiguous scan lines with acceptable crosstalk between adjacent detector channels. Future designs may require only 16 active elements per assembly plus two crosstalk elements, allowing 8 spare channels.

Minor changes will be required in the layout in that experience gained in the assembly techniques has indicated means for improving the design. The changes are as follows:

1) Two vendors supplied array assemblies for this contract: UDT and EG&G.

2) Assembly personnel at SBRC were able to weld directly to the array substrate, therefore eliminating additional jumpers to the common substrate. This is desirable for the reason that reliability is improved because of fewer weld joints. The change

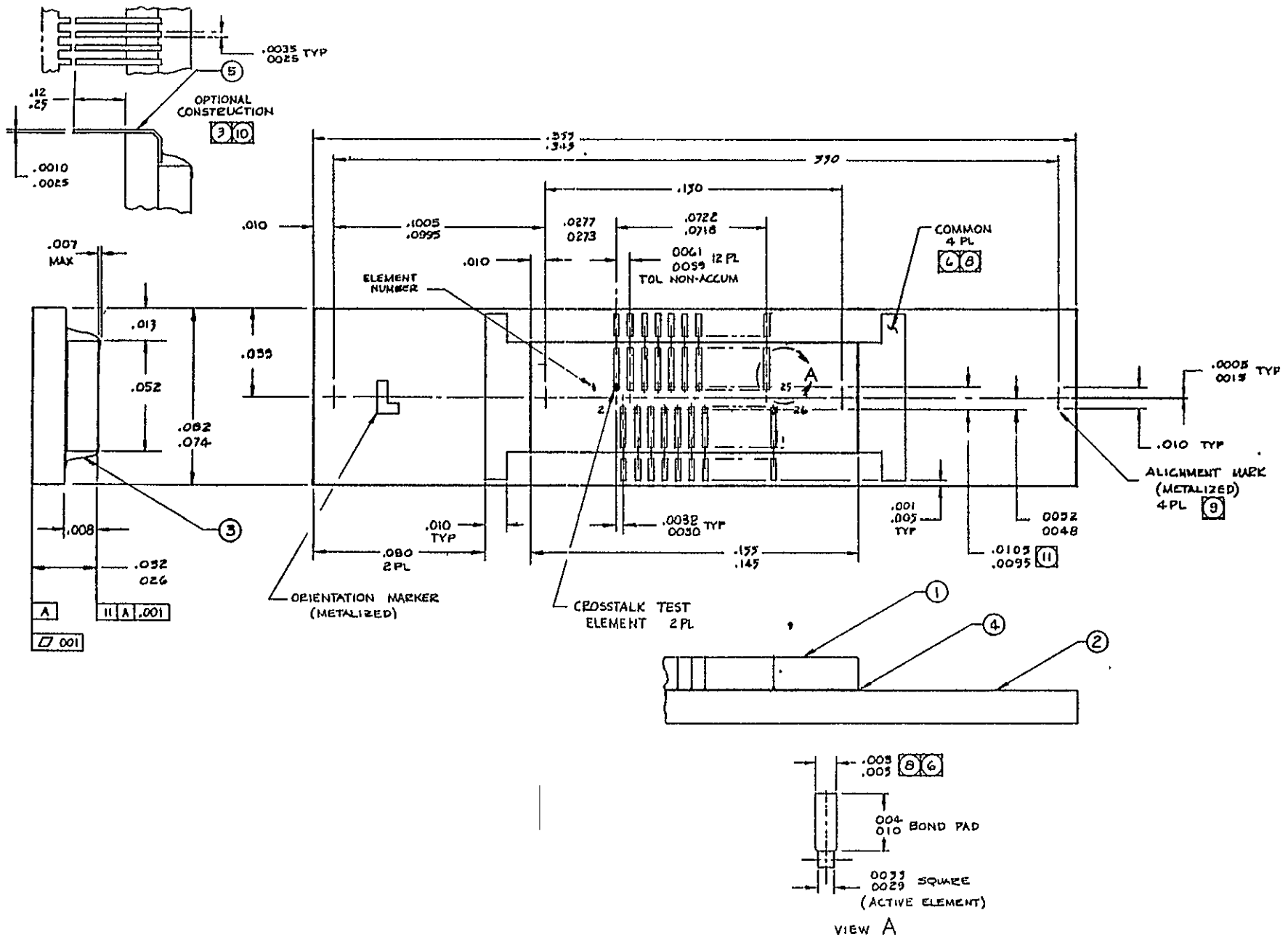
.0035
.0025 TYP
5
.12
.25
OPTIONAL
CONSTRUCTION
3 10
.0010
.0025
.357
.343
330
.130
.010
.1005
.0995
.0277
.0273
.0722
.0718
.010
.0061
.0059 12 PL
TOL NON-ACCUM
COMMON
4 PL
4 8
.007
MAX
ELEMENT
NUMBER
.013
.052
.055
.082
.074
A
25
26
2
1
.0005
.0015 TYP
.010 TYP
ALIGNMENT MARK
(METALIZED)
4 PL 9
.008
3
.010
TYP
.0032
.0030 TYP
.080
2 PL
.155
.145
.001
.005
TYP
.0052
.0048
.0105
.0095 11
.032
.026
A
11 A .001
.001
ORIENTATION MARKER
(METALIZED)
CROSSTALK TEST
ELEMENT 2 PL
1
4
2
.003
.005 8 6
.004
.010 BOND PAD
.0033
.0029 SQUARE
(ACTIVE ELEMENT)
VIEW A

Figure 3.4-3

would mean increasing the width of the array substrate to provide a more optimum "Fan-Out" of the detector bonding pads on its surface. This would be accomplished without increase in the overall width of the package.

The wider array would also facilitate handling. The bonding of the array to the support frame and the wiring was otherwise successful.

3.4.6 Resistor Array

The resistor array containing 15 resistive elements of 10^9 ohms each (2 spares) was successfully integrated into the assembly (see Figure 4.3-3 for layout). A design change however may be incorporated to increase the size of the array for future systems for the following reasons:

1) To allow a larger centerline spacing between elements.
2) Provide areas for trimming the resistors to the drawing requirements (the delivered resistances were 10^9 + 100 percent, - 50 percent).
3) To enhance the design so that other vendors will respond for procurement. Only one responded for the present contract (ELTEC).
4) To facilitate handling and tests because of the larger size.
5) To allow minimization of undesirable effects due to distributed capacitance along the feedback resistor to the common substrate and to other resistors.

3.4.7 Conclusions

The conceptual studies in this phase of the program have provided an insight into the feasibility of the SiPDA assembly. The integration of state of the art devices will allow the packaging to be accomplished effectively. The density and associated reliability features have been

improved by a significant factor over the earlier MSS and VISSR detector packaging designs. The completed design integrated with the final mechanical configuration shows promise of being a highly reliable and maintainable system. A complete set of drawings for the FPA is included in Appendix C.

3.5 AMPLIFIER CIRCUIT

The preamplifier schematic is shown in Figure 3.5-1. It is divided into three sections: a preamplifier, boost amplifier, and low pass filter. A current mode preamplifier is used to reduce electrical crosstalk at the input. Because of the close spacing of the detectors within the array, there will be some capacitive coupling between adjacent detector output leads. The magnitude of a signal coupled across this capacitance at a given frequency depends on the magnitude of the source signal and the impedance of the sending and receiving modes. Figure 3.5-2 shows a crosstalk model for voltage and current mode circuits. Taking some typical values, C_f = .05 pF, C_c = .05 pF, K = 1000, C_{in} = 5 pF, the model gives 0.1 percent crosstalk in the current mode case and 1 percent in the voltage mode.

The current mode amplifier frequency response typically extends to 3 to 5 kHz, using a 1 X $10^9\Omega$ feedback resistor, whereas the voltage mode amplifier can roll off as low as 30 Hz. Thus, in the current mode a boost factor of about 10 is required instead of 100.

The preamplifier itself is divided into two parts. The input stage is located adjacent to the detector on the focal plane and the remainder is located some distance away. This division is made since it is desirable to have the preamplifier as close as possible to the detector to minimize pickup and input capacitance, but there is not room for the complete preamplifier at the detector array.

The input stage should provide a low output impedance to reduce pickup along the cable to the remainder of the preamplifier and should be as simple as possible to allow packaging within the immediate neighborhood of the detector array. Also power dissipation must be minimized so as not to

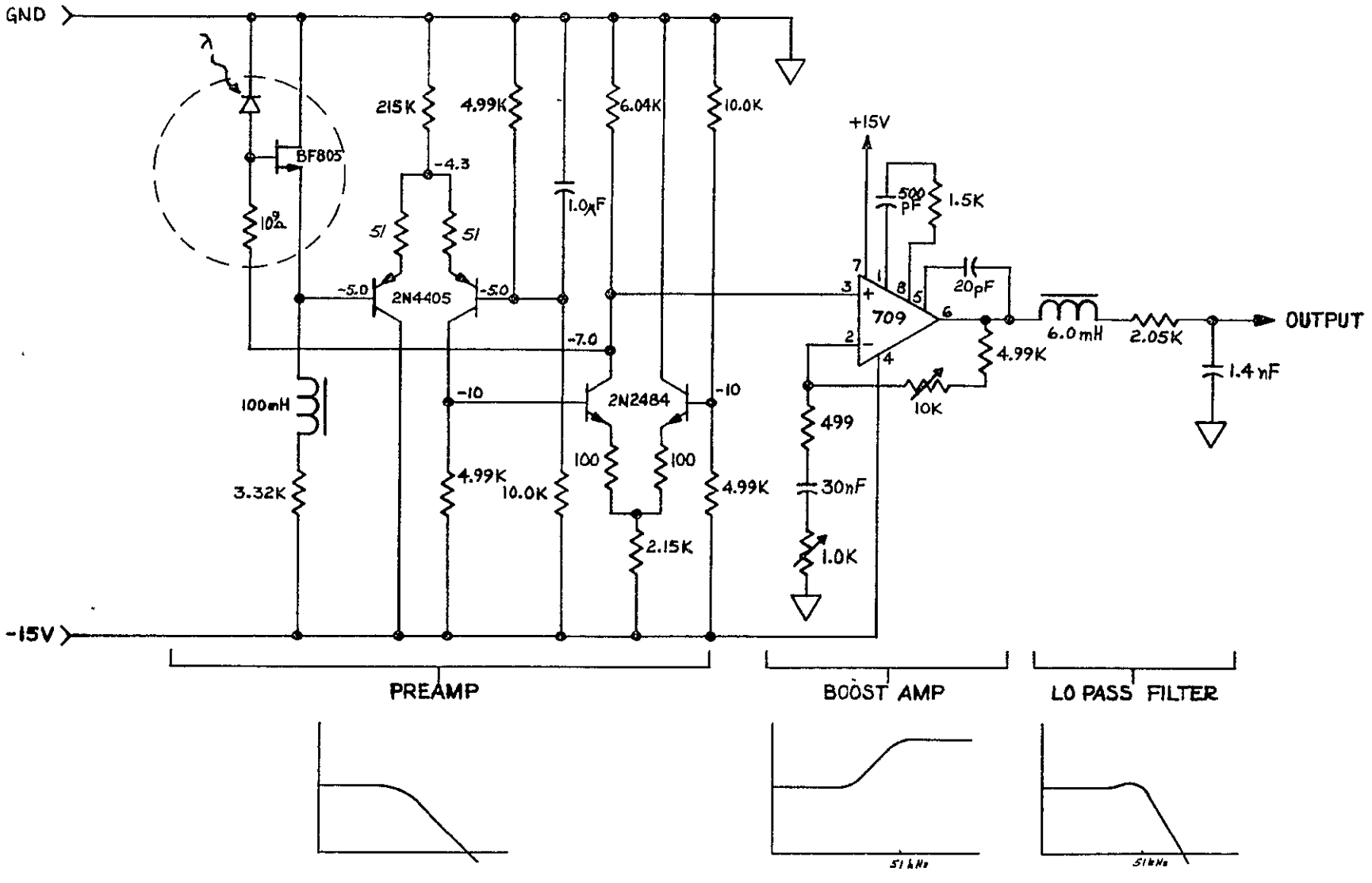

Figure 3.5-1. Detector/amplifier schematic diagram

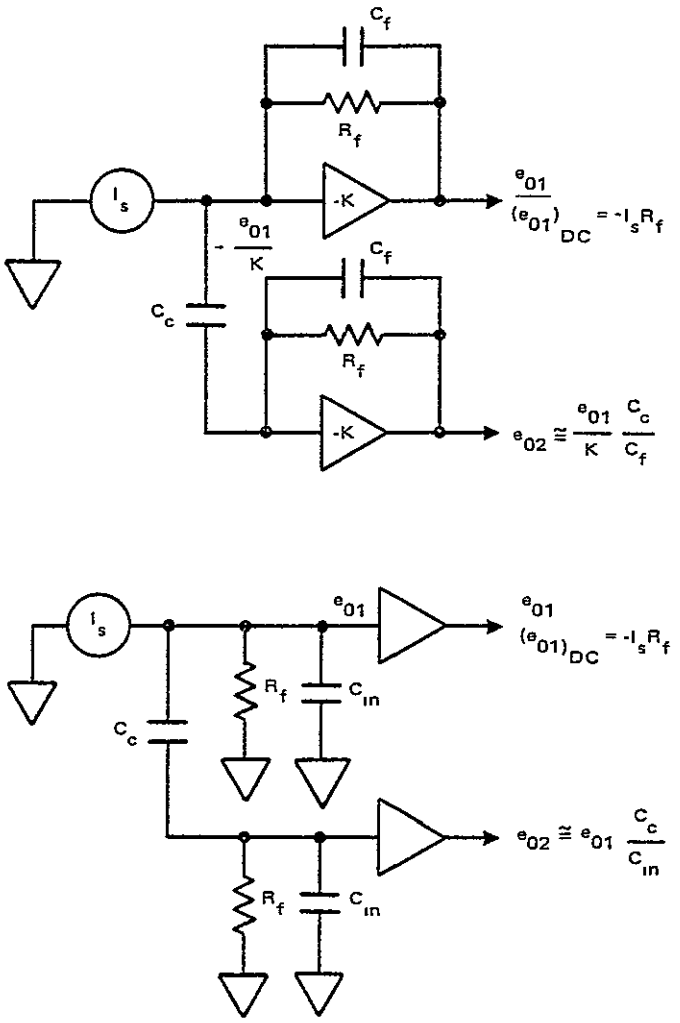

Figure 3.5-2. Crosstalk in adjacent current and voltage mode channels

increase the temperature more than about 20°C above ambient. As the temperature increases, transistor and detector leakage currents increase and become significant noise contributors. It is difficult to design a package to remove a great deal of heat and still maintain low capacitance to ground, therefore low dissipation is important.

A single FET source follower seemed to satisfy all these requirements best. It has the disadvantage that there will be some second stage degradation of the input FET noise voltage. For the circuit shown, there is second stage noise generated by the $\bar{e}_n$ of the differential bipolar pair (0.70 nv/$\sqrt{Hz}$ each) and the thermal noise of the two 50Ω resistors (0.91 nv/$\sqrt{Hz}$ each). This gives an rss total of 1.62nv/$\sqrt{Hz}$. Since the FET source follower gain is typically 0.92, this noise must be multiplied by 1.08 to refer it to the preamplifier input. The result is that the 2.4 nv/$\sqrt{Hz}$ FET $\bar{e}_n$ is degraded by about 24 percent by the second stage. This is acceptable since $\bar{e}_n$ is not the dominant noise source for frequencies below about 200 kHz. The 3-pole Butterworth filter at 50 kHz has rolled the noise off almost 40 dB by 200 kHz. (See Section 3.6.2 for details of noise.)

The closed loop frequency response of the detector-preamplifier rolls off anywhere between 2 and 10 kHz, depending on the particular layout. The boost amplifier following the preamp has the transfer function shown in Figure 3.5-1 to provide a rising response to compensate the preamplifier's falling response out to 52 kHz. The combined preamplifier and boost amplifier response will then be approximately flat from dc approaching 50 kHz, down 3 dB at 52 kHz and rolling off at 20 dB/decade for frequencies >>50 kHz. The signal and noise levels are sufficiently high at the preamp output that no measurable noise is added due to the boost amplifier. Another way to say this is that the signal to noise ratio is determined at the preamplifier output and signal and noise are amplified and filtered equally in the following stages.

The LRC filter at the boost amplifier output provides two complex conjugate poles which, acting with the 52 kHz real pole in the boost amplifier, generate a 3-pole Butterworth filter response at 52 kHz.

3.6 AMPLIFIER SIGNAL AND NOISE TESTING

Tests of the completed focal plane array indicated two major difficulties; the high frequency noise was excessive and the frequency response was not such that it could be boosted by means of a simple RC filter to produce a flat response to the desired corner frequency of 52 kHz. Also the signal response rolled off much earlier than was expected based on tests of the individual detector hybrid circuits completed earlier.

3.6.1 Frequency Response Measurements

Figures 3.6-1 and 3.6-2 show plots of unboosted and boosted frequency response for several channels using the UDT detector array connected into the focal plane assembly (FPA) package. It is seen that the unboosted response is down anywhere from 6 to 8 dB at the corner frequency which causes a 3 to 5 dB sag in the boosted response around the unboosted corner frequency. The opposite of this effect was observed during the earlier single detector hybrid testing where the unboosted response was down only 2 dB at the corner, resulting in a +1 dB response in the boosted response at the unboosted corner frequency. The effect is attributable to two causes. One is stray capacitance from the feedback resistor to ground and to the FET source lead acting with the feedback resistor shunt capacitance. The two capacitances produce a complex pole pair in the frequency response which may have a damping factor greater or less than unity depending on their relative magnitudes. By making further tests with identical components in various layouts, the dependency of this effect on layout was demonstrated. Figure 3.6-3 shows the response of a UDT detector array from the same lot connected in the same circuit, but mounted in a flat planar configuration on a sapphire "sunburst" substrate. This layout used a chip feedback registor, rather than one of the array resistors. This signal response is down 3 dB at the 7 KHz unboosted corner, although it appears to have a small amount of sag in the 2 to 5 KHz area. This is probably due to the second of the causes, namely detector secondary time constants. A non-ideal detector frequency response can be produced if the modulated signal light energy strikes the detector chip outside its active area. Thus if several hole-electron pairs

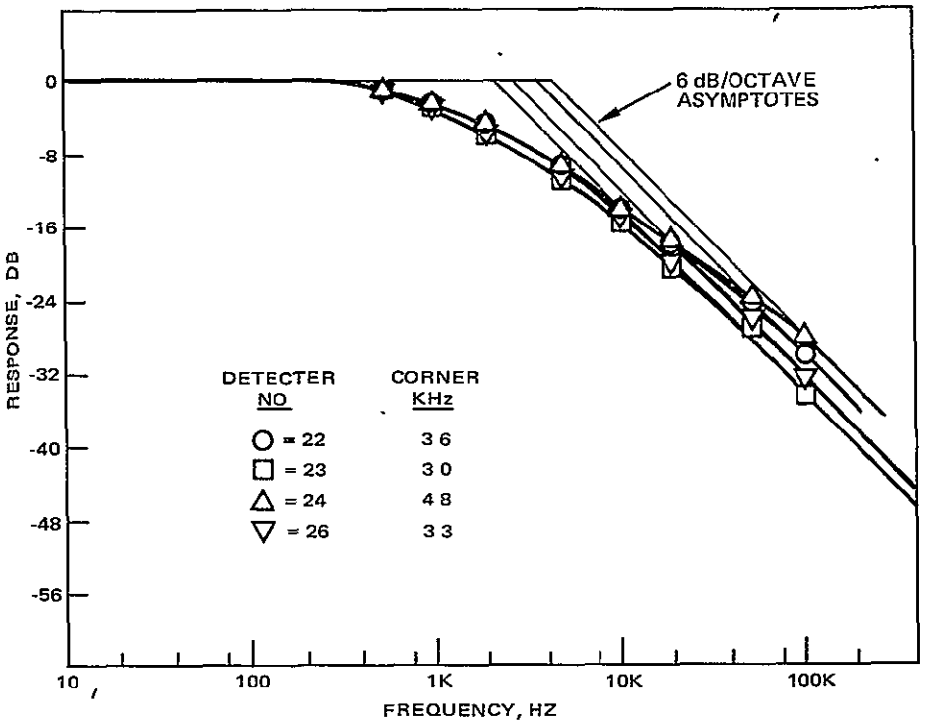

Figure 3.6-1. UDT array unboosted response

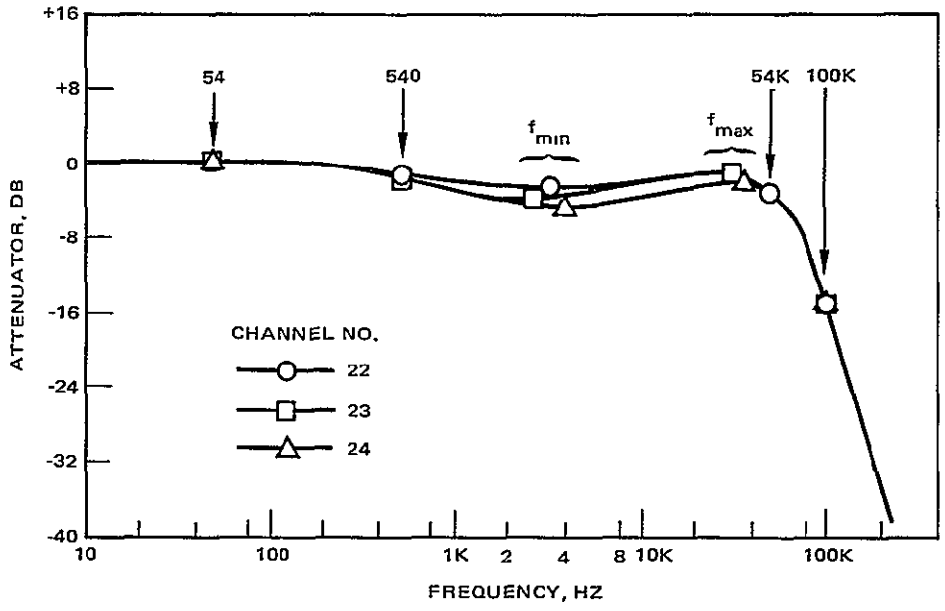

Figure 3.6-2. UDT array boosted response

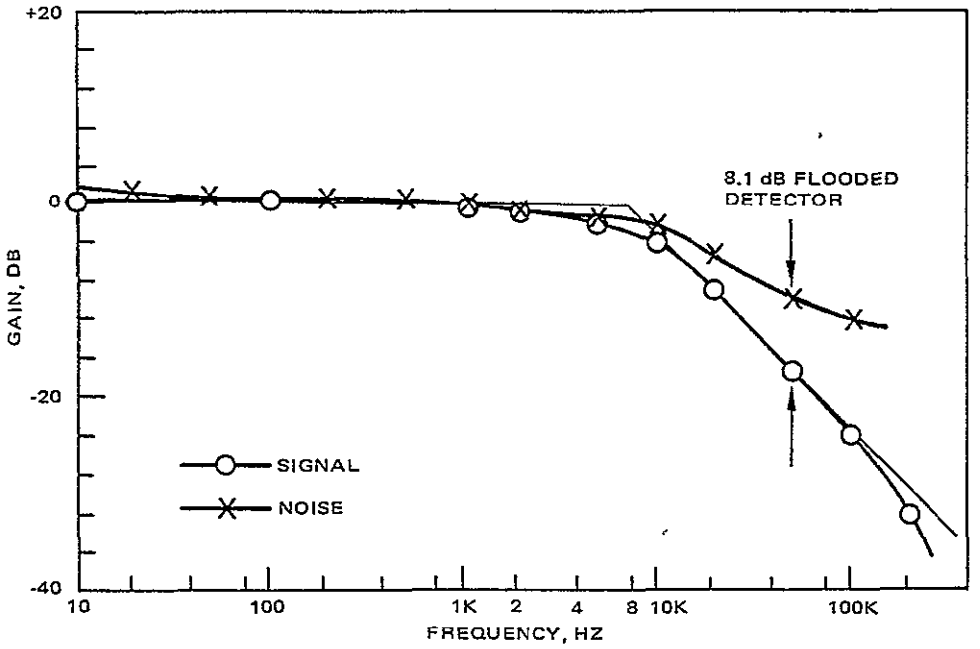

Figure 3.6-3. Signal response improvement using planar layout

are produced some distance from the junction, a few will diffuse into the depletion under the effect of their concentration gradient. This requires some time, so that if the number of carriers produced outside the depletion region becomes comparable with the number produced inside, then a "secondary time constant" in the step response is produced which leads to the frequency response shown in Figure 3.6-4. The dotted lines show the curves as they would be if the inactive chip areas were perfectly masked. The extent of the spurious response depends on the ratio of exposed inactive to active chip area and the incident energy pattern. To determine the presence of absence of this effect, a test setup is being constructed that can focus the modulated light intensity into a small spot about the size of the detector. Results are not available at the time of this writing, but improvement is expected based on the contour plots made earlier on the UDT array. These showed about 20 percent of the low frequency signal current was due to energy falling outside the active area. It is reasonable to expect that some "destructive interference" due to phase shift would occur at or below 50 kHz.

To summarize, it is expected that the frequency response problem can be solved by careful amplifier layout to reduce stray capacitance and by improved detector masking.

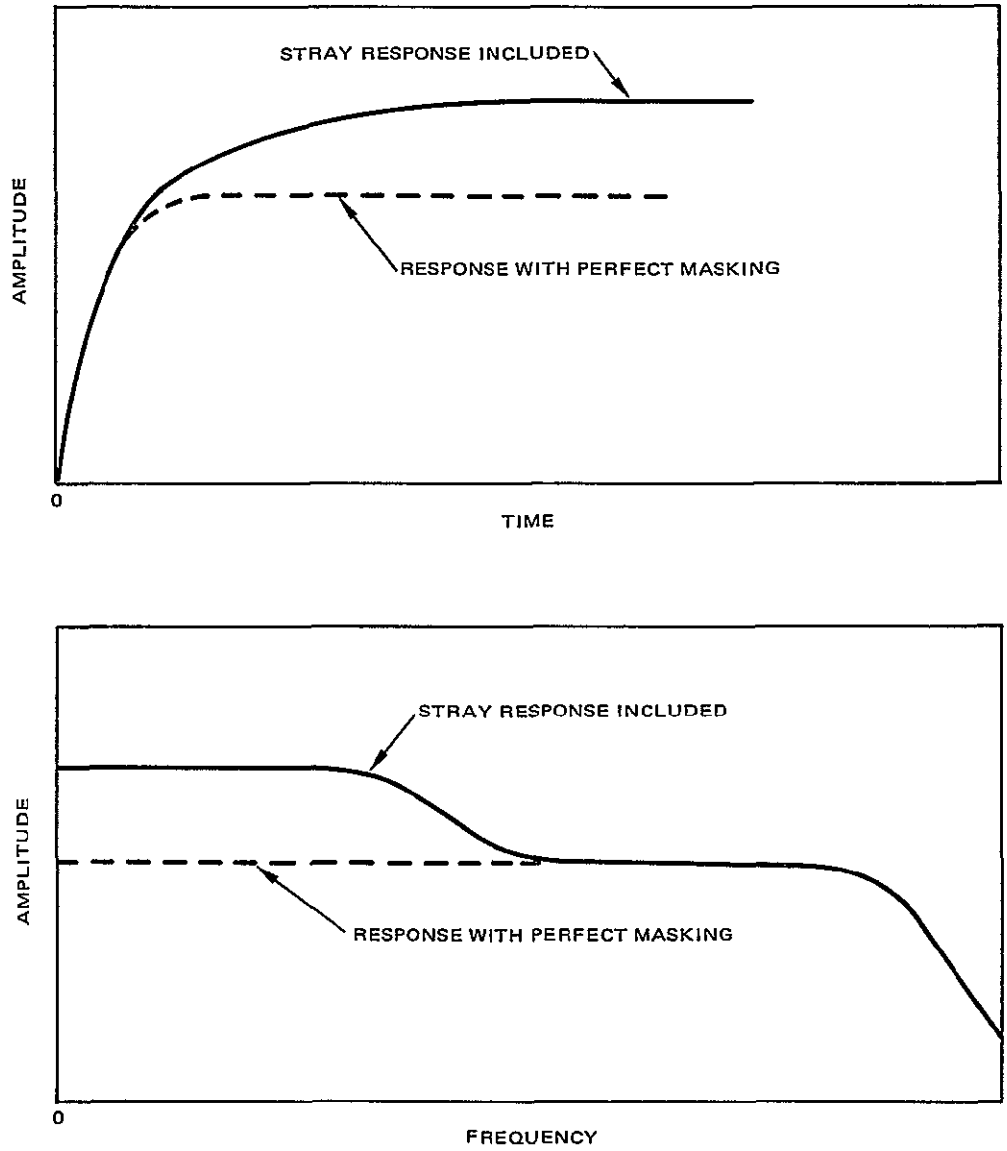

Figure 3.6-4. Detector secondary time constant and frequency response

3.6.2 Noise Model

The various noise sources are plotted in Figure 3.6-5 for the following assumed parameters which are worst case specification values:

Parameter	Symbol	Value
Amplifier Input Noise Voltage	$\bar{e}_n$	$3nV/\sqrt{Hz}$
Feedback Resistor Thermal Noise Voltage	$\bar{e}_r$	$4.05\ \mu V/\sqrt{Hz}$
Amplifier Input Noise Current	$\bar{i}_n$	$6 \times 10^{-16}\ A/\sqrt{Hz}$
Input Capacitance	C_{in}	5 pF
Dielectric Loss Tangent	$\tan \delta$	.003
Detector Leakage Current	I_D	30 pA

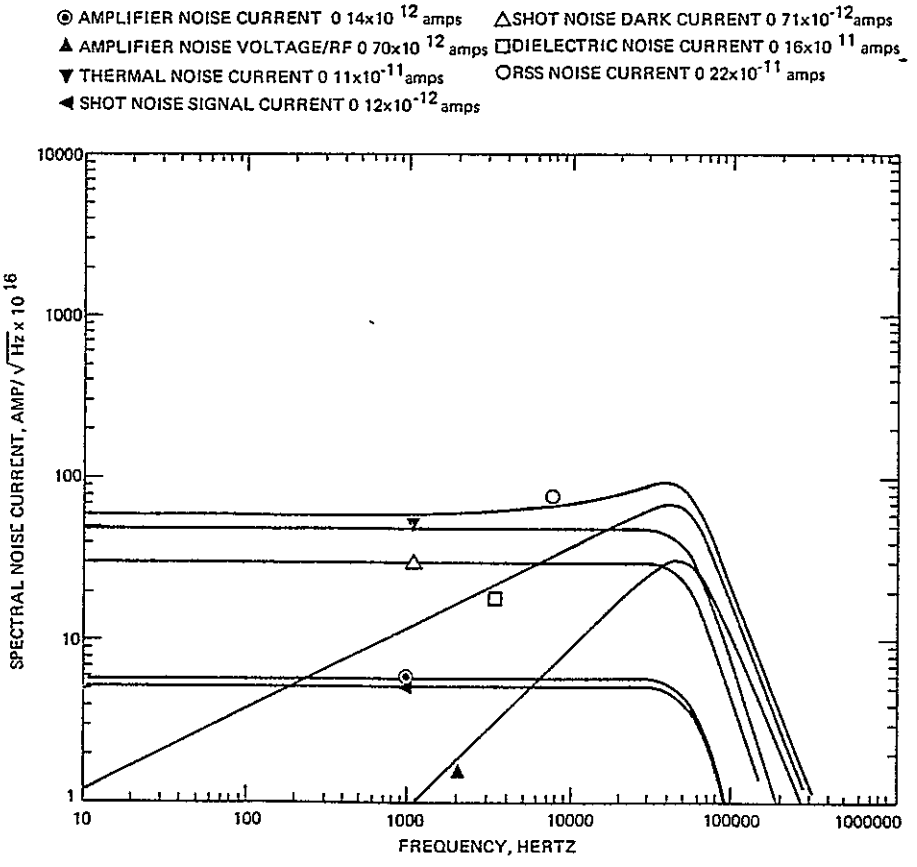

Figure 3.6-5. Rss noise currents versus frequency with boost

Figure 3.6-5 and previous calculations show that for these assumed parameters the spectral noise should be up 6 dB about the thermal noise of the feedback resistor at 50 KHz. Low frequency (zero signal) noise is due primarily to the feedback resistor thermal noise. The high frequency noise boost is due to dielectric loss resistance noise current which increases with frequency at the rate of 10 dB/decade, and to $\bar{e}_n$ boost which increases with frequency at the rate of 20 dB/decade. In the noise model, these two components are equal at approximately 200 kHz with the dielectric loss resistance noise dominating below 200 kHz.

3.6.3 Noise Tests

The various sources in Figure 3.6-5 are shaped by a 3-pole Butterworth filter at 54 KHz, then summed (rss) to form a composite curve. A noise integration (neglecting the signal shot noise) shows the wideband noise to be about 2.1 mv. Wideband noise tests on the hybrid circuits, reported a previous document, agreed well with this calculated value and had a basically flat frequency response. All efforts to date have been unsuccessful in duplicating this result using the array detectors with the focal plane assembly or other modified assemblies.

Results seem to vary considerably depending on the detector array, the channel within the array, and the type of layout. In general there are two problems. The first is that each individual channel operating by itself is too noisy, and the second is that all the channels operating together are even noisier.

Considering the first problem, although wideband noise measurements have been obtained as low as 2.4 mv on FPA channels, a more typical single channel value is 3.3 mv. Figures 3.6-6 and 3.6-7 show data taken on a UDT array channel where the original FPA layout was modified to move the source lead away from the feedback resistor. The wideband noise in this channel was 2.5 mv. The layout modification is shown in Figure 3.6-8. The idea was to build a channel fairly well removed from the others, and to locate the FET source output trace away from the feedback resistor. The wideband noise was not bad. The spectral noise is up about 8 dB above thermal noise at 50 KHz, instead of the desired 6 dB. However,

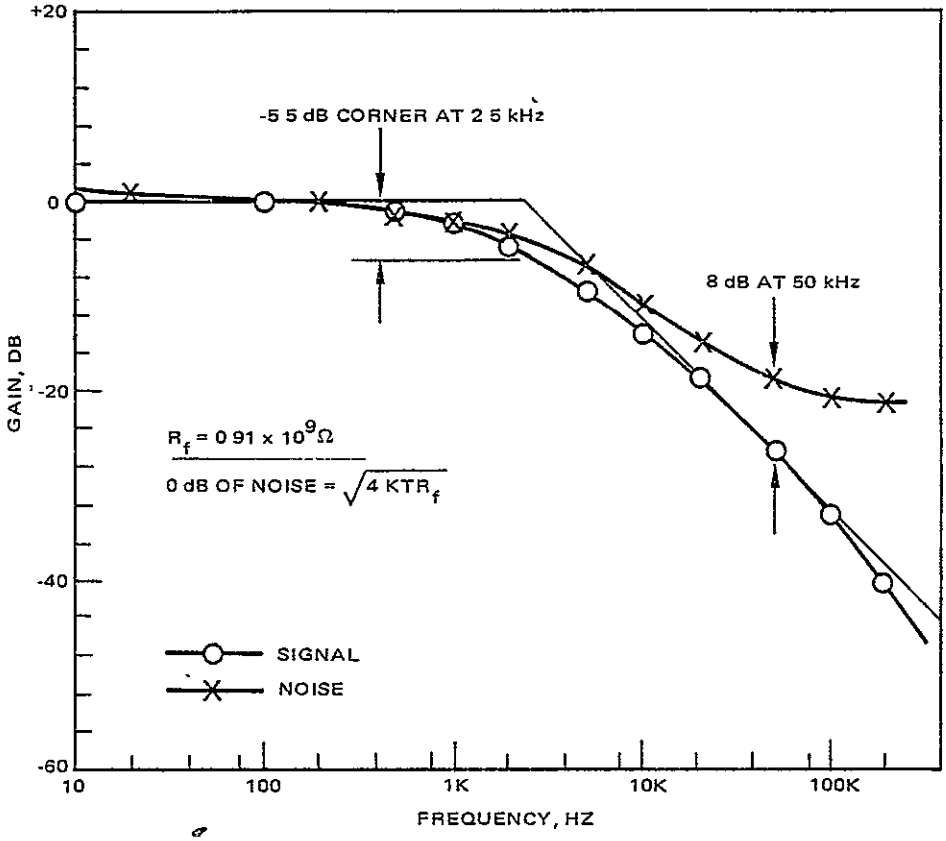

Figure 3.6-6. UDT FPA single channel unboosted response, layout modified

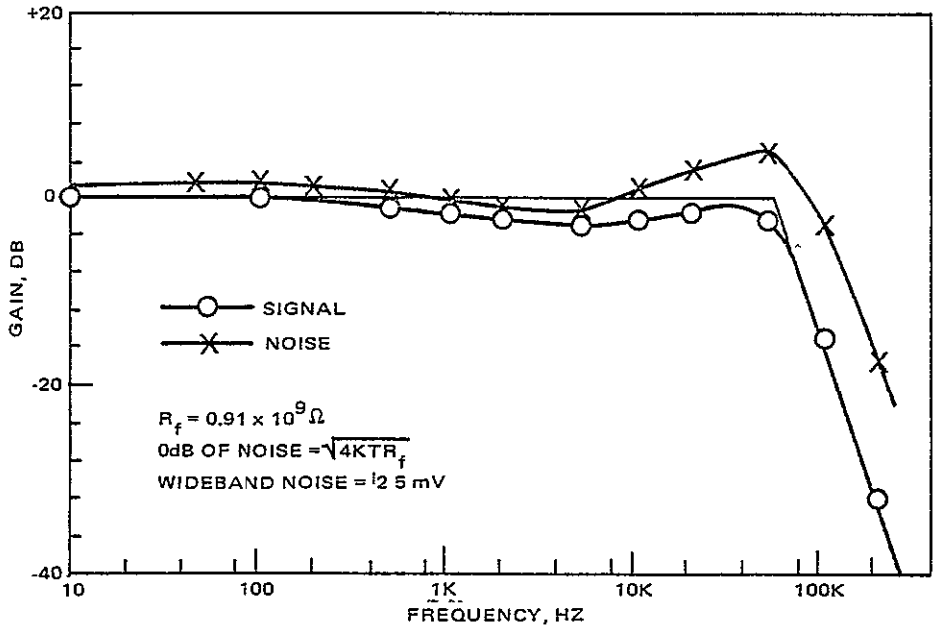

Figure 3.6-7. UDT FPA single channel boosted response, layout modified

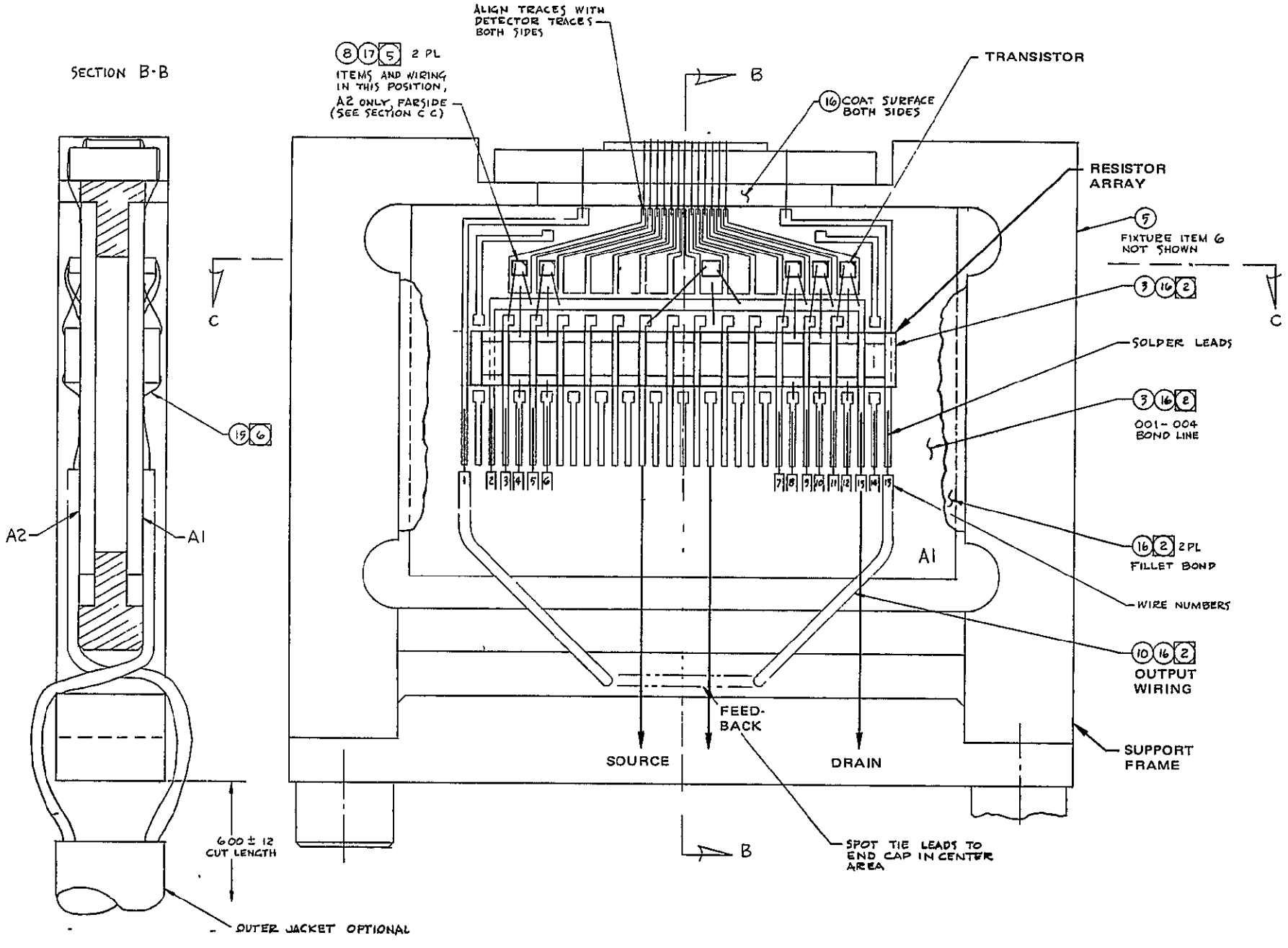

Figure 3.6-8. UDT array FPA, modified layout

boosted spectral plot (Figure 3.6-7) shows a sag of about 2.5 dB at 5 kHz. This could be due to detector secondary time constant as mentioned earlier.

To check the effect of the resistor array (15 resistors on a single substrate) and to further isolate the resistor from circuit traces, a discrete chip resistor was used in place of one of the array resistors. The individual resistor chip was simply glued onto the resistor array and connected as shown in Figure 3.6-9. The spectral signal and noise plots, unboosted and boosted, are shown in Figures 3.6-10 and 3.6-11. They are not significantly different from those of Figures 3.6-6 and 3.6-7, but the wideband noise was measured at 3.3 mv instead of 2.5. The only explanation for this other than measurement error is that a different FET chip was used with the discrete resistor. This brought up the possibility that some of the FET chips were not meeting the noise specification. More will be said about this later.

To check the effect of the UDT detector in the layout, a Hewlett-Packard 4205 detector chip was installed in place of the UDT detector on a FPA circuit board. The configuration is shown in Figure 3.6-12. The unboosted and boosted spectral response is shown in Figures 3.6-13 and 3.6-14. Noise is about 8.3 dB above thermal noise at 50 KHz and the wideband boosted noise is 2.8 mv. The boosted signal response tends to peak rather than sag with this detector. The peaking or sagging appears to be detector related, based on comparison of this data with that shown in Figure 3.6-11.

To determine if the FET chips were meeting the noise specification, thirteen of them were silver epoxied to a circuit of the type shown in Figure 3.6-12, and connections were made using micro-probes. In this way there was no possibility of degrading the chip performance as a result of bonding the leads to the metalization. According to these measurements, about 1/3 of the devices met the noise specification at 50 kHz, and another third were slightly (25%) over. A good electrical connection was difficult to obtain using the probes because the chip pads are so small, but fairly consistent results were obtained with a little practice.

TI, Ltd. in England was contacted to determine if the chips were tested for noise before delivery. The answer was that they can test noise

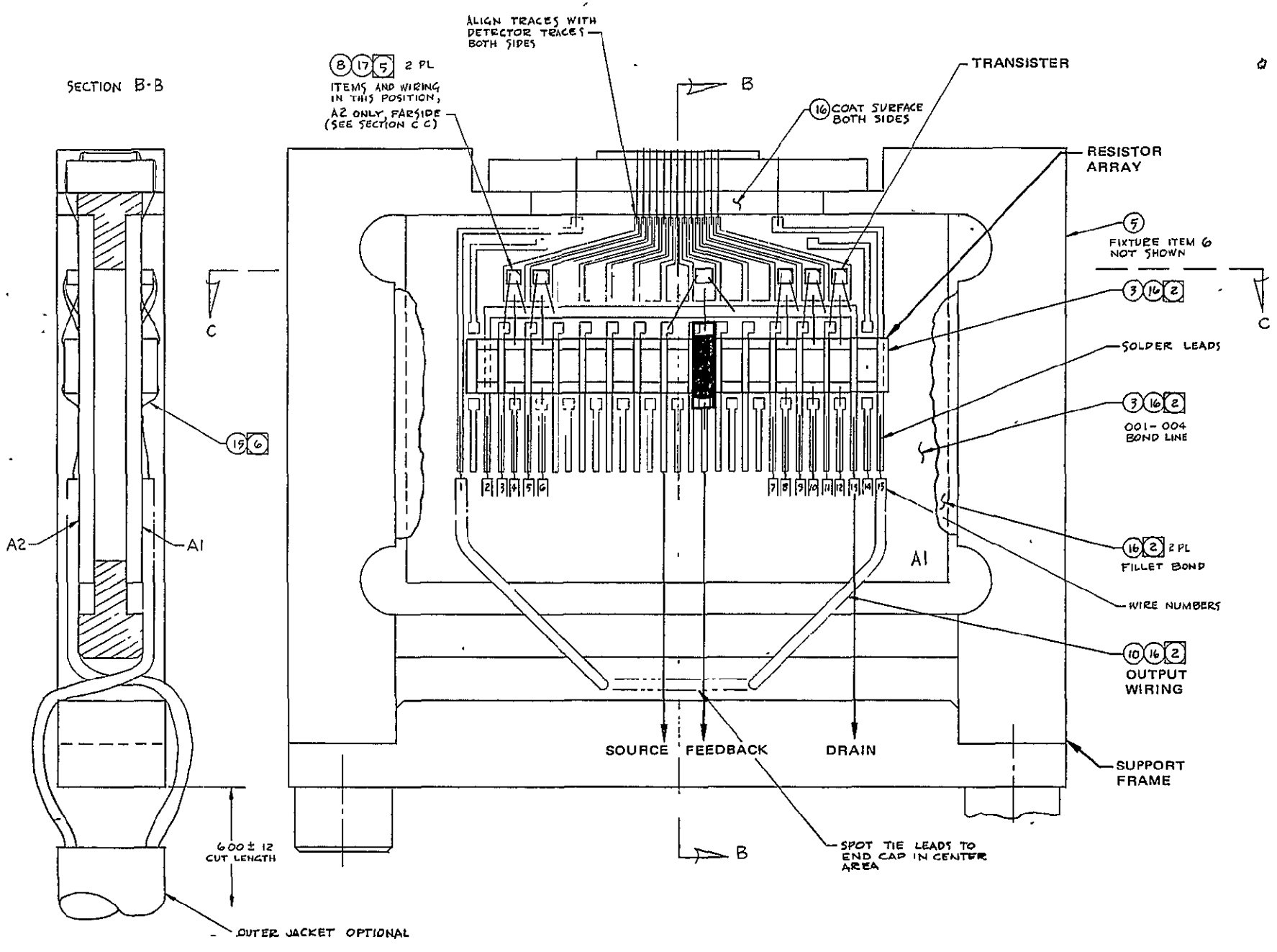

Figure 3.6-9. UDT FPA with discrete resistor

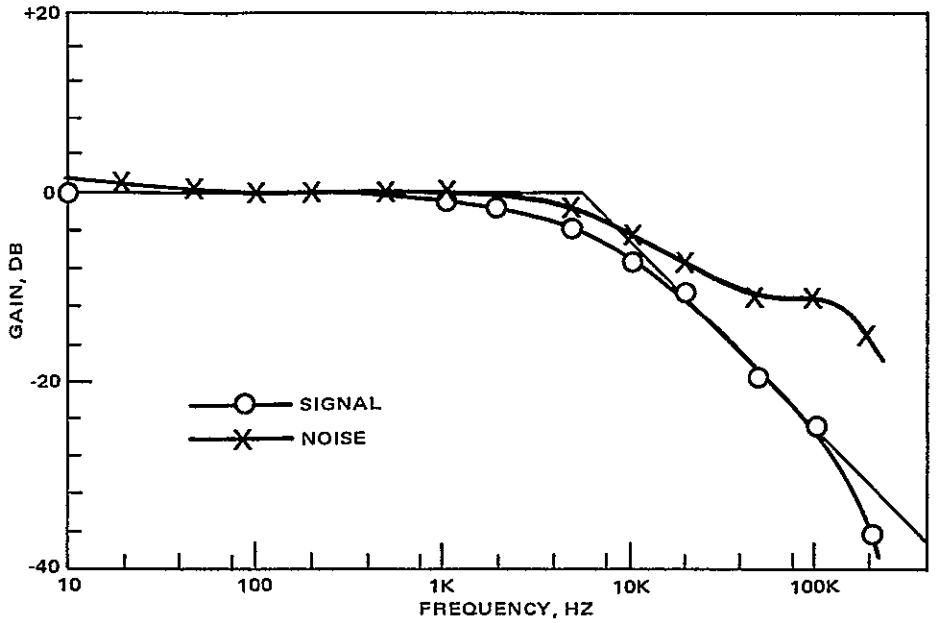

Figure 3.6-10. UDT remote source channel with discrete chip resistor, unboosted

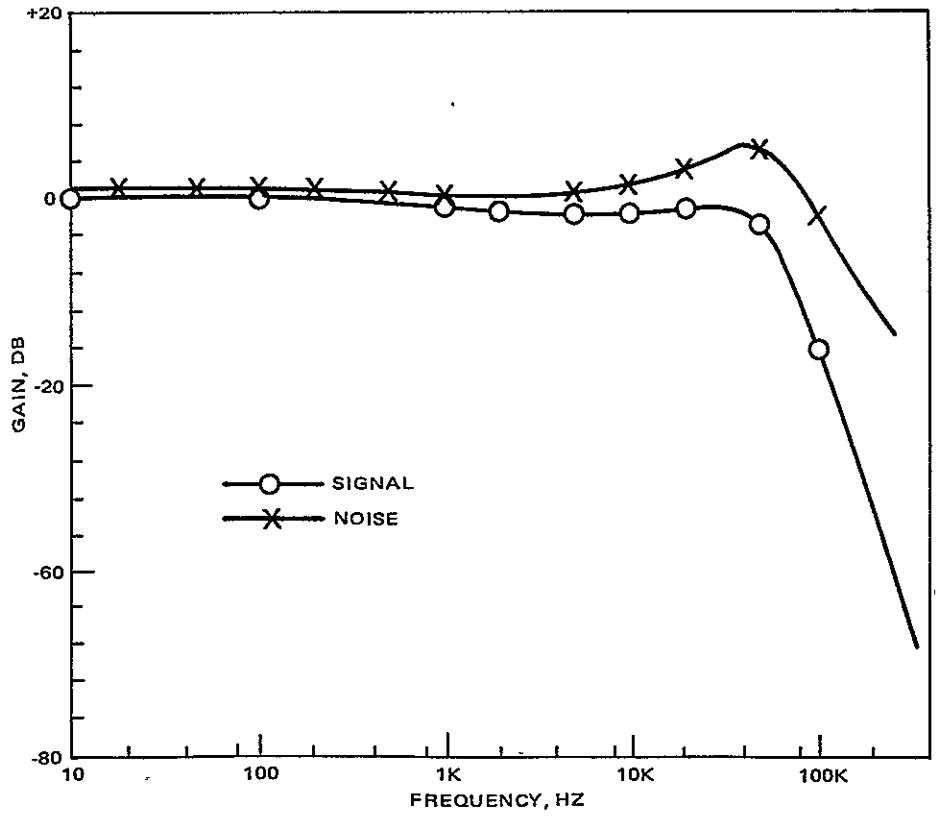

Figure 3.6-11. UDT modified layout FPA with discrete resistor, boosted

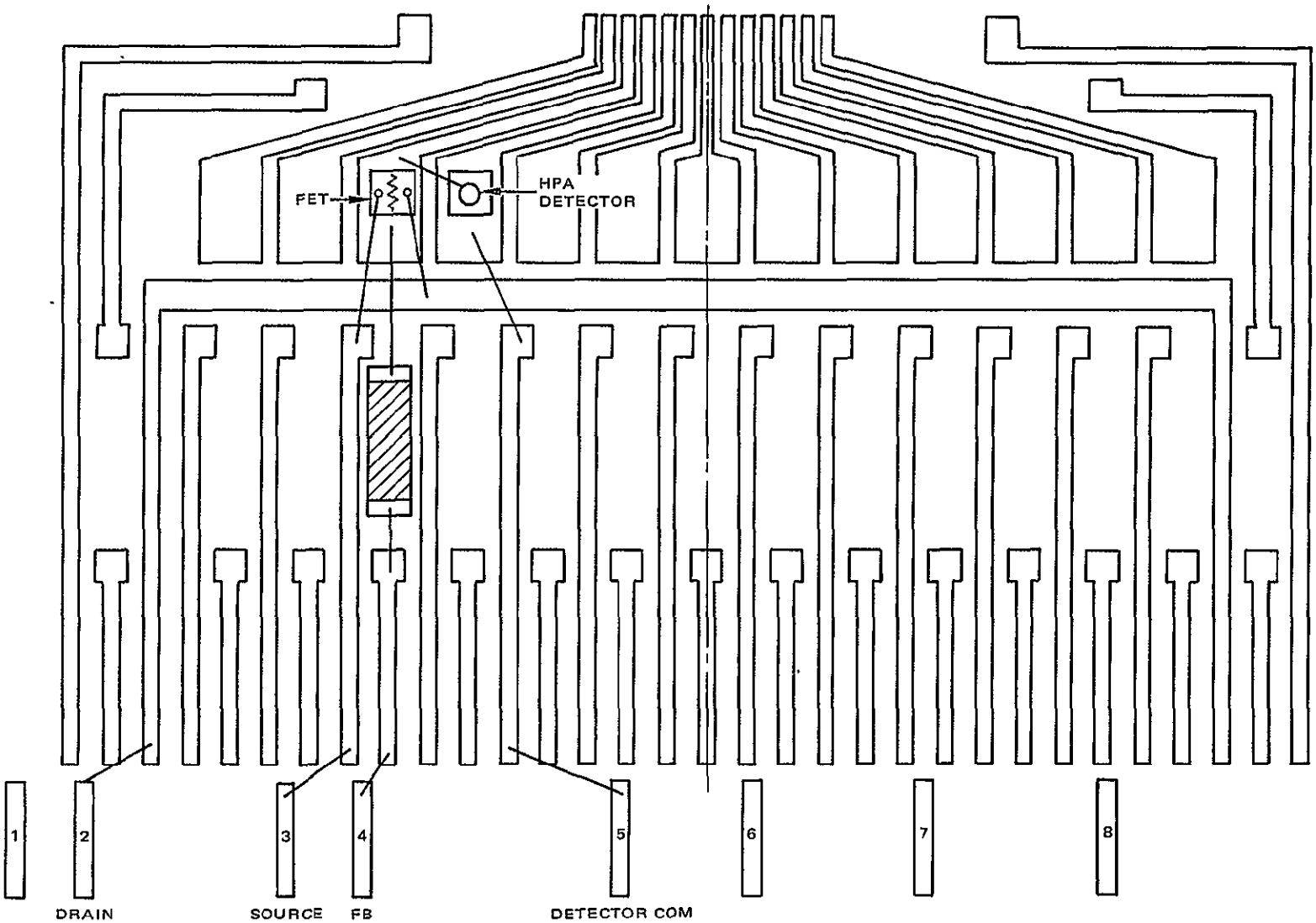

Figure 3.6-12. HPA 4205 layout

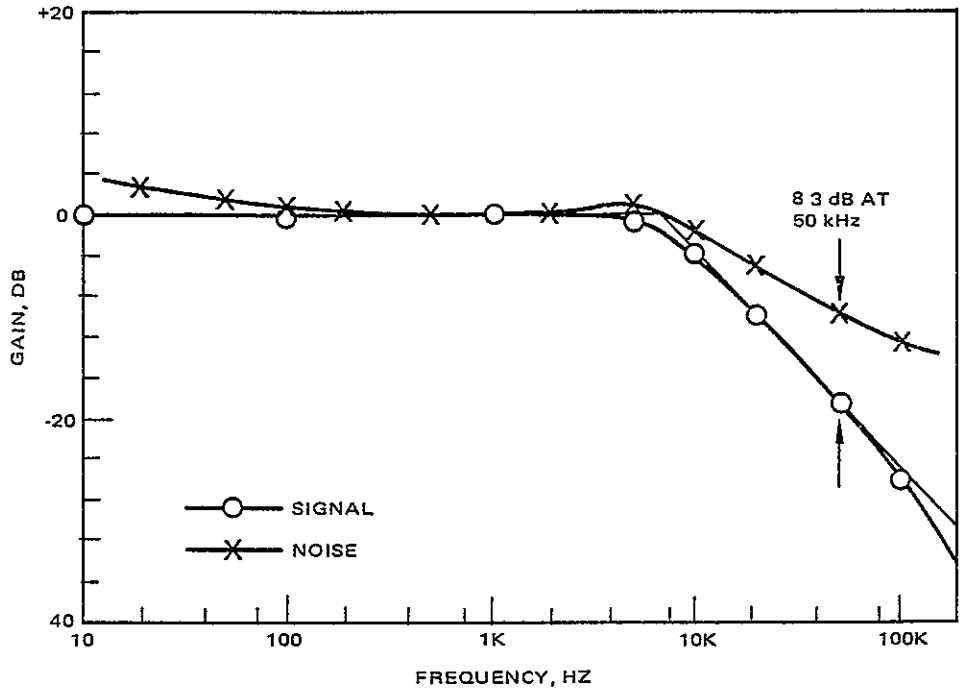

Figure 3.6-13. Unboosted spectral noise with HPA detector

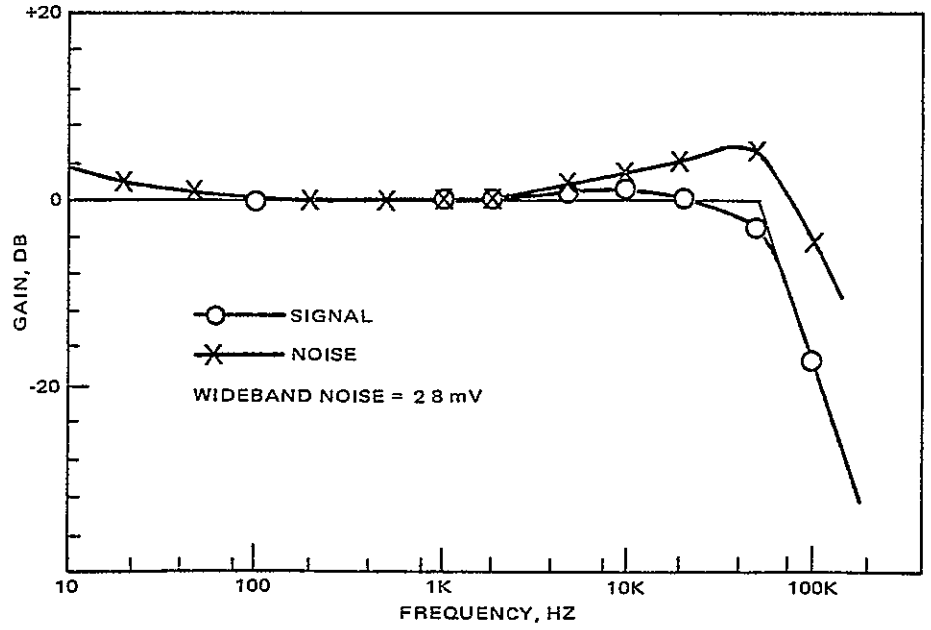

Figure 3.6-14. Boosted spectral noise with HPA detector

of an encased device only. They take a sample lot of about 30 chips from each wafer, put them in cans and check the noise. If the 30 are all good, the several thousand individual devices on the wafer are considered to be good also.

After learning of this, chips were purchased in TO-18 cans and after checking them on commercial noise measuring equipment for $\bar{e}_n < 2.4$ nv/$\sqrt{\text{Hz}}$ at 50 kHz, the chips were removed from the cans for use on the arrays. The technique used was to saw off the header lead upon which the chip is mounted, immediately below the chip. The gate contact of the FET is located on the bottom of the chip. The source and drain wire bonds, which are made to the top of the chip, were left intact. The chip, wires, and lead stub were transferred to the test circuit and the lead stub was conductively epoxied to the sapphire substrate. The gate connection to the detector and feedback resistor was made by bonding to the top of the lead stub (which is larger in diameter than the FET chip) and the source and drain leads, still attached to the chip were bonded to the test circuit pads.

Some $\bar{e}_n$ tests on the preamplifier circuit were made using an "ex-canned" device at the front end. The test circuit is shown in Figure 3.6-15. The results are shown in Figure 3.6-16. They compare with the 3.0nv/$\sqrt{\text{Hz}}$ used in the computer calculation of Figure 3.6-5.

It was also desired to measure the input capacitance of the preamp since this is the major factor in the magnitude of the high frequency noise. This was done by making a frequency response test from the noninverting bipolar input stage transistor base, as shown in Figure 3.6-17. Measurements were made with and without the detector connected. The results are shown in Figures 3.6-18 and 3.6-19. The gain e_o/e_s is nearly unity at very low frequency, then starts to increase due to the effect of R_f and C_{in}. C_{in} is determined by the frequency where the low frequency response is up 3 dB.

$$C_{in} = \frac{1}{2\pi R_f f + 3\text{dB}}$$

Such a calculation yields about 2.5 pF with the detector and about 1.5 pF without it. These values are for the apparent or unbootstrapped input capacitance. In determining noise effects, the bootstrapped gate-to-source

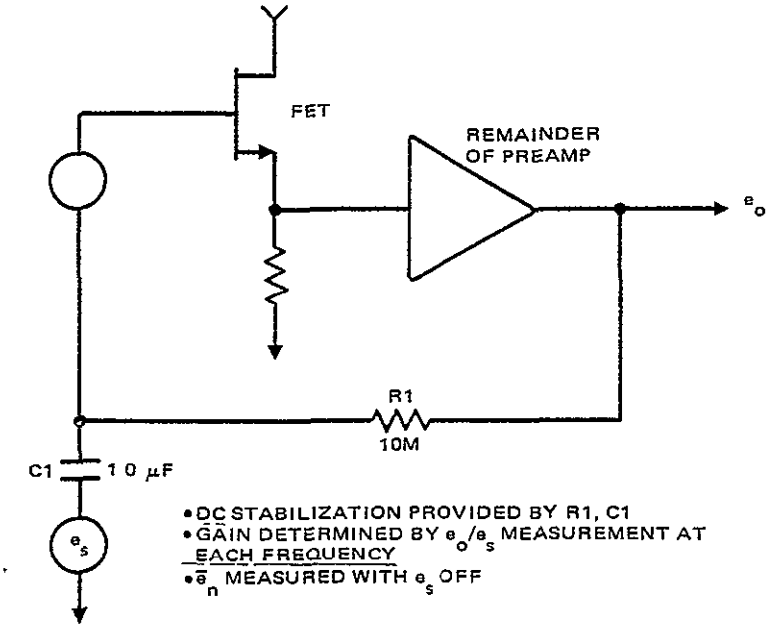

Figure 3.6-15. Circuit to measure $\bar{e}_n$ of preamplifier input FET

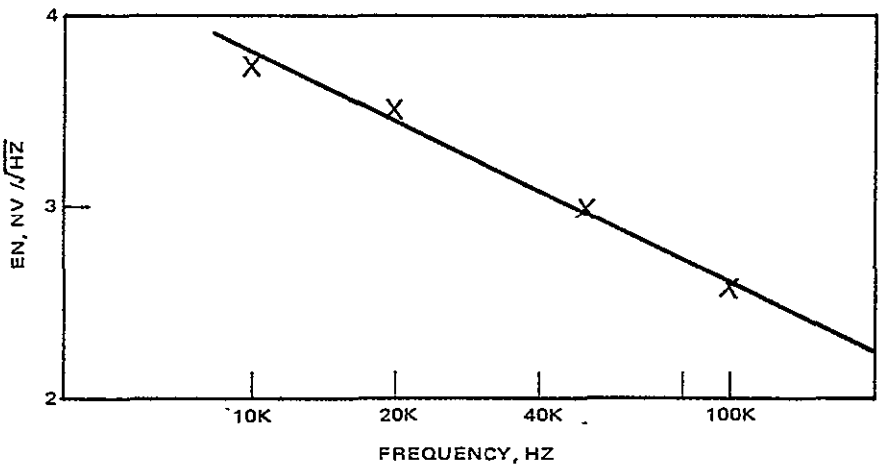

Figure 3.6-16. Preamplifier e_n versus frequency

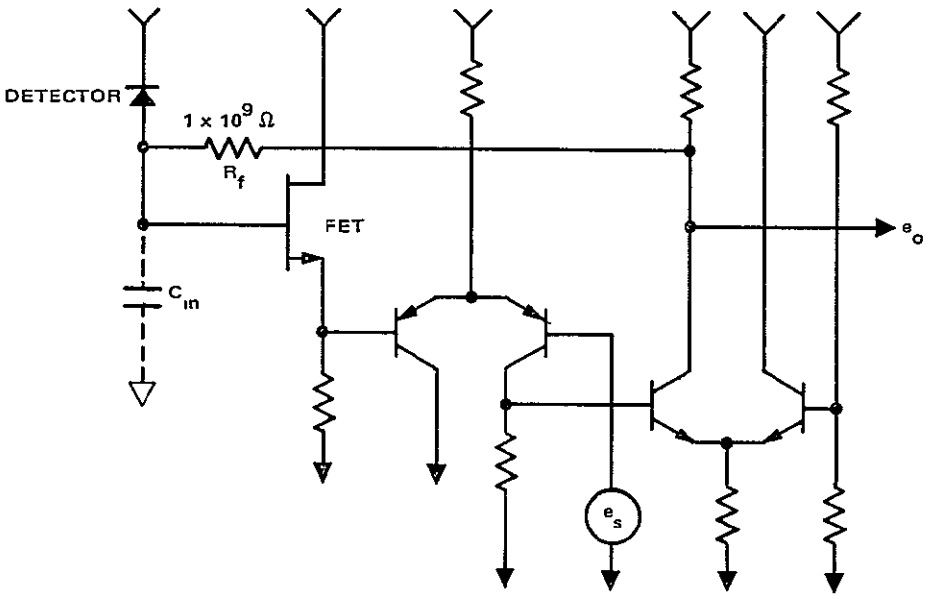

Figure 3.6-17. Circuit for measurement of C_{IN}

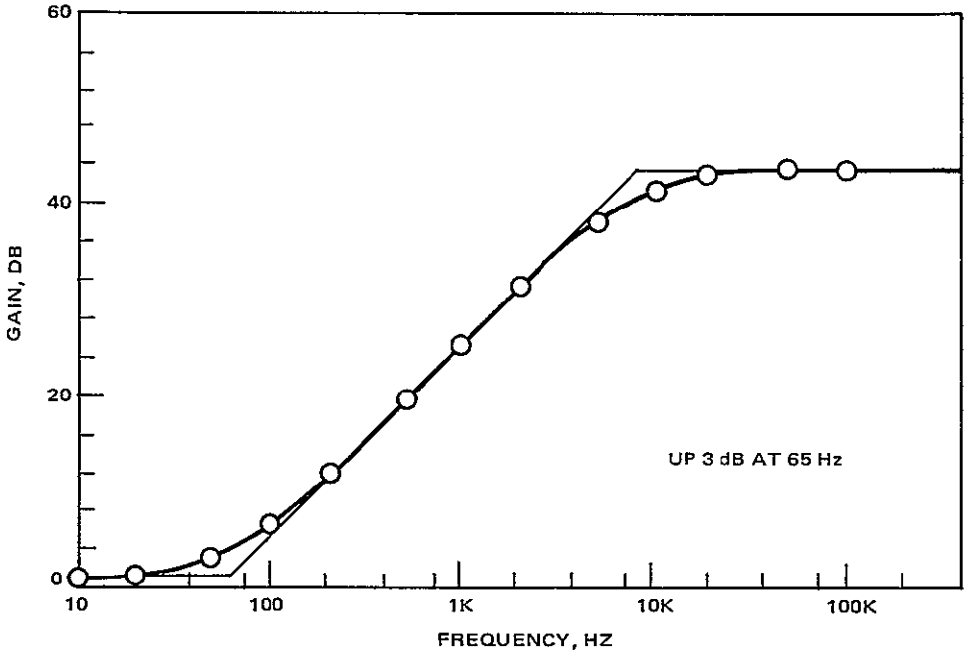

Figure 3.6-18. Input capacitance measurement with UDT detector

capacitance C_{gs} of the input FET, typically 2.2 pF per the data sheet, must be added. This brings the total to 4.7 pF, which compares well with the 5 pF used in the noise model calculation.

Detector leakage current was also measured and found to be anywhere between 5 and 10 pA depending on the array, the site and the reverse bias. This is well below the 30 pA used in the calculation. In summary, all the known parameters affecting noise have been tested with the exception of the FET $\bar{i}_n$ and $\tan\delta$, the C_{in} loss tangent. The reason these have not been tested is primarily because it is very difficult to do so. The FET $\bar{i}_n$, being specified at $6 \times 10^{-16} A/\sqrt{Hz}$, is dominated by the thermal noise of R_f and by dielectric loss resistance noise above about 1 KHz. Because $\bar{i}_n$ is the shot noise of the gate leakage current, calculable by the shot noise formula, it is expected to be flat with frequency. At 50 KHz it would be over an order of magnitude below the dominant noise source. Since our excessive noise is at high frequencies only, it is not expected that $\bar{i}_n$ should be causing the problem.

A high loss tangent could easily be the cause of excess high frequency noise. The problem is that the majority of our input is device capacitance. The $\tan\delta$ of these devices cannot be altered. High quality dielectric materials such as sapphire and alumina in the substrates and circuit boards have been used wherever there has been a choice.

3.6.4 Additional Frequency Response and Noise Measurements

In making the C_{in} tests, it became apparent that here was a way to make frequency response tests without a detector. After turning up at low frequency, the gain e_o/e_s (see Figures 3.6-18 and 3.6-19) increases, then levels off to a constant value at high frequency. The feedback resistor shunt capacitance C_f, may be calculated from the frequency at which the high frequency gain is down 3 dB. Stated another way, the transimpedance frequency response will be flat in the area where the plot of Figure 3.6-18 is rising, and will fall off at -20 dB/decade in the area where Figure 3.6-18 is flat. In this way the optical frequency response obtained by illuminating the detector may be compared with the electrical frequency response with and without the detector. Signal and noise plots may also be made. Figure 3.6-20 shows the electrical frequency response and spectral noise of a

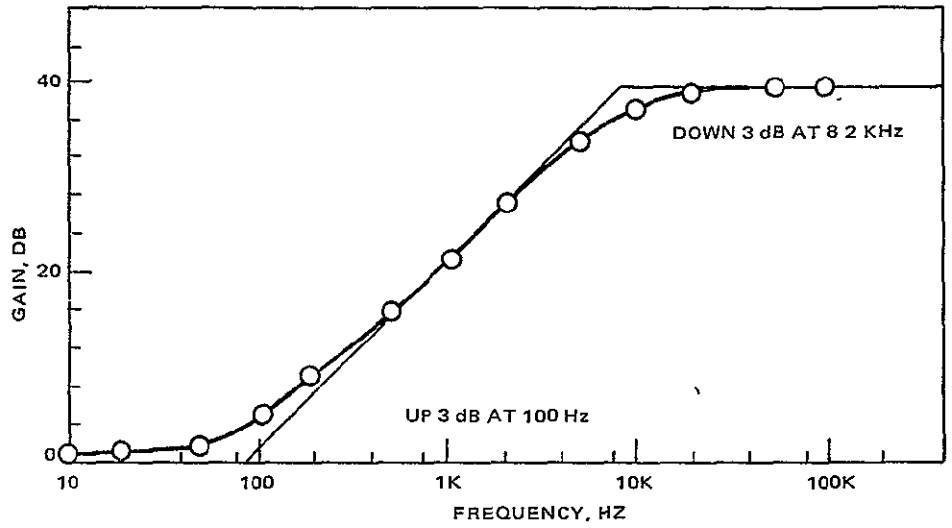

Figure 3.6-19. Input capacitance measurement without UDT detector

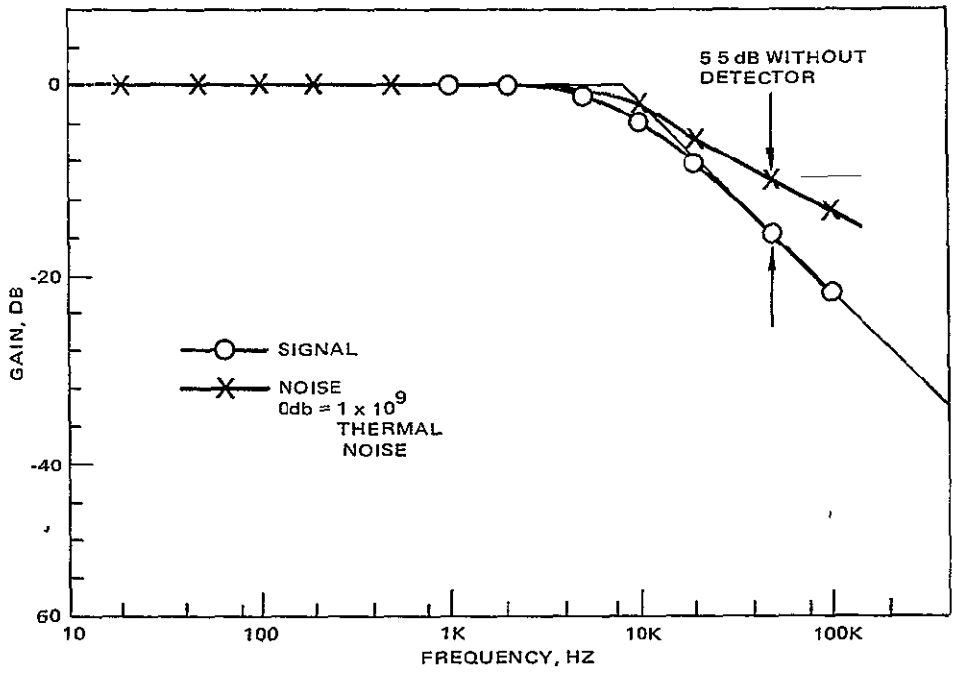

Figure 3.6-20. Signal and noise plot using electrical input signal without detector

single channel with no detector. The noise is up 5.5 dB above the signal level at 50 kHz. The plot was repeated in Figure 3.6-21 with a UDT detector array added. The 50 kHz noise is now up 6.7 dB. The increase is attributable to the 1 pF increase in C_{in} caused by the detector.

The plot was repeated again as shown in Figure 3.6-22, with an optical input signal. The noise was the same, but the frequency response was down an additional 1.4 dB at 50 kHz, making the "signal-to-noise ratio" at 50 kHz 1.4 dB worse. The noise is 8.1 dB up, in this case, which is very typical of earlier plots with optical inputs. Further testing will determine whether a focused light signal will produce a better optical signal response.

The second noise problem, mentioned earlier, is that a channel operating in the neighborhood of other operating channels is noisier than it is if its neighbors are turned off. This is particularly noticeable if one of the neighbors happens to be excessively noisy. In tests of the original UDT FPA, channel 24 exhibited the best noise performance. The wideband noise of channel 24 varied from 3.6 mV with the other channels turned off to 4.2 mV with the other four channels operating. The excess noise was primarily due to the adjacent channel (channel 22) as the wideband noise in channel 24 was 3.7 mV with all channels operating with the exception of channel 22. There was some indication that the frequency response of a particular channel can be affected by its neighbors. In the above test, the boost on all 5 channels was adjusted so the optical frequency response was down 3 dB at 54 kHz with all channels operating. After channel 24's neighbors had been turned off, not only did its noise go down, but its frequency response went up. Upon readjusting its boost for -3 dB at 54 kHz, the wideband noise was 2.9 mV. This interaction between channels is related to the layout of the FPA. These problems can be largely eliminated by incorporating the following guidelines in future layouts.

1) Greater channel-to-channel spacing to obtain better isolation.
2) Ground plane shields between traces and ground barriers between feedback resistors also to help reduce cross-talk.
3) Reconfigure ground planes around the feedback resistors to improve frequency response.
4) Include ground planes beneath the FETs to aid in removing the heat generated by them. It is undesirable to have a

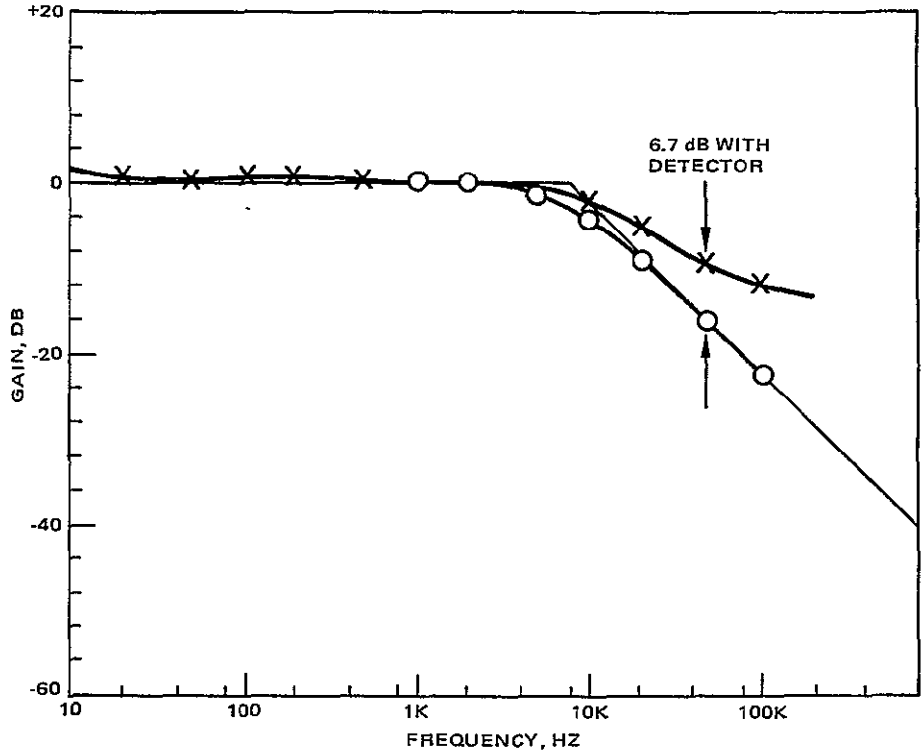

Figure 3.6-21. Signal and noise plot using electrical input signal and UDT array detector

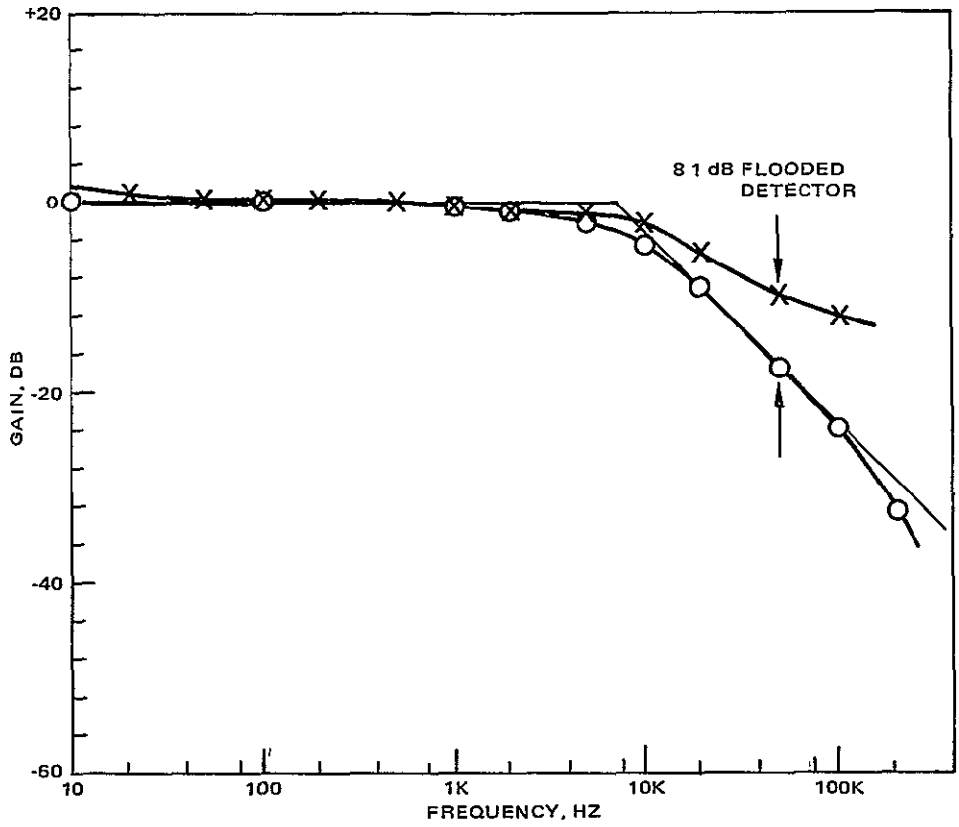

Figure 3.6-22. Signal and noise plot using optical input signal to UDT array detector

chip temperature over about 50°C, because leakage current increases to the point where it becomes a significant noise contributor.

(To further aid in reducing the chip temperature, reduction of the drain current I_D has been considered. The penalty for doing this is increased $\overline{e}_n$ and reduced g_m. The currently used parameters are specified at I_D = 3.0 mA on the data sheet, which is the current at which test operations have been conducted. At 5 volts the voltage between source and drain of the FET, V_{DS}, 15 mW per channel are dissipated. Tests show that if I_D were cut in half, $\overline{e}_n$ would increase by about 15 percent and the device transconductance g_m would decrease by about 20 percent. Further study is required to determine the effect of this variation on the system performance, but it would seem from the plot of Figure 3.6-5, that $\overline{e}_n$ could be increased 15 percent without serious degradation.)

3.7 SUMMARY

Because of time limitation research on the contract has been terminated, but work should be continued on refining the design of the arrays and assembly packaging to correct problems which now have been clearly identified. Such continued work is being carried on by Hughes/SBRC. As of this printing, the indications are that the probability of resolving the herein reported discrepancies with redesigned hardware is close to unity.

4.0 SCAN MIRROR ASSEMBLY

4.1 TASK DESCRIPTION

The Scan Mirror Assembly, SMA, breadboard development was undertaken to investigate certain critical design parameters that were known to significantly affect the overall TM performance. Design goals for these parameters were defined and the main purpose of the subject program was to prove how well these individual goals could be met. It is therefore worthwhile delineating these specific critical parameters:

- Mirror Fabrication. As a baseline for the TM SMA the Multispectral Scanner (MSS) was flight proven. However, the MSS mirror is significantly smaller. Increasing the size of the MSS mirror while utilizing the same fabrication techniques was a possible approach. However there was a strong desire to minimize spacecraft momentum transfer effects and this suggested a mirror of significantly less inertia than could be achieved by the MSS approach. A new, lightweight, brazed beryllium mirror structure was proposed based on a 51 cm diameter model which had been successfully built and polished. As a design goal it was required that the mirror remain flat over a 20°C temperature range and under the dynamics of operation. A total flatness goal of 0.9 micrometers was set; however a meaningful MTF specification was not defined at the start of the program.
- SMA Line Scan Accuracy. At the beginning of the program the SMA was defined to operate with the logic and basic mechanics of the MSS SMA. As such it would have a quasi-linear scan in one direction (forward) and would have a torqued and quite non-linear scan in the reverse direction. The TM system scans in both directions for efficiency, so the non-linear rescan would be highly undesirable. A low risk (minimal change to MSS) design was the basic program philosophy, and a means for

torquing during the turnaround had not yet been demonstrated. The along scan repeatability of the MSS was adequate, and the goal was to demonstrate equal performance in a larger SMA. The measured cross-axis motion of the MSS SMA exceeded the TM requirement, but significant improvement could be achieved: by careful balancing of the mirror on its flexural pivots, by individually matching the shear stiffness of the flexural pivots, and by adjusting the bumpers to create equal and opposite forces on the mirror.

Thus the scope of effort originally consisted of developing a new mirror technology and of scaling up an MSS-type SMA to demonstrate along scan repeatability and cross-axis motion parameters. Two events came to pass which indicated that a basic scope change was desirable. The first of these was the completion of an IR&D effort which strongly indicated that a torque-while-turn-around design existed which could be adapted to the TM SMA without major changes to the new mirror (which by that time had been fabricated and was in the process of being polished). The second event was the cross-axis measurements taken on the MSS-type SMA utilizing a dummy mirror. These measurements showed that the mass of the MSS-type bumpers was causing significant cross-axis motion. The torque-while-turn-around concept utilized extremely light bumpers. It was thus proposed to include the new torque-while-turn-around concept, to re-build the SMA appropriately and to re-test. The expected pay-off was: reduced cross-axis motion, reduced vibration, and a nearly linear scan and rescan.

With NASA consent and approval, direction was received to stop all testing of the MSS-type SMA and to fabricate necessary parts, re-assemble and test a torque-while-turn-around TM SMA. The results of this testing are the principal content of this report on the SMA.

4.2 RESULTS SUMMARY

The test results demonstrate the feasibility of the SMA and lightweight mirror design concept. The original SMA specification (DS 31649-001) contemplated a quasi-linear forward scan (≈2 percent) followed by a quite non-linear reverse scan. This would require a computer to make the two functions equal, linear, and of the same scan length. In the final breadboard

configuration the goal was to achieve repeatable along scan registration without computer corrections.

Scan Mirror Assembly Results

Figure 4.2-1 presents SMA test results in summary form by comparing the original goals, the revised goals and what has been demonstrated by test or analysis. Each parameter in Figure 4.2-1 is briefly discussed below.

- Scan Frequency. The baseline flight design scan frequency has changed from 9.78 to 7.1 Hz. The tested design can be operated easily between 5 and 11 Hz. As the frequency is increased, the energy put in during turn-around must increase. All else being equal, this requires lengthening of the torque pulse. Ultimately this increase would reduce scan efficiency. For this reason, most data was taken at 9.2 Hz to show a healthy margin over the requirement. Higher efficiency at frequencies in excess of 11 Hz would require more voltage to the torquer or a torquer with larger torquing coils.

- Scan Linearity. The linearity was defined originally as the ratio of scan velocity at a particular scan angle divided by the average scan velocity over the total scan angle. For a truly torque free scan the linearity would be 100 percent by definition. For the forward scan of MSS or both scans of the TM, the predominant torque is from the flex pivots. For this program it was originally assumed that the reverse scan would contain the energy restoring torque pulse. Thus the original design goal for linearity was +3.7/-7 percent (measured from 100 percent) during the untorqued scan and ±20 percent during the rescan. The actual linearity of the TM SMA as tested and computed for a vacuum environment was +1.3/-2 percent. This was based upon the mirror scan natural frequency, the scan angle and the average scan rate as measured. However a device has been built and tested on IR&D funds which applies a magnetic torque which approximately cancels the flex-pivot restoring torque. By measuring the net static torque on the mirror as a function of scan angle the in-vacuum linearity can be predicted assuming no significant eddy-current torques exist in the torquer. From this it can be shown that the maximum angular deviation from a truly

Parameter	Original Goal (DS 31649-001)	Present Goal	Achieved	
			By Test on SMA	By Other Means
Scan Frequency	9.78 ±0.01 Hz	7.1 Hz	Any desired frequency between 5 and 11.0 Hz Most tests at 9.2 Hz to show margin	
Scan Linearity ($\theta(t)/\dot{\theta}$ for avg scan)	+3 7/-7 0% forward ≈20% reverse	New Definition θ actual = θ linear ±21.3 microradians (0.5 IFOV)	Not applicable but equal to +1.3, -2.0%	<10 microradians Tested upon IR&D device
Along Scan Repeatability (Object Space)	4 μrad RMS with "rubber banding" and knowledge of fwd/rev. scan functions	4.2 μrad RMS without 'rubber banding 1.0 μrad with processing	~4 1 urad RMS without "rubber banding"	Analysis of test setup errors suggests that the real error may be one-half the measured values
Cross Scan Error (Objective Space Non-nested)	2 μrad RMS (Mirror) = 2 x 1 73 = 3.5 μrad in object space for 60° Mirror	3.0 μrad RMS in object space	4.0 μrad RMS worst case in object space 2.0 μrad RMS nominal	Approx 1.0 μrad RMS achievable with optimum pivots and mirror mass
Scan Amplitude	0 2595 rad		~0.27 radian in test setup	
Scan Efficiency	>80%	No known change	84.2% at 7.1 Hz 79 6% at 9 2 Hz	Note Turn around time of 11.6 ms could be shortened somewnat
Phase Stability	Locked to clock within 5 msec		≤17 μsec	
Start-up Time	≤30 sec			≤10 sec
Mirror Inertia to Cause Less than 2.5 Microradians SC Motion with 1000 Slug ft^2 SC and 0 1297 rad Mirror Motion	≤0 231 in. lb$_f$, sec^2		0.292 in lb$_f$ sec^2 because of retrofit to mirror	≤0 230 in. lb$_f$ sec^2 calculated with flex pivots on CG and magnesium torquer mounting plates
Power	≤20 watts		~7 watts	

Figure 4.2-1. Results summary for SMA.

linear scan can be closely matched to constant earth surface scanning rate. This variable angular rate cannot be achieved with constant angular rate scanners which scan the earth surface at a variable, hence nonlinear rate.

A device which removes flex pivot restoring torque, was not incorporated into the breadboard TM SMA for several reasons: (1) its operation had already been demonstrated on an IR&D SMA; (2) adding the hardware to the already-built, flight-type mirror would be cumbersome from a mechanical design point of view and

would not be cost-effective from a knowledge-gathering viewpoint; (3) quantitative linearity measurements would require total redesign of the test equipment. The appropriate place to incorporate this device is in the Engineering Model phase, since there is no question that the desired degree of scan linearity can be obtained; feasibility has been well proven.

- Along Scan Repeatability. The original goal specified in the Development Specification was that the expected along scan separation of two IFOV's on adjacent scan lines and whose object space scan angle is identical be less than 1/10 of an IFOV (or ≤ 4.2 microradians) when processed and printed by the ground station. The ground station was assumed to know the times of crossing a beginning and end fiducial ground angle and to know the times of all video data. The assumed processing technique "rubber-banded" all scans between the start and stop fiducial times to a constant, processed scan length. And in addition, it was assumed that the basic forward and reverse nominal scan functions of mirror angle versus time were known and used in the processing. With the implementation of torque-while-turn-around, the requirement goal was changed to 0.1 IFOV unprocessed. This means that the difference in forward and reverse scan pairs should be less than 4.2 microradians. This goal has essentially been met. The measured value of the scan-to-rescan standard deviation is about 4.1 microradians. When scan periods are normalized it has been shown that measured data taken on the breadboard SMA in a helium tent provides along scan repeatability with an expected deviation of less than a microradian in object space.

- Cross-Scan Error. This is the measure of the deviation in the along-track direction. It amounts to overlap and underlap in the raster format of the picture; the latter represents a loss of data that is not recoverable. The original SMA design goal was to keep the rms value of cross-scan error under 3.5 microradians in object space for a sensor system whose nominal incident-to-reflected scan mirror ray is 60 degrees. This corresponds to a rms goal of 2.0 microradians for the cross-scan mirror angle itself. The design goal has recently been changed (because of system error budgeting and a change in IFOV size) to require that the object space cross-scan error be less than 3 microradians, rms, independent of sensor/SMA geometry.

  Actual measurements taken on the breadboard SMA indicate that cross-axis error is caused by the existence of first-mode, rigid-body motion of the mirror bouncing on the flex-pivots (which are springs in shear). To a large extent, however, the cross-axis vibration so described is correlated from scan to rescan. To the

extent that this motion in the scan and rescan traces nest with each other, no cross-axis error exists (except for mapping error but this error can be made much less than the specification of 1/2 IFOV). Measurements show that the true non-nested cross-scan error is a function of the exact scan frequency chosen and the particular natural frequency of the mirror (in the first-mode motion described), which is presently 320 Hz. The rms value of the resulting cross-scan error (scan-to-rescan) was measured for slightly differing scan frequency and found to be between about 1 and 2.8 microradians (mirror coordinates). This suggests that in the flight system, where the SMA period is predetermined exactly, the natural first mode frequency should be tuned for best cross-axis results. In object space the cross-axis error would then be 1.4 and 1.8 microradians rms for a 90 degree and 60 degree mirror respectively. The worst-case cross-axis motion measured near a vibrational resonant peak was 4 microradians in mirror coordinates.

- Scan Amplitude. The required scan amplitude is ≥0.2595. In actual practice all tests have been run with a scan amplitude greater than this minimum requirement. The scan amplitude for test purposes is the active scan angle and must be less than the angle between bumper contacts; this has been assured by placing the scan measuring split diodes slightly inside of the angle defined by the bumper contacts. It should be pointed out that the scan angle is adjustable on the breadboard and scan angles larger and smaller by a factor of two are quite feasible.

- Scan Efficiency. Scan efficiency, for a quasi-linear scan mechanism, is simply the percent time spent actively scanning. The design goal of the development specification was 80 percent minimum (the active forward plus active reverse scans, divided by the total mirror period). The turn-around time thus determines the scan efficiency once the total period is specified. The turn-around time is defined by the bumper spring length and can be adjusted. Once adjusted, the turn-around time is largely independent of scan frequency. The turn-around time includes all of the time spent between active scans (a bit larger than the bumper/mirror contact time). On the test unit the scan efficiency was 79.6 percent at 9.2 Hz where most of the data on jitter and scan repeatability were taken. This corresponds to 84.2 percent at 7.1 Hz. In an optimized design, the bumper spring length can be shortened to decrease the turn-around time and further increase scan efficiency, perhaps to 90 percent (estimated).

- Phase Stability. The requirement that the phase time lead or lag between the control clock and the SMA not change by more than 5 milliseconds in five years can be easily met with the torque-while-turn-around logic of the breadboard SMA. Changes in phase measured over several minutes do not exceed three microseconds. Assuming major changes in the electronic or mechanical parameters (simulated by significantly varying an electronic input) result in phase changes of less than 17 microseconds. It should be pointed out, however, that the start of scan should not be controlled directly by the master clock, but by an SMA output (magnetic bumper pick-off or by the baseline Scan Mirror Monitor device).

- Start Up Time. The MSS SMA does not have a special start logic and is self starting. The TM SMA breadboard is not self starting. No attempt has been made to put a realistic start-up logic on the present breadboard. This is because the present breadboard self centers the mirror at rest with its uncompensated flex pivots.

  The breadboard is easy to start by applying a momentary voltage to the magnetic pick-off circuit (but its rest position is always at mid-scan). The actual flight mirror, at rest, may assume any position. The proper logic for the flight system would apply a small voltage to the torquer to place the mirror in contact with one particular bumper. This voltage would persist for 3 to 7 seconds to insure that the mirror is at rest. Then a fixed-length pulse would be applied to drive the mirror away from the bumper. During this start-up sequence, the normal logic would be inhibited. At the end of the fixed pulse the logic would be freed and the mirror would coast into the opposite bumper. This logic was built and demonstrated on the IR&D unit (which had flex-pivot torque compensation). The end result is a simple, reliable "SMA-On-Off" switch.

- Mirror Inertia. The present breadboard mirror (including torquer components and counter weights) has unnecessary inertia. This is because the redesign of the mirror and bumpers for the torque-while-turn-around set-up changed the location of the center of gravity with respect to the flex-pivot axis. Additional counter-weight was required to move the c.g. back onto this axis. In a proper redesign the flex-pivots would be slightly relocated, there would be no MSS-type bumper cups, the torquer magnetic structure would be lightened and the counterweight would be much smaller. There is no problem in meeting the desired inertial goal of 0.231 in-lbs-sec^2 with a 60° mirror.

- Power. The design goal of less than 20 watts drive power was based upon what might be achieved with MSS-type logic. In early tests of the TM SMA with MSS-type logic about 40 watts were required. The torque-while-turn-around concept brings about a sharp reduction in power consumption. In recent tests of the SMA about 7 watts is used by the drive electronics at 9.2 Hz scan frequency. At other operating frequencies the power required is

approximately proportional to the square of the operating frequency.

Scan Mirror Flatness Measurements

The original specification for mirror quality was in terms of flatness over the operating environment. The defined operating environment consists of the operating dynamic loads and the temperature range: $20 \pm 10^{\circ}C$. Flatness is the largest spacing obtained between a flat plate placed in contact with the mirror and the mirror itself. A design goal of 0.9 micrometers, maximum, was set.

A proper criteria for the mirror surface should be based upon an assessment of the scan mirror contribution to image blur. The SMA, scan line corrector, and optics all contribute to the image blur, and the detector geometry and following electronic filters also affect system MTF. Originally a lack of system definition dictated that the above simple flatness criteria be used based upon what was thought to be reasonably attainable. In addition a requirement was placed upon the polishing vendor that the mirror be polished flat to within 1/4 wavelength (λ = 0.6328 micrometers) at the polishing temperature of $20^{\circ}C$ over the clear aperture of the mirror. Because of a series of problems that occurred during the fabrication of the mirror blank, it proved difficult to obtain this desired flatness. In addition, these problems delayed the program to the point where it became necessary to accept the mirror in order to complete other tests. The mirror was flat to 1/2 wavelength at that point. Subsequent thermal testing showed that over $\pm 20^{\circ}F$ temperature range the peak static flatness error measured was 0.158 micrometers. This is well within the specified goal.

The smallest change in flatness that can be discerned by the dynamic flatness test is 0.2 micrometers. Dynamic flatness testing was done at a conservatively high scan rate (10 Hz) and no motion was detected. Thus the basic requirements, as specified, were met with margin.

The thermal tests showed a print-through of the mirror blank core pattern which appeared as the temperature was raised or lowered from $20^{\circ}C$

(the polishing temperature). Although the perturbations of the core print through are small and within the flatness requirement, the spatial frequency is high (3/4 inch core). The slopes could be significant and degrade system MTF. The planned test procedure could not handle this case.

Through analysis the effect of the print through on MTF was bounded, but only loosely. Tighter bounding was achieved by a special test procedure. This involved a line spread measurement of the sample mirror which showed that only a 6 percent degradation will occur at $\pm 10^{\circ}C$ from the polishing temperature. Experience has now shown that in future manufacture, far less aluminum braze alloy need be used and hence less print through will result on subsequent mirrors. But even this tested case shows performance that exceeds the TM system requirement. There is, therefore, no question regarding the ability to achieve sufficient surface quality over the specified $20 \pm 10^{\circ}C$ temperature range.

4.3 BASELINE SMA DESCRIPTION

This section describes the logic, mechanics and electronics of the breadboard TM SMA. It is largely a functional description of this newly developed SMA.

The original program plan called for building an SMA which adopted the logic, electronics, and bumper design of the MSS SMA. Initial developmental test on this unit, using a dummy mirror, showed that the cross axis error could not be reduced to within the design goal. As discussed in section 4.1 the program was redirected towards producing and testing a torque-while-turn-around SMA. It therefore seems inappropriate to describe the operation and hardware of the abandoned MSS-type approach. The remainder of this section is devoted to a description of the present baseline.

4.3.1 Logic

A scan mirror assembly requires that periodic torques be applied to maintain speed. Bang-bang SMA's can produce very linear and repeatable bidirectional scanning if, and only if, the torque can be applied

during the unused portions of the scans, i.e., the turn-around periods. In order to minimize the power requirement, spring "bumpers" are utilized to store the mirror's kinetic energy during turn-around. This significantly reduces the torquer's requirement to provide energy. A problem inherent with a torque-while-turn-around system is torquer inefficiency. In the first place, torque power transferred to the mirror is the product of torque and mirror speed as indicated in Figure 4.3-1.

To achieve maximum scan efficiency the turn-around period should be as short as possible. But all electromagnetic torquers possess some time constant. Thus the steady state torque for a given applied voltage cannot be achieved throughout the torque pulse (as it essentially can when torque is applied during an active scan). The requirement that torque be terminated prior to the end of turn-around (so as not to offset the active scan) limits the duration of the torque pulse further. The power transferred to the mirror is degraded by the fact that the mirror speed is far from constant during turn-around. Thus for a given size magnetic torquer, the turn-around torquer is hampered by time constants and slow mirror speed.

To enable a torque-while-turn-around system to work the coefficient of restitution of the bumper must be maximized, i.e., the less energy lost during turn-around, the less energy must be replaced. In an MSS-type bumper the two major causes of energy loss are the mass of the bumpers and the larger dampers. Bumper mass subtracts energy in the following manner:

$$\text{Initial Mirror Energy prior to Impact} = \frac{I_m \dot{\theta}_{in}^2}{2}$$

Since energy is conserved (without dampers)

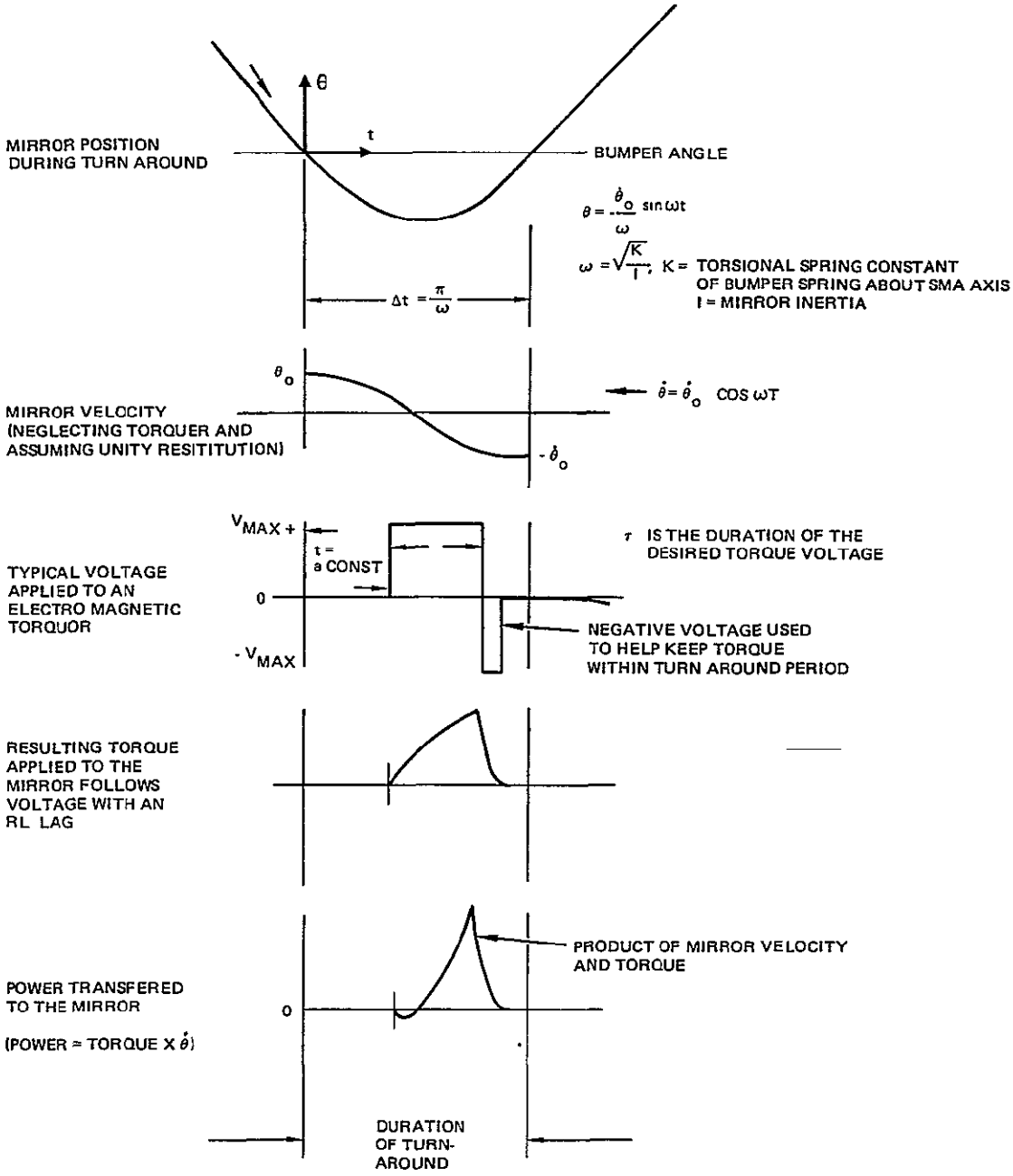

Figure 4.3-1. Typical torque functions during turn-around.

$$\frac{\left(I_m + mr^2\right)\dot{\theta}_{out}^{\,2}}{2} = \frac{I_m \dot{\theta}_{in}^{\,2}}{2}$$

where m and r are the mass and distance from the pivot axis of the bumper moving mass. θ_{out} is the speed the mirror would leave with if no torque pulse were added. Thus the energy lost to the bumper mass is

$$\frac{mr^2\,\dot{\theta}_{out}^{\,2}}{2} = \frac{\left(\frac{I_m + mr^2}{I_m}\right)\dot{\theta}_{in}^{\,2}}{2}$$

By minimizing the bumper mass, this energy loss is minimized. In addition, if no dampers are used which damp the motion of the mirror, then no damping loss will occur. In practice the new bumpers provide no mirror damping and have such small mass that the energy loss is predominately due to contact friction. This subject is discussed further in the mechanics section (Section 4. 3. 2) however for the purpose of explaining the logic it is sufficient to state that the coefficient of restitution as a function of θ is known and is approximately constant. The mechanical energy lost at each bumper contact (turn around) is thus approximately a function of the square of the scan rate, $\dot{\theta}$:

$$\text{E lost mechanically} = \frac{I_m\left(\theta_{in}\epsilon\right)^2}{2}$$

where ϵ is the coefficient of restitution with no torque input ($\epsilon = \theta_{out}/\dot{\theta}_{in}$ untorqued). Consider now the manner of adding energy to the mirror. Figure 4. 3-2 shows the motion as a function of time and in a phase plane. The basic stability requirement is that, given a perturbation from stable operation, perturbations decay with time.

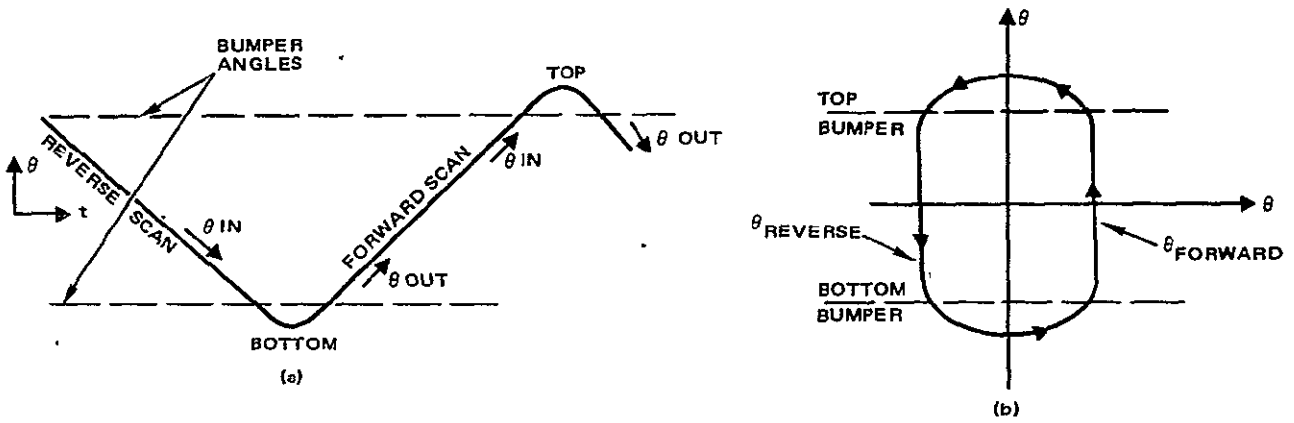

Figure 4. 3-2. SMA motion versus time, and in-phase plane.

In the general case one needs consider only a single operating cycle. Assume that Figure 4. 3-2 shows a steady state operating condition. Then if there is a perturbation in $\dot{\theta}$ (say in the reverse scan), for stable operation, the magnitude of this perturbation must be reduced after two bumper contacts, i. e. , during the next reverse scan. There is no basic stability requirement that $\dot{\theta}$ forward equal θ reverse. Since energy is lost mechanically at each turn around, energy must be added during at least one turn around. If the coefficient of restitution is strictly defined as,

$$\epsilon = \frac{\dot{\theta}_{out}}{\dot{\theta}_{in}}$$

independent of whether energy is added or not then as a corollary to the basic stability requirement,

$$\epsilon_T \epsilon_B = 1$$

where the subscripts denote the top and bottom bumper. This equation indicates that the two coefficients need not be equal and, in fact, it is

perfectly possible to drive the system on only one turn around while taking a passive loss on the other. However since it is desirable to have equal scan speeds in each direction, and since it is undesirable to allow a perturbation in velocity to propagate for a longer time than necessary, it is best that controlled energy be added during both turn arounds.

In proceeding with the development of the logic, for simplicity, it is first assumed that both bumpers act identically, that is $\epsilon_T = \epsilon_B = 1$, nominally. Stability can now be viewed on a plot of energy as a function of operating speed as shown in Figure 4.3-3. Using this figure as a guide it is instructive to look at the mirror energy taken out by the bumper. It is the quadratic function previously discussed, $\Delta E_{lost} = I_m\left(\dot{\theta}_{in}\epsilon\right)^2/2$.

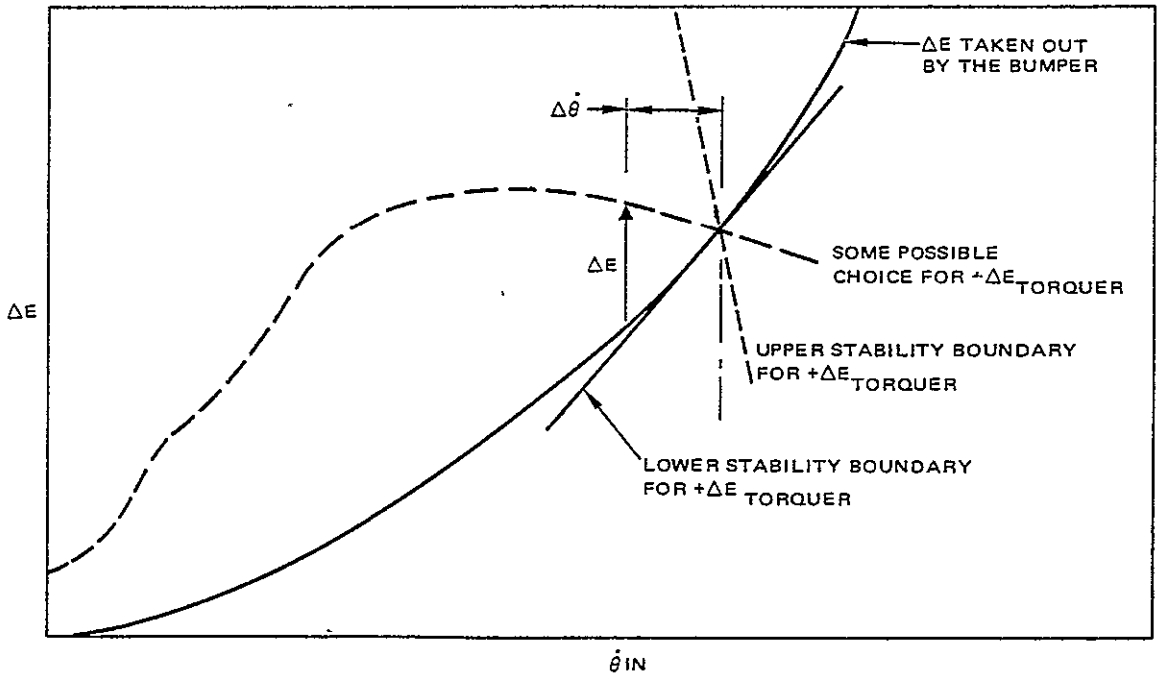

Figure 4.3-3. Choosing a stable torquing function.

If some proper function of $\dot{\theta}_{in}$ is chosen, as shown in the figure, which puts energy in, then the SMA will operate at the intersection of these two functions. Still assuming that these functions are identical for top and bottom bumpers, the identical intersection will thus provide

$\dot{\theta}_{in} = \dot{\theta}_{out} = \dot{\theta}_{forward} = \dot{\theta}_{reverse}$. Now the question of how to choose the best input function will be addressed.

There are two absolute stability boundaries. The lower stability boundary is the tangent to the ΔE_{lost} curve. This boundary describes a situation in which not enough energy is supplied to keep the SMA running. The upper boundary is defined such that a $\Delta\dot{\theta}_{in}$ (displacement from the nominal operating point) causes a net ΔE so great that $|\dot{\theta}_{out} - \dot{\theta}_{in}| > \dot{\theta}_{in}$. For this case a small error would grow without bounds. With a simple speed control every input function between these two bounds is stable. The stability bounds become closer together only when we consider the noise response and the effect of control loops with inherent lags. From a simplistic standpoint an upper bound might be that value such that ΔE net is sufficient to reduce the input error $\left(\Delta\dot{\theta}_{in}\right)$ to zero in one turn around. The problem with this is that a control system cannot differentiate between noise and error. To reduce noise throughput, the gain should be lowered from this simplistic case. Note that the initial upper stability boundary is, by definition, the point of no damping; the case where an error is removed in one turn-around corresponds to critical damping; and what is being suggested to minimize noise is a slightly over damped case. Before further synthesizing a proper energy input function it is necessary to postulate how the operating point (crossover of input and loss functions) is established.

There are two requirements: one is to maintain a constant scan rate and the other is to synchronize the total scan cycle to a reference clock. Both of these requirements can be done with a phase-lock loop. From Figure 4.3-3 it can be seen that if nothing changed with age, i.e., if the input and output functions stayed where they were initially set, a constant energy input function could be defined and adjusted to a desired and unchanging scan rate, $\dot{\theta}_d$. Figure 4.3-4 describes how a clock can be used to correct for changes that can occur in the input and output functions.

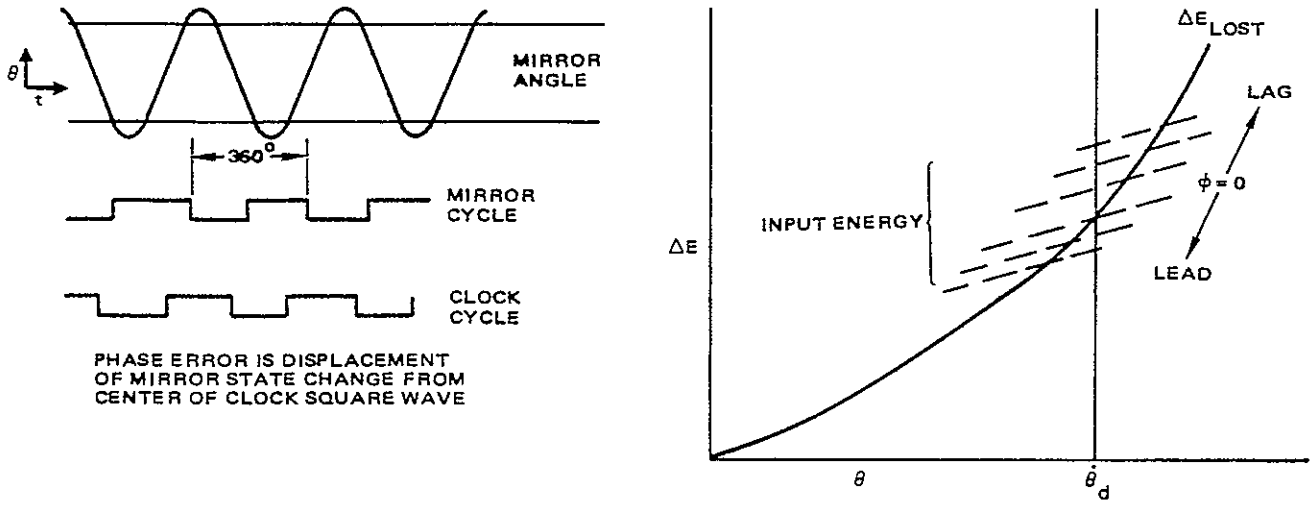

Figure 4.3-4. Phase control added to a constant input.

If the duration of the torque pulse were the control function, a constant value of this torque pulse length will produce an input energy function which is approximately proportional to scan rate, $\dot{\theta}_{in}$. From Figure 4.3-1 this can be derived. The power transferred to the mirror is the product of torque and mirror speed. Thus for a constant length torque pulse

$$\Delta E_{added} = \int_0^{\tau} T\dot{\theta}\, dt$$

where τ is the constant torque pulse duration and τ starts after a fixed time delay following the instant of bumper impact. To a first approximation the torque function does not significantly change $\dot{\theta}$ during the turnaround (ϵ with no torque pulse is about 0.975). But $\dot{\theta} = \dot{\theta}_{in} \cos \omega t$ from Figure 4.3-1. Therefore ΔE_{added} is proportional to θ_{in}.

Figure 4.3-4 shows how the phase between the SMA and a reference clock can be measured and used to shift the ΔE_{added} function as a function of a lead or lag phase error. The logic of the TM SMA is based upon the fact that an electromagnetic pick off responds to each instance wherein

the mirror makes first contact with the bumper. Thus the time of a fixed angle (actually two angles) is measured. This time, or any time corresponding to a fixed angle, provides a measure of a series of SMA cycles. By comparing this series of events with a reference clock it is easy to derive an analog measure of the phase between the clock and the SMA. The phase voltage looks like:

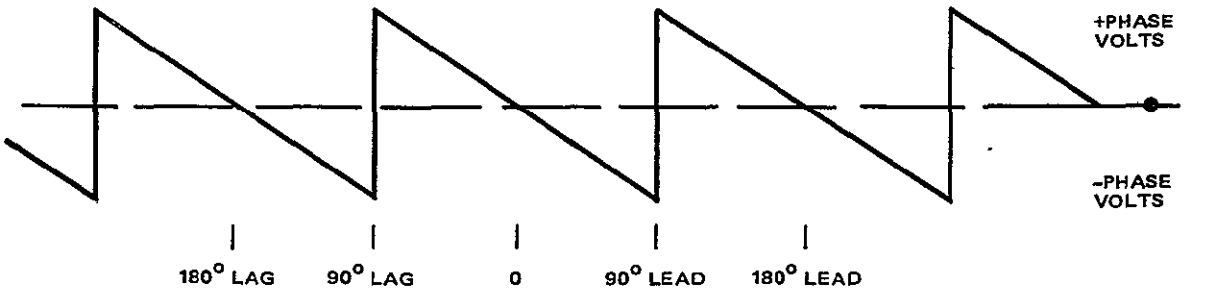

Notice that a linear phase voltage is developed over a $\pm 90^{\circ}$ range of phase shift between the clock and the SMA. Using this voltage the duration of the torque pulse can be controlled. With reference to Figure 4. 3-1 we can write:

$$\tau = \tau_o + \tau_\phi \phi$$

which states that the torque pulse is of constant duration, τ_o, if no phase error exists, and grows with a gain, τ_ϕ, as a linear function of the phase error. The net effect of this logic, in Figure 4. 3-4, is to raise the level of the input energy function as a quasi-linear function of SMA lag. The shape of the input energy function remains unchanged, i. e., the slope with respect to $\dot{\theta}$ is unaffected. In closed loop operation, the steady state behavior is as follows:

1. Assume τ_o is picked such that the operating frequency exactly matches the clock. Then after start up, the SMA will lock to the clock with exactly no phase error. The desired operating or cross-over point, $\dot{\theta}_d$, is now established.

2. Now assume that τ_o, τ_ϕ or the energy lost function drifts to slightly different values. The net result is that the energy input function will raise or lower to establish exactly the same previous value of $\dot{\theta}_d$. The SMA is still locked to the clock but now a constant phase error will exist.

The phase lock loop thus raises and lowers the energy input function by a fixed amount to establish a balanced phase error which maintains $\dot{\theta}_d$ and also maintains the operating frequency of the SMA identical to the clock. The next consideration is how to set the limits on the gain τ_ϕ.

Since the loop has usable phase limits of $\pm 90^o$ the gain must be large enough to produce changes in τ which can move the input energy function far enough up or down to cover all drifts that can occur in τ_o, τ_ϕ, or the energy loss function. In practice a term, capture range, can be defined. This is the range over which the drive clock can be changed without exceeding a $\pm 90^o$ phase shift. This range is a direct function of τ_ϕ. For the operating breadboard TM SMA this range is slightly more than $\pm 1/2$ Hz. Thus the lower limit on phase gain is that value required to limit long term phase shift to less than 90^o. The upper limit on phase gain is more complicated.

The phase angle is measured on a stable basis at each instant of bumper impact. Phase errors then require a controlled value of τ to be applied. But on any one measurement there exists noise. In order to precisely lock the SMA frequency without responding to noise, the phase signal is filtered in the following manner

$$\phi = \sum_{n=1}^{\infty} \phi_A \, Ae^{-bn}$$

n = 1, 2, ...; 1 is the last impact, 2 is the previous impact, etc.

Thus the phase locked loop is less responsive to noise at the expense of being slow. However, since no sudden changes in the electronic or mechanical parameters are expected to occur, this should present no penalty. Unfortunately the lag in the phase loop tends to cause oscillatory behavior of $\dot{\theta}$.

From Figure 4.3-4 it can be seen that the $\dot{\theta}$ behavior is related to the angle between the input energy and energy lost in the neighborhood of the cross-over point, $\dot{\theta}_d$ as in the following sketch.

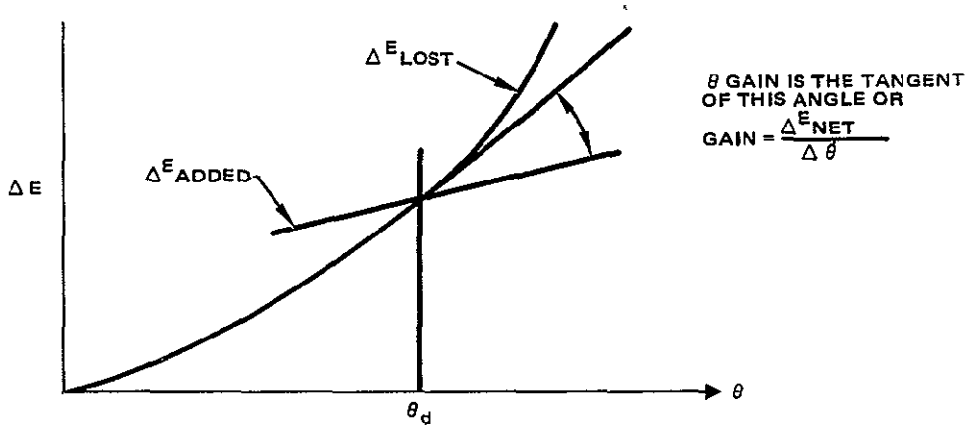

The operating $\dot{\theta}$ gain for $\tau = \tau_o + \tau_\phi \phi$ is rather low since the two energy functions do not cross each other at a very steep angle. One is a quadratic and the other a positive linear function. In order to see the relationship

between $\dot{\theta}$ gain and phase gain, τ_ϕ, a simple frequency domain system is shown below.

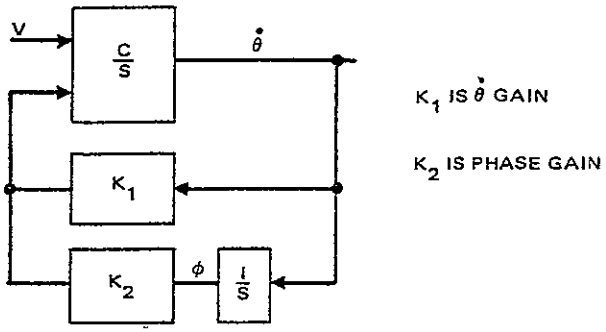

The transfer function is $CS/(S^2 + CK_1S + CK_2)$ and the denominator is the full quadratic of a simple harmonic oscillator. If K_2 is too large with respect to K_1 then the transfer function is oscillatory and could be unstable. If K_2 is zero (no phase lock) the system is always exponential and is always stable.

For the case of the TM SMA the value of the $\dot{\theta}$ gain with a constant τ input and no phase control is sufficient to cause stable "open loop" operation. However, with the phase control adjusted to provide ±1/2 Hz capture range, the system is underdamped and the speed continues to hunt with rather large fluctuations. Thus it can be seen that the upper limit of the phase gain depends upon the slope of the input energy function or $\dot{\theta}$ gain. Thus far the input energy function has been described only for the case where τ is independent of $\dot{\theta}$.

The mirror speed cannot be accurately measured at the instant of bumper impact. Yet to use $\dot{\theta}$ in the control loop requires that it be measured with very little error since errors would propagate. Therefore, what is implemented is a nearly equivalent measure of time. Figure 4.3-5 shows how a time is obtained which is strongly related to $\dot{\theta}$. If t_A could be easily measured, then $\dot{\theta}$ at the time of interest, t_n, could be closely approximated by $\theta_{scan}/(t_n - t_A)$. This would be a rather noise free measurement of $\dot{\theta}(t_n)$. However, the TM SMA measures only the times of bumper impact, t_n, t_{n-1}, t_{n-2}, ... etc. The approximation used is

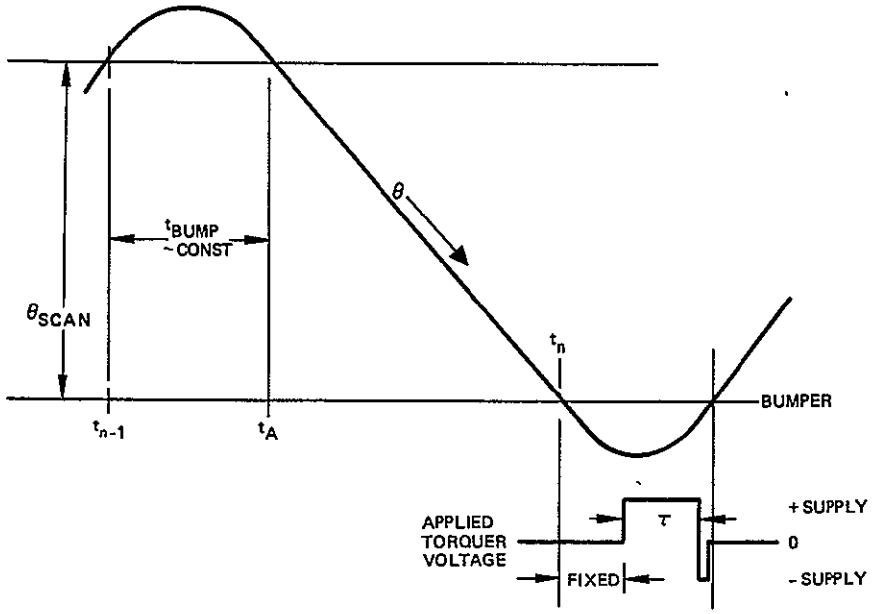

Figure 4.3-5. Developing a Variable $\dot{\theta}$ Gain.

$$\dot{\theta} = \frac{C}{(t_n - t_{n-1} - t_1)}$$

where

t_1 is a constant approximation of t_{bump}.

For small variations in the neighborhood of the operating point it can be shown that this is an exact approximation, given that C can be arbitrarily chosen. This approximation is, however, sensitive to fluctuations in the turn around time which are independent of $\dot{\theta}$. $\dot{\theta}$ information is used to rotate the input energy function, as shown in Figure 4.3-4, in a clockwise manner about the intersection point. A summary of the logic is shown in Figure 4.3-6. A pair of electromagnetic pickoffs utilizes the velocity of the leaf spring bumpers to measure the instant of mirror/bumper impact. Because of subsequent ringing, these pickoffs are followed by a device which measures a threshold crossing and then self inhibits for a duration sufficient to insure that ringing will not yield further threshold crossings. The two resulting signals are combined to form a pulse train of bumper impacts. The state of the pulse train determines which of the bumpers was last hit. The pulse train is compared with a reference clock for phase and the result filtered. This signal,

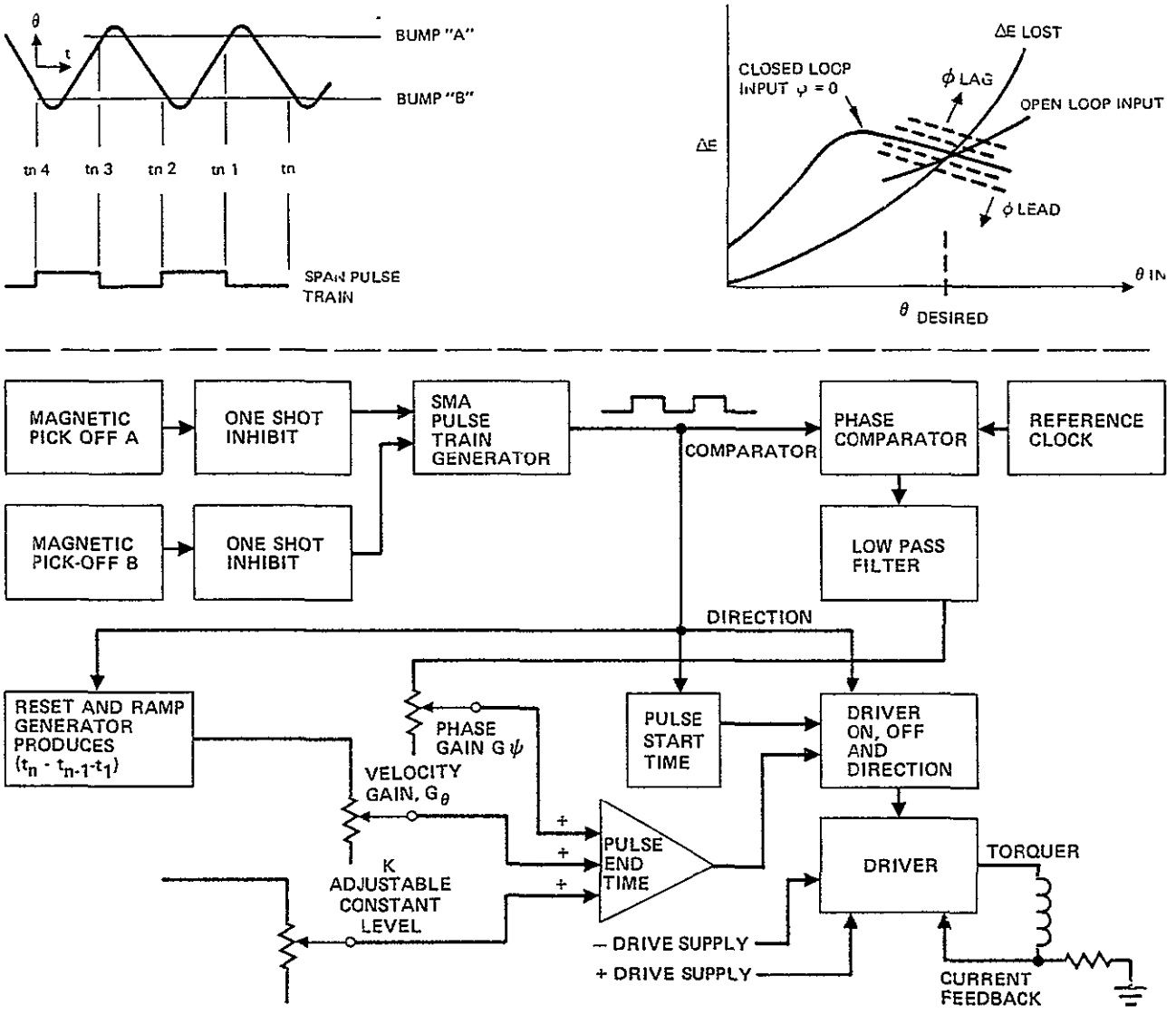

Figure 4.3-6. Simplified logic block diagram.

when multiplied by a preset but variable gain, becomes the phase control signal. The SMA pulse train is also used to obtain the velocity control signal

$$G_{\dot{\theta}}(t_n - t_{n-1} - t_1)$$

where

t_1 is a constant and equal to the nominal value of $t_n - t_{n-1}$.

The phase and velocity control signals are added to a constant (level) to produce the torquer duration, τ.

$$\tau = K + G_{\dot{\theta}} (t_n - t_{n-1} - t_1) + G_{\phi} \text{ (phase error)}$$

Note τ has the value K when the gains and levels are adjusted such that the SMA is running at its nominal speed with no $\dot{\theta}$ or phase error. Should a perturbation in speed occur after the bumper impact at t_{n-1}, the gain, $G_{\dot{\theta}}$, will decrease the next pulse length, τ, if the speed is high and the converse. In concept, the phase control will do very little unless the constant, and preset level changes; in which case the phase loop will compensate the level change by accepting a balancing phase error.

The above logic has been described assuming both bumper pairs are mechanically and electrically identical. It is also important to show what happens when the bumpers are not equal. Consider first unequal coefficients of restitution. Then, as discussed previously.

$$\epsilon_A \epsilon_B \equiv 1$$

However, ϵ_A need not equal ϵ_B, although it is an objective in the design to make these coefficients mechanically equal. If ϵ_A and ϵ_B are not equal the scan rates will not be equal.

The second parameter of the turn around is its duration. From Figure 4.3-1 it can be seen that each turn around time is primarily a function of the leaf spring constant in torsion about the flex-pivot axis. The spring constant of each bumper can be adjusted by adjusting the length of the leaf in cantilever and equal turn-arounds are closely approximated. For the purposes of the remainder of the logic discussion it will be assumed that the sum of the two turn-around times is constant.

Considering unequal bumper characteristics, Figure 4.3-7 helps to explain the system behavior. For stable operation the period, T_p, must nominally be a constant. In addition, it is assumed that $T_A + T_B$, the sum of the two turn around times, is a constant. Thus, if we define $\dot{\theta}_{B,A}$ as the nominal average scan rate going from bumper A to B, and $\dot{\theta}_{A,B}$ conversely, we have

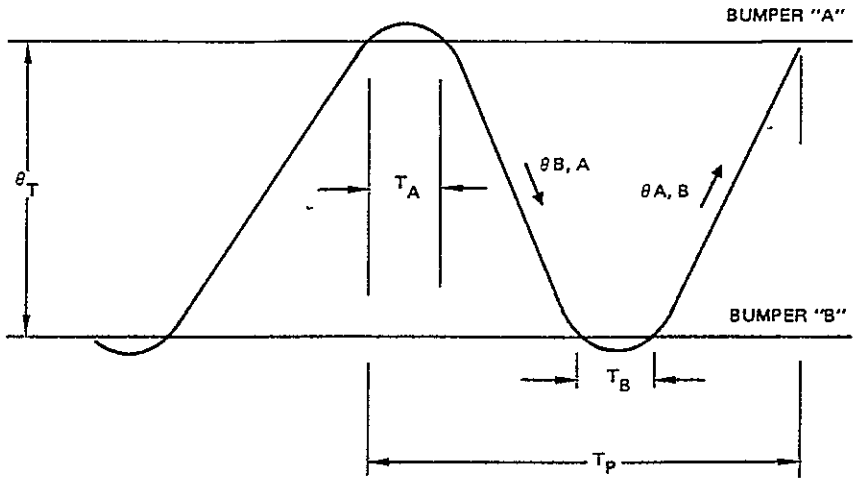

Figure 4.3-7. Definition of times.

$$\frac{\Delta\theta}{\dot{\theta}_{B,A}} + \frac{\Delta\theta}{\dot{\theta}_{A,B}} = T_p - T_A - T_B$$

a constant which states that the total period is constant. From this equation and the relationship, $\epsilon_B = \dot{\theta}_{A,B}/\dot{\theta}_{B,A}$, one may conclude

$$\dot{\theta}_{B,A} = \frac{(1 + \epsilon_B)\Delta\theta}{\epsilon_B (T_p - T_A - T_B)}$$

$$\dot{\theta}_{A,B} = \epsilon_B \dot{\theta}_{B,A}$$

which is to state that if the coefficients are not equal, the scanning rates are also unequal and uniquely determined by the coefficients of restitution. Figure 4.3-8 shows such stable operation for the general case wherein the energy loss curves for each bumper are different and the constant levels (K) are different for each bumper. Two operating speeds result, neither of which is at a crossover point.

From this discussion a number of conclusions can be drawn regarding the operation of the basic logic as implemented and tested on this program.

- Suitable gains, G_ϕ and $G_{\dot{\theta}}$, can be found which when combined with a suitable level K will produce a torque while-turn-around time, τ, which will produce stable operation.

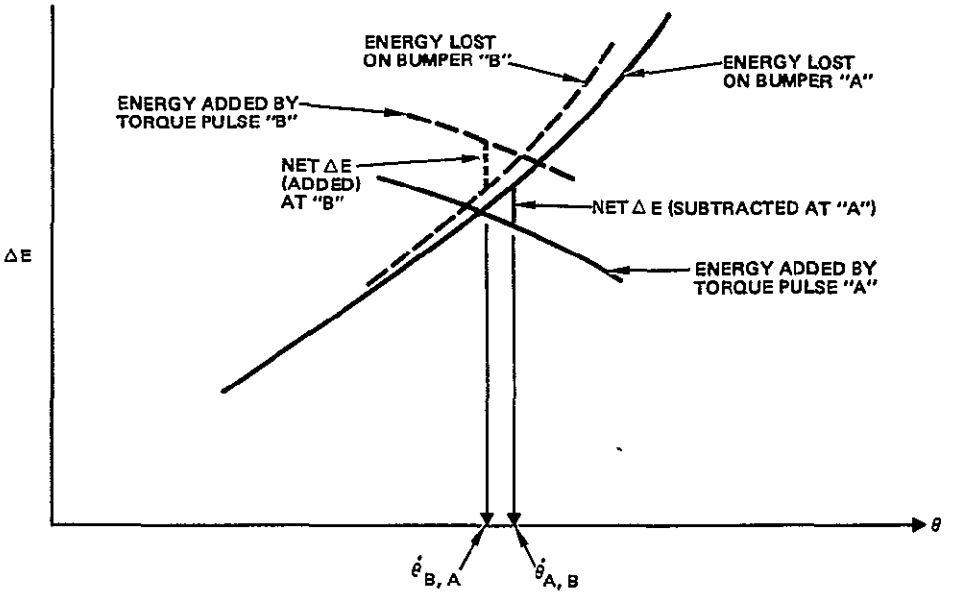

Figure 4.3-8. Stable operation with $\epsilon_B \neq \epsilon_A$.

- Stable operation will consist of two speeds (a forward and reverse scan speed) which remain fixed if the turn around times remain fixed and if the coefficients of restitution remain fixed.
- If, in addition, the coefficients of restitution are equal, then the scan speeds will be identical.

These conclusions have been born out in all tests performed on this program. Before concluding this section it is worthwhile to describe how the logic might be improved. Specifically, it would simplify the ground processing if both scan speeds were forced to be identical and equal to a constant.

Since the turn around time will vary predominantly with changing spring constant and since this is a function of temperature, a constant turn around time may be difficult to maintain to the desired level of precision passively. If the TM temperature remains within the narrow bounds which MSS has experienced, there should be no problem.

If the two active scan periods are controlled to be equal (but not necessarily constant) then ground readout can be at an equal and constant rate, forward and reverse, without systematic image blur. If, in addition, the scan periods can be held to a constant, then constant readout rate will

produce no mapping error. As explained in Section 4.4.2, the test equipment was not capable of determining if long term drifts exist in the turn-around time. They most likely do not, but if they do, then it is possible that the sum of the two active scan periods might drift by as much as 5 microseconds over a few hours. It will thus be possible to make the individual scans, forward and reverse, equal to a constant within 5 microseconds and mapping errors of less than 1/2 IFOV over a frame can be assured. This is because the IFOV dwell time will be approximately 10 μsec in the flight system.

Nevertheless it is a rather simple matter to make the two scan speeds absolutely equal. From Figure 4.3-8 it can be seen that if the two energy input functions are moved in level alone in such a way as to cause the cross-over points to occur at identical values of $\dot{\theta}$, ϵ_A will equal ϵ_B and $\dot{\theta}_{A,B}$ will equal $\dot{\theta}_{B,A}$. Since an active measure of the scan times in both directions is possible using the planned scan angle monitor, logic to produce equal scan rates is easy to implement. Figure 4.3-9 suggests the implementation

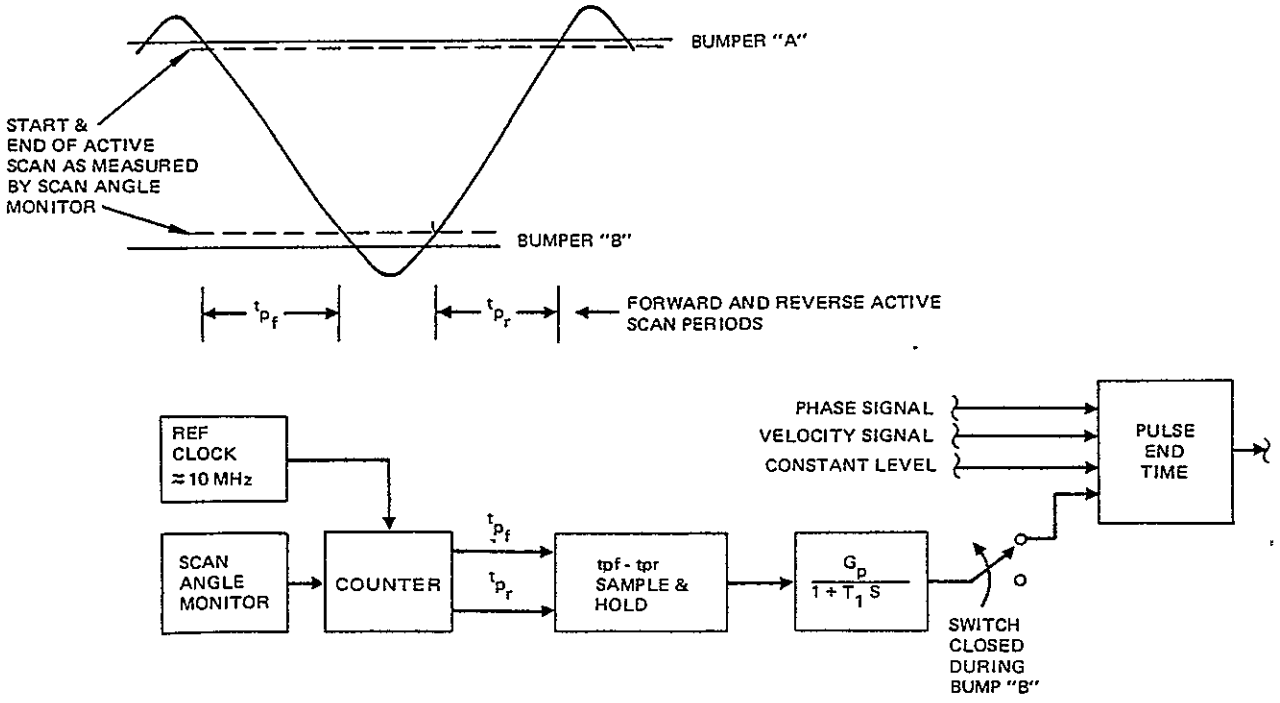

Figure 4.3-9. Suggested logic to provide equal forward and reverse scan periods.

Two counters would measure the active scan period in both directions for each cycle. The difference, accurate to about 0.2 microseconds, would be filtered with a low pass time constant on the order of 10-50 seconds. This signal would then be used on one of the two torque pulses. Since expected system drifts are very slow, the long time constant is compatible with the system and assures that there is minimal crosstalk between this loop and the phase control.

A "hands-on" equivalent to this control has been accomplished by watching two active scan period counters and adjusting one of the two driver power supply voltages. This adjustment causes the level of one input energy function to raise and lower with respect to the other input. In practice it is easy to "hand-control" the two scans such that they are equal to within a microsecond.

4.3.2 Mechanics of the SMA

This section describes the SMA mechanical design including: the mirror design and structural analysis; the torquer design; the flex pivots and their impact upon performance; the flex pivot compensator and measurements of linear scans; the bumper design and analysis of cross-axis motion effects; and mechanical measurements which are required for system analysis.

SMA Mechanical Overview

Figure 4.3-10 is a sketch of the breadboard SMA indicating the major subassemblies. The mirror is mounted to the housing on two flex pivots. The housing is anchored to a magnesium fixture. On the housing are two bumper holders each of which holds one bumper assembly comprised of two bumper springs. The housing also holds the coil subassembly of the torquer. The magnet subassembly of the torquer is mounted to the back of the mirror. The magnesium fixture is mounted to a granite slab under a set of extender blocks. A photograph of the SMA is shown in Figure 4.3-11.

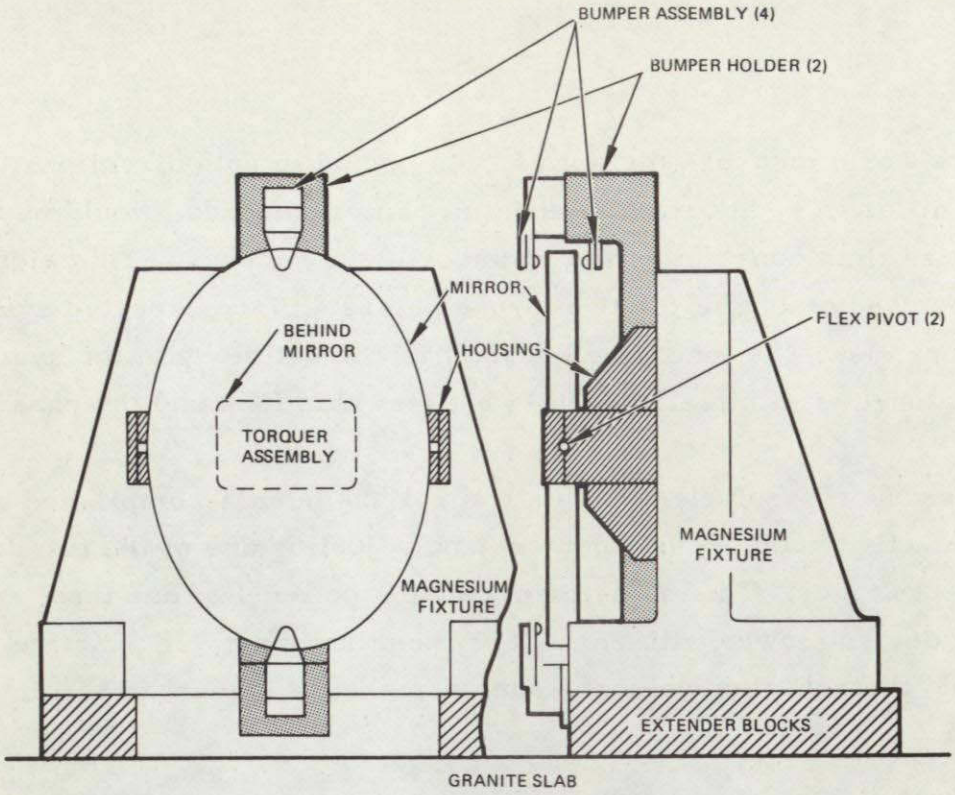

Figure 4.3-10. Sketch of breadboard TM SMA showing major subassemblies and supports.

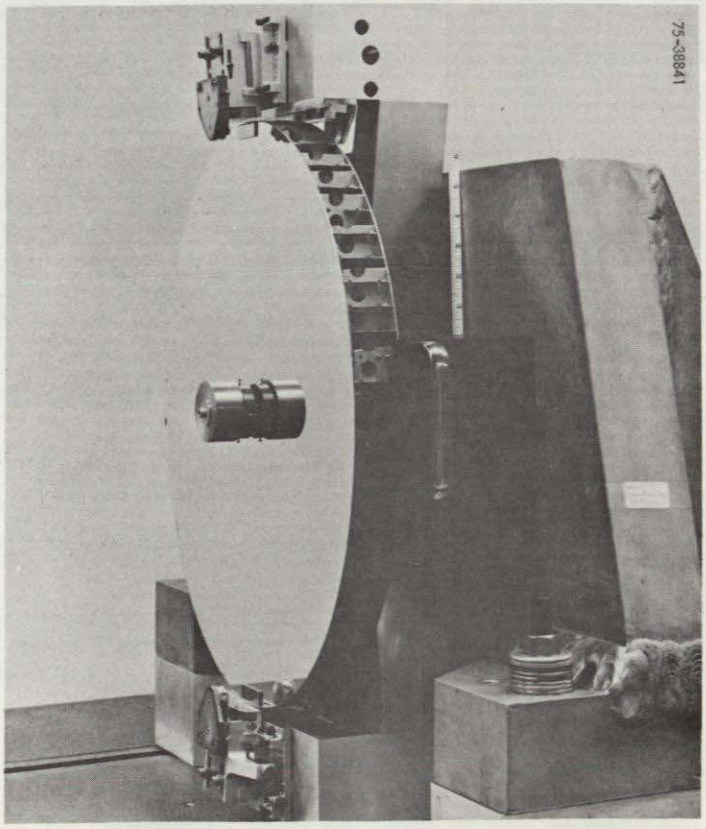

Figure 4.3-11. Breadboard SMA.

This breadboard SMA has evolved from the original TM SMA which was designed with MSS-type bumpers. In order to minimize the net force on the mirror, it was decided to use "end-type" bumper assemblies. This is a concept that has been proven to be most ideal and has been selected for the flight model. The bumper holders are cantilever fixtures (on the breadboard only) designed to adapt the housing to the bumper assemblies. The magnesium fixture was also originally designed to hold the MSS-type SMA. Once the end-type bumpers were installed the magnesium fixture required additional granite slab clearance, hence the extender blocks.

In operation the mirror rotates on the flex pivots in a sinusoidal fashion with a natural frequency of about 1.9 Hz. This sinusoidal motion is stopped each time a bumper is hit as shown in Figure 4.3-12. The turn around motion is the result of the mirror contacting the leaf springs of two bumper assemblies, one at each end of the mirror. The turn-around motion is also sinusoidal with a duration equal to the half period of a sinusoid whose frequency, approximately 60 Hz, is that determined by the mirror inertia and effective bumper spring constant.

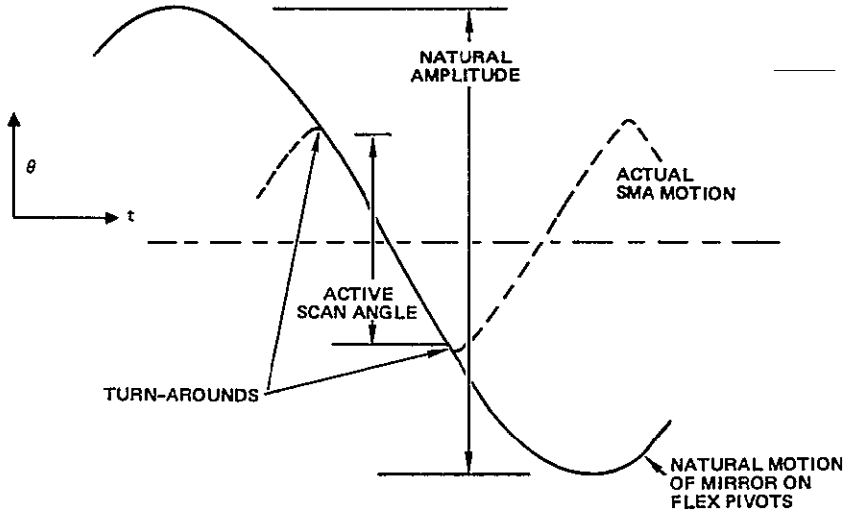

Figure 4.3-12. Scan motion.

The linearity of the scan angular velocity is determined by the portion of the natural sinusoid that is used for the active scan angle. The center of the natural sinusoid is adjusted to be essentially the center of the active scan angle. The flight model will also employ a magnetic device which will further linearize the scan. This device was developed and proven on an IR&D project.

The following brief review of the design requirements introduces the more detailed description of the SMA assemblies.

The mirror should be of minimal inertia to minimize the purturbations to the scanner optics and the spacecraft. Minimum inertia also minimizes the electrical drive power since drive power is directly proportional to mirror inertia. The mirror inertia is proportional to the third power of the mirror major axis dimension which, in turn, is related to the nominal reflection angle which the mirror provides between nadir and the telescope axis.

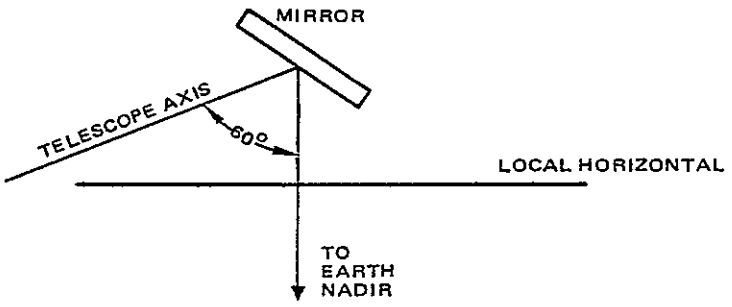

The breadboard mirror is 19 inches long corresponding to a 60-degree angle. If the telescope axis were horizontal as in MSS, a 90-degree mirror would be required which would be 25 inches long. This would increase the mirror inertia by about 130 percent.

The mirror pivot design should provide a repeatable and nearly linear scan. The use of flex-pivots as opposed to bearings does provide truly repeatable torques during active scans.

The mirror should have minimal bending motion as a free body, i.e., it should act as a perfectly rigid body. This can best be achieved by minimizing the forces acting on the mirror and by maximizing its stiffness-to-weight ratio.

The mirror should have minimum cross-scan (or cross-axis) motion. This can be accomplished by minimizing the applied forces which cause cross-axis motion and by providing maximum shear stiffness in the pivot mounts. Flex-pivots are inherently flexible in shear as well as in torsion.

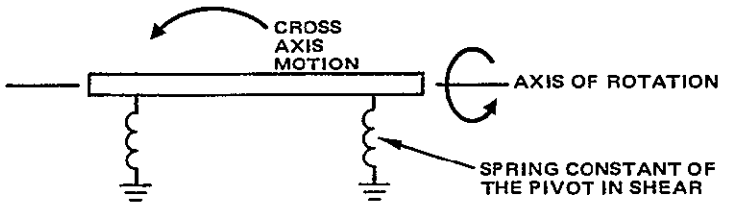

This in turn requires careful selection of flex pivot design to maximize shear stiffness. Since the original breadboard SMA design did not include any feature for balancing out flex pivot torsional force on the mirror, the pivots were selected so as to minimize the mirror's natural frequency (~1.9 Hz) in order to maximize scan velocity linearity. The ratio of shear/flexural stiffness on Bendix pivots is at least a factor of 3 higher than that achievable with designs optimized for minimizing cross-axis mirror motion, but these were selected because of proven reliability (lifetime).

At a given scan frequency and active scan period the product of turn-around-time and torque is a constant and establishes scan efficiency. The fraction of total period spent in turn-around determines scan efficiency. The breadboard SMA has an adjustable turn-around time. Throughout the program effort was made to use no more than 20 percent of the total cycle in turn-around (80 percent minimum scan efficiency). The two forces used to produce turn-around torque should be equal and opposite and the torque profile should be as smooth as possible. The smoothest theoretical turn-around force would be achieved by a massless bumper spring which would absorb zero mirror momentum while reversing the mirror motion.

The bumper springs should be at rest upon initial impact. This is a requirement for along-scan motion repeatability. This requirement states

that the springs used for turn-around should be damped in some manner. In addition the rest position of the springs should be fixed in space. This requires a relatively rigid housing and mounting fixture.

The torquer should not disturb the motion of the mirror during either forward or reverse active scans. Thus the torque energy must be supplied during turn-around and the mirror should be mechanically and magnetically free of the torquer during active scan. This requires that the torquer system have as short a time constant as possible (air core coils are therefore preferable to iron core coils).

A method must be provided for sensing the time of bumper impact. This is done in the bumper assembly via electromagnetic coils.

With this overview of the basic SMA mechanical design requirements as an introduction, the remainder of this section is devoted to a description of the mechanical hardware components.

Mirror Design and Structural Analysis

Prior to starting the mirror design, it was determined that there were three possible contenders for the mirror substrate configuration; all were based upon the use of beryllium since it is a material of high stiffness/weight ratio. These contenders were: the MSS-type design utilizing machined solid block; a machined eggcrate with a brazed back face; and a brazed eggcrate assembly design.

Figure 4.3-13 lists some preliminary estimates for the inertia of the bare mirror (without inserts, counterweights, or torquer components attached) as a function of design parameters. Three mirror widths were used: 16, 15.5 and 15 inches. Where brazed joints were involved, the mass of aluminum alloy in 0.05 inch fillets was included. The construction of brazed eggcrate designs starts with individual webbs which are slotted to form an eggcrate web assembly. This assembly is brazed between front and back sheets to form the final mirror blank. The construction of the machined

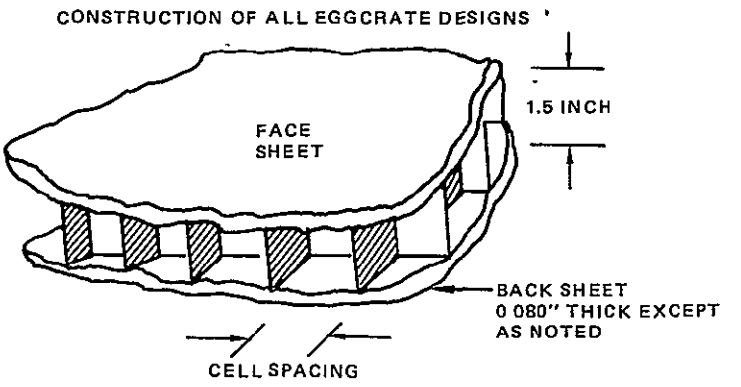

CASE	MIRROR	DESIGN	WALL THICKNESS	CELL SPACING	FACE SHEET THICKNESS	$I_{16.0}$	$I_{15.5}$ (IN-LB-SEC^2)	$I_{15.0}$
1	BRAZED	EGGCRATE	0 016	0 75	0 100	.180	158	.139
2	BRAZED	EGGCRATE	0 016	0 75	0 075*	158	139	122
3	BRAZED	EGGCRATE	0 016	1.00	0.133	228	200	176
4	BRAZED	EGGCRATE	0 016	1 00	0 100	190	167	146
5	BRAZED	EGGCRATE	0 020	0 75	0 100	0 186	.164	143
6	BRAZED	EGGCRATE	0 020	0 75	0.075*	0.163	.143	.125
7	BRAZED	EGGCRATE	0 020	1 00	0.133	0.235	207	.181
8	BRAZED	EGGCRATE	0 020	1 00	0 100	0 196	172	151
9	MACHINED	EGGCRATE	0 020	0.75	0 100	0 190	167	146
10	MACHINED	EGGCRATE	0 020	0 75	0 075*	0 166	146	128
11	MACHINED	EGGCRATE	0 020	1 00	0 133	0.240	.211	.185
12	MACHINED	EGGCRATE	0 020	1.00	0 100	0 200	.176	.154
13	MSS TYPE		0 040	1.50	0 150	0 245	216	189
14	MSS TYPE		0 040	1 50	0 200	0 298	262	229

*BACK SHEET THICKNESS = 0 075

Figure 4.3-13. Preliminary mirror inertia estimates.

eggcrate starts with a solid blank of approximately the final thickness. The eggcrate "holes" are machined out by electro-discharge machining (EDM) leaving a face sheet and web structure. The back sheet is then brazed on to create a rigid blank. The minimum allowable web width was thought to be about 0.020 inches as limited by this machining technique. EDM appeared to be the only allowable machining method that would not produce residual stresses. The MSS-type design is a simple scale-up of the MSS mirror wherein a solid blank is EDM'd from the blank edge, radially inward.

The two types of eggcrate constructions would each allow a mirror of less inertia than could be achieved by the MSS EDM technique. The natural symmetry of the brazed eggcrate strongly influenced its choice because of thermal considerations. The chosen design incorporates a 3/4 inch eggcrate pattern with a nominal 0.080 inch front face sheet and a 0.068 inch back sheet.

The brazing alloy used is aluminum-silicon. Due to expected thermal stresses between brazing alloy and the beryllium core material, it was decided to limit the brazing alloy to the region of the front and rear sheets to minimize possible show through of the aluminum posts which would otherwise connect between front and back optical surfaces. At temperatures above or below the polishing temperature the factor of a higher thermal expansion of aluminum compared to beryllium was the effect which was to be avoided. To facilitate this, "stop flow" holes were put in the core strips so that aluminum brazing material would not flow across from front to back along the webb nodes. A reduced copy of the mirror blank drawing (3439382) is shown in Figure 4.3-14 (sheet 1, 2 and 3).

The design inertia and weight of the bare mirror were estimated to be 0.217 in-lb-sec^2 and 3.7 pounds. The two inserts on the 16 inch axis are for the 3/4 inch diameter flex pivots. The fore-aft location of the flex-pivots was based upon the added weight of an MSS-type torquer. When fabrication started, no definitive weight estimates existed for the new torquer hardware which would permit torquing during turnaround. The central insert is

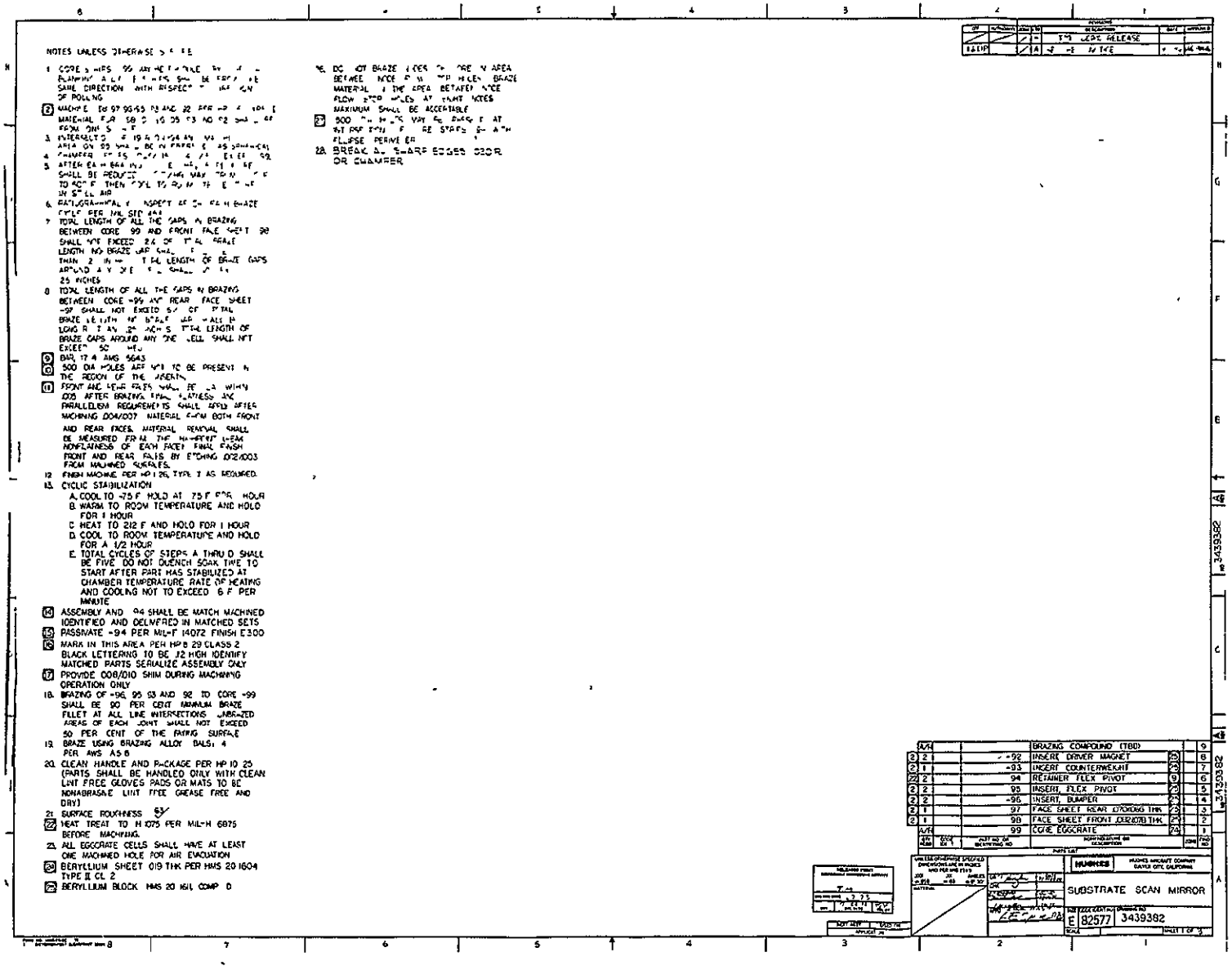

Figure 4.3-14. Mirror blank drawing. (Sheet 1 of 3)

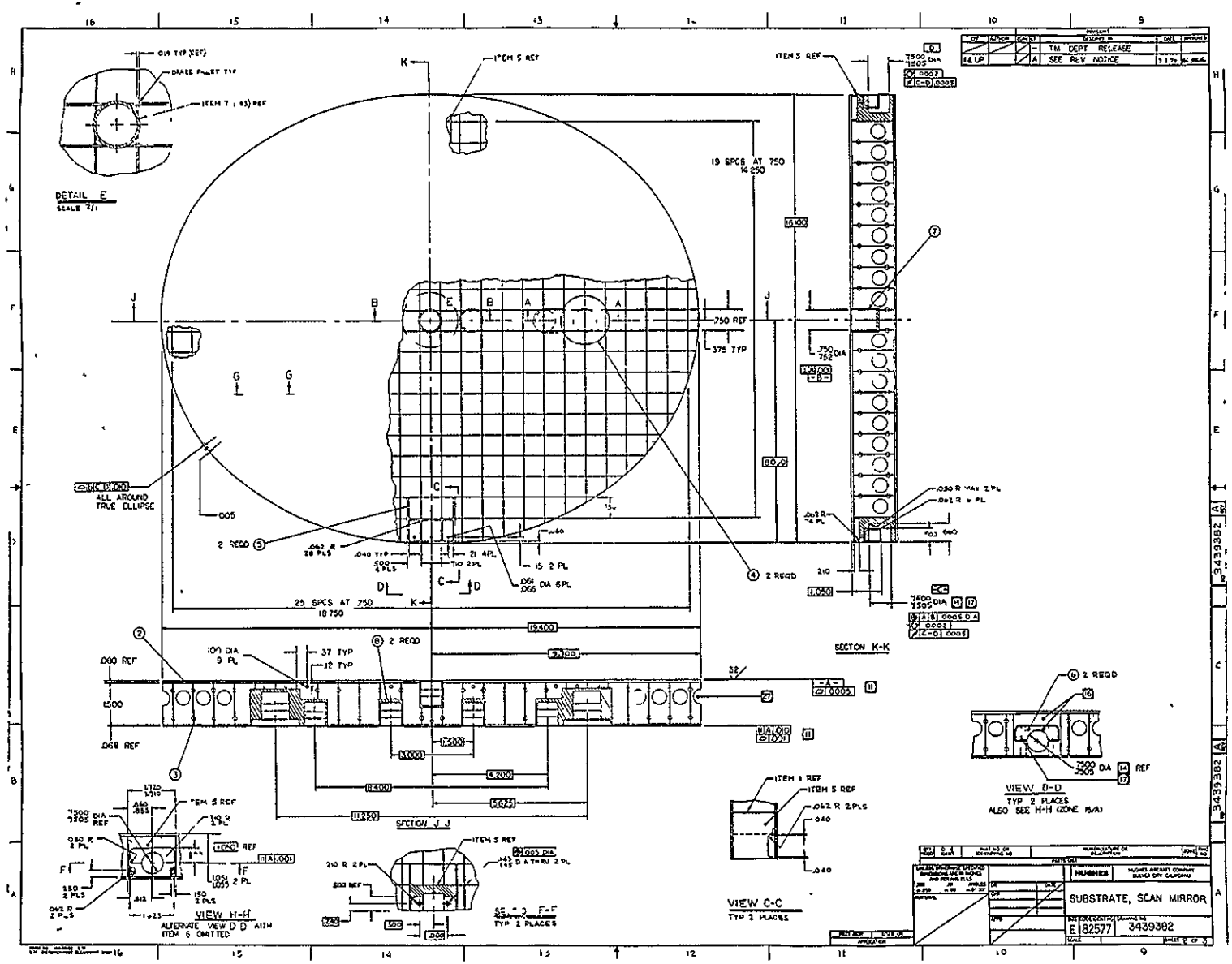

Figure 4.3-14. Mirror blank drawing. (Sheet 2 of 3)

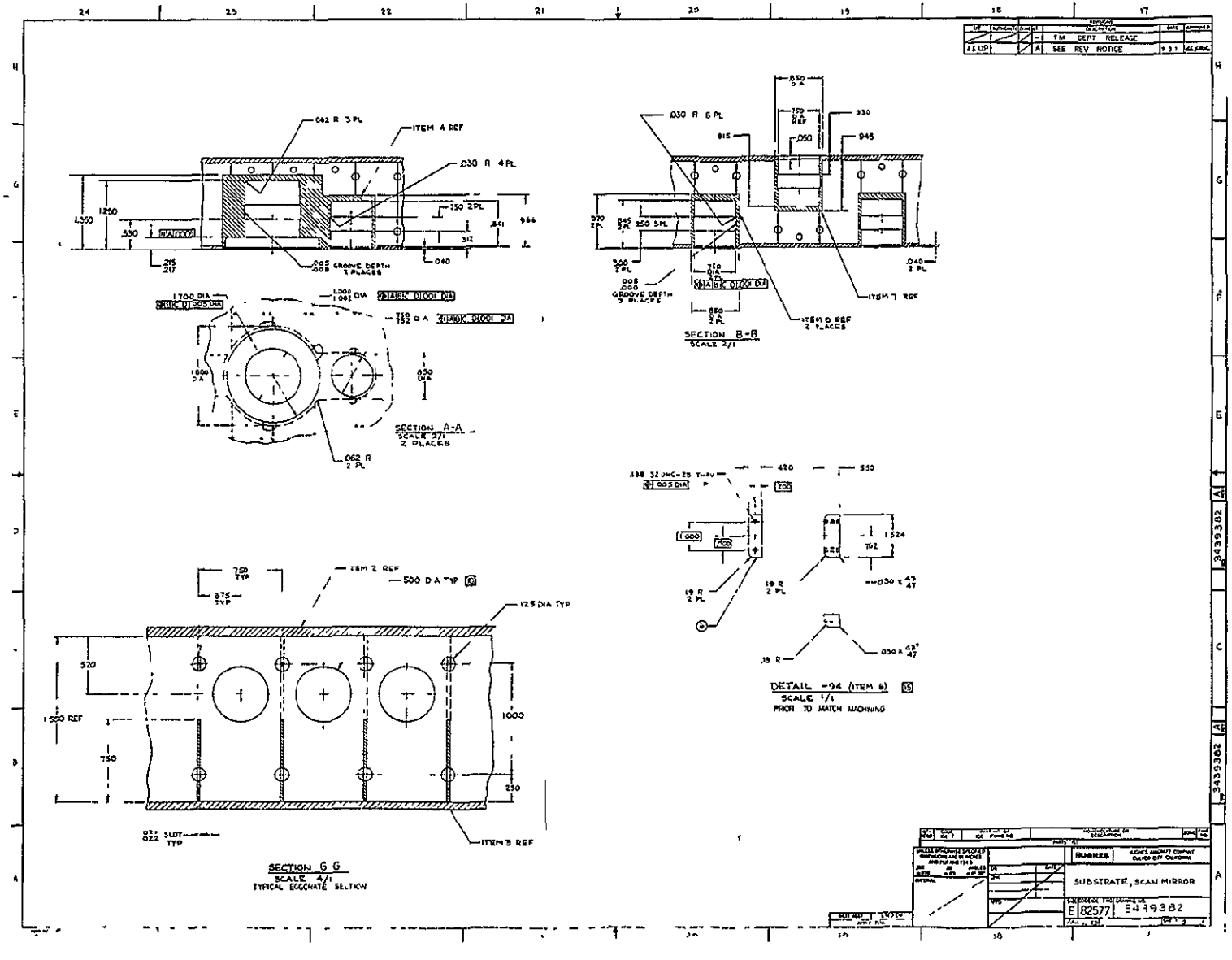

Figure 4.3-14. Mirror blank drawing. (Sheet 3 of 3)

for the counter weight that is used to achieve final balance. The two inserts outboard of center along the major axis serve two purposes: the inboard holes accept the magnet assembly of the torquer and the outboard holes were designed to accept the bumper cups for the MSS-type bumpers.

In the next phase of development a slight mirror redesign would eliminate the two bumper cup holes and bumper inserts would be added at the ends of the major axis. In addition, the flex pivot inserts would be redesigned to nominally place the center of gravity on the scan axis. When the new parts were added to the original breadboard for testing with the torque-while-turn-around leaf spring bumpers the total weight of the assembly mirror was increased to about 7.5 pounds to maintain balance, thus a 3 pound reduction would occur with the flight model.

Prior to PDR a dynamic structural analysis of the mirror was performed to check two criteria: stresses must be sufficiently low that fatigue and permanent mirror surface quality degradation will not occur; and dynamic deformations must be small enough as to not degrade MTF. Preliminary stiffness/inertia calculations showed that the mirror should bend less than the MSS mirror and dynamic flatness measurements of the MSS mirror showed no deleterious bending. Thus there was significant reason for optimism.

In an a priori analysis, two areas of uncertainty exist: the exact nature of the turn-around forces and the validity of the structural model. In the preliminary analysis mentioned above, the turn-around forces were assumed to be half-sinusoids. This approximation is exact only for massless spring bumpers. The model approximation used was a simple beam. Forces were based upon the location of MSS-type bumpers at an operating frequency of 9.78 Hz, and an 8 m.s. turn-around time was assumed.

Results of the analysis indicated that dynamic flatness should be well within optical requirements. The analysis recognized that the dynamic deflection of any particular point on the mirror surface woud be defined by the equation

$$\delta = \sum_i A_i \Delta_i \sin \omega_i t$$

with A_1 representing some dynamic factor, Δ_1 representing some static factor, and ω_1 the natural frequency of a particular mode, i, of motion. The dynamic factor for half-sine acceleration inputs is a function of the ratio of the half-sine exciting frequency, ω_e to the natural frequency of the system, ω_n, specifically which has been plotted in Figure 4.3-15.

$$A = Z \left[\frac{\frac{\omega_e}{\omega_n} \cos \frac{\pi}{2} \frac{\omega_n}{\omega_e}}{\frac{\omega_e^2}{\omega_n^2} - 1} \right]$$

The following modes of deflection were identified and studied:

δ_1 = Torsion of the mirror about the flex pivot *

δ_2 = First mode bending of mirror due to bumper loads

δ_3 = First mode bending of mirror due to a 5 percent imbalance in the bumper loads

δ_4 = Deformation due to torquer (MSS type) and counterweight inertias

δ_5 = Deformation due to flex pivot shear vibration.

The total maximum deflection during scan was computed to be 0.7 microinches occurring at the mirror end points and resulting in a peak slope error of 0.11 microradian. The simplified model used for the calculations was such that the predicted mirror response would be somewhat in error, but the magnitudes were so small compared to the allowable dynamic deformations (12 microinches) that further analysis did not seem warranted at that time.

---

*There will be no significant deflection in this mode in the flight design because the flexpivot torque will be countered by the flex pivot compensator (see discussion on page 4-54).

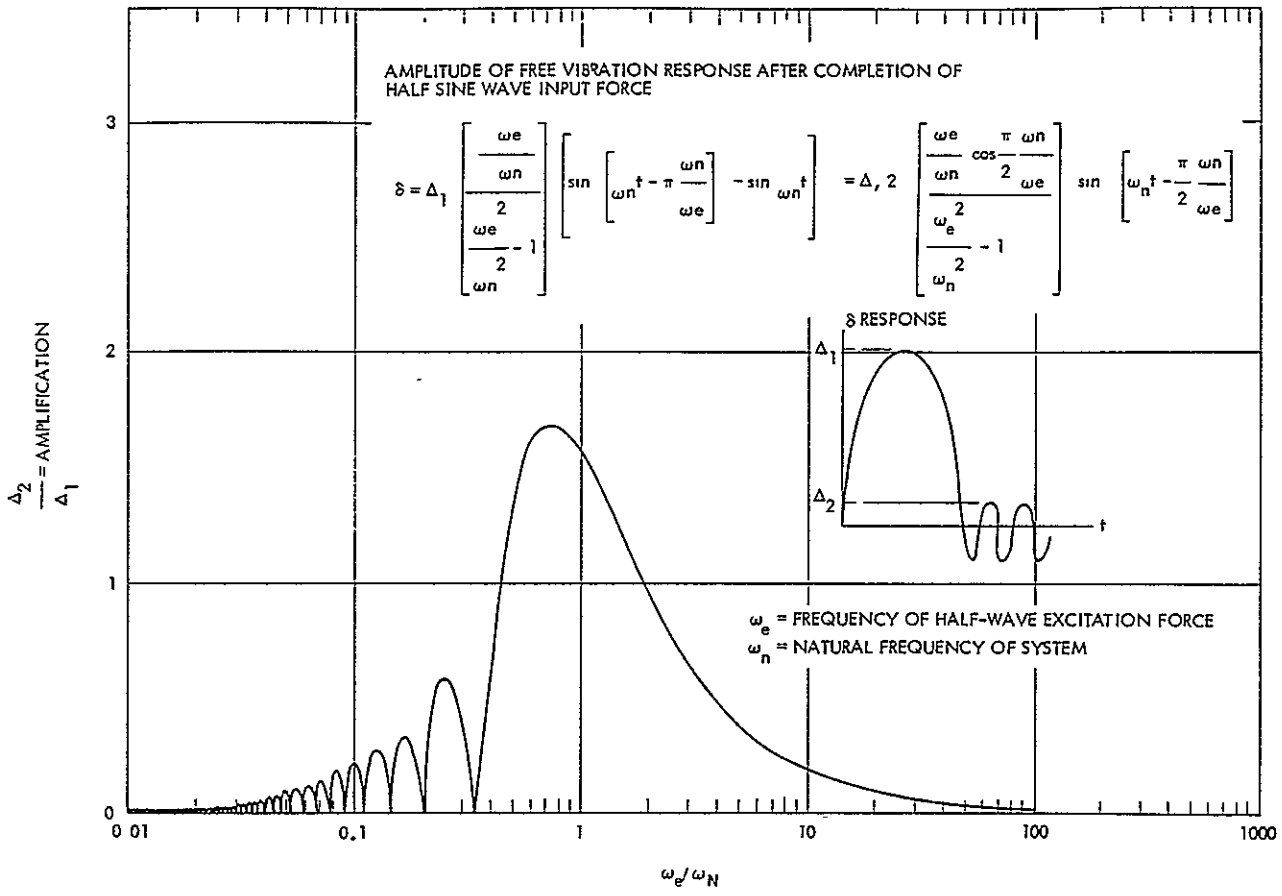

Figure 4.3-15. Dynamic amplitude.

After assembly, the mirror was tested by optical techniques for dynamic flatness (see Section 4.5) and no deflection within the resolving capability of the instrumentation (8 microinches) was noted. After final testing of the SMA, accelerometers were placed on the mirror, running at 10 Hz, and two distinct modes of motion were measured. A 330 Hz mode, associated with deformation due to vibration of the mirror in shear on the flex pivots, was measured with a peak amplitude of 2.0 microinches compared with a 0.7 microinch calculated. A 2350 Hz mode, associated with δ_2, δ_3 and δ_4, was measured at 3.5 microinches. This high frequency mode quickly damps out during scan while the 330 Hz mode does not. These measured results are of significance since they include the important effects of the non-sinusoidal components of the turn-around forces. The effect of bumper mass is to create high frequency slapping which, in turn, causes significant response (at 2700 Hz for example) that would not be seen in the early structural analysis. Of all of the techniques used to determine dynamic deformation, this last one, based upon accelerometer measurements is the most definitive. Thus it can be concluded that the real deformations are significantly less than 12 microinches which would be required to cause a noticable degradation in system MTF.

The question of peak stresses, however, can be determined by purely analytic techniques. Shear stresses were calculated according to beam

theory; that is, it was assumed that the mirror was a beam with bumper forces acting as shear loads as follows:

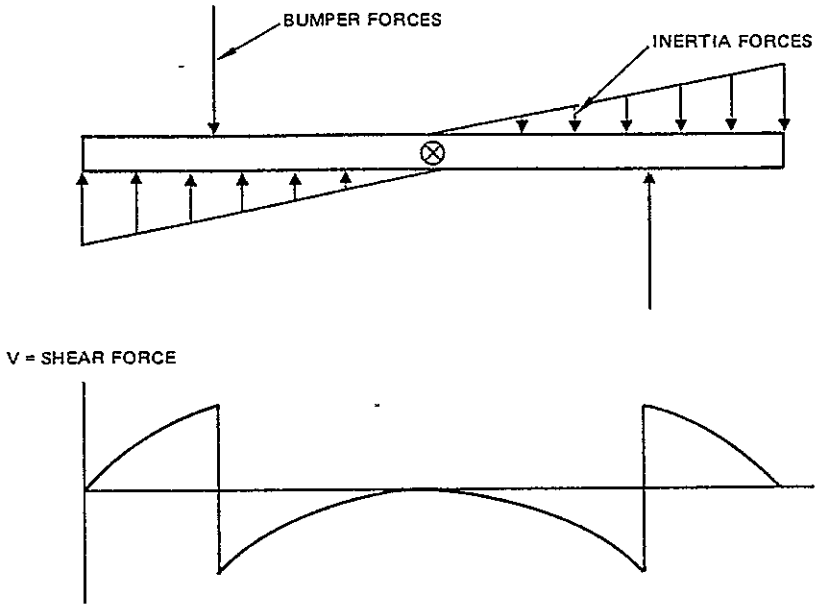

Inertia forces account for the slopes in the shear diagram. Beam equations for flexural shear stress were then used to calculate stress for each of two extreme conditions. The first condition was based upon the conservative assumption that all shear was carried only by the four center core strips. Under that assumption, the maximum shear stress would be 300 psi. The other (lower) extreme condition was based upon the assumption that all panels carried shear equally. Shear stress under that condition would be 55 psi.

The core strips contain 0.5 in diameter holes around which higher stresses might be expected. Those holes, however, were not present in the vicinity of the bumper cups; consequently, 300 psi remained an upper limit on shear stress.

The shear buckling stress for a simply supported plate without holes would be 145,000 psi without correction for plasticity. That value exceeded even the 70,000 psi tensile stress for beryllium, suggesting that core panels were probably not susceptible to buckling.

It should be noted that the actual failure stress would have been affected by the presence of holes and by the fact that 45 percent of the lengths

of the strips near the mirror edges were actually free rather than simply supported as assumed. It was not only dificult but impossible to calculate failure strength accurately, but conservative judgement placed that value somewhere above 10,000 psi based upon the above calculation. Consequently, even with the beam approximations used in calculating stresses, the margin of safety was large enough to inspire a large degree of confidence in the design.

A stress concentration of approximately 600 psi exists in the core panels near the counterweight. This is not in an optically critical area on the face sheet and also would not pose any problem in fatigue. The magnet assembly induces no shear and only small tensile and compressive stresses in the core panels thus producing maximum face sheet stresses of about 20 psi.

The modification to the stress estimate caused by the new end-mounted bumpers and lower operating frequency will be to reduce all stresses somewhat. In the final design an insert will be provided at each end of the mirror to pick up the turn-around force and distribute them optimally into the mirror.

Torquer Design

The torquer used on the original breadboard SMA was designed to operate with MSS-type logic and bumpers. It had been used earlier on an IR&D prototype SMA to aid in the development of new control logic. Figure 4.3-16 is a photograph of the IR&D SMA. The mirror-mounted torquer components consist of a mounting plate holding eleven magnet plates. Each plate holds two magnets and the end plates contain an iron flux path. The support housing-mounted components consist of a mounting plate and ten epoxy encapsulated coils. The coils contain no iron and thus permit a short time constant for torque buildup. This feature made it possible to retain this torquer for use in the later torque-while-turnaround redesign. It has, in fact, performed very well in this short torque pulse mode, however, a lighter design will be used to further increase stiffness on the next model.

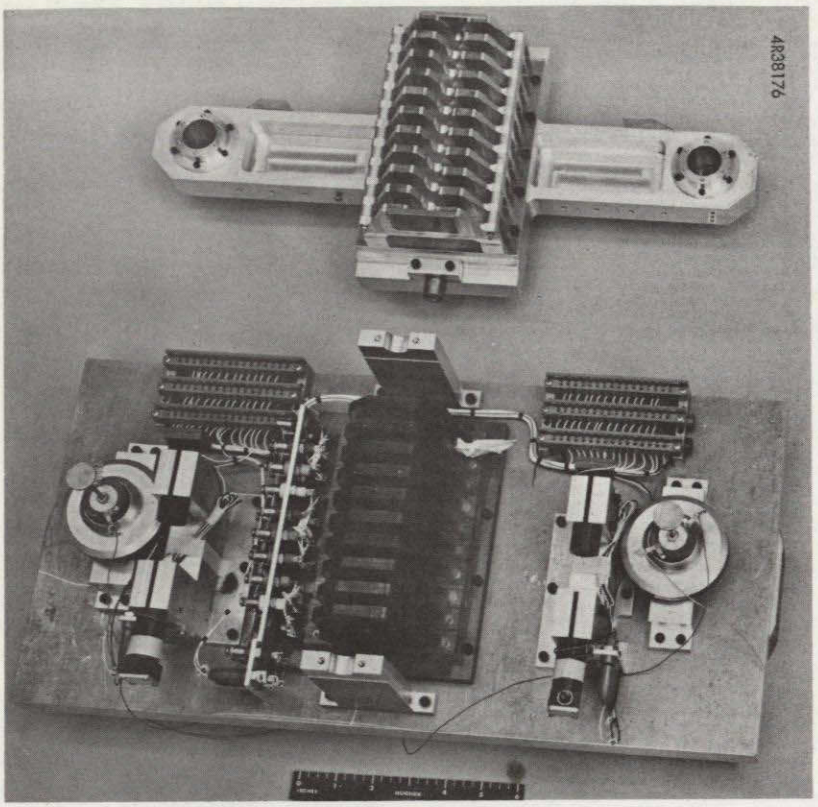

Figure 4.3-16. Torquer components shown on early IR&D SMA hardware.

This new design would utilize the same added inertia to the mirror but would rearrange the magnetic structure to achieve higher flux density and thus higher torque per $\sqrt{\text{watt}}$ with a lower time constant. This new design is shown in Figure 4.3-17.

The existing prototype coils and the suggested coils are of identical size and construction. However a change in the wire size (holding the total wire weight constant) could be utilized to adjust the impedance to the driver. At present this impedance has been adjusted by selecting a particular series-paralleled combination of wiring the ten coils. Both designs are capable of applying torque in either direction and at all scan angles. Thus these torquers

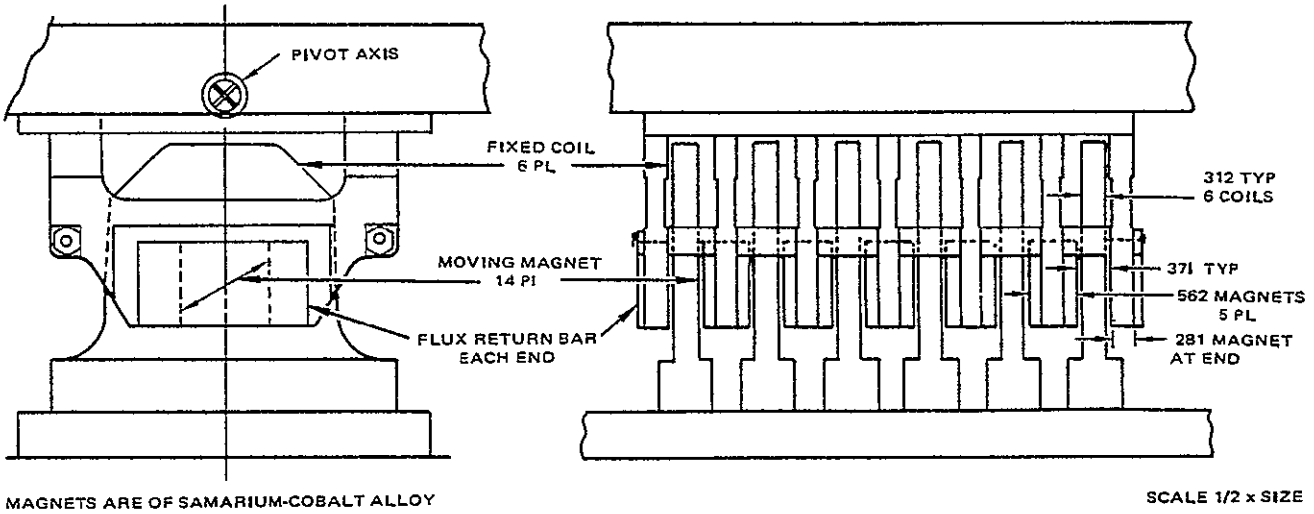

Figure 4.3-17. Suggested redesign of torquer.

can be used to start the SMA. A comparison between the parameters of the existing torquer and the torquer shown in Figure 4.3-17 is as follows:

	Breadboard Torquer	Redesign Calculated
Inch-pounds per $\sqrt{\text{watt}}$	2.54	3.15
Flux density in gaps, kilogauss	3.2	4.8
Time constant, milliseconds	3.1	2.4
Inertia added to mirror, lb-in^2	10.4	10.4
Mass unbalance, lb-in	2.9	2.9

The effect of the force imbalance created by the torque pulse is negligible. The decreased time constant and increased torque for the same power input would probably reduce the total drive power by at least 30 percent.

Other torquer designs have been investigated with the goal of reducing mirror inertia and torquer time constant. As yet no better design has been found.

Flex Pivot Choice and its Effect Upon Performance

Because of the along-scan repeatability requirement, no random torque can be allowed during the active scan. This precludes any form of

bearing except the flex pivot. A flex pivot, however, has two disagreeable characteristics: it torques the mirror proportional to angular deflection and it is not infinitely rigid in shear. During this program all flex-pivots used on the SMA were obtained from the Bendix Corporation. The fatigue life of these units has been proven and they were used on the MSS. The Bendix design is unique in that they are cylindrical in form factor and tend to rotate at an imaginary plane through the center:

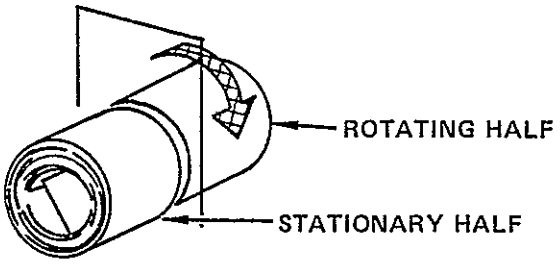

They are thus easy to mount in a variety of applications. The disadvantage of the design is that supports for the flexure are cantilevered from the mounting surface resulting in a loss in shear stiffness.

Pivots were selected from the following chart abstracted from the Bendix catalog:

Nominal Dia	Cat. No.	Wt (Oz.)	Load Capacity Pounds V_c	V_t	Torsional Constant Lb-In-Rad^{-1}	Dia (In)	Length (In)	Mounting Length (In)
3/8"	5012-400	0.1312	225 0	225.0	22.0	0.3750	0.600	0 285
	5012-600	0 1216	80.0	113.0	2.75			
	5012-800	0 1136	9 9	31 5	0.331			
1/2"	5016-400	0 3152	400.0	400.0	52.0	0 5000	0 800	0.380
	5016-600	0.2928	141.0	200.0	6 50			
	5016-800	0.2704	17.7	56 3	0.813			
5/8"	5020-400	0.6144	625.0	625 0	106.0	0.6250	1.000	0.475
	5020-600	0.5696	221 0	312.0	13 3			
	5020-800	0.5280	27.6	87.8	1 69			
3/4"	5024-400	1.0880	900.0	900 0	182 0	0.7500	1 200	0.570
	5024-600	1.0080	318.0	450.0	22.8			
	5024-800	0.9344	38 9	127 0	2.85			
7/8"	5028-400	1.7280	1220.0	1220 0	289.0	0.8750	1.400	0 670
	5028-600	1.6	431.0	610.0	36.1			
	5028-800	1 485	53.0	172.0	4.44			
1"	5032-400	2.584	1600.0	1600.0	431 0	1 0000	1.600	0.770
	5032-600	2.397	566.0	800.0	53.8			
	5032-800	2.221	70 7	225.0	6.73			

The shear load capacity is measured in two orthogonal directions: V_c puts both flexures in compression while V_t puts one flexure in tension and one in compression.

The first basis of selection was to pick a pivot which would see no greater launch stress than the MSS pivot. It was assumed that the MSS and TM launch environments would be identical. Therefore it was required that

$$\frac{V_c \text{ TM Pivot}}{V_c \text{ MSS Pivot}} \geq \frac{\text{Mass TM Mirror}}{\text{Mass MSS Mirror}}$$

The second basis of selection was to require that the torsional constant be such that the SMA natural frequency would be about 2 Hz or less. Pivot number 5024-600 met both requirements. The torsional stiffness results in a natural frequency of 1.88 Hz with the mirror assembly, as built and the shear load requirement was met. The shear stiffness of this pivot, as mounted, is 33,000 lbs/in for each pivot.

It is important to consider the effect of the shear constant on cross-axis motion. If we consider the scan mirror to be much stiffer than the flex pivot on which it is mounted, the following is a model of the SMA in a two dimensional, cross-axis sense:

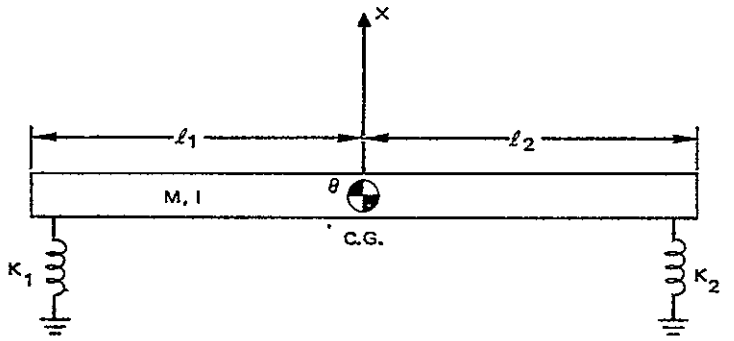

The two springs of stiffness k_1, and k_2 are the flex pivots in shear, and lengths ℓ_1 and ℓ_2 determine the location of the c.g. of the mirror whose mass is M and whose inertia is I. The motion of the mirror for this two dimension model is a translation, x and a rotation θ. The equation of motion in matrix form is

$$\begin{bmatrix} M & O \\ O & I \end{bmatrix} \begin{bmatrix} X \\ \theta \end{bmatrix} = \left[\begin{array}{c|c} k_1 + k_2 & k_2\ell_2 - k_1\ell_1 \\ \hline k_2\ell_2 - k_1\ell_1 & k_1\ell_1^2 + k_2\ell_2^2 \end{array}\right] \begin{bmatrix} X \\ \theta \end{bmatrix} = 0$$

as a force free body (after leaving bumpers). The solution of this equation yields two modes of motion. In the first mode both springs compress and expand in phase. The natural frequency of this mode is 330 Hz for the SMA as built. In this mode the center of gravity tends to move up and down and the mirror rotates to the extent that $\ell_1 k_1$ does not equal $\ell_2 k_2$. In the second mode the compression and expansion of the two springs are out-of-phase and the mirror tends to move up and down very little but rotates about the c.g. The natural frequency of the TM SMA second mode is 1200 Hz. The first mode is excited by net forces on the mirror through the c.g. The second mode is excited by net torques on the mirror. In a dynamic sense, applicable to the SMA, the power spectrum of the forces and torques applied determine the magnitude of motion of each mode. However with the real SMA the situation is not two dimensional and each pivot contains two dimensions of shear. What can be concluded, however, regarding the minimization of cross-axis motion is the following:

- For the second mode. Minimize cross-axis torque applied by the bumpers. Minimize all forces or torques occurring at high frequencies (near the mode natural frequency). Maximize flex pivot shear stiffness since, for a given energy put into the mirror in the second mode, the angular deflection is proportional to $k^{-1/2}$.
- For the first mode. Balance the mirror and select equal pivots to make $k_1\ell_1 - k_2\ell_2 = 0$. This will tend to straighten the mode shape and minimize θ for a given x (only θ causes cross-axis motion). Minimize the net forces on the mirror, especially at mode frequency. Maximize the flex pivot shear stiffness.

The general subject of minimizing cross-axis motion will be discussed further in other sections, however with respect to selecting flex pivots it is clear that an attempt at matching should be done and it was. A test fixture was built that allowed matching the pivots in shear to one percent. However, in SMA tests it was found that no significant change in first mode cross-axis motion could be achieved by this selection process. The reason is only

partially understood but a few facts are clear. In three dimensions the shear stiffness at each mirror/housing interface is two dimensional and dependent upon the stiffness of the mounting as well as that of the pivot. The pivots were matched in one dimension. Selection of pivots on the basis of two dimensional shear stiffness is possible (given enough pivots) but probably not useful, since a major portion of the loss of stiffness is clearly in the mounting technique.

The other clear fact regarding the relationship of the pivots to cross-axis motion is the desire for increased stiffness. Unfortunately, the ratio of shear stiffness to torsional stiffness is fixed for a particular design. Thus for Bendix pivots the only way to increase shear stiffness would be to accept a higher mirror natural frequency which would degrade the scan linearity. (With the new flex pivot compensator, discussed in the next section, it is possible to accept a higher torsional stiffness, and thus this is a legitimate design parameter.) The Bendix design does possess a poor shear/torsional stiffness ratio and this fact was intensely studied.

A project was undertaken to analyze and test a flex pivot design that will have greater shear stiffness than the Bendix pivot with equal torsional stiffness and fatigue life. Initial calculations indicated that the cantilevered supports of the Bendix flex pivots contribute about half of the loss in stiffness. The proposed design was a classical flex pivot where the flexure supports are directly mounted (bolted) to the mirror and housing rather than clamped as with the Bendix pivots.

A set of pivots was built with flexures of exactly the same dimension as those used by Bendix. Figure 4.3-18 shows the design drawing. Analysis of the "ideal" shear stiffness indicated 490,000 lbs/in. "Ideal" refers to the flexures alone. It was not expected that "ideal" stiffness could be obtained, however, some improvement over the 33,000 lb/in achieved by the Bendix design was expected.

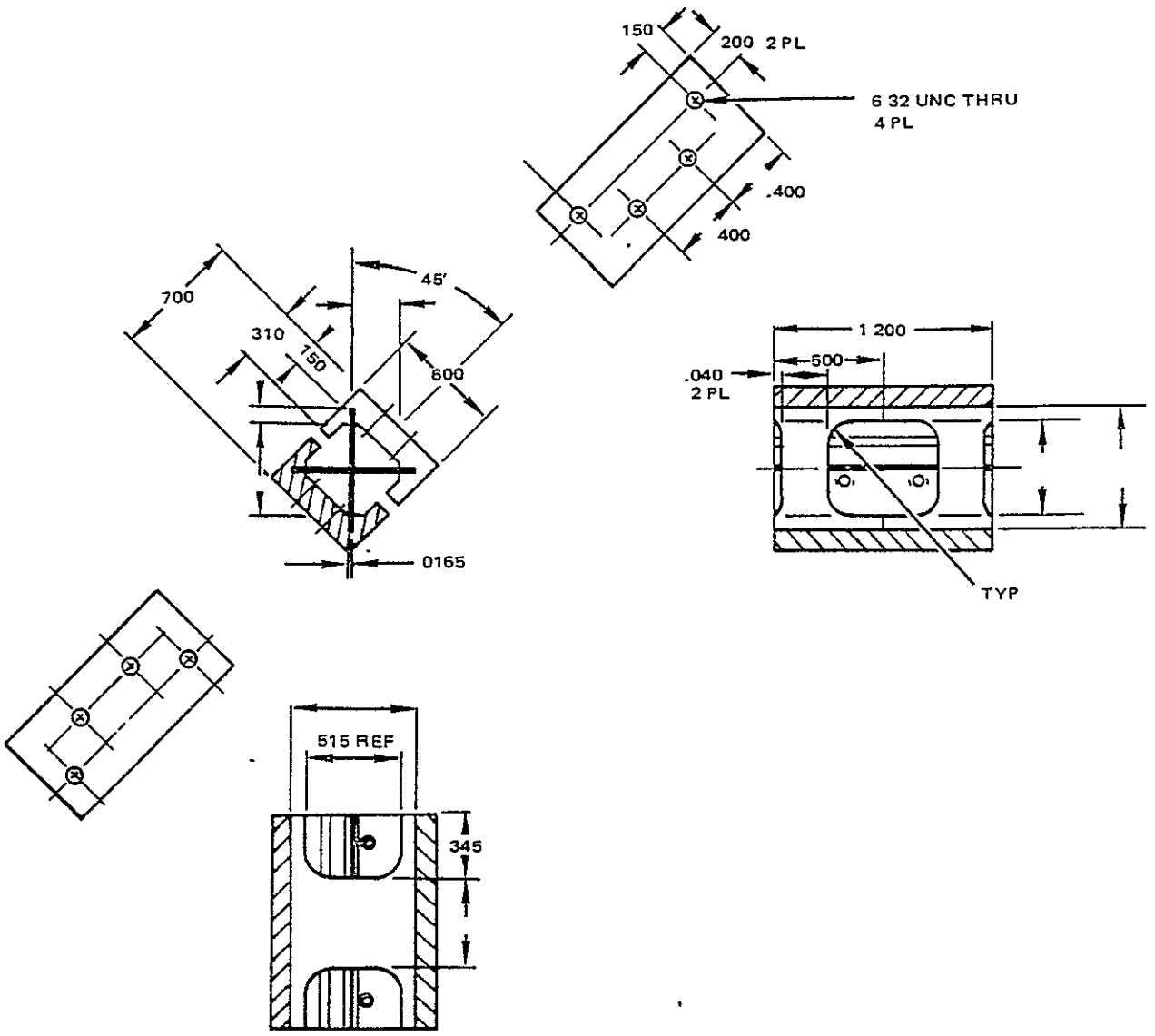

Figure 4.3-18. Classical flex pivot built and tested.

The test set-up consisted of a pair of pivots mounted to a base and connected by a rigid bar. A similar set-up was built to test Bendix pivots. It was realized that the mounting stiffness of these test set-ups probably exceeded that of the TM SMA. The test fixtures were mounted on an Instron test machine and force-deflection data taken. The pivots were rotated such that both axes (V_c and V_t) could be tested. The test results, shown in Figure 4.3-19, indicate that the classical design is at least 2.6 times as

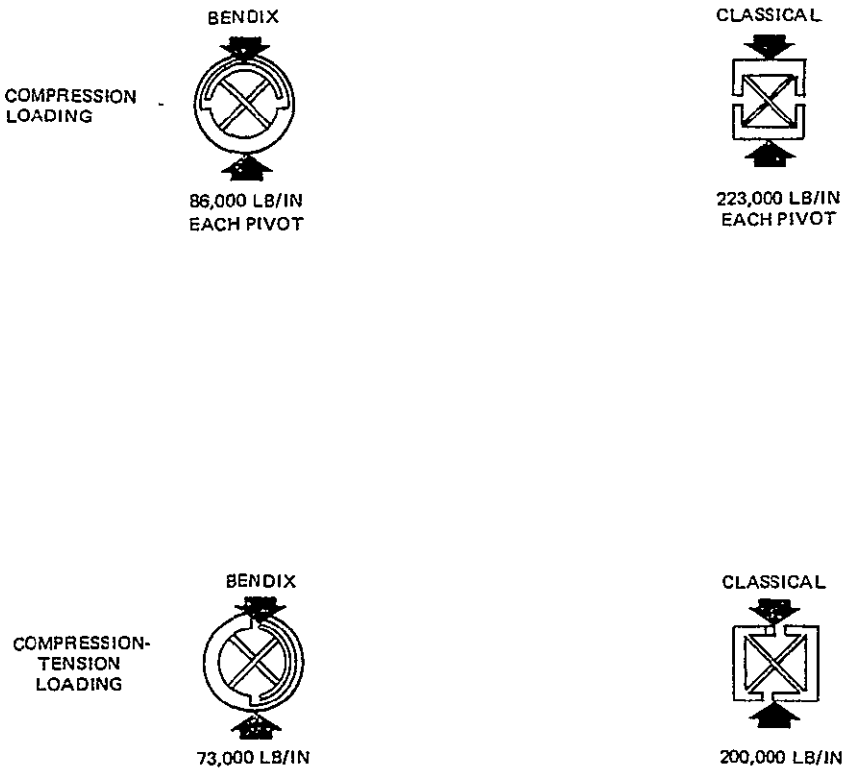

Figure 4.3-19. Comparable shear stiffness test results.

stiff as the Bendix design. The difference between the shear stiffness of the Bendix pivot, as tested above (73,000 lb/in) and as mounted in the TM SMA (33,000 lb/in) is in the rigidity of the mounting. The equivalent stiffness of the present design can be conservatively estimated by assuming that the stiffness of the test set-up was infinite. From the sketch

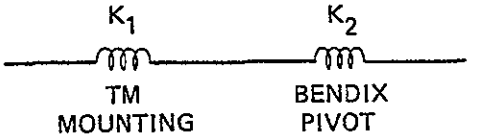

the mounting stiffness may be calculated

$$\frac{1}{k_1} + \frac{1}{k_2} = \frac{1}{k_t} = \frac{1}{33,000} = \frac{1}{k_1} + \frac{1}{73,000}$$

to be k_1 = 60,300 lbs/in. Now even if no increase could be achieved in the stiffness of the mounting then a simple replacement of the classical pivot for the Bendix type would yield (with k_3 = 200,000)

$$k_t = \frac{k_3 k_1}{k_3 + k_1} = 46,000 \text{ lbs/in}$$

or a 40 percent increase in effective shear stiffness. By a reasonable design effort directed at increasing the mounting stiffness, it is expected that the classical pivot will yield a net increase of 100 percent. This would increase the natural frequency of both cross-axis modes and decrease the cross-axis angular amplitude for a given energy level by the square root of the stiffness increase. However, since most energy inputs tend to decrease with higher frequency it is reasonable to expect that this substitution could reduce by about a factor of two, the presently measured cross-axis motion.

Such a substitution could not be made without proof of fatigue life, however, it is strongly recommended that such steps be taken prior to finalization of the flight design.

A final problem with Bendix flex pivots is the fact that the axis of rotation shifts with deflection. This is true for both the Bendix pivot and the classical pivot as tested. This shift is shown in Figure 4.3-20. If two pivots behaved identically then no cross-axis motion would result. Unfortunately, no two pivots are exactly identical and this causes a repeatable cross-axis motion as a function of scan angle. Since it is repeatable no scan-to-scan cross-scan error results and forward and reverse scans nest perfectly. However, a mapping error does result. By carefully selecting pivots and by rotating the pivots relative to each other in their mounts, this nested cross-axis motion can be minimized. The test log book shows that for one mounting

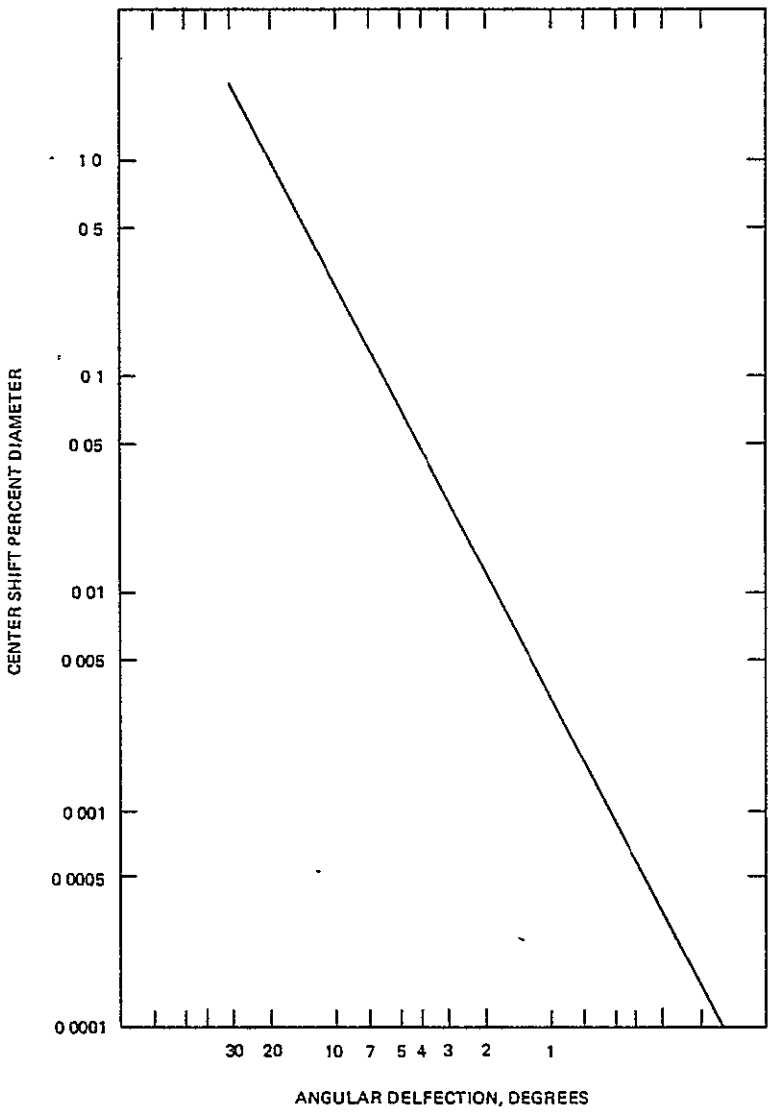

Figure 4.3-20. Center shift of common flex pivots.

arrangement the nested motion was less than 4 microradians. Generally, about 20 microradians of the nested motion result from flex pivot center shifts.

Figure 4.3-21 shows a design for a flex pivot of the classical type which will have a minimal center shift. It consists of two classical flexure pairs mounted such that their center shifts are complementary.

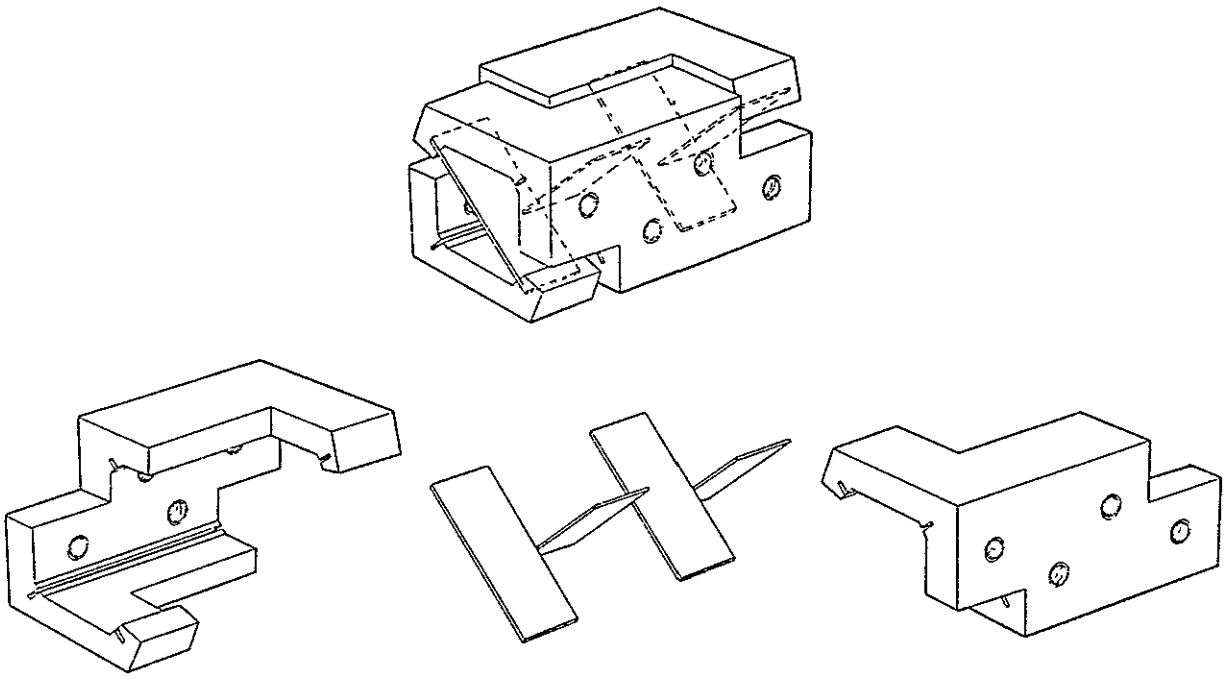

Figure 4.3-21. Minimal center shift classical flex pivot.

However, since the natural center shift is restrained, the compression in each flexure is increased (by about 20 percent for the scan angles as large as $\pm 5^{\circ}$ of mirror motion). Should it prove desirable to reduce built-in mapping errors in the cross scan direction, pivots of this type should be built and tested.

The Flex Pivot Compensator

Scan linearity is defined as the nominal or average scan rate at a specific scan angle referenced, in percent, to the average scan rate over the entire active scan (half scan only). Thus the linearity of a constant speed scan would be 100 percent at all points along the scan angle. Referring to Figure 4.3-12 it can be seen that the flex pivot causes a sinusoidal scanning motion. At the start of the subject contract a design goal was set to

control the linearity to stay between 93.0 and 103.7 percent during the forward scan (where no torque occurred).

As part of the formal measurement program linearity is measured with the SMA running in air. These measurements are subject to inaccuracies of air drag and the uncertainty in placements of position measuring diodes (see Test Procedure).

A more accurate measure of linearity, for pure flex pivot effects can be obtained by measuring the mirror natural frequency, ω, the total object space active scan, θ_s, and the time required to scan, t_p, the total angle. Assuming that the rest position of the mirror is equidistant between start and end of active scan and equidistant between turn-arounds and assuming no air drag nor significant residual torquer effects, the following sketch can be used to develop an exact measure of linearity:

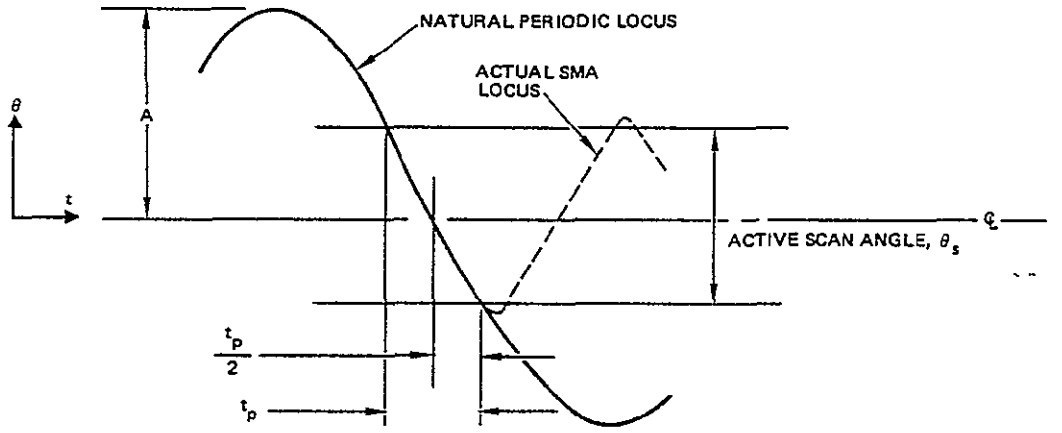

Define: $\theta = A \sin \omega t$ where $t \equiv 0$ at $\mathbb{Q}$ crossing

Then $\dot{\theta} = A \omega \cos \omega t$

and we can calculate the average scan rate over the active scan angle,

$$\bar{\dot{\theta}} = \frac{\int_0^{t_p/2} A\omega \cos \omega t \, dt}{t_p/2} = \frac{A \sin (\omega t_p/2)}{t_p/2}$$

But $\bar{\dot{\theta}}$ also equals θ_s/t_p, both of which are known. Thus we can solve for A. Then the maximum scan speed is

$$\dot{\theta}_{max} = \dot{\theta} \, (t = 0) = A\omega$$

and the minimum scan speed is

$$\dot{\theta}_{min} = \dot{\theta} \, (t = t_p/2) = A\omega \cos \, (\omega t_p/2)$$

for the TM SMA with end bumpers and running in helium, the following were measured:

$t_p = 0.043$ sec

$\theta_s = 0.273$ rad (in object space)

$\omega = 11.8$ rad/sec

therefore:

$$\bar{\dot{\theta}} = \frac{\theta_s}{t_p} = \frac{0.273}{0.043} = 6.35 \text{ rad/sec}$$

{ NOTE: θ_s is the object space angle and not the mirror angle }

$$\bar{\dot{\theta}} = \frac{A \sin (\omega t_p/2)}{t_p/2} \Rightarrow A = \frac{\bar{\dot{\theta}} \, (t_p/2)}{\sin (\omega t_p/2)} = \frac{6.35 \, (0.0215)}{\sin (11.8 \times 0.0215 \text{ rad})}$$

$$A = \frac{6.35 \, (0.0215)}{\sin (0.254 \text{ rad} = 14.5^{\circ})} = \frac{6.35 \, (0.0215)}{0.25} = 0.544 \text{ rad}$$

$$\dot{\theta}_{max} = A\omega = 0.544\ (11.8) = 6.43 \text{ rad/sec}$$

$$\dot{\theta}_{min} = A\omega \cos(\omega t_p/2) = 6.43 \cos(14.5^{\circ}) = 6.43\ (0.968) = 6.22 \text{ rad/sec}$$

Expressed in percent:

$$\bar{\dot{\theta}} = 6.35 \text{ rad/sec} = 100\%$$

$$\dot{\theta}_{max} = 6.43 \text{ rad/sec} = 101.3\%$$

$$\dot{\theta}_{min} = 6.22 \text{ rad/sec} = 98\%$$

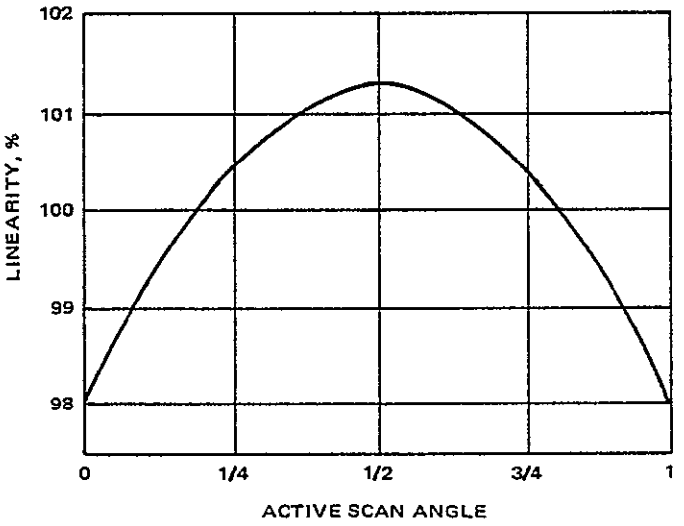

About the time that the torque-while-turnaround feature was added to the breadboard it became apparent that a new goal for scan linearity should be established to eliminate the need for ground processing correction to linearize the scan. This may require that the actual nominal scan angle should not deviate repeatably from a linear scan by more than 21.3 microradians at any along scan location. This is a restriction for the existing flex pivots. The

difference between the actual scan angle and the linear scan angle is given by

$$\Delta\theta = A \sin \omega t - \bar{\dot{\theta}}\, t$$

where

$\bar{\dot{\theta}}\, t$ is the linear scan angle

$A = 0.54387$ rad/sec

$\bar{\dot{\theta}} = 6.3488$ rad/sec

plotting the difference, $\Delta\theta$, against the linear angle $\bar{\dot{\theta}}\, t$ gives the curve shown in Figure 4.3-22, and it can be seen that the departure of 560 microradians far exceeds the goal of 21.3 microradians or less.

As part of an IR&D project a spring compensator was built and tested. This device consists of two "E" magnet and armature bars on either end of the pivot axis of the mirror as indicated in the following sketch

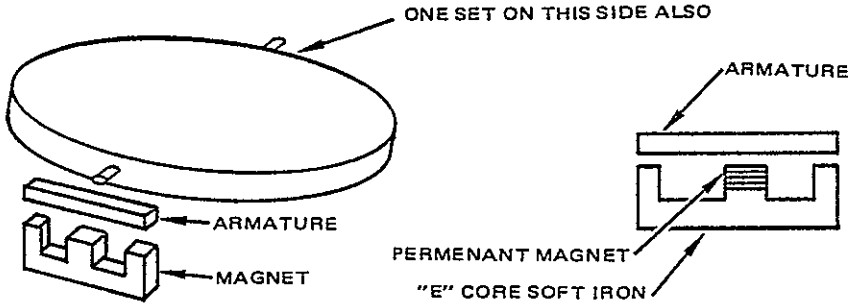

The torque produced by the set-up is

$$\frac{Q\Delta}{(P - \Delta^2)^2}$$

where Δ is the motion of the armature over one pole divided by the nominal air gap when the armature is centered. P is a dimensionless ratio of air gap

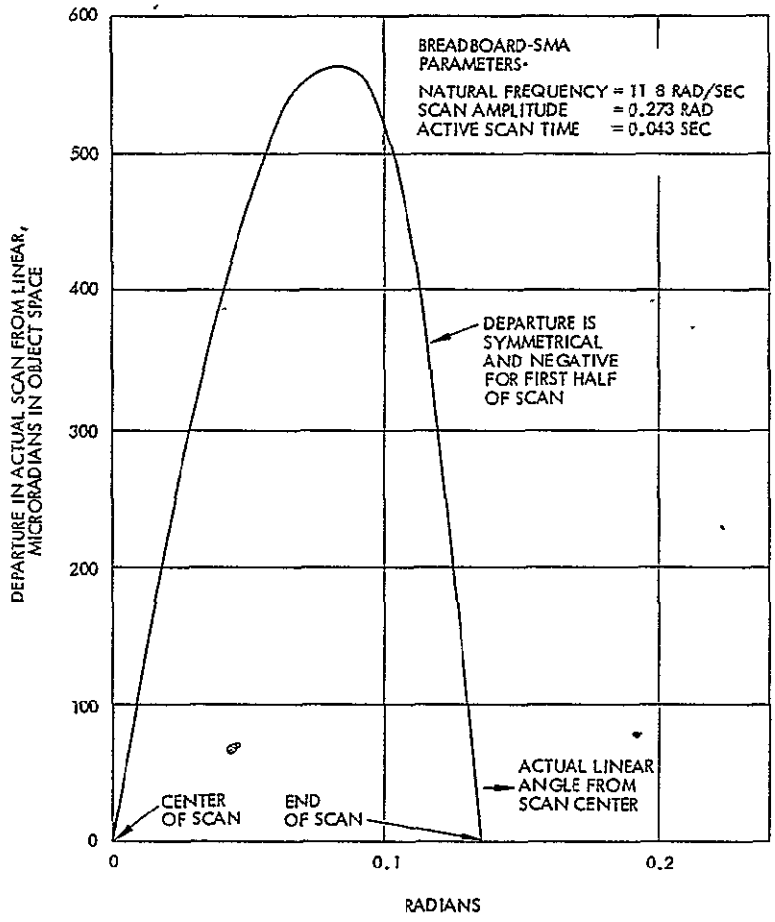

Figure 4.3-22. Departure of scan from linear.

length end areas (≈ 4). Q is dependent upon the strength of the magnet. The torque curve is zero at zero deflection and increases with increasing deflection in a slightly greater than linear manner. For the test set-up (which did not have exactly the same characteristics as the breadboard TM SMA) the torque curves are shown in Figure 4.3-23. Both the flex pivot torque and the E magnet torque were individually measured. The E magnet was adjusted to produce a net torque cross over at the center of scan (a natural phenomenon if centering is exact) and at two points near the end of scan. The concept is to reduce the net torque at all scan angles and to make the average torque as a function of scan angle (measured from the center to

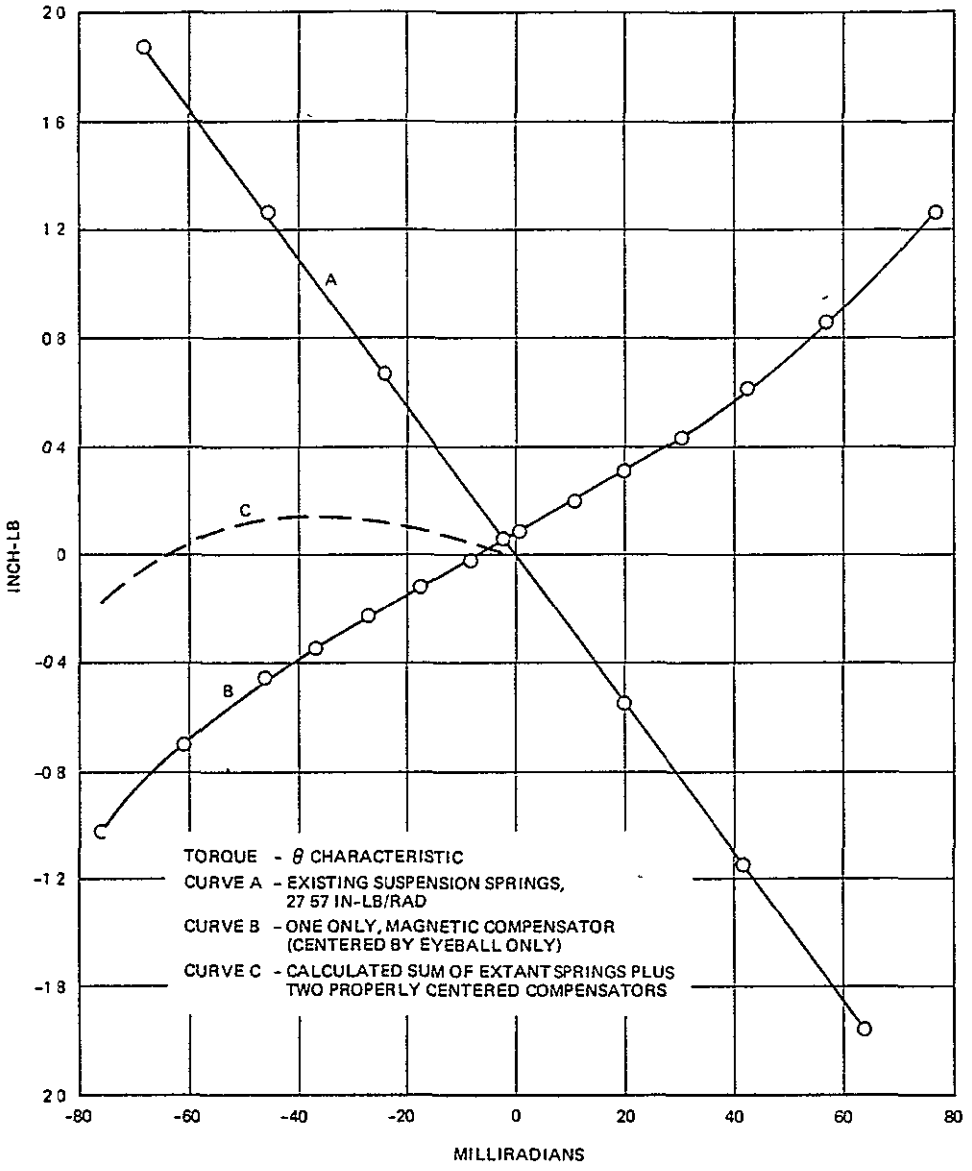

Figure 4.3-23. Torque curve for IR&D magnetic compensator set-up.

one extreme) zero. Since the E magnet torque is non-linear this can only be done approximately. It is important to note, however, that as curve A of Figure 4.3-23 increases (increased pivot torsional constant), curve B can be increased equally by supplying greater magnetic strength. The percent difference in curves A and B will remain constant and thus curve C,

the resultant, is directly dependent upon the strength of the flex pivot. There is thus a trade-off between linearity and flexural stiffness.

The conversion from torque-position data to time-rate or time-position is somewhat complex. We start without knowledge of initial mirror rate and only know the total angle and total scan time. By numerically or graphically integrating the torque-position curve increments of energy are obtained. These increments are then divided by half the mirror inertia, and the square of an assumed initial rate is added. Then the square root of the sums gives a set of rates as function of position. By dividing equal increments of angle by these rates unequal increments of time are obtained. When these Δt's are added up the exact time of the scan is not obtained so a new initial rate is chosen and the process is repeated.

Expressed in algebraic terms,

$$\omega \text{ as } f(\theta) = \sqrt{\omega_o^2 + \frac{2}{J}\int T \, d\theta}$$

$$\Delta t = \frac{\Delta\theta}{\omega(\theta)}$$

One iteration using an assumed initial rate of 3.333 rad/sec was accomplished and the rates tabulated.

By taking running totals of these Δt's, and listing beside them the running totals of a set of equal Δt's which add up to the same half-scan time, the difference between these columns will be the time by which the mirror arrives late or early at each value of scan angle. These lead or lag times can be multiplied by the appropariate rates to get angular departures from linearity. These departures are shown in Figure 4.3-24. It can be seen that the largest corrected departure is about 23 microradians. A greater departure for the same set-up applied to the TM should be expected because the natural frequency of the TM mirror is higher. As seen from Figure 4.3-24 the uncompensated object space departure is 230 x 2 = 460 microradians compared to 560 microradians for the TM mirror shown in

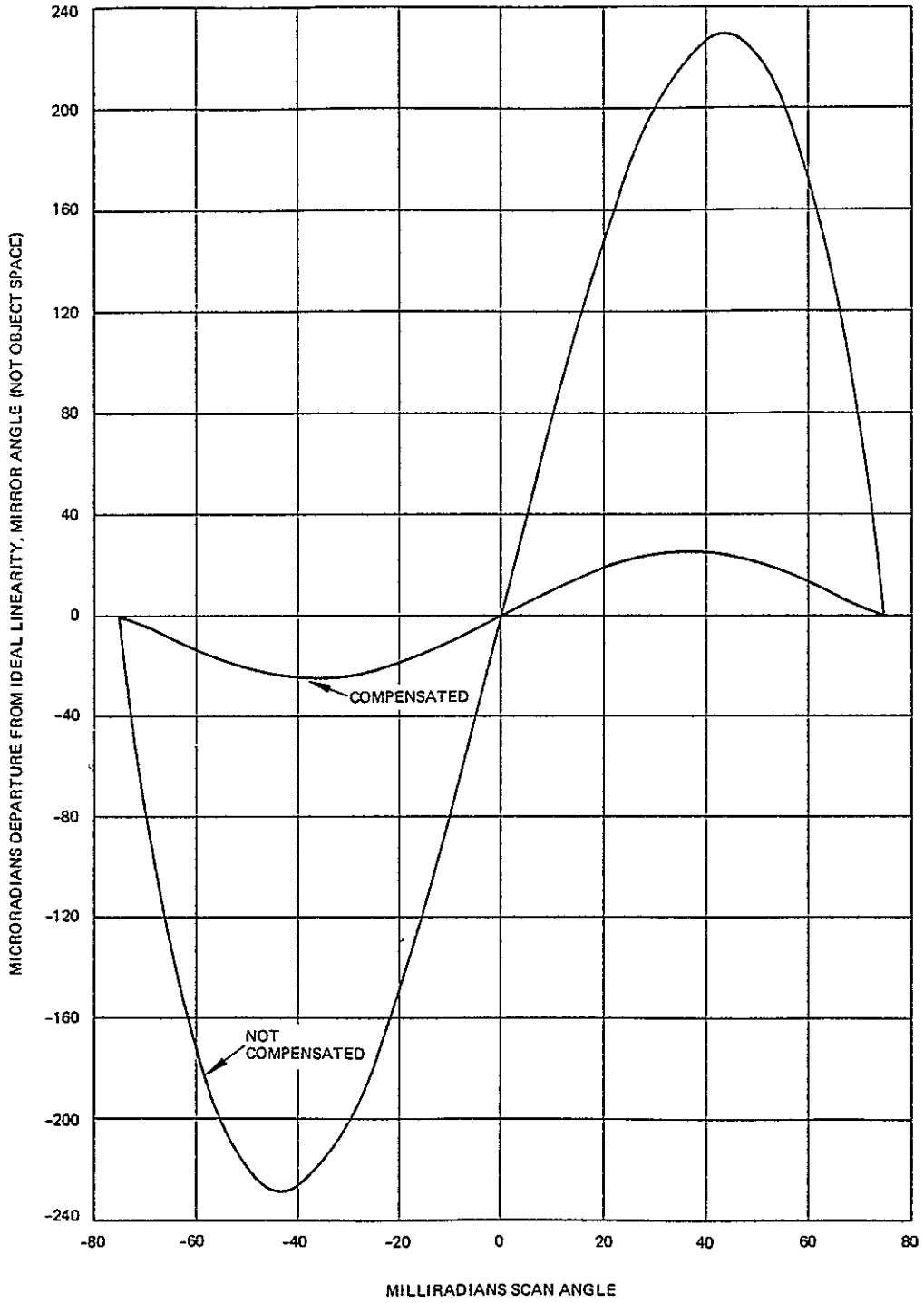

Figure 4.3-24. Departure from linearity for actual E magnet test set-up.

Figure 4.3-22. However, since building and testing the compensator, a much more linear E magnet arrangement has been found. There is a possible improvement by about a factor of three in linearity:

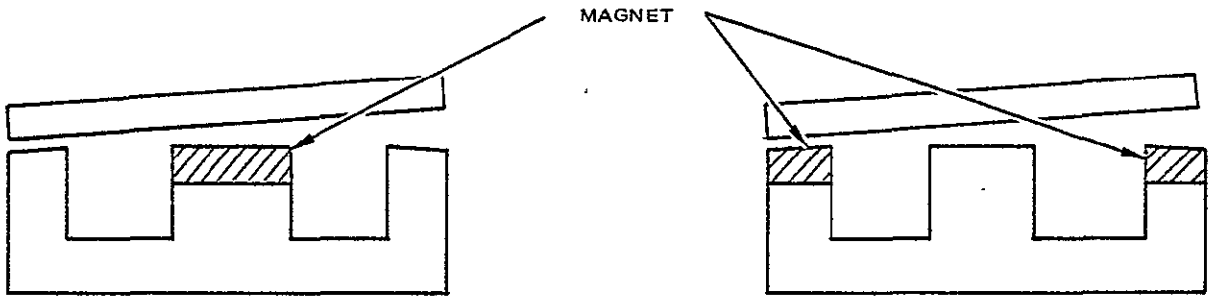

The reason for the change is the Δ in the demominator of torque equation:

$$T = \frac{Q\Delta}{(P - \Delta^2)^2}$$

The ceramic magnet material used has a permeability almost equal to air, thus an inch of magnetic material is equivalent to an inch air gap. As presently configured, the nominal air gap is 0.25 inches and the corrective motion is $\pm$ 0.187 inches. As a function of scan, Δ goes from -0.75 to +0.75. The magnet is 0.5 inches long. With the magnets on the ends of the E, Δ would range between $\pm$ 0.25. In addition, the value of P decreases slightly so the maximum torque output is about constant. But the change in $(P - \Delta^2)$ is much less. The resultant peak net torque can be reduced to 4/13 of its preset value and thus no problem in meeting the desired 21.3 microradian maximum perturbation from linearity is foreseen. This technique also offers a control of sufficient precision to shape the angular scan velocity profile to be nonlinear in a prescribed way so as to result in a linear scan rate over the curved earth surface. A perfectly constant angular scan rate produces scene displacements in the image of approximately 500 microradians according to a profile which is quite similar to that produced by the flex pivots and shown in Figure 4.3-22, but of opposite polarity.

Thus far we have assumed that residual torquer forces can still the neglected. Such forces will be quite small and will be a linear function of scan speed. Therefore if any non-constant scan rate is seen it could easily be exactly removed by applying a very small constant current to the torquer during active scan. This brings up the more basic problem of quantitative knowledge regarding linearity.

For the breadboard SMA the analytic determination of linearity shown in Figure 4.3-22 is correct to within a few percent, since flex-pivot torques predominate overwhelmingly. But when the flex-pivot forces are essentially cancelled by the E magnet, angular linearity based on integration of statically measured torques (as in Figure 4.3-24) will no longer be a reliable estimate. The present test set, which was deemed adequate to measure the linearity requirements initially specified, cannot accurately measure the uprated linearity requirements. The test set accuracy is deficient in two ways: neither air nor helium sufficiently approximate the zero density of space; the five-diode placement technique does not yield sufficient information and the information it does yield is in error because of the uncertainty in diode location.

What will be required is a vacuum chamber test with a laser interferometer and/or a diode placement technique which is insensitive to the knowledge of diode separation. One such set-up consists of placing a moving pair of split diodes in the path of a reflected laser beam as shown in Figure 4.3-25.

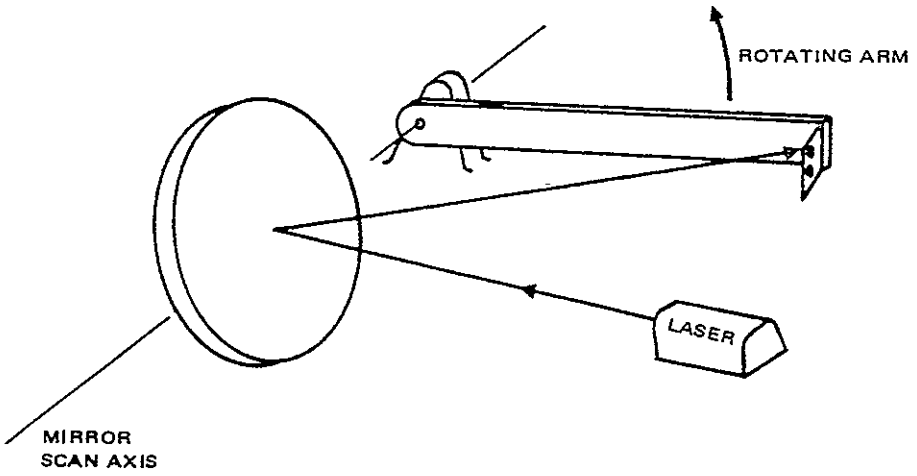

Figure 4.3-25. Suggested high accuracy linearity test set.

The set-up consists of an arm which can be rotated about the scan axis and fixed at any approximate angle. A laser beam is located such that its reflected ray describes a cone about the scan axis. Two diodes on the movable arm intercept the reflected conical ray path in a perfect circle. The conical scan angle between the two diodes is exactly equal to a specific change in scan angle for all positions of the arm. (Actually this is true only if the arm length doesn't change and if the mirror surface passes through the scan axis. These two anomalies can be corrected by simple mathematical adjustment and measurement of the temperature of the arm.) The angle between diodes is set approximately equal to 1/20 of the total scan. With the SMA running the arm is approximately positioned at 20 equal scan increments along the total scan and the time of diode pair traversal of the beam measured. Not shown in the figure are diodes near the top and bottom of the scan used to measure the total scan angle. These diodes need not be accurately located, their purpose being to correct for any change in the nominal scan rate. The inaccuracy of measuring the time between traversal of two diodes has previously been shown to have a standard deviation of less than 1 microsecond. The procedure for measuring linearity is as follows.

Define linearity,

$$L(\theta) = \frac{\dot{\theta}(\theta)}{\bar{\dot{\theta}}}$$

where $\dot{\theta}(\theta)$ is the nominal value of $\dot{\theta}$ for a scan whose average scan rate over the full scan is $\bar{\dot{\theta}}$.

Define $T(\theta)$as the average value of the time of traversal of the total scan (out board diodes) during the measurement of $\Delta T(\theta)$ which is the average time of traversal of the diode pair on the arm set at a particular θ.

Then even with slow drifts or fluctuations in the scan period

$$L(\theta) = \frac{\dot{\theta}(\theta)}{\bar{\dot{\theta}}} = \frac{\overline{\Delta T}}{\Delta T(\theta)} \cdot \frac{T(\theta)}{\bar{T}}$$

where $\overline{\Delta T}$ is the average value of $\Delta T(\theta)$ over the twenty angular samples and $\overline{T}$ is the average value of $T(\theta)$ over the twenty samples.

Now plot $L(\theta)$ against θ and piecewise integrate to produce the angular deviation in the nominal scan from a perfectly linear scan.

$$\Delta\theta(\theta) = \int_0^{\theta} (L(\theta) - 1)\, d\theta$$

Note that an error in the estimate of $\Delta\theta$, the departure from linearity can only come from an error in $L(\theta)$. By definition the average value of $L(\theta)$ is unity so no constant error can exist. The most difficult error to detect would be a slope error in $L(\theta)$. If it is required that the maximum allowable error in the knowledge of $L(\theta)$ is that which could cause $\Delta\theta(\theta)$ to be less than 2 microradians anywhere (this is sufficiently small compared to the desired linearity goal where $\Delta\theta(\theta)$ is to be less than 21.3 microradians) than from the sketch

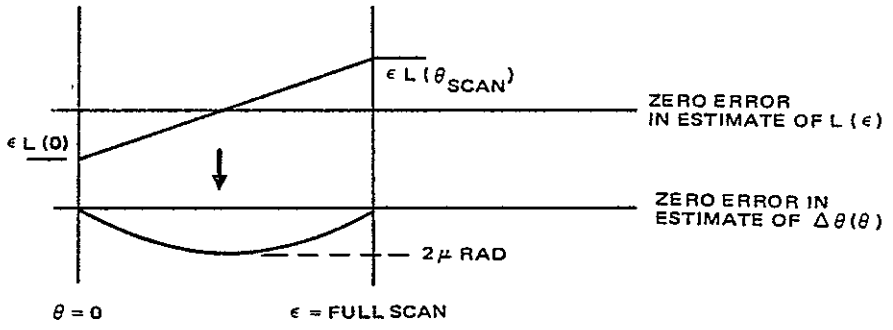

we have

$$\max \epsilon\Delta\theta(\theta) = \frac{\epsilon L(o)}{2} \cdot \frac{\theta_{scan}}{2} \Rightarrow \epsilon L(\theta) < \frac{4 \times 10 \times 10^{-6}}{.26} = 0.15 \times 10^{-3}$$

which states that the maximum allowable error in measuring linearity, $L(\theta)$, should be less than 0.15×10^{-3}. The total scan time is about 44×10^{-3} seconds, so ΔT will be about 2×10^{-3} seconds. $\Delta T(\theta)$ will be measured with fifty consecutive readings, each of which has an expected error of less than 0.1×10^{-6} seconds. Thus the expected error in $\Delta T(\theta)$ will be $0.1 \times 10^{-6}/\sqrt{50}$ or 0.014×10^{-6} seconds. The expected error in $L(\theta)$ will thus be

$$\epsilon L(\theta) = 0.014 \times 10^{-6}/2 \times 10^{-3} = 0.007 \times 10^{-3}$$

which is a factor of twenty better than the requirement.

The point of presenting all of this under the subject of flex pivot compensator is to show why inclusion of the compensator on the TM breadboard SMA during this contract would not yield useful data. The test equipment available under this contract simply could not measure the improvement. It makes more sense to include the compensator after other parameters, such as the flex pivot torsional stiffness, are finalized and under a situation where vacuum chamber testing can be justified.

The Bumper Design

Once it became clear that the MSS-type logic and bumpers would be abandoned, the design and location of the new leaf spring bumpers began. Test data from the IR&D SMA was used to develop and reduce to practice the new logic. The principal constraint was that the mirror had been fabricated to the old design.

Two basic principles were adhered to in the conceptual design of the new bumpers: (1) the bumpers were to have minimum moving mass; and (2) the bumpers would be damped between impacts but no damping would be applied to the mirror. The position of the bumpers must be predictably fixed during each impact so as to produce accurate impact timing pulses for mirror control.

These two principles guarantee that a minimal amount of mechanical energy is removed from the mirror during turn-around and thus ease the problem of restoring the lost energy with a short torque pulse.

An important effect of the first principle is the reduction of high frequency forces upon the mirror which cause cross-axis motion. Figure 4.3-26 presents an analysis of turn-around forces for the TM SMA with MSS type bumpers. The ideal case of a massless turn-around spring would produce a smooth sinusoidal turn-around force on the mirror whose frequency is a

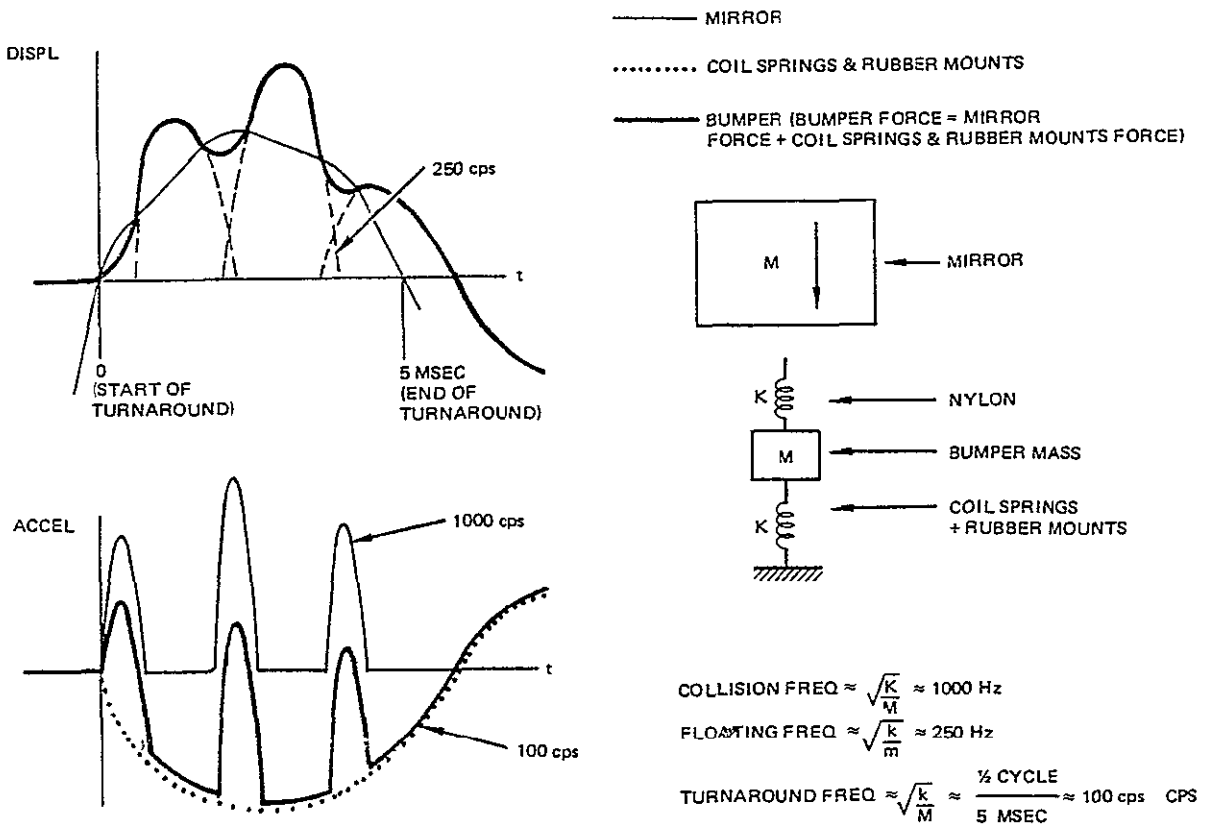

Figure 4.3-26. Turn-around dynamics with MSS-type bumpers.

function only of the mirror inertia and spring constant of the turn-around spring. However, for the case of the MSS-type bumpers, the bumper mass is so large that much higher frequency force components exist. The first mode natural frequency of the mirror on the flex pivots is about 320 to 330 Hz and the second mode is about 1000 to 1200 Hz. It is therefore extremely important to reduce all high frequency components of turn-around forces.

The chosen concept used to achieve the desired goals was a single tapered leaf spring backed by a rubber bumper. The tapered leaf spring has the property that bending moment at any station along the axis of

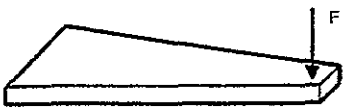

the spring is proportional to the distance from the impact force, but the spring cross sectional area is also proportional to the same distance. Therefore the peak compressive and tensile stress is constant at all stations (approximately). Since one of the objectives of the spring design is to minimize moving mass and since the energy that the spring must absorb and return during turn-around is fixed, this objective is achieved by making the peak stress constant throughout the length of the spring.

The spring need deflect in only one direction during turn-around if separate springs are used for each turn-around. This allows placement of a damper on one side of the spring which will stop the spring after turn-around but will not damp the motion of the mirror.

Upon abandoning the MSS-bumper concept, the TM SMA was equipped with a dummy mirror which could be quickly fitted with leaf spring bumpers to try out the torque-while-turn-around logic on the TM SMA. A sketch of this quick adaptation is shown in Figure 4.3-27. This bumper assembly

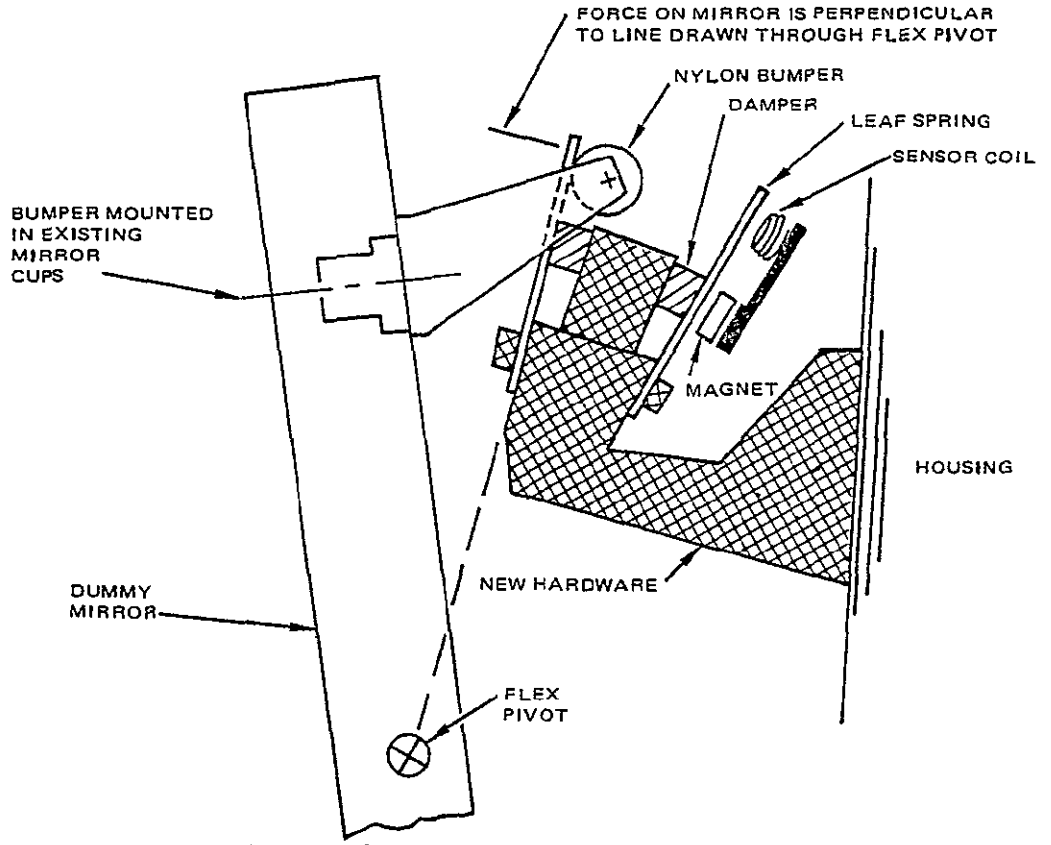

Figure 4.3-27. Quick adaptation of leaf spring concept to the TM SMA with the dummy mirror.

(one on each end of the mirror) employs a cylindrical nylon bumper mounted on the back of the mirror utilizing the existing cups in the mirror which previously contained the mirror mounted, MSS-type bumper parts. The leaf springs are arranged in such a manner that relative motion between the nylon bumper and the steel spring is minimized during spring deflection with the objective of minimizing friction and wear. The placement of the bumpers is such that a pair of springs makes contact upon each turn-around. This allows a period of almost a full cycle for the rubber dampers to bring the spring to rest prior to the next impact. Also shown on the sketch is an electromagnetic device whose output closely approximates the velocity of the tip of the spring. This device can be used by the logic to measure the time of bumper impact. The output of the sensor coil is shown in the sketch below:

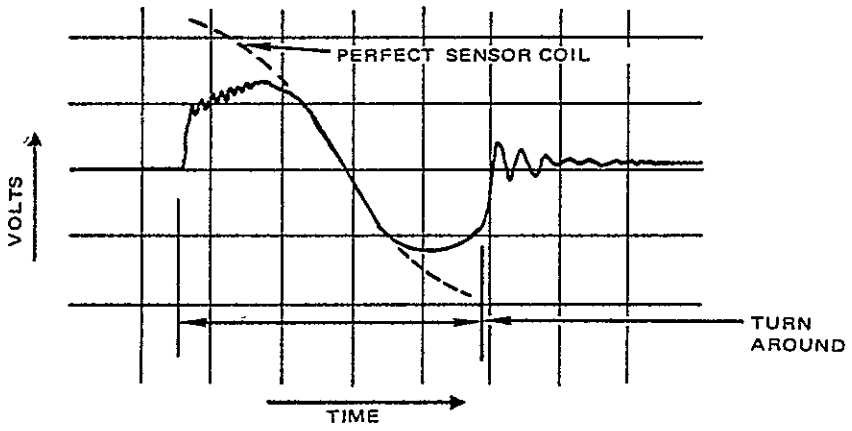

At the start of turn-around the spring velocity quickly approaches that of the mirror. There is then a low magnitude extremely high frequency (about 45 KHz) ringing of the spring which is quickly damped out by the nylon bumper. The motion of the spring is then essentially quiet until the mirror leaves the spring. At this point it rings with its natural cantilever frequency. Were it not for the existence of the damper, the spring would ring

throughout the scan period. However, as seen in the sketch, the motion of the spring is reduced to zero in a period about equal to the turn-around time, leaving plenty of margin prior to the next impact. It should be pointed out that the sketch indicates that the spring nominal motion is not a perfect sinusoid. This is simply because the "gain" of the magnetic assembly is low at the start and end of the turn-around, and high in the middle, because the leaf-spring/coil gap closes with increased deflection.

Initial data taken on the TM SMA with the dummy mirror and "rear-mounted" bumpers was quite encouraging. Along-scan repeatability appeared acceptable, but more important, no second mode motion of the mirror on its flex pivots was measurable. Thus a major breakthrough in the reduction of cross axis motion had been achieved. However there were several known deficiencies in this quick adaptation. As shown in the following sketch the net nominal force on the mirror was not zero:

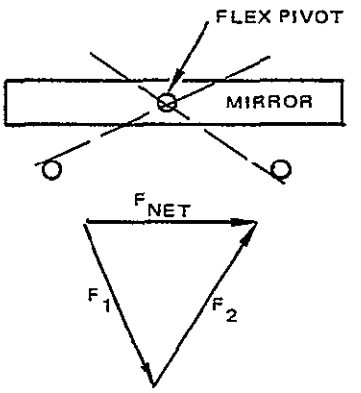

To minimize friction, the spring face must be a projection of a line through the flex pivot (for this design), thus the two turn-around forces are equal but not opposite and a net force on the mirror results. A second deficiency in the design is the inability to precisely control the position of the contact force in the direction defined by the scan axis: A flat spring contacting a cylindrical surface provides an indeterminant point of contact. Lastly, the design did not provide for easy adjustment of several parameters. The

parameters that might be adjusted (if for no other reason than to parametrically understand their effect upon cross-axis motion) are:

1. Spring constant (spring length)
2. Simultaneity of contact of a spring pair
3. Position of the damper to vary the damping time
4. Position of contact along the scan axis

Several bumper arrangements were considered for the final breadboard configurations with the goal of improving the above known deficiencies. As a starting point the choice of simple leaf springs was questioned. The motion of the point of contact on the mirror is a large arc about the pivot axis. For simple tapered leaf springs, the motion of the point of contact is approximately on a circle of radius equal to half the leaf spring length as demonstrated in Figure 4.3-28. Thus the point of contact on the mirror moves in a large arc while the point of contact on the spring moves in a small arc. These two points cannot be made to traverse the same locus.

Two alternative spring choices are shown in Figure 4.3-29. The first of these is a "wishbone" consisting of two leaf springs. The traversal of the point of contact is much more linear for this device but the moving mass is greater than for the simple tapered leaf spring. The second approach places a coil in a slightly preloaded condition against two cups. This device produces a linear travel but again, is relatively massive. In addition, there would be some question regarding the repeatability of seating the cups.

For the breadboard TM SMA with its restriction of an already-fabricated mirror, techniques such as the coil spring device were not realistic approaches. For reasons of simplicity and to minimize mass it was felt that, at this time, the baseline approach of a simple, tapered leaf spring should be maintained. The only question remaining was thus, where to mount the springs. That is, how far from the flex pivots and how far from the central plane of the mirror blank they would be mounted. If the contact surface on the mirror is parallel to the mirror surface, the normal force of the

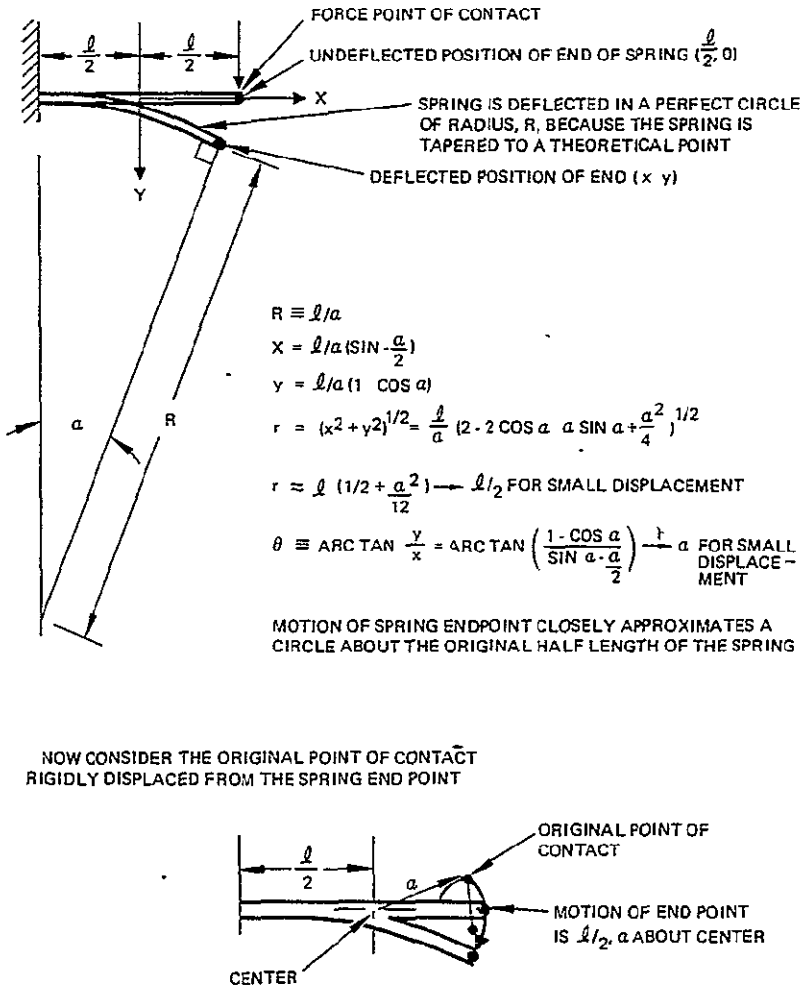

Figure 4.3-28. Motion of the original point of contact for any tapered leaf spring.

spring (the only force except friction) will be perpendicular to the mirror surface and the pair of turn-around forces will be equal and opposite. Thus a slight modification of the design of Figure 4.3-27 as indicated in the

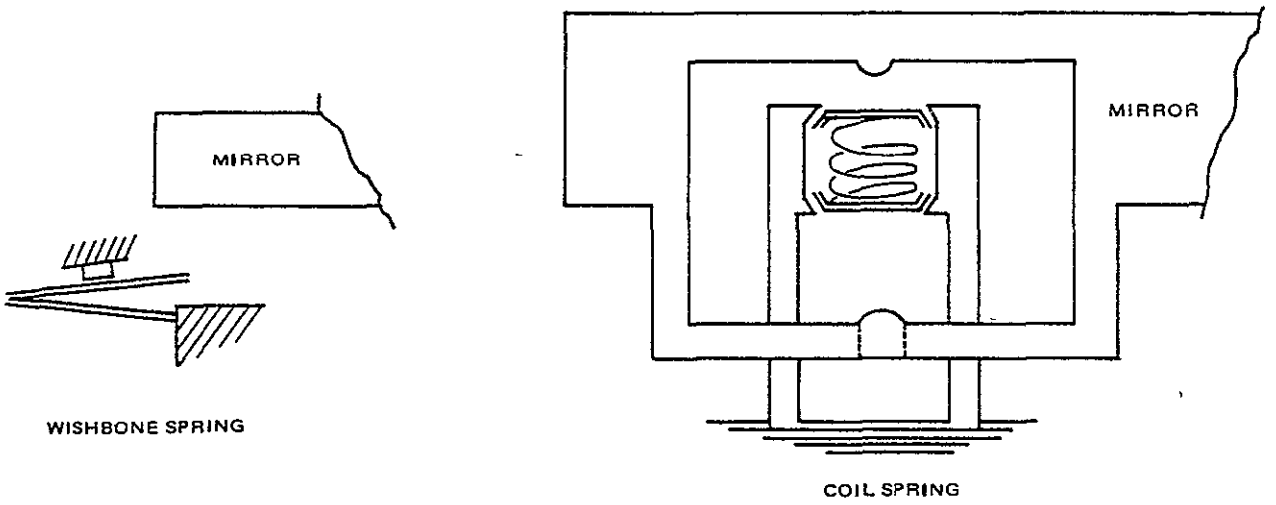

Figure 4.3-29. Alternate springs designated for quasi-linear deflection locii.

following sketch would cause the net force on the mirror to be zero (except for friction):

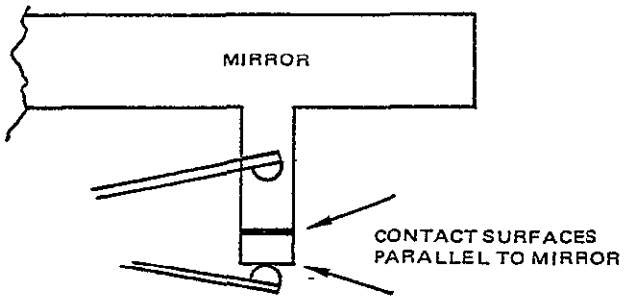

This would require a contact radius on the spring to provide point or line contact as the spring deflected. There are three reasons why it was felt that the contact should be near the mirror end. First, analysis of deflection of the mirror showed that there was no great advantage in requiring the forces to go through the center of percussion as they did in the MSS and the early TM design. Second, end mounting would be extremely attractive for a flight-design since it would allow direct mounting of the bumper assemblies to the scanner structure. The scanner structure must be a necessary link in transmitting bumper loads and torques to the rest of the optical path and to the spacecraft. It thus must be quite rigid to minimize angular errors. To add

additional rigid structure behind the mirror would only be required if the bumper assemblies are behind the mirror. In addition, placing the bumpers at the end of the mirror will tend to minimize the scanner length. Third, placing the bumpers at the end of the mirror tends to reduce the forces required for turn-around. The torque-time function is independent of length and is only dependent upon mirror inertia, scan speed and turn-around-time allowed. However the force required is inversely proportional to the lever from the pivot axis, and the energy stored in the spring is a constant independent of this distance. The equivalent moving mass of the bumper is linear function of the stored energy since the spring design sizes the mass on the basis of an allowable working stress. The rotational inertia of the moving bumper mass about the flex pivot axis unqieuly determines the energy loss directly to the mass

$$\Delta E_{\text{bumper mass}} = \left(\frac{I_{\text{mirror}} + M_{\text{bumper}} r^2}{I_{\text{mirror}}} \right) \frac{M_{\text{bumper}} r^2 \dot{\theta}_{\text{in}}^2}{2}$$

but additional energy is lost to friction at the spring/mirror contact point

$$\Delta E_{\text{friction}} = \mu \int F ds$$

where F is the normal force of one turn-around spring, μ is the coefficient of friction (0.2 → 0.4) and the integral is over the displaced distance of sliding of the contact point. All estimates of these two energy losses indicate that for leaf springs the predominate loss is frictional. This loss is reduced by reducing the normal force. Maximizing the lever arm of the bumper thus reduces the net forces transferred to the scanner, reduces the mass of the bumper and thus the components of high frequency ringing which disturbs the mirror in cross axis motion, and reduces the energy loss.

A proper end-bumper design would place the bumper contact point outboard of the mirror to reduce the net size of the bumper assembly and to avoid optical occlusion. Thus a final flight configuration would look like:

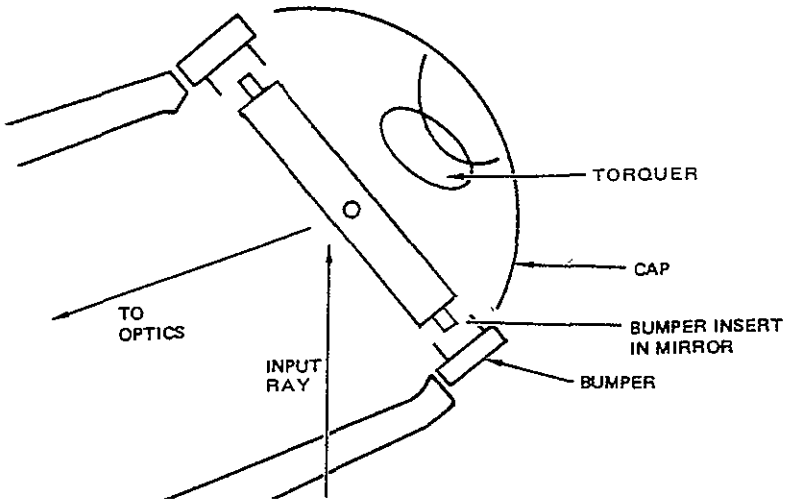

However for the already polished mirror it seemed inadvisable to braze or bond an insert into the mirror eggcrate structure. For completion of the tests it was not required that the full optical aperture be available. A simple solution, suitable for breadboard purposes, was to glue a stainless steel striker plate on to the front and rear mirror surfaces. This resulted in the bumper design pictured in Figure 4.3-30 and sketched in Figure 4.3-31.

This bumper assembly was designed to allow adjustment of several parameters. These adjustments, and the general operation of the assembly can be best described through the use of Figures 4.3-30 and 4.3-31. The mirror and stainless striker plate are clearly seen in Figure 4.3-30. The striker plate makes contact with the nylon bumper pad (1)*. This pad lessens vibration due to contact and provides a rounded surface to maintain a point contact during spring deflection. The tapered leaf spring (2) is sandwiched between two spring holders (3). The spring constant can be varied by adjusting the length of the spring that protrudes from the holders:

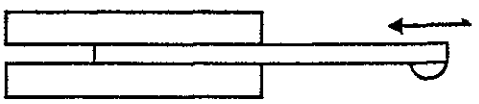

*Parenthetical numbers refer to callouts on Figure 4.3-31.

C-3

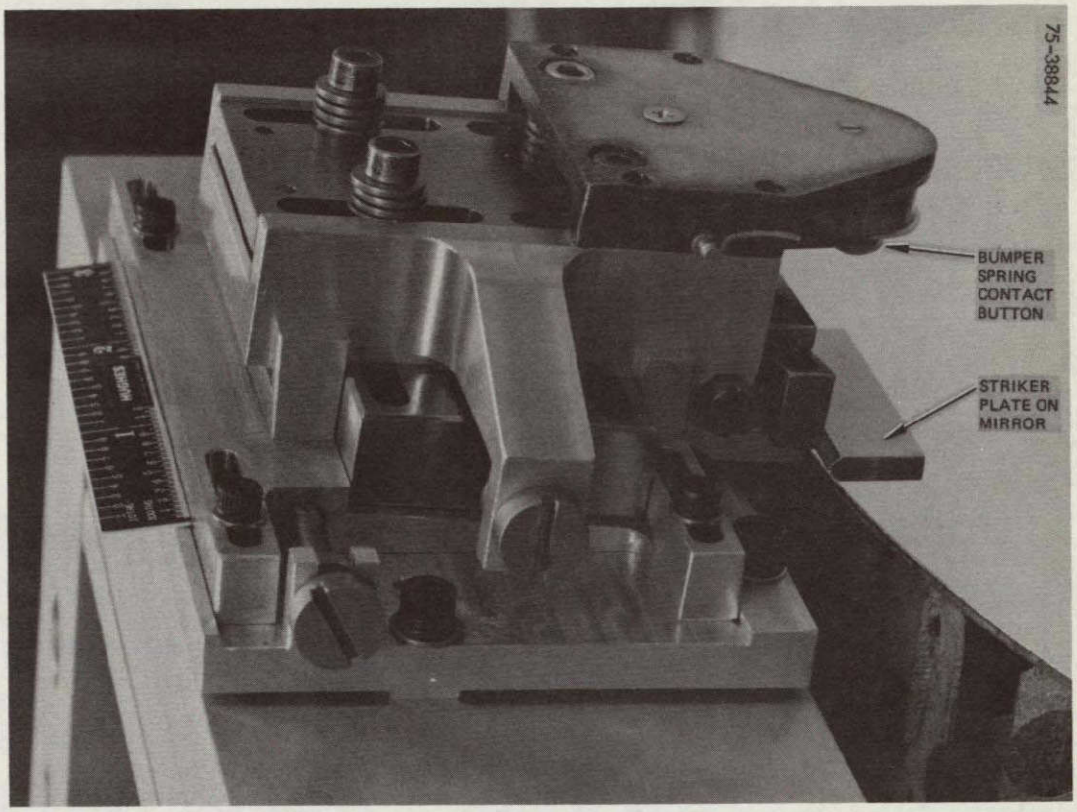

Figure 4.3-30. TM breadboard SMA bumper photo.

In addition the point of contact of the nylon pad can be moved in and out along the major mirror axis by adjusting the position of the spring holder on the channel block (4). A requirement for simultaneity of impact of opposing springs (on diagonally opposite ends of the mirror) is met by raising and lowering the channel block (4) with respect to orthogonal translator (5). The simultaneity adjustment screw (6) raises and lowers the orthogonal translator through the use of two height wedges (7). After this adjustment, four screws accessible from the top of the top spring holder are tightened, clamping the spring tightly in the spring holders and rigidly clamping all of above mentioned parts to the orthogonal translator. The orthogonal translator

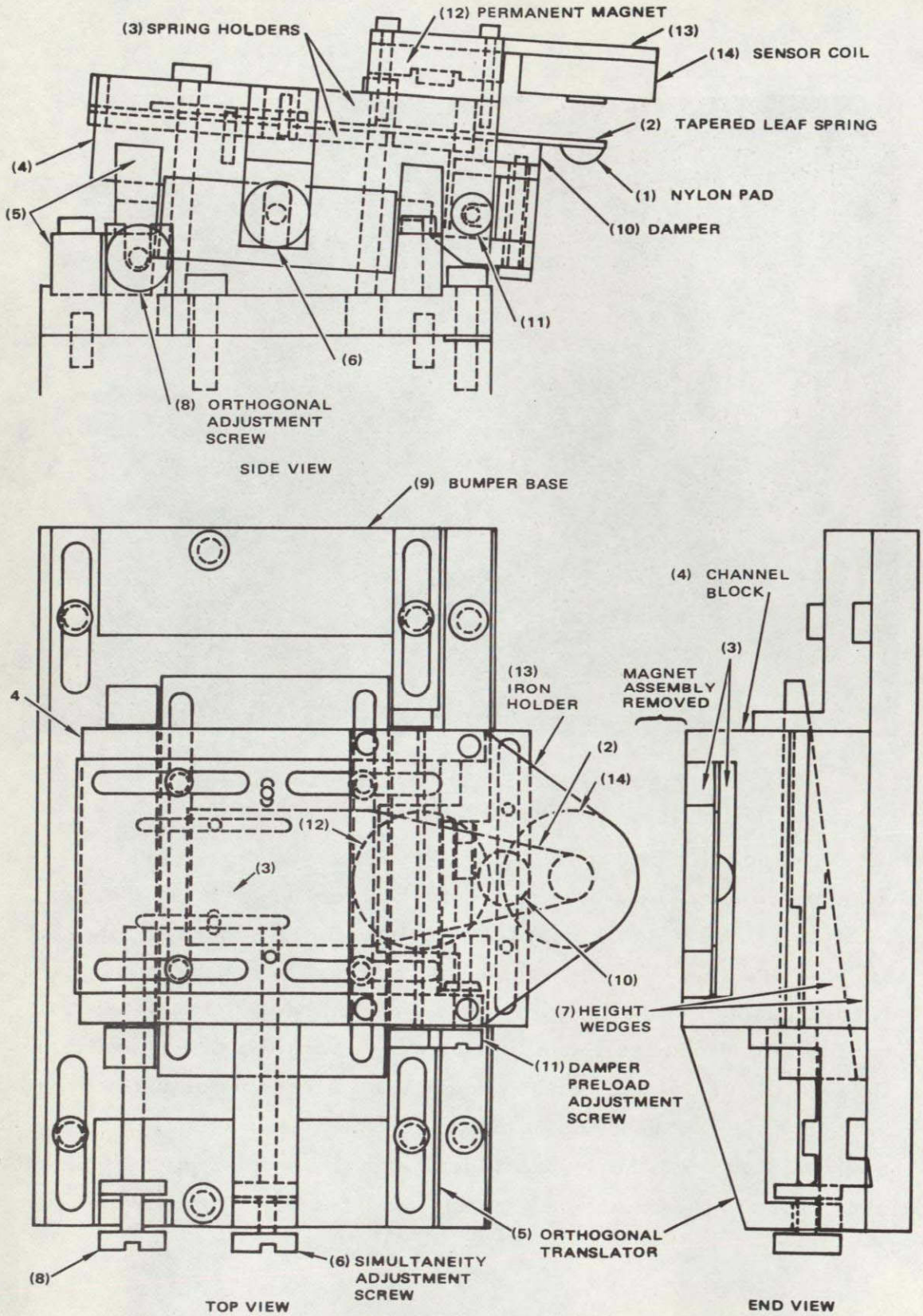

Figure 4.3-31. TM breadboard SMA bumper sketch.

adjusts the pad contact point in a direction normal to the mirror major axis (along the scan axis) by the use of the orthogonal adjustment screw (8). After adjustment four screws (two seen near the ruler in Figure 4.3-30) clamp the above parts to the bumper base (9). The silicon rubber damper (10) can be raised and lowered with respect to the leaf spring by a second wedge mechanism through the damper preload adjustment screw (11). This allows minimizing the damping effect on the mirror while assuring that the spring is fully damped prior to the next mirror contact. The electromagnetic sensor consists of a permanent magnet (12), an iron holder (13), and a sensor coil (14). The magnetic path is completed through the steal leaf spring and the coil output is a measure of the speed of the spring tip (multiplied by a variable gain caused by the changing gap).

The highly adjustable bumper design permitted a variety of design sensitivity tests to be made on the breadboard. In the flight model no continuously variable adjustments are thought necessary. The orthogonal adjustment will not be required at all and cross axis motion will not be degraded by normal manufacturing tolerances. But this was not known when the breadboard bumper was designed. It is probable that spring length will not be adjusted, but for the breadboard, several turn-around times were tested. There will be a requirement for an adjustment of impact simultaneity, however, this would be done with shims which are more difficult to adjust but provide a more secure and reliable mount. The damper preload adjustment would also probably be done with shims. With all of these adjustments out of the way, the sensor assembly will be placed on the other side of the leaf spring. This accomplishes two objectives: the iron holder and sensor coil would not obstruct the optical path and the magnetic gap would be smallest at the instant of impact which increases the signal output. The assembly might look like the following sketch:

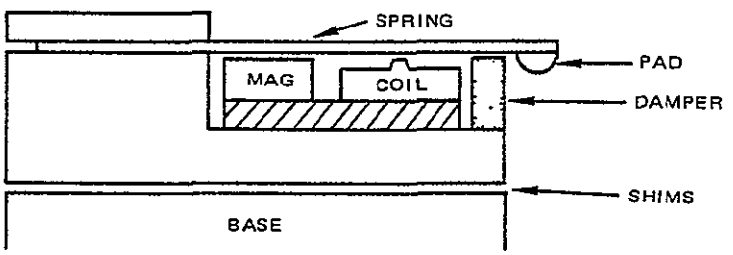

Energy is lost during turnaround in two ways. First, energy is transferred from the mirror to the spring mass and left-lost-in the spring mass after turnaround. This energy loss is easily calculated and is less than 0.1 percent of mirror energy per turnaround. Second, energy is lost in friction at the contact point between the mirror and the spring. This energy loss, although not easily calculated, could be as high as 1 percent of mirror energy at each turnaround based on measurements made with and without lubrication.

Friction forces affect cross-axis motion since they are of nearly the same magnitude as net bumper forces and are of an uncontrollable, erratic frequency. This effect of friction is of far greater importance than energy loss. Friction forces are expected to be the major contributor to cross axis motion. The related problems of contact wear and material selection also must be addressed in conjunction with their effects upon friction.

In order to reduce friction forces, an analysis of bumper contact geometry has been developed. The analysis provides a first-order method of finding a combination of contact radius and spring angle to provide as much rolling and as little sliding friction as possible. The analysis is of a a rotating and translating radius in contact with a rotating and translating flat surface. The purpose is to calculate some geometry in which the distance that the contact point travels on the flat surface will be equal to the distance the contact point travels on the round surface. The procedure is first-order because it considers only the total distance travelled and does not consider the variation in velocity along the way. Examination of the numbers developed for the TM design suggests that the effects of ordinary fabrication tolerances will exceed the effect of expected velocity variations. Therefore the analysis is considered adequate.

Two geometries are illustrated. The first (Figure 4.3-32) assumes that the flat mirror contact surface and the leaf spring are parallel at initial contact. The second (Figure 4.3-33) allows these surfaces to have an angle, θ_{MB}, between them.

The analysis is fairly general and may be applied to many conditions of rotating and translating radii in constant contact with a rotating and translating flat surface. The mirror and bumper rotation during turnaround at maximum spring deflection, θ_M and θ_B, are calculated based upon the dimension of the mirror and bumper, the speed and inertia of the mirror,

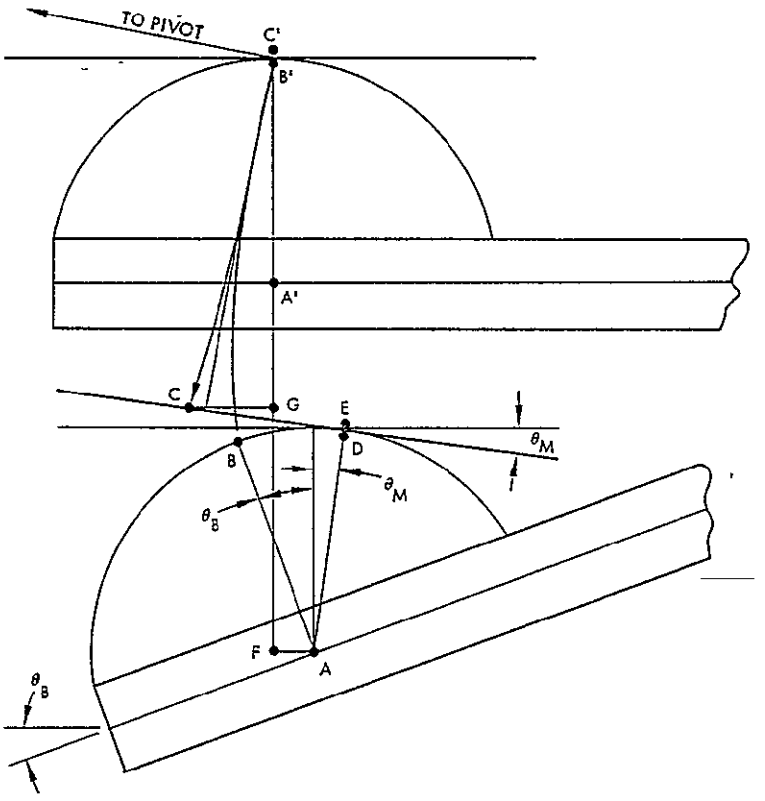

FOR NO NET SLIDING, REQUIRE CE = BD WHERE,

$$CE = \left[\frac{\theta_B + \theta_M}{360^\circ}\right] (2\pi)\ AD$$ WHERE AD = AB UNLESS BUMPER IS NOT ROUND ABOUT A

$$BD = \frac{CG}{\cos \theta_M} + \frac{FA}{\cos \theta_M} + AD \tan \theta_M$$

Figure 4.3-32. Geometry of spring/mirror motion (simple case).

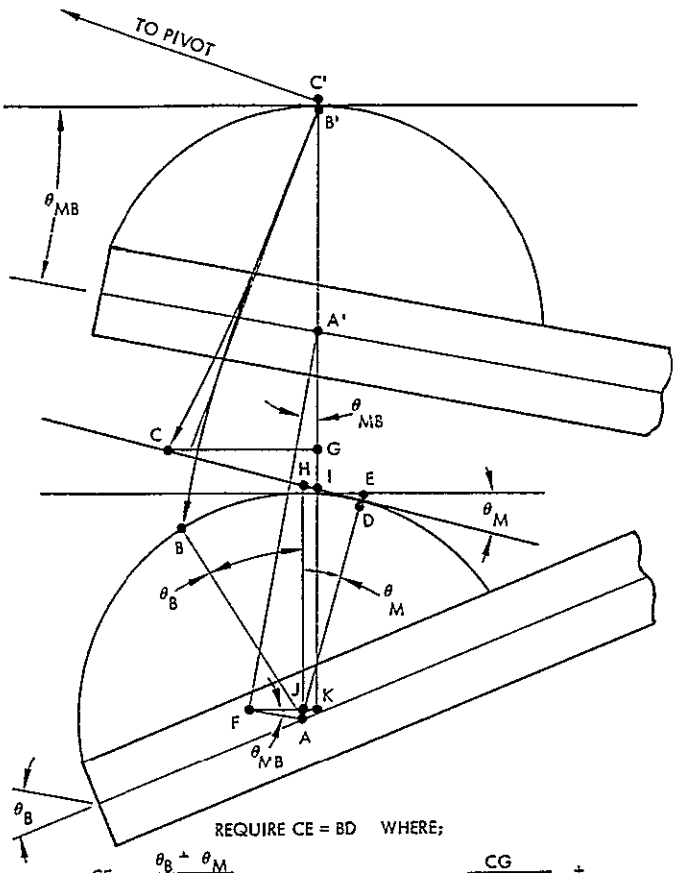

REQUIRE CE = BD WHERE;

$$CE = \frac{\theta_B + \theta_M}{360^\circ} (2\pi) AD \quad \text{AND} \quad BD = \frac{CG}{\cos\theta_M} +$$

$$(HE-HI) = \frac{CG}{\cos\theta_M} + AD \tan\theta_M - \frac{JK}{\cos\theta_M}$$

$$JK = FK - FA\cos\theta_{MB} = A'F \sin\theta_{MB} - FA\cos\theta_{MB}$$

$$BD = \frac{CG}{\cos\theta_M} + AD\tan\theta_M - \frac{A'F\sin\theta_{MB}}{\cos\theta_M} + \frac{FA\cos\theta_{MB}}{\cos\theta_M}$$

$$BD = \frac{CG}{\cos\theta_M} + \frac{FA\cos\theta_{MB}}{\cos\theta_M} + AD\tan\theta_M - \frac{A'F\sin\theta_{MB}}{\cos\theta_M}$$

Figure 4.3-33. Geometry of spring/mirror motion (general case).

and the desired turn around time (utilizing Figure 4.3-28 for an approximation of the tapered leaf spring motion, A'F and FA).

Whether or not the simple case of $\theta_{MB} = 0$ or some other θ_{MB} should be used remains uncertain. The basic problem is that it is impossible to determine exactly when there is slipping and where the point of contact sticks. From an energy standpoint, and assuming sliding friction prevails, the natural desire would be to minimize $\mu \int Fds$, or to minimize the total travel (on either surface) of the contact point. An alternative would

be to minimize the relative velocity at the contact point when the normal force F is largest (a linear function of spring displacement, maximum at maximum deflection). For the present breadboard the choice was to minimize energy loss and this turned out to be: $\theta_{MB} = 0$.

The actual dimensions of the bumper pad were sized under the assumption that there would be an initial flattening of the nylon. This phenominon is a natural one, was encountered on MSS and on TM with MSS type bumpers, and can be reasonably predicted. With a spherical pad a point contact exists. This point contact produces infinite stress and thus a flattening yield of the nylon will occur until the stress is reduced, locally, below the yield point.

Photographs of four types of tapered leaf springs are shown in Figure 4.3-34. The right-most spring was used with the rear-mounted bumper wherein the nylon cylinder was carried on the mirror. The initial deformation pattern shows that the forces were not equal along the line contact. The first spring from the left was the first one used on the final breadboard. The extremely small deformation of the nylon pad (permanent set) is barely visible. The next spring to the right utilized a titanium pad. This pad clearly wore rather than yielding to a work-in position. It was tried because it would not yield (very much) under the known loads and, if wear were not a problem, could be expected to be manufactured to finer tolerances. It was an unusable choice. The spring with the large spherical pad was designed to allow greater SMA running speeds. At some time it may prove desirable to "life-test" the mirror structure by running the SMA at speeds significantly greater than any planned real-life speed. This spring was designed for 20 Hz operation. Unfortunately it would not fit the existing bumper assembly and cut-outs were required (the notches on either side of the spring). Nevertheless this spring has been used at speeds up to 15 Hz. The larger bumper pad was used when it was realized that frictional forces far out weighed forces due to spring inertia. The larger pad provides a larger spherical radius, and as would be expected, less initial yield deformation. After two months of testing (averaging about 4 hours per working day) no noticable change in the initial yield spot was seen.

During the final weeks of breadboard testing, two additional button materials, rubber and Delrin AF, were tried to compare friction and wear characteristics. Wear and set were found to be imperceptible on both button types, but the rubber appeared to excite the second mode of mirror cross axis jitter by a greater amount than any of the other materials. The choice was then narrowed down to nylon and Delrin AF, with Delrin AF showing a slight advantage over nylon in yield and wear characteristics.

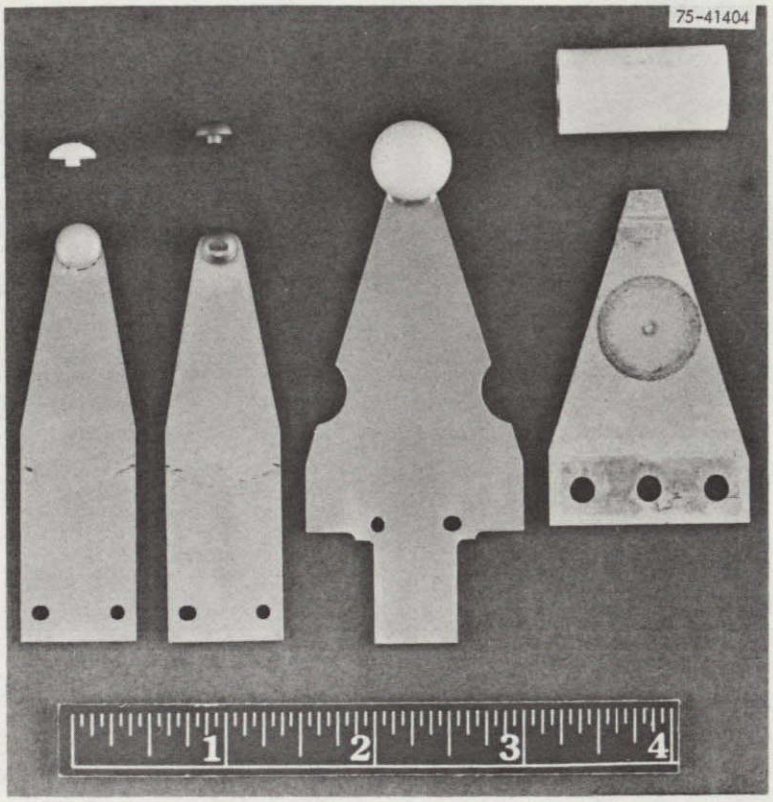

Figure 4.3-34. Photos of four leaf spring designs used in development.

4 3.3 TM Electronics

The electronics control system used to implement the previously described logic is described by the schematic shown in Figure 4.3-35. An analog timing control has been adapted from an earlier IR&D project for this breadboard design. Although the desired performance has been demonstrated with this electronic design, considerations of long term stability may make a digital processor more desirable for the flight version. However the analog approach did offer a very straightforward method of utilizing well-developed monolithic op-amps and logic elements. Preliminary implementation concepts of the required functions with digital processing have been examined and found to offer a direct conversion to digital form of the tested analog controls.

In the analog electronics, mirror timing information is derived from magnetic coil pickups that generate a pulse when the mirror contacts the turn-around spring. These pulses are input to voltage comparators (Q_{20}, Q_{21}) whose thresholds are set to eliminate false triggering between turnarounds. The leading edge of the comparator outputs triggers monostable oscillators (Q_{22}, Q_{23}) that hold their changed state for a little less than half a scan period. In the breadboard electronics, this time has been set at 30 msec. The function of these one shots is to produce a timing reference that has a sharp leading edge and also to inhibit any false triggering that might be caused by ringing in the output of the magnetic coil as the mirror leaves the spring bumper at the start of scan. Figure 4.3-36 shows the waveforms for the coil output and resulting processing. Trace Three is the unprocessed output of the pickoff coil It is a measure of the leaf spring velocity. The ringing of the spring just after the mirror has left turn-around can be seen. Also, a stray pick-up between turn arounds caused by the alternate turnaround torque pulse can also be seen. Trace Two shows the output of the comparator and how it is triggered on the sharp rise of Trace Three.

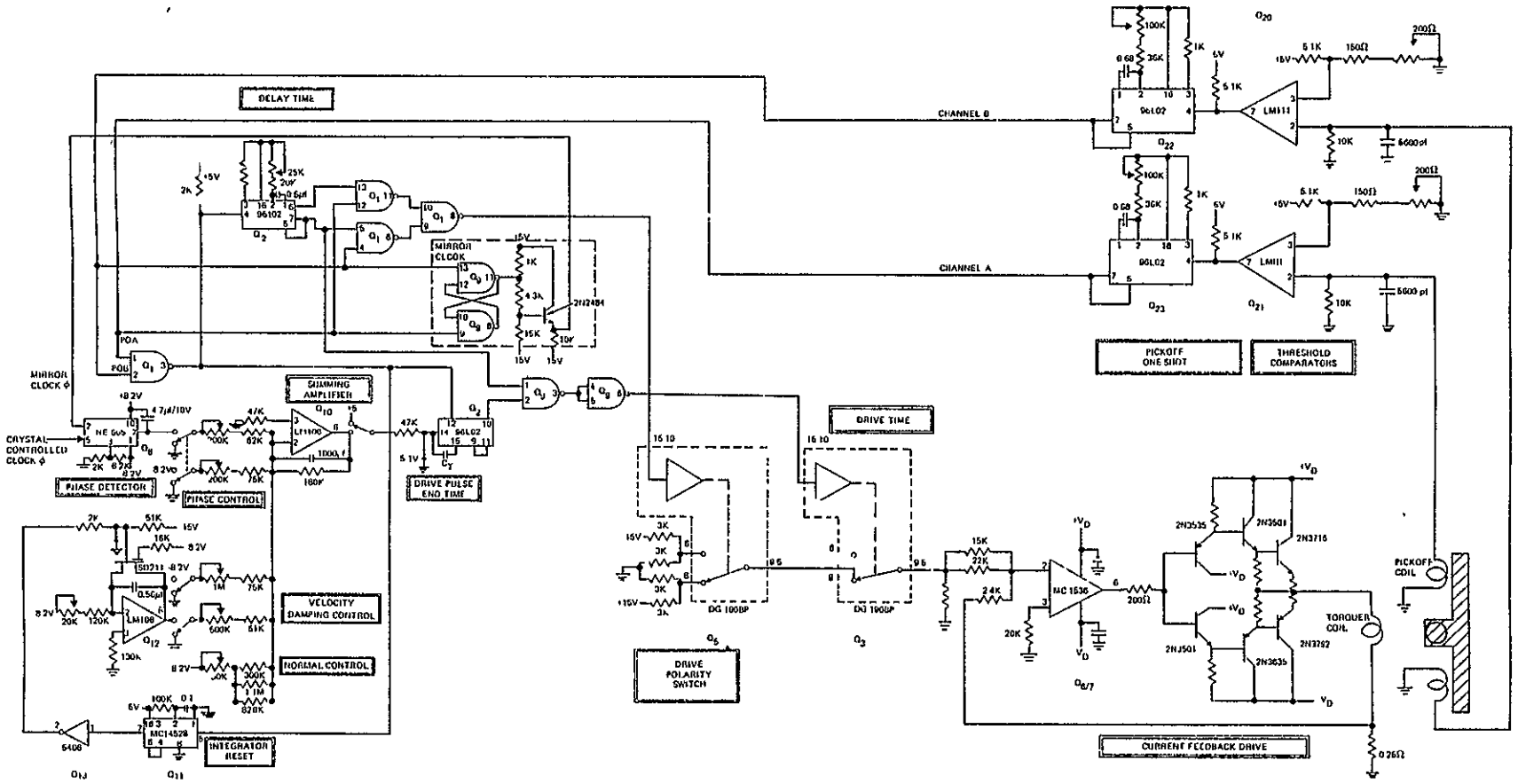

Figure 4.3-35. SMA electronics diagram.

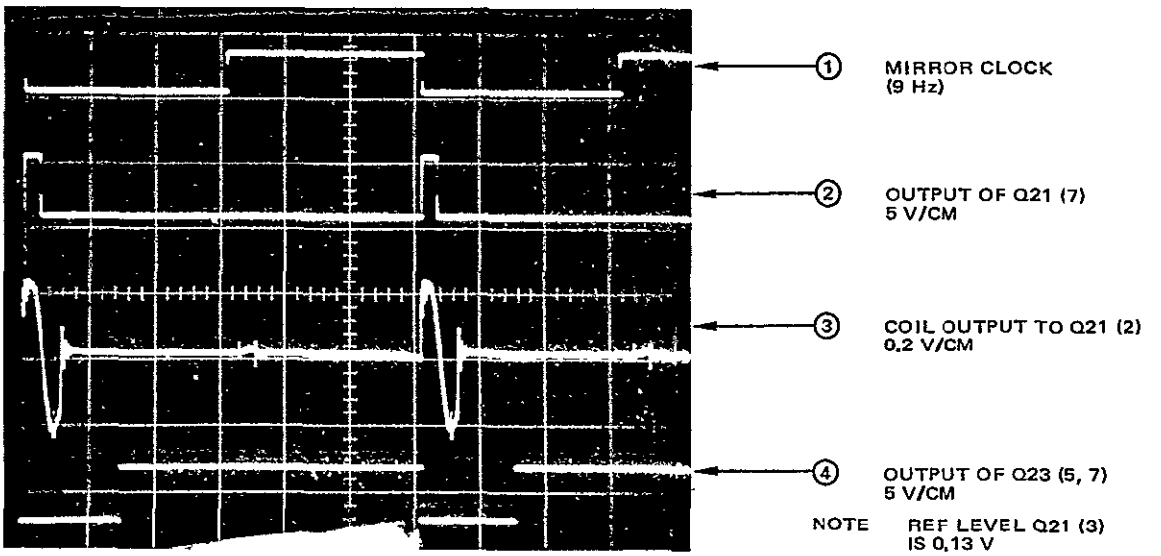

Figure 4.3-36. Channel A pickoff and resulting signals.

Trace Four is the resulting output of the one-shot, i.e., a pulse which spans the complete turnaround period plus the ringing of the spring thus preventing false triggering during this period. The two one-shot outputs (Channel A and B) enter a nand gate Q1 (1&2) that inverts and combines the two pulse trains. These outputs also enter Q9 (9&13) to produce the "Mirror Clock" signal shown in Trace One. This Mirror Clock signal is compared to the reference clock to determine the phase error.

The leading edge output of the nand Gate Q1 (3) is used to trigger both a drive pulse delay monostable, Q2 (4) and a drive pulse end monostable, Q2 (12). With reference to Figure 4.3-5, the drive pulse delay is the fixed time between the bumper impact and the start of the applied voltage to the torquer. The drive pulse end is that time after bumper impact at which the drive voltage is commanded to stop the drive current. The difference of these two times is the control variable, τ, or drive time.

Figure 4.3-37 shows, again, the mirror clock at an expanded time base as Trace One. And for reference, the coil output is again shown in Trace Two. Because of the expanded scale, the ringing is easier to see. Trace Three of this scope photo shows the delay pulse waveform relative to

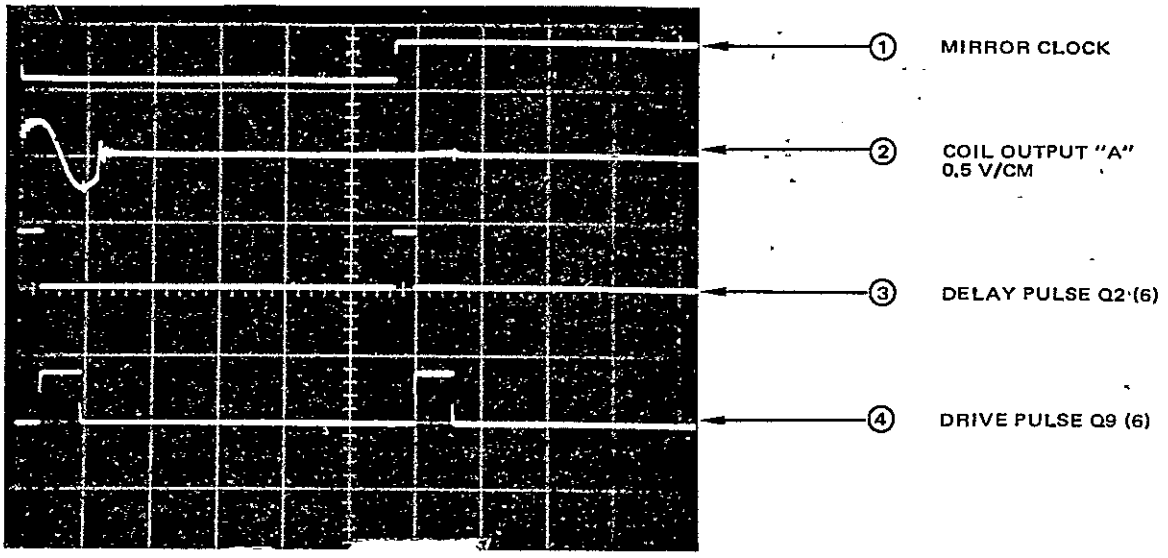

Figure 4.3-37. Producing a drive pulse.

the coil output. The drive pulse end is not shown, but Trace Four shows how the delay pulse, Q2 (6) and the drive pulse end Q2 (9, 11) are combined to produce the torquer drive on-time pulse whose duration is the control variable, τ .

The delay pulse from Q2 (6) has a sign (±) as determined by which bumper was last hit. This information is entered at Q1 (12&4) producing the drive polarity control Q1 (8). The drive pulse duration Q9 (6) is multiplied by the polarity control in the drive polarity generator, Q5 and Q3, thus producing a drive voltage pulse of proper polarity, Q3 (9, 5). The length of the drive pulse delay time is set such that initiation of the torque pulse occurs slightly before the point of maximum spring compression. This point is optimized to maximize drive efficiency. The absolute setting is not critical. The repeatability of this time interval, however, is quite critical.

The length of the drive pulse width, τ , is the controlling element of mirror operation. Control circuits that generate error voltages based on mirror phase and velocity information are summed with a nominal constant voltage input to provide the controlling voltage input to the drive pulse end time monostable. The output of this monostable is a rectangular pulse that

is initiated by the mirror impact with the spring and terminated at a time set by the input voltage and a timing capacitor, C_T. For a fixed value of C_T, the pulse length is inversely proportional to the absolute value of the input voltage. The largest input to the control loop summing amplifier (Q10) is provided by the constant nominal voltage. With the phase and velocity loops switched off, the nominal voltage is set to drive the mirror at the desired frequency. The monostable output pulse length is constant in this open loop form of operation. In this mode, the mirror exhibits very small scan period to scan period differences but drifts significantly over a large number of scans.

Velocity control is implemented by an integrator (Q12) that develops a negative ramp function at the output of the summing amplifier. The start of this ramp is set by a fixed delay after mirror impact with the spring. When summed with the nominal input, the effect of the velocity loop is to decrease (or increase) the voltage input to the drive pulse width monostable if the mirror runs slower (or faster) than desired. This results in an adjustment of the pulse width for the next torque pulse that tends to correct the speed of the mirror, thus seeking a constant velocity for each scan.

The phase control loop provides long term frequency control by referencing scan operation to a stable crystal controlled oscillator. In the case of the breadboard system, a 16 MHz crystal was used in conjunction with frequency dividers to provide a reference period that was stable to better than one part in 10^6. The phase detector section of a phase locked loop integrated circuit, Q8, is used to generate an error voltage proportional to the difference in phase between the mirror clock pulse train and the crystal reference clock. A zero error voltage is produced by this circuit when the two clocks are 90 degrees out of phase. Lead or lag by the mirror clock relative to the reference clock results in a proportional voltage increase or decrease at the output of the phase discriminator. The signal is filtered by an RC circuit to provide a smooth, noise free average of the phase error as measured over past cycles. Gain and offset adjustments are provided for each control loop by potentiometers in series with the input to the summing amplifier.

Figure 4.3-38 is a scope photo that shows how the velocity control affects the drive pulse length. Trace One is the drive pulse duration, Q9 (6),

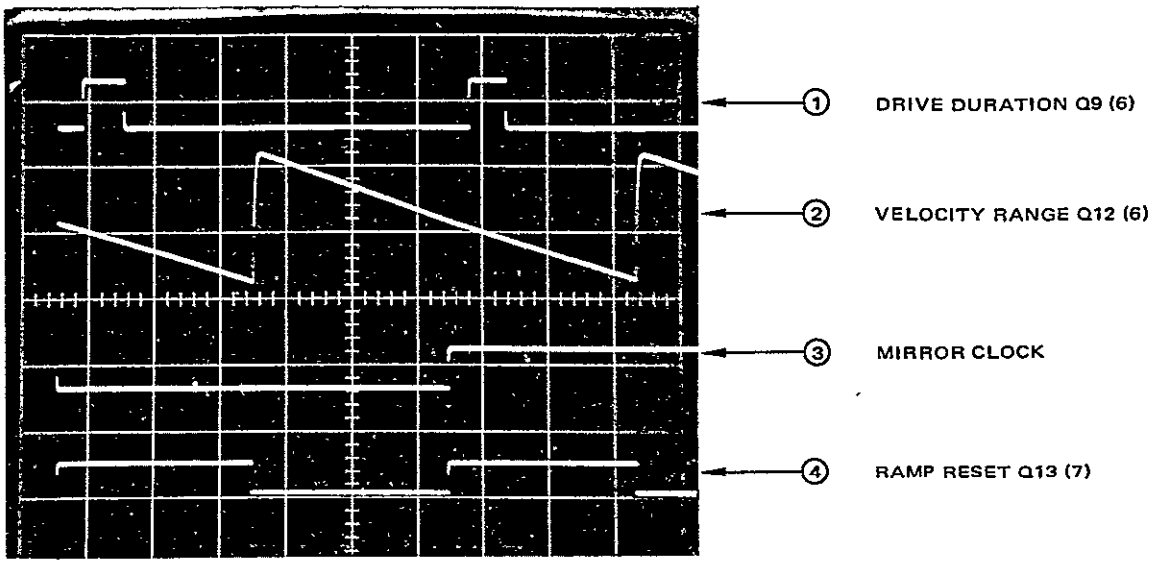

Figure 4.3-38. Velocity ramp.

and Trace Three is the mirror clock. Trace Four is a delay pulse created by each bumper pulse from the output at Q1 (3). This delay pulse thus starts when the mirror clock state changes. The delay pulse is created in the integrator reset, Q11, and is used to create a ramp which closely approximates the free scan time of forward or reverse scan. This ramp is shown in Trace Two and is created by Q12. This ramp voltage is subtracted from the constant input (and phase error input) at the summing amplifier, Q10. Its effect is to reduce the voltage out of the summing amplifier if the mirror strikes the bumper late and to increase the voltage if the impact is early. A late impact implies a slow mirror speed, thus the reduced voltage causes the torque drive duration to increase in turn putting extra energy into the mirror. The reason that the reset of the ramp is delayed past the drive pulse is that, for noise reasons, it is important that the ramp, and total control voltage in and out of Q10, not be disturbed during the integration which turns off the drive pulse at Q2.

The actual drive circuitry, Q6, 7 and the following transistors, is a current feedback driver. The drive voltage to the torquer coil is either off or full on (± a preset drive voltage). Since the drive current slowly lags the

drive voltage as a result of the torquer inductance, there is a lag in the current rise at the start of the drive pulse. This lagging response is solely determined by the impedance and the step voltage input, V_d. However when the drive circuit is told to stop, the current feedback provides total opposite drive polarity and a step of 2 V_d is created. Thus the turn-off response is twice as great as the turn-on response. Then as the driver voltage (feedback current) approaches zero, the mode of operation is no longer saturated and the torquer drive current is held at zero throughout the free scan.

Since the building of these analog electronics, the requirement that the two scan times (forward and reverse) be equal has been analyzed. The existing electronics do not do this, nor were they so intended. The present analog electronics simply phase lock the mirror clock (SMA cycle) to the reference clock in a reasonably noise free manner. The relationship between the positive half cycle on the mirror clock (say forward scan) and the reverse half cycle is such that they tried to be equal. But small differences in the coefficients of restitution and the torquer drive circuitry, if not compensated, keep these times from being exactly equal. As explained in Section 4.3.1, the logic to make the scans equal in duration to within a microsecond or better requires digital logic.

When this requirement for a digital control loop is implemented there is no reason for not digitizing the entire logic. The threshold comparators would still be analog, but the phase loop, damping or velocity loop, and constant input should all be digitized and operated from the same crystal used to equalize the scan periods. Since the Scan Angle Monitor, SAM, monitors both the scan periods (active forward and reverse half cycles) and provides the start time for the multiplexer, it should be the sensor used to establish the length of the drive pulse. It is also the best source of damping and phase data. A direct conversion to a digital mechanization would be as follows, using Figure 4.3-39 as a guide.

The delay for the start of the i^{th} torquer pulse, τ_1, should be a constant and should be measured from the i^{th} bumper impact, $t_b(i)$. This assures that a given torquer pulse, τ_2, will be timed identically with the motion of the mirror and bumper to put a consistent amount of energy into

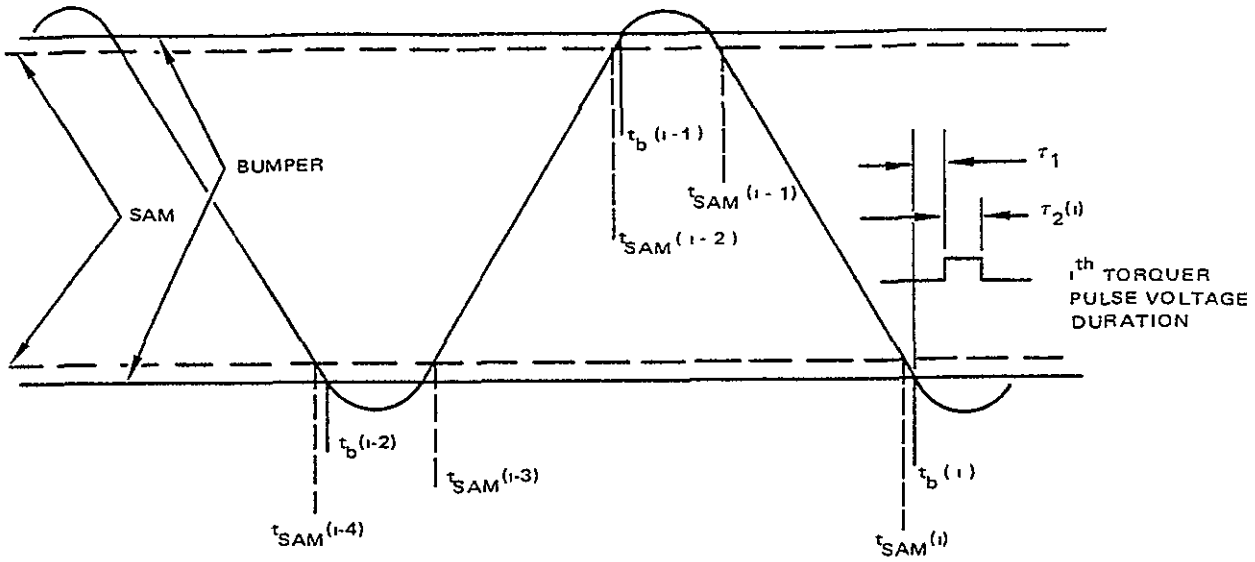

Figure 4.3-39. Information for digital logic.

the mirror. This follows the existing logic except that τ_1 would be controlled by the digital clock operating at 10 MHz.

The torque time, $\tau_2(i)$, would be computed digitally based upon the reference clock and the extreme in SAM times. The logic would be identical to the existing electronics with the addition of equal scan period control. Defining

$$\text{Error in Period} \equiv \Delta p(i) = \left[t_{SAM}(i) - t_{SAM}(i-1)\right] - \left[t_{SAM}(i-2) - t_{SAM}(i-3)\right]$$

$$\text{Phase Error} \equiv \text{Period}(i) = \text{time between } t_{SMA}(i-1) \text{ and the reference clock state change}$$

$$\text{Scan time damping Error} \equiv \Delta t_1 = \left[t_{SMA}(i) - t_{SMA}(i-1)\right] - C$$

where C is the nominal value of $t_{SMA}(i) - t_{SMA}(i-1)$

then the control function would be

$$\tau_2 = \tau_o + G_{\dot{\theta}} (\Delta t_1) + \frac{G_{\phi}'}{1+\tau_p s} (\phi_{error}) + \frac{G_p}{1+\tau_p s} (\Delta p)$$

where the phase and period errors are filtered values. (Phase is similarly filtered in the present electronics).

The net effect of this digital representation of the logic would be, in addition to equalizing the scan periods, to reduce errors in the pulse times to the control capability of digital electronics based upon a 10 MHz (0.1 μsecond) clock. Since all of the gains are far less than unity (milliseconds per unit error equivalent to a millisecond) and since the error times are measurable to about a tenth of a microsecond, the total error in τ_2 would be about a tenth of a microsecond and predominantly due to quantization.

Again it should be pointed out that the existing analog electronics was built as a design tool. It has served its purpose well and does not contribute to any measured errors in along scan repeatability. It has enabled testing of the logic and established gain procedures and sensitivity. With the exception of the period control loop, no logic changes are suggested. However, with the digital requirement of period control, an all digital system is an obvious and easy-to-implement design choice.

4.4 SMA PERFORMANCE TESTS AND ANALYSIS

This section describes and discusses the tests that were performed on the breadboard SMA and analyzes the results. The tests performed are of two types: formal tests done in compliance with the Test Plan and Test Procedure (TP 31891-350), and additional diagnostic tests which allow a deeper understanding of the SMA. This section is arranged to follow the order or the paragraphs of the test procedure. In this manner each formal test will be described and other tests relating to the intent of the formal test will be so grouped. Analysis related to individual tests will be placed with the relevant tests.

The formal procedure was used to test the flight-type mirror with bumpers mounted on the rear of the mirror. This data is appended. The SMA was then modified to include the end-mounted bumpers and all forward tests were repeated. In general this section will address tests of the latest baseline assembly with end-mounted bumpers.

4.4.1 Test Set-Up Description

This subsection presents a brief overview of the test station, special setups and a definition of terms. Detailed descriptions of the test equipment are given in the referenced Test Procedure document.

Figure 4.4-1 is a photograph of the test set-up on the granite slab. Portions of the rack mounted test-station electronics can be seen at the right. The rear of the magnesium holding fixture and a few of the SMA components are visible. All slab-mounted components have been raised on blocks to accommodate the end-mounted bumpers. The laser, which is used in measuring all scan parameters, is seen mounted in a rigid housing. It is important that all equipment related to angular measurements be rigidly mounted to the slab and have low amplitudes of vibration at any of their natural mechanical frequencies. Next to the laser is a vertical track with three split optical diodes (and their preamps) attached. Using the lens as shown, the laser beam is scanned, by reflection off the SMA, across the three split diodes (which can be placed anywhere along the scan). The time that the laser beam crosses any split diode can be measured to 0.1 microsecond accuracy. Next to the split diode track is a position sensitive photo

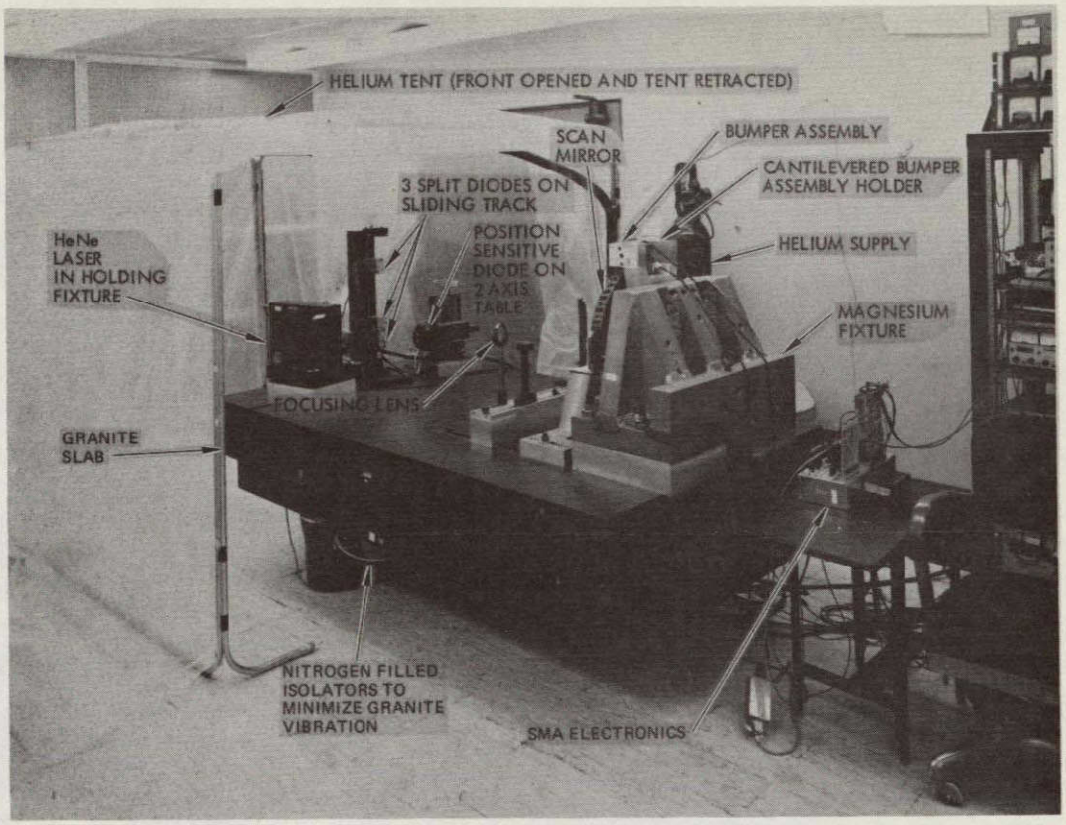

Figure 4.4-1. Test setup showing granite slab and related equipment.

diode mounted on an x-y mount. This diode is arranged to be sensitive to horizontal displacement of the laser beam and thus measures cross-axis motion of the scan mirror.

The scan mirror assembly electronics is attached to the bumper sensor coils through two twisted leads (seen going to the top bumper assembly) and to the torquer coil assembly (remaining wire over the magnesium housing). The other wires to the SMA electronics go to power supplies and to an oscilloscope as shown in Figure 4.4-2. In this figure the helium tent is shown in position. The majority of testing was done in an ambient air environment with the tent retracted. However certain along-scan measurements were degraded by random fluctuations of pressure upon the mirror. Pure helium would reduce the atmospheric density by a factor of seven and reduce random disturbances to the motion of the mirror along the scan

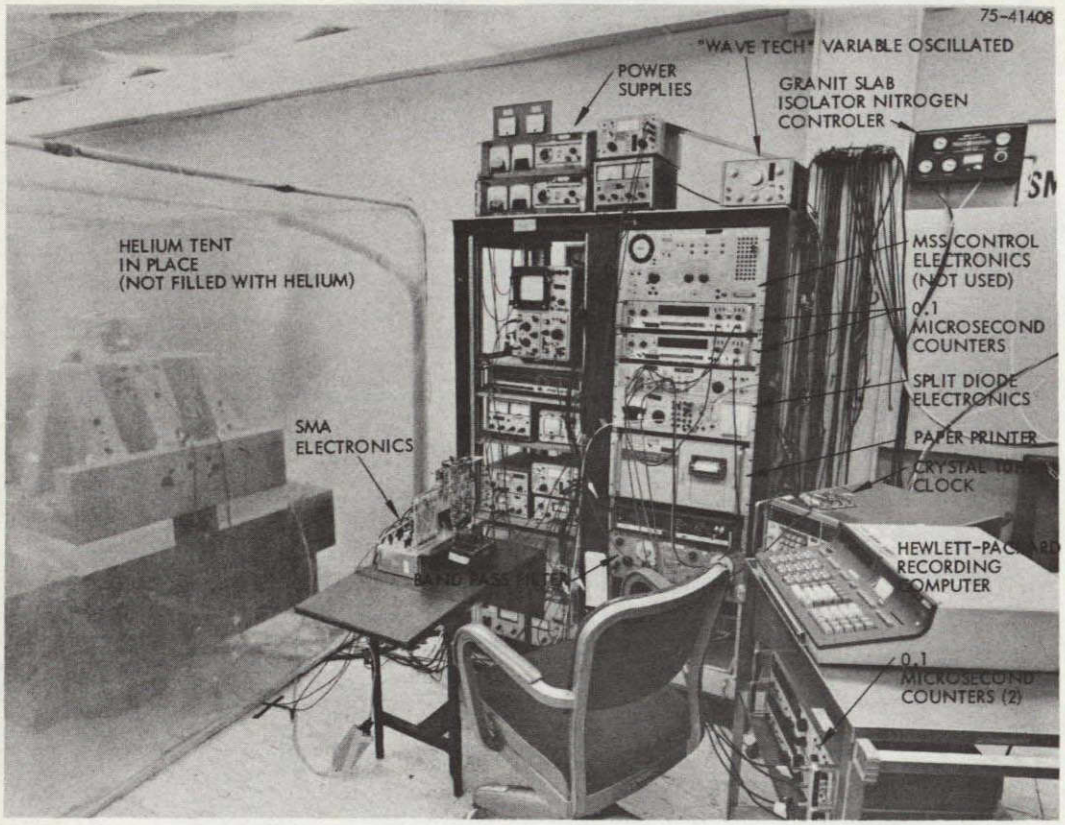

Figure 4.4-2. Test setup showing electronic portion of test station.

direction. It is, at best, only a crude approximation to a vacuum environment.

The position sensitive diode (cross-axis motion) is monitored on the rack mounted oscilloscope which is its basic data recorder.

The split photo diodes, after preamplification to maintain S/N, are processed in the split diode electronics shown in the figure. As the laser beam crosses a split diode (actually two diodes with a line separation) the following signal results:

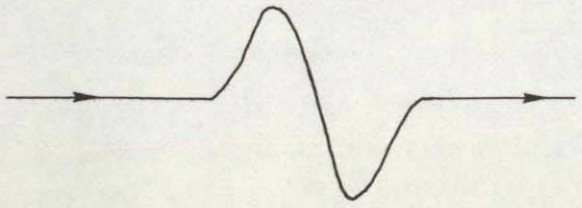

The diode electronics can tell the direction of motion and thus trigger on a positive going and negative going zero crossing, separately, enabling one to use both directional zero crossing epochs. Counters mounted above the split diode electronics count time to 0.1 microseconds and these times can be printed on a paper printer. The printer will print two times at once at a rate slightly above 10 Hz. However a significant time must exist in a print cycle for resetting.

An auxiliary set of two counters and a Hewlett Packard computer can be used to record and print times in a similar manner and at a greater rate. In addition, this computer will store up to one hundred time measurements and will process this data. This computer thus yields a quick look at the statistical properties of along scan measurements.

Figure 4.4-3 is representative of a typical scan profile, that is, angle vs. time. Several terms used throughout this analysis are defined in terms of this figure:

- Scan Amplitude: The useful portion of the total scan angle is defined, for test purposes, as the angle between the two monitoring points (split diodes). On the flight configuration these points will be monitored with the MSS-type Scan Angle Monitor.
- Turn Around Time: The time the mirror is in contact with the bumper spring at one extreme of the cycle. Since the turn around must be accomplished outside the useful portion of the scan, some small angle must exist between the monitored angle and bumper contact. The effective turn around time is therefore the total time (A and C in Figure 4.4-3) between active scans.
- Active Forward and Reverse Scans: Duration B and D are the useful scan sequence. For purposes of consistency the forward scan is defined as B.

Tests are performed with either of two basic test set-ups on the slab. All along scan measurements utilize the split diode array to measure the time of specific angle crossings. The cross-scan set-up utilizes the position sensitive diode and a porro (roof) mirror to amplify the cross scan angular motion of the scan mirror.

Two techniques are used for measuring cross axis motion in the basic test set up. These are referred to as the "even" and "odd" bounce techniques since the laser beam is forced by the porro mirror to make

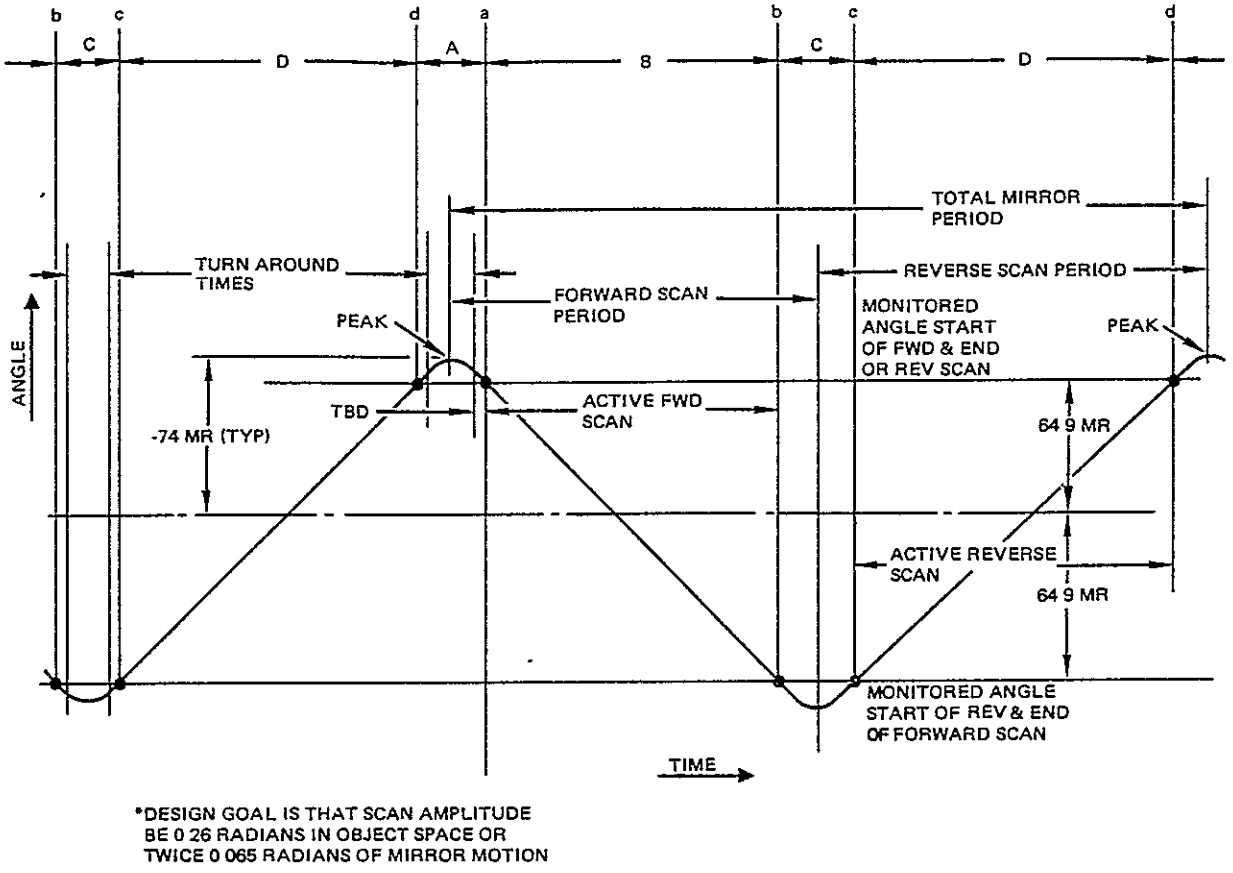

Figure 4.4-3. TM mirror scan profile.

four bounces off the scan mirror in one case and five bounces in the other. These two techniques are diagrammed in Figure 4.4-4. For each bounce off of the scan mirror the laser beam rotates through an angle twice as large as the cross axis deflection of the mirror. After an odd number of bounces, the final reflected beam will swing up and down with the scan angle just as though no porro mirror were in the path of the beam. However, with an even number of bounces, the reflected beam will not scan up and down as the scan mirror rotates but will stay fixed on the detector diode. The detector diode is sensitive to cross axis deflection (and unfortunately also to changes in beam intensity). The cross axis deflection, δ, is given by:

$$\delta = F2N\theta_x$$

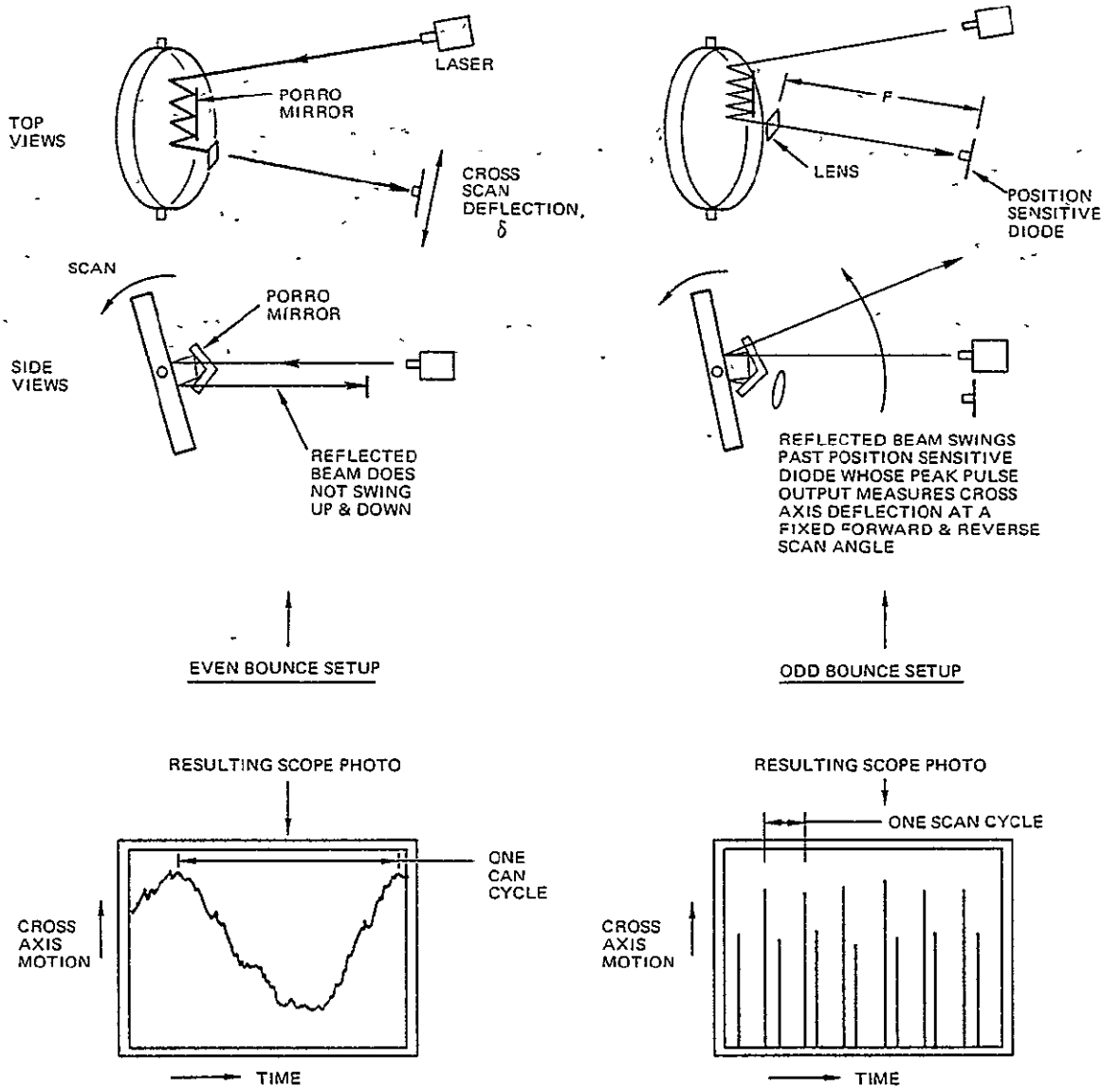

Figure 4.4-4. Two setups for measuring cross-axis motion.

where

F = distance between lens and diode (focal length)

N = number of bounces off of the scan mirror

θ_x = cross axis angular motion of the scan mirror

For our tests N = 4 or 5. This magnification allows the signal to be sufficiently greater than the noise to obtain meaningful data.

A typical scope record for the even bounce technique shows a complete scan. In order to interpret cross axis motion, it is necessary to compare amplitudes at the same scan angle in forward and reverse scans. Most of the motion shown on the photo is "nested" and does not contribute to cross-axis smear. The nested motion does, however, produce mapping errors. The nested motion is due to unbalanced behavior of the flex pivots and to light power effects such as dirt or scratches on the porro mirror (since the detector diode is power sensitive). The even bounce set-up is used primarily as a diagnostic tool since it shows the entire scan at a glance.

The odd bounce photo, as shown in Figure 4.4-4 records the cross-axis deflection at the exact same spatial scan angle on forward and reverse scans. This technique gives a direct reading of scan-to-scan cross axis motion at one spatial scan angle. It is thus far more accurate (in concept) since no nested motion is recorded. However, in order to determine the overall quality of cross-axis behavior, the diode must be moved to several positions along the scan. Unlike the sketch of Figure 4.4-4, about 50 pairs of scans can be recorded on one photo; thus both systematic and random behavior can be evaluated. By taking several photos several minutes apart, any long term effects can be measured.

4.4.2 Scan Frequency and Turn Around Times

Using the along scan set-up, a diode is adjusted to coincide with the point of contact of the mirror with the bumper spring. The formal data (see data package I) was taken with a helium atmosphere and with the clock set to produce 9.06 Hz (period of 110.2475 milliseconds which includes 2 scan periods and 2 turnaround periods). The total angle between the two diodes, as measured from the mirror, was 268 milliradians. This is slightly larger than the requirement of 259.5 to demonstrate a wider choice of scan angles.

Total Scan Period

With the SMA and test-set adjusted as above, the total period of the SMA was measured by recording the time between positive zero crossings of one of the aforementioned diodes. Because of the nature of the phase lock loop, the average period will always be identical to the clock. However the

period does fluctuate from cycle to cycle. The measured standard deviation of this fluctuation in 50 successive cycles was 2.8 microseconds. The minimum and maximum periods measured were 110241.2 and 110251.6 microseconds respectively.

It should be pointed out that there is no hard and fast upper or lower limit on scan frequency. There is some upper limit at which the spring life, as presently designed, would be degraded. For the existing configuration an upper limit of around 15 Hz causes the springs to deflect into, and touch the sensor coils. This simply means that much higher speeds would require adjusting the configuration of the bumper parts. There is no real lower limit on the SMA speed. However, as presently configured, frequencies that are too low would not deflect the bumper spring fast enough to cross the trigger threshold. The present configuration has been operated smoothly below 5 Hz.

Turnaround Period

With the same test-set up, the turn-around times were measured as the time between positive and negative crossing of each of the two split diodes. Again using 50 samples the following was measured.

Turn-around A, average period = 10,754.9 μs,
standard deviation = 1.7 μs

Turn-around C, average period = 11,586.3 μs
standard deviation = 2.1 μs

The above data was measured on 11-7-75.

The turn-around-time is adjustable by changing the cantilever length of the springs. The proper turn-around is that which provides the required scan efficiency while not exciting vibrational modes in the mirror on the flex pivots or in the supporting structure. The following chart (Figure 4.4-5) shows the relationship between turn around time and scan efficiency for quasi-linear scans as a function of scan frequency.

Thus if the turnaround times are set in the nominal range of 8-10 milliseconds, a scan efficiency of 85 percent or better will be obtained in the 7 to 9 Hz SMA frequency range. And even in the extreme case of

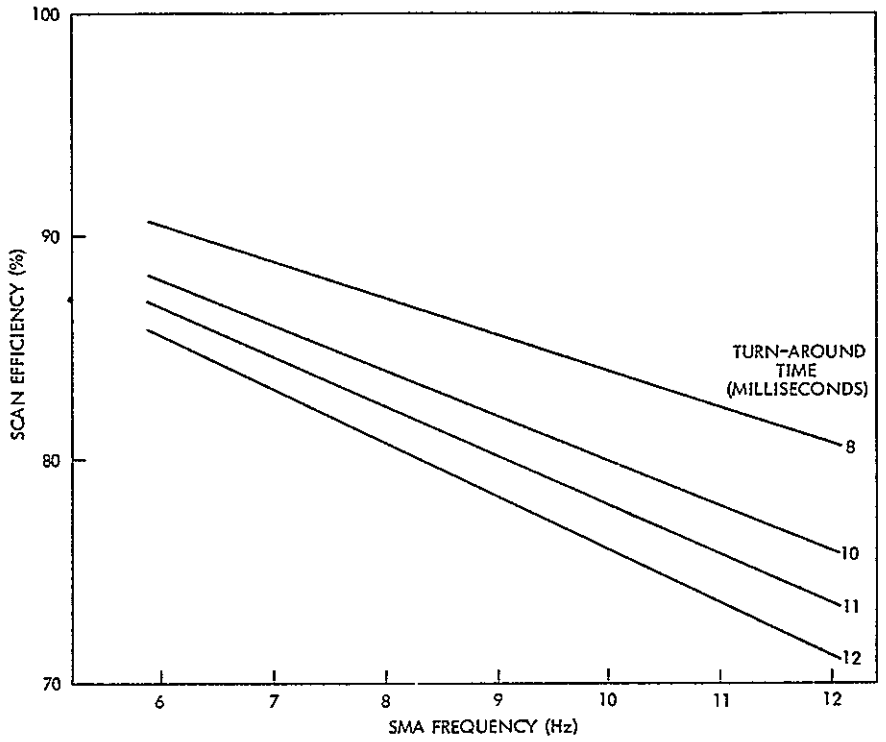

Figure 4.4-5. Scan efficiency versus a function of scan frequency and turn-around time.

11.5 ms turnaround, the scan efficiency would be 79 percent at 9 Hz and 83.5 percent at 7 Hz.

Since taking the above data a question arose regarding the long term stability of the active forward and reverse scans. Measurements were taken that indicated that the total active scan time, within the scan cycle, was slowly drifting by several microseconds. As seen in the sketch, the total scan time is the sum of the forward and reverse active scan periods, t_f and t_r. The total cycle period, T_{cycle}, must be constant (except for random noise) and equal to the reference clock period. This fact has been tested and found true. But the cycle, T_{cycle}, is equal to the sum of the total scan time, t_T, and the two turn-around times, t_{b1} and t_{b2} plus a small amount to account for the separation between photodiode and bumper pick-off angles. Thus the only way that the total scan time can vary (on a long term average) is for the turnaround times to vary.

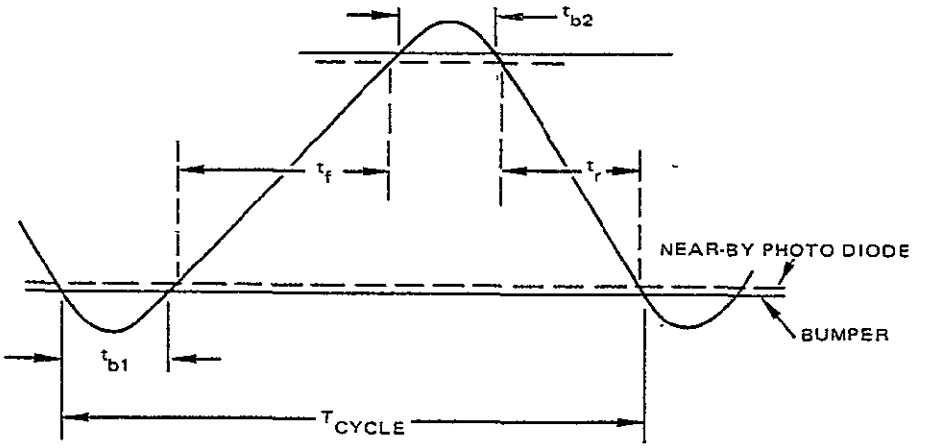

For the above reason the question was first reduced to an attempt at determining the fluctuations, if any, that might be occuring in the turn around times. In order to test the turn around time a diode is placed near the bumper impact angle as shown in the sketch below.

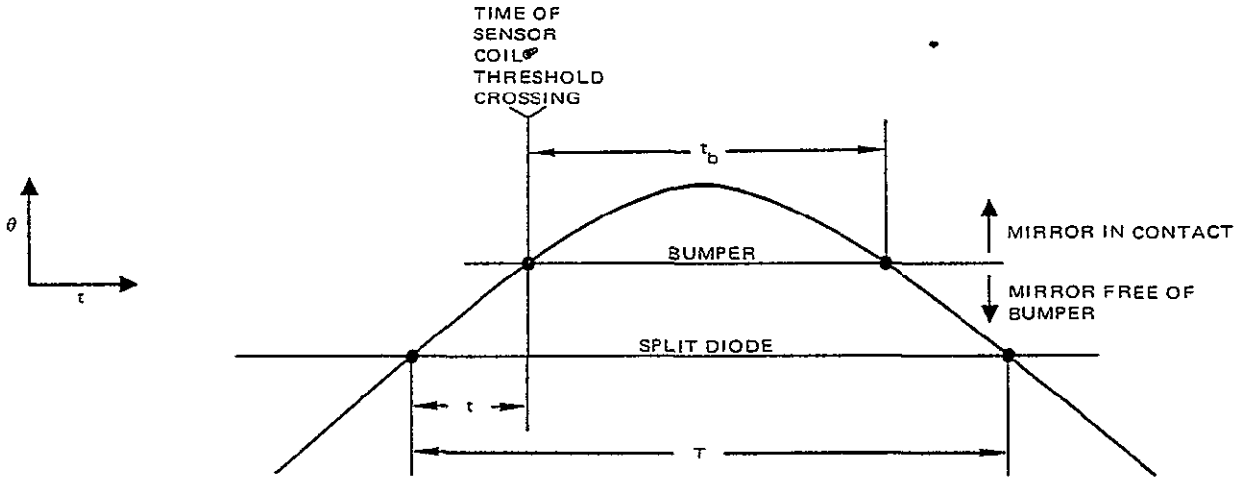

In order to measure possible drifts in the turn-around time, it is not sufficient to measure the time between photo-diode crossings, T, alone. As the temperature changes, the angle between the photodiode and the bumper may well change and thus T might be expected to drift even if t_b is constant. What is required is a measure of bumper contact, t_b. The bumper pick-off coil gives a measure of the time of contact, but no equivalent time can be measured at the end of contact. By assuming that the split diode (measured

on either end of turn-around) can only move up or down with respect to the bumper contact angle, the true turn around time should equal t_b where

$$t_b = T - 2t$$

A test was run with the reference clock set for a period of 111009.1 microseconds. T is measured between diode crossing for 50 consecutive cycles at the same time t is measured between the first crossing of the diode and the bumper sensor coil output circuit. Each data point allows an average for each measurement and a standard deviation. The error in the average can be expected to be much smaller than the standard deviation (by a factor of about $\sqrt{50}$). By measuring t and T several times over greater than a three hour period with the SMA running continuously, the following data was produced.

Time	Temp °F	T (50 Point Avg) microsec	σT microsec	t (50 Points) microsec	σt microsec	Turn Around Time (T - 2t) microseconds
10:35	69.0	12014.6	1.98	536.8	0.35	10,941.8
10:36	—	12018.2	1.89	540.6	0.24	10,937.0
11.00	69.6	12038.9	1.59	553.5	0.18	10,941.9
11:15	69.8	12031.0	2.33	550.5	0.76	10,940.0
12:20	70.0	12058.1	1.62	561.3	0.47	10,935.5
12:49	70.0	12051.6	1.01	558.9	0.44	10,935.8
1:15	70.1	12060.8	3.40	564.6	1.53	10,932.6
1:18	—	12074.8	1.73	572.3	0.64	10,930.2
1.57	70.1	12064.7	1.36	568.1	0.66	10,928.5
2:03	—	12078.1	1.63	576.4	0.58	10,925.3
2:04	—	12080.0	1.50	577.7	0.64	10,924.6

It is apparent that the temperature, as monitored at the bumper assembly did not change by very much. It would appear that the time between diode crossings, T, varied by about 65 microseconds over the test period. This could, conceivably be due to temperature related motion of the diode with respect to the bumper angle. But when the diode-to-bumper time

is subtracted from either side of the time, T, the resulting turn-around time still appears to vary by about 15 microseconds. The results of this test would, if left unquestioned, suggest that the average turnaround times will not remain constant and that the nominal total scan period will thus not remain constant.

Such a change in turn-around times could not be explained upon the basis of temperature. Then too, any kind of wear would cause a monotonic change, which was not the observed case at all. An investigation of MSS SMA related space history showed no indication of slowly changing turn-around time. But the above long-term, split diode tests had never been done on the MSS. Finally, in January, the diodes and related circuitry were brought into question. The exact quantitative nature of the signal output of the split diodes is not completely understood. However measurements have been taken showing that the short term noise is extremely small. The standard deviation of the noise created by measuring a time with two split diodes has been shown to be less than 0.1 microseconds (many samples of 50 consecutive measurements). The question of long term stability revolves around understanding how a split diode measurement could slowly shift or drift. The possible explanations are several: the laser power distribution within the beam could shift; the angle of the laser could shift with temperature, causing changes in its position when crossing a diode; the diode (actually two diodes with a separation) could have temperature dependent characteristics; the threshold circuits (one for each direction of diode crossing) could shift with time. But rather than determine how the photo diode set-up could produce apparent drifts in measurements, a test was devised to determine whether or not such a problem existed.

By running the SMA in helium, in the closed loop mode, two times could be measured whose relationship would show up any diode related drift. The following sketch indicates the test. By obtaining the average value of t and T (50 data points each) over a long period it is possible to differentiate between diode drifts and actual changes in the scan period. Of course the average cycle time will, on the average, equal the reference clock, and the reference clock must be shown to be constant.

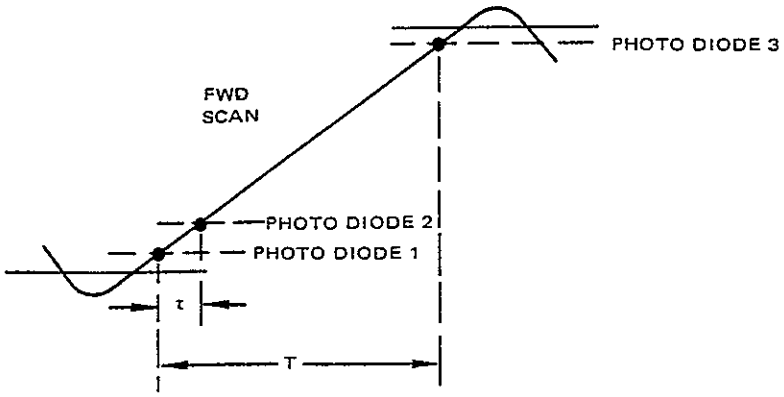

If the scan time actually changes, then because of the nature of the non-torqued scan, the velocity of scan will change, essentially equally, throughout scan. Therefore we can predict results for all possible situations.

1. If diode No. 1 drifts, t and T will drift by an equal and correlated amount.
2. If diodes No. 2 or No. 3 drift, t or T will be individually changed.
3. If the scan period alone is actually changing, then the change in t will be less than the change in T by a factor of T/t (about 20.3 for the actual test)

The following data was taken on 1/14/76 where the bars over t and T indicate a 50 measurement average; the SMA was run continuously from 10:06 AM to 2 30 PM.

Time of Day	$\bar{t}$ (μs)	σt (μs)	$\bar{T}$ (μs)	σT (μs)	Ref Clock (μs)	Notes
10 06	2136.0	0.22	43400.2	1.65	111009.1	
10 10	2137 8	0.15	43403 5	1.49		
10·12	2137.3	0.37	43405 6	1 49		
10.17	2137 2	0.15	43405.6	1 68		
10 24	2137.0	0.14	43403.7	1.32		
10 27	2136.9	0.16	43403.7	1.89		
10:35	2136.2	0.15	43399.8	1.44		
10:45	2135.8	0.18	43398.8	1.94		
10:55	2135 9	0.11	43398.1	1.77		
11.05	2135 4	0.13	43398.2	1.82		
11.18	2135.4	0.28	43394.7	2.28	111009 1	
11 30	2135.2	0.44	43395.9	1.85		
11 40	2134.6	0.73	43396.8	1.41		
11 50	2134.6	0.27	43396.4	1.77		
1.20	2131.9	0.79	43395.2	2.58	111009 1	} Helium level high in tent. Possible air effect.
1 30	2132.1	0.78	43394.7	2.28		
1 40	2133 4	0.19	43398.6	2.56		
1 50	2134.3	0.95	43403 6	2.44		
2 00	2136.0	0.52	43404.7	1.96		New helium added.
2.10	2135.7	0.79	43403.2	2.14		
2.20	2135.2	0.49	43402 1	1.78	111009.1	
2 30	2135.0	0.24	43401.5	1.82		

This data is plotted in Figure 4.4-6. $\Delta\overline{T}$ is the change in $\overline{T}$ from its first measured value at 10:06 AM. $\Delta\overline{t}$ is a similar curve for the short scan segment. If all of the fluctuations in $\Delta\overline{T}$ were due to changes in initial scan velocity, then $\Delta\overline{t}$ should look like $\Delta\overline{T}/20.3$ since T is nominally 20.3 times as long as t. Thus if all of the fluctuation in $\Delta\overline{T}$ were attributed to changes in scan line length (velocity) there is a 4 microsecond discrepancy in Δt! It must therefore be concluded that some elements of the test setup are fluctuating during each scan and are producing apparent (to the controller) changes in the turnaround periods over long term. There is also seen in the listed data and the plots of Figure 4.4-6 a direct correlation in the magnitude of $\Delta\overline{T}$ and $\Delta\overline{t}$ with the amount of air present in the tent and with the times of helium replacement.

Until a more elaborate test setup incorporating a vacuum chamber can be obtained, no definitive statements can be made as to the actual error sources responsible for timing errors.

To be absolutely conservative, at this time, it should be assumed that some small, slow variation in turn around times exists. This implies that the two active scan periods (forward and reverse) on the breadboard are not absolutely equal to a constant. As described in Section 4.3 (see Figure 4.3-6), logic can be added to make the two scans equal to each other (nominally within a microsecond). It is desirable that any slow drift over tens of seconds in the active scan half cycles not exceed 0.5 IFOV or 5 microseconds. This goal has been reached. It also appears from the above analysis of the data on Figure 4.4-6 that this drift magnitude applies over periods of many hours. As more of the diagnostic testing data is analyzed, the suggestion increases that almost all of the measured magnitudes of drift are largely attributable to test setup error sources and not to the SMA. This anomaly has been proven to apply to the MSS SMA laboratory test data since errors measured in the laboratory were not found to exist in the data measured from the instrument in orbit.

4.4.3 Start-Up Time

The logic for mirror start-up on the flight instrument was not installed on the breadboard SMA. A simple starter was employed on an IR&D

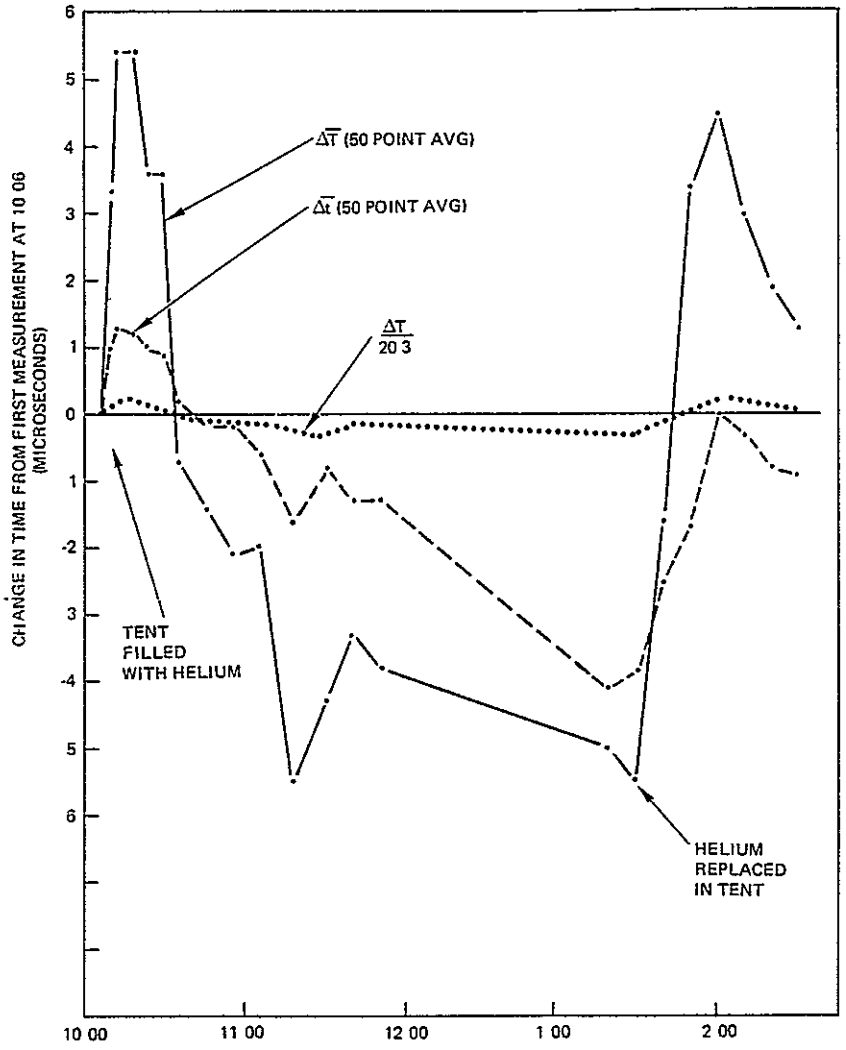
CHANGE IN TIME FROM FIRST MEASUREMENT AT 10 06 (MICROSECONDS)
6
5
4
3
2
1
0
1
-2
3
-4
5
6
$\overline{\Delta T}$ (50 POINT AVG)
$\overline{\Delta t}$ (50 POINT AVG)
$\frac{\Delta T}{20\ 3}$
TENT FILLED WITH HELIUM
HELIUM REPLACED IN TENT
10 00
11 00
12 00
1 00
2 00

Figure 4.4-6.

SMA but this is not directly applicable to the flight-type system. See Section 4.2 subtitled "Start-Up Time" for a description of the baseline start-up logic tested elsewhere.

4.4.4 Scan Center

The Development Specification set a design goal that the rest position of the mirror be within ±4.3 milliradians of the center angle between the two bumpers (or spit-diodes in this case). This was accomplished by adjustments during the initial installation of the mirror into the SMA The pivot holding blocks were loosened, the mirror was positioned and the blocks retightened until the above requirement was met. This adjustment assures that the torque produced by the flex pivots will be equal in both scan directions thus helping to insure along scan registration for bidirectional scanning.

4.4.5 Scan Linearity

The original breadboard design goal for linearity, which is perturbed primarily by the flex pivot restoring torque, was to be between +3.7/-7 percent. The precision of the test procedure designed for this purpose was entirely adequate. However when it later became an objective to produce scans whose angle at any time is no further from a linear angle ($\theta = Ct$) than ±21.3 microradians, that procedure became marginal. The new objective can be met with a special test setup within a vacuum chamber which permits temperature and air turbulence to be adequately controlled. Since such a facility was not available, the originally planned test setup was used. This employs three split diodes.

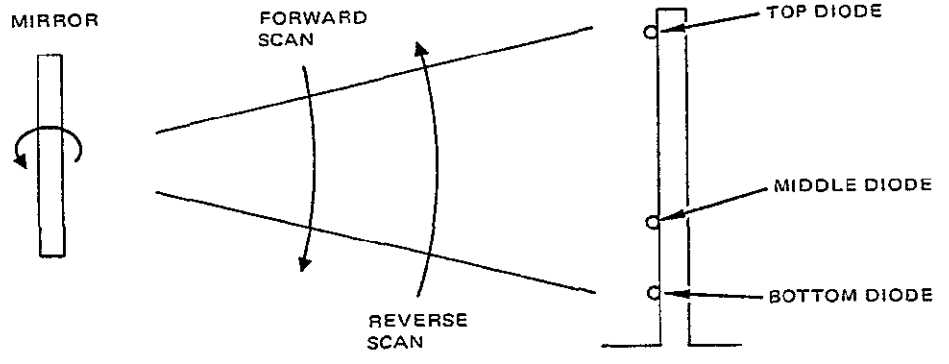

This middle diode is individually set at five, near-equally spaced, positions between the two end-of-scan diodes. Since linearity is defined as the average scan speed at a particular along scan angle expressed as a percentage of the average speed taken over the entire active scan angle, we may write

$$L = \text{average value of} \left\{ \frac{\theta(\theta)}{\dot{\theta} \text{ for a scan}} \right\}$$

For the case of the uncompensated flex pivot torque, the scan angle is a portion of a sinusoid perturbed by air drag (the formal test was done in air). A reasonably good functional form for the mirror position is

$$P(x) = Ax^3 + Bx^2 + Cx$$

where

θ_T = total angle of scan (0.268 radians in test)

$P(x)\theta_T$ = scan angle at time of middle diode

$$x = \frac{t_2 - t_1}{t_3 - t_1}$$

$t_2 - t_1$ = time between top diode and middle diode for forward scans

$t_3 - t_1$ = time between top and bottom diode for forward scans

The test for forward scans was performed as follows. The two times involved in x are measured with the SMA running in air at 9.06 Hz. x is measured several times at each location of the middle diode (10 measurements were used at each diode location. Then all x were least square fitted to the polynomial P(x) under the condition P(0) = 0, P(1) = 1 identically. The scan speed (non dimensional) is given by

$$\dot{P}(x) = 3Ax^2 + 2Bx + C$$

The routine is repeated for reverse scans where now

$$x = 1 - \left(\frac{t_2 - t_3}{t_1 - t_3} \right)$$

and is a measure of angle in the same sense. The resulting data is plotted in Figure 4.4-7. On the same figure is shown the theoretical value that would be obtained in a vacuum. The accuracy of the measuring technique is about one percent.

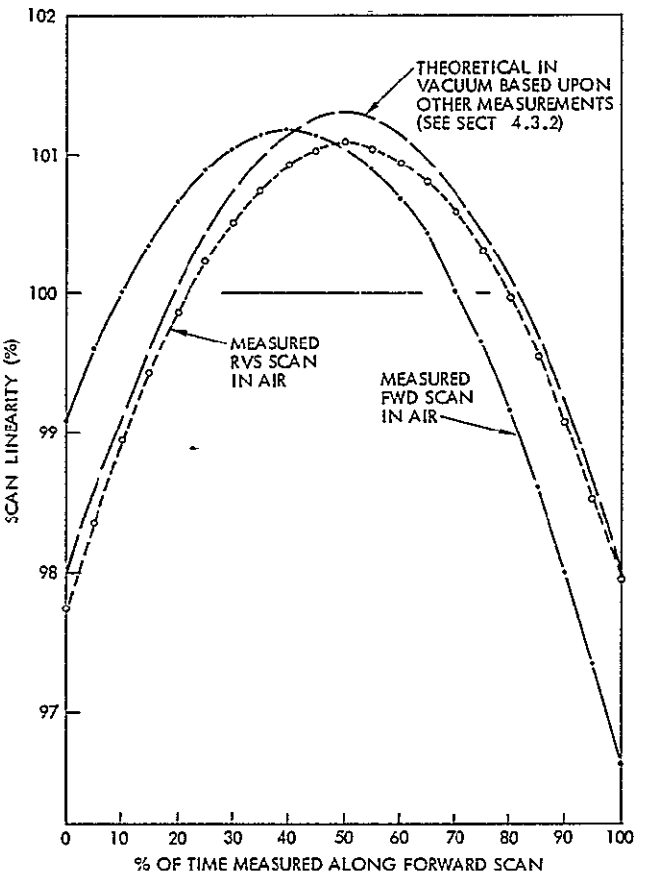

Figure 4.4-7. Measured linearity in air and theoretical linearity (uncompensated) in vacuum.

4.4.6 Scan Amplitude

The scan amplitude was arbitrarily set at 0.268 radians which is slightly larger than the original requirement of 0.2595 radians. It should be

noted, however, that the basic design is not sensitive to scan amplitude. For instance, should it be desirable to double the scan amplitude the net effect would be:

1. A proportional increase in momentum transfer to the space craft, e.g., 5 rather than 2.5 μrad spacecraft rigid body motion.
2. A tendency to create bumper obscuration of the clear aperture. This would require a minor redesign to place the mirror/bumper contact points slightly behind the mirror front surface:

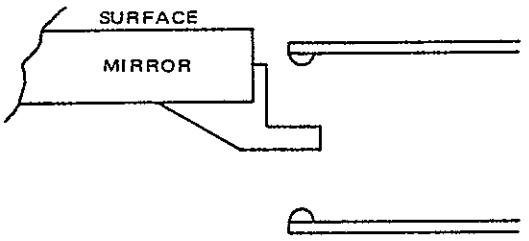

3. For the same cyclic rate, the scan rate would double and the power requirement would quadruple. To maintain the same scan efficiency, the turn-around time must remain constant thus requiring that greater torque capability be designed into the torquer (approximately double).

4.4.7 Phase and Phase Stability

The design goal that the phase angle between the driving clock and the SMA not change by more than the equivalent of 5 milliseconds over the life of the unit is difficult to prove in this program. At an operating frequency of 7 Hz, 5 milliseconds corresponds to a change in phase angle of about 12.6 degrees.

It is possible to measure the time between a clock zero crossing and an output of a bumper sensor, this being a measurement of phase. This has been done and this measurement watched for several hours. The largest noted drift in this parameter was 17 microseconds. This, however, is a short term measurement in a parameter which would be expected to change measurably only after a very long time. A proper estimate requires an analysis based upon the expected changes that might occur in the SMA. Refer back to the basic control equation:

$$\tau = \tau_0 + G_{\dot{\theta}}(\Delta t) + G_{\phi}(\Delta\phi)$$

where:

τ is the duration of the applied voltage which produces the torquer pulse.

G_θ is the frequency loop gain

Δt is the difference between the actual value and nominal value of the time between the two most recent bumper impacts

G_ϕ is the phase loop gain

$\Delta\phi$ is the error in phase, i.e. the difference between the clock and the pulse train created by the bumper impacts. Actually $\Delta\phi$ is zero when the phase is 90^o. $\Delta\phi_{max}$ is limited by $\pm 90^o$.

From measurements taken with the unit running at 7.09 Hz and with the lowest available setting of the phase loop gain (G_ϕ = 0.021 ms/deg) the equation becomes

$$\tau = 2.74 + 0.021\,\Delta\phi \text{ (in milliseconds)}$$

where the frequency loop is ignored because its nominal contribution to τ is zero. For a 5 millisecond change in phase (12 6 degrees) to occur, the constant term (τ_0 = 2.74 milliseconds) would have had to drift by 9.7 percent. Without catastrophic failure, there is no way that this could occur electronically. The constant term is established by a well regulated power supply and by a well specified monostable. The other source of change to the constant term is the mechanics of the bumper. As presently measured, the coefficient of restitution of the bumper is 0.974 at 7 Hz in Helium. As the coefficient of restitution reaches unity, the energy required to be added during each bounce and the torquer on time are reduced to zero. A slight change in restitution would then cause a very large relative change in the torquer time. For the actual case at hand the energy required at each turn around is

$$E = C(1 - \epsilon^2)$$

where C is a constant and ϵ is the coefficient of restitution. Then

$$\frac{dE}{E} = \frac{-2\epsilon^2}{1-\epsilon^2} \cdot \frac{d\epsilon}{\epsilon}$$

By measurement it has been shown that a constant extra microsecond of torquer-on-time causes a decrease of 40 microseconds of scan time, t_p. That is if

$$\frac{d\tau}{\tau} = \frac{1}{2740}$$

then

$$\frac{dt_p}{t_p} \quad \text{will be} \quad \frac{-40}{60,000} \quad \text{(at 7.0 Hz)}$$

or

$$\frac{d\tau}{\tau} = -0.55\frac{dt_p}{t_p} = 0.55\frac{d\dot{\theta}}{\dot{\theta}}$$

We now have the relationship between an increased scan speed and its causative increased torque time. Energy can be related to scan speed by

$$\frac{dE}{E} = \frac{2d\dot{\theta}}{\dot{\theta}}$$

Thus

$$\frac{d\tau}{\tau} = 0.55\frac{d\theta}{\dot{\theta}} = \frac{0.55}{2}\frac{dE}{E} = -\frac{0\ 55}{2} \cdot \frac{2\epsilon^2}{1-\epsilon^2}\frac{d\epsilon}{\epsilon} = 10.4\frac{d\epsilon}{\epsilon}$$

for the measured case wherein ϵ equals 0.974. For the phase lag not to change by more than 5 millisecond at the lowest gain setting (corresponding to a change in τ of no more than 9.7 percent) implies that

$$\frac{d\epsilon}{\epsilon} \leq \frac{9.7\%}{10.4} = 0.9\%$$

The mechanical question thus becomes, will the coefficient of restitution change, over a mission lifetime by more than 0.9 percent.

Over periods of several hours, no significant change in ϵ is measurable. It has been predicted that temperature could possibly change ϵ by changing the effective spring constant of the tapered leaf spring. However no change in ϵ was noted when the temperature was changed by $8^{\circ}F$. The other possible cause for changing ϵ might be wear of the nylon button contact. Significant wear has not been seen in over 1000 hours of operation. The following measurement of ϵ is used:

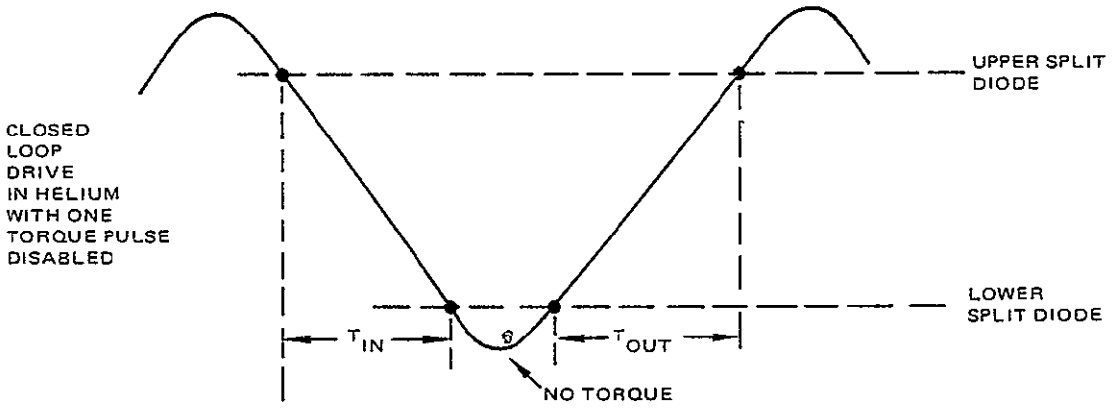

Then coefficient restitution, ϵ, is defined as

$$\epsilon = \frac{T_{in}}{T_{out}}$$

where the average of over 50 measurements is used. This result will vary depending upon the exact placement of the diodes. If the diodes were both close to the bottom bumper, the slowdown effect of helium would be minimized and the measurement would depend more upon the mechanical parameters. On the other hand, moving the diodes further apart tends to eliminate diode measurement noise from the calculation.

With the diodes moved to extreme poisitions (each near a bumper) the following results were measured on the first day after assembly and again after the bumper contact points had been worn into their stabilized configuration as shown below:

Date	Drive Frequency	T_{in}	T_{out}	ϵ
11-7-75	9.06 Hz	44350.3 μs	43338.7 μs	0.97719
12-18-75	9.00 Hz	43911.3	42832.6	0.97543

The difference in the absolute values of T_{in} and T_{out} is not significant, as the diode positions had been moved and not re-located exactly. It is also known from previous test measurements that ϵ is a function of operating frequency such that

$$\frac{d\epsilon}{df} = 0.0024/\text{Hz}$$

With this correction factor, the change in ϵ, as measured over the wear-in period is about 0.165 percent. Some additional contact surface wear will occur over a full mission lifetime but this is estimated to be small compared to the initial wear-in experienced at the time of this measurement.

To summarize, it is improbable that a 5 millisecond change in the phase "angle" will occur because:

a. With the lowest phase gain possible a 0.9 percent change in ϵ is required to exceed 5 milliseconds and the measured change was 0.165 percent after wear-in.

b. The optimum phase gain setting is not the minimum one but rather a factor of two greater (shown later in Section 4.4.10) thus requiring twice as large a change in ϵ.

It should also be pointed out that should a situation present itself (such as a mechanical design change) that would cause a slow drift in phase angle, then a simple integration in the phase loop would hold the time average phase angle identically to zero.

4.4.8 Along Scan Image Displacement Repeatability

The basic design goal, established in the Development Specification, is that adjacent scans (forward and reverse) when processed on the ground, conformally map object space with no greater than 4 microradians expected error between scans. It is assumed that the total scan angle, θ_T, is monitored by an MSS-type Scan Angle Monitor that correctly records the time of the start and stop of the scan in both directions. It is assumed that the scan will be mapped such that one end of the scans (say the start of forward scans and the stop of reverse scans will be aligned. The following sketch suggests how this might look when so mapped.

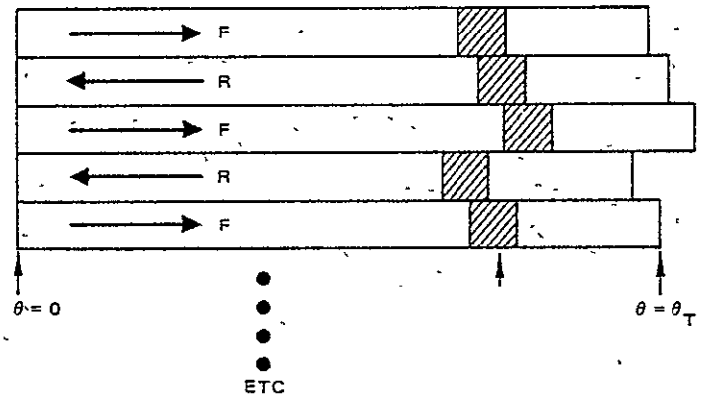

The first IFOV, at $\theta = 0$, would thus always be perfectly registered for all scans. The crosshatched IFOV at θ_1 shows some degree of misregistration. The basic goal is that the expected value or standard deviation of $\theta_{1\ \text{Forward}} - \theta_{1\ \text{Reverse}}$ rms averaged over all 1 from 0 to θ_T not exceed 4 microradians.

At the beginning of this program it was assumed that torque would be applied during the reverse scan and that the scan functions for each direction would be quite dissimilar. It was also assumed that the difference between the scanning functions would be systematic and known a priori. With appropriate processing the nominal forward and reverse scanning functions could thus be made to equal identically. In addition it was assumed, based upon experience from MSS, that, after processing for the difference in the scanning functions, the remaining random error between scans would be primarily due to a single parameter, namely the random error in average scan speed (this average is taken over an entire scan). Since data processing would be required to compensate the scan functions, this major source of statistical error could then be removed by linearly justifying each scan line. The following sketch defines the times that were measured for the procedural tests to measure along scan repeatability. The raw and unprocessed measure of the object space location of a middle diode (θ) would be the time between start of scan (T_1 for forward scans and T_3 for reverse scans) and the time that the middle diode (T_2) was crossed. Assuming that the two scanning functions were known and that the individual scans were linearly justified

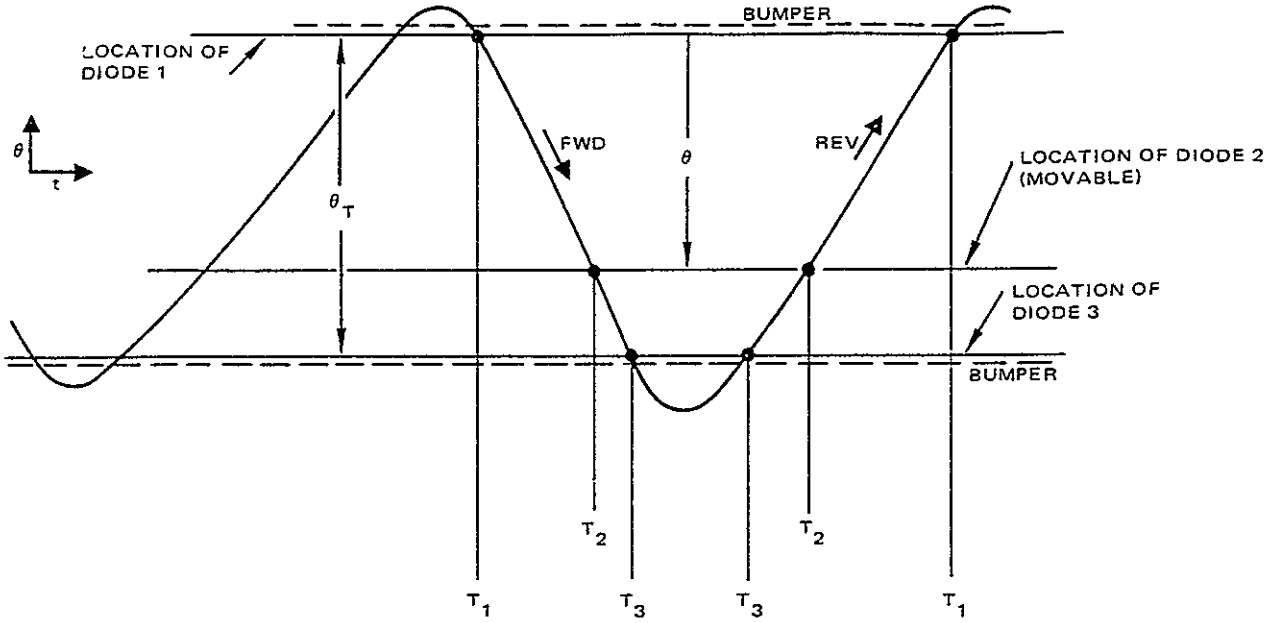

based upon the measured time of total scan allows a measureof the random error for any scan. For forward scans the random i^{th} error is

$$\epsilon\theta_{f_i}(\theta) = \left[\left.\frac{T_2 - T_1}{T_3 - T_1}\right|_i - \left.\frac{T_2 - T_1}{T_3 - T_1}\right|_{AVG}\right]\theta_T; \qquad i = 1, 3, 5 \ldots$$

and for reverse scans

$$\epsilon\theta_{r_i}(\theta) = \left[\left.\frac{T_1 - T_2}{T_1 - T_3}\right|_i - \left.\frac{T_1 - T_2}{T_1 - T_3}\right|_{AVG}\right]\theta_T; \qquad i = 2, 4, 6 \ldots$$

The scans are numbered consecutively where the first is arbitrarily a forward scan and the second is a reverse, etc. From these measured statistical errors in the forward and reverse scans, the difference or misregistration between scans can be developed

$$\Delta\theta(\theta)_1 = \epsilon\theta_{r2}(\theta) - \epsilon\theta_{f1}(\theta)$$

$$\Delta\theta(\theta)_2 = \epsilon\theta_{r2}(\theta) - \epsilon\theta_{f3}(\theta)$$

$$\Delta\theta(\theta)_3 = \epsilon\theta_{r4}(\theta) - \epsilon\theta_{f3}(\theta)$$

$$\Delta\theta(\theta)_4 = \epsilon\theta_{r4}(\theta) - \epsilon\theta_{f5}(\theta)$$

$$\vdots$$

$$\Delta\theta(\theta)_{i\ \mathrm{ODD}} = \epsilon\theta_{r_{i+1}}(\theta) - \epsilon\theta_{f_i}(\theta)$$

$$\Delta\theta(\theta)_{i\ \mathrm{EVEN}} = \epsilon\theta_{r_i}(\theta) - \epsilon\theta_{f_{i+1}}(\theta)$$

The expected value of the scan to scan deviation is thus

$$\sigma\theta(\theta) = \left\{ \frac{1}{N-1} \sum_{i=1}^{N} \left(\Delta\theta(\theta)_i\right)^2 \right\}^{1/2} \qquad \text{where N is large}$$

This is the quantity that could be tested at several angles, θ, by moving the middle diode. Then the expected value over all angles could be obtained by rms averaging several measured angles. Because of the linear justification $\sigma\theta(\theta)$ will be identically zero at $\theta = 0$ and $\theta = \theta_T$.

The procedural tests were based upon the above assumptions but were perturbed by two constraints. First the test equipment (borrowed from MSS for these tests) was not capable of recording consecutive forward and reverse scans at the same time. The mechanical printer simply did not have time to reset between print requirements. One could record consecutive values of $T_2 - T_1$ and $T_3 - T_1$ for forward scans, and then record a string of reverse scan parameters ($T_1 - T_2$ and $T_1 - T_3$).

The second perturbation is that it was originally planned to conduct all tests in air. This was done, however it was found that the statistical fluctuations of air drag swamp the results that would have been obtained in vacuum or space.

In any case, the procedural test consisted of measuring $\sigma(\epsilon\theta_f(\theta)$ and $\sigma(\epsilon\theta_r(\theta)$ and then assumed no correlation.

$$\sigma\theta(\theta) \qquad \text{assumed equal to} \qquad \left\{\left(\sigma\theta_f(\theta)\right)^2 + \left(\sigma\theta_r(\theta)\right)^2\right\}^{1/2}.$$

This assumption was found to be overly conservative when it was later shown that positive autocorrelation exists in scans in each direction and positive correlation exists between forward and reverse scans. The measured results of these procedural tests in air are shown in Figure 4.4-8.

Very little can be concluded from this data, other than the fact that air swamps the real noise. It is quite obvious that if no forces act upon the mirror during its free travel, and if the scan function is as linear as it is known to be (Figure 4.4-6), then linear justification will reduce the rms error at any point to well under a microradian. It has also been shown that the noise in measuring the time between two diode crossings is less than 0.1 microsecond (see Log Books) which should contribute about a

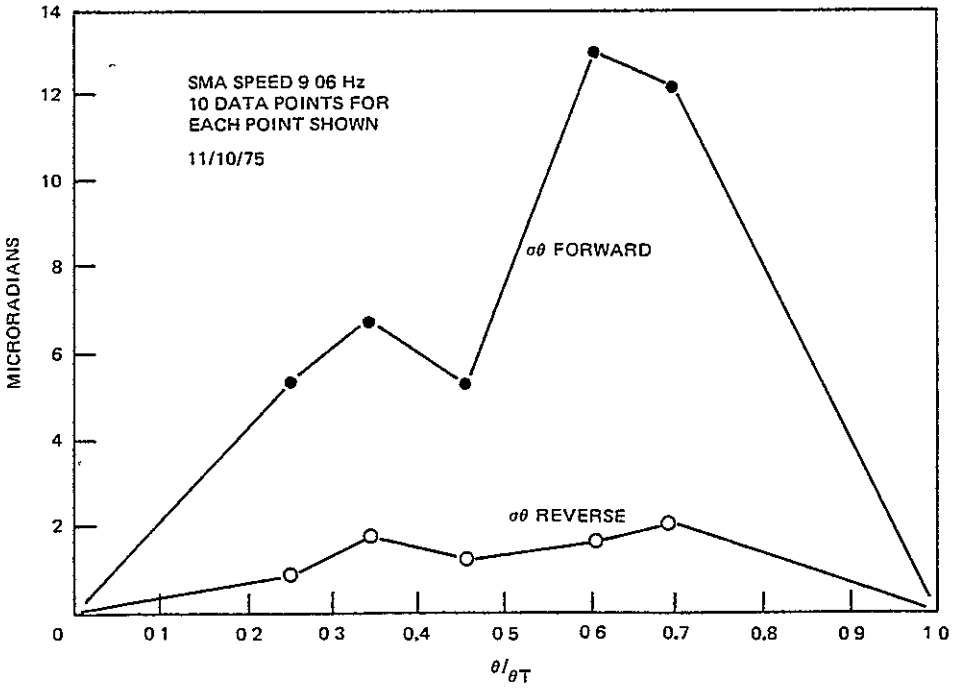

Figure 4.4-8. Results of procedural tests in air of along scan repeatability.

microradian error. It is therefore clear that these measurements could only have meaning if done in a more benign environment than air.

To test this hypothesis, the worst case of Figure 4.4-8 (forward scan) was repeated in a helium tent at $\theta/\theta_T = 0.46$. Fifty values of $T_2 - T_1$ and $T_3 - T_1$ were measured. The results were (see Log Book for data):

$$(T_2 - T_1) \text{ average} = 20404.7\ \mu s, \text{ STD DEV} = 0.93\ \mu s$$

$$(T_3 - T_1) \text{ average} = 44277.6\ \mu s, \text{ STD DEV} = 1.808\ \mu s$$

$$\sigma\theta_f\ (\theta/\theta_T = 0.46) = 1.4\ \mu \text{radians}$$

which is significantly less than was measured in air. Again it should be pointed out that in all probability the true error is smaller than computed since at least 1 μ radian can be attributed solely to photodiode measurement noise and, although helium is a more benign environment than air, it does not approach that of a vacuum. No estimate of what perturbations are caused by helium seems possible without actually testing in a vacuum. All that can be concluded from the aforementioned testing is that, in a vacuum, the along scan repeatability after linear justification would be expected to be better than 1.4 microradians.

Further procedural-type tests at other angles were not attempted in helium because the basic goal had changed. With the design change to torque-while-turn-around operation, the two scan functions were made nearly identical. In addition the statistical fluctuation in mirror speed appeared to be much less than expected. The new goal was to achieve less than 4 microradians rms repeatability with minimal or no processing.

Prior to testing for torquing in turnaround, a change in the test setup was accomplished. Using a Hewlett Packard recording computer full forward scans ($T_3 - T_1$) and full reverse scans ($T_1 - T_3$) can be measured in succession. In this way, 100 consecutive scans can be recorded by the computer (50 forward and 50 reverse). Figure 4.4-9 is a data sample taken

Forward Scans (microseconds) (50)	Reverse Scans (microseconds) (50)	Scan-to-Scan Differences (microseconds)	
44008.5	43907.8	100 7	
44007.9	43908.0	100.5	
44006.4	43907.9	100.0	90.8
44006 3	48908.1	98.3	99.1
44006.6	43907.3	99.0	99.7
44007.7	43908.4	98 2	99.0
44004.6	43908.0	99.7	99 6
44004.4	43904.8	99.8	98.9
44006.0	43908.0	97.4	97.8
44007.8	43907.8	98 2	96.2
44008.4	43909.7	98.1	97.1
44008.6	43909.7	98.7	96.0
44008.1	43908.9	99.7	97.3
44008 4	43908.7	99.4	97 6
44006.3	43908.8	99.6	99 5
44005.6	43906.9	99.4	101.1
44006.3	43907.4	98.2	99.7
44007.2	43908.2	98.1	100.8
44006.0	43908.7	98.5	98 5
44006.6	43907.0	99 0	100.8
44004.3	43907.0	99.6	99.1
44005.3	43906.7	97.6	97.4
44006.3	43907 7	97.6	98.3
44006.2	43908.5	97.8	96.5
44006.8	43909.0	97.2	97.0
44008.1	43908.7	98.1	97.5
44007.8	43908.1	100.0	99.0
44007.1	43907.5	100.3	99.9
44006.4	43908.6	98.5	99.2
44004.8	43907.7	98.7	97 4
44003.7	43906.4	98 4	97.5
44004.0	43904.5	99.2	98.8
44005.6	43905.9	98.1	99.8
44006.7	43908.2	97.4	100.1
44009.0	43909.9	96.8	98.3
44007.3	43909.0	100.0	96.8
44005.5	43908.5	98.8	97.2
44006.0	43907.0	98.5	99.4
44006.9	43907.7	98.3	99.9
44005.1	43907.6	99.3	99.9
44006 4	43906.6	98.5	98.5
44006.7	43908.4	98.0	99.8
44005.2	43908.0	98.7	99.8
44007.4	43907.5	97.7	99.9
44007.4	43908.9	98.5	98.8
44008 7	43908.9	98.5	98.0
44008.8	43910.0	98.7	98 4
44008.0	43909.6	99.2	97.8
44007.4	43908.7	99.3	98.7
44007.7	43908.9	98.5	99.0
			98.8
Scan Avg 44006.7	Rescan Avg 43908.0	Avg	98 7
Scan Std Dev 1.3	Rescan Std Dev 1.1	Std Dev	1.1

Note that maximum fluctuation from average is 2.7 microseconds corresponding to 16.5 microradians

Figure 4.4-9. Measurement of 100 consecutive scans.

on 11/7/75 with the SMA running in helium at 9.2 Hz. The first column contains scans 2, 4, 6, 8 ... etc. The second column contains scans 1, 3, 5 ... etc. The last two columns contain the scan to scan differences.

$$\Delta_1 = \text{scan 2 - scan 1}$$

$$\Delta_2 = \text{scan 2 - scan 3}$$

$$\Delta_3 = \text{scan 4 - scan 4}$$

etc.

The standard deviation of the scan differences, 1.1 microseconds, when multiplied by the nominal scan rate of 0.268 rad/0.044 sec = 6.1 rad/sec, provides the scan-to-scan expected repeatability at the end of forward scan or $\theta = \theta_T$. Thus 1.1 microseconds corresponds to 6.7 microradians, rms at one end of the picture:

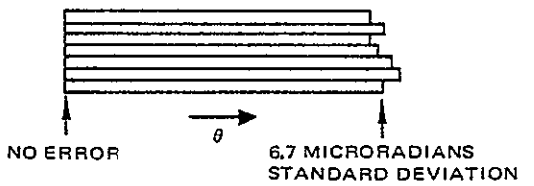

Since one must assume that the error is primarily related to a systematic error in average scan rate, the average value of the expected scan-to-scan error over the entire scan angle would be only half as large or 3.4 microradians. The underlying assumptions are, again, that the scan speeds in both directions nominally stay the same.

When this timing error is related to flight operating conditions where an IFOV dwell time will be approximately 10 microseconds, the 1.1 microsecond error, reached only at the end of scan, equates to 0.11 IFOV.

It is important to note that Figure 4.4-9 shows a fairly strong positive correlation between successive scans. The relationship is of the form

$$\sigma\Delta t = \left\{ \left(\sigma t_f\right)^2 + \left(\sigma t_r\right)^2 - 2\rho_{f,r}\sigma t_f \sigma t_r \right\}^{1/2}$$

where

$\sigma\Delta t$ is standard deviation in the scan time differences

σt_f and σt_r = the standard deviations in the forward and reverse scan times respectively

$\rho_{f,r}$ is the correlation between forward and reverse scans.

If successive scans were totally uncorrelated, $\rho_{f,r} = 0$, then

$$\sigma\Delta t = \left\{\left(\sigma t_f\right)^2 + \left(\sigma t_r\right)^2\right\}^{1/2} = \left\{(1.3)^2 + (1.1)^2\right\}^{1/2} = 1.7$$

but in fact, $\sigma\Delta t$ equals only 1.1 which suggests a reasonable degree of positive correlation

$$\rho_{f,r} = \frac{\left(\sigma t_f\right)^2 + \left(\sigma t_r\right)^2 - (\sigma\Delta t)^2}{2\sigma t_f \sigma t_r} = \frac{(1.3)^2 + (1.1)^2 - (1.1)^2}{2(1.3)(1.1)} = 0.59$$

The fact that there is positive correlation simply means that if the speed is perturbed in one direction during a scan, then the perturbation will propagate but diminish for successive scans.

This data, was quite encouraging and the major remaining questions were how closely could this performance be maintained over long periods and at other scan frequencies. The following data summary shows the net frequency effect (data taken on 11-7-75) (T_{for} and T_{rev} are 50 pt averages)

SMA Freq. (Hz)	$T_{FORW.}$ (μs)	σt_f (μs)	T_{rev} (μs)	σt_r (μs)	$\sigma\Delta t$ (μs)	$\sigma\theta_{end}$ (μrad)
7	61768	3.2	61603	3.2	2.3	10.0
7.5	56802	2.0	56645	2.0	1.6	7.5
8.0	52469	1.4	52328	1.5	1.4	7.1
9.0	45272	1.3	45135	1.2	1.1	6.5
9.2	44015	1.5	43908	1.3	1.1	6.7

From this data it can be concluded that the time deviation will grow as the scan time grows, but the scan rate tends to compensate resulting in a nearly constant standard deviation in the angular error. The one point at 7 Hz tends to refute this but it suspected that the electromagnetic pick-up was a bit noisy at this low rate. As configured during this test, the pick-up flux path was poor and operation below 6.7 Hz was impossible because the initial deflection rate of the spring produced insufficient voltage to cross the threshold. This problem has since been solved by a minor redesign of the bumper assembly. Noise free pulses can now be generated at speeds well below 5 Hz. The first attempt to measure scan period repeatability over long operating times was inconclusive. Figure 4.4-10 shows data taken on 11/18/75 over a two hour period.

Time	T_{for} (μs) 50 pt. avg.	T_{rev} (μs) 50 pt. avg.	$\sigma\tau_f$ (μs)	$\sigma\tau_r$ (μs)	$\sigma\Delta t$ (μs)	Total Active Scan Time per Cycle, $T_{for} + T_{rev}$ (μs)	
11:00 AM	44640.6	44631.0	1.68	1.48	1.48	89271.6	
11.03	44641.3	44634.1	1.39	1.60	1.24	89275.4	
11:06:30	44646.1	44632.2	2.08	1.68	1.35	89278.3	Data taken at 9.00 Hz in helium
11.10	44647.3	44630.3	1.34	1.35	0.98	89277.6	
11.22	44643.0	44627.6	1.89	1.79	1.22	89270.6	
12:10 PM	44645.3	44622.0	1.30	1.30	0.98	89267.3	
12:55	44639.8	44611.8	1.69	1.78	1.46	89251.6	

Figure 4.4-10. Extended measurement of forward and reverse scans.

The data indicates an average scan rate change with time. Over two hours time the forward scan period seemed to drift over a ±3.5 microsecond range. As previously described (see Figure 4.3-9 and neighboring text), the logic does not presently contain a loop to keep the forward scan equal to the reverse scan. However the total active scan time (forward plus reverse) should remain equal to a constant unless the turn-around-time drifts. The data tabulated in Figure 4.4-10 indicates a ±5 microsecond drift in total active scan time.

It is because of this apparent drift that the test of turn-around time was made on 12/16/75 (see text following Figure 4.4-5). And as a result of all such tests, the test to determine if the photo-diode circuits were drifting was made (see Figure 4.4-6 and neighboring text). The conclusion reached is that the test set-up does drift to the extent that the quantitative constancy of the active scan periods can not be determined. Only rough bounds to the possible drifts of the forward and reverse scan periods can be estimated. It is quite possible that if the scans were forced to be equal (by a control loop) that the total drift of any active scan period would be less than a microsecond. It is also possible, but not probable, that the drift of the active scan period could be as large as ±5 microseconds after an hour or so. A new test set-up should be built during the next program phase to resolve this question.

The important parameter of scan-to-scan registration, which can be evaluated from the $\sigma\Delta t$ data in Figures 4.4-9 and 10, appears to be bounded by values of 0.98 and 1.48 microseconds (at 9.0 - 9.06 Hz). Assuming a somewhat conservative figure of 1.4 microsecond as the expected misregistration of full scan lines results in an expected value of 4.1 microradians misregistration for any two IFOV's over all scan angles. This is less than 0.1 IFOV's. An MSS-type Scan Angle Monitor would then permit line-to-line justification through on-board or ground processing. This would further improve registration by a factor of about three.

4.4.9 Cross Scan Measurements

Cross scan motion of the mirror is rotation of the mirror-normal, perpendicular to the scan direction. This motion causes an overlap or underlap of the scan line bundle as it traverses the scanned swath. Cross scan motion can be divided into two categories which are defined as "nested" and "non-nested." Nested motion is that which repeats exactly for all forward scans and repeats in an inverse sense for all reverse scans. The following sketch shows pure nested and non-nested cross axis motion of successive scan line bundles.

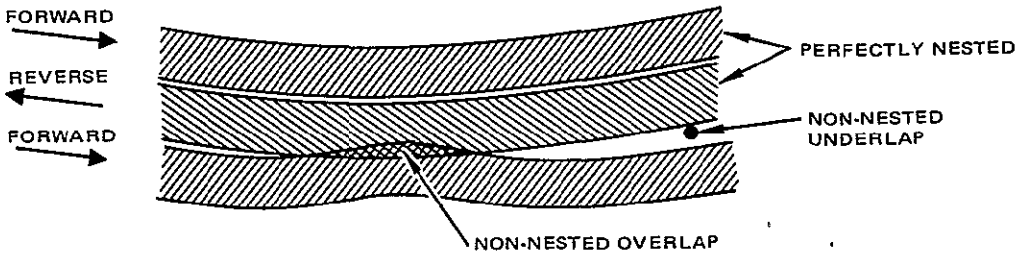

The design goal is to keep the rms value of the non-nested cross scan motion well below 4 μ radians in object space. The nested motion is less critical since its effect is to create a mapping error which can be as large as 20 μ radians. Nested motion, which has been demonstrated to be systematic and constant in nature, can be removed, therefore, by ground processing (if desired).

The nature and source of non-nested cross axis motion, sometimes referred to as cross axis jitter, was briefly introduced in Section 4.3.2 wherein it described how first and second mode motion of the mirror on its flex pivots provide the major source of this undesirable mirror motion.

Two types of cross-scan measurement techniques were described in Section 4.4.1. As previously described, the even bounce technique measures an entire scan period and shows both nested and non-nested motion. The odd bounce technique measures only non-nested motion, but allows measurements of several cycles. An example of both types of measurement is shown in Figure 4.4-11.

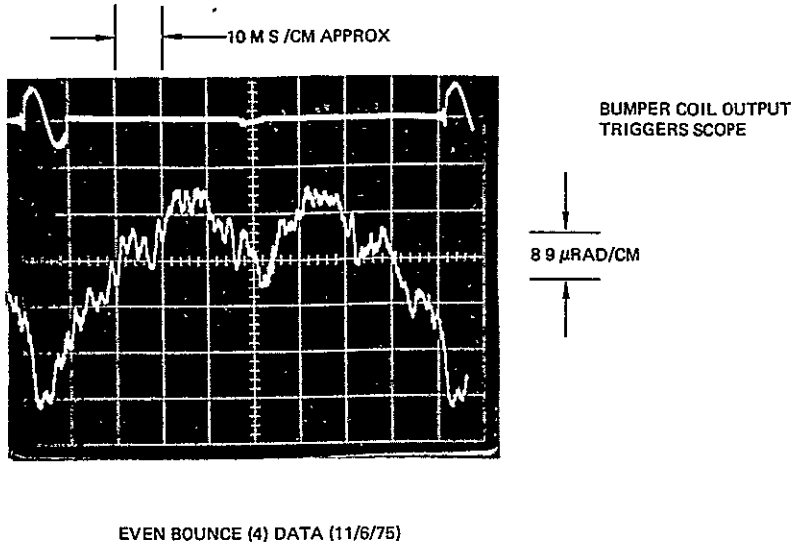

Figure 4.4-11. Examples of even and odd bounce cross-scan data.

The top trace of the even bounce photo shows the output of one of the pick-off bumper coils. This signal is used (with a delay) to trigger the scope. This photo shows all of the cross scan motion, most of which nests perfectly. In this photo the total nested motion is about 40 μ radians or about an IFOV. As previously described, it is possible to rotate one flex pivot with respect to the other and to thus reduce this systematic motion. In addition it is possible to design a flex pivot which has minimal center shift. The cross-scan motion created by the flex pivots is not necessarily monotonic with scan

angle, but is a simple and unique function of scan angle (once the laser noise, mirror dust and detector peculiarities are removed). If the photo trace is folded over such that the scan would lie on top of the inverted rescan then the following sketch illustrates the result:

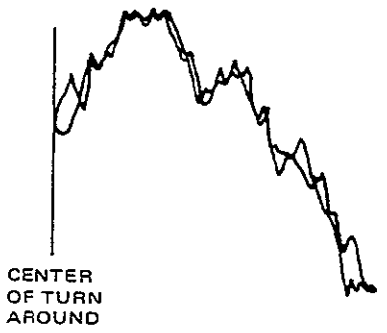

The low frequency part of the strongly nested result is due to flex pivot center shifts. The higher frequency, but nested motion, is primarily due to dirt on the mirror surface and on the surfaces of the porro mirror. The position sensitive diode is also power sensitive and thus such dirt results in apparent, but imaginary, nested cross-scan motion. A careful analysis of such a sketch would indicate some non-nested cross-axis motion. This particular trace indicates a worst case peak forward to reverse scan difference of 4 microradians. Because of the power sensitivity of the diode and the resulting high frequency nested components of the output, the even bounce technique is not a sufficiently accurate way to determine quantitative non-nested motion but is a very useful analytic tool. One can observe where along the scan non-nested motion exists; the power spectrum of cross-axis motion (with appropriate filters); and how random is the motion in time.

The odd-bounce technique, exemplified by the lower photo of Figure 4.4-11, is an analytic tool of another sort and is the preferable technique for obtaining quantitative estimates of non-nested motion or real jitter. Since the diode is temporarily stationary, only one optical path is used independent of scan direction. The principal measurement error sources are then variations in the laser output and variations caused by air turbulence. These variations have been measured with the SMA inoperative and have been shown to contribute less than half a microradian of error. The diode must

be calibrated for each position, but this calibration then holds for all tests at a given detector position. Thus all data taken over a period of time is calibrated and all deviations are truly non-nested cross-axis motion. By carefully examining the first spike in each pair of spikes in the lower photo, a small cyclic fluctuation in the forward scan, cross axis motion can be measured. The same phenomena can be measured for reverse scans (second spike of each pair). This analytic tool allows computation of the randomness of cross-axis motion at a given scan location and indicates the coupling of vibrational frequencies. The true overlap and underlap can easily be measured for each scan (forward-reverse-forward, etc.) by measuring the differences in heights of each pulse pair.

As planned in the Test Procedure, the odd bounce technique was used to measure non-nested cross axis motion at five positions along the complete scan. The SMA was operated in air and a minimum of 63 cross-scan differences were measured for each position in the scan. The SMA was operated at 9.06 Hz. The results were:

Diode Location Along Scan (fraction of full scan)	Mean Fwd-Rvs Cross-Scan Motion (microradians)	RMS Scan-to-Scan Motion (microradians)
0.009	-0.25	1.16
0.275	-4.07	4.08
0.415	-0.34	0.71
0.662	-0.90	1.46
0.968	1.25	1.56

The mean of the above results is the average position of all forward scans less the average position of all reverse scans, while the rms of the above results is the root-mean-square of the difference between successive scans. The following sketch indicates how these results are obtained from a typical photo. Thus the mean indicates a systematic and time invariant non-nested cross scan motion while the rms value indicates the expected amount of misalignment or smearing. The rms value includes random effects and is the better indicator of the critical parameter of smear or over/under lap. From

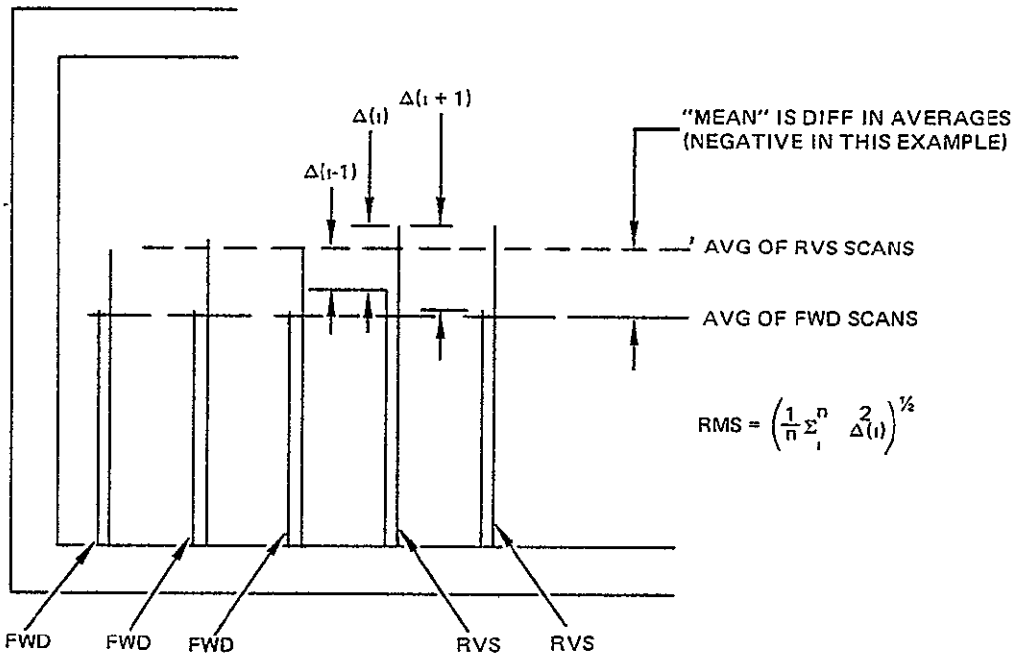

this limited data it can be seen that there is a bit less than a microradian of random cross axis motion. It appears that there may also be a periodic fluctuation in the systematic cross-scan, non-nested motion as a function of scan angle.

For this reason many more data points were taken than required in the formal procedure. The position sensitive diode was moved up and down in quarter inch increments. Figure 4.4-12 is a plot of this extensive data. (The rms value of the differences at each mean position are plotted). From

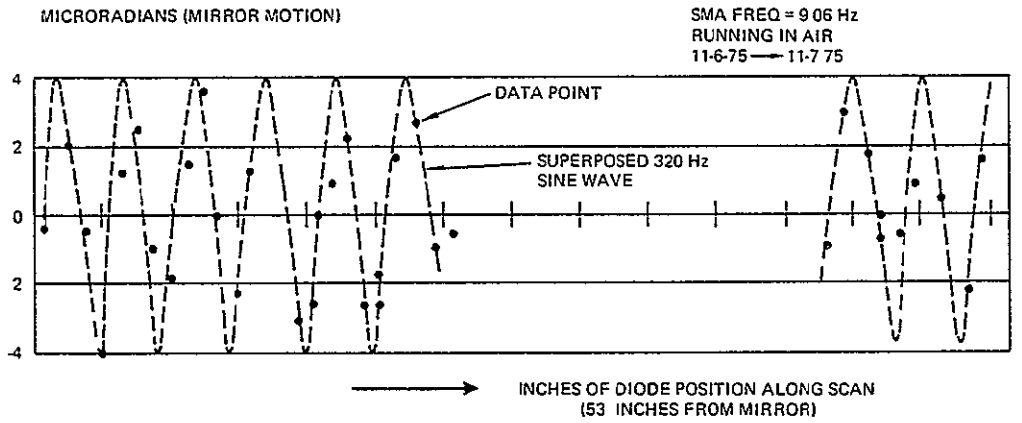

Figure 4.4-12. Non-nested cross-scan motion in air.

this plot it appeared that a sine wave of 4 microradians amplitude could fit to the data points. Since the first mode of the mirror on its flex pivots was measured for this set-up at 320 Hz an attempt was made to superimpose a 320 Hz, 4 μrad sine wave. As seen in Figure 4.4-12 the fit is quite good. This indicates that the major form of non-nested motion is caused by an interaction of the mirror natural frequency on its flex pivot supports with the drive frequency. That is, the phase of mirror motion is almost constant for forward scans and separately constant for reverse scans. The drive frequency then determines whether forward cross-axis motion and reverse cross-axis motion are in or out of phase (or in between).

Other data was taken as a function of small variations in drive frequency, and the general result was that the peaks of scan-to-rescan cross axis motion fluctuated between 1 and 4 microradians. This should be expected if Figure 4.4-12 is a worst case drive frequency for a mirror natural frequency of 320 Hz. One would expect there to be some point where the phase of the cross scan motion of the mirror during forward scans identically equalled the phase during reverse scans. It was found that the maxima and minima followed each other, occurring at each 0.3 Hz increase in drive frequency. The maxima all tended to be near but never exceeded 4.0 microradians. This test was checked between 7 Hz and 13 Hz. There was absolutely no monotonic relationship with drive frequency noted within this range.

Limited testing of this sort was repeated in helium (it being a rather difficult and dangerous process to move, adjust and calibrate each diode in a helium atmosphere). No significant difference was noted. However one interesting phenomena was noted: the phase of the cross axis motion in air (causing a worst case) would not produce a worst case phase in helium. The exact case of Figure 4.4-12 was repeated in helium with no changes to the equipment except the addition of helium. (This data is shown in the log book.) Significantly better results were recorded. Apparently the helium atmosphere slightly changed the natural first mode frequency of the mirror away from 320 Hz and the forward and reverse motions tended to cancel. It can be concluded that the SMA breadboard as-built, whether operating in helium,

air, or vacuum, will have a systematic cross-scan, non-nested motion of the form

$$\theta_x = A \sin \left(n \frac{\theta_s}{\theta_{st}} \right) + \theta_{xn}$$

where

θ_x is the non-nested motion in radians

A is a peak amplitude between 0 and 4 μ radians

θ_s is the scan angle

θ_{st} is the total scan angle (0.268 rad for our case)

n is a function of the first mode natural frequency and the active scan period and was equal to h = 320 x 0.044 = 14 for the case shown in Figure 4.4-12

θ_{xn} is random noise whose rms value is less than one microradian.

The expected value of this jitter which contributes to overlap and underlap is the rms of this function. For a conservative worst case, the rms value would be 2.8 microradians. This value is considered to be the worst rms case for several reasons. It is the worst case ever measured on the final baseline as tested, and several cases were measured. Measurements were taken before the nylon bumpers were worn into their final configuration, during wear-in, and after wear-in. In addition, cross axis measurements were taken at several adjustments of bumper impact time, bumper location, turn-around time, and damper preload setting. Several flex pivots were substituted and the mirror counterweight was also completely removed to unbalance the system. Cross scan non-nested motion never exceeded 4.1 microradians peak or 2.8 microradians rms.

Now because the location of the SMA in the scanner has not been fixed, the above reference to cross-scan motion has always been in mirror coordinates. However the real requirement is in object space. The following

sketch depicts the nominal position of the mirror with respect to the scanner and the nadir:

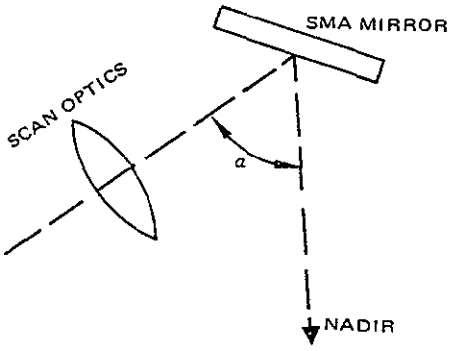

The object space cross-scan motion is thus related to mirror motion by

$$\theta_{\text{object space}} = \theta_{\text{mirror}}\, 2 \cos \frac{\alpha}{2}$$

For the contemplated situations wherein the angle, α, is about 90 degrees, the 2.8 microradians rms of mirror motion corresponds to 4.0 microradians of object space motion. Should an extreme angle of 60 degrees be chosen, the equivalent object space motion would be 4.9 microradians.

Thus far this discussion has described performance testing and provided a conservative estimate of the cross scan motion that can be expected from the breadboard SMA. The remainder of this section will discuss the present limitations that cause cross scan motion with the result that conservative predictions can be made regarding the predicted performance of the flight system.

Present Limitations

It had been speculated that bumper/mirror contact friction might be a significant source of cross-scan energy. This appeared reasonable since frictional forces were expected to have a magnitude of roughly 0.2-0.3 times the normal forces and random in amplitude from impact to impact with a power spectrum that includes the first mode natural frequency of 320 Hz. To test this hypothesis, cross scan motion was measured before and after

the contact surfaces had been lubricated with DuPont Slip Spray. A factor of two improvement in cross-scan motion was observed after lubrication. Friction is therefore definitely a major cross-scan energy source. This conclusion was further established by the fact that a significant increase in cross-scan motion did not occur when the unit was operated on two rather than four bumpers which causes a large increase in net normal forces but little change in frictional forces. Friction can be further reduced by optimal choices in materials and contact configurations.

Another limitation in the present breadboard was discussed in Section 4.3.2 with respect to the flex pivots. The Bendix flex pivot is only half as stiff in shear as a flex pivot of conventional design. With a conventional flex pivot of the same torsional stiffness as the Bendix pivots used in the breadboard, the magnitude of the cross-scan deflection would be reduced by a factor of the square root of two.

In addition, the existing mirror mass is about three pounds heavier than it should be as a result of the design change to leaf spring late in the program. A reduction in mass of this magnitude will significantly increase the natural frequency of the first mode motion of the mirror on its pivots. Such an increase will also cause a decrease in the cross axis deflection.

Finally, the existing bumper support structure is cantilevered from the holding fixture. This, also, was an add-on design, and although an attempt to maximize rigidity was made, the cantilevered supports vibrate at a well defined natural frequency of 115 Hz. This caused the selection of specific turn-around times which would not excite these cantilevers. In the flight design, without the cantilevers, shorter turn-around times could, and probably would, have been selected. As the turn-around time shortens, normal forces increase but more importantly, the vibration spectrum caused by friction shifts upward in frequency away from the first mode mirror frequency. Tuning of the first-mode/drive frequency relationship then becomes more feasible.

Growth Potential for the Flight System

The nature of the present breadboard test program is such that the results obtained should be different from what would be predicted for a flight model.

The scanner support structure when designed will be maximally stiff along the axis of the bumper forces. Conversely, the granite slab and the 280-pound magnesium support fixtures, despite their large mass and intrinsic stiffness, could not be arranged so that these properties would counteract the bumper loads in an optimal way. In the flight system, the bumper assemblies will be directly mounted to the scanner support structure.

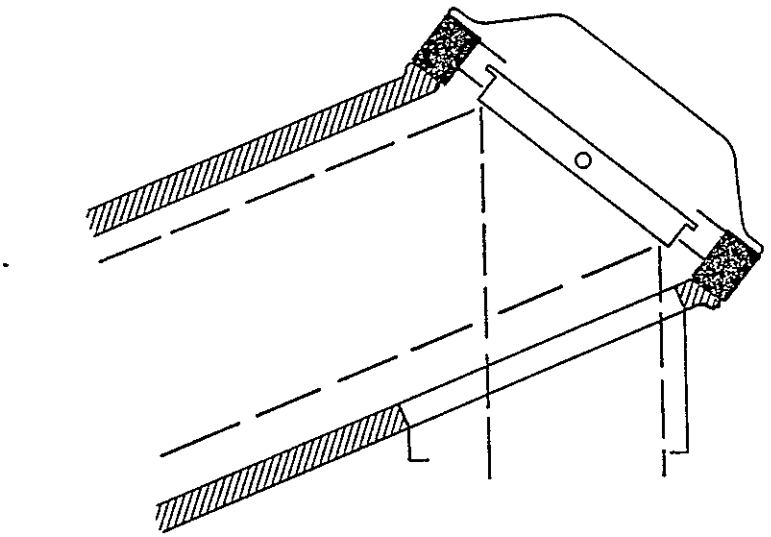

Since the bumper assemblies are directly mounted and not cantilevered, the natural frequency of the mount should be at least as high as on the present breadboard. In essence, the breadboard with its add-on design for conversion to the new bumpers is not particularly rigid.

The potential for reducing the effect of contact friction has not been quantified. The most promising concept appears to involve a slight change in contact geometry. The present bumper geometry was chosen to minimize the total sliding travel between the mirror and bumper contact points. This choice causes the directions of motion of the bumper and mirror contact points to be non-colinear when the maximum normal force occurs (at maximum spring

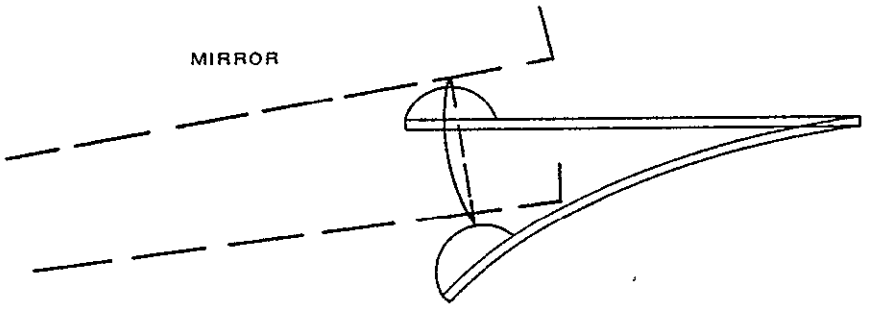

deflection). Since testing it has become apparent that yield or wear in of the nylon bumper pad occurs almost solely at the point of maximum deflection. Therefore it would appear that a significant decrease in friction would occur if the relative geometry were rotated such that less or zero sliding forces exist at maximum deflection. It is conservatively felt that improved geometry will reduce the frictional energy input to cross-scan motion by a factor of two.

Reducing the mirror mass by three pounds is a natural expected improvement. It is also true that use of conventional flex pivots is a natural improvement. The mounting of conventional pivots is easier and there is no reason to expect any change in fatigue life. The same fabrication processes would be utilized.

Optimal tuning of the first-mode mirror frequency to the drive frequency will involve the selection of flex pivots for shear constant, fine tuning of the mirror mass and elimination of atmospheric loads. The potential for cross axis motion reduction has been shown to be large, but large improvements are not needed at the expense of criticality in the selection and tuning process.

In summary, test data substantiates a conservative estimate of 4.0 microradians rms cross-scan non-nested motion in object space for the flight system. Slight changes in design and material selection can be conservatively said to offer substantial improvements to these measured results. It is felt that 1.0 microradians rms is achievable with a 60-degree mirror.

4.4.10 System Gains and Gain Margins

As part of the program a determination of the system gains, time delays and gain margins was accomplished. Since this SMA is a time domain and not a frequency domain servo, and since certain factors within the gains are dependent upon mechanical effects which are difficult to quantify, a pure analytic determination of gains was not attempted. Instead, actual test data were used to determine the settings of gain parameters and their effects upon performance.

Unlike the MSS SMA, stability is insensitive to gain settings. The stability gain margins are huge for the torque-while-turn-around logic. The most critical measure of performance is along-scan repeatability. And thus, the standard deviation in the active scan half cycle (forward or reverse scans) was selected as the measure of performance. The control equation (see Section 4.3.1 and 4.3.3),

$$\tau = K + G_{\dot{\theta}} (\Delta T) + G_{\dot{\phi}} (\phi \text{ error}) \quad ,$$

describes the terms that were to be determined by test

K = the nominal torquer drive voltage on-time with no error in the time between the last two bumper impacts and no phase error

G_{θ} = the increase in torquer on time for positive error (increase) in the time between the last two bumper impacts. This is referred to as the damping gain.

$G_{\dot{\phi}}$ = the increase in torquer on time (m.s.) for a degree of steady phase error between the mirror clock and the reference clock. This is the phase loop gain and is positive if the SMA tends to lag the reference clock.

Prior to starting the gain parameter tests a new electronics box was fabricated. The main reason for building the new electronics box was that the older breadboard was difficult to adjust and difficult to connect to the SMA and power supplies. The new electronics was packaged in a chassis box with simple connectors. Thus the SMA and power supplies were easy to connect and such connection could be made reliably without undesirable

ground loops. In addition multi-turn dial potentiometers were installed in place of the trimpots which had been used to adjust the gain and levels of the constant, K, and the two control loops.

The first step in gain determination was the establishing of the nominal τ or constant, K, as a function of operating drive frequency in helium. Figure 4.4-13 is used to reference the required terminology. Each time a

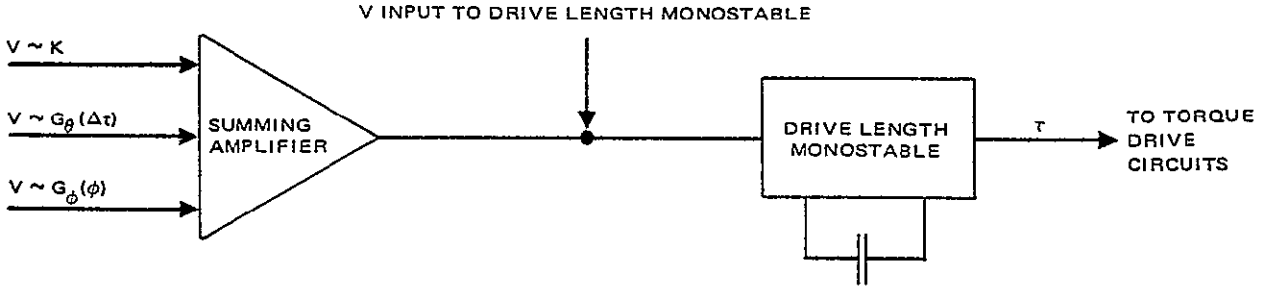

Figure 4.4-13. Terminology for gain determination.

gain potentiometer setting is changed, the d.c. level of the loop at the input to the summing amplifier changes a small amount. Thus in normal operations (with no phase error), these levels must be zeroed in order that the input proportional to K contains the entire d.c. input. With this in mind, it is possible to obtain the relationship between the K input pot setting, the input to the summing amplifier; the torque drive time, τ; and the number K (which is nominally equal to the torque drive time); and the drive frequency. The following table lists the data taken in open loop operations.

K Dial Pot Setting	Drive Monostable Input (Volts)	τ, K (m s)	Scan Period (m.s)	Scan Frequency (Hz)	
4.56	5 111	3.05	97.1	10 30	Open Loop Operation Monostable Capacitor at 0 0202 μf.
5 00	5.190	2 95	116 4	8 59	
5 50	5 285	2.88	121.95	8.200	
5 80	5.344	2 82	124 11	8 057	
6.00	5.382	2.80	126.5	7 905	
6.30	5 444	2.74	141.2	7.082	
4 70	5 138	3 00	97.9	10.215	
5.00	5 191	2.96	99.8	10 020	
5.50	5.287	—	121.95	8.200	
4 30	5.064	3.10	96.3	10 381	
4.00	5.012	3 15	95.88	10 430	
3.50	4.927	3.25	80.50	12.422	
5 32	5.250	2.91	110.7	9 033	

Each scan period measurement consists of an average of 50 data points. The scan frequency is then obtained as the period reciprocal. The data is plotted in Figure 4.4-14. It can be seen that the electronic behavior was quite stable with time and changing pot settings, however the resulting mirror speed was not.

The next step is the determination of the phase gain, G_ϕ. In closed loop operation, the equation to be used is

$$\tau = K + G_\phi (\phi \text{ error})$$

Where the damping term will be ignored because it contributes nothing when operation is steady and it is the steady state gain, G_ϕ, that will be determined. With the clock at 9.0 Hz and with the phase pot set at zero (this pot is adjustable from zero to about 9.5 and produces some gain when set at zero because

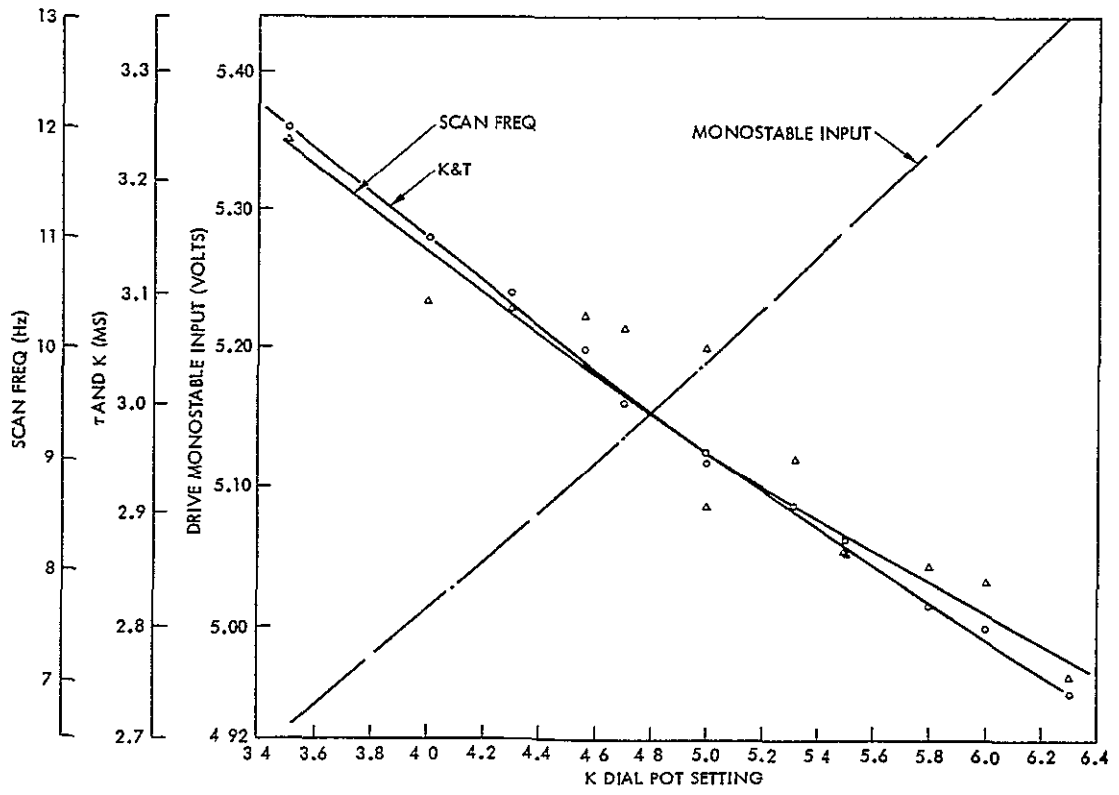

Figure 4.4-14. Open loop measurements.

of a shunting resistor), the K dial pot is adjusted to produce zero phase error. The pot is read and the drive time measured. At this point

$$G_\phi \text{ dial pot} = 0$$

$$K \text{ dial pot} = 5.52$$

$$\tau = K + G_{\phi_o}(0) = K = 2.85 \text{ m.s.}$$

The clock is now adjusted upwards until τ increases by 0.3 m.s., the phase error is no longer zero and read as 14 degrees by comparing the reference clock and the mirror pulse train clock on an oscilloscope. The K dial pot is now adjusted to reduce the phase error to zero and then the clock is returned to produce 9.0 Hz. The phase error is measured as a check and it was, in fact 14 degrees. The gain can now be computed

$$G_{\phi_o} = \frac{\Delta\tau}{\Delta \text{ phase}} = \frac{0.3}{14^o} = 0.021 \text{ m.s/deg}$$

This is the phase gain at G_ϕ dial pot = 0. A second check was made for a G_ϕ dial pot setting of 6. For this case

$$G_{\phi_6} = \frac{\Delta\tau}{\Delta \text{ phase}} = \frac{0.3}{8.65^o} = 0.035 \text{ m.s/deg}$$

Neither of these measurements are more accurate than about 5 percent.

As a second technique, the phase loop was opened (so that it could not effect the monostable) and the phase loop output, referenced to the monostable input, was read when a specific phase error was held by manually controlling the frequency with the K dial pot. This allowed measuring the phase loop input to the monostable per degree phase error. This was done as a function of G_ϕ dial setting thus producing G_ϕ in volts/deg for each dial

setting. From Figure 4.4-14 the relationship between volts at the monostable input to change in τ is seen to be

$$\frac{\Delta\tau}{\Delta V \text{ input}} = 1.1 \text{ m.s/volt}$$

Thus the above G_ϕ in volts per degree can be converted to G_ϕ in milliseconds per degree (in the neighborhood of 9 Hz operation). This is plotted below in Figure 4.4-15. Also shown on the plot are the two previously calculated check points performed by a completely closed loop test. The check is sufficiently accurate for the purpose of determining phase gain margins.

Finally the $G_{\dot\theta}$ gain was determined as a function of its dial pot settings. Again by holding the speed of the SMA constant, in open loop operation, the output of the damping loop, referenced to the monostable input can be measured as a function of change in the time between bumper impacts. Using the

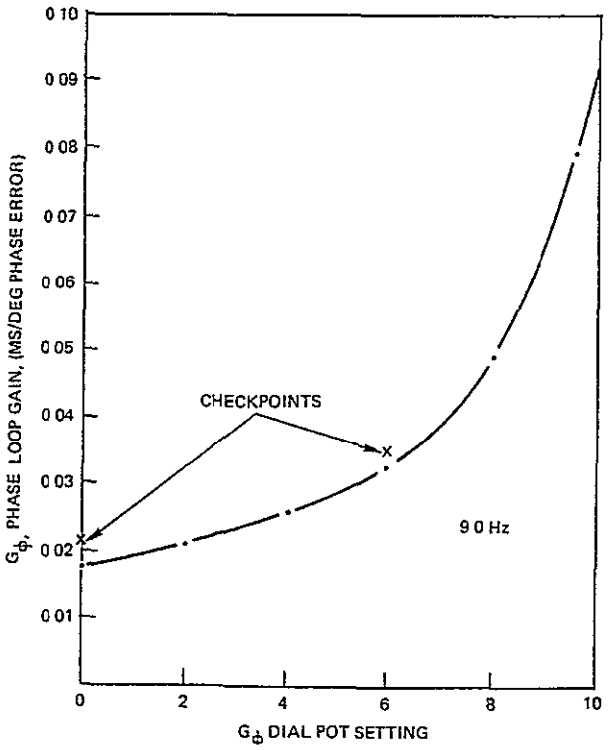

Figure 4.4-15. Phase gain in neighborhood of 9 Hz for various gain pot settings.

1.1 ms/volt factor previously discussed, the $G_{\dot{\theta}}$ damping gain is plotted in Figure 4.4-16. Now the entire equation for drive time can be established, given the desired operating speed and the optimum (as yet to be determined) gain pot settings. For instance, for 9.0 Hz with the phase pot at 7 and the velocity pot at 7

$$\tau = 2.95 \text{ m.s} + 0.10 \text{ s/s } (\Delta t) + 0.03 \text{ m.s/deg } (\phi \text{ error})$$

where Δt is in milliseconds and ϕ error is in degrees. Similarly, for 7.09 Hz with the same gain settings,

$$\tau = 2.74 \text{ m.s} + 0.10 \text{ s/s } (\Delta t) + 0.03 \text{ m.s/deg } (\phi \text{ error})$$

The next investigation was to determine the optimum gain settings and how sensitive to gain settings is the repeatability of scans. The 9.0 Hz

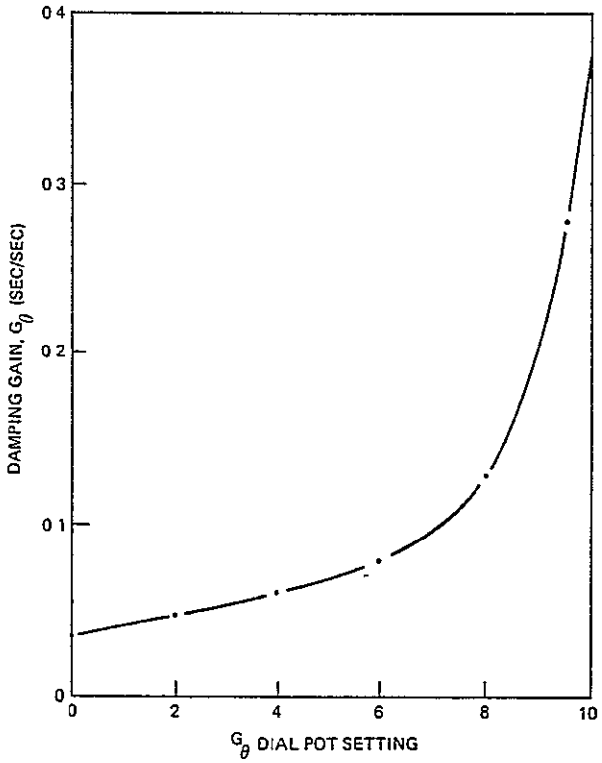

Figure 4.4-16. Damping gain in the neighborhood of 9 Hz for various gain pot settings.

operation was used and the standard deviation in the forward scan length was computed from a continuous string of 50 scans or more. At least three runs were made for each data point and the averages plotted. Figure 4.4-17 shows

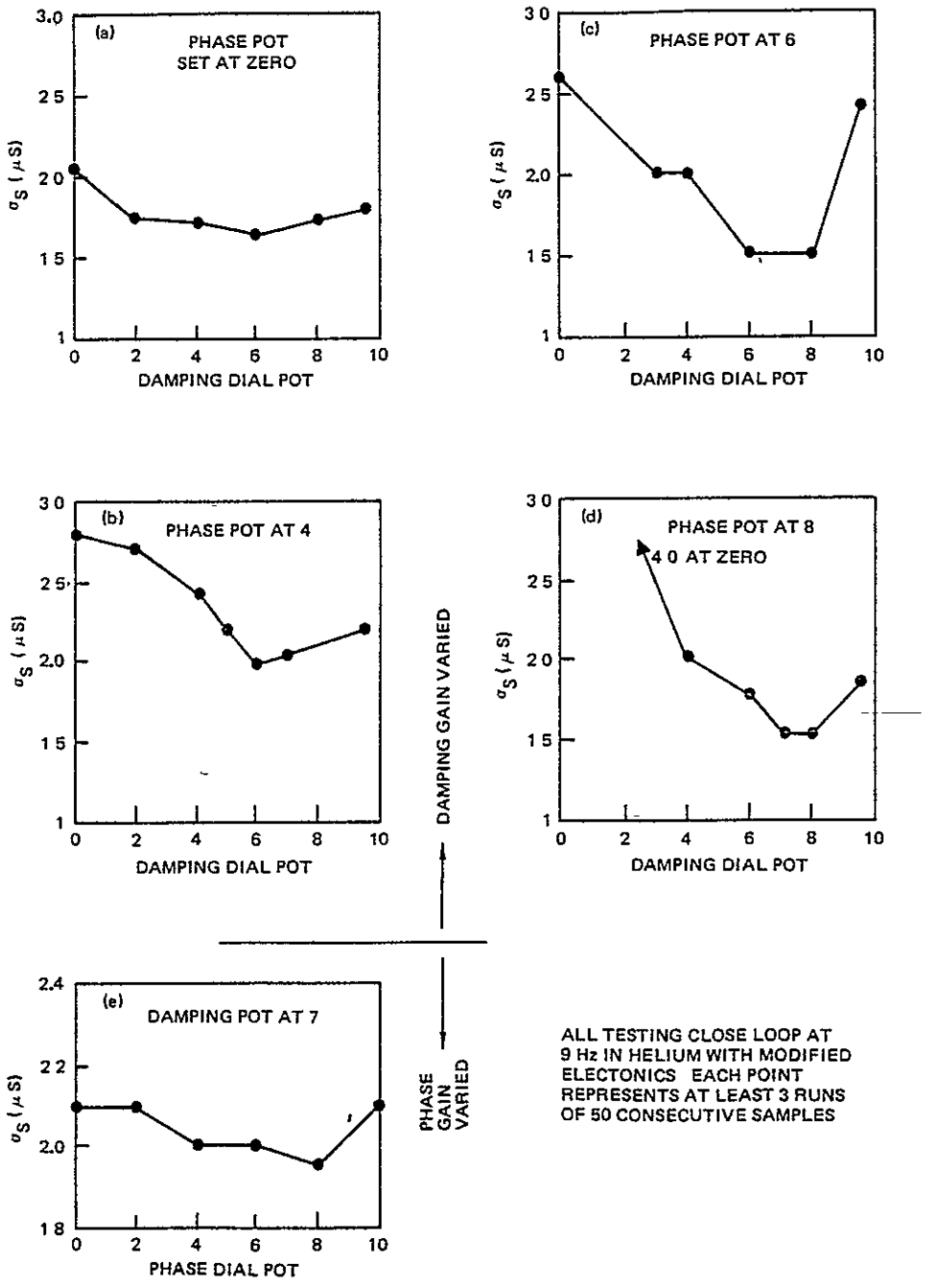

Figure 4.4-17. Scan repeatability data as a function of phase and damping loop gains.

the effect of changing both gain settings, one at a time. Sketches (a) through (d) indicate that a minimum error in repeatability might be achieved with a phase pot set at about 5 on the dial while the damping pot was set at about 7. Sketch (e) holds the damping pot fixed to indicate the effect of changes in the phase gain pot. It would appear from sketch (b) and (c) that if the damping pot were set at 7, then a plus or minus change of 1 in the phase pot will make no noticeable change in along scan repeatability. Sketch (e) indicates that changes from the nominal phase setting of 5 could be at least ±1 without significance. Figure 4.4-15 shows that at a phase pot setting of 5 a ±1 variation would require a 20 percent change in electronic drift, while Figure 4.4-16 shows that a ±1 variation from the optimum would require a 22 percent change in the damping loop gain. Obviously the electronic components should not be expected to drift by this amount.

From the above data it can be concluded that gain settings are not critical and can be easily selected to ensure significant gain "margin." Electronic drift should not change the performance significantly. To this point, the discussion has involved steady state conditions. That is, no noise effects have been analyzed and all gains have been assumed, and tested, as constants. The damping gain is a constant, however the phase gain is not. As seen in Figure 4.3-35, the phase detector (NE 565) contains a filter consisting of a 3.6K ohm resistor and a 4.7 μf capacitor (time constant equals 17 m.s.). This filter smooths the phase measurements made at each bumper contact such that

$$G_\phi(S) = \frac{G_\phi}{1 + 0.017\,S} = \frac{G_\phi}{1 + \tau_\phi\,S}$$

causing the phase signal to be insensitive to measurement noise. The choice of the filter time constant is made by assuring that it is long enough to remove noise, while short enough to control drifts that could occur in the electronics. In the modified electronics this controlling capacitor was replaced with a bank of 5 switched capacitors. Figure 4.4-18 shows the effect of varying τ_ϕ on the forward scan standard deviation. The conclusion is that the phase filter time

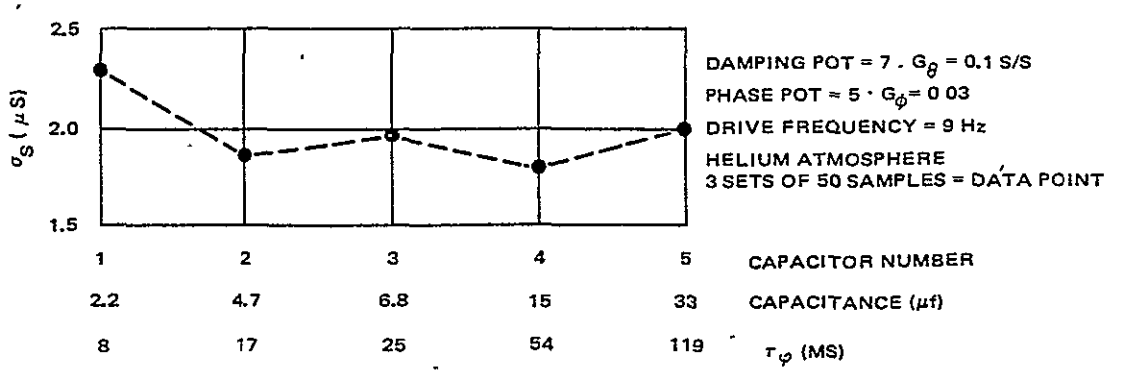

Figure 4.4-18. Effect upon scan deviation of phase loop filters.

is not a critical parameter from a noise standpoint. It was set at 17 ms for the data presented in Figure 4.4-17.

A special test was also performed to determine the transient response to a step K input. The electronics was modified such that a resistor which controlled the nominal input, K, to the summing amplifier was shunted with a resistor and switch.

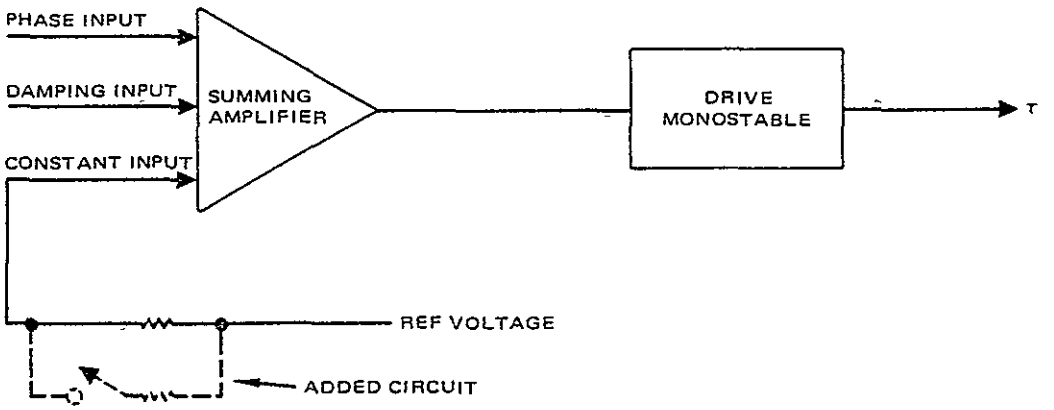

With the SMA running with the switch open, the active forward scans were timed and recorded. With the recorder running, the switch was closed to produce an instant step change in K. The resulting record shows the transient behavior of the SMA. Figure 4.4-19 shows the effect of the phase gain. It is the phase loop which makes up for any change in the nominal drive time and which is responsible for returning the SMA frequency to the drive command of the reference clock. As can be seen in the figure, with the phase

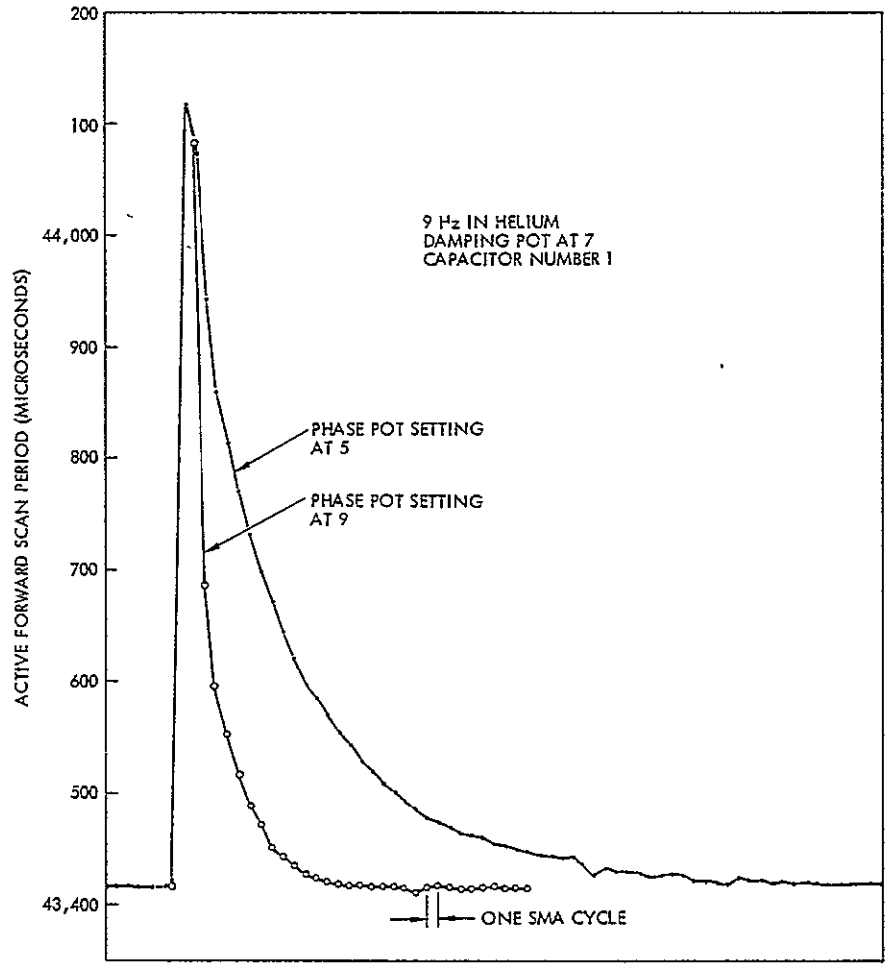

Figure 4.4-19. Transient behavior versus phase gain.

dial pot set at 5, about 50-60 cycles are required to bring the forward scan period back to its original value. With a phase dial pot setting of 9 (a gain increase of about 2.4), the scan period is corrected in about 17 cycles. The step changes in K were abnormal and only gradual drifts are expected in actual operation.

Figure 4.4-20 shows the transient behavior as a function of damping gain. The damping term can be thought of as a lead correction. Well before the phase error has had a chance to build up, the damping (or velocity) loop senses the effect of a step change in K. Thus the figure shows that as the damping gain is increased the peak excursion is reduced. A comparison between Figures 4.4-19 and 4.4-20 shows that the damping loop is far more

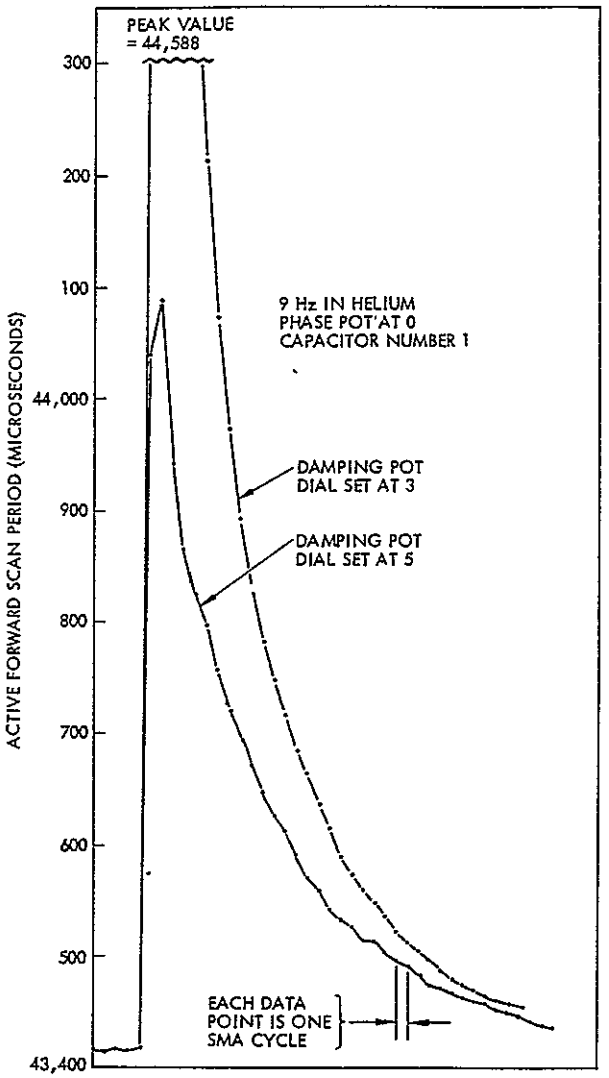

Figure 4.4-20. Transient behavior versus damping gain.

powerful than the phase loop early in the disturbances. However, after several cycles, the total phase error is significant and the phase loop is the predominant controller. As seen in Figure 4.4-20, a large change in damping gain (a factor of about 1.4) does not significantly affect the total time required to return the forward scan period to its original value.

Similar plots were made with variations in the phase loop time constant, τ_ϕ , but, as expected, no significant effect was noted.

4.4.11 Mechanical Noise and Loop Control of Noise

It is important to know where in the SMA noise originates and how well the logic and electronics suppress the random growth of noise. The following sketch is used to aid in the discussion of this question. The most pertinent

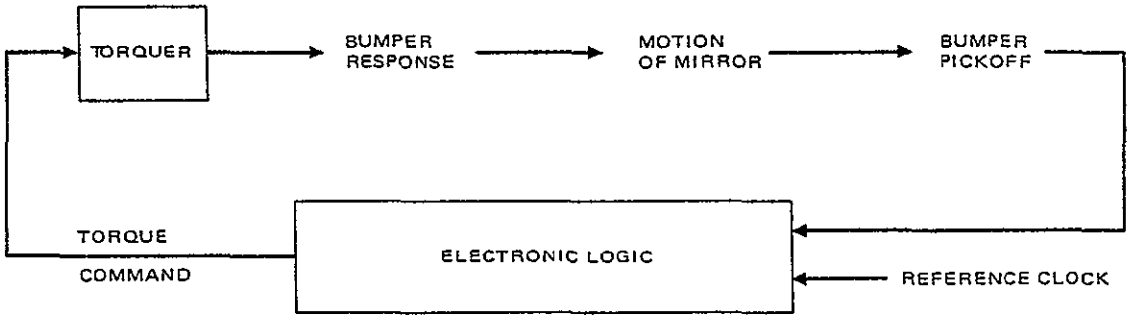

effect of noise is random changes in the active scan times. From the sketch it can be seen that some noise inputs can theoretically be filtered so as not to cause mirror motion perturbations.

Starting with the control clock, it can be seen that high frequency clock noise can be filtered by the phase comparator so as not to affect the torque command. Clock drifts, on the other hand, will obviously affect mirror motion and thus cannot be allowed. Bumper pick-off noise can be filtered out of the phase loop (if it is not strongly auto correlated) but cannot (or at least is not in the present logic) be filtered out of the damping loop. For this reason measurements were taken of the time between a split diode crossing and the bumper coil output. In this test the split diode was regularly located quite close to the bumper contact point. The split diode is known to possess measurement noise of less than a microsecond rms. The standard deviation of the resulting time measurement was measured several times and all values were between 0.1 and 0.2 microseconds. The conclusion reached was that the uncorrelated noise produced by the bumper sensor coil and threshold circuitry is small indeed and would thus not contribute to perturbations of the mirror motion.

There is no reason to believe that the torquer is a source of noise. This leaves three noise sources. mechanical bumper noise, noise created by

the air or helium atmosphere used to test the SMA, and noise created within the electronics.

As yet no conclusive technique for separately measuring bumper mechanical noise and atmospheric effects has been devised. Tests have determined that operation in helium creates smaller scan period fluctuation than operation in air. And it has been presupposed that operation in vacuum will show further improvements, but the degree of improvement has not been determined.

In order to measure the combined noise created by the bumper mechanics and helium atmosphere, a test was devised. Figure 4.4-21 is used to describe this test and shows the data taken. The SMA was operated in helium at 9.06 Hz. A split diode was located near each bumper such that full forward and reverse scan periods could be measured. Torque was not applied at one turn-around. That is, a switch on the electronics was installed that would cause the logic to torque at the "top" bumper but not at the "bottom" as shown in the figure. The split photo diodes were arranged to record T_{in} and T_{out} in succession such that for each passive turn-around, the previous scan (T_{in}) and the succeeding scan (T_{out}) were measured. Fifty such correlated data points were recorded and plotted in the figure.

If no perturbations occured during a turn-around, and if the atmosphere (helium) did not affect the scans, then

$$T_{out} = \frac{T_{in}}{\epsilon} \text{ identically}$$

where ϵ is the nominal coefficient of restitution. The data was processed for average values of T_{in} and T_{out} and a linear fit to the data was passed through this point (this checked with a slope of $\epsilon = T_{in}/T_{out}$). Thus with no mechanical or atmospheric perturbations, the data points should all fall on this ideal line. The error in T_{out} by which a data point missed the line was measured and defined as Δi for the i^{th} data point. Then the average and standard deviation of the Δs were taken:

$$\overline{\Delta} = -0.03 \text{ microseconds}$$
$$\sigma\Delta = 0.74 \text{ microseconds}$$

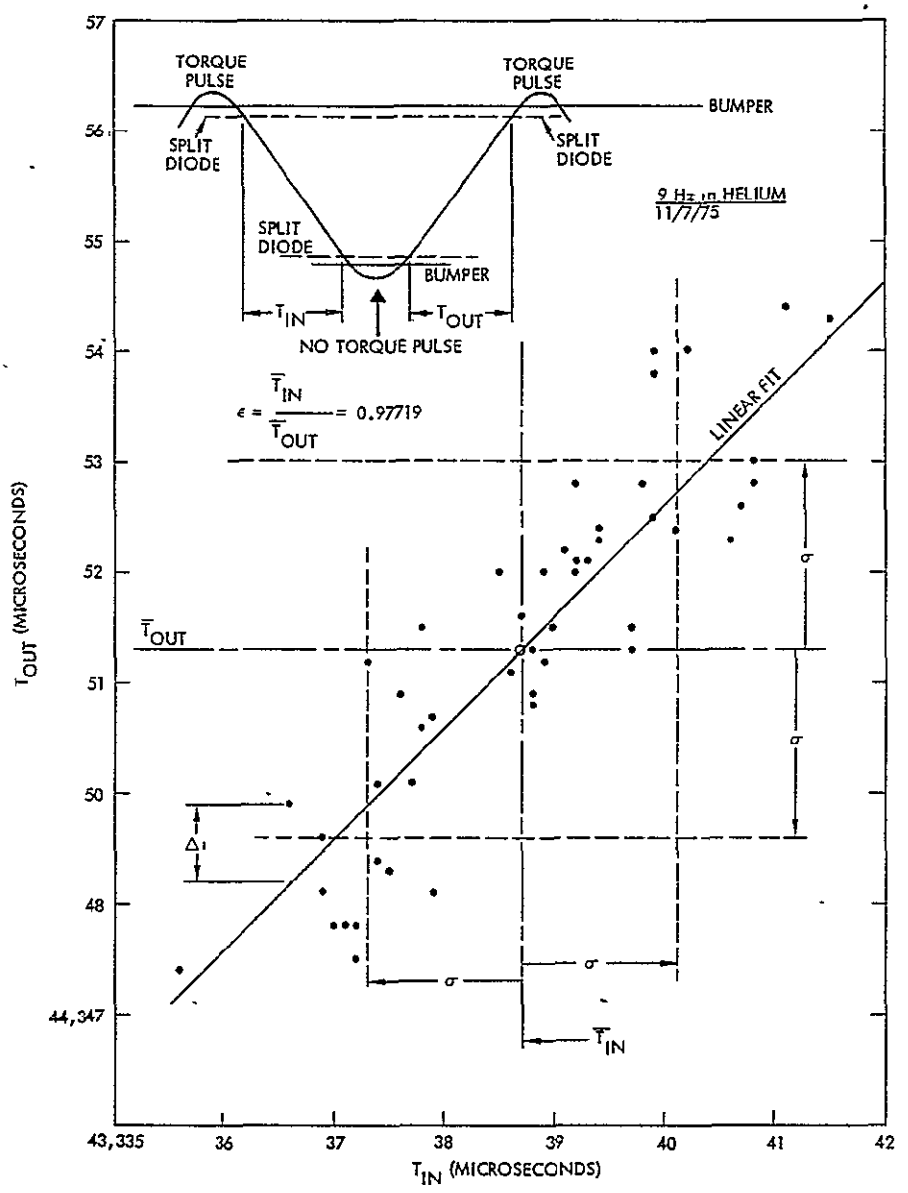

Figure 4.4-21. Data used to obtain mechanical noise.

In addition the standard deviations of T_{in} and T_{out} were obtained

$$\sigma T_{in} = 1.4 \text{ microseconds}$$

$$\sigma T_{out} = 1.7 \text{ microseconds}.$$

It would be expected that σT_{out} would be larger than σT_{in} since no correction is made during the passive turn-around and the noise created at that turn-around would add to the noise of the previous scan.

The conclusion is that the bumper and atmosphere produce noise equivalent to 0.74 microsecond rms measured at the end of a succeeding scan. There is no way that the control system can reduce the total noise in the system tested below this value since it can only operate upon the noise after the succeeding scan. Some of this noise should be due to helium and some due to nonoptimum bumper design. With both bumpers operating the total system noise should be slightly better than $\sigma T_{in} \approx 1.1$ microseconds. (See Figure 4.4-9 showing data taken immediately prior to the data of Figure 4.4-20.)

The last part of the question involves how much noise is created within the electronics and how well does the electronics handle the growth of the total noise input. The electronics cannot reduce the total noise below the real values of mechanical noise. In fact, noise is known to propagate through several bounces. Examination of a time plot of a typical series of scan period measurements provides some insight as to the possible magnitude of timing errors created by electronic disturbances. Figure 4.4-22 is such a plot. Successive forward and reverse scan period errors from the respective mean periods are plotted from left to right. The first point plotted is a forward scan with zero error and the second point is for the following reverse scan, etc. It can be seen that the first 44 scan periods ($\approx$2.5 seconds) were reasonably unperturbed with an rms value of less than 0.5 microsecond. Suddenly, a disturbance occurred which initially produced peak errors of more than 2 microseconds, reducing to half this value after about 1 second This data, taken on the final day of testing, clearly suggests the introduction of a transient perturbation in the electronics which probably involved the drive or laser power or both.

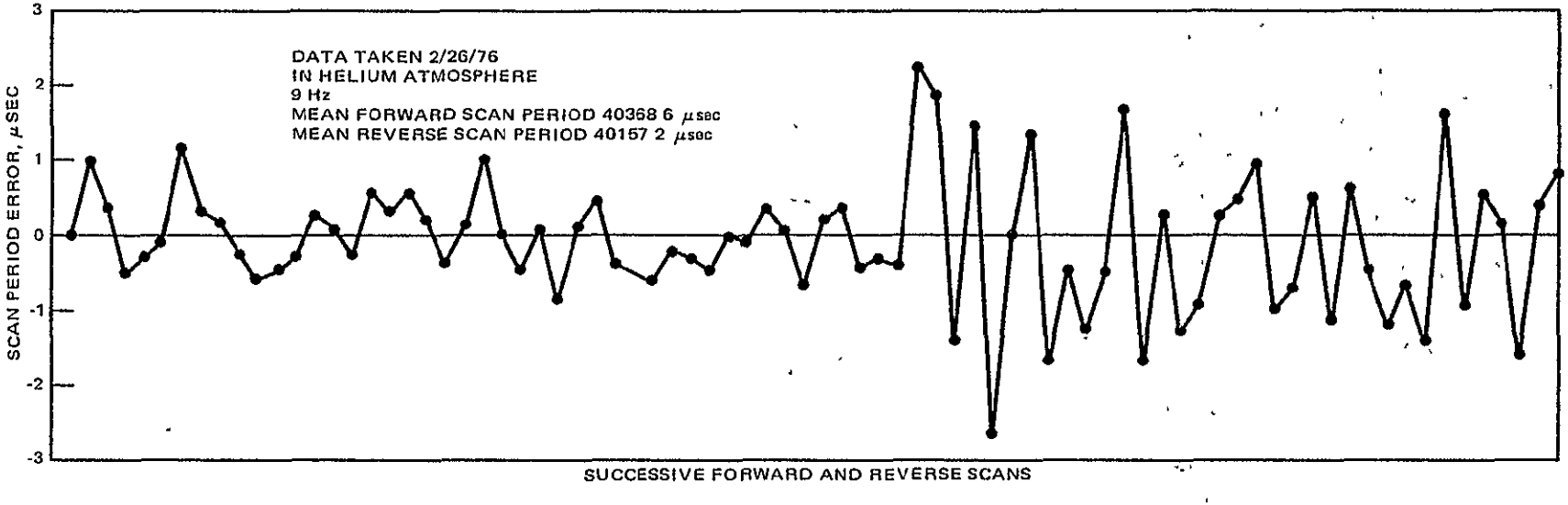

Figure 4.4-22. Instantaneous scan period errors versus time (zero mean)

4.5 MIRROR FABRICATION AND TESTING

The basic design of the beryllium scan mirror has been previously described in Section 4.3. This section discusses the blank fabrication, polishing, and mirror testing. This then leads to the conclusion that the new, lightweight construction is suitable for Thematic Mapper over the full range of the desired environmental conditions.

4.5.1 Blank Fabrication

At the beginning of the program it was anticipated that the blank fabrication and mirror polishing would be a critical path in the program schedule. In order to uncover unforeseen problems early, two additional mirrors were fabricated. The first was a small, 15 x 23 cm sample of the brazed beryllium structure. This sample would allow the mirror manufacturer (Grant and Kamper of San Diego) an opportunity to try out the brazing techniques specified on the mirror blank drawing. In addition this sample would allow the polishing vendor (Applied Optics Center of Burlington, Mass.) the same opportunity. Once polished, flatness tests on this sample were intended to be performed prior to final assembly and brazing of the flight-type mirror blank. The other additional "mirror" fabricated was the dummy mirror which was a beryllium cruciform which could be used for initial SMA tests prior to delivery of the flight-type mirror.

During fabrication of the sample mirror several detail fabrication problems were encountered and solved. The sample blank delivery date was delayed but it was hoped that the information gathered would aid in fabricating the large mirror. The sample mirror was deliberately built with brazed eggcrate joints (no stop-flow holes) on one half and unbrazed joints on the other half. The object was to see if a "posting" effect would print through the mirror surface under temperature cycles. Further processing delays in the sample occured at the polishing vendor. Specifically, the time to remove material was greater than the vendor anticipated. One result of these delays was that the decision to not braze the joints in the eggcrates had to be made prior to thermal flatness testing of the sample.

Interferograms of the sample mirror at various temperatures are shown in Figure 4.5-1a through e. The test set-up is shown in Figure 4.5-2.

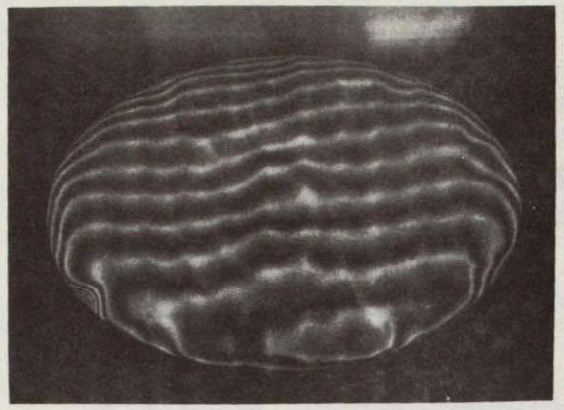

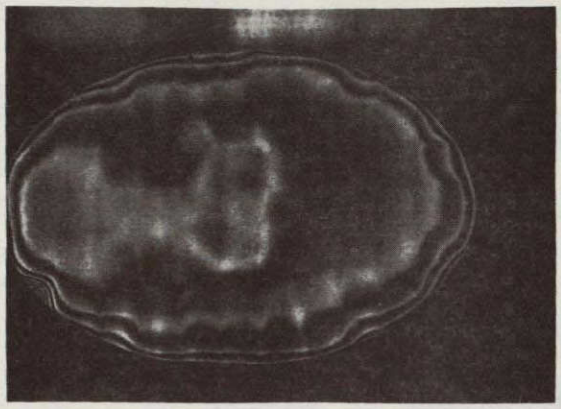

4°C

COMMENTS:

1. CORE PATTERN "SEE THRU" IS APPARENT
2. APPROX A 2 FRINGE EDGE ROLL-DOWN
3. DISREGARDING EDGE ROLL DOWN, THE FLATNESS OF EITHER SIDE IS ABOUT 1 FRINGE

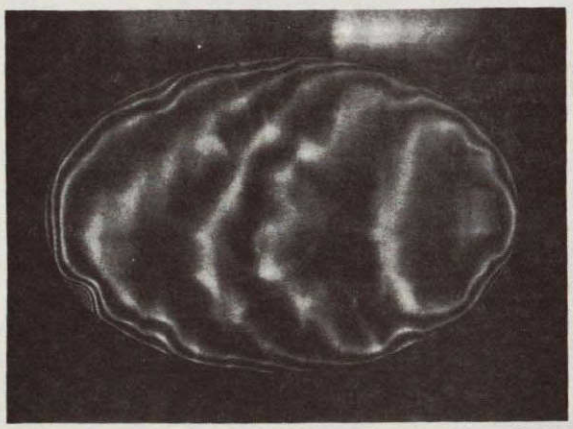

Figure 4.5-1a. Sample mirror interferograms.

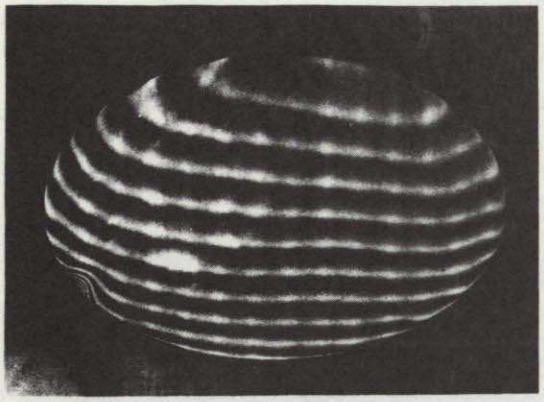

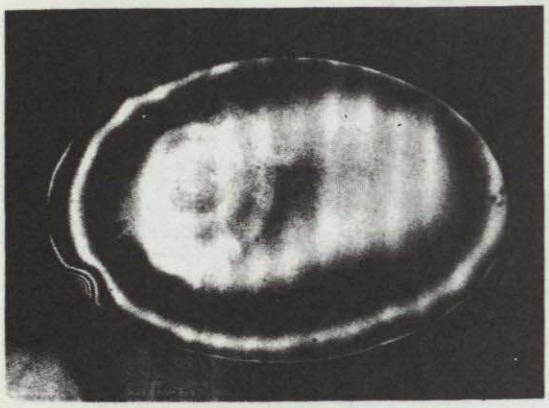

13°C

COMMENTS:

1. EDGE ROLL DOWN IS ~0.5 FRINGE
2. THE ACTIVE MIRROR IS FLAT ALONG MAJOR AXIS

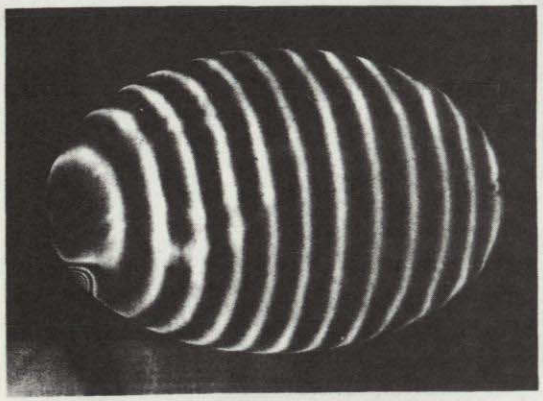

Figure 4.5-1b. Sample mirror interferograms.

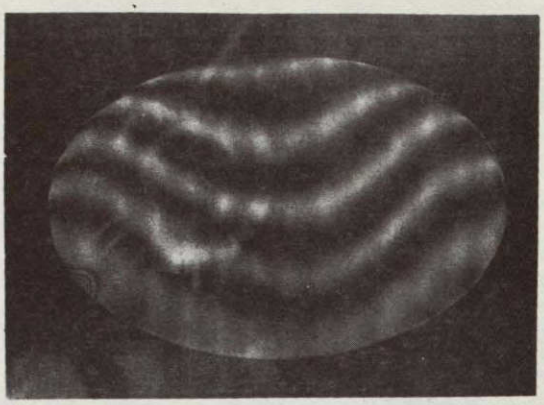

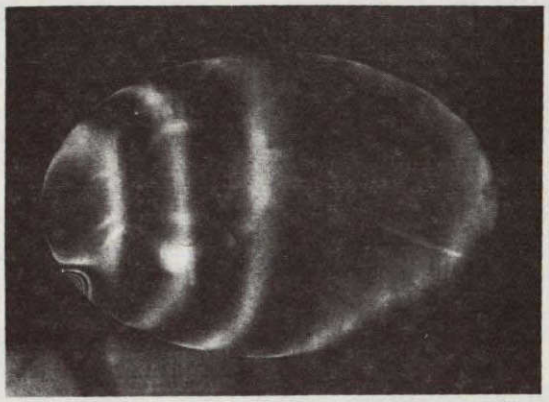

20°C

1. PHOTOS NEAREST THE POLISHING TEMPERATURE
2. THE MIRROR SURFACE IS CONCAVE ALONG THE MAJOR AXIS (CREASE DOWN MINOR AXIS AND BENT UP ON EITHER SIDE) BY ABOUT 1.5 FRINGES
3. LITTLE OR NO PRINT THRU SEEN

Figure 4.5-1c. Sample mirror interferograms.

24°C
ROOM
TEMPERATURE

1. BENDING ABOUT MIRROR MINOR AXIS IS MORE APPARENT AT THIS ELEVATED TEMPERATURE
2. EACH HALF OF MIRROR IS FLAT TO 0.5 FRINGE
3. EGGCRATE STARTING TO PRINT THRU

Figure 4.5-1d. Sample mirror interferograms.

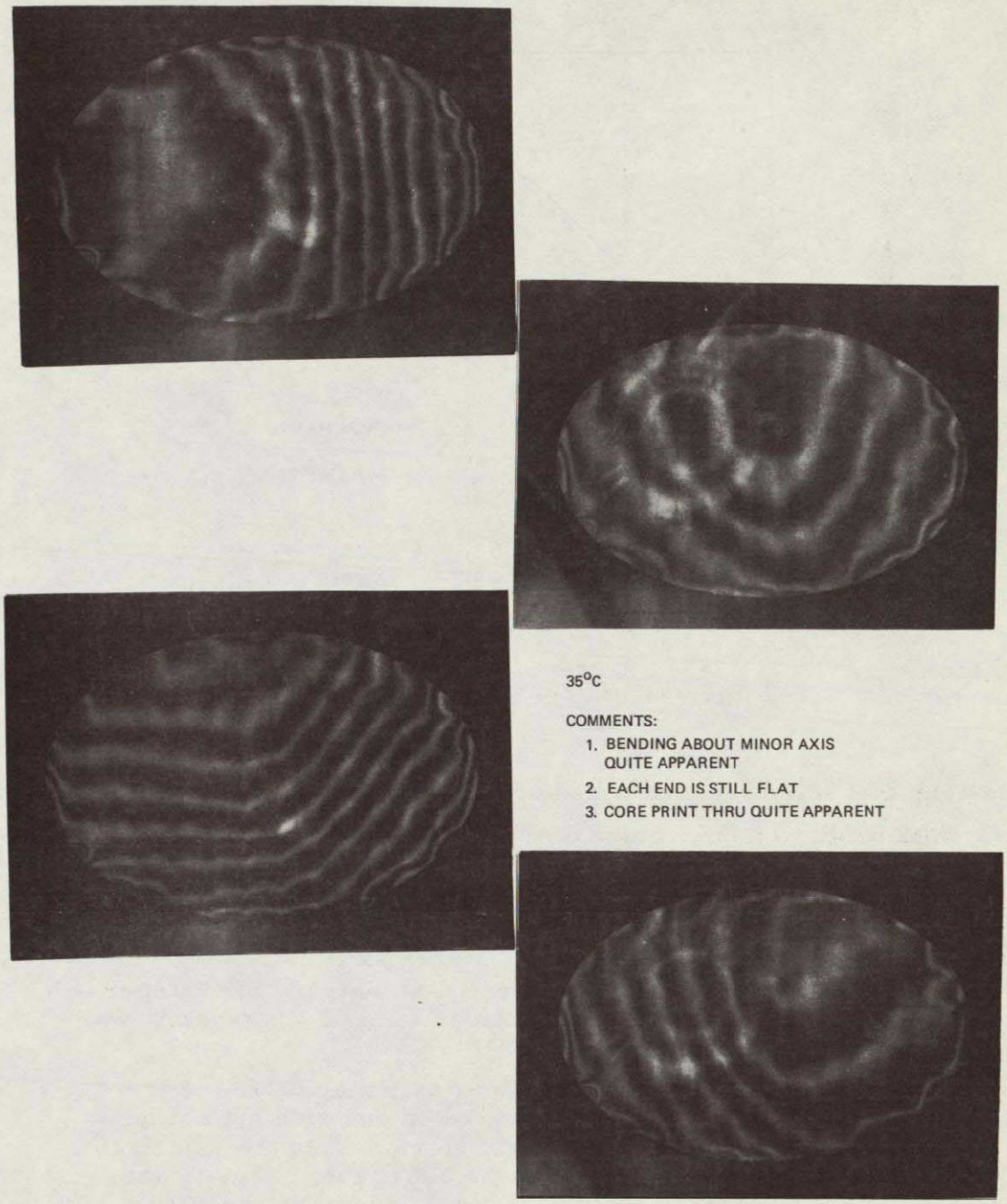

Figure 4.5-1e. Sample mirror interferograms.

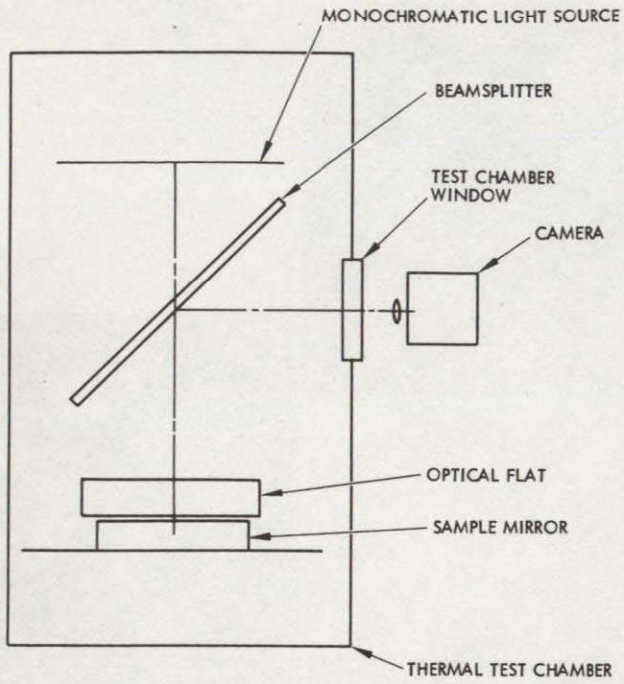

Figure 4.5-2. Sample mirror thermal flatness test equipment setup.

Conclusions that were reached based upon sample mirror tests and that were directly applicable to manufacture of the flight-type mirror were as follows:

1. Posting due to the brazed eggcrate joints was not evident. Therefore either core design can be used without expected degradation.
2. Eggcrate pattern can be expected at high and low temperature extremes. No conclusion as to MTF degradation was initially made.
3. Bending about the mirror minor axis may be due to the fact that core nodes were brazed on one side but not on the other. Or the cause could be related to the existence of an insert in the center of the back face. Thus it was not known if the existence of many inserts in the flight-type mirror would cause temperature warpage of the figure.
4. The edge roll off on the sample mirror surface increased with temperature perturbations. The same effect should be expected on the flight-type mirror. Edge roll could be a problem if it extended into the clear aperture. Since edge roll on the sample extended 0.10 inch into the mirror face, the planned oversize (0.1 inch) of the flight mirror may be marginally acceptable.

These conclusions would have led to building the flight type mirror a bit larger to allow greater edge roll outside of the clear aperture, but the fabrication cycle was too far downstream to allow this change. No other changes would be indicated from these conclusions and the only concern was the possible effect upon mirror figure of the inserts. Only subsequent testing of the flight-type mirror would prove that the bending problem seen in the sample mirror was not due to inserts but rather to the asymmetrical brazing of core nodes.

As the flight-type mirror blank progressed in its fabrication process several new problems arose that were not uncovered by the sample mirror. There are two ways to achieve the elliptical profile. The parts of the blank can be sized prior to brazing, as was done for the sample mirror, or they can be assembled in an oversized condition and the entire blank profiled after brazing by an EDM "band saw" technique. Because it would require sending the blank to a separate vendor for profiling, which would have added to the schedule, it was decided to pre-cut the face sheets just as had been done with the sample mirror. The basic fabrication plan is shown in Figure 4.5-3.

This choice was a mistake. In the braze oven all parts must be jigged and the assembly weighted to cause tight braze joints between the core and the face sheets. Although jigging was a simple matter with the sample mirror with its single insert, pre-profiling made jigging much more difficult with the large mirror. There were simply no edges upon which to jig.

During the rear face sheet brazing operation, the insert bosses moved from their index positions on the rear face sheet, thus forcing the mirror front face sheet out of flat:

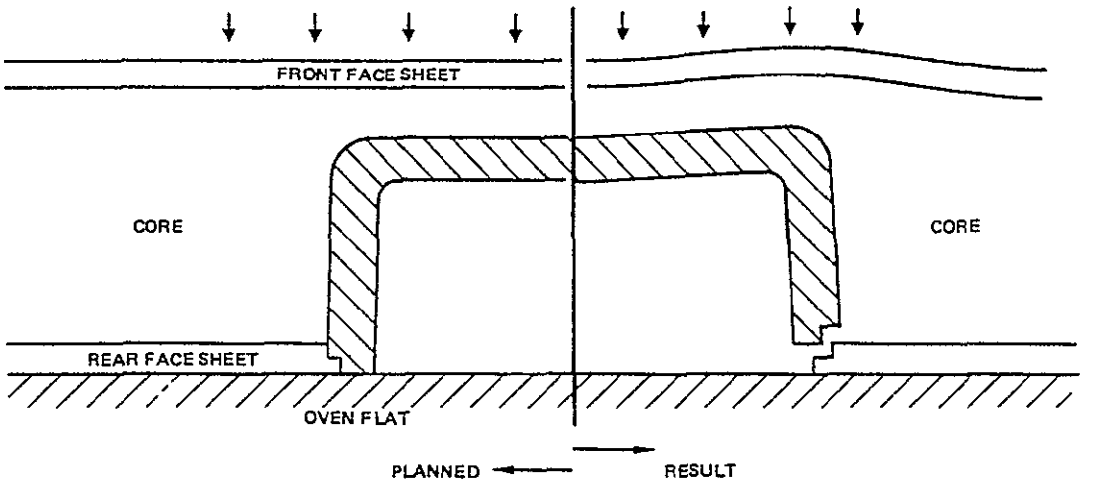

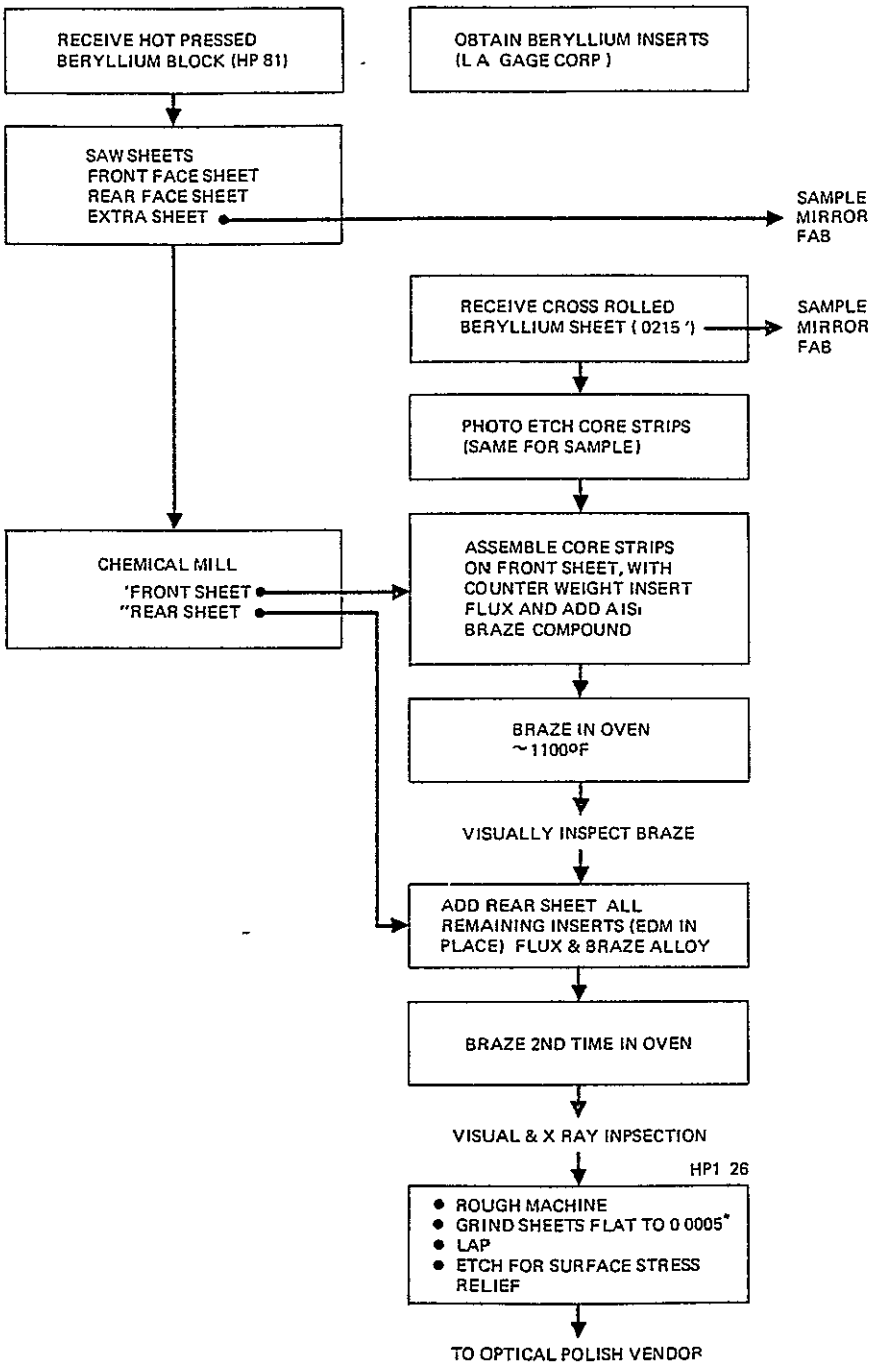

Figure 4.5-3. Flight type mirror blank fabrication plan.

During the planned second braze operation the rear face sheet is on a flat in the oven. Braze flux and alloy foil are placed on the rear face sheet and the previously brazed subassembly and all of the remaining inserts are placed on top of the rear face sheet. The parts are held in place laterally and weighted down from the top. The temperature of brazing is near the yield point of beryllium. Thus the result of improper fixturing was to put a 0.040 inch bump in the front face sheet.

Rather than scrap the part an attempt was made to flatten the face sheet by turning it over in the oven and pressing the face sheet against the oven flat. (It would have been impossible to have unbrazed all parts and started over, since each braze cycle causes the flux and braze alloy to etch away (dissolve) beryllium.) This attempt worked to an extent, after several oven cycles. The face sheet flatness was brought to within 0.015 inch. However, the total of six braze cycles, that it had now been subjected, created other problems. Prior to each braze cycle the entire interior was flushed with flux. To do otherwise would insure that the alloy would ball-up and leave the joints. This repeated application of flux and alloy took its toll on the beryllium. The results were voids in some brazed areas and migrated braze alloy into some non-braze areas. Several of the core nodes were completely brazed between the stop-flow holes. Pitting and etching of the exterior of both front and rear face sheets was caused by excessive flow of flux and braze alloy during the repeated oven braze cycles and by an unexpectedly high wetting characteristic on the HP-81 face sheet material (not on the cross-rolled core strips).

All of these problems can be substantially alleviated on subsequent units by eliminating some of the insert bosses and by leaving the mirror blank in a rectangular configuration until after all brazing (followed by an EDM profile operation). This makes jigging far simpler and will keep flux and braze alloy off the exterior surfaces of both face sheets.

Upon inspection after the final brazing operation the decision was made to proceed with final machining and grinding since the polish vendor thought it would be possible to polish the part flat even with the blank fabrication discrepancies. During the final grinding operation (performed at Los Angeles Gage Corporation), a compromise was required. The front face was already too thin to grind to a final print dimension of 0.080 inch. Yet there were

several small but deep pits distributed over the mirror surface and a rather deep scar along one edge and extending inward about 3/8 inch. Again, these were caused by flux and braze alloy. The part was ground to a flat which left a few pits and a small (approximately one square inch) remaining edge scar. The final front face thickness was between 0.060 and 0.065 inch. The remaining print through bump, due to the unseated boss had been removed.

It was concluded that if this blank could be polished, the few front face sheet imperfections would not interfere with the planned tests. Thus this imperfect mirror blank might be expected to allow successful completion of the remainder of the program.

In addition, a series of improvements to the fabrication process were developed and demonstrated on a small sample by Grant and Kamper. This provided assurance that a proper blank could be fabricated with a single oven braze cycle.

4.5.2 Mirror Polishing and Coating

The slow rate of achieving figure on the sample mirror was repeated on the flight-type mirror. Several re-estimates, by A.O.C., of the polish completion date resulted. The slow polish rate was attributed to two factors. First, the substrate material seemed to be unusually hard. Apparently A.O.C. had not polished the HP-81 beryllium in such large sizes before. The material does yield an excellent surface quality and no change in the material call-out on future mirrors is warranted. The fact of slow polish rate will simply be accepted and planned for. The second problem was the existence of severe pitting. These pits tended to break down the edges of the polishing lap which, in turn, scratched the mirror and required cyclic lap re-fabrication.

Finally on 11 June HAC was alerted by AOC that the desired figure had just about been reached and a HAC representative was sent to AOC to check figure and accept the mirror (actually a thermal cycle, re-check, coating and buy-off would follow this check of flatness). Unfortunately AOC had made an error in the test set-up and procedure and thus thought the mirror was flat when, in fact, it was cylindrical.

The scan mirror was tested using a Ritchey sphere test set-up and a laser interferometer. The equipment layout is shown in Figure 4.5-4. The Ritchey test permits the testing of large flat mirrors in an uncollimated beam of light. The flat mirror under test is used as a folding mirror in the test. To thoroughly test the scan mirror surface in the Ritchey test, the mirror's surface flatness is examined with the scan mirror major axis in one orientation and then with the scan mirror axis rotated 90 degrees. The interferograms shown on the left side of Figure 4.5-5 show the results of the Ritchey test. It was determined from these interferograms that there was still approximately 2 fringes of concave power along the short axis of the mirror. This represents approximately 0.7 wavelength since the test set-up makes 2.8 fringes equal to 1 wavelength. This conversion is due to the scan mirror being mounted at 45 degrees with respect to the sphere and because the laser light is reflected off the mirror twice. The requirement for the scan mirror is ±1/4 wavelength over the entire clear aperture of the mirror. The test wavelength is 0.6328 micrometer.

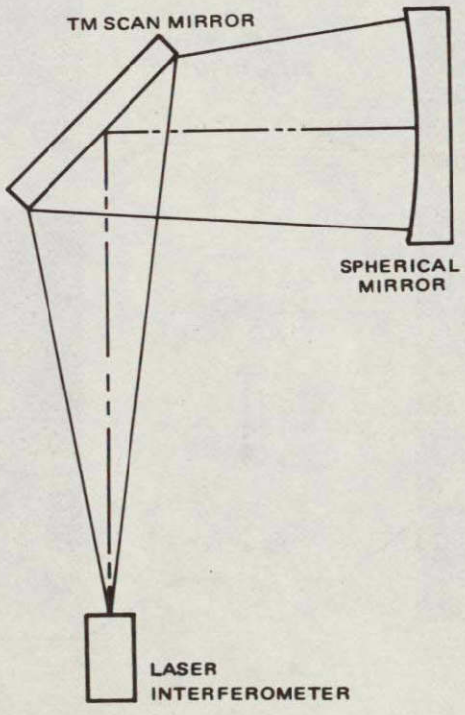

Figure 4.5-4. Equipment layout for Ritchey test at AOC on 11-13 June, 1975.

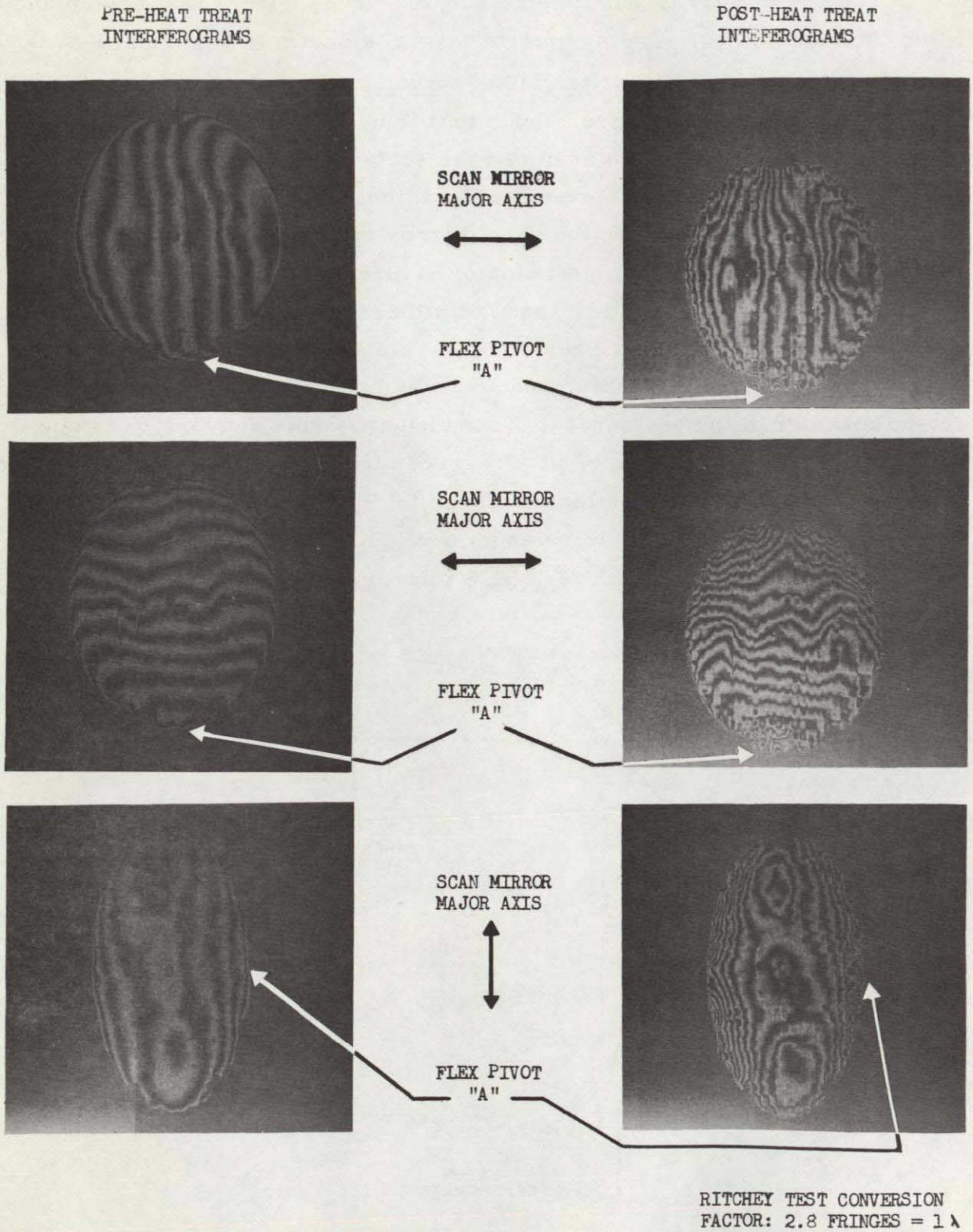

Figure 4.5-5. Ritchey test interferograms taken at AOC on 11-13 June 1975.

The mirror had thus been polished to a cylinder rather than a flat, and this had occurred because of a procedural error in testing, i.e., by testing the mirror in only one axis with the Ritchey sphere they were inadvertently focusing out the astigmatism. Had AOC rotated the mirror they would have quickly seen the problem. The test procedure and polishing cycle was reviewed and it then appeared that further polishing and proper checking would produce a flat mirror.

However, the mirror was nearly flat and this seemed like a good time to test for temperature stability. The mirror drawing requires a post-polishing 98°C thermal cycle flatness check. This check, which is a customary requirement for all metal mirrors, assures flatness over a military-type storage environment and assures stability after hot coating operations. The mirror is not required to be flat at 98°C, but it is not expected to warp due to that exposure.

The morning after the heat treat a second set of interferograms were taken. These pictures are shown on the right side of Figure 4.5-5. The interferograms showed how the eggcrate print-thru occurred over the entire front surface. The print-thru was more pronounced around the flex pivot block labeled "A" in Figure 4.5-5. Print-thru occurred on the back surface only in the area of flex pivot "A". After reviewing the post heat treat interferograms, it was decided to put the mirror back into polish.

At that point it was questioned whether the sample mirror had been subjected to this final thermal cycle or not. It was therefore decided to perform the test on the sample mirror at HAC. The results indicate that a permanent print-thru problem did not occur on the sample mirror after the 98°C temperature cycle. The interferograms of the sample mirror at HAC were taken using a Fizeau interferometer. No evidence of permanent honeycomb see-thru or increased edge roll off was detected.

The question of why the sample mirror behaved properly while the flight-type mirror warped was paramount. The poor behavior could be blamed only upon differences between the two mirrors. One difference is the construction. The sample mirror has a thicker face sheet and has been through far fewer braze cycles. These braze cycles cause the braze material to etch into the face sheet. It is quite probable that the braze material, whose

coefficient of thermal expansion is twice that of beryllium, has eaten its way well up into the underside of the face sheets. The cure is simply to make the flight mirror like the sample, and in fact, future substrates will be limited to one or at most, not more than two braze cycles and a final face sheet thickness in excess of 0.080 inch. A second difference between the two mirrors is the grinding and polishing history on the flight type mirror caused by the braze material and the pits on the face sheet. It is conceivable that excessive polishing or grinding forces in conjunction with a thin face sheet causes residual stresses which were relieved at 98°C. Here again, this conforms to the fact that the sample mirror, which was not pitted, did not experience a problem due to the 98°C cycles.

The plan of action from this point was thus to obtain a flat mirror, reduce the post polish thermal cycle to 38°C and finish the rest of the program objectives without repeating the 98°C thermal cycle. The sample mirror was evidence enough that a flight-type mirror could be made to withstand a 98°C thermal cycle. The critical questions at that juncture were whether or not a mirror could be fabricated to the requirement of 1/2 fringe and what thermal in-use variations could be tolerated.

On 19 and 20 June a second HAC representative met with AOC personnel to again go over procedures and the permanent print-through problem as well as to assess polishing progress. At that time AOC was confident that they could meet the full print requirements for static flatness. However, the additional time required for polishing was difficult to quantify. In order to accelerate delivery and yet still allow accuracy for dynamic and thermal flatness, it was agreed upon to allow a one inch rolled edge around the mirror (0.1 inch per print). This minimizes the amount of material which must be removed to attain final flatness and hence delivery time, yet maintains a high quality figure over approximately 90 percent of the area for accurate test measurements.

On 26 June a HAC representative arrived at AOC and inspected interferograms which clearly indicated that the mirror was still 1.2 fringes out-of-flat. AOC agreed.

The figure of the mirror was essentially flat over the central half of the area; the outside half rolled down all the way around. The plan for obtaining flatness was to dish out the center, leaving a toroidal mound near the edge. Then the toroidally high area would be worked outward. It was decided to continue the polishing process but to send interferograms by telecopy machine directly to HAC Culver City to allow Hughes concurrence in the progress and direction without round trips to Boston. By 9 July 1975 is was clear from the interferograms that further progress was not being made. The mirror was not within the 1/2 fringe goal and in fact had a large edge roll (~ 1 fringe). At this point delivery of the mirror to allow continuation of testing at Hughes had become critical.

It was determined by Hughes that the mirror was satisfactory for the purpose of all remaining tests. That is thermal effects could be measured, dynamic performance was measurable with the existent figure, and all SMA tests could be performed. In addition, although the existent mirror was not as flat as could normally be expected for metal mirrors of this size, there were known techniques for easing the polishing problem. Specifically, the mirror could be thinly coated with nickel (one or two thousands of electroless nickel) and this surface is known to be easier to control than beryllium. Then too, a flight mirror would have a significantly thicker face sheet which would tend to ease the edge roll-down problem. Lastly, it still had not been determined just how flat the mirror must be. Hughes, accordingly, told AOC to coat the mirror and the mirror was delivered and put into thermal flatness testing on 17 July 1975.

It should be pointed out that the mirror was coated with aluminum rather than silver. This choice was possible since there were no plans to test the mirror for qualities of the coating such as reflectivity, absorptivity, polarization, scattering, etc. The choice permitted a quick turnaround with less risk of damaging the surface. The flight mirror will be silver coated. The aluminum coating was sufficient for this program's needs.

At this point in time the remaining questions outweighed the conclusions. The ability to polish the HP-81 beryllium has been established, but the required and achievable figure quality had not.

4.5.3 Mirror Testing and Analysis

The critical tests of flatness were performed in accordance with the Test Plan and Test Procedures. The procedures were changed in only two ways. (1) Tests were performed in a thermal chamber to enable measurement of flatness over the 20 ±10°C temperature range, and (2) Tests were performed prior to and after bonding operations to check the effect of bonding-induced stresses and gravitational effects of the magnet assembly.

This was an extensive change in the scope of the static flatness measurements compared to the original plan. The need for this change was to assure that the cause of the bend down the middle at high and low temperatures on the sample mirror would not be present.

The thermal/static flatness tests were accomplished and reported in IDC 72123/87, "Thermal Flatness Test Report" by R.A. Johnson, dated 6 August 1975; and IDC 72123/113, "Post-Bonding Test Report" by R.A. Johnson, dated 23 September 1975. Prior to bonding, the mirror was tested using a Tinsley Unequal Path Interferometer at temperatures of 11, 15, 20, 23, 26, and 32°C. Interferograms were taken at each temperature and each interferogram was reduced to determine the flatness at each temperature. Two effects were quickly noted.

The "bend-down-the-middle" seen on the sample mirror was not seen in the flight type mirror. This data confirmed the hypothesis that the sample mirror behavior of bending down the middle was due to the fact that the sample mirror was made with complete braze posting on one side and no braze posting on the other. In fact, the overall figure of the mirror behaved quite well over the temperature extremes tested (which were slightly greater than the 20 ±10°C required). The flatness of the flight-type mirror at the polishing temperature was not within the 1/2 fringe requirement required by the polishing drawing. However, the temperature behavior or change in flatness from the figure at 70°F was quite good, as shown in the following table

Temperature, °C	ΔT, °F	Peak to Peak Fringes	
		Vertical	Horizontal
11	−18	0 45	0 42
15	−10	0 30	0 05
20	0	0	0
23	3	0 20	−0 05
26	8	0 22	0 55
27	11	0 25	0 35
32	20	0 05	0

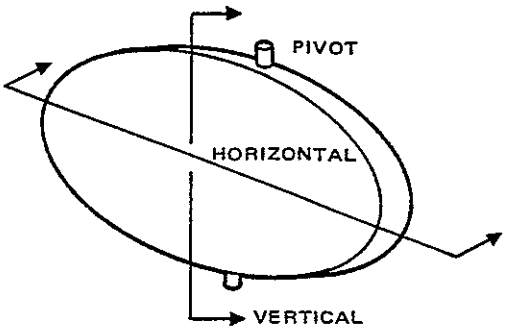

After bonding and assembling the torquer magnets to the mirror, the mirror was again statically tested at room temperature. The mirror was tested with the pivot axis in both a horizontal and vertical mount. No bending of the mirror due to bonding was noted. However, the magnet mass caused a 1/8 fringe mirror bend when the pivot axis was vertical and a 1 fringe bend when the pivot axis was horizontal. This static bending due to gravity is not pertinent to flight performance; however, it is an indication that inertial forces caused by the magnet mass during turn around should be considered as a possible cause of any dynamic changes in flatness.

The second effect of thermal variations was the core pattern that could be seen in the interferograms. The perturbation of the surface due to the core pattern at temperature extremes is less than 1/8 fringe, which is well within the overall flatness requirement. However, due to the high spatial frequency of this pattern, the slope errors could conceivably degrade the mirror MTF. The interferogram test method cannot be used to evaluate the magnitude of the core print through effect upon MTF.

The first step in understanding the total effect upon MTF of the figure errors and core print through was taken by utilizing an analytic model. This was reported in IDC 7212.1/136, "TM Scan Mirror MTF Degradation Analysis" by W. W. Goodridge dated 17 September 1975. The analytic model is only as good as the estimate of the surface error used in the model. By reading the interferograms one can estimate the figure errors quite well. However the core print through errors can only be bounded. This resulted in the following estimated bounds on figure and core print through errors.

Surface Errors in Wavelength at 0.6328 μm
for flight-type mirror as fabricated.

	Temperature, °C				
	10	16	21	27	32
Probable Figure Errors	0.13	0.08	0.06	0.11	0.13
Pessimistic Figure Errors	0.26	0.16	0.12	0.22	0.26
Lower Bound on Core Errors	1/20	1/40	1/40	1/20	1/16
Upper Bound on Core Errors	1/8	1/16	1/32	1/8	1/4

These estimates were then utilized in the analytic model to produce MTF degradations. The analytic model (developed in the above mentioned IDC) separately models the effect upon MTF of the low spatial frequency figure errors and the high spatial frequency print through errors. For figure errors the MTF degradation, $T(\nu)$, as a function of spatial frequency, ν, can be expressed

$$T(\nu) = e^{-(2\pi\omega)^2 (1 - \phi_{11}(\nu))}$$

where ω^2 is the variance of the wavefront errors in wavelength squared, and $\phi_{11}(\nu)$ is the auto-correlation function of the perturbations expressed as a function of spatial frequency. For this particular case where $\omega < \lambda/8$ and the errors have a low spatial frequency content, the transfer function is independent of the form of the error, and depends only upon the magnitude of the wavefront error. Figure 4.5-6 expresses the MTF of the figure errors for various magnitudes of the figure error (λ/n) as a function of normalized spatial frequency ($\nu_n = \nu/\nu_o$ where $\nu_o = D/\lambda$ in cycles/radian).

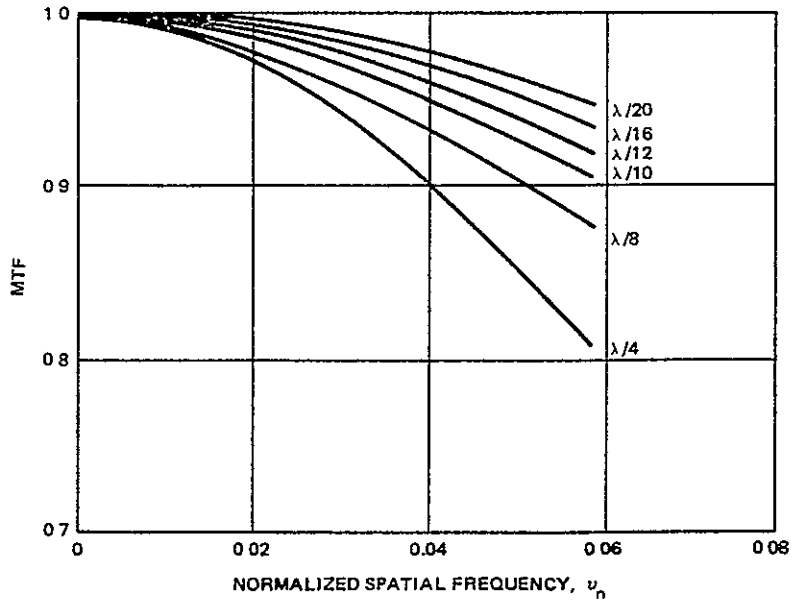

Figure 4.5-6. MTF for figure errors.

However it is the degradation in system MTF due to scan mirror imperfections that needs to be determined rather than scan mirror MTF per se. For a circular aperture the perfect lens MTF in terms of the normalized spatial frequency, ν_n, is

$$T_I(\nu_n) = \frac{2}{\pi}\left[\cos^{-1}(\nu_n) - \nu_n \sin\cos^{-1}(\nu_n)\right]$$

Then the degradation factor is $T(\nu_n)/T_I(\nu_n)$ and this degradation factor for figure errors is plotted in Figure 4.5-7.

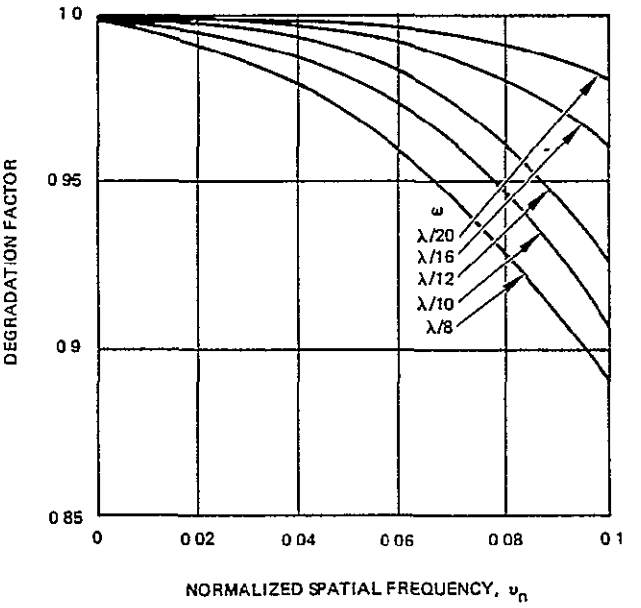

Figure 4.5-7. Degradation factors for figure errors.

An example of the use of this figure is as follows: For Band 5, the wavelength is 1.65 μm. From the table, the pessimistic figure error at 32°C is 0.26 wavelengths at 0.6328 μm. Therefore the curve selected from Figure 4.5-7 is

$$\omega = \frac{0.26 \times 0.6328}{1.65} = 0.0996 \rightarrow \lambda/10$$

The IFOV is 42.6 microradians and the cut-off frequency is 1/2 (IFOV) or 11.7 cycles/mrad. The diffraction cut-off frequency for a 40.6 cm diameter aperture is $\nu_o = D/\lambda = 242$ cycles/m radians at 1.65 μm. By dividing, the normalized spatial frequency is obtained, $\nu_n = 11.7/242 = 0.048$. Therefore Figure 4.5-7 is entered at $\omega = \lambda/10$ and $\nu_n = 0.048$ obtaining a degradation factor of 0.98; that is, a loss in MTF of 2 percent from the MTF of a perfect 40.6 cm diameter aperture.

Now in addition to the basic figure errors, the print-through of the eggcrate pattern must be considered. The degradation factor for the print-through errors and the degradation factor for the figure errors can then be multiplied to obtain the total degradation factor for the mirror as a function of temperature (factor of 1 implying no degradation). To evaluate the higher frequency errors the following equation as developed in "Geometric Versus Diffraction Predictions of Properties of a Star Image in the Presence of Isotropic Random Wavefront Disturbance," by R. V. Shack, Technical Report 32, Optical Science Center, University of Arizona, 16 September 1968, is used:

$$T(\nu_n) = e^{-1/2(2\pi\omega/\ell_c)^2 \nu_n^2}$$

where here:

σ_ω is the departure, rms, in lens units

n is the rms correlation length of the departure

ν is the angular spatial frequency in cycles/mr

D is the optical diameter

$\omega = (\sigma\omega)/\lambda$

λ is the optical wavelength

$\nu_n = \nu/(D/\lambda)$

$\ell_c = n/D$

This equation can also be normalized to obtain the factor of MTF relative to a perfect aperture. Then by combining the factor for figure with the factor for the print-through errors, the total expected degradation can be obtained. This results in the estimation shown in Figure 4.5-8.

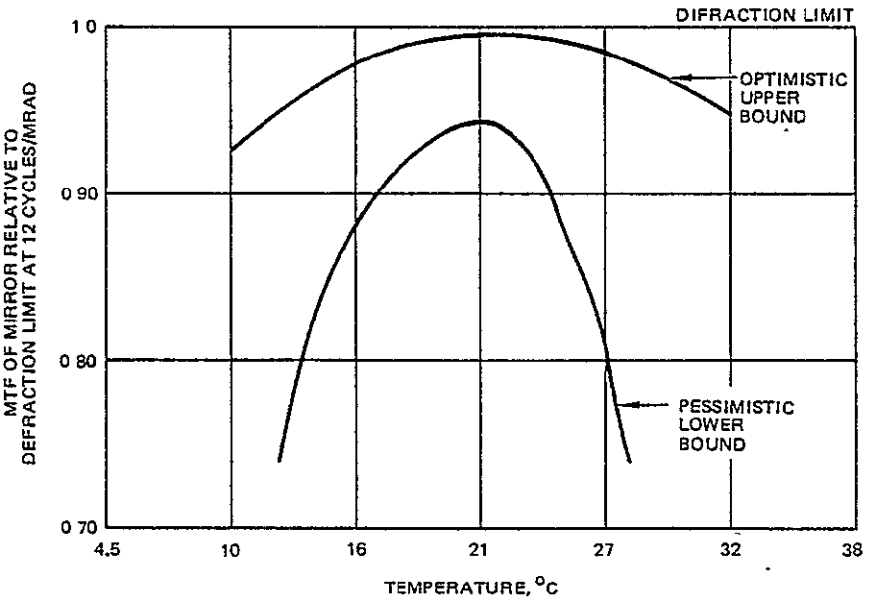

Figure 4.5-8. Upper and lower bound of mirror MTF based upon analysis and interferogram data expressed as a function of temperature at 12 cycles/mrad.

Two boundaries are shown. The upper bound (optimistic) is based upon the probable figure errors of the mirror (not including edge roll off) and the lower bound on core errors as previously tabulated. The lower bound is based upon doubling the measured figure errors (pessimistic figure errors in the table) and by using the upper bound on the core errors. Three facts are clear: The bounded MTF curves are not very close together, The uncertainty in the core errors is the largest contributor to the uncertainty in MTF; If the pessimistic estimate is used, a very narrow temperature range would be permissible.

In order to get a better estimate of what the true MTF degradation as a function of temperature will be, a second type of test was performed. This test set-up is shown in Figure 4.5-9. The objective of this test is to directly

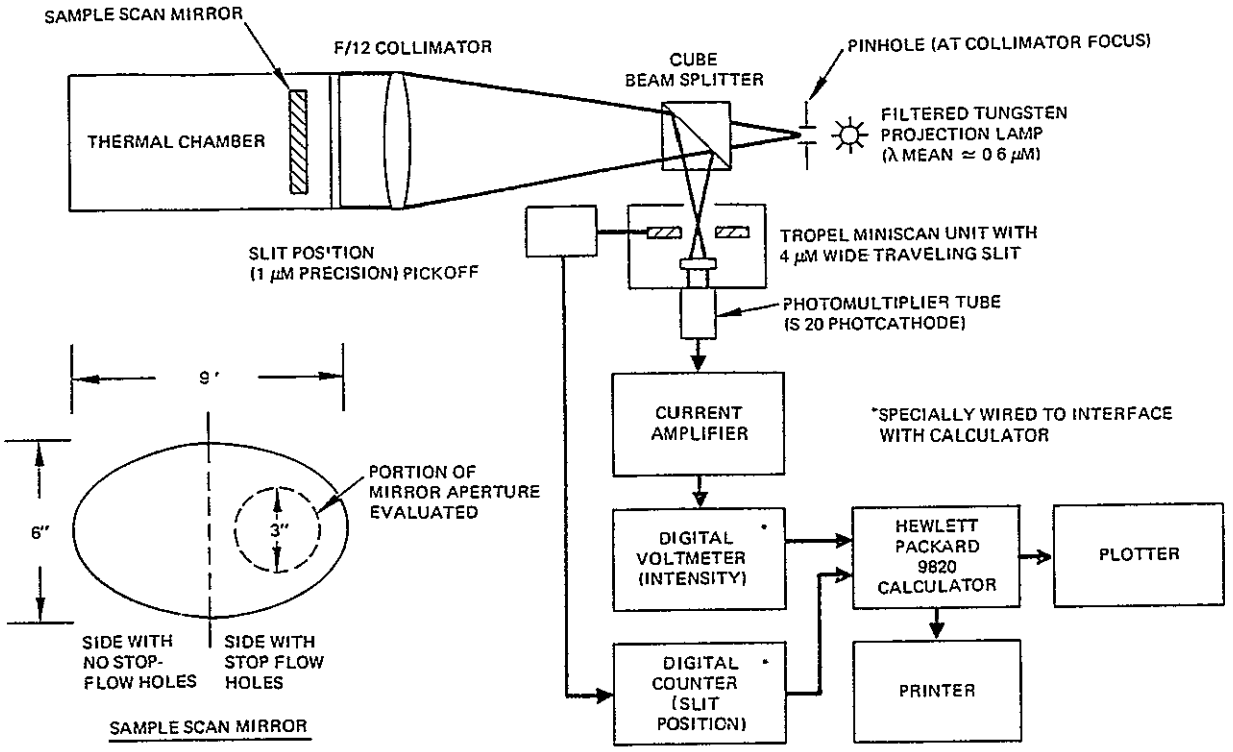

Figure 4. 5-9. Thematic Mapper sample scan mirror MTF measurement setup.

measure the line spread function of the mirror under the conditions of the temperature environment. The technique utilizes a slit scanner. The image of a point source, located at the focus of a collimator and after reflection off of the mirror under test and reimaged through the collimator and beam splitter, is scanned with a narrow slit resulting in a line spread function (LSF). The MTF is obtained by taking the Fourier Transform of the LSF. Errors in the mirror flatness change the LSF and hence the MTF. In this set-up, with the mirror normal to the incident wavefront, surface errors are doubled.

Since the basic objective is to determine how well a flight quality mirror will perform with respect to temperature dependent core print-through, the test was performed using the sample mirror. The sample mirror was manufactured with the proper front face sheet thickness while the flight type

mirror has a much thinner than desired front face sheet. Fortunately this technique does not require testing the entire surface. The only requirement is that the area tested be representative of the high spatial frequency deformations and that there be several cycles of core per diameter of the test area.

The sample mirror was located in a thermal chamber and the LSF measured at temperatures between 21° and 32°C. In addition the LSF was measured using a reference mirror installed in place of the sample mirror. The test set-up automatically plots the LSF, taking 200 points and plotting every other one, as shown in Figure 4.5-10 (for the 21°C case). Each data point consists of the average of 50 measurements. In this fashion RMS noise values were reduced to one point in 5000, and highly repeatable data resulted.

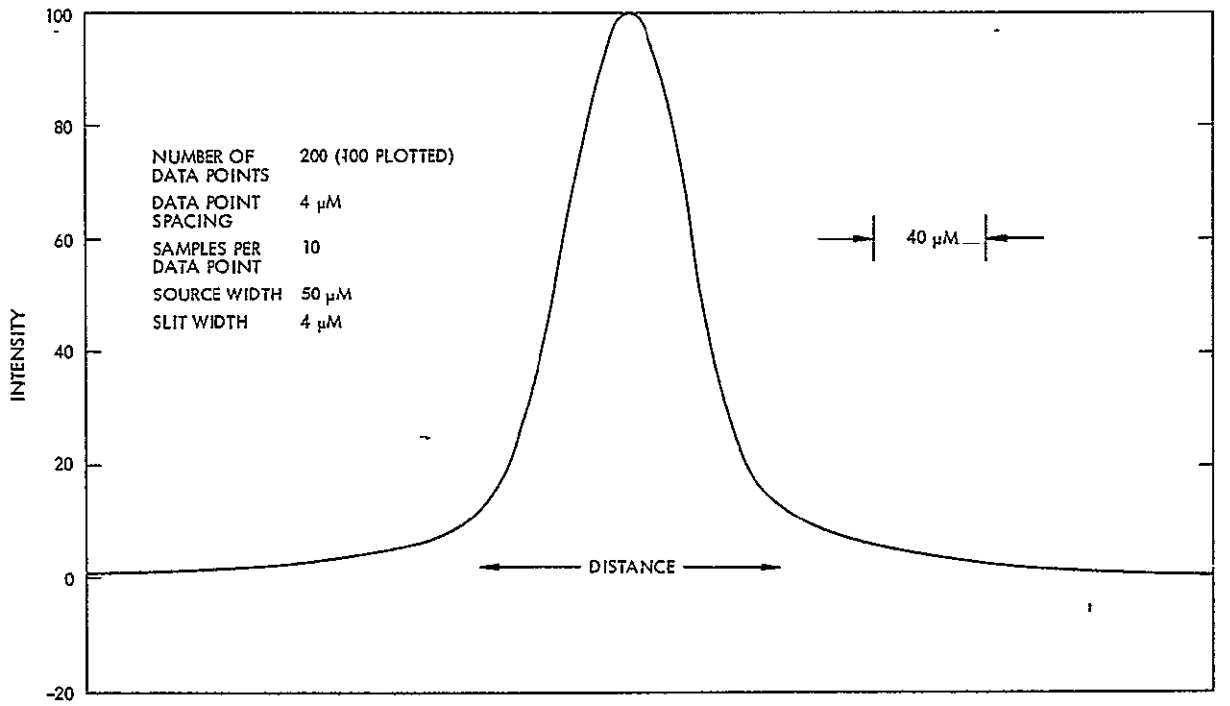

Figure 4.5-10. Measured line spread function at 21°C.

If one visually compares the resulting plotted line spread function at 21°C and 32°C, by overlaying the computer produced curves, a barely discernable skirt spreading can be detected at the higher temperature. However, for the required data reduction accuracy, these curves were not used and the measured data is used numerically and directly.

The measured data includes the effect of finite source and slit size along with test-set aberrations. However, these were compensated for by deconvolving the slit and source width from the measured data (accomplished by dividing the resulting measured MTF by the transfer functions of the source and slit). Since the frequencies of interest are between approximately 0.1 and 0.7 of the slit cut-off frequency and because of the low noise value obtained, accurate estimates of MTF can thus be obtained. The effects of set-up aberrations were computed relative to a baseline system with the reference mirror installed.

As discussed previously, performance estimates are derived in terms of degradations at angular spatial frequencies below 12 cycles/mrad. The system angular frequency in cycles/mrad can be converted to test station linear spatial frequencies in cycles/mm by dividing by the collimator focal length of 914 mm. Thus 12 cycles/mrad corresponds to $12/(10^{-3} \times 914) = 13$ cycles/mm in the test-set. (The slit cut-off frequency is 18 cycles/mm.)

The measured MTF versus mirror temperature is shown in Figure 4.5-11. Please note that the scale of this figure is chosen to illustrate the MTF at all frequencies involved. Actual data and not this figure, were used to compute MTF degradation. The following table expresses the mirror MTF as a percentage degradation from the baseline system. Essentially these results show that for a properly manufactured mirror substrate, such as the sample mirror, there will be a negligible effect caused by core print through at temperature extremes (only the higher extreme was tested, however, it has been previously demonstrated by interferograms that the behavior of print through is nearly symmetrical in both perturbations of temperature). This test data confirms that the optimistic upper bound of Figure 4.5-8, which was based upon estimates taken from interferograms is essentially correct. Over the design environmental goal of 20 ±10°C, all

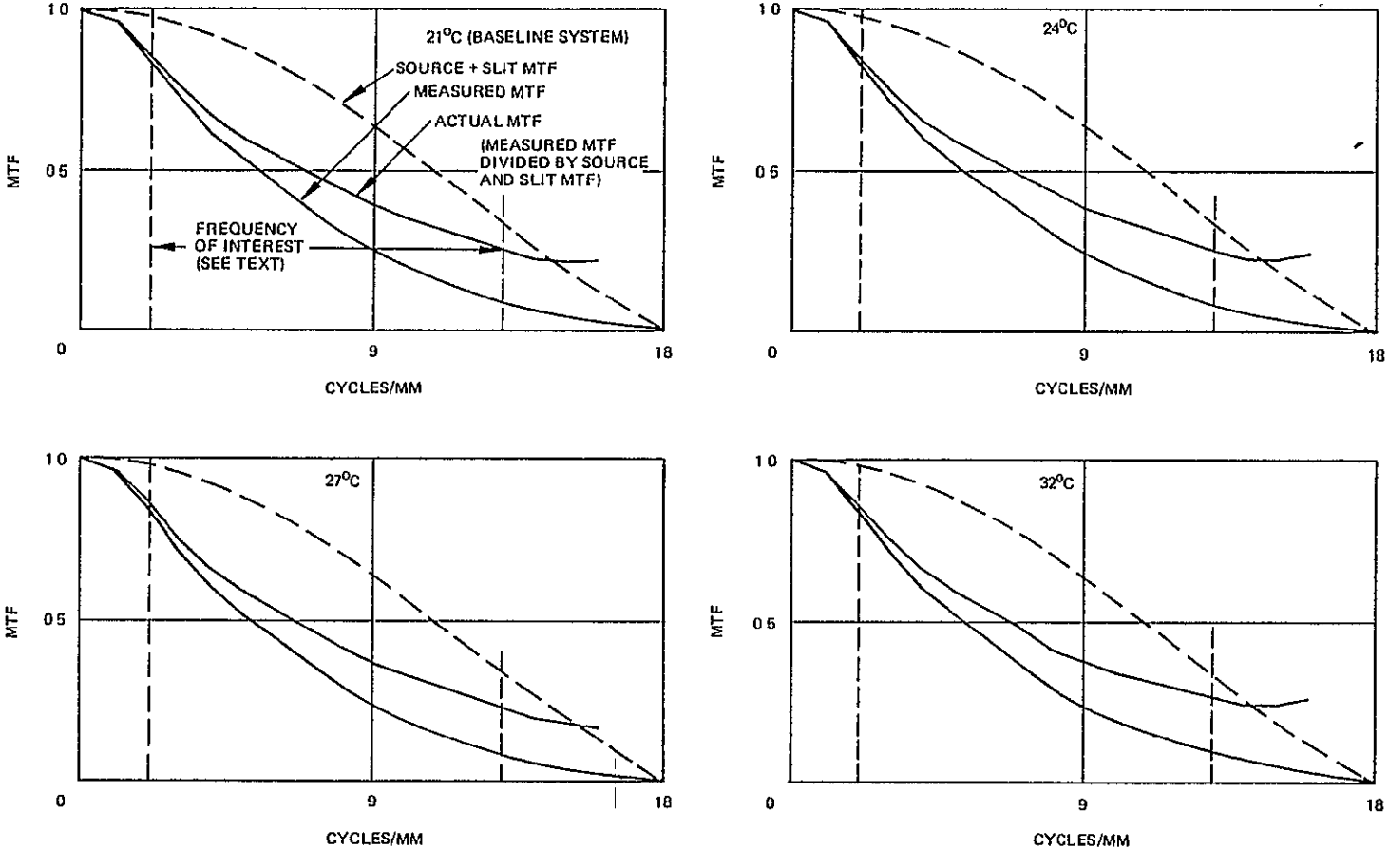

Figure 4.5-11. Measured MTF versus mirror temperature.

Temperature (°C)	MTF Degradation	
	Spatial Frequency	
	6 cycles/mrad (6.5 cycles/mm at test station)	12 cycles/mrad (13 cycles/mm at test station)
21 (baseline system)	0	0
24	0.2 percent	1.3 percent
27	0.7 percent	3.4 percent
32	1.5 percent	6.2 percent

data and analysis indicates that the mirror will cause no more than about a 6 percent degradation in MTF at 1/2 the system cut-off frequency of 12 cycles/mrad.

The original mirror manufacturing plan has now been revised based upon uncovered problems and measured results. In future fabrication more than two braze cycles will not be allowed. Grant and Kamper have suggested a lay-up technique allowing only one braze cycle. Total braze alloy will be minimized. Mirror profile will be established by EDM after brazing and prior to heat treat thereby ensuring ease of jigging and ensuring that no flux or braze alloy touch the reflecting surfaces of the mirror blank. In addition this will ensure that a blank is fabricated with a nearly constant and flat (12 μm) face sheet. Polishing ease will be increased by ensuring through the above mentioned techniques, that no significant pitting exists. The final polished surface specification will be changed to reflect angular surface departures rather than height departures, thus specifying the figure as it relates to MTF.

In summary, the results based upon tests of the large flight-type mirror and of the sample mirror show that brazed beryllium eggcrate construction can yield a mirror that meets all TM requirements. In addition, this technique has growth potential that should be explored for other systems requiring larger, lightweight mirrors.

5.0 NEW TECHNOLOGY

Periodic surveys of the contractual effort have been made throughout the period of the contract. These consisted of monthly and quarterly examinations of each breadboard assembly and part design, as well as test concepts and special test equipment, for evidence of advances in the state of the art. The results of these periodic surveys were then reported in the formal monthly and quarterly reports. No instance of advanced design qualifying as "new technology" was found.

The underlying theme of the program was to adhere to proven techniques and design experience in order to assure a successful demonstration of feasibility, and under that guideline such advances were not expected to be incurred. As an example, the initial design for the Scan Mirror Assembly (SMA) was simply a scale up of the flight proven Multispectral Scanner SMA. However, midway through the program, one application of advanced technology did occur, but the new design was added to the SMA only after it had been proven on an earlier IR&D breadboard development project. This involved the application of a design for scan mirror torquing in which drive torque is applied as a very short but controlled pulse during the period that the mirror is bounding off the scan reversal springs.

All other techniques such as the Scan Line Corrector mechanism and the photodiode arrays were based upon extensive earlier hardware implementations.

Appendix A

MASS PROPERTIES OF SCAN LINE CORRECTOR

Reference: SBRC Layout 2792-1, Scan Line Corrector

Mass Moment of Inertia Summary

	$lb\text{-}in\text{-}sec^2 \times 10^{-6}$
Upper Mirror	10.3
Lower Mirror	6.9
Channel Sections	21.6
Mirror Support Plates	0.6
Bottom Flange	2.2
Top Flange	1.1
Flex Pivot Adapter, Nut	0.9
Flex Pivot Adapter	0.7
Total SLC	44.3
Tachometer	2.5
Motor	34.4
Total	81.2

Ix, Iy For Center Rectangles

The three stiffening rectangular plates on the mirror backs have dimensions as follows:

Large Mirror a=.76", b=.24"

Small Mirror a=.62", b=.19"

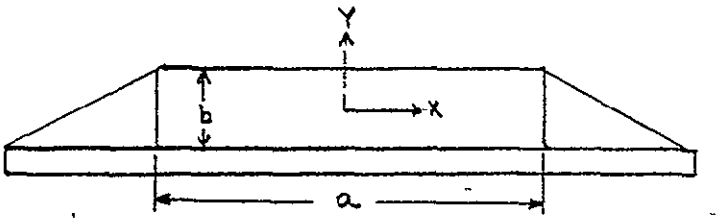

$$Iy = \frac{mba^3}{12}$$

$$Ix = \frac{mab^3}{12}$$

Large Mirror

$$Ix = \frac{(1.607E\text{-}5)(.76)(.24)^3}{12} = 1.407E\text{-}8$$

$$Iy = \frac{(1.607E\text{-}5)(.24)(.76)^3}{12} = 1.411E\text{-}7$$

Small Mirror

$$Ix = \frac{(1.607E\text{-}5)(.62)(.19)^3}{12} = 5.695E\text{-}9$$

$$Iy = \frac{(1.607E\text{-}5)(.19)(.62)^3}{12} = 6.064E\text{-}8$$

Ix, Iy For Simicircular Sections

From Roark p.75

$$Ix' = \frac{M\pi R^4}{8}$$

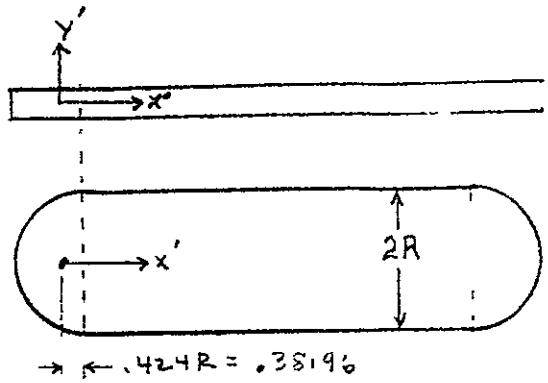

Iy' can be found by noting that Iy about the axis of a disk is

$$\frac{1}{2}(m\pi R^2)R^2 = \frac{\pi}{2} mR^4$$

so one half this value applies to a semicircle which we transfer to the cg as

$$Iy' = \frac{\pi}{4} mR^4 - (m\pi R^2)(.4244R)^2 \qquad \text{(Parallel Axis Theorem)}$$

$$Iy' = mR^4 \left(\frac{\pi}{4} - .4244^2\right) = .60528mR^4$$

Large Mirror (same as Small Mirror)

$$Ix' = \frac{m\pi R^4}{8} = \frac{(1.607E\text{-}5)(\pi)(.45)^4}{8} = 2.587E\text{-}7$$

$$Iy' = .60528\ (1.607E\text{-}5)(.45)^4 = 3.988E\text{-}7$$

Ix, Iy For Mirrors

For Rectangular section

$$Iy = \frac{mab}{12}(a^2 + b^2)$$

$$Ix = \frac{mba^3}{12}$$

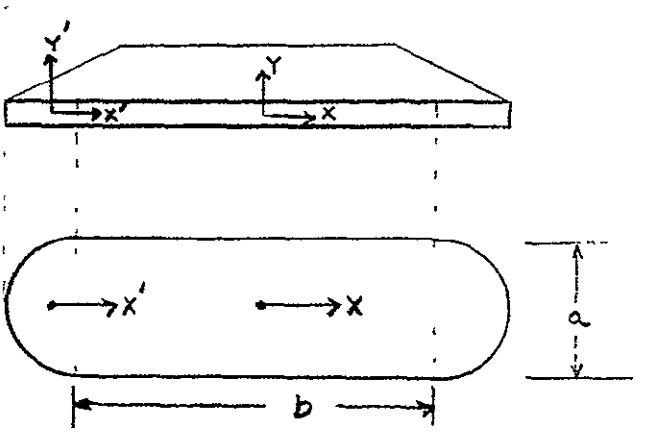

Large Mirror a=.9, b=1.2

Small Mirror a=.9, b=0.8

Large Mirror

$$Ix = \frac{(1.607E\text{-}5)(1.2)(.9)^3}{12} = 1.172E\text{-}6$$

$$Iy = \frac{1}{12}(1.607E\text{-}5)(.9)(1.2)(.9^2+1.2^2) = 3.254E\text{-}6$$

Small Mirror

$$Ix = \frac{(1.607E\text{-}5)(.8)(.9)^3}{12} = 7.81E\text{-}7$$

$$Iy = \frac{1}{12}(1.607E\text{-}5)(.8)(.9)(.9^2+.8^2) = 1.398E\text{-}6$$

CG of Mirrors

Establish XY global system as shown where the origin is at the center of the mirror. From symmetry the mirror cg is located as shown some distance $\bar{Y}$ above the origin.

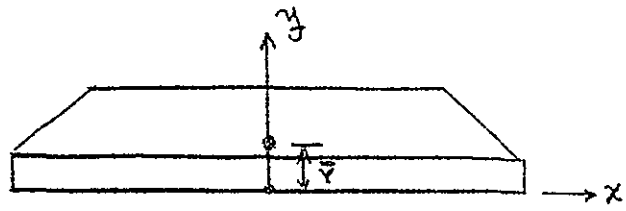

(Large Mirror)

Section	Mass	$\bar{y}$	Mass($\bar{y}$)
Main Rectangle	1.7356E-5	.030	5.2067E-7
Semicircles(both)	1.0223E-5	.030	3.067E-7
Support Rectangle(all)	8.7935E-6	.180	1.5828E-6
Support Triangles(all)	6.595E-6	.140	2.638E-7
	ΣM=4.297E-5		$\Sigma M\bar{y}$=2.674E-6

$$\bar{Y} = \frac{\Sigma M\bar{y}}{\Sigma M} = 0.0622"$$

(Small Mirror)

Section	Mass	$\bar{y}$	Mass($\bar{y}$)
Main Rectangle	1.157E-5	.030	4.571E-7
Semicircles(both)	1.0223E-5	.030	3.067E-7
Support Rectangles	5.679E-6	.1555	8.831E-7
Support Triangles	4.03E-6	.123	4.957E-7
	ΣM=3.15E-5		$\Sigma M\bar{y}$=2.032E-6

$$\bar{Y} = \frac{\Sigma M\bar{y}}{\Sigma M} = .0645"$$

Ix, Iy For Triangular Plates

The six triangular supports (three on each end of the mirror) on each mirror are approximately identical in size with the following base and altitude.

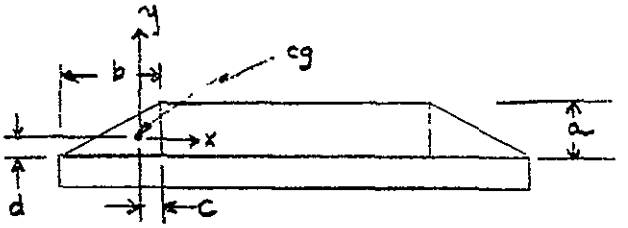

Large Mirror a=.24", b=.57", c=.19, d=.08

Small Mirror a=.19", b=.44", c=.146, d=.063

(each mirror):

$$Ix = \frac{mba^3}{36}$$

$$Iy = \frac{mab^3}{36}$$

Large Mirror

$$Ix = \frac{(1.607E\text{-}5)(.57)(.24)^3}{36} = 3.5174E\text{-}9$$

$$Iy = \frac{(1.607E\text{-}5)(.24)(.57)^3}{36} = 1.984E\text{-}8$$

Small Mirror

$$Ix = \frac{(1.607E\text{-}5)(.44)(.19)^3}{36} = 1.347E\text{-}9$$

$$Iy = \frac{(1.607E\text{-}5)(.19)(.44)^3}{36} = 7.2248E\text{-}9$$

Calculation of Mass Per Unit Area (Mirrors)

m = mass per unit area

Volume of beryllium per unit area is V_B = .060"-2t where t is thickness of nickel plating.

Volume of nickel per unit area is V_N=2t. If ρ_B and ρ_N are the mass densities of Be and Ni, then

$$m = (.060"-2t)\rho_B + 2t\rho_N$$

ρ_B = (.067 lb/cu in)/(386) = 1.73575E-4 lb-sec^2/in^4

ρ_N = (.2853 lb/in^3)/(386) = 7.39E-4 lb-sec^2/in^4

t = 0.005 inches.

m = (.060 - 2(.005)) 1.7357E-4 + 2(.005)(7.39E-4)

m = 8.6785E-6 + 7.39E-6

m = 1.607E-5 lb-sec^2/in^4 mass per unit area

Calculation of Ix, Iy at Mirror CG (Large Mirror)

Large Mirror

Establishing X-Y origin at cg:

$$Icg = Io + d^2M$$

Main Rectangle

$$Iy = Iy' = 3.254E-6$$

$$Ix = Ix' + r^2M = 1.172E-6 + (1.7356E-5)(.032)^2 = 1.190E-6$$

Simi Circles (both)

$$Iy = Iy' + r^2M = 2(3.988E-7 + (.98^2)(5.11E-6)) = 1.06E-5$$

$$Ix = Ix' + r^2M = 2(2.5878E-7 + (.032)^2(5.11E-6)) = 5.28E-7$$

Rectangles (Support)

Center Rect. $Iy = Iy' = 1.411E-7$

$$Ix = Ix' + r^2M = 1.407E-8 + (.12 - .0022)^2(2.93E-6)$$

$$= 5.47E-8$$

Combined $Iy = 2(Iy' + r^2M) = 2(1.411E-7 + .425^2(2.93E-6)) = 1.34E-6$

Outside Rectangles $Ix = 2(Ix' + r^2M) = 2(1.407E-8 + (.12 - .0022)^2 + .425^2) \times (2.93E-6)) = 1.17E-6$

Triangles

2 Center triangles $Iy = 2(Iy' + r^2M) = 2(1.984E-8) + .57^2(6.716E-7))$

$$= 3.755E-7$$

$$Ix = 2(Ix' + r^2M) = 2(3.517E-9) + (.0778^2)(6.716E-7))$$

$$= 1.516E-8$$

Outside triangles $Iy=4(Iy' + r^2M)=4(1.984E-8 + (.425^2 + .52^2)\times (6.716E-7)) = 1.437E-6$

$Ix=4(Ix' + r^2M)=4(3.517E-9 + (.0778^2 + .425^2)\times (6.716E-7)) = 5.155E-7$

Calculation Of Ix, Iy At Mirror (Large) CG

$\Sigma Ix = 1.19E-6 + 5.28E-7 + 5.47E-8 + 1.17E-6 + 1.516E-8 + 5.155E-7$

$\Sigma Ix = 3.47E-6$ lb-sec^2-in

$\Sigma Iy = 3.254E-6 + 1.06E-5 + 1.411E-7 + 1.34E-6 + 3.755E-7 + 1.437E-6$

$\Sigma Iy = 1.715E-5$ lb-sec^2-in

Rotation of Mass Moments of Inertia About CG

We wish to find the mass moment of inertia about an axis thru the cg that is parallel to the axis of rotation. The relation (Thomson Space Dynamics p.106) for this case is

$$I_{\xi\xi} = (\ell_{\xi x})^2 Ix + (\ell_{\xi y})^2 Iy$$

where $\ell_{\xi}x$ and $\ell_{\xi}y$ are direction cosines. For SLC the angle between the axis is 45°. Therefore

$$I_{\xi} = \frac{1}{2} (Ix + Iy)$$

$$I_{\xi} = \frac{1}{2} (3.47E-6 + 1.71E-5) = 10.3E-6 \text{ lb-in-sec}^2$$

Translate to Spin Axis

Large

$Ispin = Irot + d^2M = 10.3E-6 + .01258^2(4.297E-5)=10.3E-6$ lb-in-sec^2

Calculation of Ix, Iy at Mirror CG (Small Mirror)

Small Mirror

Establishing X-Y origin at mirror CG:

Then $I_{cg} = I_o + d^2M$

Main Rectangle (reflective surface)

$$I_x = 7.81E\text{-}7 + (.0345)^2(1.157E\text{-}5) = 7.948E\text{-}7$$

$$I_y = I_{y'} = 1.398E\text{-}6$$

Simicircles (both)

$$I_x = 2\left[2.588E\text{-}7 + .034^2(5.11E\text{-}6)\right] = 5.30E\text{-}7$$

$$I_y = 2\left[3.988E\text{-}7 + .78^2(5.11E\text{-}6)\right] = 7.02E\text{-}6$$

Rectangle (Support)

Center Rect. $I_x = (5.69E\text{-}9 + .095^2(1.89E\text{-}6)) = 2.27E\text{-}8$

$I_y = 6.064E\text{-}8$

Combined $I_y = 2(6.064E\text{-}8 + .425^2(1.89E\text{-}6)) = 8.04E\text{-}7$

Outside Rectangles $I_x = 2(5.69E\text{-}9 + (.1178^2 + .425^2)(1.89E\text{-}6)) = 7.47E\text{-}7$

Triangles

Center Triangles $I_y = 2(7.2248E\text{-}9 + .456^2(6.7E\text{-}7)) = 2.94E\text{-}7$

$I_x = 2(1.347E\text{-}9 + .059^2(6.7E\text{-}7)) = 7.37E\text{-}9$

4 Outside Triangles

$I_y = 4(7.2248E\text{-}9 + (.425^2 + .456^2)(6.7E\text{-}7)) = 1.07E\text{-}6$

$I_x = 4(1.347E\text{-}9 + (.425^2 + .059^2)(6.7E\text{-}7)) = 4.99E\text{-}7$

$\Sigma I_x = (.7948 + .530 + .0227 + .747 + .00737 + .499)E\text{-}6 = 2.6E\text{-}6$

$\Sigma I_y = (1.398 + 7.02 + .06064 + .804 + .294 + 1.07)E\text{-}6) = 1.06E\text{-}5$

Rotate about cg

$$I\xi\xi = \frac{1}{2}(Ix + Iy) = \frac{1}{2}(2.6E\text{-}6 + 1.06E\text{-}5) = 6.62E\text{-}6$$

Translate to rotation axis

$$Ispin = 6.62E\text{-}6 + .08768^2(3.15E\text{-}5) = 6.862E\text{-}6$$

Mass Moment of Inertia of Yoke

Each Channel section has area = .052

Length = 2.7, $VOL = .052(2.7) = .1404in^3$

Weight = $(.1404in^3)(.067\ lb/in^3) = .0094068\ lb$

Mass = Weight/G = $2.437E\text{-}5\ \frac{lb\text{-}sec^2}{in}$

Mass Moment of about rotation axis = $Io + r^2M$

For Each Flange

Icenter of web = $Io + r^2M = 9.135E\text{-}9 + (.71^2 + .075^2)\ 4.2E\text{-}6$

Ic = 2.15E-6

Total about center of web

$= 2Ic + Io = 2(2.15E\text{-}6) + 6.16E\text{-}7$

$= 4.916E\text{-}6$

Total about cg of cross section

Icg = $Io - R^2M = 4.916E\text{-}6$

$-.017^2(2.43E\text{-}5) = 4.91E\text{-}6$

I about Spin Axis Each Channel Section

$I = Icg + r^2M = 4.91E\text{-}6 + .492^2(2.43E\text{-}5) = 1.08E\text{-}5$

So for both sections the total is 2.16E-5

Moment of Mirror Support Plates

Void = Rectangle + 2 Semicircles

Rectangle = $(0.5)(.6) = .30\ in^2$ $I = \frac{bh^3}{12} = \frac{.6(.5)^3}{12} = .00625$

Each Semicircle = $\pi R^2 = \pi(.25)^2 = .1963\ in^2$ $I = \frac{\pi}{8}R^4 = \frac{\pi}{8}(.25)^4$

$= .001534$

Total I of Void = $.00625 + 2(.001534) = 0.009318\ in^4$

Solid Parallelogram

$I = \frac{bh^3}{12} = \frac{1.6(.75)^3}{12} = .05675\ in^4$

But must subtract Void I = $.05675 - .009318 = .04743\ in^4$

Add small support bars $I_{each} = \frac{\sqrt{2}(.05)(.75)^3}{12} = .00248\ in^4$

mass/area for bars is $\frac{(.05)(.067)}{386} = 8.6787E-6$

So I (bar) = $(8.6787E-6)(.00248\ in^4) = 2.157E-8$

mass/area (plate) = $\frac{(.030)(.067)}{386} = 5.2E-6$

I (Plate) = $(5.2E-6)(.04743\ in^4) = 2.4697E-7$

I total = $2.4697E-7 + 2(2.157E-8) = 2.9E-7$

So both plates add to $2(2.9E-7) = 5.8E-7$

Top Yoke Termination

Volume = $(.2)(.75)(.9) = .045\ in^3$

Mass = $(.045\ in^3)(.067\ lb/in^3)/386$

= 7.81E-6

$I_{spin} = \frac{1M}{12}(a^2+b^2) = \frac{1}{12}(7.81E-6)(.25^2+.9^2) = 5.68E-7$

Plate at Top

Vol = $(.05)(.75)(.75) = .028$

Mass = $.028(.067)/386 = 4.88E-6$

$I = \frac{4.88E-6}{12}(.75^2+.75^2) = 4.57E-6$

Shaft Boss at Top

Volume = $.05(\pi)(.25^2) = .009817\ in^3$

Mass = $(.0098)(.067)/386 = 1.7E-6$

$I = \frac{1}{2}mr^2 = .5(1.7E-6)(.25^2) = 5.33E-8$

Bottom Yoke Termination

Vol = $(.15+.05)(.5)(.5) = 0.05$

Mass = $(.05)(.067)/(386) = 8.68E-6$

$I = \frac{1}{2}m(a^2+b^2) = \frac{1}{2}(8.68E-6)(.5^2+.5^2) = 2.17E-6$

Flex Pivot Adapter (Bottom)

For a nollow cylınder of hieght, h, inner radıus, r, outer radius r_2 and mass density, ρ; The mass moment of inertıa about the cylınder axıs is

$$I = \frac{\pi}{2}\rho h(r_2^4 - r_1^4)$$

$r_1 = .25 \quad r_2 = .3125 \quad h = .42 \quad \rho = 1.73575E-4$

$$I = (\frac{\pi}{2})(1.7357E-4)(.42)(.3125^4 - .25^4) = 6.447E-7$$

Solid Dısk

$$I = \frac{1}{2} Mr^2 \qquad \text{Volume} = .19(\pi)(.25^2) = .0373 \text{ ın}^3$$

$$\text{Mass} = (1.73575E-4)(.0373 \text{ ın}^3) = 6.475E-6$$

$$I = \frac{1}{2}(6.475E-6)(.25^2) = 2.02E-7$$

Shaft

$$\text{Volume} = (\pi)(.0625)^2(1) = .0123 \text{ ın}^3$$

$$\text{Mass} = (1.73575E-4)(.0213) = 2.13E-6$$

$$I = \frac{1}{2}(2.13E-6)(.0625^2) = 4.16E-9$$

Nut $\quad I = \frac{\pi}{2}(1.73575E-4)(.25)(.125^4 - .0625^4) = 1.56E-8$

Total = 6.447E-7 + 2.02E-7 + 4.16E-9 + 1.56E-8 = 8.66E-7

Flex Pivot Adapter (Top)

$$I_1 = \frac{\pi}{2}\rho h(r_2^4 - r_1^4) = \frac{\pi}{2}(1.73575E-4)(.4)(.32^4 - .25^4) = 7.18E-7$$

$$I_2 = \frac{\pi}{2}(1.73575E-4)(.39)(.125^4 - .0625^4) = 2.43378E-8$$

Itotal = 2.433E-8 + 7.18E-7 = 7.42E-7

Appendix B

SCAN LINE CORRECTOR TEST DATA

13.0-Hz DATA SUMMARY

$2f_s$ = 13.0 Hz

T = 0.0769 sec 0.9T = 0.0692 sec

T/7 = 0.009887 sec (seven equal increments)

Scan Deviation Data

Time (msec)	Rate (in./sec)	Displ (mils)	Cumulative Displ (mils)	Nominal Displ (mils)	Δ (mils)	Error % Full Scale
9.886	0.905	8.947	8.947	8.912	+0.030	0.048
19.771	0.902	8.917	17.864	17.834	+0.030	0.048
29.657	0.900	8.897	26.761	26.751	+0.010	0.016
39.543	0.898	8.877	35.638	35.668	-0.030	0.048
49.429	0 900	8.897	44.535	44.585	-0.050	0.080
59.314	0.901	8.907	53.442	53.501	-0.059	0.094
69.200	0.904	8.937	62.379	62.418	-0.039	0.062

displacement = 62.379 mils nominal displacement = 62.418 mils

average rate = 0.9014 in./sec nominal rate = 0.902 in./sec

Repeatability

Scan to Scan (data from all seven increments)

Worst Case = 0.07 msec = 0.66 μr

σ = 0.016 msec = 0.15 μr

30-Second Period (one frame)

Worst Case = 0.10 msec = 0.94 μr

Average = 0.067 msec = 0.63 μr

Scan Jitter (Scan to Scan)

Worst Case = 0.04 msec = 0.38 μr

σ = 0.021 msec = 0.20 μr

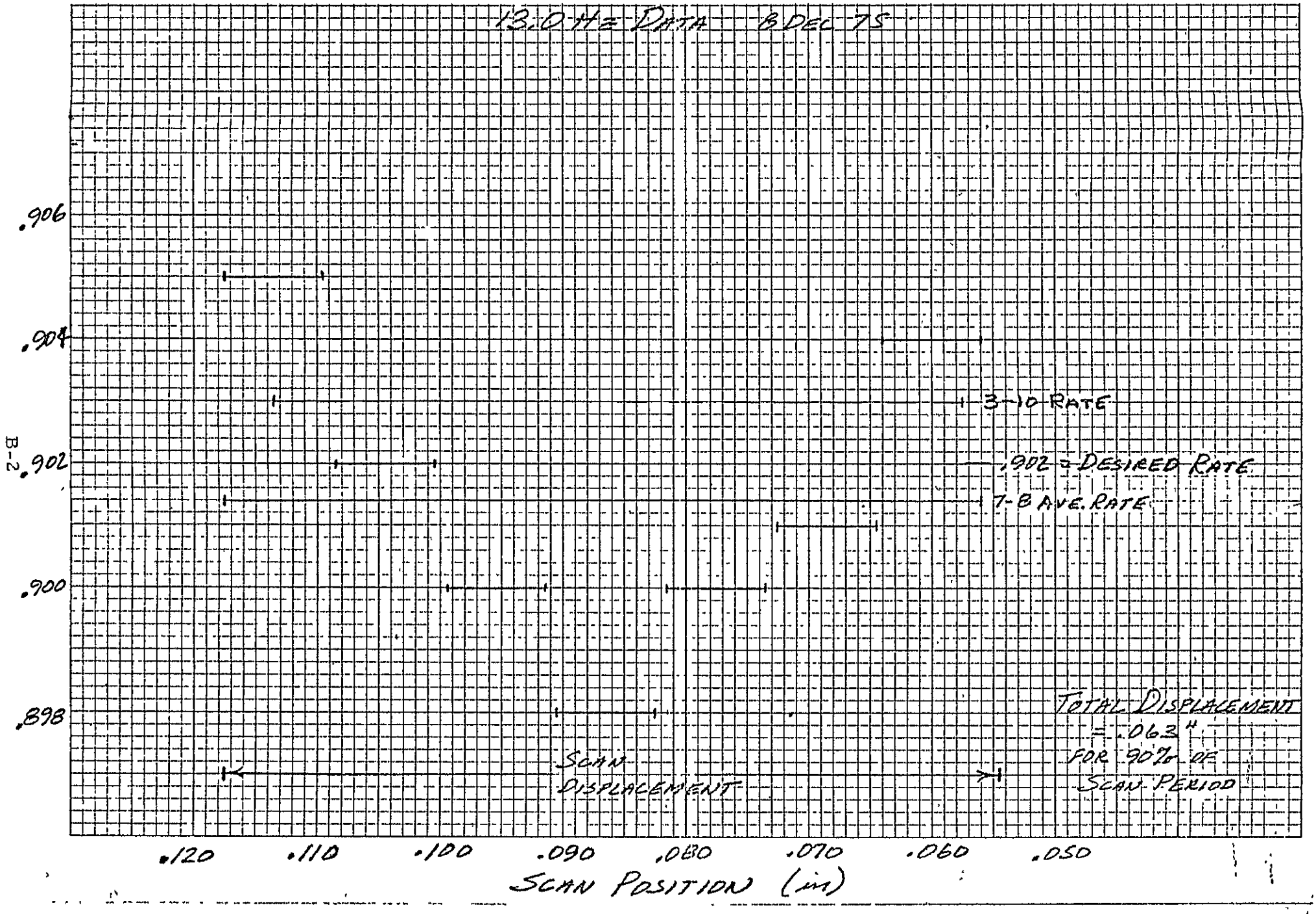
13.0 Hz Data 8 DEC 75
.906
.904
.902
.900
.898
3-10 Rate
.902 = Desired Rate
7-8 Ave. Rate
Total Displacement
= .062"
for 90% of
Scan Period
Scan
Displacement
.120
.110
.100
.090
.080
.070
.060
.050
Scan Position (in)

TEST DATA

SCAN LINE CORRECTOR

DATE 8 DEC 75

SCAN FREQUENCY 13.0 Hz

SCAN PERIOD .0769 SEC

OFFSET = 4.3V

I. SCAN RATE (2 SCAN INTERVAL DATA)

DETECTORS 3 - 10

15.5% 96.5%

TIME	MIN TIME	MAX TIME
10:37	62.06 ms	62.08 ms
	04	05
	02	05
NOMINAL TIME	02	06
SHOULD BE	04	04
62.084 ms	04	06
	03	04

TOTAL 868.63

AVE 62.045 ms

(AVE TIME/(N-1) DETECTORS) $\frac{AVE}{N-1} = \frac{62.045}{7} = 8.86$ ms

8.869 ms

SHOULD BE ~~8.9 ms ± .1 ms~~

SPACE BETWEEN DETECTORS = .008"

Detector #7

II SCAN AMPLITUDE

SHOULD BE $\geq .902 \times .9 \times \frac{1}{f}$ (in)

10%	.1175	.0069
20%	.1106	.0069
30%	.1037	.0069
40%	.0968	.0070
50%	.0898	.0070
60%	.0828	.0070
70%	.0758	.0069
80%	.0689	.0071
90%	.0618	.0065
~~100%~~ → 99.0%	.0553	

10% to 100% ≈ .063"

.1175
.0630
.25

Moving detector 7&8 through scan from 10% - 100%

Peak to Peak scan time deviation for ≈ 30 sec

8.78 - 9.03 ms
8.78 - 8.99
8.77 - 9.03
8.79 - 8.99

AVG 8.78 9.01 .911 in/sec .886 in/sec

DATE 8 DEC

III SCAN LINEARITY & SCAN TO SCAN REPEATABILITY (2 SCAN INTERVALS)

DETECTOR PAIR 7-8 VERTICAL POSN .1175

TIME	MIN TIME (ms)	MAX TIME (ms)	ΔT
10:46	8.79	8.84	.05
	84	89	.05
	85	88	.03
	80	84	.04
	84	86	.02
10:55	83	84	.01
	83	87	.04
	84	86	.02
	84	85	.01
	81	83	.02
	81	83	.02
	78	81	.03
	83	84	.01
	84	85	01
	84	87	03
11:07	84	87	03
	84	85	01
	83	83	00
	84	85	01
	82	84	02

TOTAL TIME 353.54 TOTAL ΔT .46

AVE TIME 8.8385 AVE ΔT .023

σ .0224

$$\text{RATE} = \frac{.008''}{8.838\text{ms}} = 1.905 \text{ in/sec}$$

DATE 8 DEC

III SCAN LINEARITY & SCAN TO SCAN REPEATABILITY (2 SCAN INTERVALS)

DETECTOR PAIR 7-8 VERTICAL POSN .1035

TIME	MIN TIME MS	MAX TIME MS	ΔT
	85	86	.01
	89	90	01
	85	92	07
	80	83	03
	84	85	01
	88	89	01
	87	89	02
	86	87	01
	85	87	02
	85	87	02
	83	83	00
	85	87	02
	86	88	02
	89	89	00
	85	88	03
	86	89	03
	86	90	04
	84	85	01
	88	88	00
	85	86	01

TOTAL TIME 354.59 TOTAL ΔT .37

AVE TIME 8.86475 AVE ΔT .0185

σ .0236

.902"/SEC

DATE 8 DEC

III. SCAN LINEARITY & SCAN TO SCAN REPEATABILITY (2 SCAN INTERVALS)

DETECTOR PAIR 7-8 VERTICAL POSN .0995

TIME	MIN TIME MS	MAX TIME MS	ΔT
	92	92	00
	88	89	01
	90	93	03
	88	89	01
	85	87	02
	90	90	00
	89	91	02
	89	91	02
	92	92	00
	88	89	01
	85	87	02
	87	88	01
	89	91	02
	89	89	00
	89	90	01
	89	90	01
	88	90	02
	90	92	02
	88	89	01
	90	90	00

TOTAL TIME 355.74 TOTAL ΔT .22

AVE TIME 8.8935 AVE ΔT .0118

σ .0161

R = .900"/sec

DATE 8 DEC

III SCAN LINEARITY & SCAN TO SCAN REPEATABILITY (2 SCAN INTERVALS)

DETECTOR PAIR 7-8 VERTICAL POSN .0905

TIME	MIN TIME MS	MAX TIME MS	ΔT
	90	91	01
	91	96	05
	88	92	04
	91	94	03
	91	91	00
	89	92	03
	87	93	06
	94	94	00
	92	94	02
	90	90	00
	90	92	02
	90	92	02
	91	94	03
	87	90	03
	89	93	04
	92	93	01
	90	92	02
	89	90	01
	90	92	02
	87	94	07

TOTAL TIME 356.47 TOTAL ΔT .54

AVE TIME 8.912 AVE ΔT .0270

σ .0212

R = .898 "/SEC

DATE 8 DEC

III SCAN LINEARITY & SCAN TO SCAN REPEATABILITY (2 SCAN INTERVALS)

DETECTOR PAIR 7-8 VERTICAL POSN .0815

TIME	MIN TIME MS	MAX TIME MS	ΔT
	88	90	02
	89	91	02
	89	89	00
	88	93	05
	92	92	00
10:57	89	91	02
	87	87	00
	86	87	01
	89	90	01
	88	92	04
	90	90	00
	88	90	02
	89	89	00
	88	90	02
	89	90	01
11:10	87	89	02
	86	92	06
	87	88	02
	87	90	03
	85	86	01

TOTAL TIME 355.57 TOTAL ΔT .36

AVE TIME 8.889 AVE ΔT .018

σ .0190

R = .900"/SEC

DATE 8 DEC

III. SCAN LINEARITY & SCAN TO SCAN REPEATABILITY (2 SCAN INTERVALS)

DETECTOR PAIR 3-10 VERTICAL POSN 0815

TIME	MIN TIME (MS)	MAX TIME (MS)	ΔT
	62.01	62.02	.01
	.03	.05	.02
	.02	.03	.01
	.02	.07	.05
	.04	.06	.02
	.01	.01	.00
	.05	.06	.01
	.01	.03	.02
	.02	.04	.02
	.04	.06	.02
	.03	.03	.00
	.05	.05	.00
	61.98	.01	.03
	61.99	.04	.05
	.05	.05	.00
	.01	.05	.04
	.00	.01	.01
	.00	.04	.04
	.02	.02	.00
	.03	.05	.02

TOTAL TIME 2481.19 TOTAL ΔT .37

AVE TIME 62.0298 AVE ΔT .0185

σ .0211

R = .903 "/SEC

DATE 8 DEC

III SCAN LINEARITY & SCAN TO SCAN REPEATABILITY (2 SCAN INTERVALS)

DETECTOR PAIR 7-8 VERTICAL POSN 0725

TIME	MIN TIME (MS)	MAX TIME (MS)	ΔT
	8.87	8.89	.02
	86	88	02
	87	90	03
	90	93	03
	90	91	01
	88	90	02
	86	88	02
	87	92	05
	89	90	01
	86	91	05
11:04	86	87	01
	88	90	02
	86	88	02
	87	87	00
	84	88	04
11:12	86	86	00
	85	86	01
	86	88	02
	87	87	00
	86	86	00
TOTAL TIME	355.12	TOTAL ΔT	.38
AVE TIME	8.8780	AVE ΔT	.019
σ	.0203		

R = .901"/SEC

DATE 8 DEC

III SCAN LINEARITY & SCAN TO SCAN REPEATABILITY (2 SCAN INTERVALS)

DETECTOR PAIR 7-B VERTICAL POSN .0640

TIME	MIN TIME (ms)	MAX TIME (ms)	ΔT
10:53	8.84	8.85	.01
	83	84	01
	85	88	03
	83	84	01
	84	86	02
	83	84	01
	84	85	01
	83	88	05
	84	86	02
	82	84	02
11:05	82	87	05
	82	84	02
	83	85	02
	86	87	01
	86	86	00
	83	88	05
	85	86	01
	82	83	01
	83	84	01
	84	84	00

TOTAL TIME 353.79 TOTAL ΔT .37

AVE TIME 8.845 AVE ΔT .0185

σ .0168

R = 1.904 "/SEC

DATE 8 DEC

VI. SCAN JITTER (2 SCAN INTERVAL)

TIME FROM END OF SCAN PULSE TO DETECTOR # 7

VERTICAL POSITION OF ARRAY = .1175

	MIN TIME (MS)	MAX TIME (MS)	ΔT (MS)
	8.33	8.35	.02
	32	35	03
	32	34	02
	31	32	01
	32	35	03
	32	32	00
	32	35	03
	29	32	03
	28	31	03
	31	32	01
	26	26	00
	24	28	02
	25	27	02
	29	29	00
	27	29	02
11:06	29	33	04
	34	34	00
	32	33	01
	33	34	01
	34	34	00

TOTAL TIME 332.45 TOTAL ΔT = .33

AVERAGE TIME 8.3113 (MS) AVERAGE ΔT = .0165

.0299

WORST CASE ΔT = .04

RMS = .021 ms

DATE 8DEC

IV 30 SECOND STABILITY 3-10

f 13 Hz T .0769 # OF SCANS IN 30 SEC 390

	MIN TIMEMS	MAX TIMEMS	ΔT
11:14			
	61 98	62 05	.07
	99	05	.06
	99	05	.06
	98	06	.08
	99	05	.06
	97	07	.10
	99	05	.06
	99	05	.06
	99	05	.06
	99°	05	.06

TOTAL ΔT .67

AVE ΔT .067

WORST CASE ΔT .10

DATE _____

I. SCAN REPEATABILITY - 99,999 SCANS:

f _____ T _____ TIME REQ. FOR 99,999 SCANS _____

MIN TIME _____ MAX TIME _____ ΔT

TOTAL ΔT _____

AVE ΔT _____

WORST CASE ΔT _____

14.2-Hz DATA SUMMARY

$2f_s$ = 14.236 Hz

T = 0.0702 sec 0.9T = 0.0632 sec

T/7 = 0.009026 sec (seven equal time increments)

Scan Deviation Data

Time (msec)	Rate (in./sec)	Displ (mils)	Cumulative Displ (mils)	Nominal Displ (mils)	Δ (mils)	Error % Full Scale
9 031	0.8891	8.030	8.030	8.146	-0.116	0.20
18.063	0.8922	8.058	16.088	16.293	-0.205	0.36
27.094	0.9004	8.132	24.220	24.439	-0.219	0.38
36.126	0.8995	8.124	32.344	32.585	-0.241	0.42
45.157	0.8995	8.124	40.468	40.732	-0.264	0.46
54.189	0.8997	8.126	48.594	48.878	-0.284	0.50
63.220	0.9016	8.143	56.737	57.024	-0.287	0.50

displacement = 56.737 mils nominal displacement = 57.024 mils

average rate = 0.8794 in./sec nominal rate = 0.902 in./sec

Repeatability

Scan to Scan (data from all seven increments)

Worst Case = 0 07 msec = 0.66 μr

σ = 0.0114 msec = 0.11 μr

30-Second Period (one frame)

Worst Case = 0.11 msec = 1.03 μr

Average = 0.07 msec = 0.66 μr

Scan Jitter (Scan to Scan)

Worst Case = 0.05 msec = 0.47 μr

σ = 0.028 msec = 0.26 μr

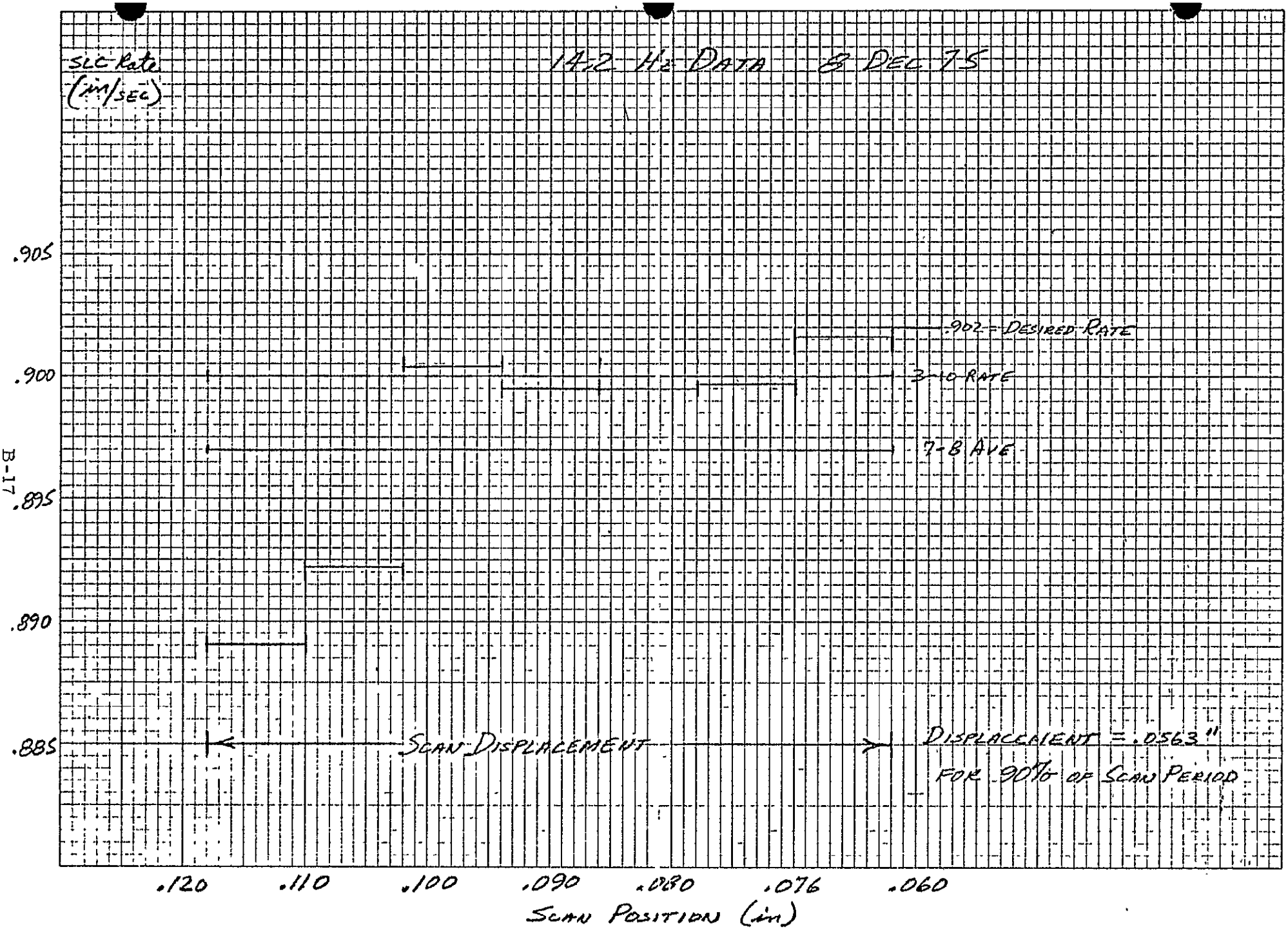
SLC Rate (in/sec)
14.2 H2 DATA 8 DEC 75
.905
.900
.895
.890
.885
.902 = DESIRED RATE
3-10 RATE
7-8 AVE
SCAN DISPLACEMENT
DISPLACEMENT = .0563"
FOR 90% OF SCAN PERIOD
.120
.110
.100
.090
.080
.076
.060
SCAN POSITION (in)

TEST DATA

SCAN LINE CORRECTOR

DATE 8 DEC 75

SCAN FREQUENCY 14.2 Hz

SCAN PERIOD .0702 SEC

OFFSET = 4.3 V

I. SCAN RATE (2 SCAN INTERVAL DATA)

DETECTORS 3 - 10

	MIN TIME (ms)	MAX TIME (ms)
13:10	62.17	62.24
	21	23
	19	23
	22	23
	22	22
	20	24
	19	24

TOTAL 871.03

AVE 62.216

(AVE TIME / (N-1) DETECTORS) $\frac{AVE}{N-1}$ 8.89 ms

Average Rate = .900

8.869 ms

SHOULD BE ~~8.9 ms ± .1 ms~~

II SCAN AMPLITUDE

SHOULD BE $\geq .902 \times .9 \times \frac{1}{f}$ (in)

detector # 7

10%	.1180
20	.1118
30	.1060
40	.0998
50	.0933
60	.0865
70	.0807
80	.0744
90	.0680
~~100~~ 99%	.0623

10% - 100% ≈ .0563"

$$.1180 - .0623 = .0557 \times \frac{90}{89} =$$

Using delayed sweep as % reader

* Moving detectors 2 & 3 through scan from 10-100%

Peak to Peak time (ms) ≈ 30 sec. SCANS

8.83	9.06
8.84	9.09
8.82	9.06
8.85	9.09

DATE 8 DEC

III SCAN LINEARITY & SCAN TO SCAN REPEATABILITY (2 SCAN INTERVALS)

DETECTOR PAIR 1-8 VERTICAL POSN .1180

TIME	MIN TIME (MS)	MAX TIME (MS)	ΔT
13:11	8.97	8.99	.02
	97	98	01
	94	98	04
	98	9 00	02
	98	01	03
	96	99	03
	01	02	01
	99	00	01
	97	99	02
	00	01	01
13:34	01	02	01
	99	00	01
	01	05	04
	00	01	01
	99	00	01
	01	03	02
	98	01	03
	02	02	00
	00	01	01
	00	02	02
TOTAL TIME	359.93	TOTAL ΔT	.35
AVE TIME	8.9983	AVE ΔT	.0175
σ	.0249		

Rate = .8891

DATE 8 DEC 75

III SCAN LINEARITY & SCAN TO SCAN REPEATABILITY (2 SCAN INTERVALS)

DETECTOR PAIR 7-8 VERTICAL POS .1100

TIME	MIN TIME (ms)	MAX TIME (ms)	ΔT
	8.96	8.99	.03
	97	98	01
	96	97	01
	98	98	00
	98	98	00
	97	98	01
	97	98	01
	95	98	03
	96	98	02
	96	98	02
	97	97	00
	94	94	00
	97	98	01
	95	97	02
	95	97	02
	95	96	01
	93	95	02
	96	97	01
	96	98	02
	94	97	03

TOTAL TIME 358.64 TOTAL ΔT .28

AVE TIME 8.966 AVE ΔT .014

σ .0143

R = .8922

DATE 8 DEC

III. SCAN LINEARITY & SCAN TO SCAN REPEATABILITY (2 SCAN INTERVALS)

DETECTOR PAIR 7-8 VERTICAL POSN .1020

TIME	MIN TIME (ms)	MAX TIME (ms)	ΔT
	8.88	8.89	.01
	88	88	00
	89	92	03
	87	89	02
	88	88	00
	89	90	01
	88	90	02
	85	87	02
	89	91	02
	89	91	02
	87	89	02
	85	86	01
	87	87	00
	89	90	01
	88	89	01
	88	89	01
	89	90	01
	86	87	01
	89	89	00
	90	90	00

TOTAL TIME 355.39 TOTAL ΔT .23

AVE TIME 8.885 AVE ΔT .0115

σ .01155

R = .9004

DATE 8 DEC

III SCAN LINEARITY & SCAN TO SCAN REPEATABILITY (2 SCAN INTERVALS)

DETECTOR PAIR 7-8 VERTICAL POSN .0940

TIME	MIN TIME (ms)	MAX TIME (ms)	ΔT
	8.89	8.90	.01
	88	88	00
	90	90	00
	88	89	01
	91	92	01
	90	91	01
	87	89	02
	90	90	00
	90	92	02
	89	92	03
13:36	89	92	03
	89	91	02
	90	91	01
	88	89	01
	87	90	03
	90	90	00
	90	90	00
	86	88	02
	88	88	00
	83	91	08

TOTAL TIME 355.75 TOTAL ΔT .31

AVE TIME 8.894 AVE ΔT .0155

σ .0178

R = .8995

DATE 8 DEC

III SCAN LINEARITY & SCAN TO SCAN REPEATABILITY (2 SCAN INTERVALS)

DETECTOR PAIR 7-8 VERTICAL POSN .0860

TIME	MIN TIME (MS)	MAX TIME (MS)	ΔT
	8.87	8.89	.02
	89	89	00
	89	91	02
	89	90	01
	91	91	00
	88	90	02
	87	88	01
	87	88	01
	91	91	00
	91	92	01
	86	88	02
	88	89	01
	87	88	01
	90	91	01
	90	92	02
	89	90	01
	88	91	03
	89	90	01
	89	92	03
	89	91	02

TOTAL TIME 355.75 TOTAL ΔT .27

AVE TIME 8.894 AVE ΔT .0135

σ .0156

R = .8995

DATE 8 DEC

III. SCAN LINEARITY & SCAN TO SCAN REPEATABILITY (2 SCAN INTERVALS)

DETECTOR PAIR 3-10 VERTICAL POSN .0360

TIME	MIN TIME (ms)	MAX TIME (ms)	ΔT
	62.23	62.25	.02
	22	24	02
	19	26	07
	21	22	01
	23	25	02
	20	23	03
	24	26	02
	20	22	02
	23	23	00
	20	25	05
	21	26	05
	23	24	01
	24	24	00
	22	22	00
	23	23	00
	23	24	01
	24	24	00
	23	23	00
	23	25	02
	20	24	04

TOTAL TIME 2489.21 TOTAL ΔT .39

AVE TIME 62.230 AVE ΔT .0195

σ .0173

R = .900

DATE 8 DEC 75

III. SCAN LINEARITY & SCAN TO SCAN REPEATABILITY (2 SCAN INTERVALS)

DETECTOR PAIR -78 VERTICAL POSN .0780

TIME	MIN TIME (ms)	MAX TIME (ms)	ΔT
	8.89	8.91	.02
	87	88	01
	87	88	01
	90	91	01
	90	91	01
13:23	91	91	00
	90	90	00
	92	92	00
	90	90	00
	89	89	00
	88	90	02
	86	88	02
	90	90	00
	87	87	00
	87	89	02
	88	88	00
	88	89	01
	88	91	03
	89	91	02
	88	90	02
TOTAL TIME	355.68	TOTAL ΔT	.20
AVE TIME	8.892	AVE ΔT	.010
σ	.0154		

$R^2 = .8997$

DATE 8 DEC 75

III. SCAN LINEARITY & SCAN TO SCAN REPEATABILITY (2 SCAN INTERVALS)

DETECTOR PAIR 7-8 VERTICAL POSN .0700

TIME	MIN TIME (ms)	MAX TIME (ms)	ΔT
13:17	8.84	8.88	.04
	88	88	00
	87	88	01
	89	89	00
	87	87	00
	88	89	01
	87	88	01
	85	88	03
	89	90	01
	85	86	01
13:38	86	87	01
	87	89	02
	89	90	01
	86	87	01
	87	87	00
	85	86	01
	87	88	01
	86	88	02
	86	88	02
	87	87	00
TOTAL TIME	354.93	TOTAL ΔT	.23
AVE TIME	8.873	AVE ΔT	.0115
σ	.0138		
	r = .9016		

DATE 3 Dec

VI SCAN JITTER (2 SCAN INTERVAL)

TIME FROM END OF SCAN PULSE TO DETECTOR # 7

VERTICAL POSITION OF ARRAY = .1180

This test is very sensitive to position setting repeatability

	MIN TIME (ms)	MAX TIME (ms)	ΔT
	7.78	7.81	.03
	75	78	.03
	75	79	.04
	79	83	.04
	78	79	.01
	67	70	.03
	68	70	.02
	66	68	.02
	67	72	.05
	66	70	.04
13:33	51	54	.03
	50	53	.03
	51	54	.03
	54	56	.03
	55	56	.02
	64	66	.02
	62	63	.01
	59	60	.01
	62	64	.02
	61	62	.01

TOTAL TIME 306.26 TOTAL ΔT .52

AVERAGE TIME 7.6565 AVERAGE ΔT .026

.0948 WORST CASE ΔT .05

RMS = .028

DATE 8 DEC 75

IV 30 SECOND REPEATABILITY #3-10

.0350

f 14.2 T .0702 # OF SCANS IN 30 SEC 426

	MIN TIME(MS)	MAX TIME(MS)	ΔT
13:46	62.19	62.30	.11
	20	29	.09
	20	26	.06
	20	27	.07
	20	26	.06
	20	27	.07
	20	27	.07
	20	28	.08
	20	26	.06
	20	26	.06

TOTAL ΔT .73

AVE ΔT .073

WORST CASE ΔT .11 MS

DATE _____

I. SCAN REPEATABILITY - 99,999 SCANS

f _____ T _____ TIME REQ FOR 99,999 SCANS _____

MIN TIME _____ MAX TIME _____ ΔT _____

TOTAL ΔT _____

AVE ΔT _____

WORST CASE ΔT _____

19.0-Hz DATA SUMMARY

$2f_s$ = 19.0 Hz

T = 0.0526 sec 0.9T = 0.0474 sec

T/6 = 0.007895 sec (six equal increments)

Scan Deviation Data

Time (msec)	Rate (in./sec)	Displ (mils)	Cumulative Displ (mils)	Nominal Displ (mils)	Δ (mils)	Error % Full Scale
7.985	0.898	7.089	7.089	7.121	-0.032	0.075
15.789	0.898	7.089	14.178	14.242	-0.064	0.150
23.684	0.902	7.121	21.299	21.363	-0.064	0.150
31.579	0.9025	7.125	28.424	28.484	-0.060	0.140
39.474	0.9025	7.125	35.549	35.605	-0.056	0.131
47.368	0 900	7.105	42.654	42.726	-0.072	0.169

displacement = 42.654 mils nominal displacement = 42.726 mils

average rate = 0.9005 in./sec nominal rate = 0.902 in./sec

Repeatability

Scan to Scan (data from all six increments)

Worst Case = 0.05 msec = 0.47 μr

σ = 0.013 msec = 0.12 μr

30-Second Period (one frame)

Worst Case = 0.08 msec = 0.75 μr

Average = 0.069 msec = 0.65 μr

Scan Jitter (Scan to Scan)

Worst Case = 0 07 msec = 0.66 μr

σ = 0.028 msec = 0.26 μr

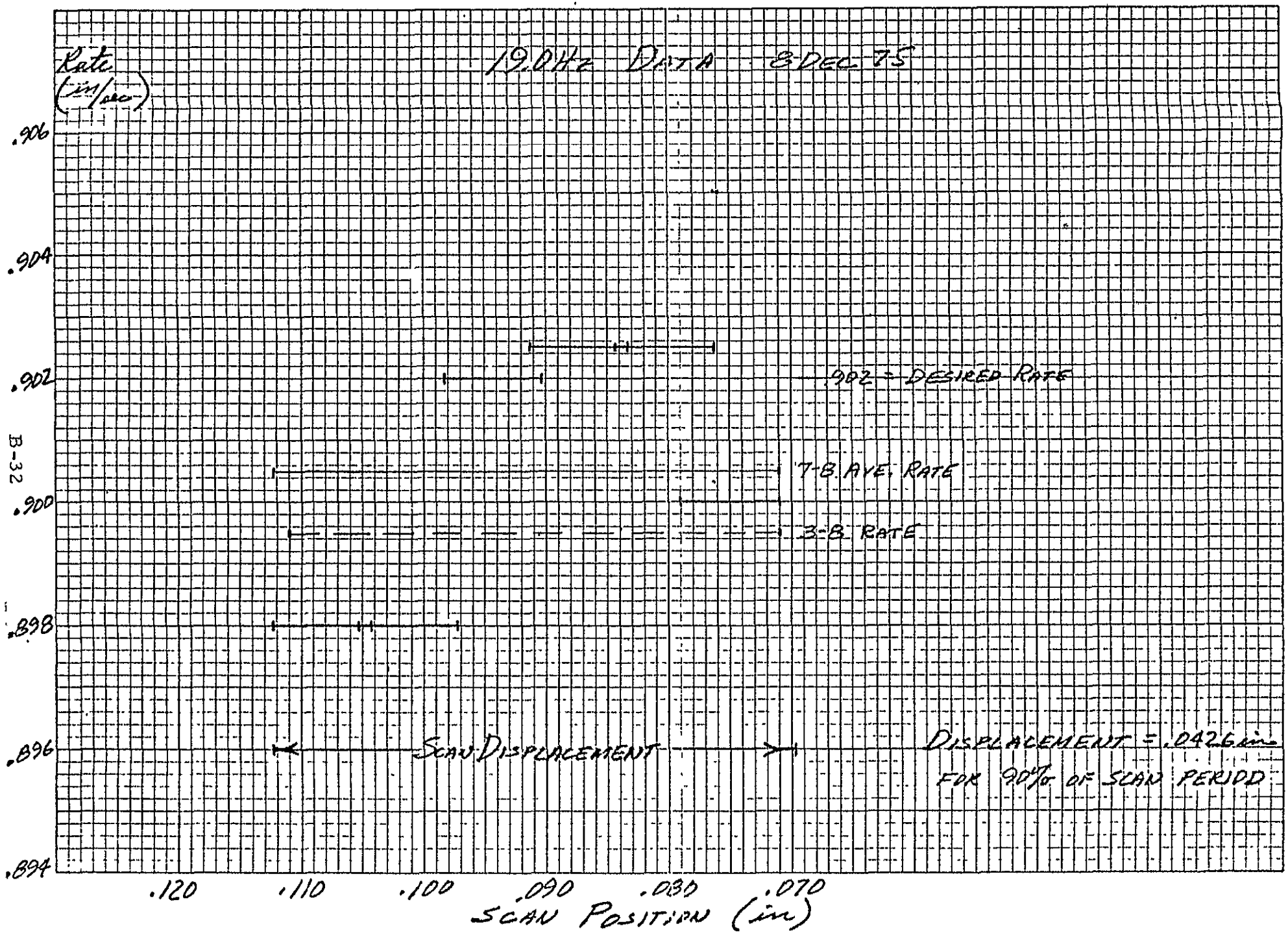
19.0Hz DATA 8 DEC 75
Rate (in/sec)
.906
.904
.902
.900
.898
.896
.894
.902 = DESIRED RATE
7-B AVE. RATE
3-B RATE
SCAN DISPLACEMENT
DISPLACEMENT = .0426 in
FOR 90% OF SCAN PERIOD
.120
.110
.100
.090
.080
.070
SCAN POSITION (in)

TEST DATA

SCAN LINE CORRECTOR

DATE 8 DEC 75

SCAN FREQUENCY 19.0Hz

SCAN PERIOD .0526 SEC

OFFSET = 3.3 ↓

1. SCAN RATE (2 SCAN INTERVAL DATA)

DETECTORS 3 - 8 @ .0790

TIME	MIN TIME (ms)	MAX TIME (ms)
14:28	44.64	44.67
	67	71
	66	69
NOMINAL SCAN TIME	66	67
SHOULD BE	65	67
44.346 ms	65	68
	64	69

TOTAL 625.35

AVE 44.668

(AVE TIME/(N-1) DETECTORS) $\frac{AVE}{N-1} = \frac{44.668}{5} = 8.93$

8.869 ms

SHOULD BE ~~8.9ms ± .1ms~~

II SCAN AMPLITUDE #7

SHOULD BE $\geq .902 \times .9 \times \frac{1}{f}$ (in)

10%	.1123	.0043
20%	.1080	.0050
30%	.1030	.0042
40%	.0988	.0048
50%	.0940	.0053
60%	.0887	.0042
70%	.0845	.0047
80%	.0798	.0048
90%	.0750	.0048 .0053
99%	.0702	

10% - 100% = .0426 in

Added test.

Worst case scan time det 7-8 slid along scan 10-100%

8.80 -	9.14 ms	.34 ms
8.83	9.15	.32 ms
8.81	9.14	.33 ms
8.84	9.16	.32 ms

$\frac{.33 \text{ ms}}{47.4 \text{ ms}} = 0.7\%$ $\frac{.32}{47.4}$

DATE 8 DEC

III. SCAN LINEARITY & SCAN TO SCAN REPEATABILITY (2 SCAN INTERVALS)

DETECTOR PAIR 7-8 VERTICAL POSN .1123

TIME	MIN TIME (MS)	MAX TIME (MS)	ΔT
14:30	8.90	8.90	.00
	90	93	.03
	89	92	.03
	90	93	.03
	91	91	.00
	89	89	.00
	90	91	.01
	91	92	.01
	91	92	.01
	92	93	.01
	90	91	.01
	88	93	.05
	92	93	.01
	91	92	.01
	91	93	.02
14:48	89	92	.03
	89	90	.01
	88	91	.03
	88	89	.01
	89	89	.00

TOTAL TIME 356.27 TOTAL ΔT .31

AVE TIME 8.9068 AVE ΔT .0155

σ .0154

Rate = .898

DATE 8 DEC

III. SCAN LINEARITY & SCAN TO SCAN REPEATABILITY (2 SCAN INTERVALS)

DETECTOR PAIR 7-8 VERTICAL POSN. .1053

TIME	MIN TIME	MAX TIME	ΔT
	91	91	00
	89	93	04
	91	91	00
	91	93	02
	91	92	01
	89	92	03
	91	92	01
	90	91	01
	90	91	01
	90	91	01
	89	90	01
	88	90	02
	89	92	03
	91	91	00
	90	91	01
14:49	88	91	03
	89	91	02
	91	92	01
	90	91	01
	89	92	03

TOTAL TIME 356.25 TOTAL ΔT .31

AVE TIME 8.906 AVE ΔT .0155

σ .0121

R = .898

DATE 8 DEC

III SCAN LINEARITY & SCAN TO SCAN REPEATABILITY (2 SCAN INTERVALS)

DETECTOR PAIR 7-8 VERTICAL POSN .0233

TIME	MIN TIME (MS)	MAX TIME (MS)	ΔT
	8.87	8.88	.01
	.86	.87	01
	85	88	03
	87	88	01
	85	87	02
	87	87	00
	84	86	02
	85	86	01
	85	88	03
	86	86	00
	86	89	03
	86	87	01
	86	87	01
	85	86	01
	85	86	01
	88	88	00
	86	87	01
	86	88	02
	88	88	00
	86	90	04

TOTAL TIME 354.66 TOTAL ΔT .29

AVE TIME 8.8665 AVE ΔT .0145

σ .0127

$R = .902$

DATE 8 DEC

III. SCAN LINEARITY & SCAN TO SCAN REPEATABILITY (2 SCAN INTERVALS)

DETECTOR PAIR 7-8 VERTICAL POSN .0913

TIME	MIN TIME (MS)	MAX TIME (MS)	ΔT
	8.86	8.87	.01
	85	88	03
	86	88	02
	84	87	03
	87	87	00
	85	88	03
	86	88	02
	86	87	01
	85	86	01
	86	88	02
	85	87	02
	85	86	01
	85	87	02
	86	86	00
	86	88	02
	86	87	01
	86	86	00
	84	87	03
	86	88	02
	85	88	03

TOTAL TIME 354.54 TOTAL ΔT .34

AVE. TIME 8.8635 AVE ΔT .017

σ .0114

R = .9025

DATE 8 DEC

III SCAN LINEARITY & SCAN TO SCAN REPEATABILITY (2 SCAN INTERVALS)

DETECTOR PAIR 7-8 VERTICAL POSN .0843

TIME	MIN TIME (ms)	MAX TIME (ms)	ΔT
	8.85	8.90	.05
	85	86	01
	84	88	04
	85	86	01
	84	89	05
	86	87	01
	86	87	01
	85	89	04
	85	88	03
	84	87	03
	87	87	00
	86	86	00
	85	86	01
	87	88	01
	87	87	00
	85	88	03
	85	87	02
	87	87	00
	86	86	00
	86	87	01

TOTAL TIME 354.56 TOTAL ΔT .36

AVE. TIME 8.8640 AVE ΔT .018

σ .0139

R = .9025

DATE 8 DEC 75

III. SCAN LINEARITY & SCAN TO SCAN REPEATABILITY (2 SCAN INTERVALS)

DETECTOR PAIR 7-8 VERTICAL POSN .0790

TIME	MIN TIME (MS)	MAX TIME (MS)	ΔT
	8.88	8.88	00
	87	89	02
	88	90	02
	89	91	02
	89	89	00
	88	92	04
	88	89	01
	89	89	00
	89	90	01
	87	89	02
	87	88	01
	88	88	00
	89	90	01
	87	91	04
	88	90	02
	88	89	01
	87	90	03
	89	90	01
	87	89	02
	88	89	01

TOTAL TIME 355.50 TOTAL ΔT .30

AVE TIME 8.8875 AVE ΔT .015

σ .0119

R = .900

DATE 8 DEC

III SCAN LINEARITY & SCAN TO SCAN REPEATABILITY (2 SCAN INTERVALS)

DETECTOR PAIR 3-8 VERTICAL POSN .0790

TIME	MIN TIME (MS)	MAX TIME (MS)	ΔT
14:34	44.63	44.65	.02
	.62	.68	06
	64	68	04
	63	65	02
	67	68	01
14:41	67	67	00
	68	68	00
	67	68	01
	64	66	02
	64	69	05
	67	69	02
	67	69	02
	66	70	04
	66	68	02
	68	68	00
14:53	67	67	00
	64	68	04
	66	67	01
	65	68	03
	66	68	02

TOTAL TIME 1786.65 TOTAL ΔT .43

AVE TIME 44.6663 AVE ΔT .0215

σ .0188

R = .8955

DATE 8 DEC

VI SCAN JITTER (2 SCAN INTERVAL)

TIME FROM END OF SCAN PULSE TO DETECTOR # 7

VERTICAL POSITION OF ARRAY = .1123

MIN TIME (MS)	MAX TIME (MS)	ΔT
5.77	5.79	.02
76	83	07
79	80	01
80	81	01
79	84	05
79	81	02
78	82	04
78	82	04
80	81	01
81	81	00
79	81	02
81	82	01
80	84	04
83	85	02
82	83	01
74	77	03
77	79	02
77	77	00
76	77	01
77	77	00

TOTAL TIME 231.89 TOTAL ΔT .43

AVERAGE TIME 5.7973 AVERAGE ΔT .0215

σ .0257 WORST CASE ΔT = .07

RMS .028

DATE 8 DEC

IV 30 SECOND REPEATABILITY

f 19.0 T .0526 SEC # OF SCANS IN 30 SEC 570

	MIN TIME (ms)	MAX TIME (ms)	ΔT
14:54	4463	4470	.07
	.63	.70	.07
	63	70	.07
	63	69	.06
	62	69	.07
	62	69	.07
	62	69	.07
	63	70	.07
	63	71	.08
	63	69	.06

TOTAL ΔT 69

AVE ΔT .069

WORST CASE ΔT .08 ms

DATE 8 DEC 75

I SCAN REPEATABILITY - 99,999 SCANS

f 19 Hz T .0526 TIME REQ FOR 99,999 SCANS 1HR 28 MIN

	MIN TIME	MAX TIME	ΔT
12/17/75	44.70	44.89	.19
12/17/75	44.63	44.86	.23
12/17/75	44.71	44.85	.14
	44.75	44.99	
	44.83	44.96	

TOTAL ΔT _____

AVE ΔT _____

WORST CASE ΔT _____

Appendix C

SiPDA MANUFACTURING DATA

DRAWING LIST

DETECTOR ASSEMBLY
SILICON PHOTODETECTOR DIODE ARRAY
(SiPDA)

NUMBER	REVISION	TITLE	SIZE	REMARKS
49733	A E03691	RESISTOR ARRAY, DEPOSITED FILM	D	RELEASED
49788	B	DIODE ARRAY, SILICON PHOTO-DETECTOR - 26 ELEMENT	2D	RELEASED
49807	A	ARTWORK DETAIL, AMP BRD	D	RELEASED
48909	A	AMP BRD - SiPDA	D	RELEASED
70373	A	FRAME ASSY, SiPDA	D	RELEASED
49812		DETECTOR ASSEMBLY, SiPDA	2D	RELEASED
70374	A	TEST FIXTURE	D	RELEASED
15483	A	PROCUREMENT SPECIFICATION, SILICON PHOTODETECTOR DIODE ARRAY	A	RELEASED
		ASSEMBLY PROCEDURE FOR THE SiPDA		

Note:

Drawings above have been furnished with earlier reports. Photo reduced copies will be included in the final report.

MODEL EFFECTIVITY	REVISIONS			
	SYM	DESCRIPTION	DATE	APPROVED
	A	INITIAL RELEASE	20 MAR 1975	

REVISION STATUS THIS PRINT
NOT MAINTAINED AFTER
JAN 1 91976
DO NOT USE THIS PRINT
UNLESS YOUR UPDEP OF INSTRUCTIONS
SPECIFY THE REVISION LEVEL SHOWN

CONTRACT NO.

PREPARED	2/10/75
CHECKED	3/20/75
APPROVED	3/20/75
APPROVED	3/20/75

SANTA BARBARA RESEARCH CENTER
A Subsidiary of Hughes Aircraft Company
GOLETA, CALIFORNIA

TITLE

PROCUREMENT SPECIFICATION
SILICON PHOTODETECTOR DIODE ARRAY

SIZE	CODE IDENT NO	NUMBER
A	11323	15483

SCALE —— | SHEET 1 OF 10

FORM NO 0122-3 (3-69)

PROJECT 2756

1. SCOPE

1.1 Scope. This specification defines the minimum technical requirements for the design, fabrication, and testing of a silicon photodetector diode array. The array is used to detect light levels at various wavelengths in a high-reliability space application.

2. APPLICABLE DOCUMENTS

2.1 The following documents, of the issue in effect on the date of request for quotation, form a part of this specification to the extent specified herein. If any conflict between this document and referenced documents exists, this document shall take precedence.

SPECIFICATIONS

Military

MIL-C-45662A	Calibration System Requirements

STANDARDS

Military

MIL-STD-202D	Test Methods for Electronic and Electrical Component Parts

DRAWINGS

SBRC

Specification Control Drawing SCD 29788	Silicon Photodetector Diode Array

3.0 REQUIREMENTS

3.1 Performance Requirements. Each individual photodiode element of the array shall meet the following performance requirements when operated at any reverse-bias voltage between 10 mV and 300 mV.

a. Responsivity - The minimum responsivity shall be as tabulated here:

Wavelength Band (μm)	0.5-0.6	0.6-0.7	0.7-0.8	0.8-1.1
Band Average Responsivity (A/W)	0.27	0.34	0.39	0.24

b. Dark Resistance - A minimum of 2×10^{9} ohm at 25°C (dark resistance is defined as the slope of the voltage current curv

c. Dark Current - A maximum of 3×10^{-11} A at 25°C.

d. Noise Current - A maximum of 4.5×10^{-15} $A/Hz^{1/2}$ at 25°C for a bandwidth of 2 Hz to 150 kHz. The increase in noise current with temperature shall be less than 6% per °C.

e. Sensitivity Pattern - At and beyond 0.0005 inch outside the sensitive area as shown on the drawing, responsivity shall be less than 5% of the peak responsivity. Within the sensitive area, the responsivity shall be constant within ± 5%.

f. Cross-talk - A non-illuminated photodiode element shall produce less than 0.5% of the signal produced by any other illuminated element.

g. Capacitance - The total capacitance per element shall be less than 1pF.

h. Response Time - The photocurrent rise and fall times shall each be 0.5×10^{-6} seconds maximum.

3.2 Environmental Requirements. The Photodiode shall operate within specification requirements during or after (as later specified) exposure to the following environments:

a. Temperature: 0 to +45°C

b. Pressure: Ground Ambient to 10^{-8} Torr

c. Vibration: Sinusoidal: 20 g's 5-2000 Hz
0.12 inch DA limited

Random:

20-50 Hz	0.1 G^2/Hz
50-80 Hz	+12 db/octave
80-900 Hz	0.6 G^2/Hz
900-2000 Hz	-6 db/octave

3.3 Mechanical Requirements

a. Dimensions - As specified on SBRC Specification Control Drawing.

b. Interconnect Pad - To be compatible with 0.001 in. connecting wires of Al or Au, bonded by ultrasonic or thermal compression means.

c. Optical Mask - If the optional optical mask is used to delineate sensitive area, the layout on the silicon wafer should be compatible with an f/6 optical system.

d. Cross-talk Test Element - One normally processed sensitive area, except that it shall be covered by an opaque layer, to serve as a detector for cross-talk from the neighboring normal uncovered elements.

e. Channel Stops - Acceptable between elements and/or surrounding the array to reduce cross-talk or stray sensitivity.

3.4 General Design Requirements

3.4.1 Useful Life. The Photodiode shall have a minimum useful life of 36 months which may include up to 24 months storage.

3.4.2 Identification and Marking. Each device package or shipping container shall be clearly marked with the manufacturer's name or registered trademark, and supplier's part number, the individual model serial number, and SBRC Specification Control Drawing number, and type number.

3.4.3 Cleanliness. The Photodiode shall have the surfaces clean and free of oil, grease, or particle contamination.

3.4.4 Workmanship. The Photodiode shall not exhibit any of the following defects except as noted when examined under a magnification of 20X:

a. Damaged or defective welding.

b. Twisted or deformed leads or terminations.

c. Flaking of lead plating or coating.

d. Evidence of burned or offset lead bonds to wafer.

e. Evidence of weld splash.

f. Particles of metal or silicon (including potentially loose particles) which exceed 10 micrometers in a major dimension.

g. Lint or other soft non-conducting particles which exceed 10 micrometers in a major dimension.

h. A bond which has less than 50% placement on the bonding pad.

i. The maximum allowable number of particles which do not exceed 10 micrometers in a major dimension shall be three (3). This applies to both types of particles as specified in f. and g. above.

4. PERFORMANCE ASSURANCE PROVISIONS

4.1 Verification Requirements. Devices supplied in conformance to this specification shall meet all requirements specified in Section 3 and 4. The lack of a specific Performance Assurance Provision designated to specific Section 3 requirement shall not relieve the product of meeting that requirement. Verification will be classified into Acceptance Verifications and Qualification Verifications. Performing Acceptance Verifications shall be the responsibility of the supplier, while Qualification will be the responsibility of SBRC.

4.1.1 Acceptance Verification Data and Test Procedure. Verification data shall be comprised of complete records of all inspections, analyses, and demonstrations performed by the supplier or his designated agency. The format for presentation of this data by the supplier shall be submitted to and approved by SBRC. All verification data furnished in accordance with this specification shall be identified by means of the serial number assigned to the device.

Data shall be reported in a manner that will facilitate following the behavior of each specimen from the beginning to the end of each inspection, analysis, or demonstration (test). This shall include explanatory comments which will aid in evaluating any unusual or abnormal events that may have occurred during the demonstrations (tests).

Two (2) copies of the Acceptance Verification Data shall be submitted to SBRC with the component parts.

An acceptance test procedure shall be submitted for approval to SBRC at least 14 days prior to start of test.

4.1.2 Part Acceptance. Prior to final acceptance of each deliverable unit, SBRC may perform such verifications as may be deemed necessary to confirm the acceptance verification data furnished by the supplier.

4.1.3 Acceptance Verifications. Acceptance Verifications are those demonstrations, analyses, and inspections that are imposed on every unit that the supplier builds. The supplier shall certify that the acceptance verifications have been performed and that all units meet the applicable acceptance and performance requirements. Failure to pass any of these verifications will be cause for rejection of the unit involved. A failure analysis shall be performed by the supplier to determine the failure under the complete cognizance of SBRC.

4.1.3.1 Inspection. A visual/mechanical inspection shall be performed to determine that the following Section 3 requirements have been met:

a. 3.3a Dimensions

b. 3.4.2 Identification and Marking

c. 3.4.3 Cleanliness

d. 3.4.4 Workmanship

4.1.3.2 Analysis. A review of the engineering documents (i.e., specifications, drawings, schematics, past history records) shall be made to verify the following Section 3 requirements:

a. 3.4.1 Useful Life

4.1.3.3 Acceptance Demonstrations. Demonstrations shall consist of tests used to verify Section 3 requirements. The demonstrations shall be performed by the supplier on 100% of the units and shall consist of functional and environmental tests.

4.1.3.3.1 Acceptance Functional Tests. Functional tests shall be performed at standard test conditions and shall be performed prior to environmental tests.

a. 3.1a Responsivity

b. 3.1b Dark Resistance

c. 3.1c Dark Current

d. 3.1d Noise Current

e. 3.1e Sensitivity Pattern

f. 3.1f Cross-talk

g. 3.1g Capacitance

h. 3.1h Response Time

4.1.3.3.2 Acceptance Environmental Test. Environmental tests shall be performed in the following order and as specified in Table I.

a. High Temperature Burn-in

b. Temperature Cycling

c. Sinusoidal Vibration

4.1.3.3.2.1 High Temperature Burn-in. The device shall be burned in for a period of 168^{+12}_{-0} hours at an ambient temperature of 55°C in the dark condition, and with 0.3 volts reverse bias applied. Dark current shall be monitored at 0, 24, 96, and 168 hours at laboratory ambient temperature plus or minus 2 hours. The dark current shall not increase by more than 20×10^{-12} amps from its initial reading. The four hour holding time at each temperature shall be considered a minimum time required at temperature. The requirements, as listed in Table I, Column B, shall be verified.

4.1.3.3.2.2 Temperature Cycling. The device shall be placed in a temperature chamber and subjected to the following:

Four cycles of 4 hours at each temperature extreme of 0°C and +45°C. Start and end temperatures shall be +25°C; changes from one temperature to another shall be made as rapidly as possible.

The requirements, as listed in Table I, Column C, shall be verified.

4.1.3.3.2.3 Sinusoidal Vibration. The Photodiode shall be subjected to the following conditions in each of the three mutually perpendicular axes:

Frequency Range (Hz)	Amplitude (g's 0 to peak)
5-2000	20.0

Amplitude limited to 0.12 inch DA. Sweep rate = 2 octaves/minute.

The requirements, as listed in Table I, Column D, shall be verified.

4.1.4 Qualification Verifications. TBD.

TABLE I

ACCEPTANCE FUNCTIONAL AND ENVIRONMENTAL TESTS

A. Functional

B. High Temperature Burn In

C. Temperature Cycling

D. Sinusoidal Vibration

1. Measure and Record Before Test

2. Measure and Record During Test

3. Measure and Record After Test

NOTE: The post-test of one environment may serve as the pre-test of the next environment if no more than 72 hours have elapsed.

SECTION 3	A	B	C	D
REQUIREMENTS	1 2 3	1 2 3	1 2 3	1 2 3

TBD

4.2 Quality Assurance Provisions

4.2.1 Inspection Responsibility. Unless otherwise specified, the manufacturer shall be responsible for the performance of all inspection requirements prior to submission for Santa Barbara Research Center inspection and acceptance. Inspection records of examinations and tests shall be kept complete and shall be available to SBRC. All inspection and test records shall be traceable to each device by means of the serial number (Section 3.4.2). The supplier shall maintain an inspection system which meets the intent of the Purchase Order Quality Attachments.

4.2.2 Acceptance and Rejection

4.2.2.1 Acceptance. The manufacturer shall understand that final acceptance of the items covered by this specification is at Santa Barbara Research Center, regardless of whether or not the items are source inspected by SBRC.

4.2.2.2 Rejection. Any assembly which fails to meet the physical, environmental, and performance requirements of this specification may be rejected and returned to the manufacturer.

4.2.3 Traceability. The Serial Number (paragraph 3.4.2) shall be supported by records which provide positive information concerning traceability of all materials and processes used in the fabrication of each device.

5. PREPARATION FOR DELIVERY

5.1 Packaging and Marking. Each device shall be packaged in such a manner as to insure that the device as packaged for transportation shall see no environments greater than those specified in paragraph 3.2 during all phases of transportation and handling.

Both the unit package and the large external shipping container shall be clearly marked with the supplier's name or registered trademark, the supplier's part number, the lot identification or data code, and the individual model serial number.

Unit packages which are received by SBRC in a damaged or broken condition will be returned to the supplier as unacceptable. Parts submitted for purposes other than for use, such as failed specimens that are being shipped to SBRC for further study, shall be packaged in accordance with the previous paragraphs but with the following additional marking: "FAILED SPECIMENS - DO NOT USE."

6. NOTES

6.1 Definitions

6.1.1 SBRC. This is to identify the Santa Barbara Research Center, Goleta, California 93017.

6.1.2 Supplier. This is to identify a manufacturer supplying a specific device being procurred by Santa Barbara Research Center to this specification.

6.1.3 Operational. Input power applied.

6.1.4 Non-Operational. No input power applied.

ASSEMBLY PROCEDURE FOR

THE SILICON PHOTODETECTOR DIODE ARRAY (SiPDA),

PROJECT 2798

DRAWING NUMBER 49812

ASSEMBLY SERIAL NUMBER _____

SiPDA Vendor _____

Release Date 6 Aug 75

By W Mast

Approval J L Engel

TABLE OF CONTENTS

1.0 SCOPE

To perform all bonding, welding, assembly and testing functions required to evaluate the integrity of the SiPDA design

2.0 PROCEDURE

Record all information pertinent to the assembly operations in the text of this procedure. Provide separate copies of the procedure for each SiPDA assembly.

NOTE: The sequence of events in the following have been indicated for specific reasons. Variations may occur with the approval of the cognizant engineer.

2.1 Kitting. Obtain all items noted in the list of materials of 49812. Record serial numbers.

49788, 26 Element SiPDA

Vendor _____ S/N _____

		A1 S/N		A2 S/N
49733, Resistor Array		_____		_____
49809, Amplifier Board		_____		_____
BF805, Transistor Chip	1)	_____	4)	_____
	2)	_____	5)	_____
	3)	_____		

2.2 Cleaning

2.2.1 Clean and inspect all items including fixtures and mounting hardware.

2.2.2 The SiPDA, Resistor Array, Amplifier Board and Transistor Chips may be cleaned prior to installation to reduce handling. Use only acetone followed by methanol.

Clean all other items using isopropyl alcohol.

NOTE: Anti-static conditions must be maintained at all times. Handle all items after cleaning with clean tools and white gloves.

Bonding Operation

Place the frame assembly 70373 in the test fixture 70374 with the array mounting surface in the number 1 position (facing up).

Mix a portion of the insulating epoxy H54, 1 gram part A to 2 drops part B. Lightly coat the array mounting surface on the frame and the side wiring surfaces shown on the drawing. (Bond Line .001-.004) Retain the balance for inspection.

Record the Mix Number _____

Carefully place the SiPDA on the frame and locate per the drawing requirements. Note dimensions and marker location. Move the array from side to side to ensure a uniform bond line. Use mylar tape on the ends only to locate during cure cycle.

Cure the bonding material at 80°C ± 5°C for 90 minutes.

Inspect array location, bonding material and record data.

Location: Center line markers within _____

.0945 - .0955 within _____

Bonding Material _____

Repeat steps 2.3.2 thru 2.3.5 for bonding the A1 and A2 amplifier boards. Place the frame assembly with the array in the number 2 position for bonding the A1 board; in the number 3 position for bonding the A2 board.

NOTE: Align the amplifier board input traces with the array output traces.

		A1	A2
2.3.7	Inspect Alignment	_____	_____
	Bonding Material	_____	_____

2.4 Array to Amplifier Board Connection

2.4.1 Place the array or amplifier boards in a position for welding.

NOTE: Various welding methods may be used and will be determined by establishing weld schedules. Use spare array samples and amplifier boards for determining these schedules.

Record sample pull tests _____

2.4.2 Weld leads to the array. Record Data as required:

Welding Method _____

Time _____

Current _____

Volts _____

Pressure _____

2.4.3 Weld leads to the amplifier board.

Welding Method _____

Time _____

Current _____

Volts _____

Pressure _____

		A1	A2
2.4.4	Inspect Wire length	_____	_____
	Shorts	_____	_____
	Weld Joints	_____	_____

2.5 Test Array per test procedure.

2.6 Output Wiring

2.6.1 Remove enough of the outer jacket from the multiconductor cable to allow the wiring of the A1 and A2 boards. Separate the wire sets, 5 and 10 conductor, and route to their respective boards per the wiring table. Fit the conductors, cut to length, strip and tin (approximately .050 minimum tinned length). Strip, tin and identify each conductor at the opposite end by wire number for subsequent installation on the vector board. Solder in place using minimum solder. Carefully remove all flux residue.

NOTE: 1) Caution - Solder must not contaminate the weld pads at the end of every other trace. Cover pads with mylar tape if required.

2) Mylar tape and spot ties may be used to hold the wires in position.

3) Use spare amplifier boards to determine soldering techniques.

2.7 Wiring and Component Bonding

Caution: Weld pad areas must not be contaminated by bonding materials. Clean immediately if contamination occurs.

2.7.1 Prepare a portion of the insulating epoxy H54. 1 gram part A to 2 drops part B.

Record the mix number _____

2.7.2 Coat all conductors and solder joints with a thin film of the epoxy.

2.7.3 Apply a thin film of the mix to the back side of the resistor array 49733. Place the array as shown on the drawing.

Retain the balance of the bonding material for inspection.

2.7.4 Prepare a portion of the conductive epoxy H20E by weight. Part A = Part B.

Record the mix number _____

2.7.5 Apply a minimum amount to the pad area or to the back of the transistor. Place the transistor locating the orientation mark as shown on the drawing. Use minimum pressure on the transistor to reduce the bond line between the chip and the pad area.

NOTE: 1) A minimum length of .005 at the end of the pad area shall be free of the epoxy for welding purposes.

2) Use spare amplifier boards and chips for developing placement techniques and for determining the amount of epoxy.

Retain the balance of the mix for inspection.

2.7.6 Cure both residual bonding samples and the assembly at 80°C ± 5°C for 90 minutes.

2.7.7 Inspect and record:

	A1	A2
Transistor orientation mark	_____	_____
Shorts between conductors	_____	_____
Bonding materials on weld pads	_____	_____
	H54	H20E
Bonding Material Samples	_____	_____

2.7.8 Repeat operations 2.6 thru 2.7.7 for the opposite board. Record data at 2.7.7.

2.8 Vector Board Wiring

2.8.1 Prepare the vector board including the flea clips and mount on the fixture as required. Strip the outer jacket from the free end of the cable leaving the 1.50 inch jacketed length specified on the drawing. Route the conductors as shown on sheet 1 and wire per the wiring table.

2.8.2 Inspection

	A1	A2	A3
Wiring per Table	_____	_____	_____
Shorts	_____	_____	_____

2.9 Component Welding

2.9.1 Weld all connections to the transistors and resistors on the A1 and A2 boards. Establish weld schedules using spare components and amplifier boards.

Record Data:	Amp. Board	Transistors	Resistors
Welding Method	_____	_____	_____
Sample Pull Tests	_____	_____	_____
Time	_____	_____	_____
Current	_____	_____	_____
Voltage	_____	_____	_____
Pressure	_____	_____	_____

2.9.2 Inspect

	A1	A2
Source/Drain Wiring	_____	_____
Resistor Array	_____	_____
Shorts	_____	_____
Wire Lengths	_____	_____

3.0 TEST PER TEST PLAN

4.0 POST TEST PROCEDURE

4.1 Conformal Coating

4.1.1 Prepare a portion of the insulating epoxy H54. 1 gram part A to 2 drops part B. Record the mix number _____.

4.1.2 Carefully apply a thin film of the mix to all connecting wires to the detector array, transistors and resistors. Coat also all board input traces and used weld pads. This applies to the A2 board only.

Retain the residual bonding material for inspection.

Caution: Coat the detector array wires only on the surface adjacent to A2 board.

4.1.3 Cure the assembly and the residual sample at $80^{\circ}C \pm 5^{\circ}C$ for 90 minutes.

4.1.4 Inspect

Wiring Shorts	_____
Bonding Material Sample	_____
Bonding Material on Wires and Welds	_____

5.0 TEST PER TEST PLAN

EPOXY TECHNOLOGY INC.

EPO-TEK H54

Insulating Epoxy

SPECIFICATIONS

NUMBER OF COMPONENTS

Two

MIXING RATIO — PARTS BY WEIGHT

Part "A"	10
Part "B" (hardener)	1

A convenient way to mix EPO-TEK H54 in small quantities is as follows:

Part "A"	1 gram
Part "B" (hardener)	2 drops

NOTE: Contents of Part "A" has a tendency to show some crystallization with time. To restore to original smooth thixotropic consistency place container "A" (without cap) in 100°C oven for 10 minutes. Remove from oven, stir thoroughly to get a uniform smooth consistency and cool to room temperature before adding Part "B" (hardener).

CURING SCHEDULE

(Bond line temperature-use anyone of the following)

150°C	5 minutes
120°C	15 minutes
100°C	30 minutes

ELECTRICAL PROPERTIES

Dielectric Strength	480 V/mil
Dielectric Constant (1 megacycle)	3.0
Volume Resistivity	5.0×10^{15} ohm-cm
Dissipation Factor (1 megacycle)	0.001

LAP SHEAR STRENGTH — 3100 psi (aluminum to aluminum)

POT LIFE — 4 hours

SHELF LIFE

One year when stored at room temperature. DO NOT REFRIGERATE

EPO-TEK H54 is a two component, unfilled epoxy for bonding or coating applications where a thin film with high insulating resistance is required, particularly at elevated temperatures. Applications for EPO-TEK H54 include bonding of active and passive components, bonding large substrates in IC packages, crossovers or coating closely spaced conductors.

EPO-TEK H54 is a 100% solids, soft, smooth thixotropic paste characterized by outstanding high temperature properties and excellent solvent, chemical and moisture resistance. Other important characteristics include a good pot life and fast curing at relatively low temperatures. EPO-TEK H54 was designed to be used in the 300°C to 400°C range for wire bonding operations.

A unique feature of EPO-TEK H54 is the built-in color indicator when the product is cured. The color changes from amber to deep red, depending upon the curing conditions. It is normal for EPO-TEK H54 to turn a very deep red when subjected to wire bonding temperatures.

EPO-TEK H54 can be applied by brush, spatula, silk screen, hypodermic needle or commercial dispensing equipment.

AVAILABILITY: $15.00 per 3 oz trial evaluation kit, FOB Watertown, Mass. Production price schedule available on request

EPOXY TECHNOLOGY INC. 65 GROVE STREET, WATERTOWN, MASSACHUSETTS 02172 (617) 926-0136

EPO-TEK H20E

Electrically Conductive, Silver Epoxy

SPECIFICATIONS

MIXING RATIO PARTS BY VOLUME (or wt.)
Part "A" (epoxy resin and silver powder) 1
Part "B" (hardener and silver powder) 1

NOTE: Mix contents of Part "A" container and contents of Part "B" (hardener) container thoroughly before mixing the two together.

CURING SCHEDULE
(minimum bond line temperature)

175°C	45 seconds
150°C	5 minutes
120°C	15 minutes
80°C	90 minutes
50°C	12 hours

PHYSICAL PROPERTIES
Specific Gravity 2.6
Color ..... Silver - Bright
Consistency ...Very soft, smooth, thixotropic paste
Lap Shear Strength ..... 1500 psi
Pass Thermal Shock — Gold backed silicon chips bonded to a gold metallized ceramic substrate will pass: 5 cycles from —62°F to +125°F
Bonded Silicon Chips (100 x 100 mils) when placed on a 300 - 340°C heat column will resist a shear force of 16 oz.

THERMAL RESISTANCE. (Junction to Case)
TO-18 package with nickel-gold metallized 20 x 20 mil chips and bonded with EPO-TEK H20E (2 mils thick)
Eutectic Die attach ..... 4.8 to 5.3°C/watt
EPO-TEK H20E ..... 6.7 to 7.0°C/watt

ELECTRICAL PROPERTIES
Volume Resistivity (rigid specification)
0.0001 to 0.0004 ohm-cm

SILICON VARACTOR

INITIAL	2 WEEKS @ 125°C	72 HOURS @ 175°C
C_j at 0 volts = 0.20 — 0.85pF	No change	No Change
R_s at 20 ma = 3.5 ohms	3.8 ohms	4.5 ohms
B_v at 10 μa = 6V — 50V max.	No change	No change

SCHOTTKY DIODE

INITIAL	2 WEEKS @ 200°C
C_j 1pF (typical)	
$V_b \geq$ 5V @ 10 μa	4.8 V @ 10 μa
$V_f \leq$ 0.4V @ 1 ma	0.32 V @ 1 ma

POT LIFE ..... 4 days

SHELF LIFE
Two years when stored at room temperature.
REFRIGERATION NOT REQUIRED

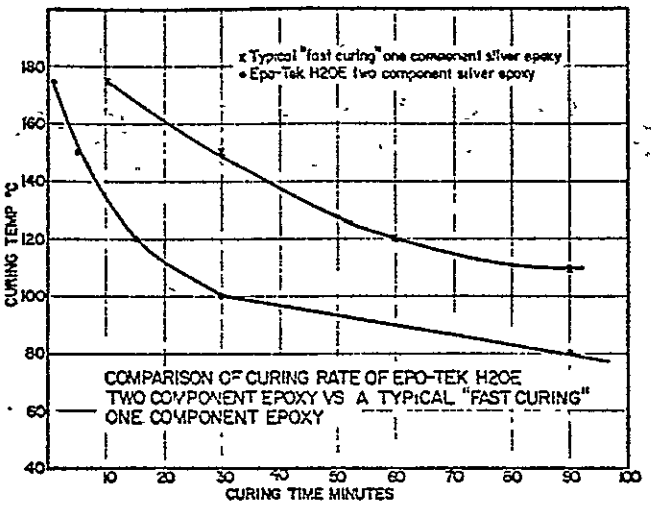

EPO-TEK H20E is a 100% solids, two component silver filled epoxy designed specifically for chip bonding in microelectronic and optoelectronic applications.

EPO-TEK H20E is a very soft, smooth, thixotropic paste. The excellent handling characteristics and the extremely long pot life at room temperatures for this unique two component system is obtained without the use of solvents. In addition to the high electrical conductivity, the short curing cycles, and the high and proven reliability of using a pure silver powder (no alloys used), EPO-TEK H20E is extremely simple to use. The pure silver powder is dispersed in both the resin and hardener and the system is designed so that it can be used in a convenient 1:1 mixing ratio by volume that is non-critical. In fact the EPO-TEK H20E is the easiest-to-use two component silver epoxy that has ever been developed for the microelectronic industry.

EPO-TEK H20E is especially recommended for use in high speed epoxy chip bonding systems where very fast cures are highly desirable. This cannot be obtained with single component systems. Because EPO-TEK H20E can be cured very rapidly it is an excellent material to use for making fast circuit repairs. EPO-TEK H20E can be screen printed, machine dispensed or stamped.

EPO-TEK H20E is designed to be used in the 300°C to 400°C range for wire bonding operations.

AVAILABILITY: 1 oz trial evaluation kit, price on request, FOB Watertown, Mass. Production price schedule available on request.

When placing an order please specify whether EPO TEK H20E is to be used by volume or weight.

EPOXY TECHNOLOGY INC. 65 GROVE STREET, WATERTOWN, MASSACHUSETTS 02172 (617) 926-0136

APPENDIX D – DATA PACKAGE 1
"PROCEDURAL TEST DATA, SMA WITH END BUMPERS"

INTRODUCTION

The attached data package contains the data collected and reduced in accordance with test procedure TP 31891-350 for the Breadboard Scan Mirror Assembly configuration. This consists of a 16 x 19 inch flight type mirror and end bumpers. Diagnostic test data on a previous configuration using the flight mirror and back-mounted bumpers is discussed in the body of the report and is compiled as data package 2, Appendix E. In the course of studying mirror performance, it was found that the ambient air significantly affects performance. In an attempt to minimize these effects, the scan mirror has been operated in a helium filled tent. Certain of the procedural tests, however, do not lend themselves to implementation in helium because of need for operator interaction with the test setup. Consequently, this data package contains data for both conditions, air and helium. The preface discussion of each test will denote the test conditions.

Several of the tests originally called for by the test procedure such as startup time and scan center, are not critical to the present design approach and are not included in these tests.

In addition to the equipment described in Section 3.0 of the test procedure, a HP9820A calculator was used for data collection and partial, on-line reduction of the data.

All of the data collected as part of the formal procedure was taken at a nominal scan period of 110.2475 msec (9.6 Hz). Notations on data sheets, however, indicate 9.2 Hz because the reference frequency was derived from a 920 kHz generator in conjunction with a nominal 10^5 frequency divider.

The performance most significantly affected by scan frequency is cross axis motion. Data for this parameter as a function of frequency is contained in the log books.

TEST SETUP

The basic scan pattern and test setup are as described by Figures 1 and 2 in the test procedure (reproduced in this report). The upper and lower split diodes are located to be approximately coincident with bumper impact. The electrical output from each split diode is processed to provide a separate output for each direction of crossing. These outputs are used to trigger electronic counters for period and time interval measurements.

Commercial pulse generators employed in earlier tests for the reference clock were found to have excessive period jitter, that would degrade scan repeatability. In order to alleviate this limitation, an HP8660B Synthesized Signal Generator was used to provide a variable yet stable frequency source of several hundred kilohertz that was then reduced by a 10^5 divider to the desired reference frequencies.

It was determined that the time interval measurement uncertainty for the setup was less than 0.2 μsec. This uncertainty was determined by time interval measurements made over very short intervals for which scan deviations would be a small fraction of a microsecond.

TEST RESULTS

Scan Frequency (4.1.2)* and Turn Around Time (4.1.4)

Data Sheet A describes the results of measurements of these two parameters for operation in helium. The most significant effect of helium operation relative to these parameters was a reduction of the scan period standard deviation (scan repeatability) by a factor of about 2 from air operation. Turnaround time deviation was not affected by the differences between air and helium operation as would be expected because of the high deceleration and acceleration forces operating during this time.

*Parenthetical numbers refer to Test Procedure paragraphs.

The difference in nominal value of the two turn around times is primarily due to differences in the placement of the split diodes relative to bumper contact. It is the variation of this value that is of significance.

Although neither of these parameters is particularly significant by itself, the small deviations observed are indicative of highly repeatable active scan times, that will be shown directly in subsequent data.

Scan Linearity (4.1.6)

Scan linearity is defined as the scan speed at a particularly along-scan angle expressed as a percent of the average speed taken over the entire active scan angle. A major limitation to the accuracy of this measurement lies in the inability, with the existing techniques used, the precisely determine the physical dimension between photodiode crossings for the several locations of the moveable diode.

Theoretically, scan linearity is the deviation of a sine wave at the mirror's natural frequency over a period of time corresponding to the active scan time. A discussion of this factor and computation of theoretical scan linearity is contained in the final technical report.

Figures 9 and 10 of the test procedure (reproduced herein) define the position and direction designations used in this measurement.

Data sheets B, C, and D describe the five moveable diode locations used in this measurement and the average partial and full scan times measured for each scan direction at each location.

Data sheet E presents the average partial to full scan time ratios for each of these locations and the standard deviation of this ratio for a sampling of ten measurements. The raw data used for these computations is contained with the data sheets for along scan repeatability.

The average time interval ratios for each location and direction contained in data sheet E and the physical dimension ratio for each location are used to compute a cubic polynominal equation that describes the position variation as a function of scan time by a least squares fit. This equation is then differentiated to provide a description of the relative scan velocity as a function of scan time.

Data sheet F describes the results of these computations and data sheet G presents a plot of relative to average rate scan rate ($\dot{\theta}$) as function of scan position for each scan direction. It may be noted that the results agree very well with the theoretical analyses (due to the flex pivot centering torque) despite the limitations associated with the physical dimension measurements.

Along Scan Repeatability (4.1.9)

This parameter provides a measure of the scan length repeatability that would exist subsequent to normalizing partial scans to their associated full scan time. As described in Section 4.1.9 of the test procedure, the value

$$\left[\left(\frac{T_2 - T_1}{T_3 - T_1}\right) - \left(\frac{T_2 - T_1}{T_3 - T_1}\right)_{AVE}\right] \theta_{Total}$$

is evaluated for the data collected at each of the locations used in the linearity test. The result of these evaluations is presented in data sheets K, L, and M. Attached to each data sheet is the raw scan data and a computer analysis performed on a sampling of ten scans. This data was taken in air.

Examination of the data tends to indicate greater scan length deviations for forward scan elements that occur right after turn around than for the reverse scan elements of same length that occur as the scan is approaching turn around. It is quite obvious that the existance of air disturbs the along-scan repeatability. (See final report for results in a helium atmosphere.)

Cross Scan Motion

The following cross scan motion measurements were obtained with the five bounce technique that provides a ten fold magnification of mirror cross axis motion. The laser beam traverses a azimuth position sensitive detector that produces a pulse amplitude proportional to the distance between center and crossing location. A scope photo is taken of the pulses produced by a series of these detector crossings. Section 4.2 of the test procedure

provides a detailed description of this technique, including calibration and data reduction.

Data sheets "T" and "W" for five locations (attached) present the scope photots, location information, and photo derived data.

The resultant computations of mean and rms deviations between forward and reverse scan position are presented in data sheet "2". This data is then plotted in data sheet "AA".

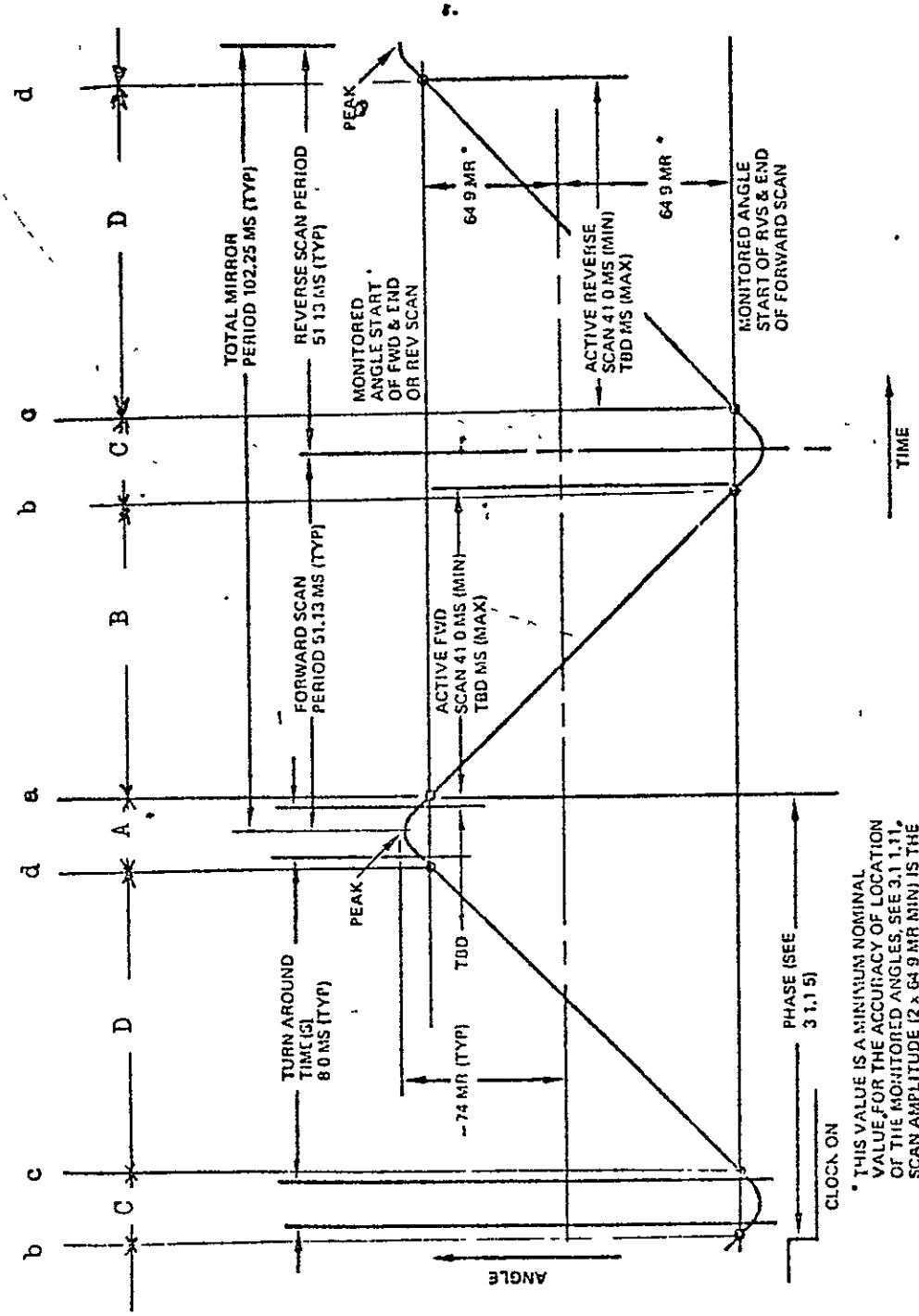

Figure 1. TM Mirror Scan Profile

TEST PROCEDURE SCAN MIRROR	BREADBOARD THEMATIC MAPPER	HUGHES AIRCRAFT CO. CULVER CITY, CALIF. CODE IDENT NO. 82577	8 SH NO.	REV LTR	TP 31891-350 NUMBER

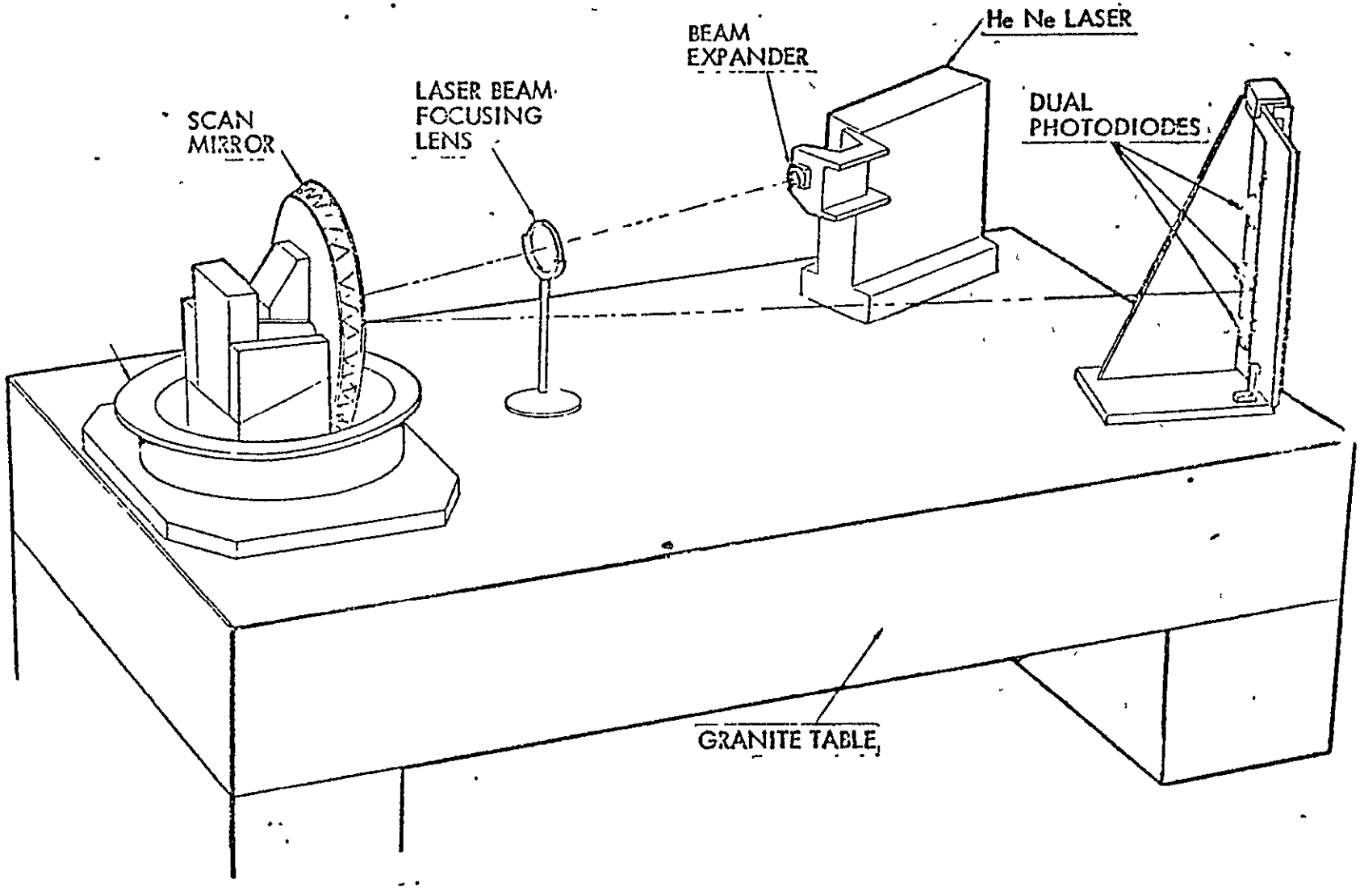

Figure 2. Test Set-Up For Along Scan Measurements Optical Components

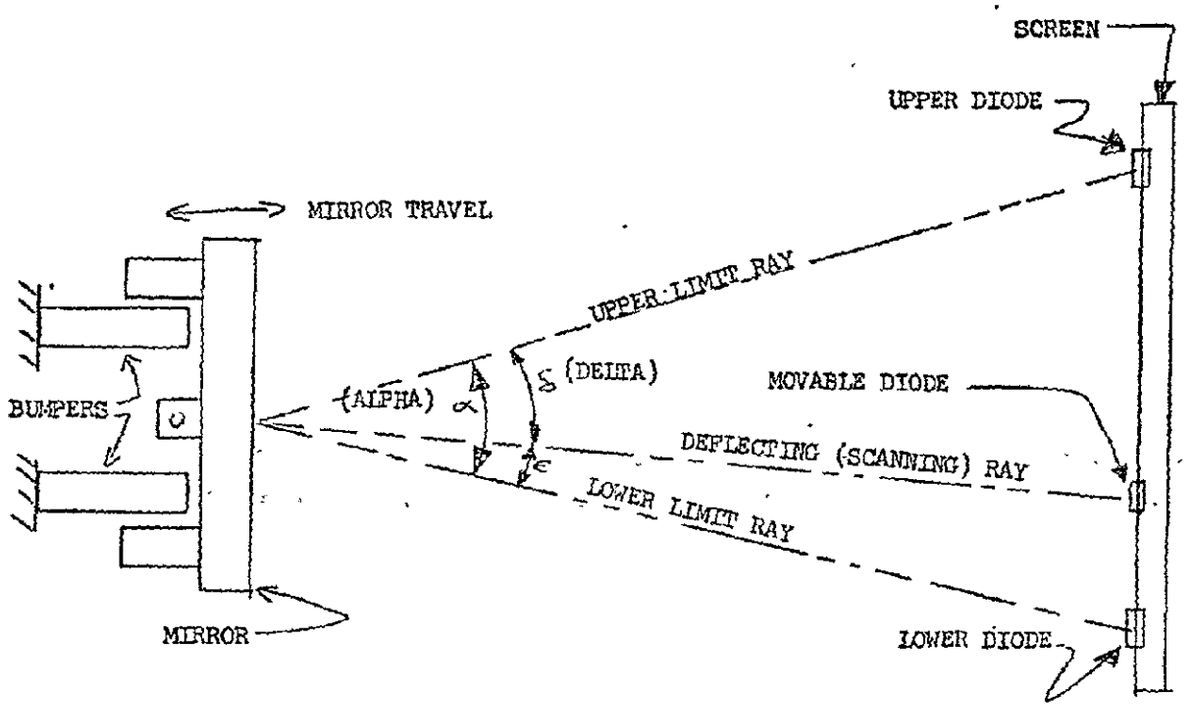

Figure 9. Scan Linearity - Diodes

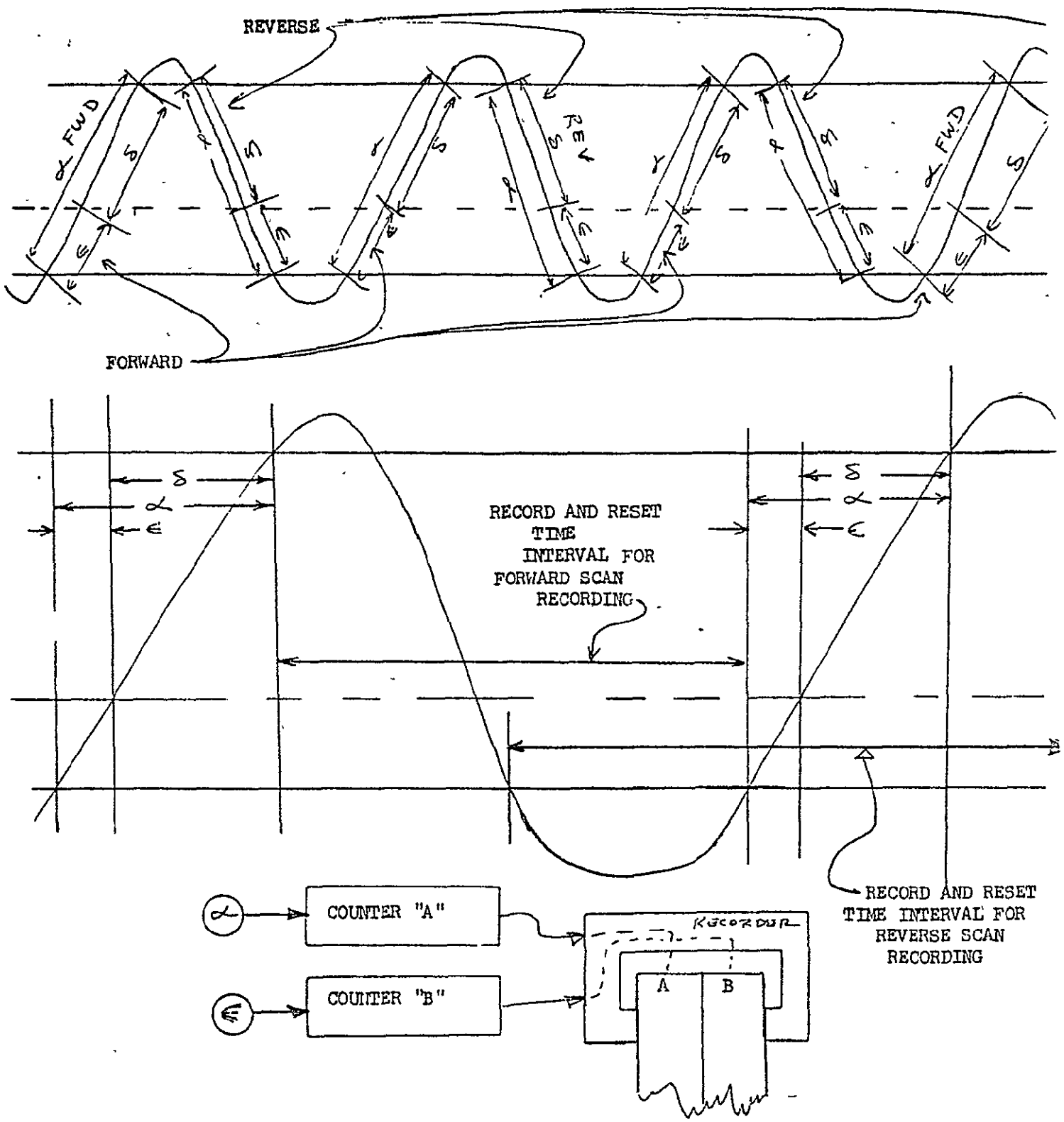

Figure 10. Scan Linearity - Timing

TEST PROCEDURE -- BREADBOARD SCAN MIRROR -- THEMATIC MAPPER	HUGHES AIRCRAFT CO. CULVER CITY, CALIF. CODE IDENT NO. 82577	32 SH NO.	REV LTR	TP 31891-350 NUMBER

		SAMPLE	SAMPLE	
4.1.2.1.4	Total Angle (milliradians) (α)	268		( )
4.1.2.2.3	Driving Frequency	9.2		( )
4.1.2.2.5	Scan Average Period	110.2475 ms		(Approx. 102 ms)
4.1.2.2.6	Scan Frequency	9.06		(Approx. 9.78 Hz)
4.1.2.2.7	Period Deviation (Increased Time)(Max)	4.1 μsec		
4.1.2.2.7	Period Deviation (Decreased Time)(Max)	7.6 μsec		
4.1.2.2.7	Attach Computer Plot to this Sheet (Deviations)	✓		
4.1.2.2.8	Standard Deviation	2.8 μsec		
4.1.3.2.4	Start Up Time	NA		(Less than 30 Seconds)
4.1.4.2.4	Turn Around Time "A" (Average)	10.7549 msec		(Approx. 8.0 ms.)
4.1.4.2.4	Turn Around Time "C" (Average)	11.5863 msec		(Approx. 8.0 ms.)
4.1.4.2.5	"A" Maximum	10.7582 msec		
4.1.4.2.5	"A" Minimum	10.7527 msec		
4.1.4.2.6	"C" Maximum	11.5897 msec		
4.1.4.2.6	"C" Minimum	11.5819 msec		
4.1.4.2.7	Attach Computer Plot to this Sheet (Deviations)			
4.1.4.2.8	Attach Computer Plot to this Sheet (Deviations)			
4.1.4.2.9	Standard Deviation "A"	1.7 μsec		
4.1.4.2.10	Standard Deviation "C"	2.1 μsec		
4.1.5.2.6	Center Scan Angle (mr) (β)			
4.1.5.2.6	Center Scan Angle (mr) (γ)			
4.1.5.2.7	Total Angle Recheck (mr) (α)			

TEST PROCEDURE -- BREADBOARD SCAN MIRROR -- THEMATIC MAPPER

HUGHES AIRCRAFT CO. CULVER CITY, CALIF. CODE IDENT NO. 82577

SH NO. 14

REV LTR

NUMBER TP 31891-350

Figure 5. Data Sheet - Type "A"

11-7-75
He
Scan period
9.2 Hz

SCAN PTS

110244.
110248.6
110249.3
110243.9
110247.3
110251.
110251.3
110248.8
110251.6
110244.4
110241.2
110249.2
110249.1
110244.
110246.
110247.
110248.
110247.2
110246.
110248.6
110245.4
110251.
110250.3
110246.4
110248.5
110246.
110245.
110249.0
110250.
110251.
110247.0
110243.8
110244.5
110245.6
110250.0
110247.
110251.4
110250.7
110248.4
110246.9
110246.3
110239.4
110242.4
110250.9
110251.1
110246.3
110247.8
110247.
110245.
11

AVG
1.
SCAN STD DEV
2.8

11-7-75
Turnaround time He
9.2 Hz

SCAN PTS

10755.3
10755.
10754.9
10754.9
10754.9
10754.5
10754.1
10755.8
10753.5
10753.
10753.2
10752.
10752.9
10752.4
10752.
10752.7
10752.9
10753.2
10753.3
10753.
10753.3
10753.
10753.9
10753.9
10753.
10753.9
10754.1
10754.0
10754.0
10754.3
10754.5
10754.
10755.0
10754.9
10755.4
10755.
10755.9
10756.0
10756.3
10756.6
10756.8
10756.9
10757.1
10757.5
10757.6
10757.6
10757.8
10758.0
10758.

AVG
SCAN STD DEV
1.7

Boulder

REPRODUCIBILITY OF THE
ORIGINAL PAGE IS POOR

Tape

11585.4
11585.5
11585.0
11586.2
11586.4
11586.6
11587.2
11587.
11588.1
11588.5
11588.6
11588.9
11586.8
11589.2
11589.6
11589.7
11589.6
11589.5
11589.2
11589.2
11589.2
11586.6
11586.3
11587.8
11587.9
11587.3
11586.4
11586.1
11585.5
11584.9
11584.9
11584.2
11584.6
11584.7
11584.6
11584.6
11584.6
11585.1
11585.0
11585.0
11584.8
11584.8
11584.9
11584.7
11584.1
11583.7
11583.4
11583.0
11583.

CAN I

RESCAN S D DEV
2.1

		SAMPLE	SAMPLE
4.1.6.2.1.3	Ten Hz Clock Signal Frequency	9.2 Hz	(Hz)
4.1.6.2.1.8	Time for Angle (α) (Average) Forward	43.7900	(ms)
4.1.6.2.1.9	Time for Angle (ϵ) (Average) Forward	10.8342	(ms)
4.1.6.2.1.10	Time for Angle (α) (Average) Reverse	43.9747	(ms)
4.1.6.2.1.11	Time for Angle (ϵ) (Average) Reverse	10.9867	(ms)
4.1.6.2.1.12	Angle (ϵ)	66.6	(mr)
4.1.6.2.1.13	Angle (α)	268	(mr)
4.1.6.2.2.3	Ten Hz Clock Signal Frequency	9.2 Hz	(Hz)
4.1.6.2.2.8	Time for Angle (α) (Average) Forward	43.7584	(ms)
4.1.6.2.2.9	Time for Angle (ϵ) (Average) Forward	14.9938	(ms)
4.1.6.2.2.10	Time for Angle (α) (Average) Reverse	43.9746	(ms)
4.1.6.2.2.11	Time for Angle (ϵ) (Average) Reverse	15.2006	(ms)
4.1.6.2.2.12	Angle (ϵ)	92.2	(mr)
4.1.6.2.2.13	Angle (α)	268	(mr)

Figure 11. Data Sheet - Type B

		SAMPLE	SAMPLE	
4.1.6.2.3.3	Ten Hz Clock Signal Frequency		9.2	(Hz)
4.1.6.2.3.8	Time for Angle (α) (Average) Forward		43.7394	(ms)
4.1.6.2.3.9	Time for Angle (ϵ) (Average) Forward		19.8417	(ms)
4.1.6.2.3.10	Time for Angle (α) (Average) Reverse		43.9517	(ms)
4.1.6.2.3.11	Time for Angle (ϵ) (Average) Reverse		26.0838	(ms)
4.1.6.2.3.12	Angle (ϵ)		122.4	(mr)
4.1.6.2.3.13	Angle (α)		268	(mr)
4.1.6.2.4.3	Ten Hz Clock Signal Frequency		9.2	(Hz)
4.1.6.2.4.8	Time for Angle (α) (Average) Forward		43.7528	(ms)
4.1.6.2.4.9	Time for Angle (ϵ) (Average) Forward		26.1768	(ms)
4.1.6.2.4.10	Time for Angle (α) (Average) Reverse		43.9569	(ms)
4.1.6.2.4.11	Time for Angle (ϵ) (Average) Reverse		26.9450	(ms)
4.1.6.2.4.12	Angle (ϵ)		164.95	(mr)
4.1.6.2.4.13	Angle (α)		268	(mr)

Figure 12. Data Sheet - Type C

		SAMPLE	SAMPLE
4.1.6.2.5.3	Ten Hz Clock Signal Frequency	9.2	(Hz)
4.1.6.2.5.8	Time for Angle (α)(Average) Forward	43.7452	(ms)
4.1.6.2.5.9	Time for Angle (ϵ)(Average) Forward	30.2151	(ms)
4.1.6.2.5.10	Time for Angle (α)(Average) Reverse	43.9508	(ms)
4.1.6.2.5.11	Time for Angle (ϵ)(Average) Reverse	30.4762	(ms)
4.1.6.2.5.12	Angle (ϵ)	186.46	(mr)
4.1.6.2.5.13	Angle (α)	268	(mr)

Figure 13. Data Sheet - Type "D"

Attach ten computer generated graphs here.

Location Diode	1	2	3	4	5
Fwd	0.247414	0.342656	0.453628	0.609721	0.690707
Rev	0.249848	0.345668	0.456951	0.612987	0.693423

Standard Deviation Values:

Location Diode	1	2	3	4	5
Fwd	1.996×10^{-5}	2.37×10^{-5}	2×10^{-5}	4.86×10^{-5}	4.59×10^{-5}
Rev	3.45×10^{-6}	6.79×10^{-6}	4.49×10^{-6}	6.02×10^{-6}	7.61×10^{-6}

Figure 14. Data Sheet Type "E"

LINEARITY COMPUTATIONS (FORWARD):
FOR DATA SET 1

RELATIVE DIODE POSITION= 0.248092

AVERAGE VALUE= 0.247414

STANDARD DEVIATION= 1.99571E-5

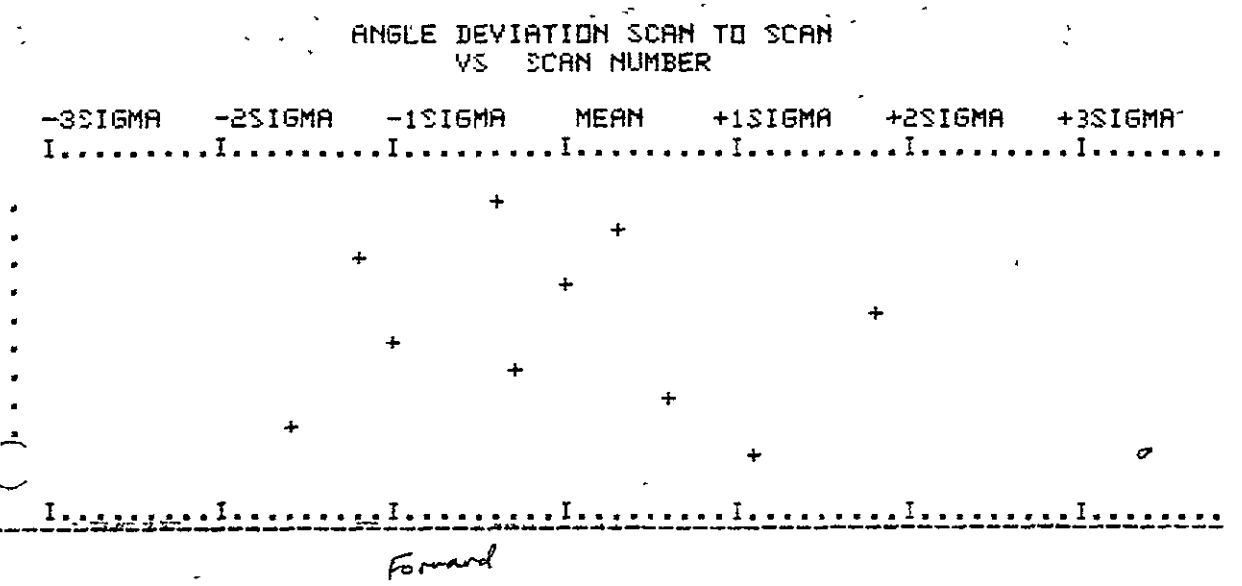

Forward

FOR DATA SET 2

RELATIVE DIODE POSITION= 0.343511

AVERAGE VALUE= 0.342656

STANDARD DEVIATION= 2.37448E-5

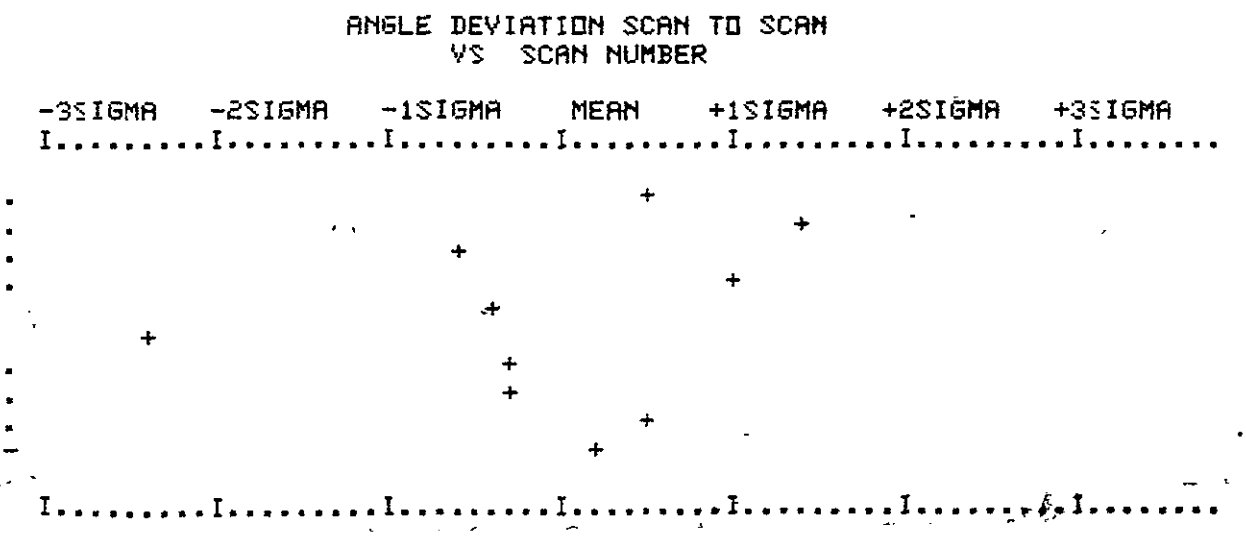

Forward

FOR DATA SET 3

RELATIVE DIODE POSITION= 0.456092

AVERAGE VALUE= 0.453628

STANDARD DEVIATION= 2.00051E-5

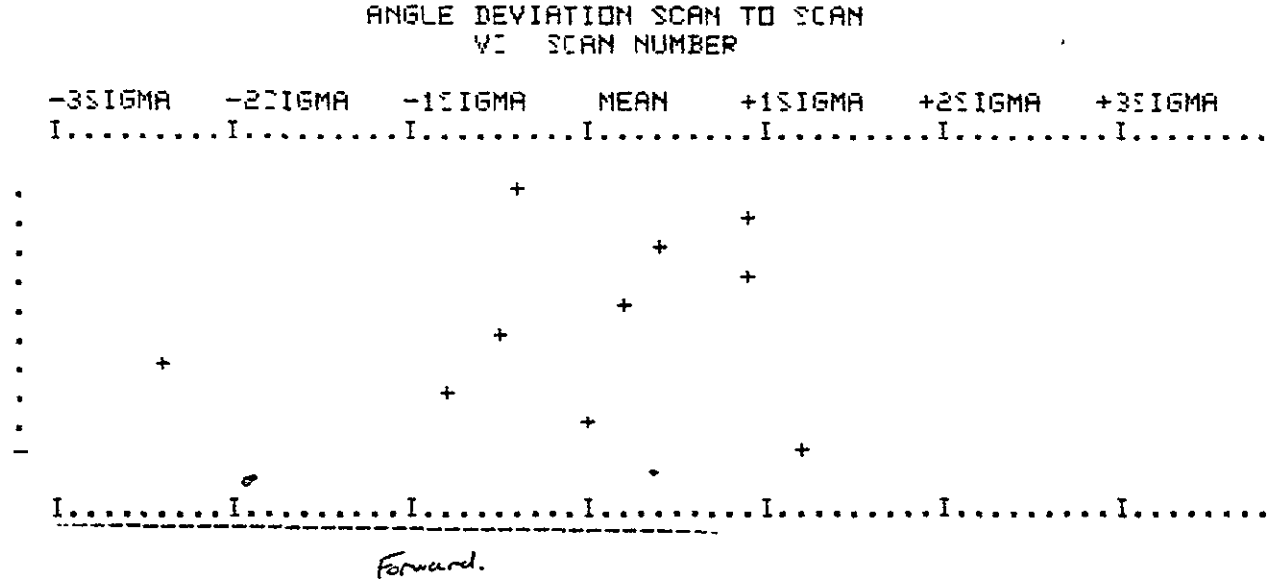

Forward.

FOR DATA SET 4

RELATIVE DIODE POSITION= 0.614504

AVERAGE VALUE= 0.609721

STANDARD DEVIATION= 4.25766E-5

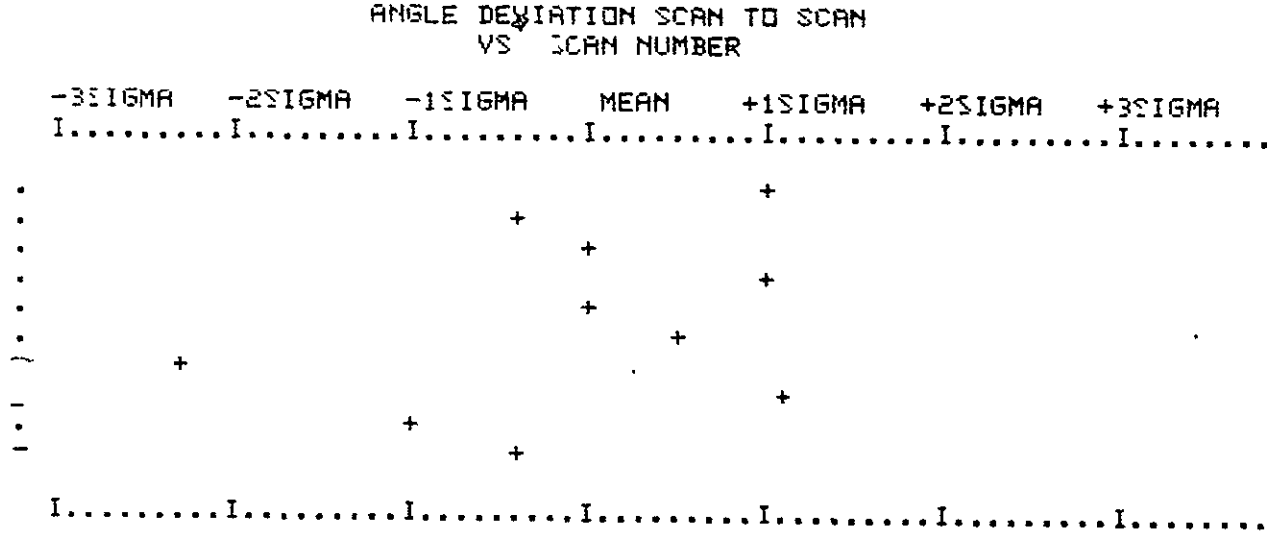

Forward

FOR DATA SET 5

RELATIVE DIODE POSITION= 0.694656

AVERAGE VALUE= 0.690707

STANDARD DEVIATION= 4.59130E-5

ANGLE DEVIATION SCAN TO SCAN
VS SCAN NUMBER

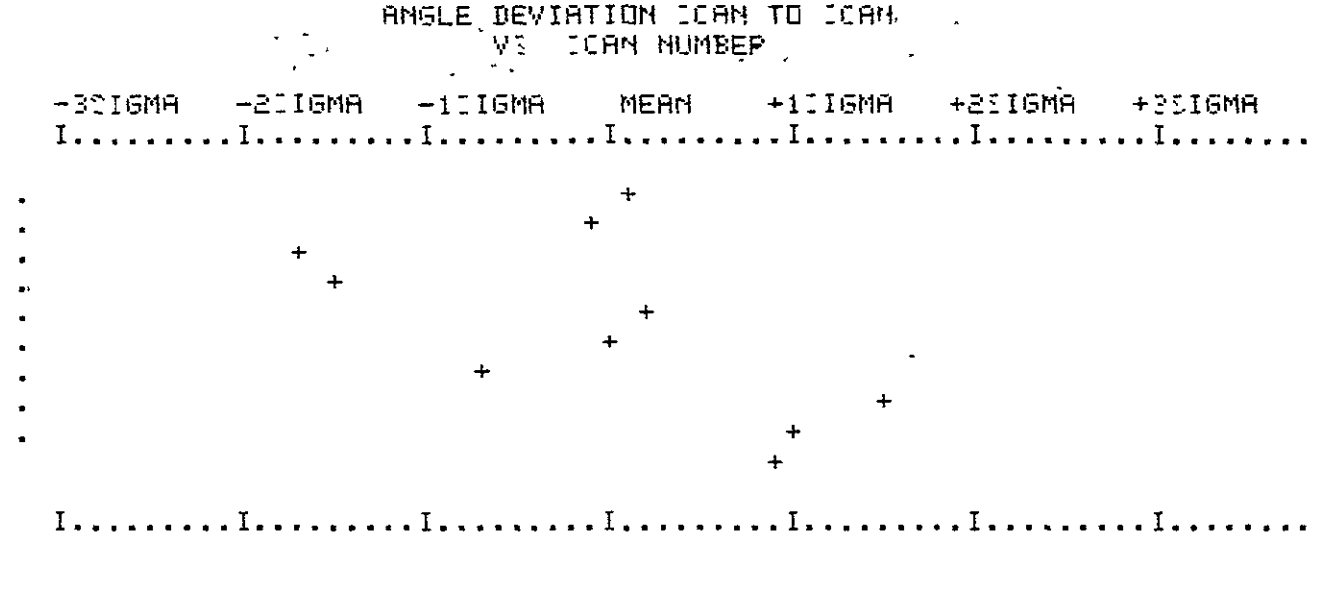

```
 LINEARITY COMPUTATIONS (REVERSE):
FOR DATA SET  1

 RELATIVE DIODE POSITION= 0.248092

 AVERAGE VALUE= 0.249345

 STANDARD DEVIATION= 3.44974E-6

                ANGLE DEVIATION SCAN TO SCAN
                     VS  SCAN NUMBER

  -3SIGMA   -2SIGMA   -1SIGMA     MEAN    +1SIGMA   +2SIGMA   +3SIGMA
  I.........I.........I.........I.........I.........I.........I.........

.                +
.                                  +
.                    +
.                                   +
.                                        +
.                 +                                    REPRODUCIBILITY OF THE
.                                        +             ORIGINAL PAGE IS POOR
.                                    +
.                                  +
.                                   +

  I.........I.........I.........I.........I.........I.........I.........

FOR DATA SET  2  Reverse

 RELATIVE DIODE POSITION= 0.343511

 AVERAGE VALUE= 0.345483

 STANDARD DEVIATION= 5.79834E-6

                ANGLE DEVIATION SCAN TO SCAN
                     VS  SCAN NUMBER

  -3SIGMA   -2SIGMA   -1SIGMA     MEAN    +1SIGMA   +2SIGMA   +3SIGMA
  I.........I.........I.........I.........I.........I.........I.........

.                                  +
.                                    +
.                                    +
.                      +
.                   +
(                                          +
.                                        +
.                                             +
.            +
-                           .          +

  I.........I.........I.........I.........I.........I.........I.........
```

FOR DATA SET 3 *Reverse*

RELATIVE DIODE POSITION= 0.456092

AVERAGE VALUE= 0.456951

STANDARD DEVIATION= 4.49774E-6

ANGLE DEVIATION SCAN TO SCAN
VS SCAN NUMBER

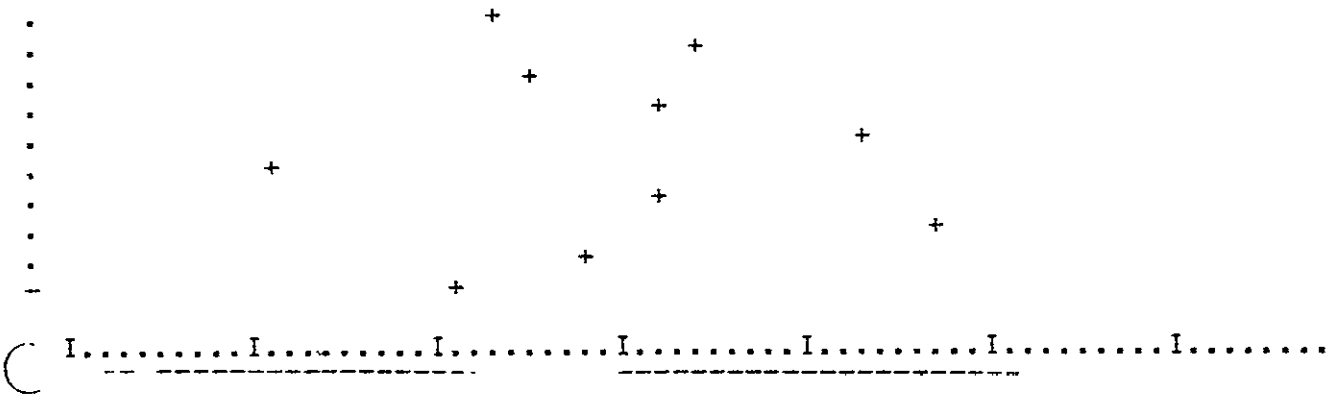

FOR DATA SET 4 *Reverse*

RELATIVE DIODE POSITION= 0.614504

AVERAGE VALUE= 0.612987

STANDARD DEVIATION= 6.02861E-6

ANGLE DEVIATION SCAN TO SCAN
VS SCAN NUMBER

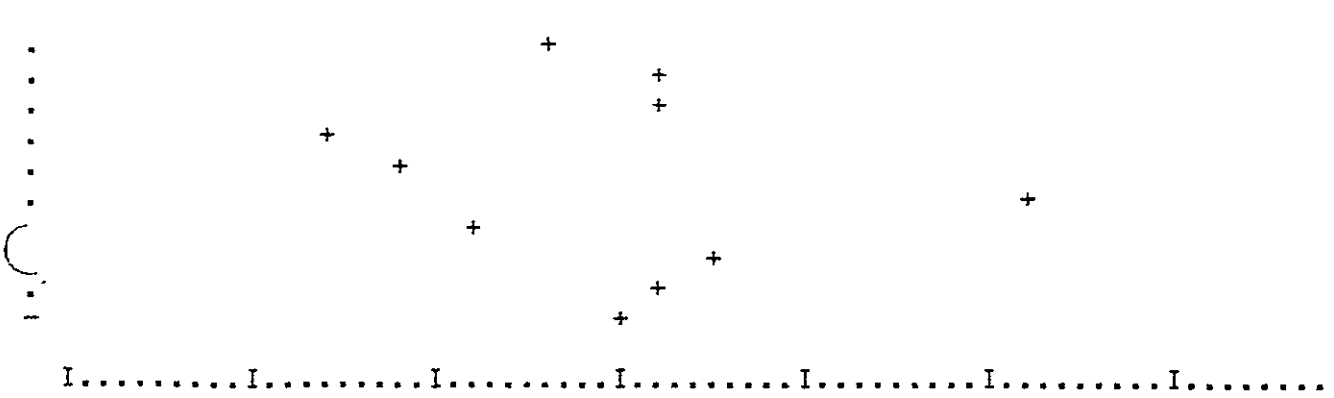

TOP DATA SET 5 Reverse

RELATIVE DIODE POSITION= 0.894E56

AVERAGE VALUE= 0.833433

STANDARD DEVIATION= 7.51441E-6

ANGLE DEVIATION SCAN TO SCAN
VS SCAN NUMBER

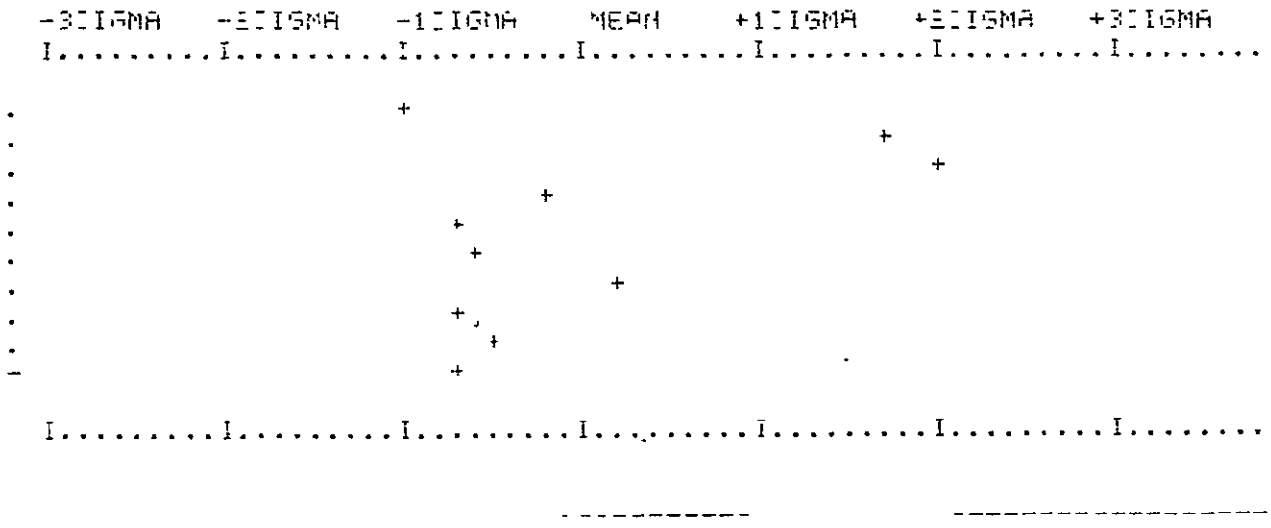

FORWARD

4.1.6.2.6.4.1

ANGULAR POSTION = P(X)=
-4.26856E-2 X^3+ 5.15397E-2 X^2+ 0.991146 X

4.1.6.2.6.5.1

ICAN RATE = PDOT(X)=
-0.128057 X^2+ 0.103079 X+ 0.991146

TIME	POSITION	ICAN RATE
0	0	0.991146
0.05	4.96808E-2	0.99598
0.1	9.95873E-2	1.00017
0.15	0.149687	1.00373
0.2	0.199949	1.00664
0.25	0.250341	1.00891
0.3	0.30083	1.01054
0.35	0.351385	1.01154
0.4	0.401973	1.01189
0.45	0.452563	1.0116
0.5	0.503122	1.01067
0.55	0.553619	1.0091
0.6	0.604022	1.00689
0.65	0.654298	1.00404
0.7	0.704415	1.00055
0.75	0.754343	0.996423
0.8	0.804047	0.991653
0.95	0.853497	0.986242
0.9	0.902661	0.980191
0.95	0.951506	0.9735
1.	1.	0.966169

4.1.6.2.6.4.2 REVERSE

ANGULAR POSTION = P(X)=
-4.28176E-2 X^3+ 6.51373E-2 X^2+ 0.97768 X

4.1.6.2.6.5.2

ICAN RATE = PDOT(X)=
-0.128453 X^2+ 0.130275 X+ 0.97768

TIME	POSITION	ICAN RATE
0	0	0.97768
0.05	4.90415E-2	0.983873
0.1	9.83766E-2	0.989423
0.15	0.147973	0.994331
0.2	0.197799	0.998597
0.25	0.247822	1.00222
0.3	0.29801	1.0052
0.35	0.348332	1.00754
0.4	0.398754	1.00924
0.45	0.449245	1.01029
0.5	0.499772	1.0107
0.55	0.550304	1.01047
0.6	0.600809	1.0096
0.65	0.651254	1.00809
0.7	0.701607	1.00593
0.75	0.751836	1.00313
0.8	0.801909	0.99969
0.85	0.851795	0.995607
0.9	0.901459	0.990881
0.95	0.950872	0.985512
1.	1.	0.979502

Figure 17. Data Sheet Type "P"

DATA SHEET "G"

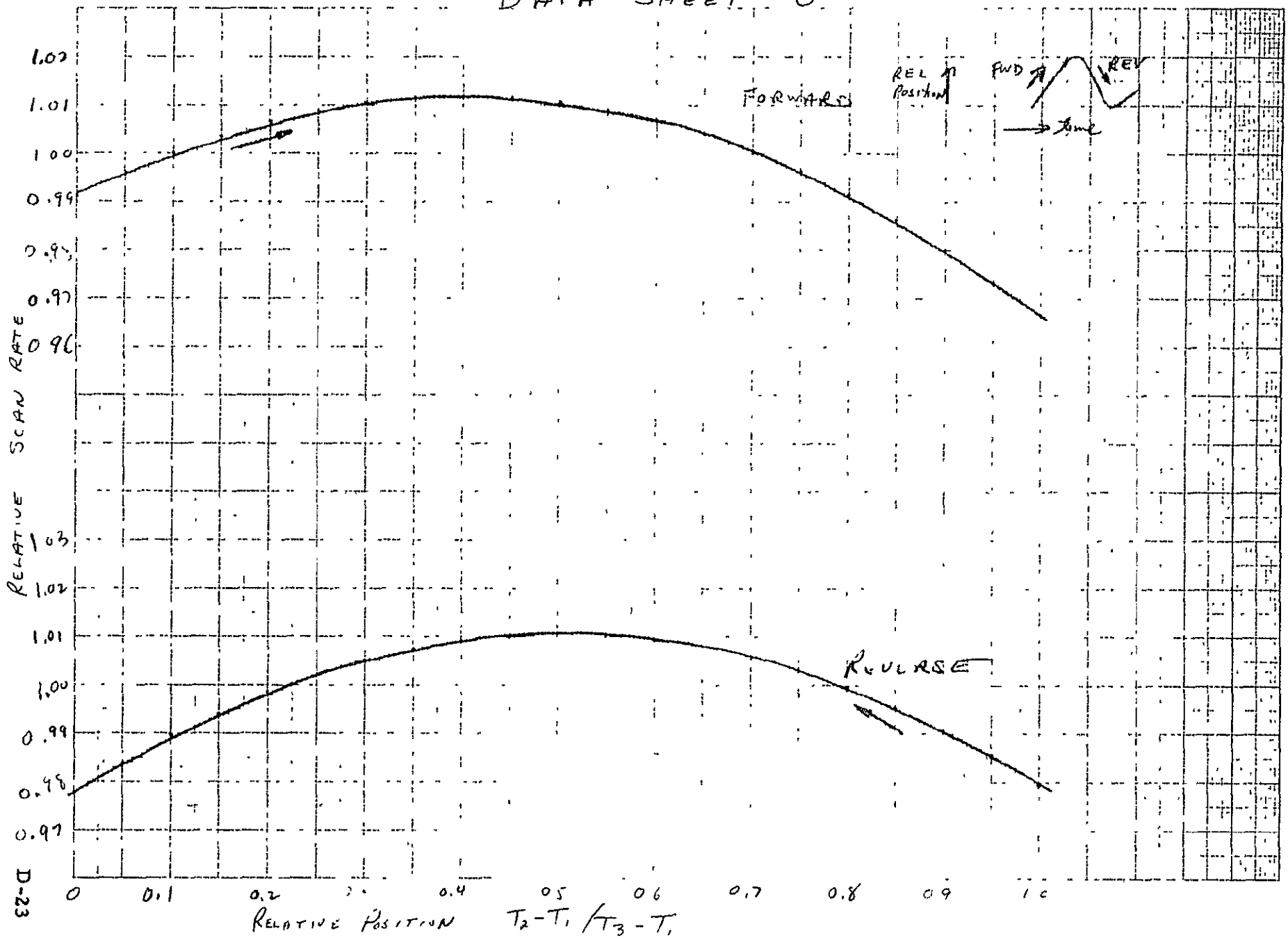
1.02
1.01
1.00
0.99
0.98
0.97
0.96
FORWARD
REL Position
FWD
REV
Time
RELATIVE SCAN RATE
1.03
1.02
1.01
1.00
0.99
0.98
0.97
REVERSE
0
0.1
0.2
0.4
0.5
0.6
0.7
0.8
0.9
1.0
RELATIVE POSITION T_2-T_1/T_3-T_1

4.1.9.1.1	Average Ratio Value - Forward:	0.2474
4.1.9.1.1	$\overline{\theta}_{FWD} = Q_{FWD}$:	66.3069 mrad.
4.1.9.1.1	σ_{FWD} (STD. DEV.):	5.35 urad.
4.1.9.1.1	Attach Deviation Plot to this Sheet	✓
4.1.9.1.2	Average Ratio Value - Reverse:	0.2498
4.1.9.1.2	$\overline{\theta}_{REV} = Q_{REV}$:	66.9592 mrad
4.1.9.1.2	σ_{REV} (STD. DEV.):	0.924 urad.
4.1.9.1.2	Attach Deviation Plot to this Sheet	✓
4.1.9.1.3	TOTAL Deviation:	5.4 urad
4.1.9.2.1	Average Ratio Value - Forward:	0.3426
4.1.9.2.1	$\overline{\theta}_{FWD} = Q_{FWD}$:	91.8318 mrad.
4.1.9.2.1	σ_{FWD} (STD. DEV.):	6.364 urad
4.1.9.2.1	Attach Deviation Plot to this Sheet	✓
4.1.9.2.2	Average Ratio Value - Reverse:	0.3456
4.1.9.2.2	$\overline{\theta}_{REV} = Q_{REV}$:	92.6391 mrad
4.1.9.2.2	σ_{REV} (STD. DEV.):	1.822 urad
4.1.9.2.2	Attach Deviation Plot to this Sheet	✓
4.1.9.2.3	TOTAL Deviation:	6.62 urad.

Figure 26. Data Sheet - Type "K"

TEST PROCEDURE -- BREADBOARD SCAN MIRROR -- THEMATIC MAPPER

HUGHES AIRCRAFT CO. CULVER CITY, CALIF. CODE IDENT NO. 82577

SH NO. 57

REV LTR

NUMBER TP: 31891-350

D-24

D-24

REPEATAB__ITY CALCULATIONS (FORWARD) FOR DATA SET

RELATIVE DIODE POSITION= 0.248092

AVERAGE ANGLE= 66.3069 MILLIRADIANS

STANDARD DEVIATION= 5.34833E-3 MILLIRADIANS

ANGLE DEVIATION SCAN TO SCAN
VS SCAN NUMBER
(FORWARD)

PEPEA~SILITY CALCULATION:(PEVEPSE) FOR DATA SE~\1

RELATIVE DIODE PO:ITION= 0.248092

AVEPAGE ANGLE= 66.9592 MILLIPADIAN:

:TANDAPD DEVIATION= 9.24399E-4 MILLIPADIAN:

ANGLE DEVIATION :CAN TO :CAN
V: :CAN NUMBEP
(PEVEP:E)

-3:IGMA -2SIGMA -1:IGMA MEAN +1:IGMA +2:IGMA +3:IGMA

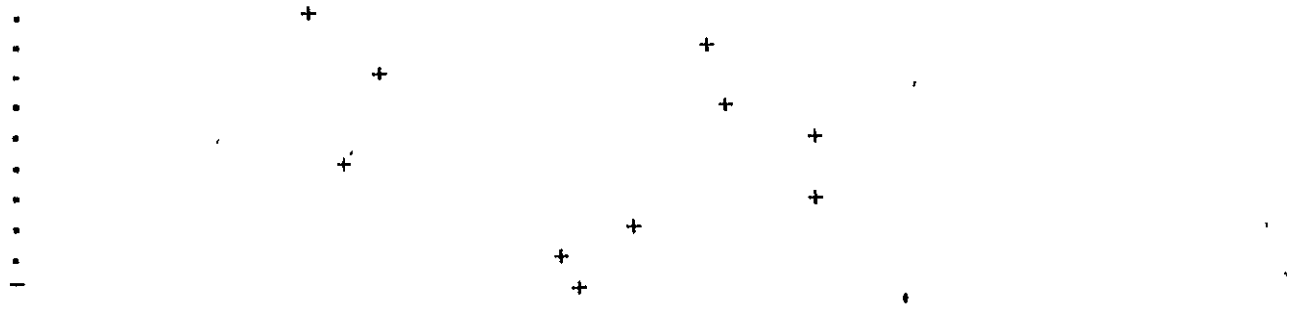

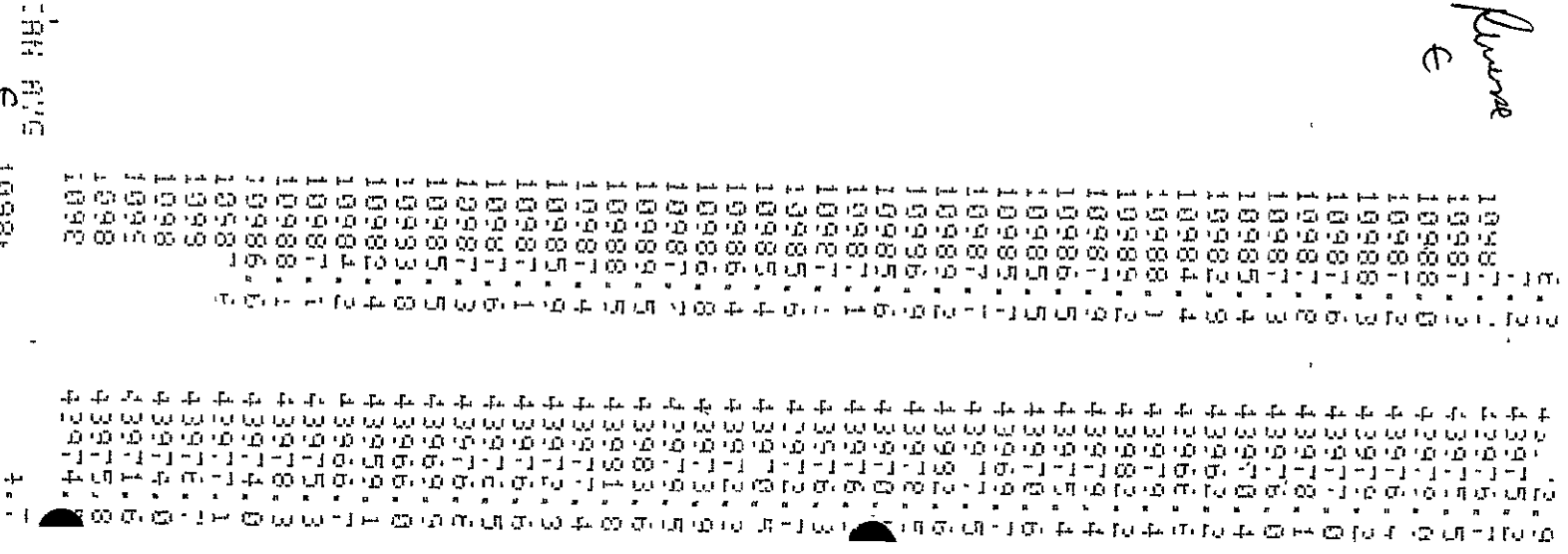

11-10-75 Laramie AIR Data
9.24 by Revenaz
Location #1
Rho = .2498
Revenaz
All P
Revenaz
TAR AVG
AH STD DEV
1.0
1.0
D-26

REPE[redacted]RILITY CALCULATIONS (FORWARD) FOR DATA SET

RELATIVE DIODE POSITION= 0.343511

AVERAGE ANGLE= 91.8318 MILLIRADIANS

STANDARD DEVIATION= 6.36378E-3 MILLIRADIANS

ANGLE DEVIATION SCAN TO SCAN
VS SCAN NUMBER
(FORWARD)

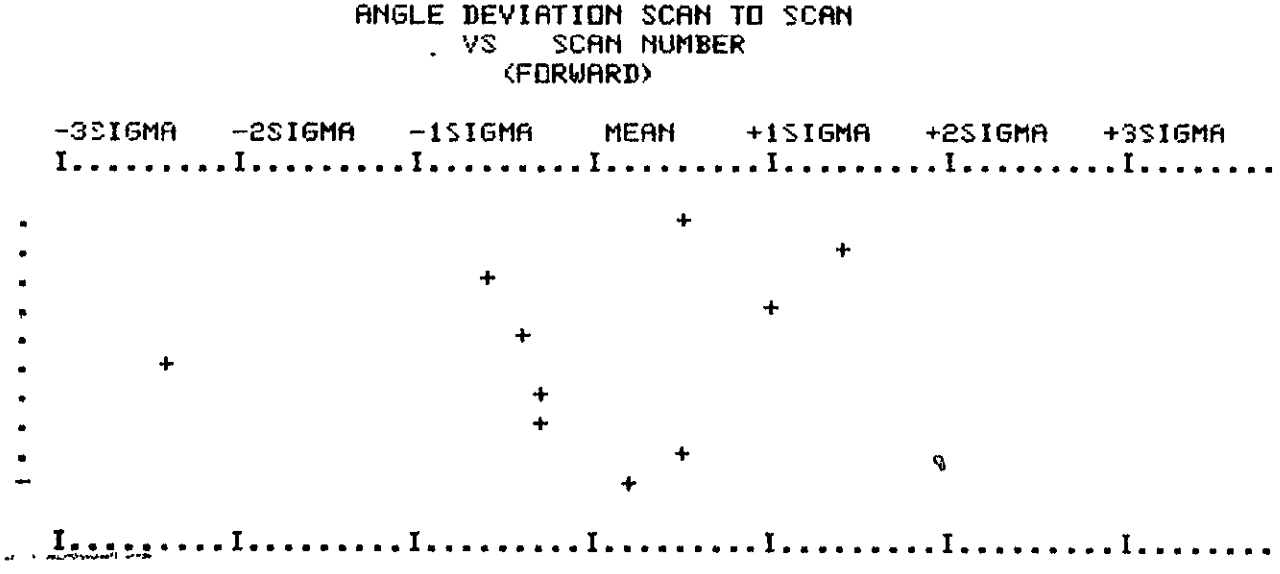

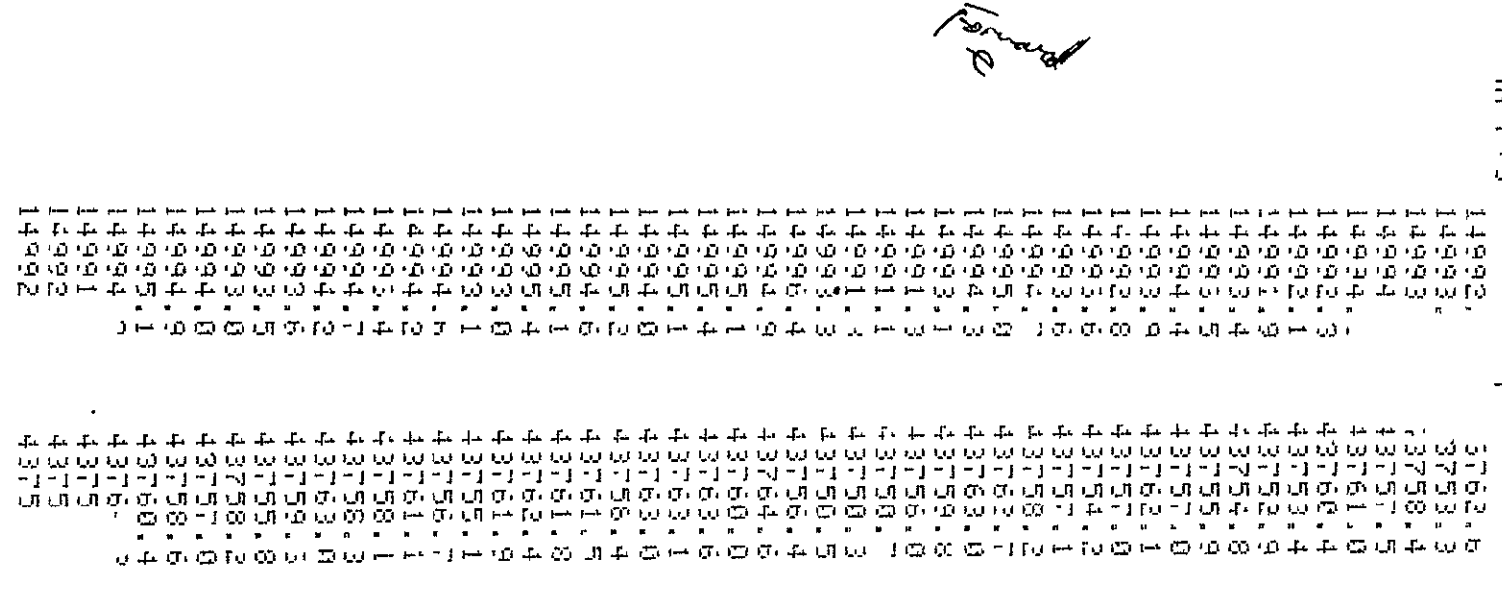

REPEATABILITY CALCULATIONS(REVERSE) FOR DATA SE 2

RELATIVE DIODE POSITION= 0.343511

AVERAGE ANGLE= 92.6391 MILLIRADIANS

STANDARD DEVIATION= 1.82186E-3 MILLIRADIANS

ANGLE DEVIATION SCAN TO SCAN
VS SCAN NUMBER
(REVERSE)

Location #2 Reverse

Te/Tc = .3456

Reverse

4.1.9.3.1	Average Ratio Value - Forward:	0 4536
4.1.9.3.1	$\overline{\theta}_{FWD} = Q_{FWD}$:	121.572 μrad
4.1.9.3.1	σ_{FWD} (STD. DEV.):	5 36 μrad
4.1.9.3.1	Attach Deviation Plot to this Sheet	
4.1.9.3.2	Average Ratio Value - Reverse:	0.457
4.1.9.3.2	$\overline{\theta}_{REV} = Q_{REV}$:	122 463 μrad
4.1.9.3.2	σ_{REV} (STD. DEV.):	1.205 μrad
4.1.9.3.2	Attach Deviation Plot to this Sheet	✓
4.1.9.3.3	TOTAL Deviation:	5 4 μrad
4.1.9.4.1	Average Ratio Value - Forward:	0.6097
4.1.9.4.1	$\overline{\theta}_{FWD} = Q_{FWD}$:	163.405 μrad
4.1.9.4.1	σ_{FWD} (STD.DEV.):	13.02 μrad
4.1.9.4.1	Attach Deviation Plot to this Sheet	✓
4.1.9.4.2	Average Ratio Value - Reverse:	0.613
4.1.9.4.2	$\overline{\theta}_{REV} = Q_{REV}$:	164.281 μrad
4.1.9.4.2	σ_{REV} (STD. DEV.):	1.616 μrad
4.1.9.4.2	Attach Deviation Plot to this Sheet	✓
4.1.9.4.3	TOTAL Deviation:	13.1186 μrad

Figure 27. Data Sheet - Type "L"

TEST PROCEDURE -- BREADBOARD SCAN MIRROR -- THEMATIC MAPPER

HUGHES AIRCRAFT CO. CULVER CITY, CALIF. CODE IDENT NO. 82577

SH NO. 58

REV LTR

NUMBER TP 31891-350

D-29

D-29

PEPEATABILITY CALCULATIONS (FORWARD) FOR DATA SET 3

PELATIVE DIODE POSITION= 0.456092

AVEPAGE ANGLE= 121.572 MILLIRADIANS

STANDARD DEVIATION= 5.36126E-3 MILLIRADIANS

ANGLE DEVIATION SCAN TO SCAN
VS SCAN NUMBER
(FORWARD)

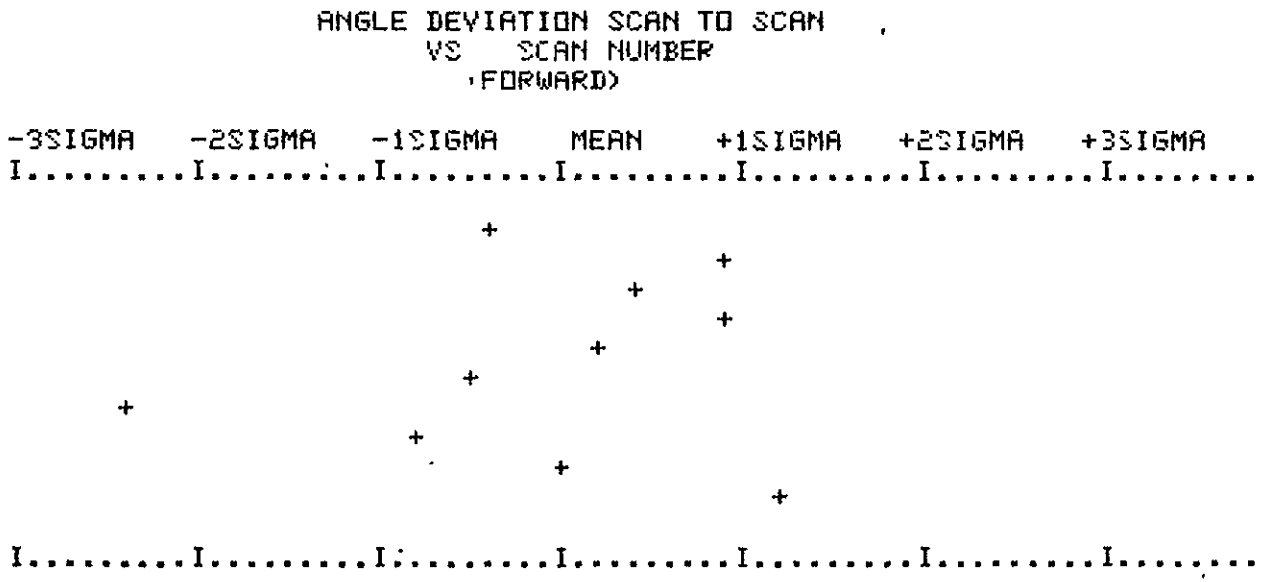

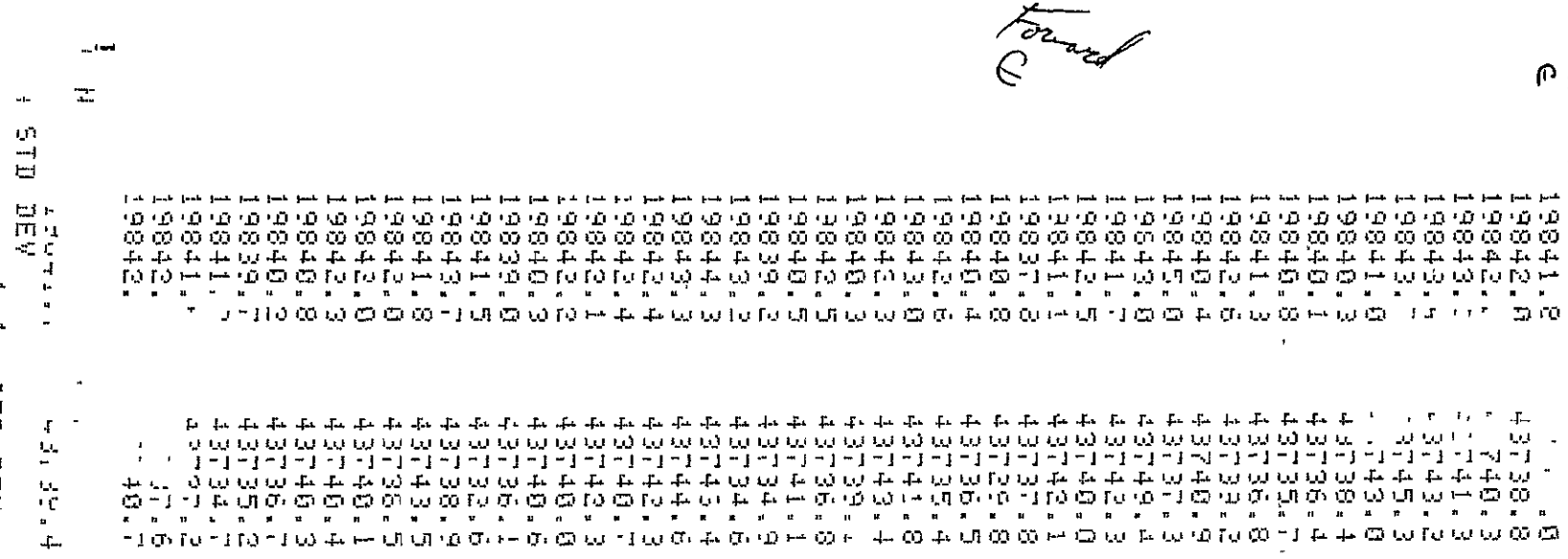

11-10-75
Location #3 Forward Scan

Forward

Re: = .4536
SCAN FTS

Nov-95

Location #3 Reverse Scan

REPEATABILITY CALCULATIONS(REVERSE) FOR DATA SET

RELATIVE DIODE POSITION= 0.456092

AVERAGE ANGLE= 122.463 MILLIRADIANS

STANDARD DEVIATION= 1.20537E-3 MILLIRADIANS

ANGLE DEVIATION SCAN TO SCAN
VS SCAN NUMBER
(REVERSE)

Re = .457

SCAN PTS

AVG

2000 -

TO DEV

1.3

STD DEV

3.0

REPEATABILITY CALCULATIONS (FORWARD) FOR DATA SET 4

RELATIVE DIODE POSITION= 0.614504

AVERAGE ANGLE= 163.405 MILLIRADIANS

STANDARD DEVIATION= 1.30188E-2 MILLIRADIANS

ANGLE DEVIATION SCAN TO SCAN
VS SCAN NUMBER
(FORWARD)

Location #4 Forward Scan

Test 6097
Tx
SCAN PTS

REPEAT ILITY CALCULATIONS (REVERSE) FOR DATA SET 4

RELATIVE DIODE POSITION= 0.614504

AVERAGE ANGLE= 164.281 MILLIRADIANS

STANDARD DEVIATION= 1.61573E-3 MILLIRADIANS

ANGLE DEVIATION SCAN TO SCAN
VS SCAN NUMBER
(REVERSE)

4.1.9.5.1	Average Ratio Value - Forward:	0.6907
4.1.9.5.1	$\bar{\theta}_{FWD} = Q_{FWD}$:	185.109 mrad
4.1.9.5.1	σ_{FWD} (STD. DEV.):	12.30 mrad
4.1.9.5.1	Attach Deviation Plot to this Sheet	✓
4.1.9.5.2	Average Ratio Value - Reverse:	0.6934
4.1.9.5.2	$\bar{\theta}_{REV} = Q_{REV}$:	185.837
4.1.9.5.2	σ_{REV} (STD. DEV.):	2.04 mrad.
4.1.9.5.2	Attach Deviation Plot to this Sheet	-
4.1.9.5.3	TOTAL Deviation:	12.4729 mrad.
4.1.9.6.1	Average Standard Deviation:	8.627 mrad
4.1.9.6.2	Attach Plot of Standard Deviation vs Angle.	-

Figure 28. Data Sheet - Type "M"

TEST PROCEDURE -- BREADBOARD SCAN MIRROR -- THEMATIC MAPPER	HUGHES AIRCRAFT CO. CULVER CITY, CALIF. CODE IDENT NO. 82577
SH NO. 60	REV LTR
NUMBER TP 31891-350	

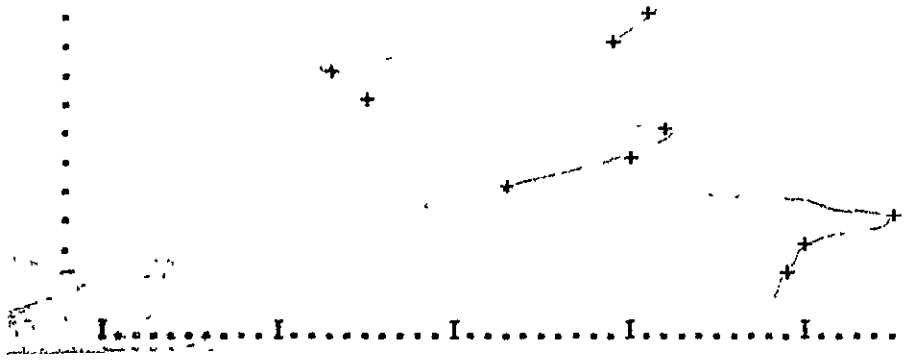

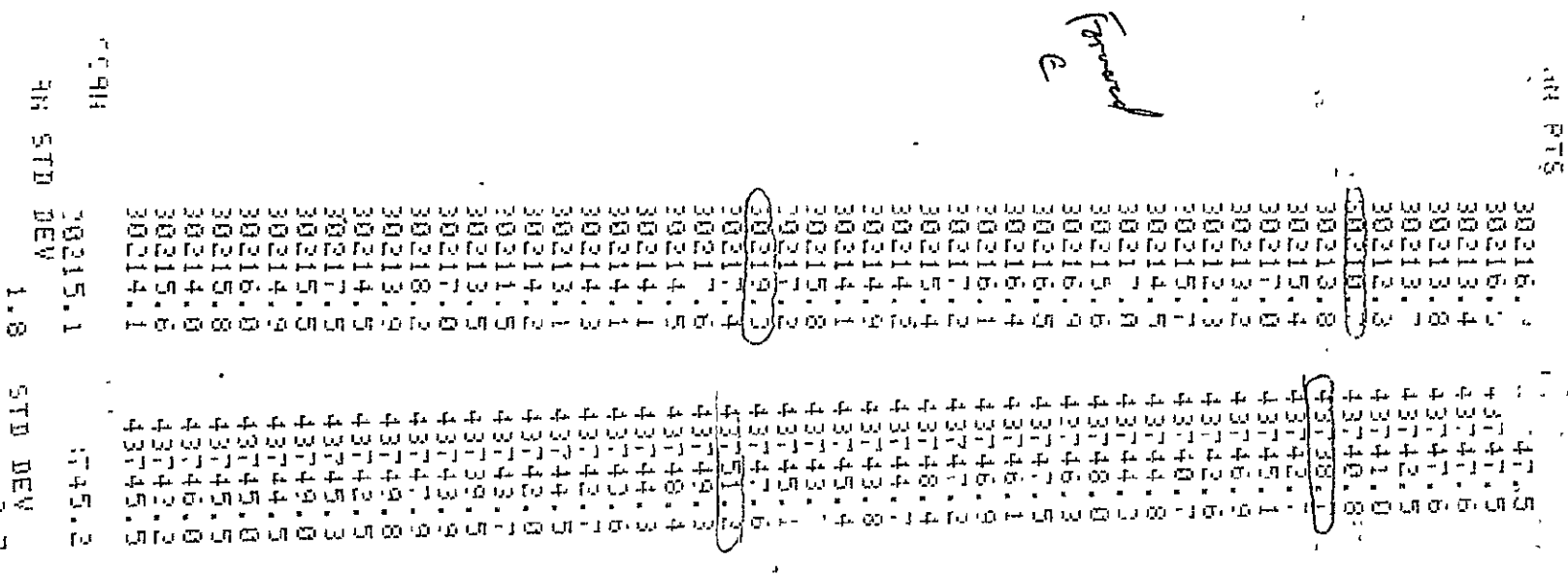

11-10-75

Location #5
Forward Scan

AIR

REPEATABILITY CALCULATIONS (FORWARD) FOR DATA SET 5

RELATIVE DIODE POSITION= 0.694656

AVERAGE ANGLE= 185.109 MILLIRADIANS

STANDARD DEVIATION= 1.23048E-2 MILLIRADIANS

ANGLE DEVIATION SCAN TO SCAN
VS SCAN NUMBER
(FORWARD)

Forward
ε

Ratio $\frac{r_\varepsilon}{r_x}$ = .6907

α↓

```
AN PTS
        30216.      47.5
        30216.5  43747.5
        30213.4  43747.6
        30213.8  43747.6
        30213.7  43742.5
        30212.3  43741.0
        30210.7  43740.8
        30213.8  43738.1
        30215.4  43742.7
        30217.0  43745.1
        30213.2  43746.9
        30212.3  43742.6
        30215.7  43740.7
        30214.5  43744.8
        30217.0  43744.3
        30215.6  43748.0
        30216.9  43746.3
        30216.5  43747.5
        30216.4  43746.1
        30216.1  43746.9
        30217.2  43747.2
        30215.4  43748.4
        30214.2  43744.7
        30214.9  43743.8
        30214.1  43745.4
        30215.8  43743.7
        30217.2  43745.1
        30219.3  43747.6
        30217.4  43751.2
        30217.6  43749.3
        30214.5  43748.4
        30214.1  43744.3
        30214.1  43743.6
        30214.3  43742.7
        30213.1  43744.5
        30214.2  43742.0
        30211.5  43743.7
        30213.5  43739.5
        30217.0  43743.9
        30218.2  43747.9
        30213.9  43749.8
        30214.5  43742.5
        30217.5  43745.3
        30215.5  43749.0
        30214.9  43744.5
        30216.0  43745.0
        30215.8  43745.5
        30214.0  43746.0
        30215.6  43742.2
        30214.1  43745.5

        30215.1     745.2
AN STD DEV
            1.8  STD DEV
                     2.7
```

REPEATABILITY CALCULATIONS(REVERSE) FOR DATA SET 5

RELATIVE DIODE POSITION= 0.694656

AVERAGE ANGLE= 185.837 MILLIRADIANS

STANDARD DEVIATION= 2.04101E-3 MILLIRADIANS

ANGLE DEVIATION SCAN TO SCAN
VS SCAN NUMBER
(REVERSE)

SCAN PTS

```
REPEATABILITY CALCULATIONS (FORWARD AND REVERSE)

AVG ST DEV OVER 5 SETS OF DATA IS 8.62674E-3 MILLIRADIANS
DOES NOT SATISFY REQUIPEMENT


            STANDARD DEVIATION OF ANGLE(MICRORAD)
            VS  DIODE POSITION ((D2-D1)/(D3-D1))

  0         1         2         3         4         5         6
  I.........I.........I.........I.........I.........I.........I

D                                                       +

D  OFF SCALE - (X,Y)=( 0.343511 , 6.61943 )

D                                                       +

D  OFF SCALE - (X,Y)=( 0.614504 , 13.1186 )

D  OFF SCALE - (X,Y)=( 0.694656 , 12.4729 )
```

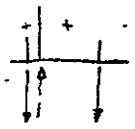

(237 μRAD/V)(.02 V/div) = 4.7 μRAD/div

11-7-75

LOCATION #5

Data Set 1

Delta Value	Photo #1	Photo #2	Photo #3
1	(-.1 div)(4.7 μRAD/div) = -.5 μRAD	-.4	-1.9
2	+.1	+.5	-.3	-1.4
3	+.4	+1.9	-.3	-1.4
4	+.2	+.9	-.2	-.9
5	.0	.0	.0	.0
6	-.2	-.9	+.2	+.9
7	-.4	-1.9	+.3	+1.4
8	-.3	-1.4	-.1	-.5
9	-.2	-.9	-.2	-.9
10	-.2	-.9	-.2	-.9
11	+.1	+.5	-.4	-1.9
12	+.3	+1.4	-.2	-.9
13	+.3	+1.4	.0	.0
14	-.2	-.9	.0	.0
15	-.3	-1.4	-.1	-.5
16	-.2	-.9	+.2	+.9
17	-.4	-1.9	+.1	+.5
18	-.3	-1.4	-.4	-1.9
19	.0	.0	-.4	-1.9
20	+.1	+.5	-.2	-.9
21	+.2	+.9	-.4	-1.9
22	+.2	+.9	-.3	-1.4
23	.0	.0	+.2	+.9
24	-.3	-1.4	+.2	+.9
25	-.4	-1.9	+.1	+.5
26	-.2	-.9	-.1	-.5
27	-.3	-1.4	-.2	-.9
28	-.1	-.5	-.3	-1.4
29	+.3	+1.4	-.3	-1.4
30	+.3	+1.4	-.2	-.9
31	+.1	+.5	-.1	-.5
32	-.2	-.9	.0	.0
33	-.3	-1.4	+.2	+.9
34	-.3	-1.4	+.1	+.5
35	-.3	-1.4	.0	.0
36			-.2	-.9
37				
38				
39				
40				

Figure 42. Data Sheet Type "W"

4.2.3.5 Measure angle "ϵ": _____ (mm)

4.2.3.5 Measure angle "α": _____ (mm)

4.2.3.5 Measure distance "ϵ": _____ (inches)

4.2.3.5 Measure distance "α": _____ (inches)

Attach three polaroid photographs to this sheet: _____

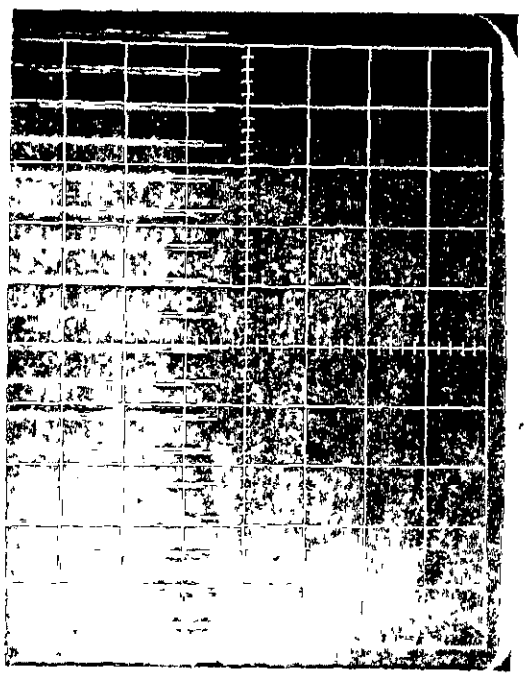

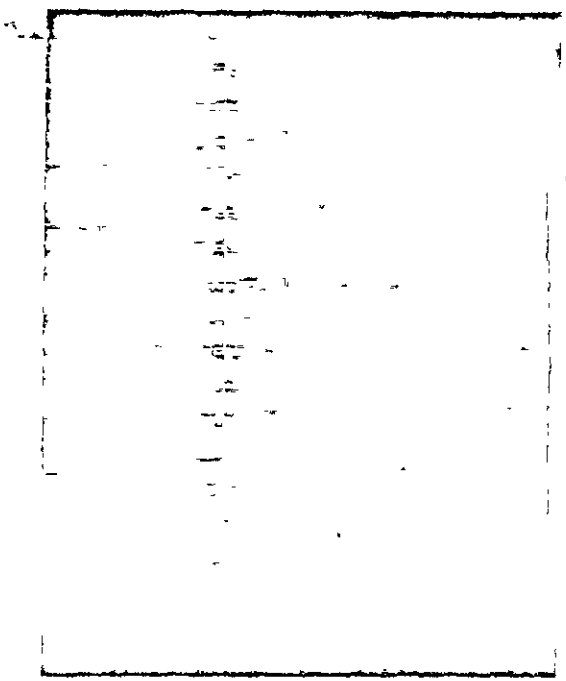

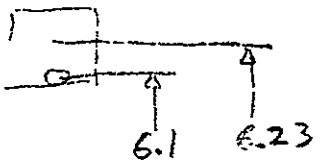

LOCATION #5 11-6-75

TURNS CW @.025 in/TURN	div	@	V/div =	V
0	+5.05	@.2		+1.01
3	2.8	.2		+.56
8	-1.3	.2		-.26
10	-3.0	.2		-.60

DIODE CALIBRATION
LOCATION #5

11-6-75

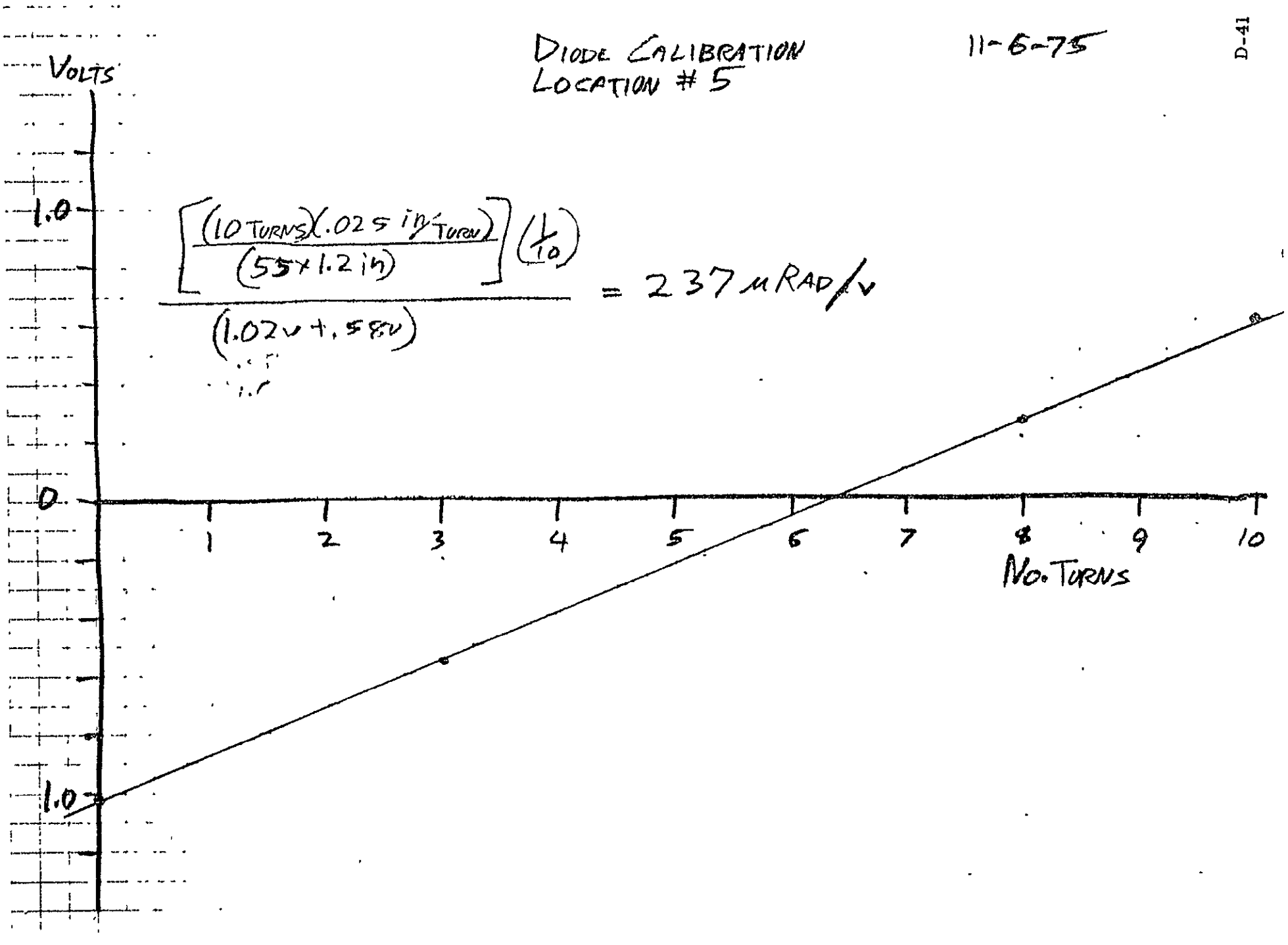

$$\frac{\left[\frac{(10\ \text{TURNS})(.025\ \text{in/TURN})}{(55 \times 1.2\ \text{in})}\right]\left(\frac{1}{10}\right)}{(1.02\text{v} + .58\text{v})} = 237\ \mu\text{RAD/v}$$

11-6-75

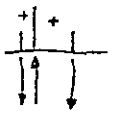

(195 μRAD/V)(.02V/div) = 3.9 μRad/div

LOCATION #2

Data Set 2

Delta Value	Photo #1	Photo #2	Photo #3
1	(-1.1 div)(3.9 μRad/div) = -4.3 μRad	-1.0 - 3.9	
2	-.6 - 2.3	-1.0 - 3.9	
3	-1.0 - 3.9	-1.0 - 3.9	
4	-1.2 - 4.7	-1.2 - 4.7	
5	-1.0 - 3.9	-1.1 - 4.3	
6	-1.1 - 4.3	-1.2 - 4.7	
7	-.9 - 3.5	-.9 - 3.5	
8	-1.0 - 3.9	-.7 - 2.7	
9	-1.1 - 4.3	-1.1 - 4.3	
10	-.6 - 2.3	-1.0 - 3.9	
11	-1.0 - 3.9	-1.0 - 3.9	
12	-1.2 - 4.7	-1.1 - 4.3	
13	-1.0 - 3.9	-.9 - 3.5	
14	-1.2 - 4.7	-1.2 - 4.7	
15	-1.1 - 4.3	-1.2 - 4.7	
16	-1.1 - 4.3	-.8 - 3.1	
17	-.9 - 3.5	-.9 - 3.5	
18	-.6 - 2.3	-1.0 - 3.9	
19	-1.0 - 3.9	-1.1 - 4.3	
20	-1.2 - 4.7	-1.2 - 4.7	
21	-1.1 - 4.3	-1.0 - 3.9	
22	-1.2 - 4.7	-1.1 - 4.3	
23	-1.0 - 3.9	-.9 - 3.5	
24	-1.2 - 4.7	-.8 - 3.1	
25	-1.2 - 4.7	-1.0 - 3.9	
26	-.7 - 2.7	-.9 - 3.5	
27	-1.1 - 4.3	-1.0 - 3.9	
28	-1.1 - 4.3	-1.2 - 4.7	
29	-1.3 - 5.0	-1.0 - 3.9	
30	-1.1 - 4.3	-1.2 - 4.7	
31	-1.2 - 4.7	-1.1 - 4.3	
32	-.9 - 3.5	-.9 - 3.5	
33	-.6 - 2.3	-.9 - 3.5	
34	-1.1 - 4.3		
35	-1.1 - 4.3		
36			
37			
38			
39			
40			
	MEAN = -3.99 σ = .77	MEAN = -3.97 σ = .53	

Figure 42. Data Sheet Type "W"

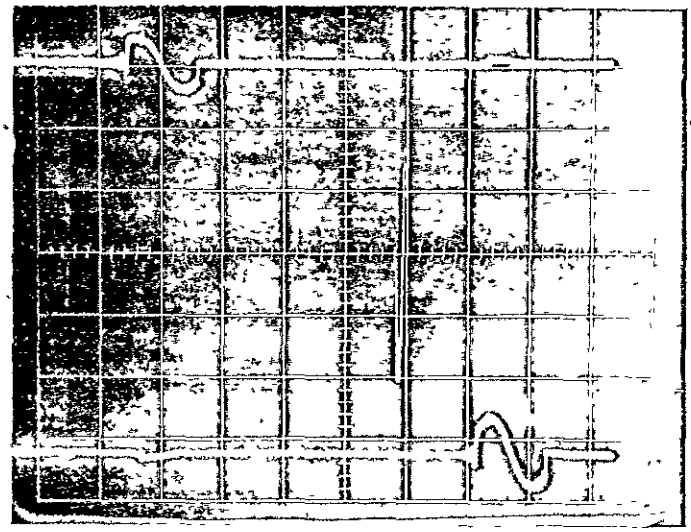

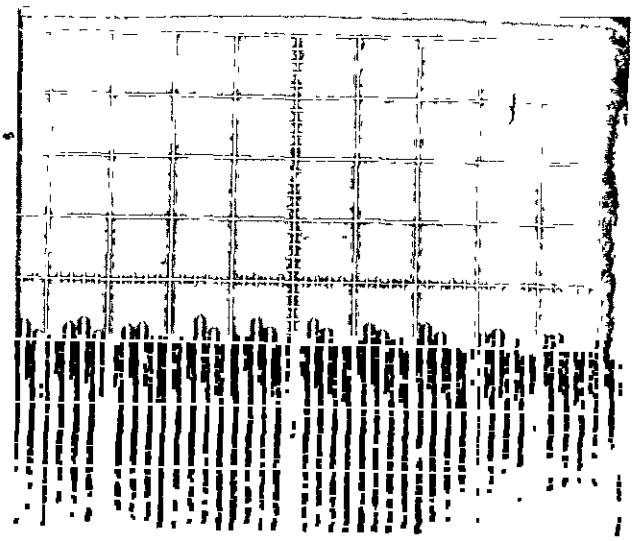

4.2.3.5 Measure angle "ϵ": _____ (mm)

4.2.3.5 Measure angle "α": _____ (mm)

4.2.3.5 Measure distance "ϵ": _____ (inch

4.2.3.5 Measure distance "α": _____ (inch

Attach three polaroid photographs to this sheet: _____

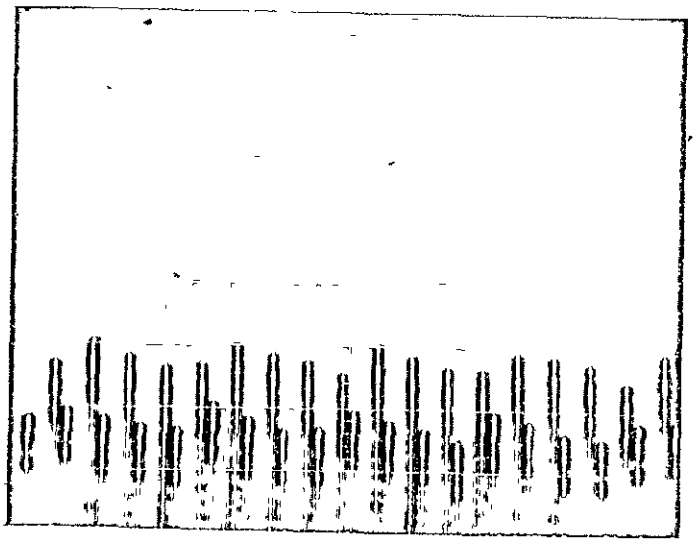

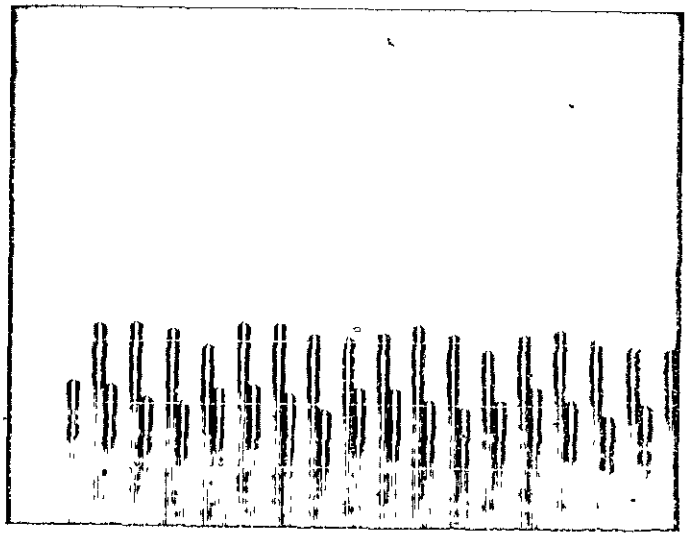

TEST PROCEDURE	BREADBOARD
SCAN MIRROR	THEMATIC MAPPER

CODE IDENT NO. 82577 | SH NO | REV LTR | NUMBER

LOCATION #2 11-6-75

9.95" dia

TURNS CW @.025 in/TURN	div	@ V/div	= V
0	+ 6.8	.2	+ 1.36
3	+ 4.0	.2	+ .80
9	- 1.9	.2	- .38
11	- 4.0	.2	- .80

DIODE CALIBRATION 11-6-75
LOCATION #2

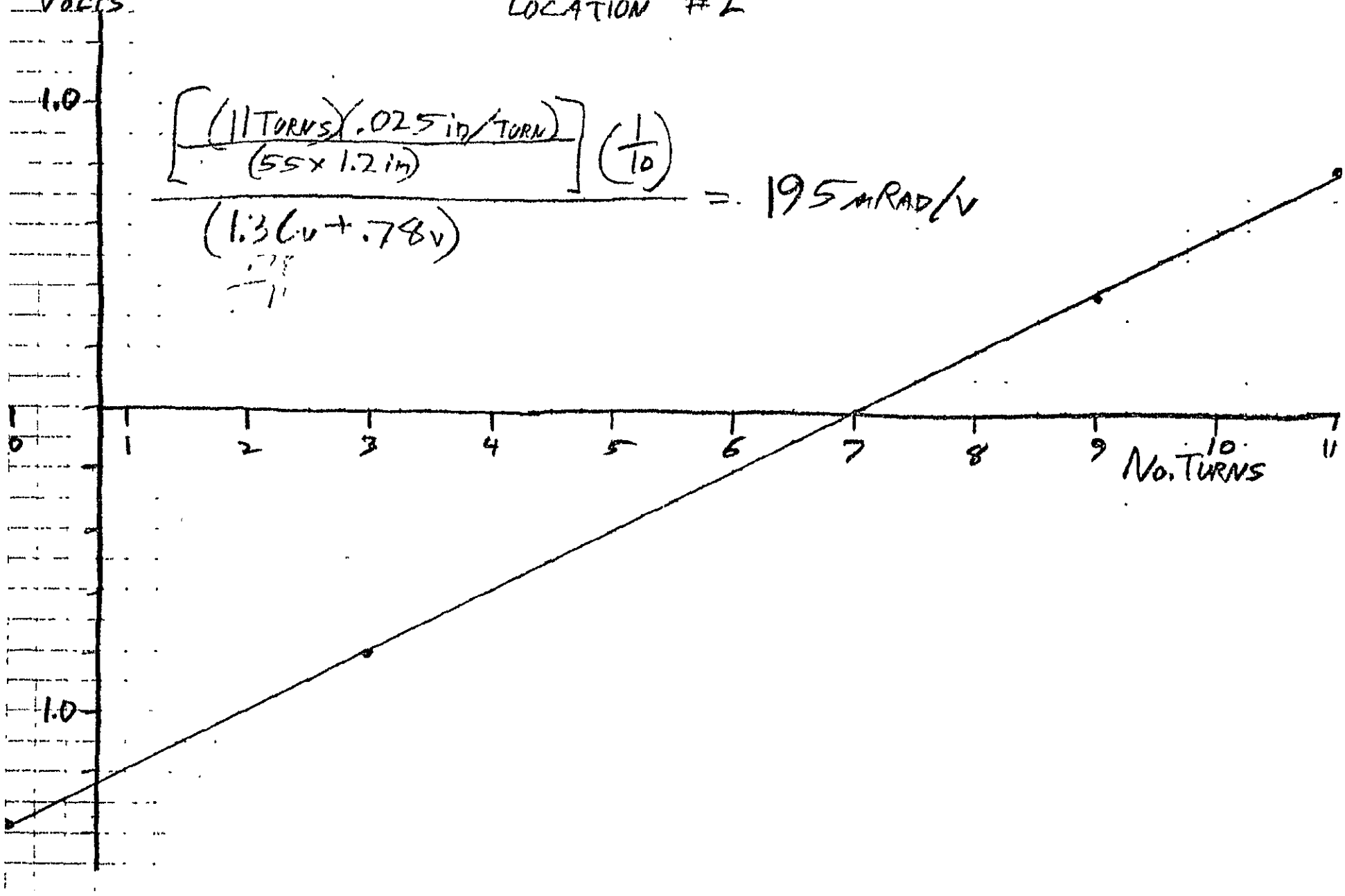

$$\frac{\left[\frac{(11\ \text{TURNS})(.025\ \text{in/TURN})}{(55 \times 1.2\ \text{in})}\right]\left(\frac{1}{10}\right)}{(1.36\text{v} + .78\text{v})} = .195\ \text{mRAD/V}$$

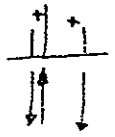

(221 μRAD/V)(.02 V/div) = 4.4 μRAD/div

11-6-75

LOCATION #1

Data Set 3

Data Value	Photo #1	Photo #2	Photo #3
1	(-2 div)(4.4 μRAD/div) = -.9 μRAD	-.2 -.9	
2	.0 .0	-.1 -.4	
3	.0 .0	0 .0	
4	+.1 +.4	-.1 -.4	
5	+.1 +.4	-.1 -.4	
6	-.2 -.9	-.2 -.9	
7	-.2 -.9	-.3 -1.3	
8	-.2 -.9	-.4 -1.8	
9	-.2 -.9	-.2 -.9	
10	-.1 -.4	-.2 -.9	
11	.0 .0	-.1 -.4	
12	+.1 +.4	.0 .0	
13	.0 .0	-.1 -.4	
14	-.1 -.4	-.2 -.9	
15	-.2 -.9	-.2 -.9	
16	-.4 -1.8	-.3 -1.3	
17	-.2 -.9	-.2 -.9	
18	-.1 -.4	-.2 -.9	
19	.0 .0	.0 .0	
20	+.2 +.9	.0 .0	
21	.0 .0	-.1 -.4	
22	-.1 -.4	-.1 -.4	
23	-.1 -.4	-.2 -.9	
24	-.3 -1.3	-.5 -2.2	
25	-.3 -1.3	-.4 -1.8	
26	-.1 -.4	-.2 -.9	
27	+.1 +.4	-.1 -.4	
28	+.1 +.4	+.1 +.4	
29	.0 0	.0	
30	.0 .0	-.1 -.4	
31	-.1 -.4	-.2 -.9	
32	-.4 -1.8	-.4 -1.8	
33	-.4 -1.8	-.4 -1.8	
34	-.2 -.9	-.3 -1.3	
35	.0 .0	.0 .0	
36			
37			
38			
39			
40			

4.-
3 9
4.9
4.2
4 7
5122.1
44

Figure 42. Data Sheet Type "W"

TEST PROCEDURE	BREADBOARD
SCAN MIRROR	THEMATIC MAPPER

4.2.3.5 Measure angle "ϵ": _____ (mm)

4.2.3.5 Measure angle "α": _____ (mm)

4.2.3.5 Measure distance "ϵ": _____ (inch

4.2.3.5 Measure distance "α": _____ (inche

Attach three polaroid photographs to this sheet: _____

LOCATION #1 11-6-75

TURNS CW @.025 in/TURN	div	@ V/div	= V
0	+5.4	@.2 V/div	+1.08
3	+3.0	.2	+.60
9	-2.1	.2	-.41
11	-4.0	.2	-.80

11-6-75

LOCATION #1

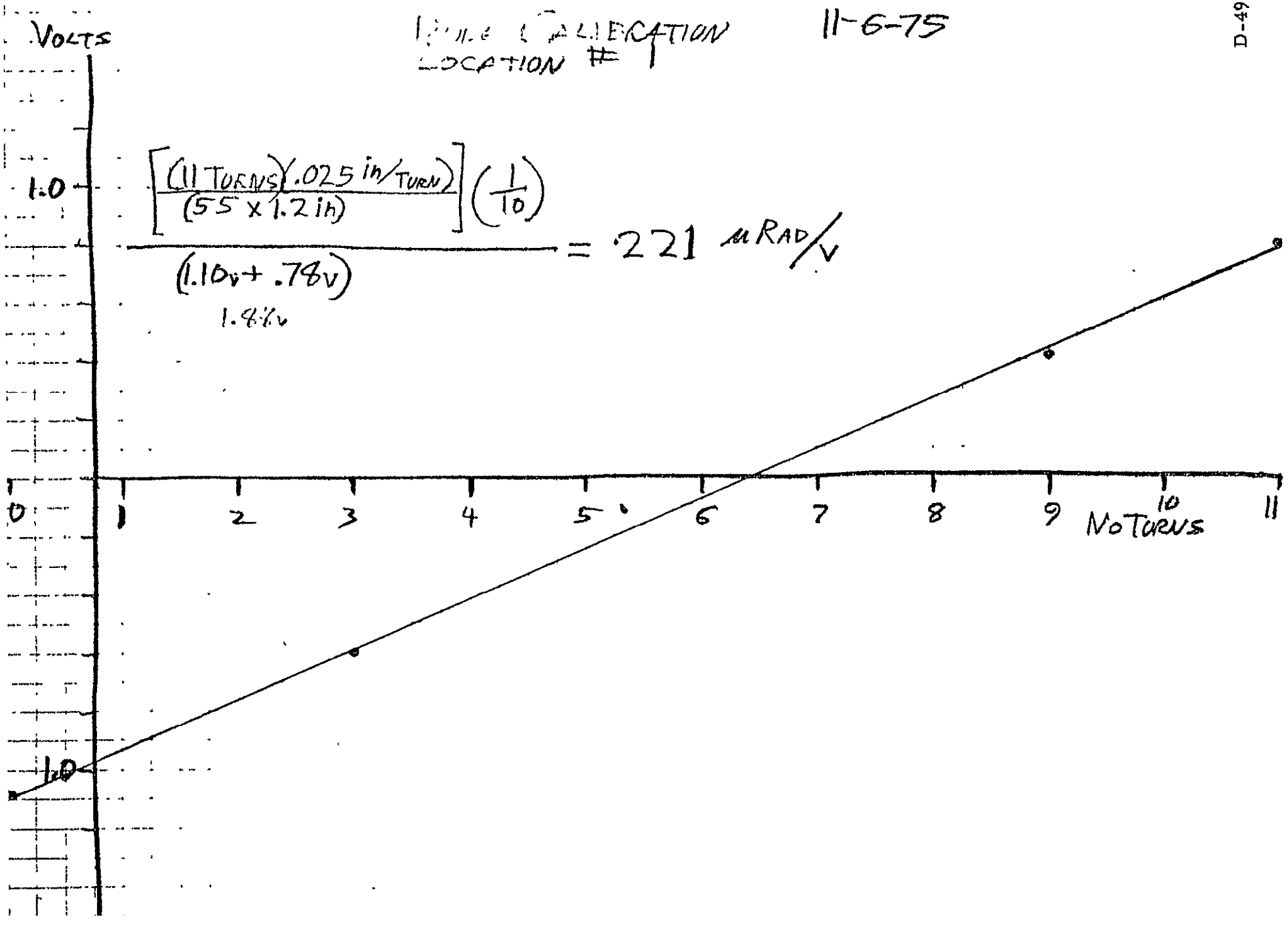

$$\frac{\left[\frac{(11\ \text{TURNS})(.025\ \text{in/TURN})}{(55 \times 1.2\ \text{in})}\right]\left(\frac{1}{10}\right)}{(1.10\text{v} + .78\text{v})} = .221\ \text{mRAD/v}$$

1.88v

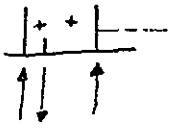

(247 μRAD/V)(.02 V/div) = 4.9 μRAD/div

11-7-75

LOCATION #3

Data Set 4

Delta Value	Photo #1		Photo #2		Photo #3
1	(-.4div)(4.9μRAD/div) = -2.0μRAD		-.1	-.5	
2	-.4	-2.0	-.2	-1.0	
3	-.2	-1.0	-.2	-1.0	
4	+.2	+1.0	-.4	-2.0	
5	.0	0	-.2	-1.0	
6	.0	.0	-.4	-2.0	
7	-.2	-1.0	-.3	-1.5	
8	-.4	-2.0	+.1	+.5	
9	-.2	-1.0	+.1	+.5	
10	-.5	-2.5	.0	.0	
11	-.4	-2.0	-.4	-2.0	
12	+.1	+.5	-.5	-2.5	
13	+.2	+1.0	-.3	-1.5	
14	.0	.0	-.3	-1.5	
15	-.4	-2.0	-.1	-.5	
16	-.5	-2.5	+.1	+.5	
17	-.4	-2.0	.0	.0	
18	-.4	-2.0	.0	.0	
19	-.2	-1.0	-.2	-1.0	
20	.0	.0	-.3	-1.5	
21	.0	.0	-.2	-1.0	
22	+.1	+.5	-.4	-2.0	
23	-.2	-1.0	-.3	-1.5	
24	-.4	-2.0	-.1	-.5	
25	-.2	-1.0	-.2	-1.0	
26	-.5	-2.5	+.1	+.5	
27	-.4	-2.0	-.2	-1.0	
28	.0	.0	-.4	-2.0	
29	+.2	+1.0	-.2	-1.0	
30	+.1	+.5	-.3	-1.5	
31	-.3	-1.5	-.1	-.5	
32			+.1	+.5	
33					
34					
35					
36					
37					
38					
39					
40					

Figure 42. Data Sheet Type "W"

4.2.3.5 Measure angle "ϵ": _____ (mm)

4.2.3.5 Measure angle "α": _____ (mm)

4.2.3.5 Measure distance "ϵ": _____ (inches)

4.2.3.5 Measure distance "α": _____ (inches)

Attach three polaroid photographs to this sheet: _____

LOCATION #3 11-6-75

TURNS CW @.025 in/TURN	div	@ V/div	V
0	5.8	@ .2	1.16
3	3.0		.6
8	-1.6		-.32
10	-3.5		-.7

Diode Calibration
Location #3

11-6-75

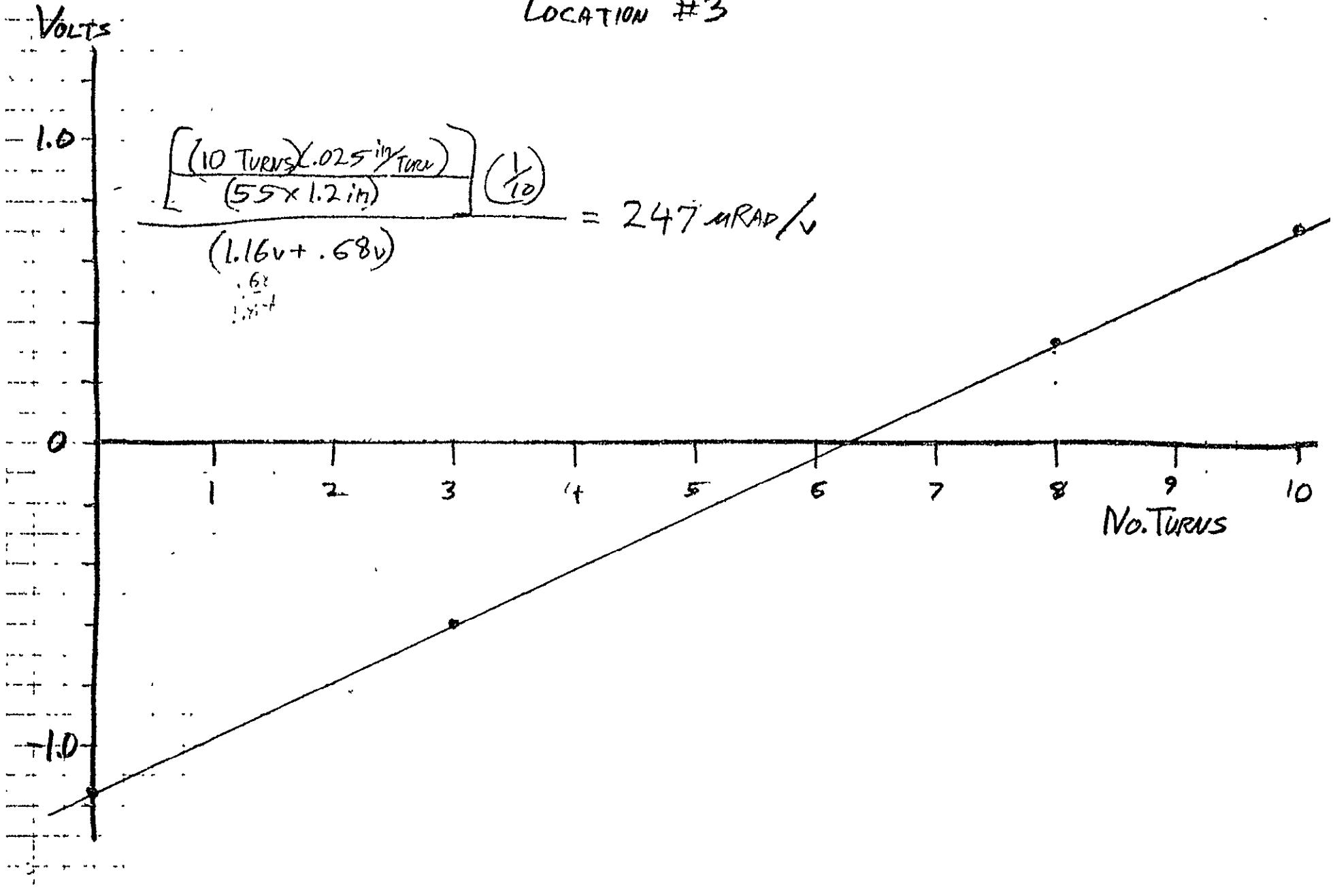

$$\frac{\left[\frac{(10\ \text{Turns})(.025\ \text{in/Turn})}{(55 \times 1.2\ \text{in})}\right]\left(\frac{1}{10}\right)}{(1.16\text{v} + .68\text{v})} = 247\ \text{mRad/v}$$

11-7-75

(210 MRAD/V)(.02 V/div) = 4.2 MRAD/div

LOCATION #4

Data Set 5

Delta Value	Photo #1	Photo #2	Photo #3
1	(+.1div)(42 MRAD/div) = +.4 MRAD	+.2 + .8	
2	+.4 + 1.7	.5 + 2.1	
3	+.7 + 2.9	.7 + 2.9	
4	+.6 + 2.5	.7 + 2.9	
5	+.3 + 1.3	.6 + 2.5	
6	+.2 + .8	.5 + 2.1	
7	+.1 + .4	.2 + .8	
8	+.1 + .4	.0 .0	
9	.0 + .0	.1 + .4	
10	+.4 + 1.7	.5 + 2.1	
11	+.5 + 2.1	.5 + 2.1	
12	+.4 + 1.7	.6 + 2.5	
13	+.5 + 2.1	.8 + 3.4	
14	+.4 + 1.7	.7 + 2.9	
15	.0 0	.2 + .8	
16	-.1 - .4	.1 + .4	
17	+.1 + .4	.3 + 1.3	
18	+.3 + 1.3	.3 + 1.3	
19	+.4 + 1.7	.4 + 1.7	
20	+.5 + 2.1	.8 + 3.4	
21	+.5 + 2.1	.8 + 3.4	
22	+.4 + 1.7	.5 + 2.1	
23	+.1 + .4	.2 + .8	
24	-.1 - .4	.2 + .8	
25	.0 .0	.1 + .4	
26	+.2 + .8	.2 + .8	
27	+.3 + 1.3	.3 + 1.3	
28	+.4 + 1.7	.6 + 2.5	
29	+.7 + 2.9	.8 + 3.4	
30	+.5 + 2.1	.6 + 2.5	
31	+.1 + .4	.4 + 1.7	
32	.0 .0	.3 + 1.3	
33	+.1 + .4	.2 + .8	
34	.0 .0	.1 + .4	
35	+.2 + .8	.2 + .8	
36	+.6 + 2.5	.6 + 2.5	
37	+.6 + 2.5	.8 + 3.4	
38			
39			
40			

Figure 42. Data Sheet Type "W"

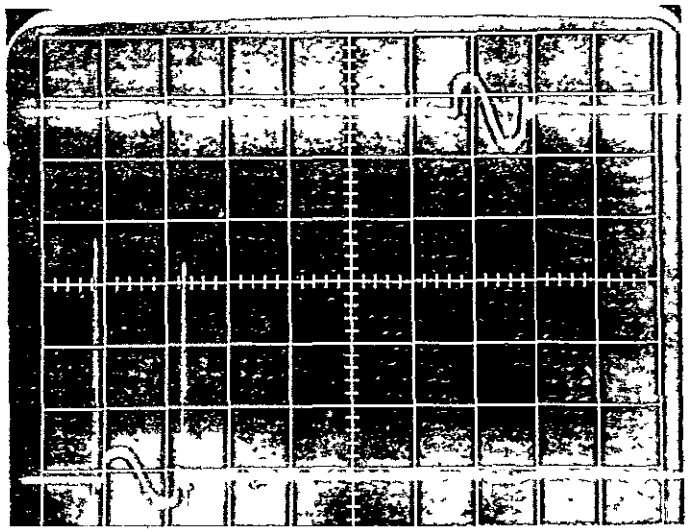

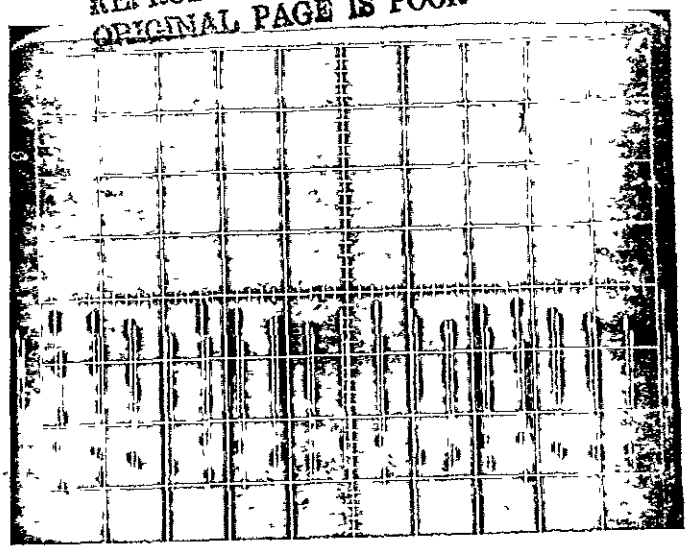

4.2.3.5 Measure angle "ϵ": _____ (mm)

4.2.3.5 Measure angle "α". _____ (mm)

4.2.3.5 Measure distance "ϵ": _____ (inch

4.2.3.5 Measure distance "α": _____ (inch

Attach three polaroid photographs to this sheet: _____

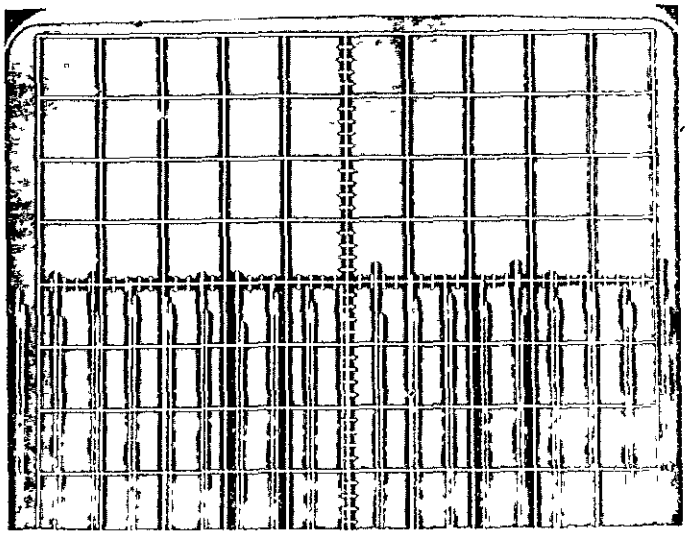

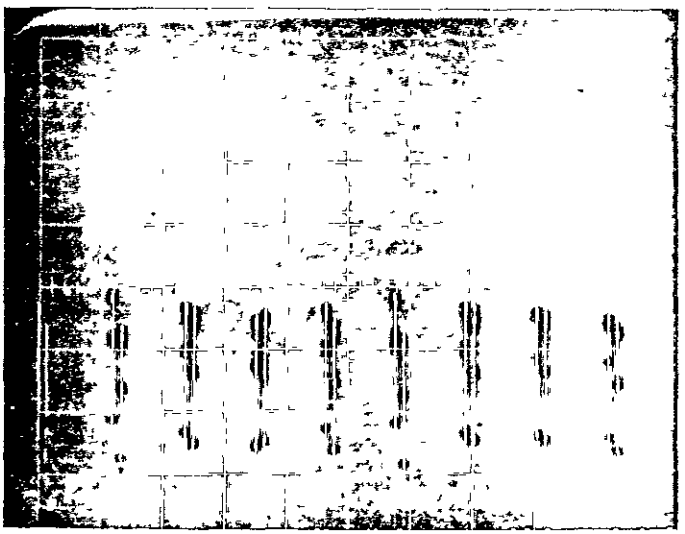

TEST PROCEDURE	BREADBOARD
SCAN MIRROR	THEMATIC MAPPER

CODE IDENT NO 82577 | SH NO | REV LTR | NUMBER

LOCATION #4 11-6-75

TURNS CW @.025 in/TURN	div	@ V/div	= V
0	5.8	@ .2	1.16
3	3.2		.64
8	-1.4		-.28
10	-3.1		-.62
11	-4.1		-.82

DIODE CALIBRATION
LOCATION #4

11-6-75

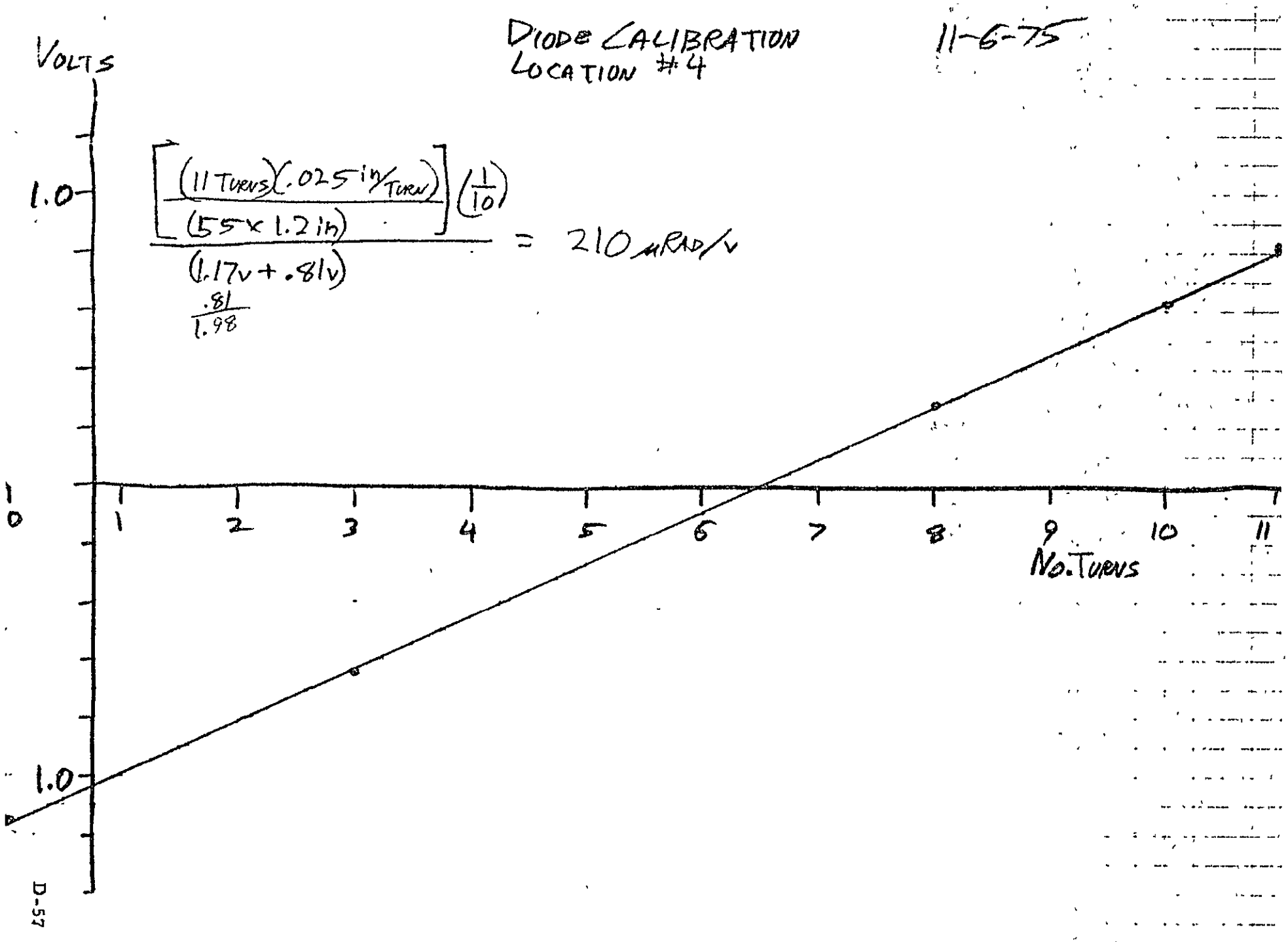

$$\frac{\left[\frac{(11\ \text{TURNS})(.025\ \text{in/TURN})}{(55 \times 1.2\ \text{in})}\right]\left(\frac{1}{10}\right)}{(1.17\text{v} + .81\text{v})} = 210\ \mu\text{RAD/v}$$

$\frac{.81}{1.98}$

CROSS-SCAN COMPUTATIONS:

FOR DATA SET 1

RELATIVE DIODE POSITION = 9.15493E-3

MEAN DEVIATION =-0.246667 MICRORADIANS

RMS DEVIATION = 1.16362 MICRORADIANS

FOR DATA SET 2

RELATIVE DIODE POSITION = 0.274648

MEAN DEVIATION =-4.01667 MICRORADIANS

RMS DEVIATION = 4.08318 MICRORADIANS

FOR DATA SET 3

RELATIVE DIODE POSITION = 0.415493

MEAN DEVIATION =-0.34 MICRORADIANS

RMS DEVIATION = 0.703799 MICRORADIANS

FOR DATA SET 4

RELATIVE DIODE POSITION = 0.661972

MEAN DEVIATION =-0.9 MICRORADIANS

RMS DEVIATION = 1.46629 MICRORADIANS

FOR DATA SET 5

RELATIVE DIODE POSITION = 0.96831

MEAN DEVIATION = 1.24667 MICRORADIANS

RMS DEVIATION = 1.55799 MICRORADIANS

Figure 45. Data Sheet Type "Z"

4.2.4.6.1.1
4.2.4.6.1.2
4.2.4.6.2.1
4.2.4.6.2.2
4.2.4.6.3.1
4.2.4.6.3.2
4.2.4.6.4.1
4.2.4.6.4.2
4.2.4.6.5.1
4.2.4.6.5.2

RMS DEVIATION FORWARD TO REVERSE (MICRORADIANS)
VS DIODE POSITION (D2-D1)/(D3-D1)

Data sheet Type 'AA'

```
DELTA          11:22          03-DEC-75


100 5,14.2
110 .13,3.9,5.9,9.4,13.75
120 30
130 -.5,.5,1.9,.9,0,-.9,-1.9,-1.4,-.9,-.9,.5,1.4,1.4,-.9,-1.4,-.9,
132 -1.9,-1.4,0,.5,.9,.9,0,-1.4,-1.9,-.9,-1.4,-.5,1.4,1.4
140 30
150 -4.3,-2.3,-3.9,-4.7,-3.9,-4.3,-3.5,-3.9,-4.3,-2.3,-3.9,-4.7,-3.9,
152 -4.7,-4.3,-4.3,-3.5,-2.3,-3.9,-4.7,-4.3,-4.7,-3.9,-4.7,-4.7,-2.7,
154 -4.3,  -4.3,-5.0,-4.3
160 30
170 -.9,0,0,.4,.4,-.9,-.9,-.9,-.9,-.4,0,.4,0,-.4,-.9,-1.8,-.9,-.4,
172 0,.9,0,-.4,-.4,-1.3,-1.3,-.4,.4,.4,0,0
180 30
190 -2,-2,-1,1,0,0,-1,-2,-1,-2.5,-2,.5,1,0,-2,-2.5,-2,-2,-1,
192 0,0,.5,-1,-2,-1,-2.5,-2,0,1,.5
200 30
210 .4,1.7,2.9,2.5,1.3,.8,.4,.4,0,1.7,2.1,1.7,2.1,1.7,0,-.4,.4,1.3,1.7,
212 2.1,2.1,1.7,.4,-.4,0,.8,1.3,1.7,2.9,2.1
```

APPENDIX E – DATA PACKAGE 2
"PROCEDURAL TEST DATA, SMA WITH BACK BUMPERS"

The data presented in this section describes the performance of the scan mirror assembly utilizing the back bumper subassembly that was used on the earlier engineering dummy mirror assembly. This data was collected and reduced in accordance with the procedures described in the Thematic Mapper Breadboard Scan Mirror Test Procedure, TP 31891-350.

The measurements taken in the procedurcal tests were in an air environment. Data taken of operation in helium is contained in the laboratory log book.

		SAMPLE	SAMPLE	
4.1.2.1.4	Total Angle (milliradians) (α) 19 of 645	295 mr	( )
4.1.2.2.3	Driving Frequency	9.2 Hz	( )
4.1.2.2.5	Scan Average Period	110,355243 msec	(Approx. 102 ms)
4.1.2.2.6	Scan Frequency	9.05	(Approx. 9.78 Hz)
4.1.2.2.7	Period Deviation (Increased Time)(Max)	110.366 msec	
4.1.2.2.7	Period Deviation (Decreased Time)(Max)	110.346 msec	
4.1.2.2.7	Attach Computer Plot to this Sheet (Deviations)	✓	
4.1.2.2.8	Standard Deviation	5 8589 msec	
4.1.3.2.4	Start Up Time		(Less than 30 Seconds)
4.1.4.2.4	Turn Around Time "A" (Average)	10.46758 msec	(Approx. 8.0 ms.)
4.1.4.2.4	Turn Around Time "C" (Average)	10.74697 msec	(Approx. 8.0 ms.)
4.1.4.2.5	"A" Maximum	10.4689	
4.1.4.2.5	"A" Minimum	10.4665	
4.1.4.2.6	"C" Maximum	10.7479	
4.1.4.2.6	"C" Minimum	10.7461	
4.1.4.2.7	Attach Computer Plot to this Sheet (Deviations)	✓	
4.1.4.2.8	Attach Computer Plot to this Sheet (Deviations)	✓	
4.1.4.2.9	Standard Deviation "A"	.4799 msec	
4.1.4.2.10	Standard Deviation "C"	.4514 msec	
4.1.5.2.6	Center Scan Angle (mr) (β)	—	
4.1.5.2.6	Center Scan Angle (mr) (γ)	—	
4.1.5.2.7	Total Angle Recheck (mr) (α)	—	

TEST PROCEDURE -- BREADBOARD SCAN MIRROR -- THEMATIC MAPPER

HUGHES AIRCRAFT CO. CULVER CITY, CALIF. CODE IDENT NO. 52577

SH NO. 14

REV LTR

NUMBER 42-31891-253

Figure 5. Data Sheet - Type "A"

4.1.2.2.7

```
MEAN AND STANDARD DEVIATION COMPUTATION

FOR DATA SET  1

A ERROR VALUE=110/1 =0.24 μsec

STANDARD DEVIATION= 5.  5.0 μsec

OPTIONAL PLOT OF DEVIATION WIDTH THE MEAN:
IF YES, TYPE A '1', IF NO, TYPE A '0'
?1

                DEVIATION WIDTH THE MEAN

 -3SIGMA   -2SIGMA   -1SIGMA    MEAN    +1 SIGMA   +2SIGMA   +3 SIGMA
 I.........I.........I.........I.........I.........I.........I.........
```

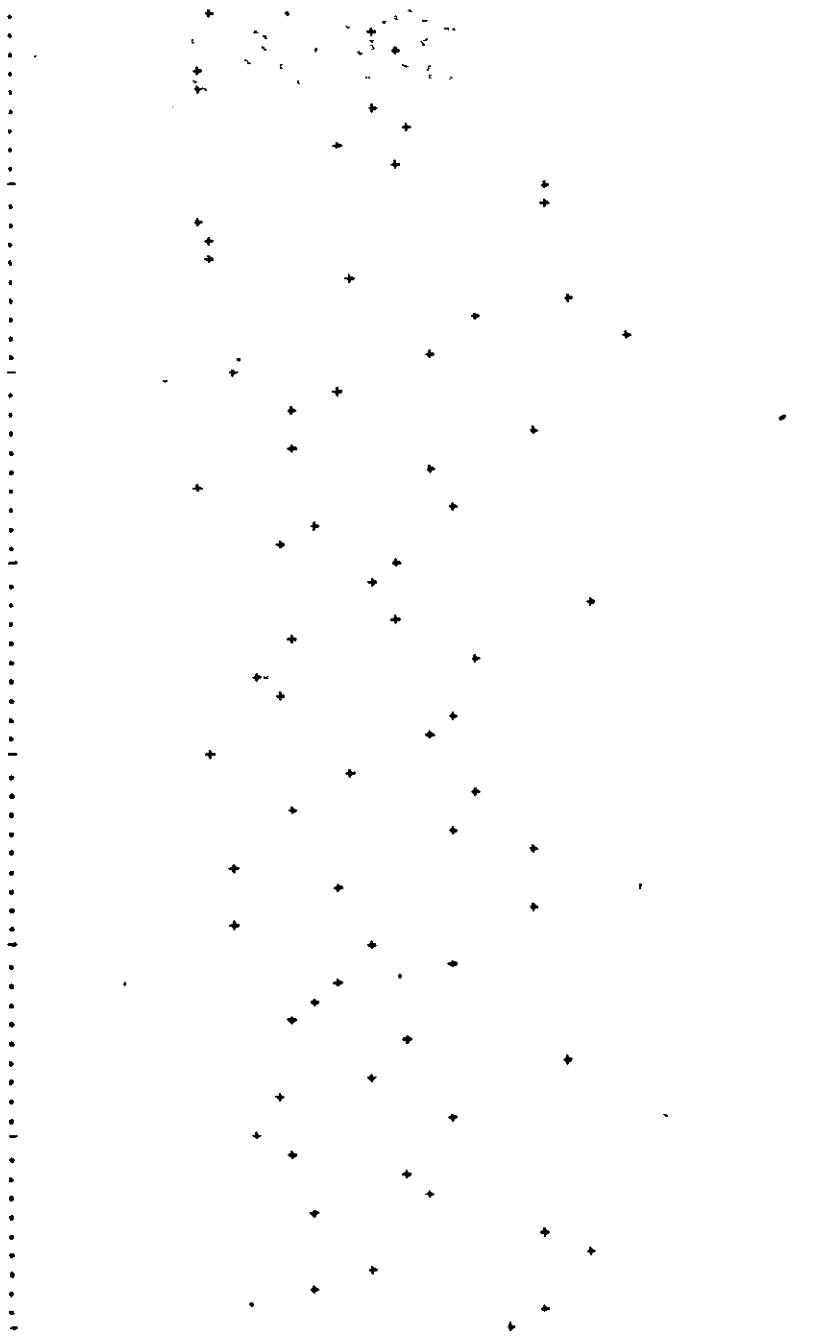

```
 I.........I.........I.........I.........I.........I.........I.........
```

Sean Reid
10-24-75 data
92 Hz closed loop?

4.1.4.2.7

10 27 75

10467 5614 msec
10.467 5614 msec

Turn Around Time (TAT)
10 24-75 data
9.2 Hz equivalent bp

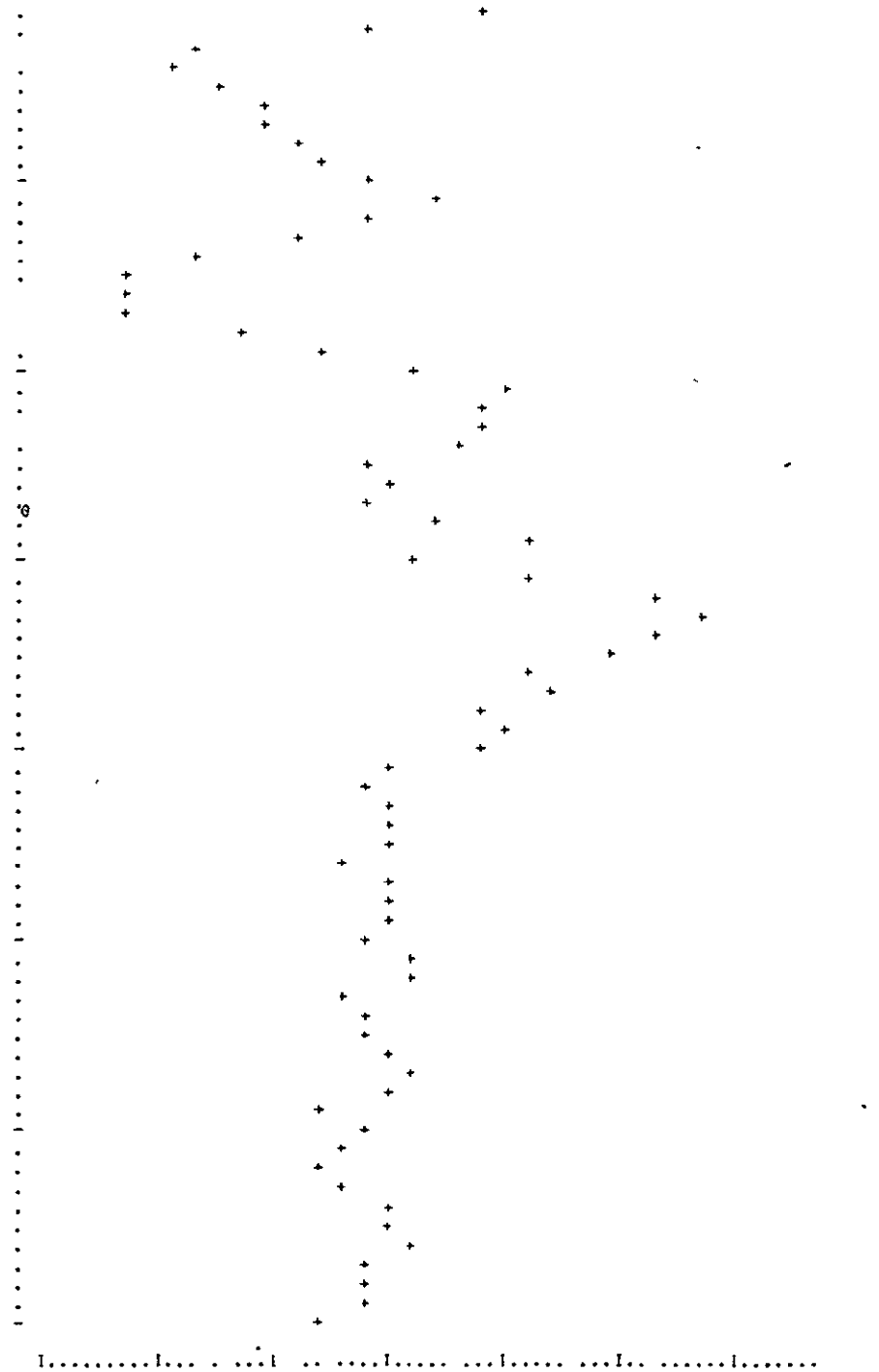

4.4.4.2.8

FOR PATH SET 2

AVERAGE VALUE= 4[illegible].771

10746.9771 msec

INNER-MOST DEVIATION= 4.[illegible]1 .4514 msec

OPTIONAL PLOT OF DEVIATION ABOUT THE MEAN
IF YES, TYPE A "1", IF NO, TYPE A "0"
?1

DEVIATION ABOUT THE MEAN

-[illegible] -2.[illegible] -1 [illegible] [illegible] +1 [illegible] +2.[illegible] +[illegible]

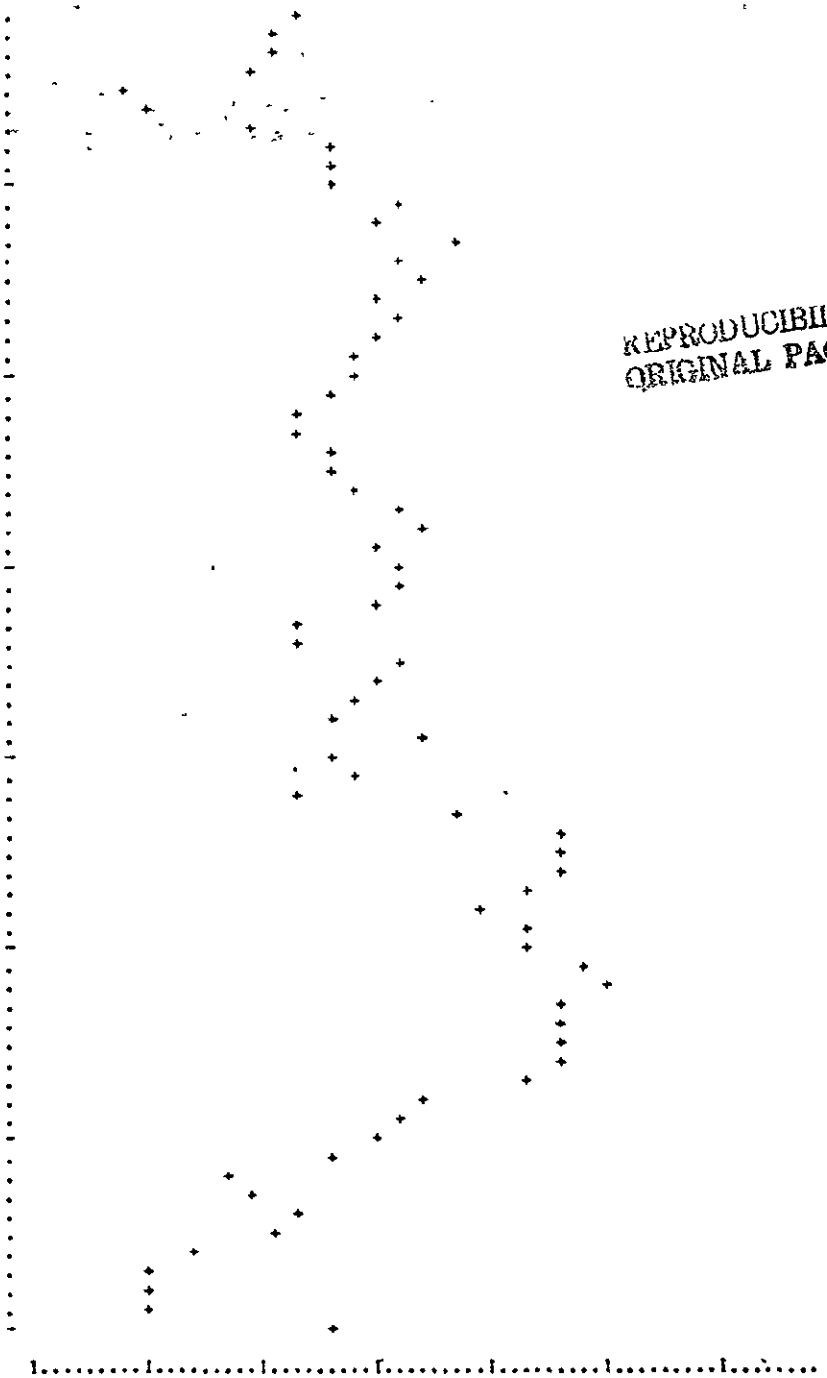

Fundamental Time (Station) 92 Hz clock 10 - 29 [illegible]

		SAMPLE	SAMPLE
4.1.6.2.1.3	Ten Hz Clock Signal Frequency	9.2	(Hz)
4.1.6.2.1.8	Time for Angle (α) (Average) Forward	44.56	(ms)
4.1.6.2.1.9	Time for Angle (ϵ) (Average) Forward	7.89	(ms)
4.1.6.2.1.10	Time for Angle (α) (Average) Reverse	44.56	(ms)
4.1.6.2.1.11	Time for Angle (ϵ) (Average) Reverse	7.95	(ms)
4.1.6.2.1.12	Angle (ϵ)	52.4	(mr)
4.1.6.2.1.13	Angle (α)	295	(mr)
4.1.6.2.2.3	Ten Hz Clock Signal Frequency	9.2	(Hz)
4.1.6.2.2.8	Time for Angle (α) (Average) Forward	44.56	(ms)
4.1.6.2.2.9	Time for Angle (ϵ) (Average) Forward	13.31	(ms)
4.1.6.2.2.10	Time for Angle (α) (Average) Reverse	44.55	(ms)
4.1.6.2.2.11	Time for Angle ($\cdot$) (Average) Reverse	13.398	(ms)
4.1.6.2.2.12	Angle (ϵ)	88.8	(mr)
4.1.6.2.2.13	Angle (α)	295	(mr)

Figure 11. Data Sheet - Type B

		SAMPLE	
4.1.6.2.3.3	Ten Hz Clock Signal Frequency	9.2	(Hz)
4.1.6.2.3.8	Time for Angle (α) (Average) Forward	44.56	(ms)
4.1.6.2.3.9	Time for Angle (ϵ) (Average) Forward	23.26	(ms)
4.1.6.2.3.10	Time for Angle (α) (Average) Reverse	44.56	(ms)
4.1.6?2.3.11	Time for Angle (ϵ) (Average) Reverse	23.38	(ms)
4.1.6.2.3.12	Angle (ϵ)	154.2	(mr)
4.1.6.2.3.13	Angle (α)	295	(mr)
4,1.6.2.4.3	Ten Hz Clock Signal Frequency	9.2	(Hz)
4.1.6.2.4.8	Time for Angle (α) (Average) Forward	44.56	(ms)
4.1.6.2.4.9	Time for Angle (ϵ) (Average) Forward	26.91	(ms)
4.1.6.2.4.10	Time for Angle (α) (Average) Reverse	44 56	(ms)
4.1.6.2.4.11	Time for Angle (ϵ) (Average) Reverse	27.03	(ms)
4.1.6.2.4.12	Angle (ϵ)	178.74	(mr)
4.1.6.2.4.13	Angle (α)	295	(mr)

Figure 12. Data Sheet - Type C

		SAMPLE	SAMPLE
4.1.6.2.5.3	Ten Hz Clock Signal Frequency		9.2 (Hz)
4.1.6.2.5.8	Time for Angle (α)(Average) Forward		44.55 (ms)
4.1.6.2.5.9	Time for Angle (ϵ)(Average) Forward		30.20 (ms)
4.1.6.2.5.10	Time for Angle (α)(Average) Reverse		44.55 (ms)
4.1.6.2.5.11	Time for Angle (ϵ)(Average) Reverse		30.29 (ms)
4.1.6.2.5.12	Angle (ϵ)		200.44 (mr)
4.1.6.2.5.13	Angle (α)		295 (mr)

Figure 13. Data Sheet - Type "D"

Attach ten computer generated graphs here.

Location Diode	1	2	3	4	5
Fwd	0.177018	0.2988	0.5221	0.6039	0.6777
Rev	0.17847	0.3007	0.5246	0.6064	0.6800

Standard Deviation Values:

Location Diode	1	2	3	4	5
Fwd	1.036×10^{-5}	1.77×10^{-5}	1.049×10^{-5}	1.082×10^{-5}	1.053×10^{-5}
Rev	1.478×10^{-5}	1.047×10^{-5}	1.408×10^{-5}	1.155×10^{-5}	1.275×10^{-5}

Figure 14. Data Sheet Type "E"

4.1.8 2.6.2

LINEARITY COMPUTATIONS (FORWARD):
FOR DATA SET 1

RELATIVE DIODE POSITION= 0.177614

AVERAGE VALUE= 0.177018

STANDARD DEVIATION= 1.02617E-5

ANGLE DEVIATION SCAN TO SCAN
VS SCAN NUMBER

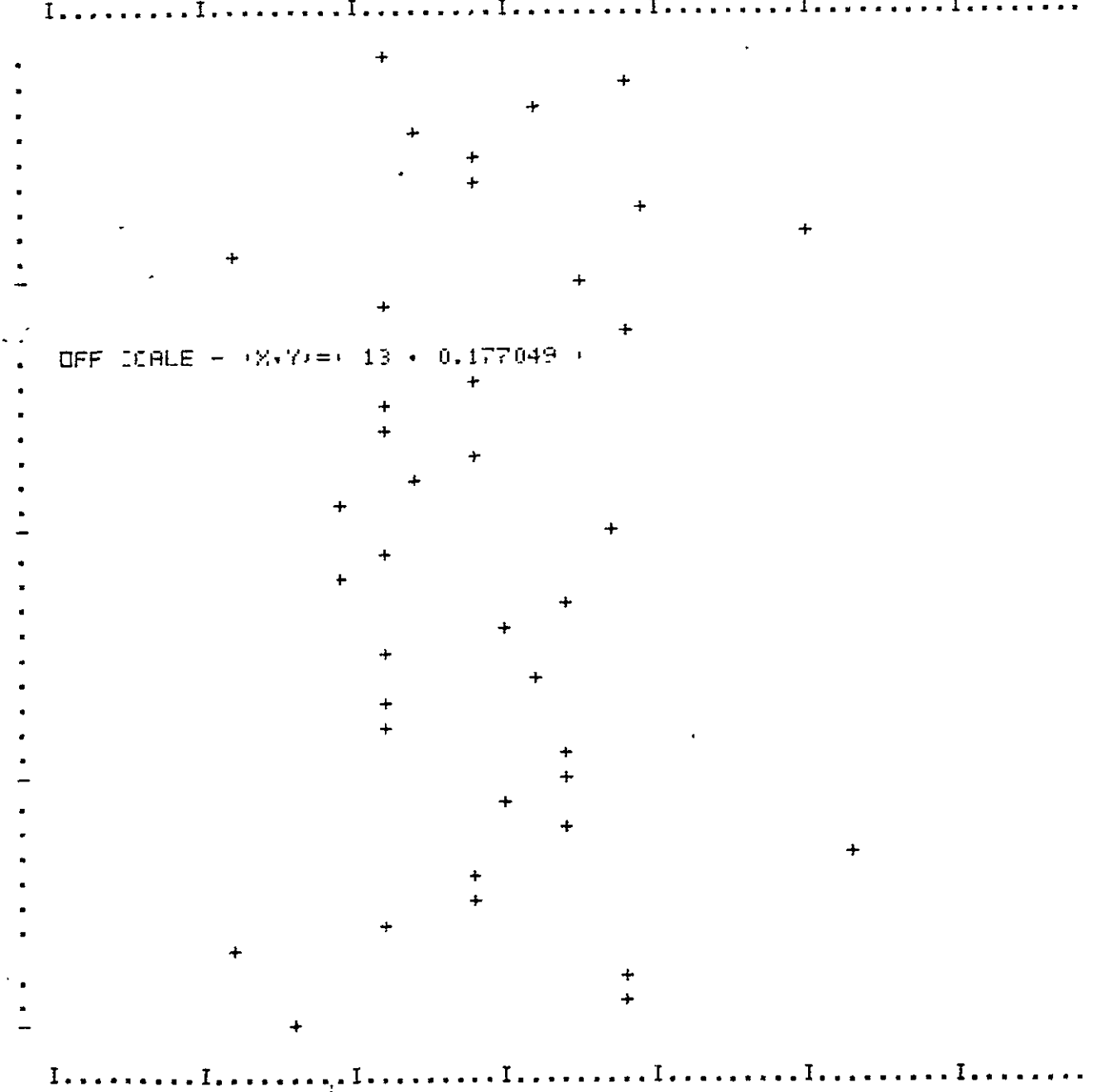

4.1.6 2 6.2 -

DATA SET 2 FORWARD

RELATIVE DIODE POSITION= 0.301104

AVERAGE VALUE= 0.298794

STANDARD DEVIATION= 1.77009E-5

ANGLE DEVIATION SCAN TO SCAN
VS SCAN NUMBER

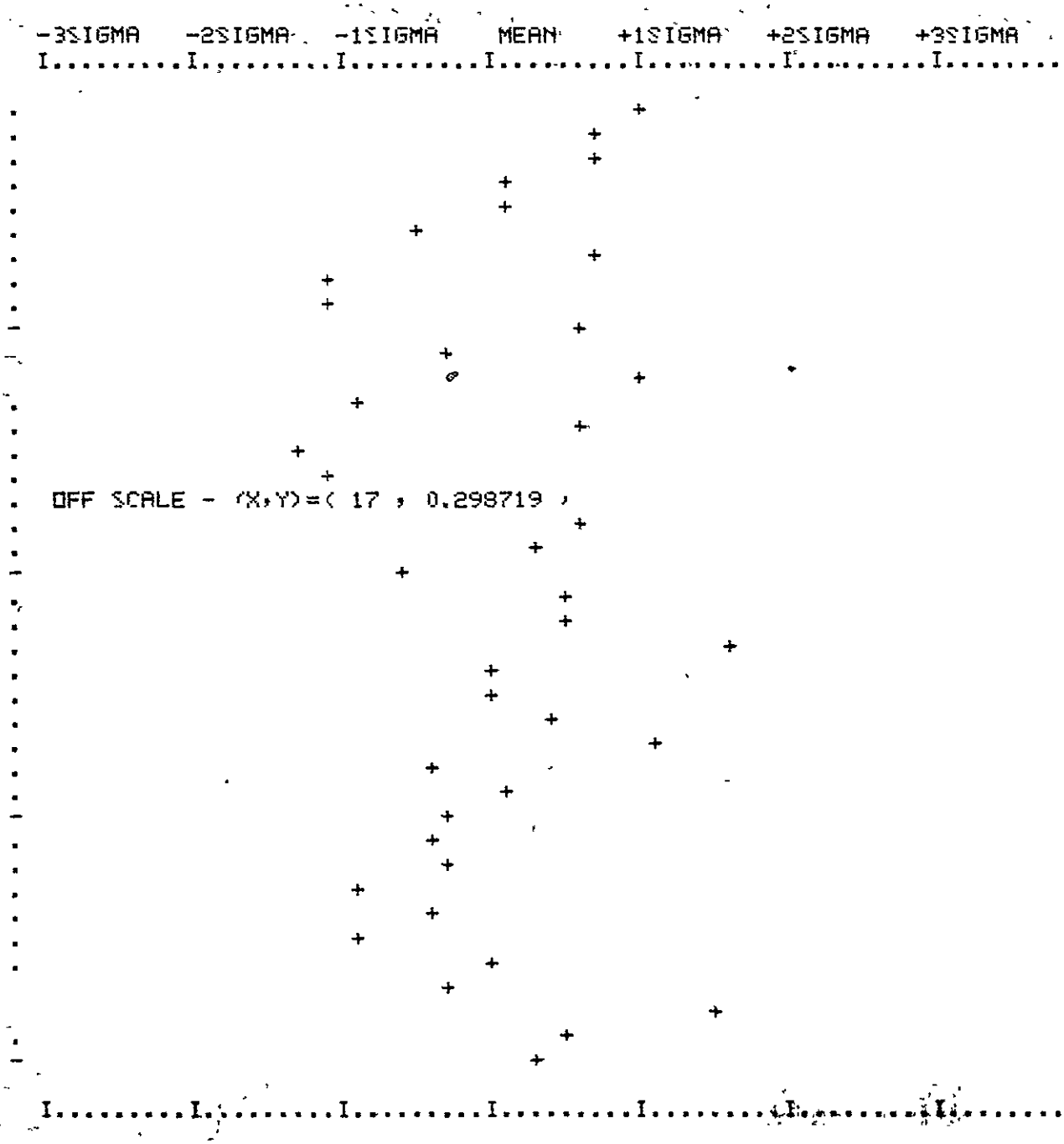

4.1.6.2.6.2

FOR DATA SET 3 FORWARD

RELATIVE DIODE POSITION= 0.522859

AVERAGE VALUE= 0.522094

STANDARD DEVIATION= 1.04935E-5

ANGLE DEVIATION SCAN TO SCAN
VS SCAN NUMBER

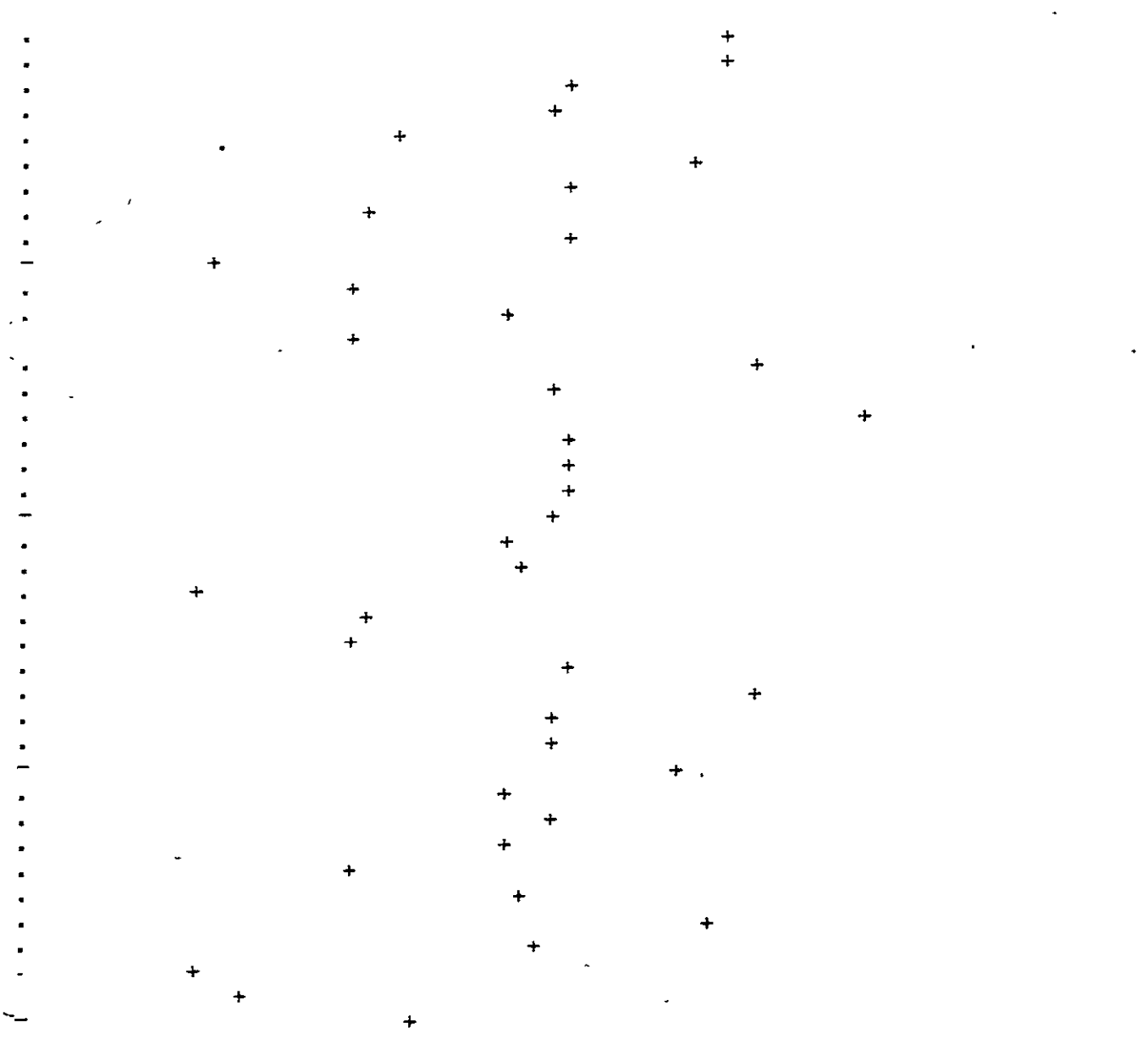

4.1.6.2.6.2

DATA SET 24 FORWARD

RELATIVE DIODE POSITION= 0.605885

AVERAGE VALUE= 0.60393

STANDARD DEVIATION= 1.08231E-5

ANGLE DEVIATION SCAN TO SCAN
VS SCAN NUMBER

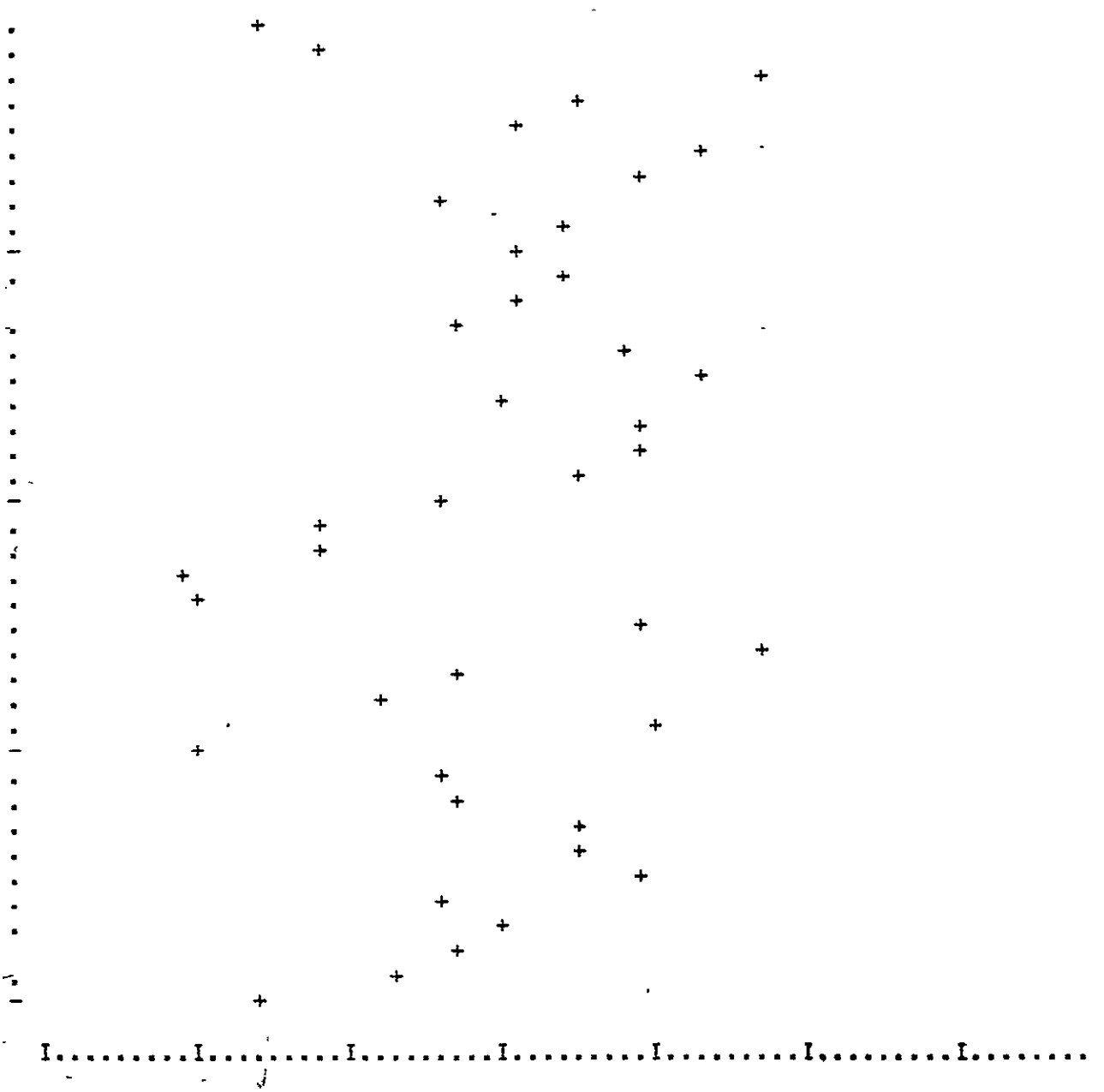

4.1.6.2.6.2

FOR DATA SET 5 FORWARD

RELATIVE DIODE POSITION= 0.679454

AVERAGE VALUE= 0.677756

STANDARD DEVIATION= 1.05322E-5

ANGLE DEVIATION SCAN TO SCAN
VS SCAN NUMBER

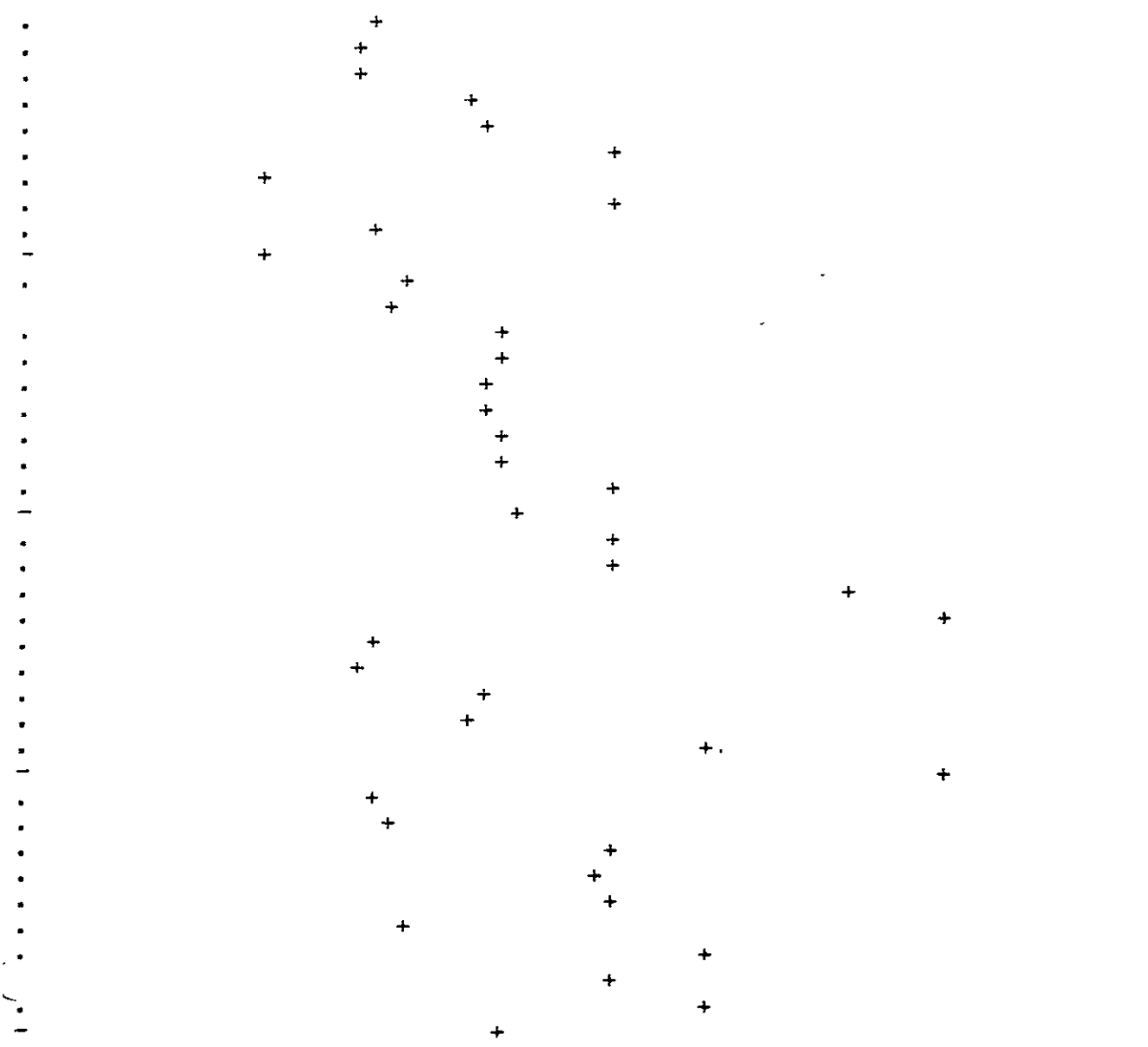

4.1.6.2.6.2

LINEARITY COMPUTATIONS (REVERSE):
FOR DATA SET 1

RELATIVE DIODE POSITION= 0.177614

AVERAGE VALUE= 0.178472

STANDARD DEVIATION= 1.47910E-5

ANGLE DEVIATION SCAN TO SCAN
VS SCAN NUMBER

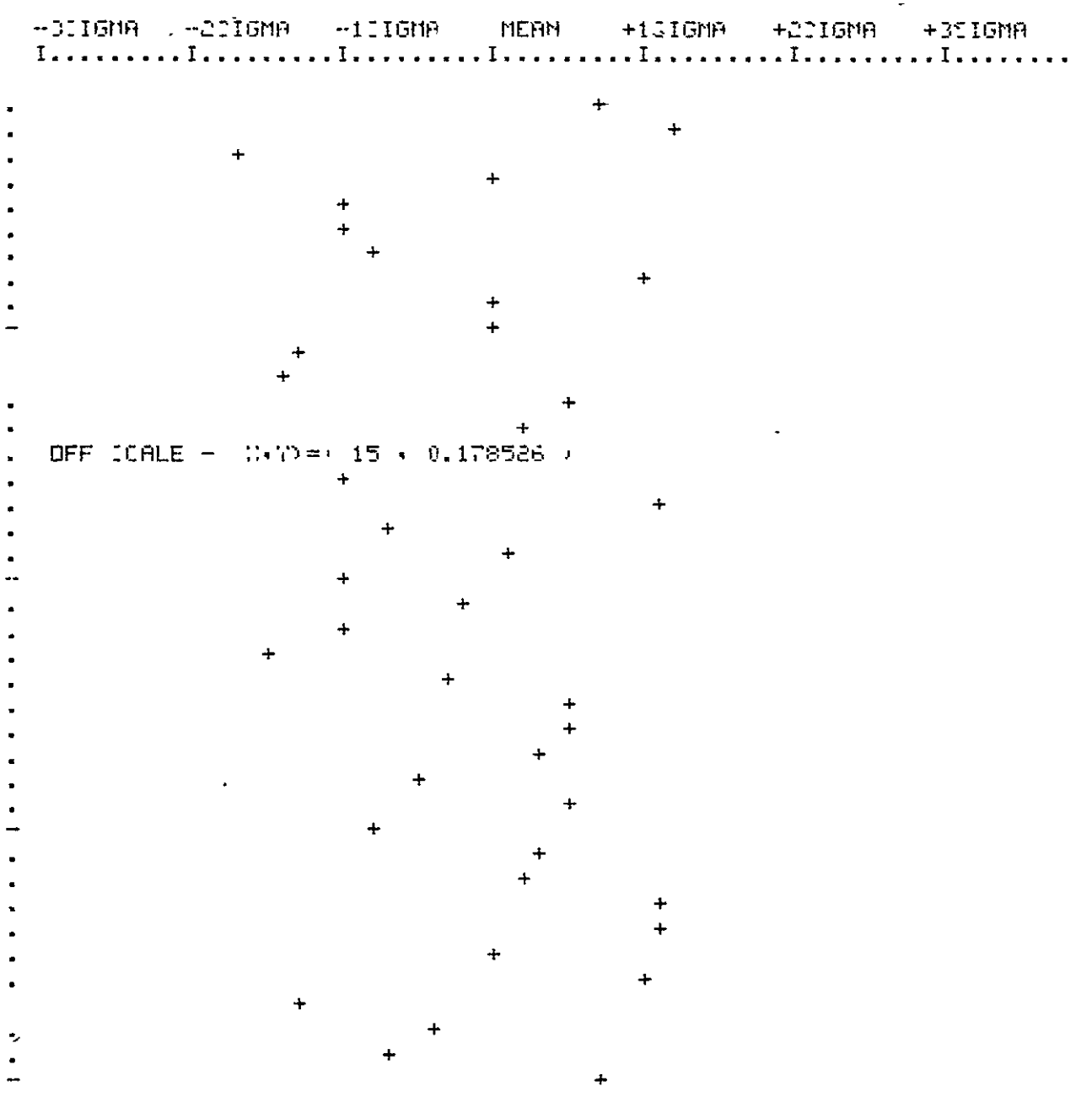

4.1.6.2.6.2

FOR DATA SET 2 Reverse

RELATIVE DIODE POSITION= 0.301104

AVERAGE VALUE= 0.300713

STANDARD DEVIATION= 1.04739E-5

ANGLE DEVIATION FROM TO FROM
VS SCAN NUMBER

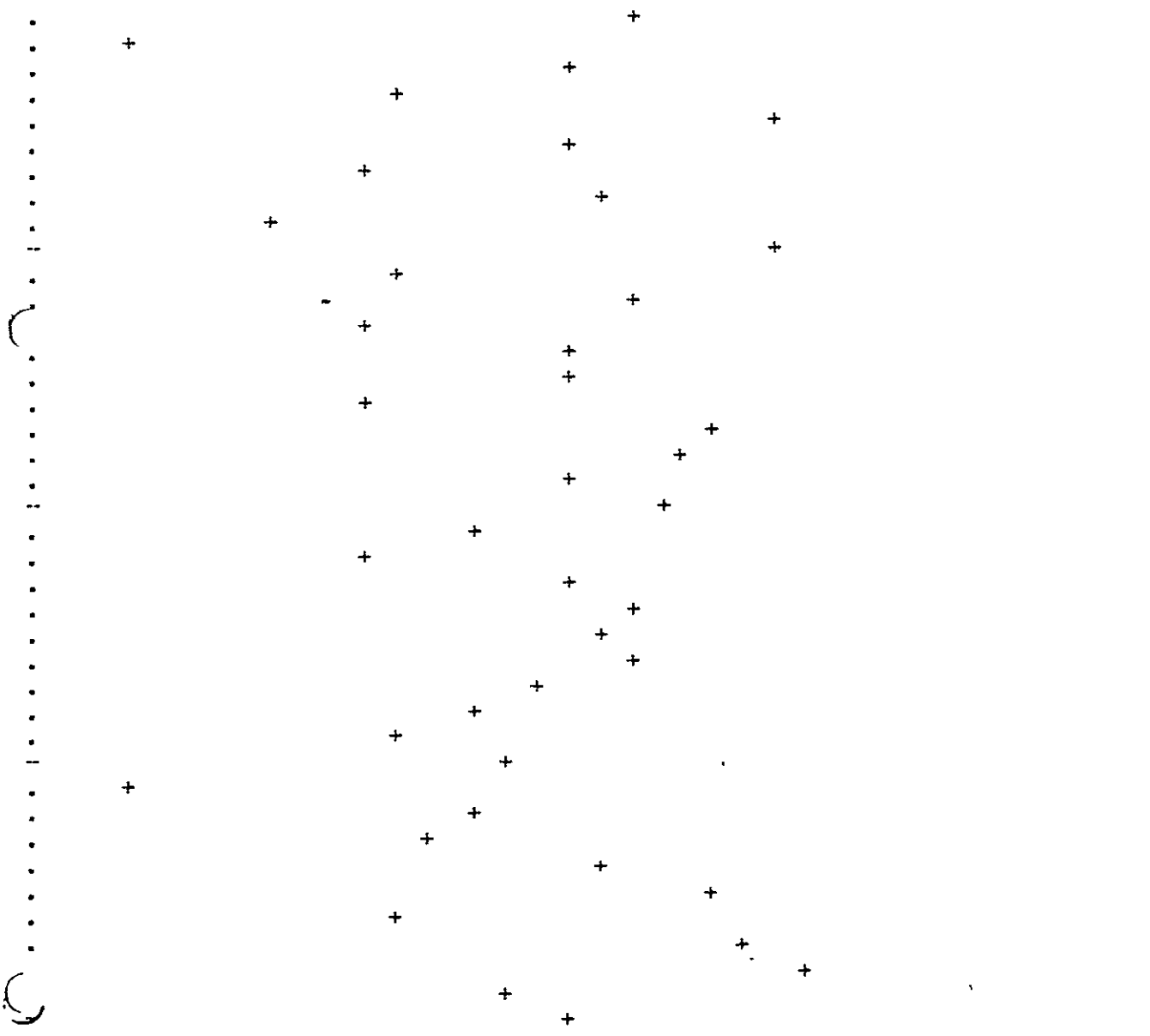

4.1.6.2.6.2

FOR DATA SET 3 Reverse

RELATIVE DIODE POSITION= 0.522059

AVERAGE VALUE= 0.524617

STANDARD DEVIATION= 1.40651E-5

ANGLE DEVIATION SCAN TO SCAN
VS SCAN NUMBER

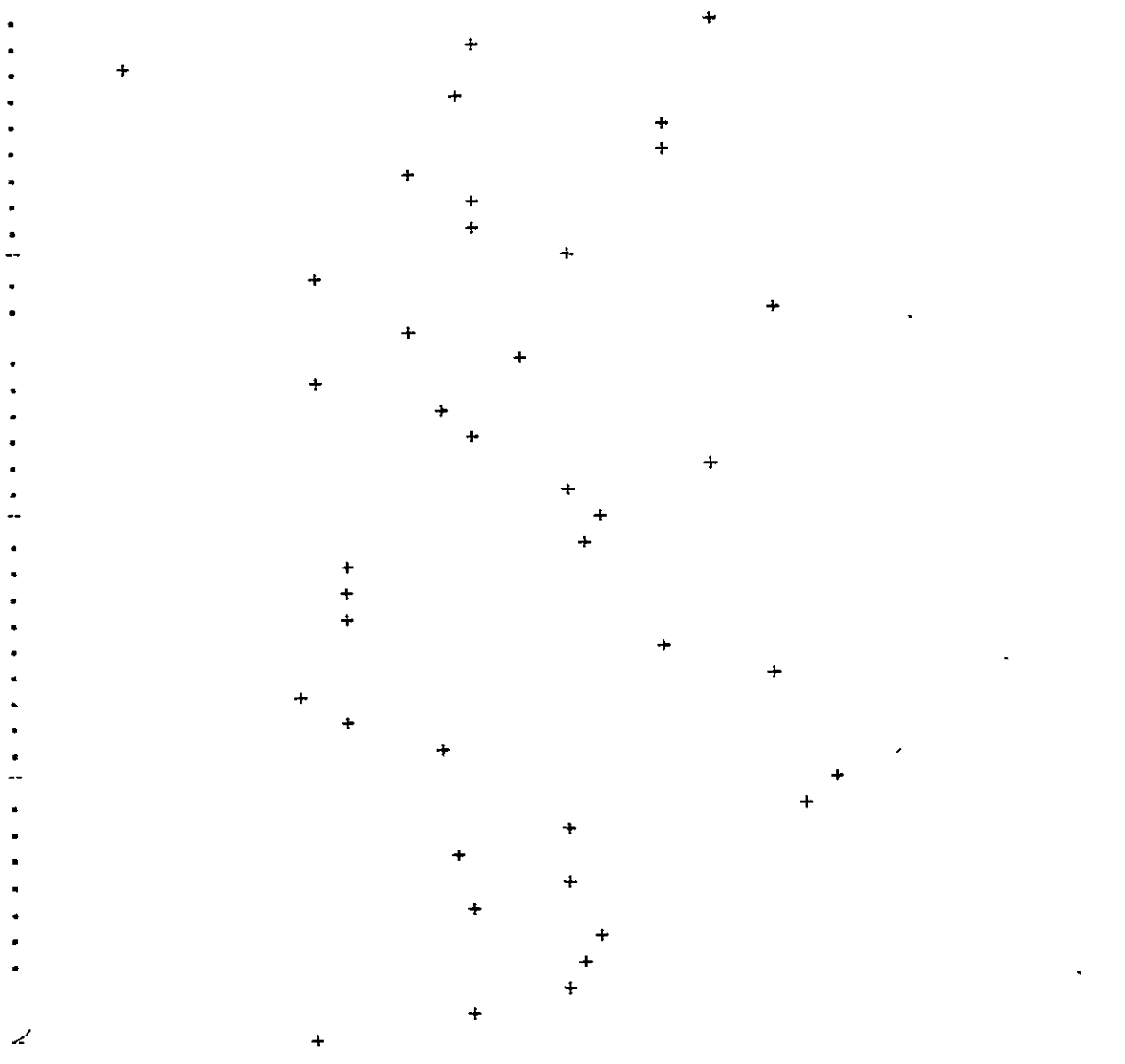

4.1.6.2.6.2

FOR DATA SET 4 Reverse

RELATIVE DIODE POSITION= 0.605085

AVERAGE VALUE= 0.606416

STANDARD DEVIATION= 1.15575E-5

ANGLE DEVIATION SCAN TO SCAN
VS SCAN NUMBER

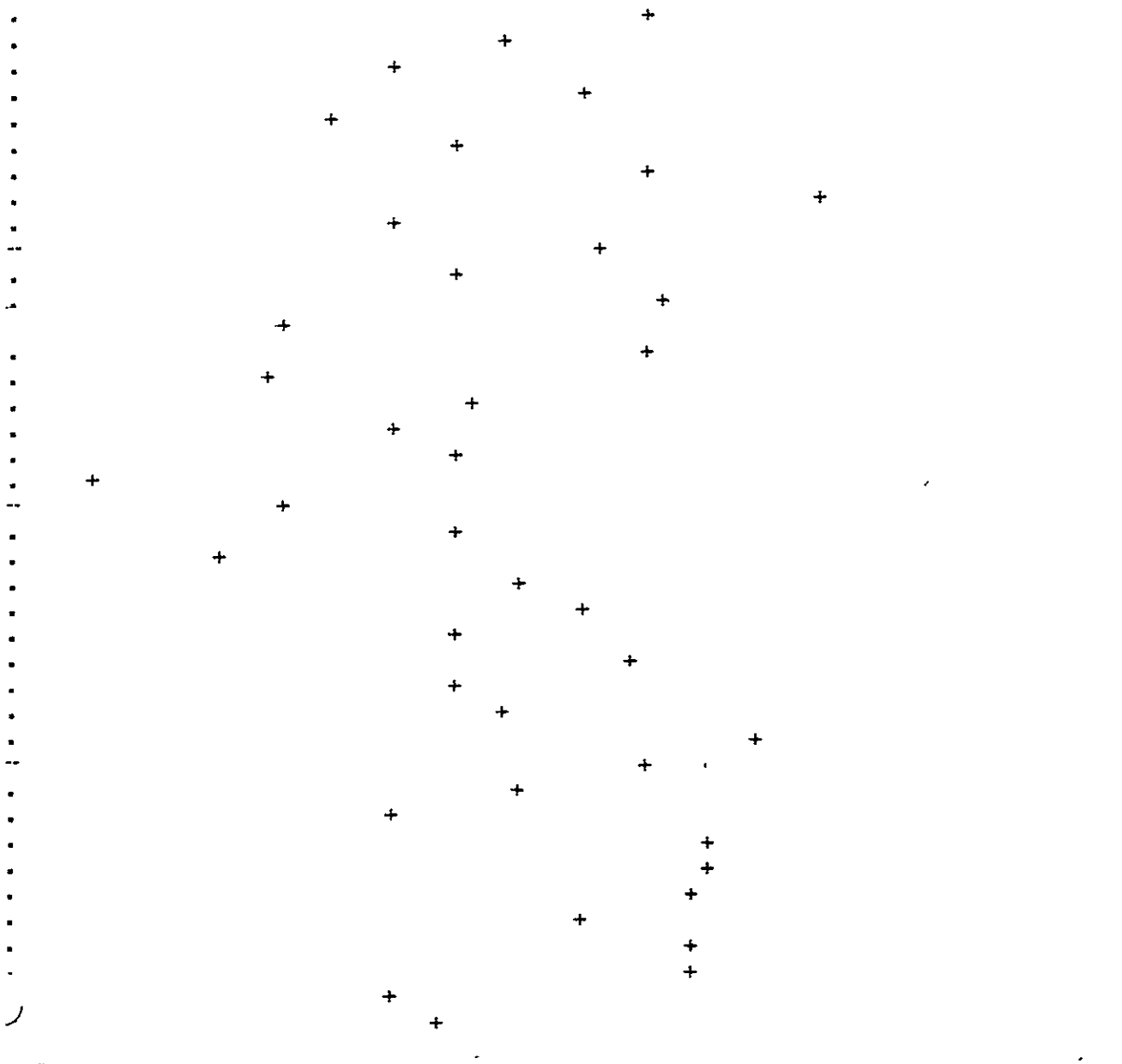

4.1.6.262

FOP DATA SET 5 *REVERSE*

RELATIVE DIODE POSITION= 0.679454

AVERAGE VALUE= 0.680057

STANDARD DEVIATION= 1.27546E-5

ANGLE DEVIATION: SCAN TO SCAN
VS SCAN NUMBER

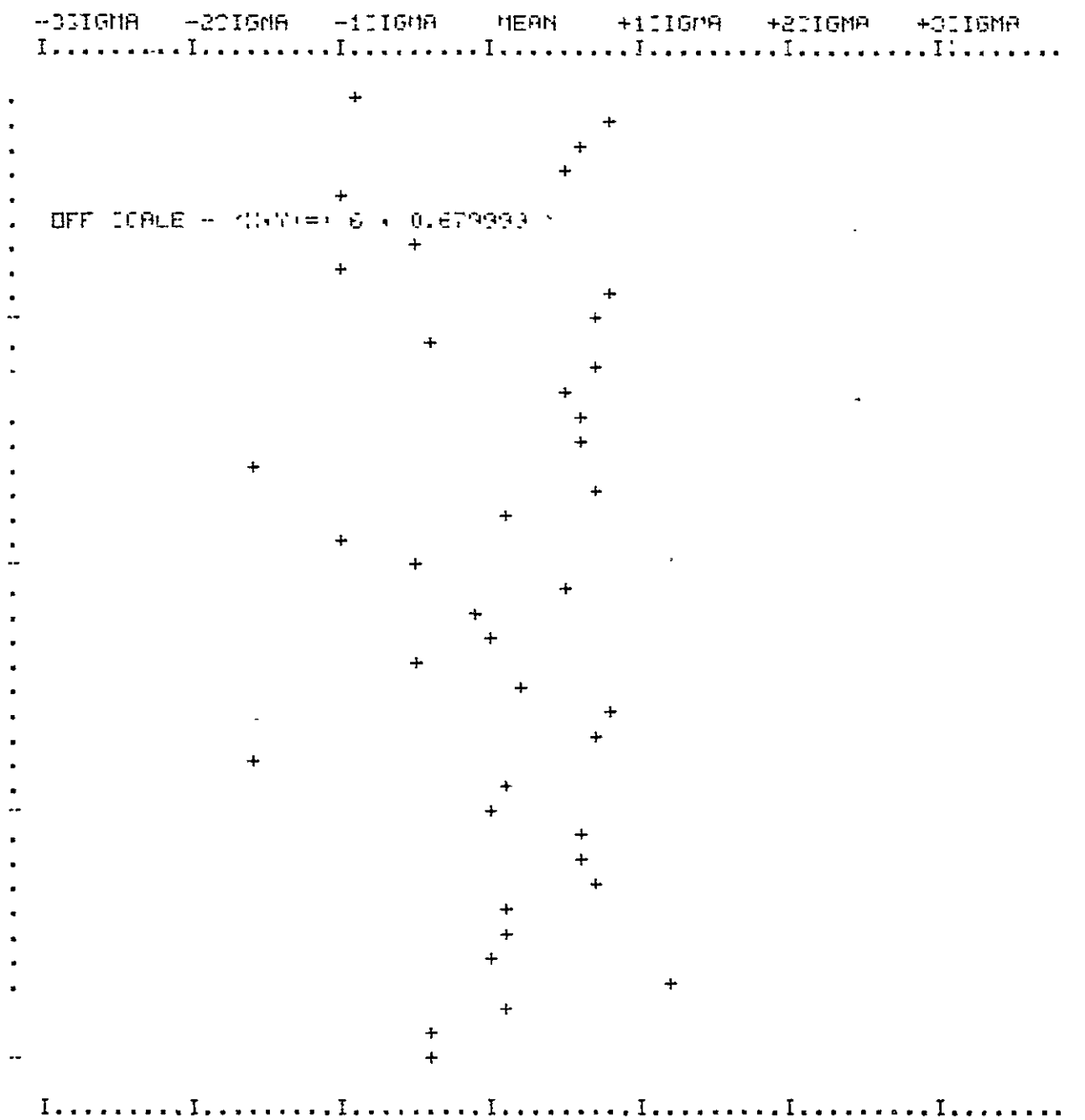

4.1.6.2.6.4.1 FORWARD SCAN

ANGULAR POSITION = P(X) =

1.22748E-3 X^3+-8.72910E-3 X^2+ 1.0075 X

4.1.6.2.6.4.2

SCAN RATE = PDOT(X) =

3.68245E-3 X^2+-1.74582E-2 X+ 1.0075

TIME	POSITION	SCAN RATE
0	0	1.0075
0.05	5.03534E-2	1.00664
0.1	0.100664	1.00579
0.15	0.150933	1.00497
0.2	0.201161	1.00416
0.25	0.251349	1.00337
0.3	0.301498	1.0026
0.35	0.351609	1.00184
0.4	0.401683	1.00111
0.45	0.45172	1.00039
0.5	0.501722	0.999692
0.55	0.55169	0.999014
0.6	0.601624	0.998352
0.65	0.651525	0.99771
0.7	0.701395	0.997085
0.75	0.751234	0.996479
0.8	0.801043	0.995892
0.85	0.850823	0.995323
0.9	0.900576	0.994772
0.95	0.950301	0.99424
1.	1.	0.993726

4.1.6.2.6.5.1 REVERSE SCAN

ANGULAR POSITION = P(X) =

3.65204E-3 X^3+-2.29737E-2 X^2+ 0.998645 X

4.1.6.2.6.5.2

SCAN RATE = PDOT(X) =

1.09585E-2 X^2+-4.59474E-3 X+ 0.998645

TIME	POSITION	SCAN RATE
0	0	0.998645
0.05	4.99269E-2	0.999442
0.1	3.90451E-2	0.999295
0.15	0.149757	0.998202
0.2	0.199666	0.998164
0.25	0.249575	0.998101
0.3	0.299485	0.998052
0.35	0.349401	0.998079
0.4	0.399324	0.99856
0.45	0.449258	0.998796
0.5	0.499205	0.999087
0.55	0.549167	0.999432
0.6	0.599149	0.999833
0.65	0.649151	1.00029
0.7	0.699178	1.0008
0.75	0.749232	1.00136
0.8	0.799316	1.00198
0.85	0.849431	1.00266
0.9	0.899582	1.00339
0.95	0.949771	1.00417
1.	1.	1.00501

DATA SHEET "F"

4.1.6.2.6.5.2

DATA SHEET "G"

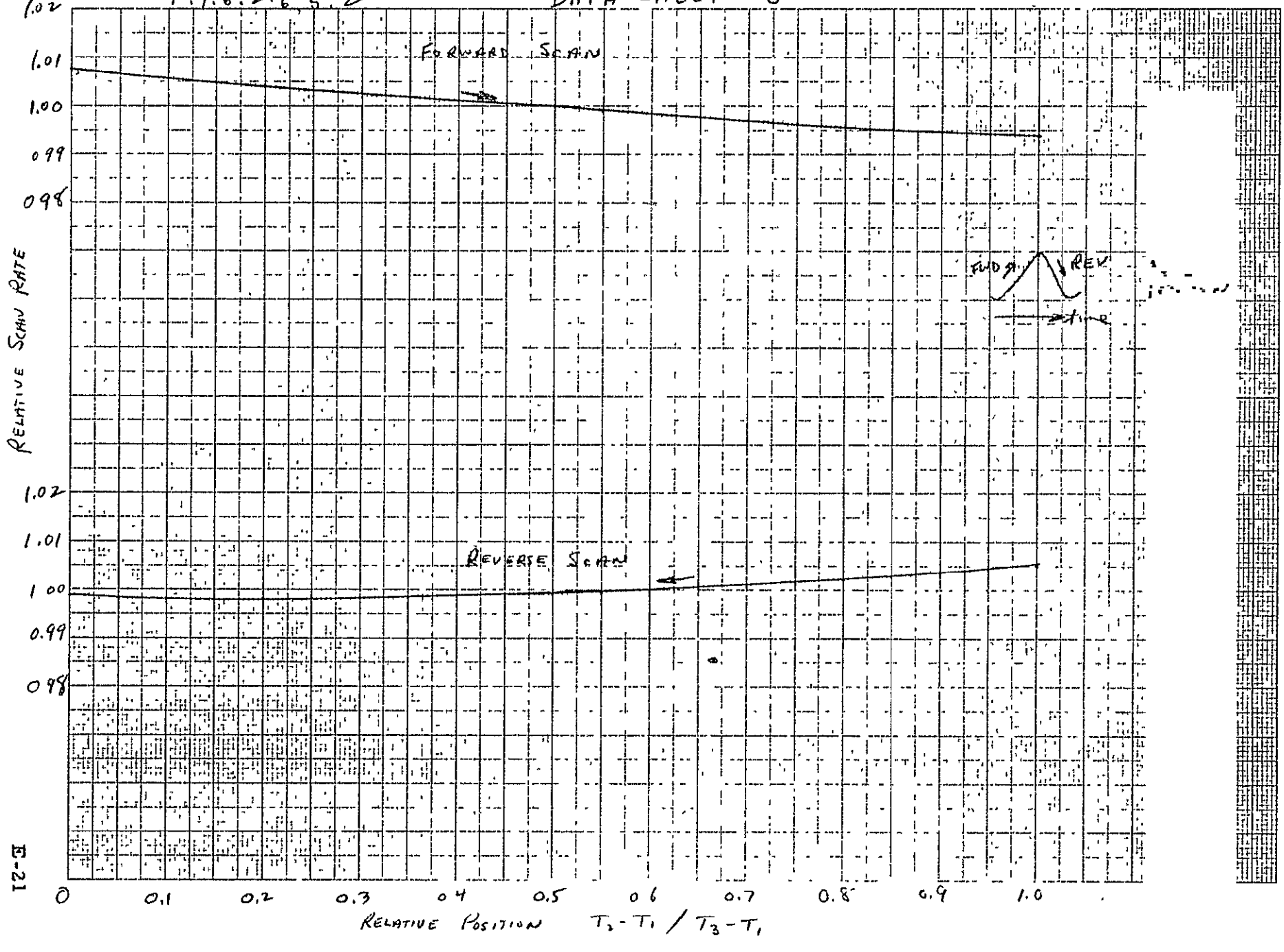

TEST PROCEDURE -- ERRADBOARD
SCAN MIRROR -- THEMATIC MAPPER

HUGHES AIRCRAFT CO.
CULVER CITY, CALIF.
CODE IDENT NO. 82377

57

4.1.9.1.1	Average Ratio Value - Forward:	0.177018
4.1.9.1.1	$\overline{\theta}_{FWD} = Q_{FWD}$:	52.22 mrad
4.1.9.1.1	σ_{FWD} (STD. DEV.):	3.03 mrad
4.1.9.1.1	Attach Deviation Plot to this Sheet	✓
4.1.9.1.2	Average Ratio Value - Reverse:	0.178472
4.1.9.1.2	$\overline{\theta}_{REV} = Q_{REV}$:	52.65 mrad
4.1.9.1.2	σ_{REV} (STD. DEV.):	4.36 mrad
4.1.9.1.2	Attach Deviation Plot to this Sheet	✓
4.1.9.1.3	TOTAL Deviation:	5.3 mrad
4.1.9.2.1	Average Ratio Value - Forward:	0.298794
4.1.9.2.1	$\overline{\theta}_{FWD} = Q_{FWD}$:	88.14 mrad
4.1.9.2.1	σ_{FWD} (STD. DEV.):	5.22 mrad
4.1.9.2.1	Attach Deviation Plot to this Sheet	✓
4.1.9.2.2	Average Ratio Value - Reverse:	0.300713
4.1.9.2.2	$\overline{\theta}_{REV} = Q_{REV}$:	88.71
4.1.9.2.2	σ_{REV} (STD. DEV.):	3.09 mrad
4.1.9.2.2	Attach Deviation Plot to this Sheet	✓
4.1.9.2.3	TOTAL Deviation:	6.08 mrad

Figure 26. Data Sheet - Type "K"

4.1.9.1.1 30 Oct 75

REPEATABILITY CALCULATIONS (FORWARD) FOR DATA SET 1

RELATIVE DIODE POSITION= 0.177614

AVERAGE ANGLE= 52.2202 MILLIRADIANS

STANDARD DEVIATION= 3.0217E-3 MILLIRADIANS

ANGLE DEVIATION SCAN TO SCAN
VS SCAN NUMBER
(FORWARD)

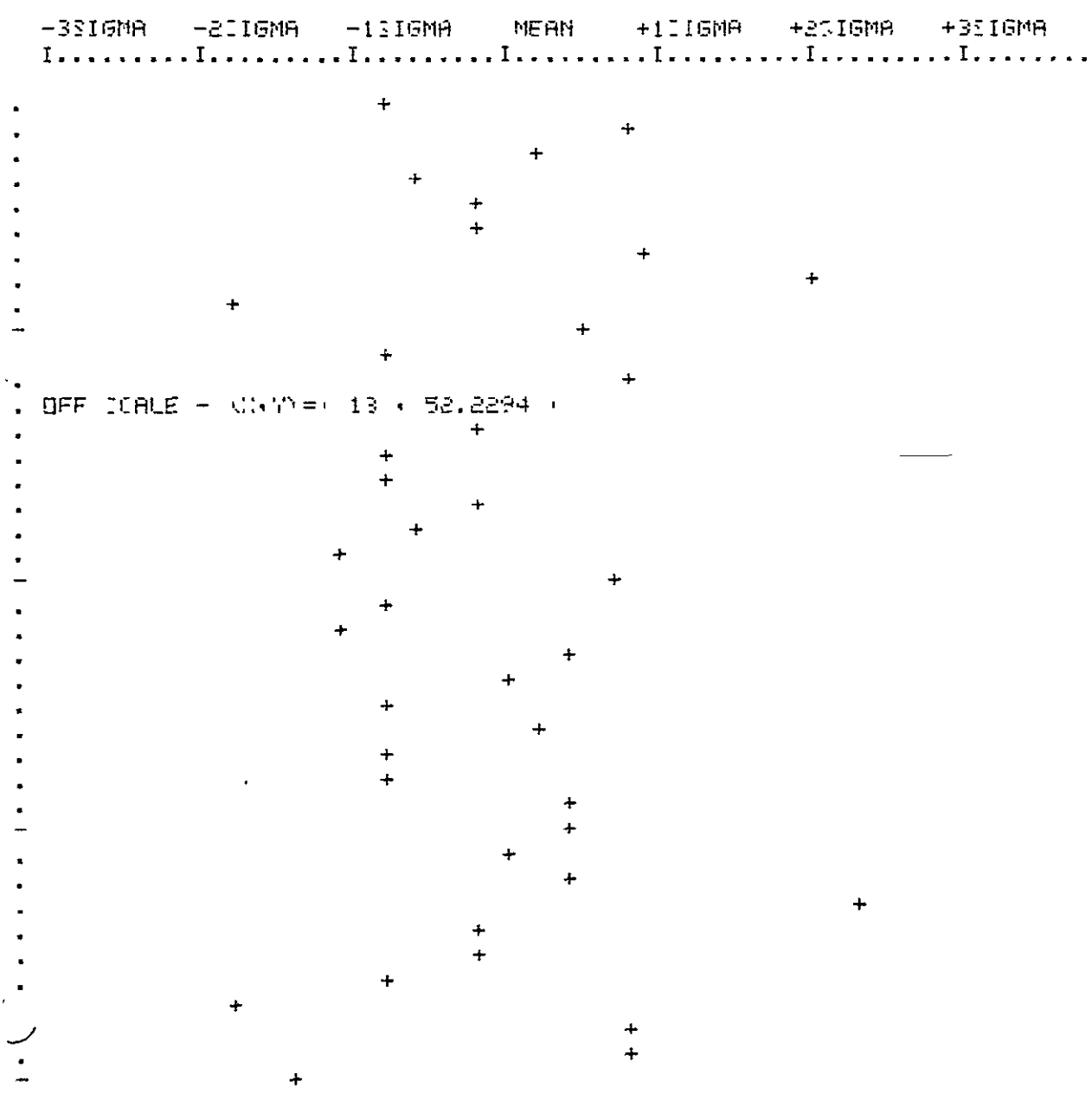

4.1.9.1.2

REPEATABILITY CALCULATIONS (REVERSE) FOR DATA SET 1

RELATIVE DIODE POSITION= 0.177614

AVERAGE ANGLE= 52.6493 MILLIRADIANS

STANDARD DEVIATION= 4.36061E-3 MILLIRADIANS

ANGLE DEVIATION SCAN TO SCAN
VS SCAN NUMBER
(REVERSE)

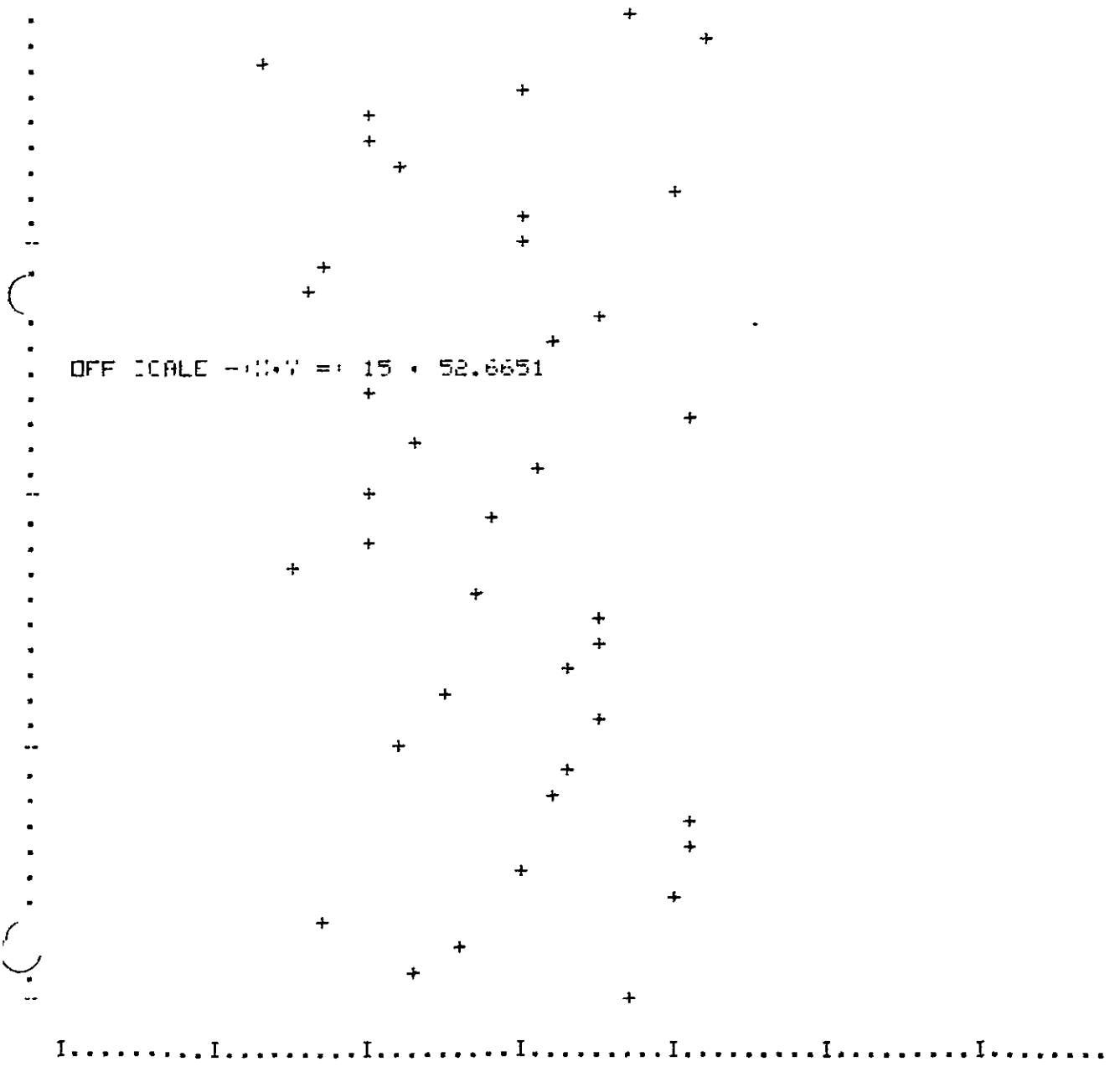

4.1.9.2.1

REPEATABILITY CALCULATION: 'FORWARD' FOR DATA SET 2

RELATIVE DIODE POSITION= 0.301104

AVERAGE ANGLE= 88.1443 MILLIRADIANS

STANDARD DEVIATION= 5.22172E-3 MILLIRADIANS

ANGLE DEVIATION SCAN TO SCAN
VS SCAN NUMBER
'FORWARD'

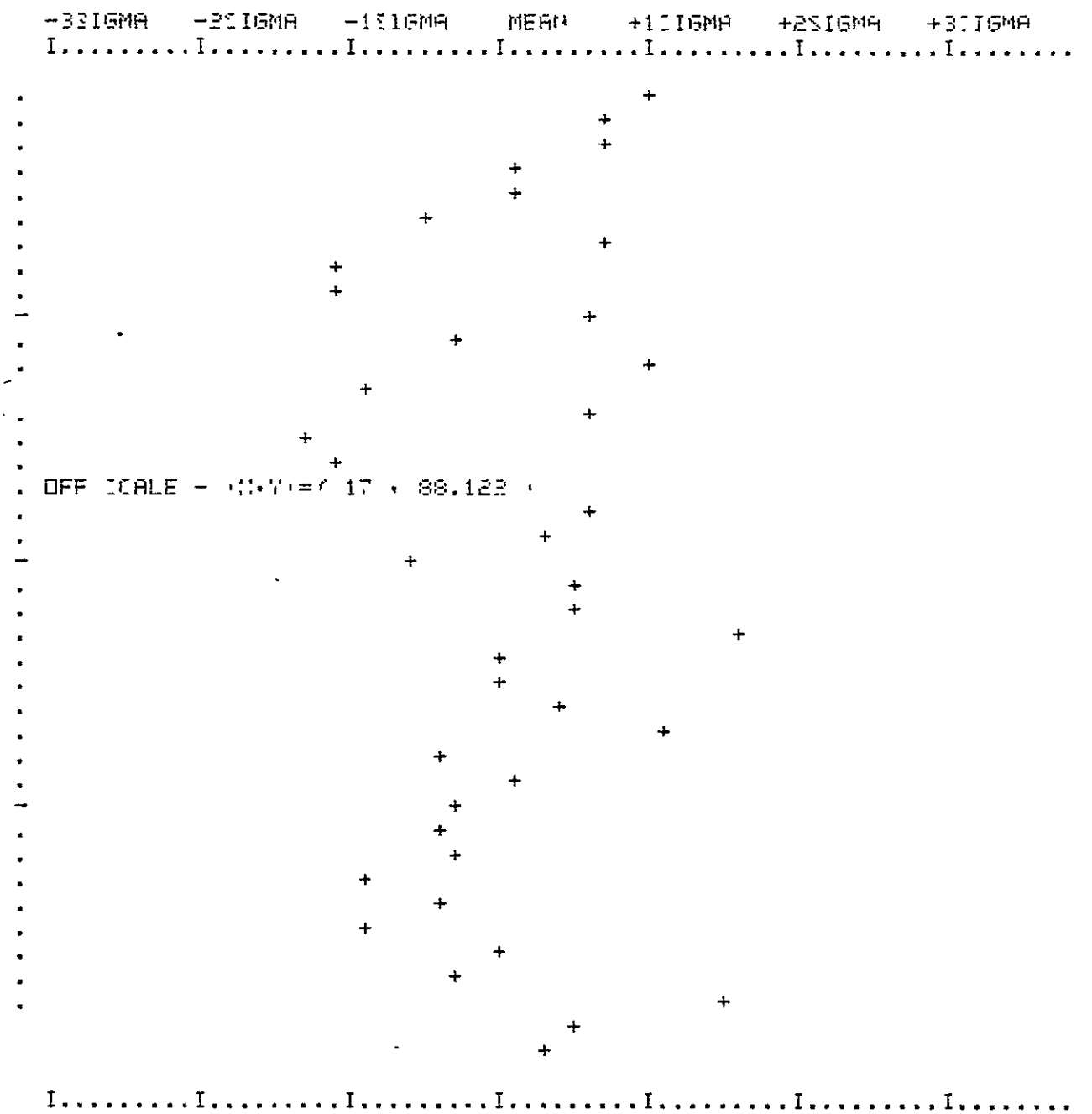

4,1,9,2,2

REPEATABILITY CALCULATIONS (REVERSE) FOR DATA SET 2

RELATIVE DIODE POSITION= 0.301104

AVERAGE ANGLE= 88.7104 MILLIRADIANS

STANDARD DEVIATION= 3.08982E-3 MILLIRADIANS

ANGLE DEVIATION SCAN TO SCAN VS SCAN NUMBER (REVERSE)

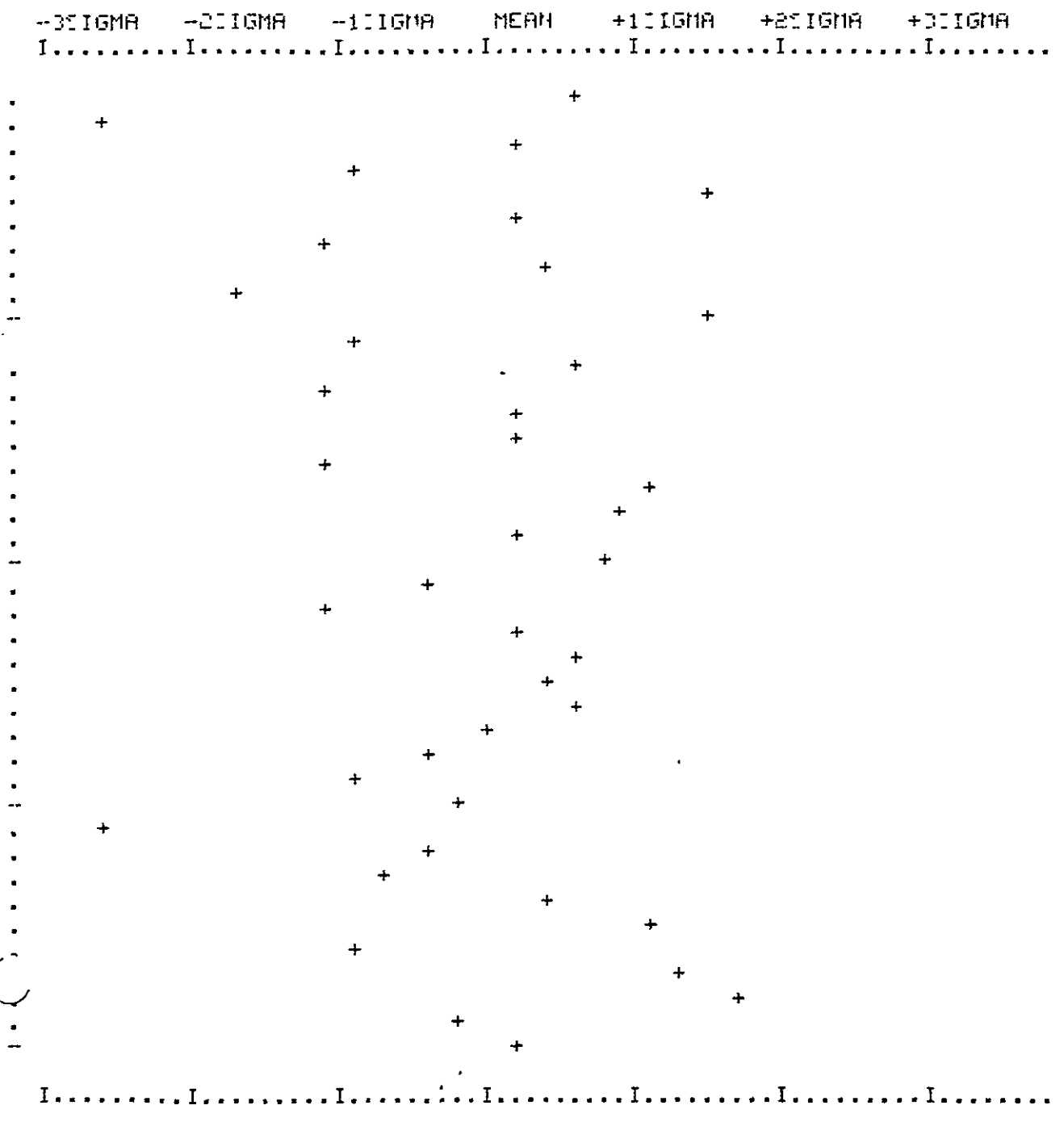

TEST PROCEDURE -- BREADBOARD SCAN MIRROR -- THEMATIC MAPPER	HUGHES AIRCRAFT CO. CULVER CITY, CALIF. CODE IDENT NO. 82577
	SH NO. 58
	REV LTR
	NUMBER ITP 31891-350

4.1.9.3.1 Average Ratio Value - Forward: 0.522094

4.1.9.3.1 $\overline{\theta}_{FWD} = Q_{FWD}$: 154.018 μrad

4.1.9.3.1 σ_{FWD} (STD. DEV.): 3.096 μrad

4.1.9.3.1 Attach Deviation Plot to this Sheet -

4.1.9.3.2 Average Ratio Value - Reverse: 0.524617

4.1.9.3.2 $\overline{\theta}_{REV} = Q_{REV}$: 154.762 μrad

4.1.9.3.2 σ_{REV} (STD. DEV.): 4.155 μrad

4.1.9.3.2 Attach Deviation Plot to this Sheet -

4.1.9.3.3 TOTAL Deviation: 5.17 μrad

4.1.9.4.1 Average Ratio Value - Forward: 0.60393

4.1.9.4.1 $\overline{\theta}_{FWD} = Q_{FWD}$: 178.159 μrad

4.1.9.4.1 σ_{FWD} (STD.DEV.): 3.19 μrad

4.1.9.4.1 Attach Deviation Plot to this Sheet -

4.1.9.4.2 Average Ratio Value - Reverse: 0.606416

4.1.9.4.2 $\overline{\theta}_{REV} = Q_{REV}$: 178.893 μrad

4.1.9.4.2 σ_{REV} (STD. DEV.): 3.41 μrad

4.1.9.4.2 Attach Deviation Plot to this Sheet -

4.1.9.4.3 TOTAL Deviation: 4.67 μrad

Figure 27. Data Sheet - Type "L"

4.1.9.3.1

REPEATABILITY CALCULATIONS (FORWARD) FOR DATA SET 3

RELATIVE DIODE POSITION= 0.522859

AVERAGE ANGLE= 154.018 MILLIRADIANS

STANDARD DEVIATION= 3.09589E-3 MILLIRADIANS

ANGLE DEVIATION SCAN TO SCAN
VS SCAN NUMBER
(FORWARD)

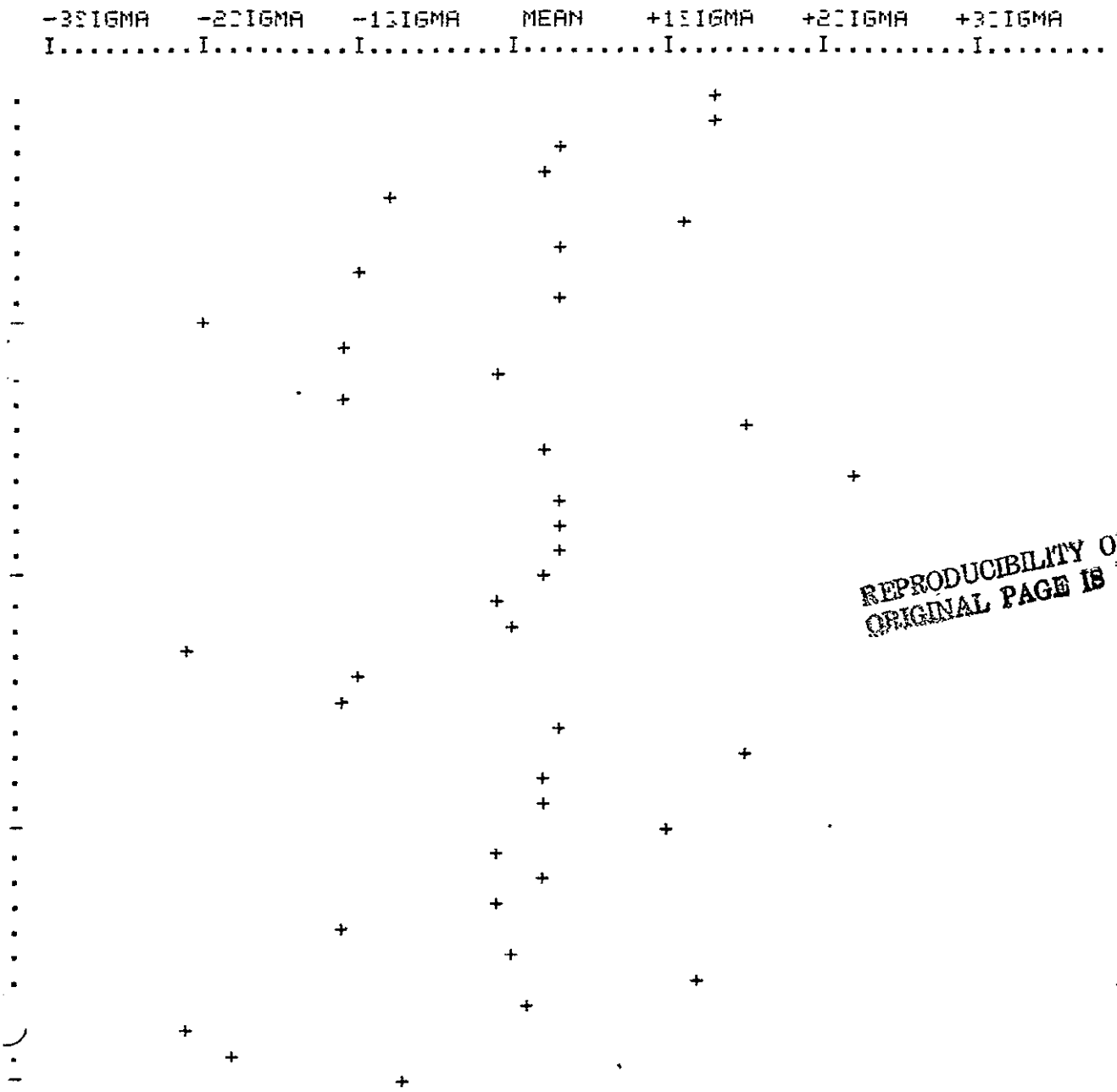

4.1.9.3.2

REPEATABILITY CALCULATION: REVERSE FOR DATA SET 3

RELATIVE DIODE POSITION= 0.522059

AVERAGE ANGLE= 154.762 MILLIRADIANS

STANDARD DEVIATION= 4.154E0E-2 MILLIRADIANS

ANGLE DEVIATION: SCAN TO SCAN
VS SCAN NUMBER
REVERSE

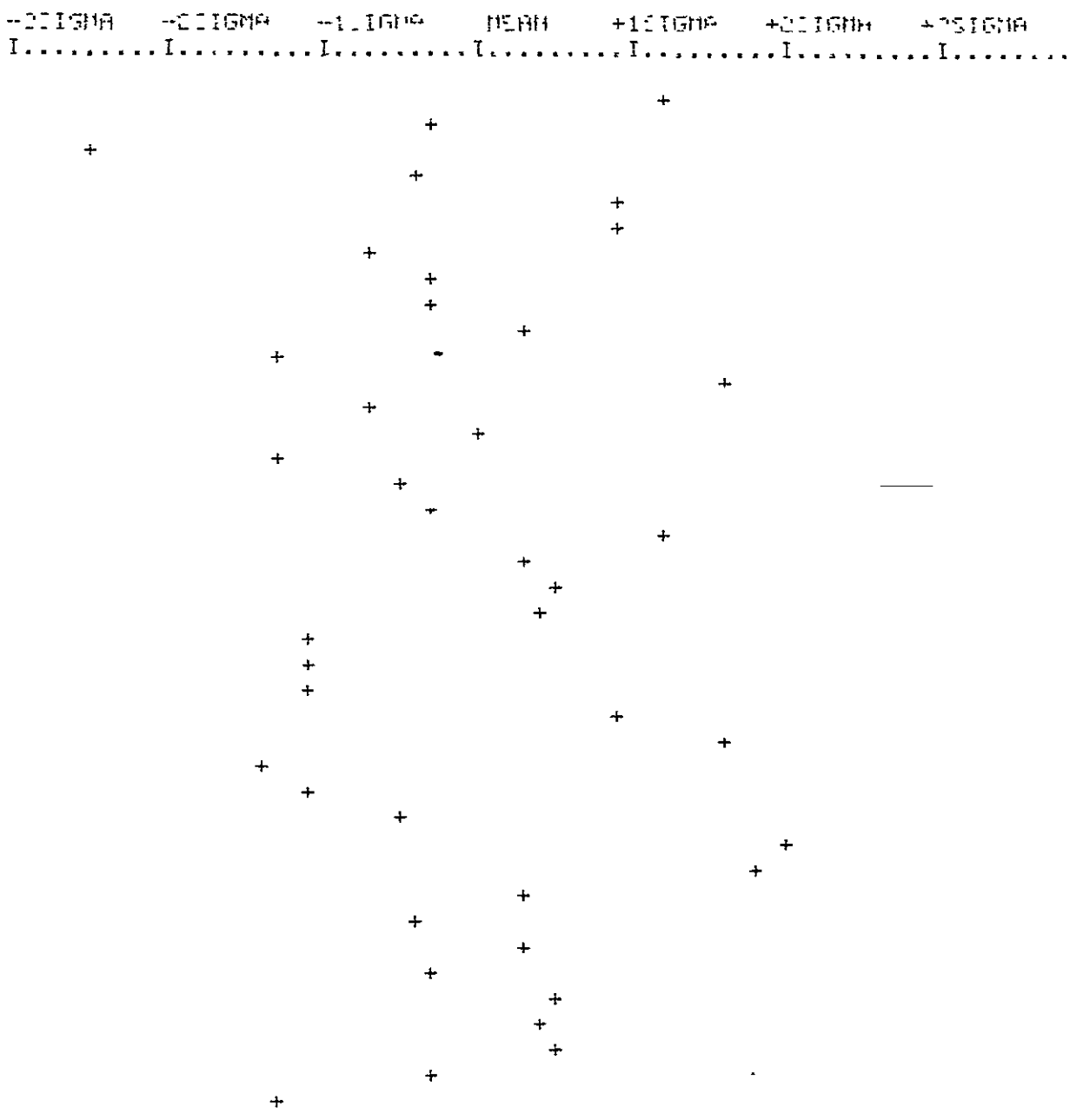

4.1.9.4.1

REPEATABILITY CALCULATIONS (FORWARD) FOR DATA SET 4

RELATIVE DIODE POSITION= 0.605885

AVERAGE ANGLE= 178.159 MILLIRADIANS

STANDARD DEVIATION= 3.19295E-3 MILLIRADIANS

ANGLE DEVIATION SCAN TO SCAN
VS SCAN NUMBER
(FORWARD)

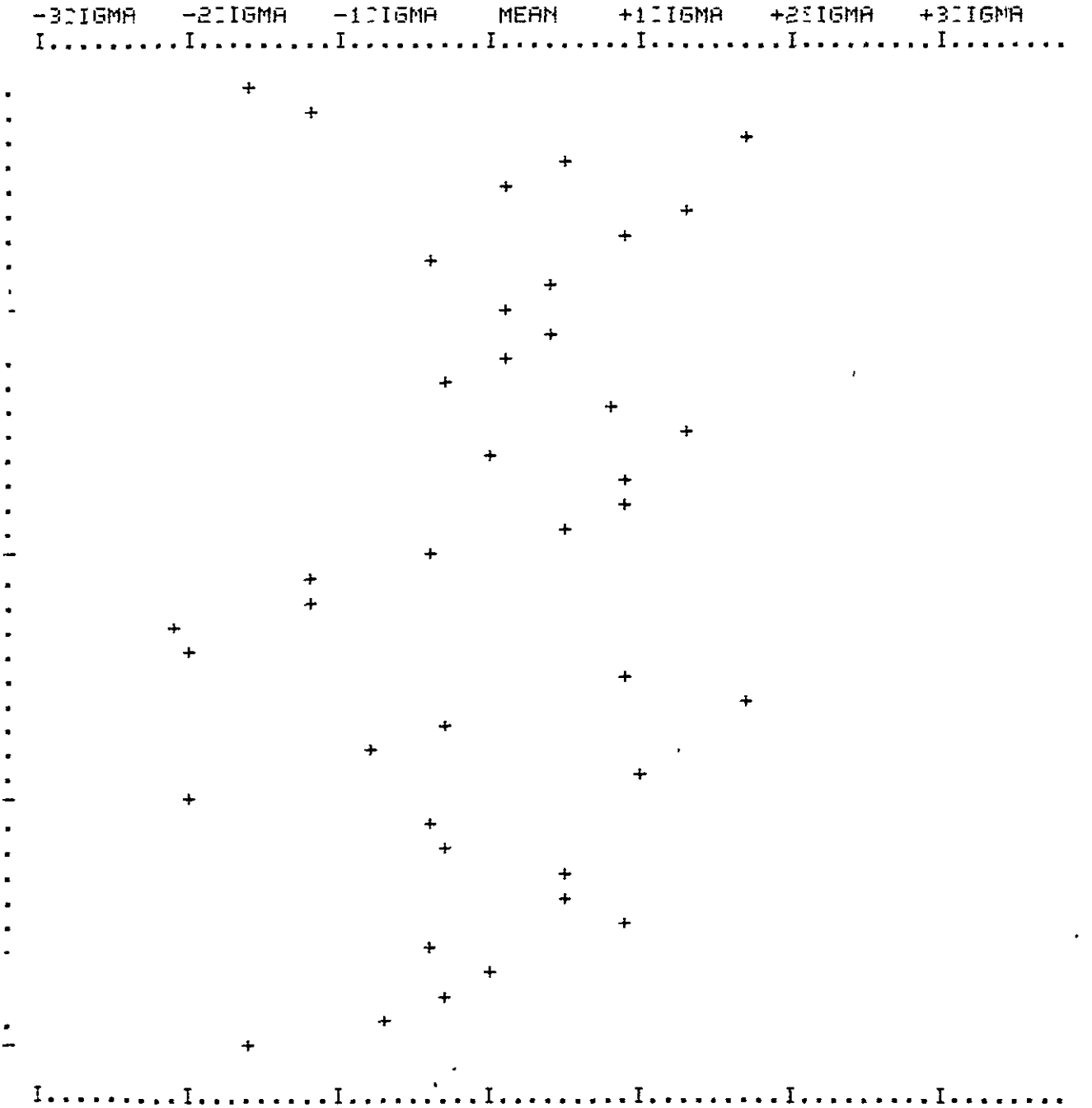

4.1.9.4.2

REPEATABILITY CALCULATION: 'REVERSE' FOR DATA SET 4

RELATIVE DIODE POSITION= 0.605035

AVERAGE ANGLE= 173.092 MILLIRADIANS

STANDARD DEVIATION= 2.40645E-2 MILLIRADIANS

ANGLE DEVIATION SCAN TO SCAN
VS SCAN NUMBER
'REVERSE

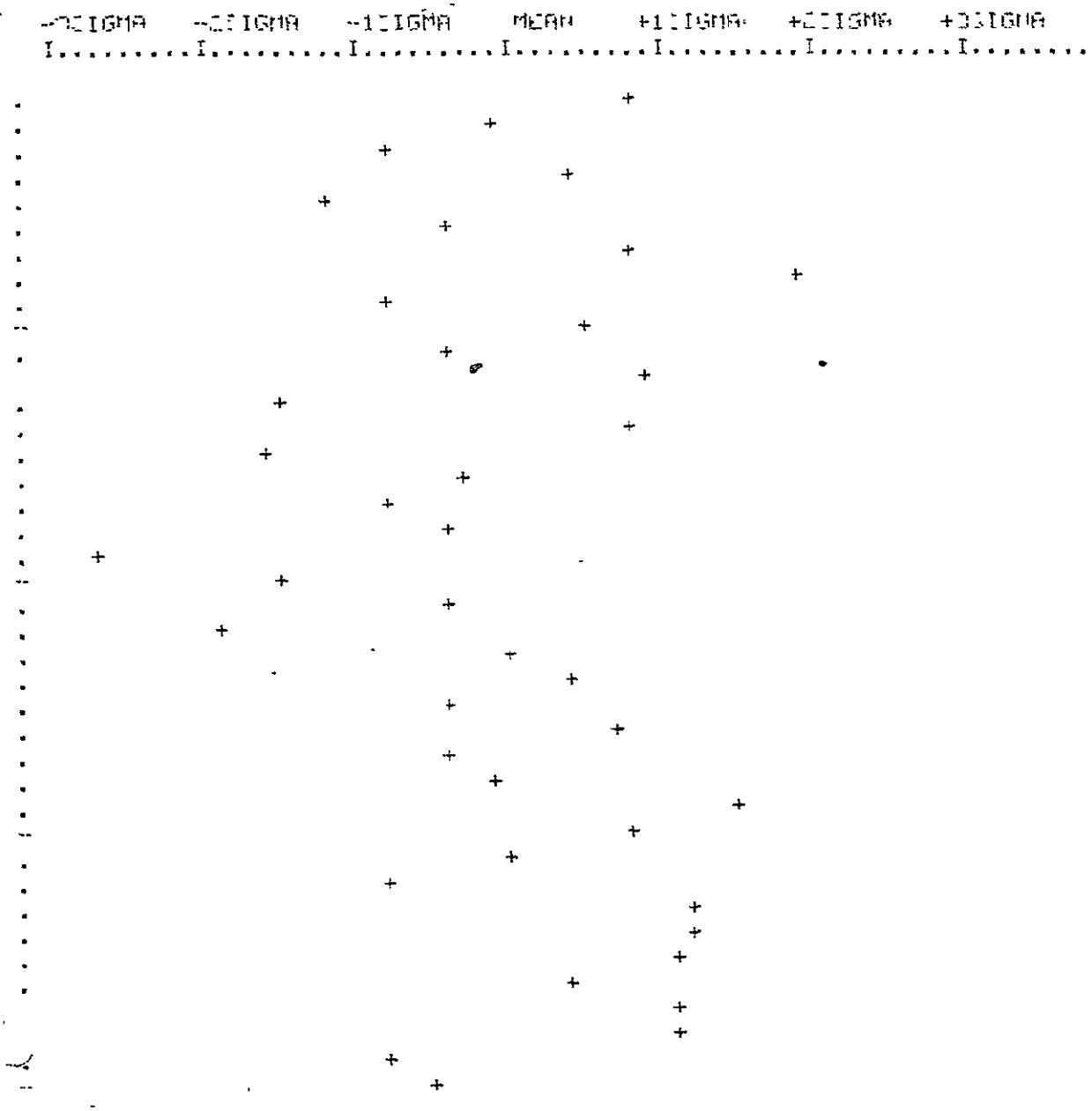

4.1.9.5.1	Average Ratio Value - Forward: 0.677756
4.1.9.5.1	$\overline{\theta}_{FWD} = Q_{FWD}$: 199.938 mrad
4.1.9.5.1	σ_{FWD} (STD. DEV.): 3.107 mrad
4.1.9.5.1	Attach Deviation Plot to this Sheet ✓
4.1.9.5.2	Average Ratio Value - Reverse: 0.680057
4.1.9.5.2	$\overline{\theta}_{REV} = Q_{REV}$: 200.617 mrad
4.1.9.5.2	σ_{REV} (STD. DEV.): 3.76 mrad
4.1.9.5.2	Attach Deviation Plot to this Sheet ✓
4.1.9.5.3	TOTAL Deviation: 4.877 mrad
4.1.9.6.1	Average Standard Deviation: 5.22 mrad
4.1.9.6.2	Attach Plot of Standard Deviation vs Angle. ✓

Figure 28. Data Sheet - Type "M"

TEST PROCEDURE -- BREADBOARD SCAN MIRROR -- THEMATIC MAPPER	HUGHES AIRCRAFT CO. CULVER CITY, CALIF. CODE IDENT NO. 82577
SH NO. 60	REV LTR
NUMBER TP 11891-350	

4.1.9.5.1

REPEATABILITY CALCULATIONS (FORWARD) FOR DATA SET 5

RELATIVE DIODE POSITION= 0.679454

AVERAGE ANGLE= 199.930 MILLIRADIANS

STANDARD DEVIATION= 2.10718E-3 MILLIRADIANS

ANGLE DEVIATION SCAN TO SCAN
VS SCAN NUMBER
(FORWARD)

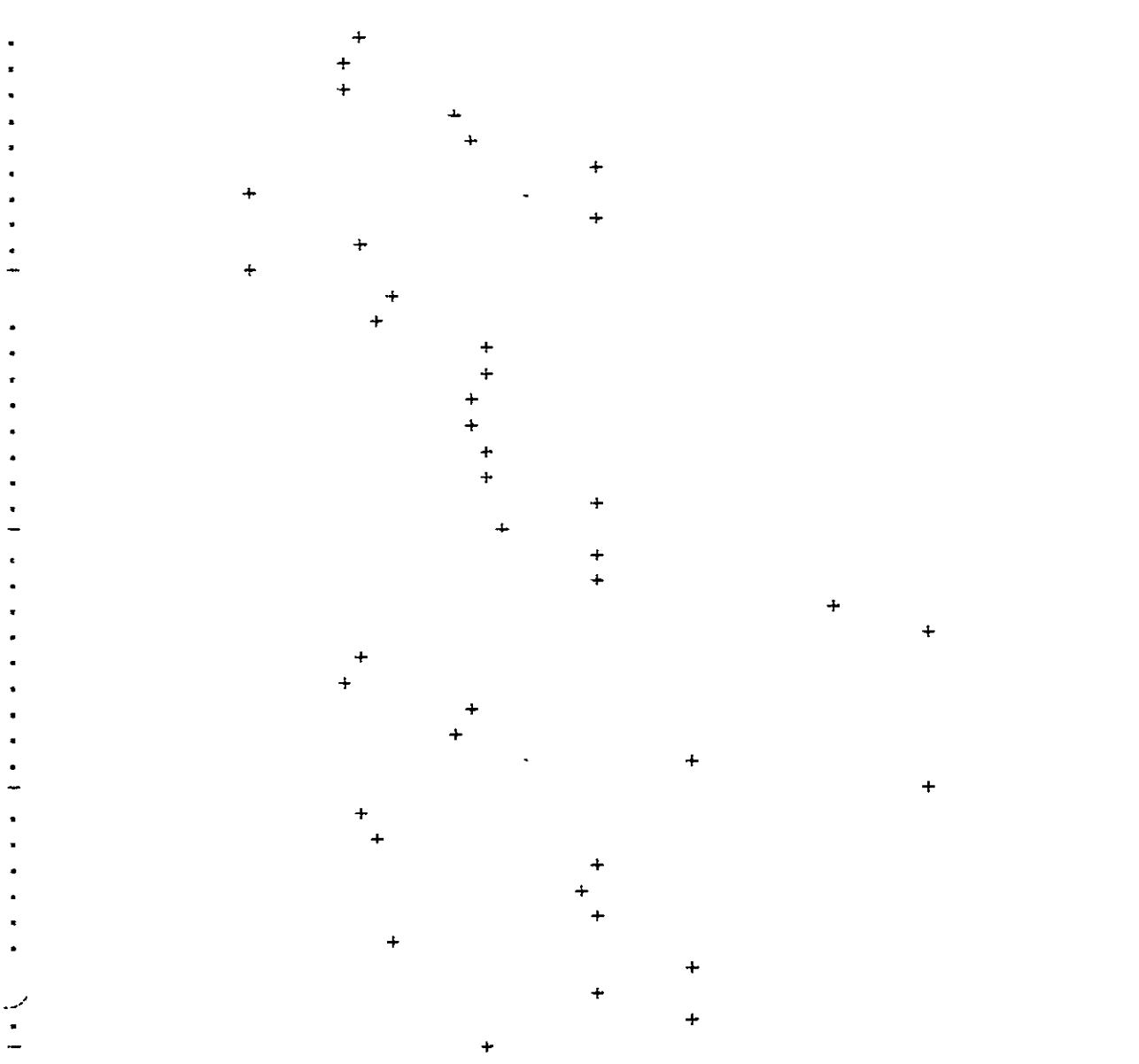

4.1.9.85.2

REPEATABILITY CALCULATION (REVERSE) FOR DATA SET 5

RELATIVE DIODE POSITION= 0.679454

AVERAGE ANGLE= 200.617 MILLIRADIANS

STANDARD DEVIATION= 3.76306E-2 MILLIRADIANS

ANGLE DEVIATION SCAN TO SCAN
VS SCAN NUMBER
(REVERSE)

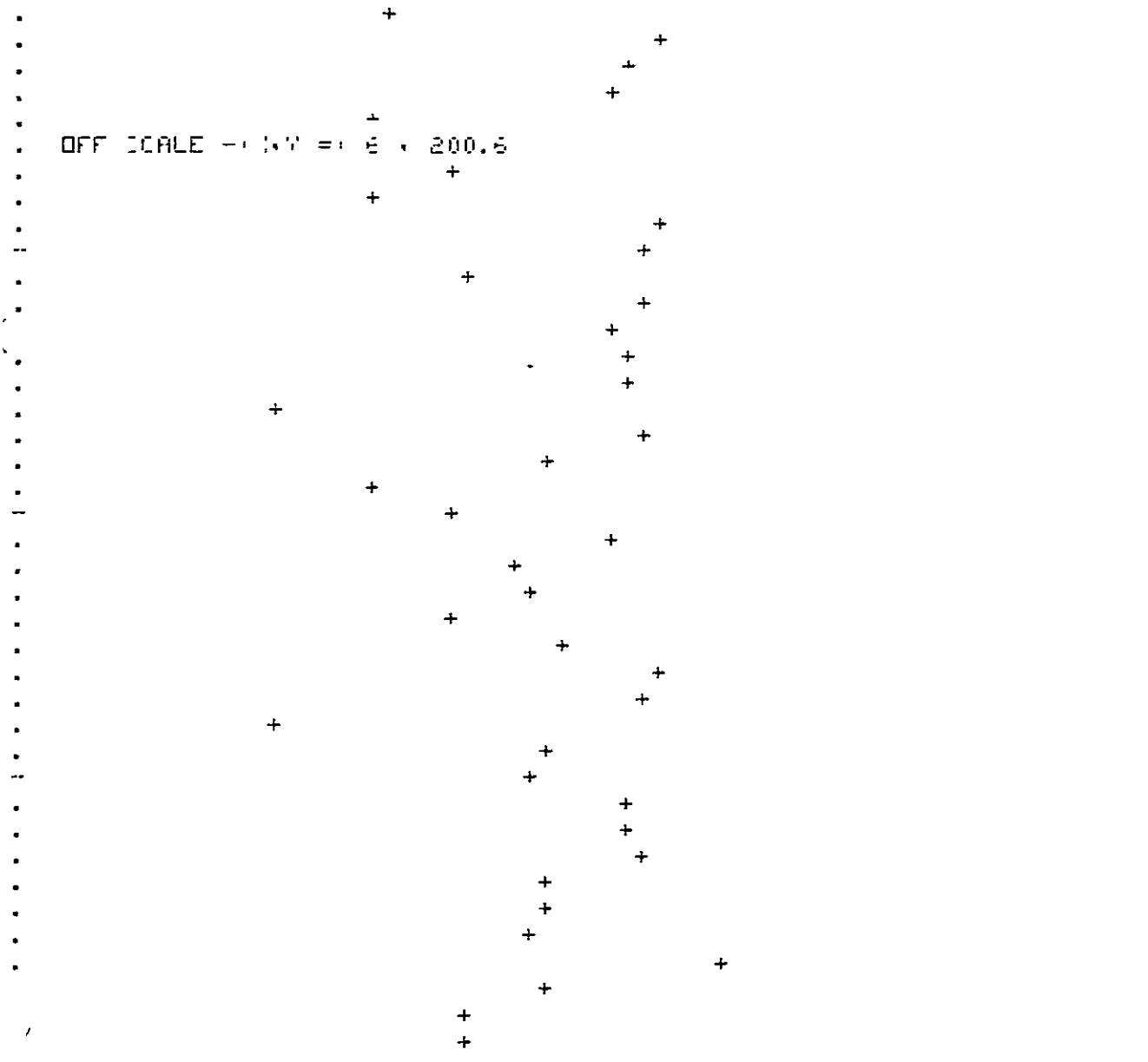

4.1.9.6.2

REPEATABILITY CALCULATIONS (FORWARD AND REVERSE)

AVG ST DEV OVER 5 SETS OF DATA IS 5.00160E-3 MILLIRADIANS
DOES NOT SATISFY REQUIREMENT

STANDARD DEVIATION OF ANGLE MICRORAD
VS DIODE POSITION (D2-D1 (D3-D1

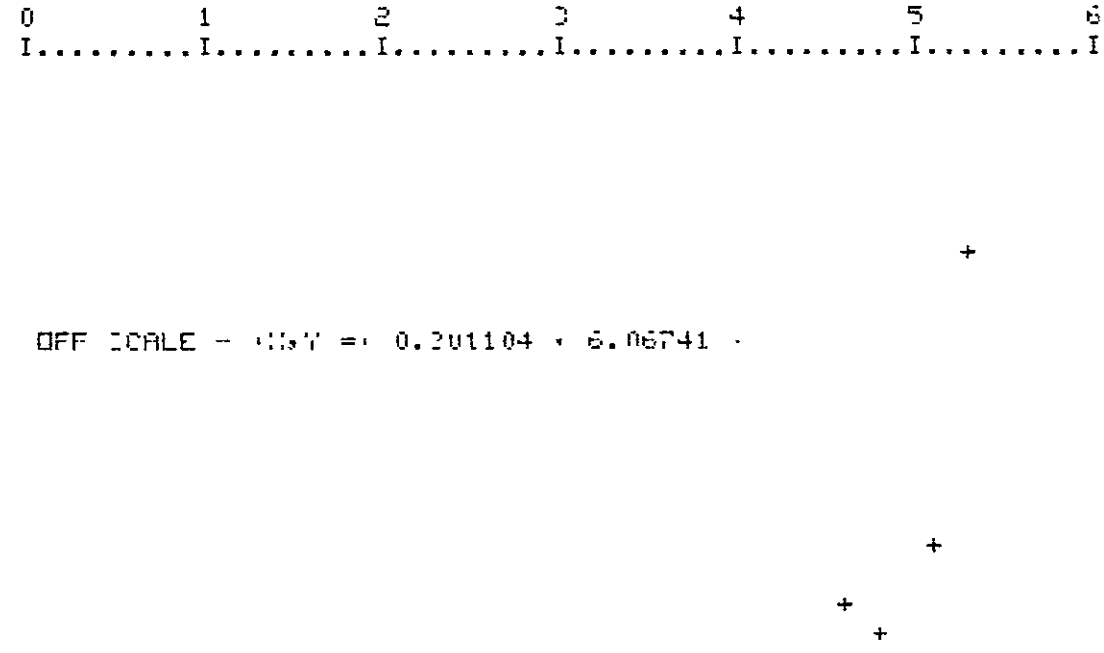

10-24-75

Data Set 1 (222 μRAD/V)(.02 V/div) = 4.4 μRAD/div

LOCATION #4

FWD REV

Delta Value	Photo #1		Photo #2		Photo #3	
1	(-4div)(4.4μRAD/div)=-1.8μRAD		-.8	- 3.5	-.4	- 1.8
2	-.5	- 2.2	-.7	- 3.1	-.7	- 3.1
3	-.6	- 2.6	-.4	- 1.8	-.8	- 3.5
4	-.7	- 3.1	- 3	- 1.3	-.6	- 2.6
5	-.8	- 3.5	-.2	- .9	-.6	- 2.6
6	- 8	- 3.5	-.5	- 2.2	-.4	- 1.8
7	- 9	- 4.0	-.6	- 2.6	-.2	- .9
8	- 7	- 3.1	-.6	- 2.6	-.3	- 1.3
9	-.3	- 1.3	-.7	- 3.1	-.3	- 1.3
10	-.2	- .9	-.7	- 3.1	-.6	- 2.6
11	-.4	- 1.8	-.5	- 2.2	-.6	- 2.6
12	-.9	- 4.0	-.3	- 1.3	-.7	- 3.1
13	-1.0	- 4.4	-.2	- .9	-.7	- 3.1
14	- 8	- 3.5	-.5	- 2.2	-.5	- 2.2
15	-.9	- 4.0	-.5	- 2.2	-.2	- .9
16			-.6	- 2.6	-.1	- .4
17			-.9	- 4.0	-.2	- .9
18						
19						
20						
21						
22						
23						
24						
25						
26						
27						
28						
29						
30						
31						
32						
33						
34						
35						
36						
37						
38						
39						
40						

Figure 42. Data Sheet Type "U"

4.2.3.5 Measure angle "ϵ": _____ (mm)

4.2.3.5 Measure angle "α": _____ (mm)

4.2.3.5 Measure distance "ϵ": _____ (inches

4.2.3.5 Measure distance "α": _____ (inches

Figure 38. Data Sheet Type "N"

LOCATION #4

No. TURNS	div	V
0	+5.1@.2v/div	+1.02
3	+5.5@.1	+.55
8	-2.8@.1	-.28
11	-4.2@.2	-.84

DIODE CALIBRATION
LOCATION #4
10-24

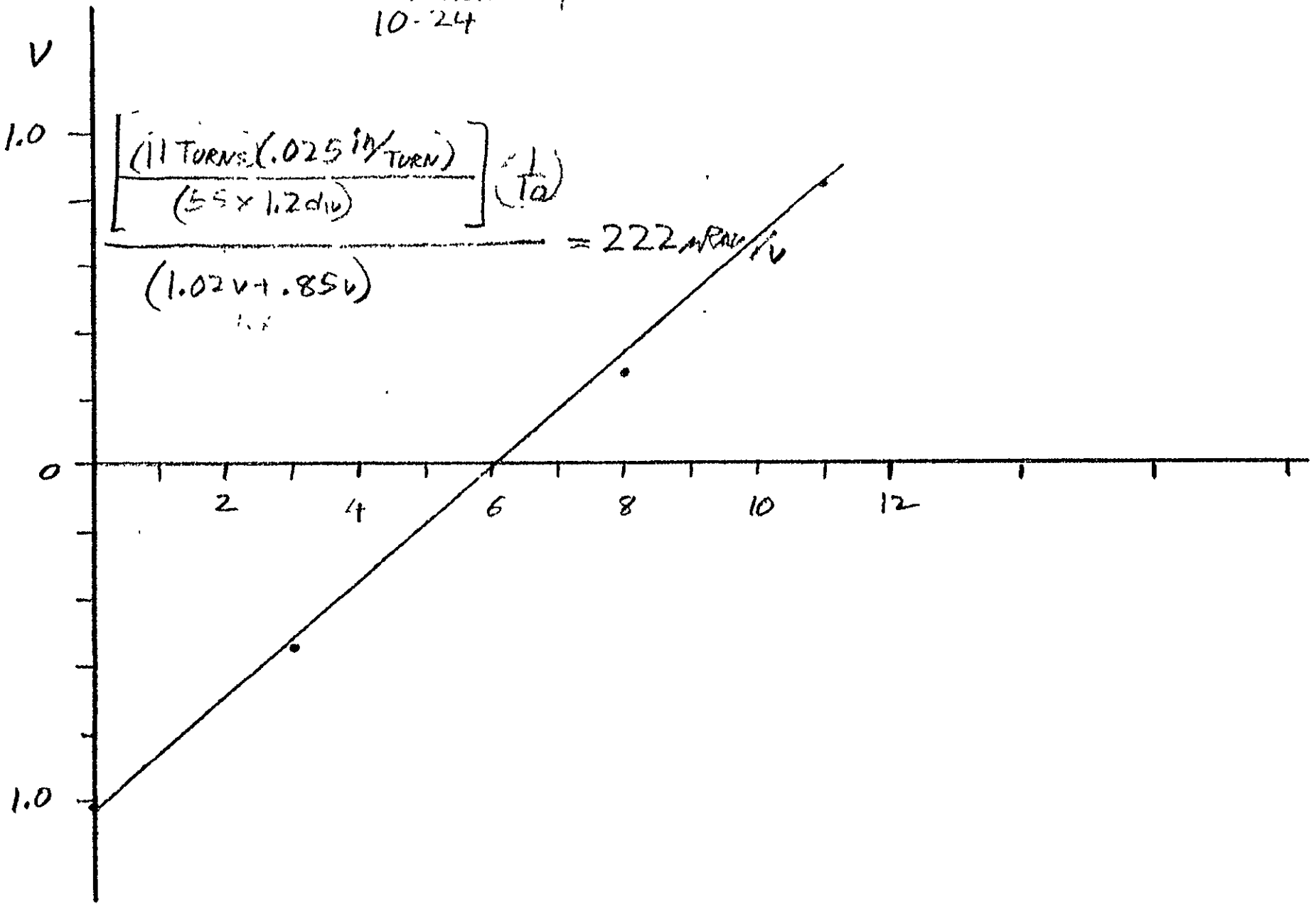

10-24-75

DATA SET 2 — (187 μRAD/V)(.02 V/div) = 3.7 μRAD/div

FWD ↓ REV ↑

POSITION #2

Delta Value	Photo #1 μRAD		Photo #2		Photo #3
1	-1.3 div x 3.7 μRAD/div = -5.0 μRAD		-1.0	-3.7	
2	-.7	-2.7	-1.1	-4.3	
3	-.5	-1.9	-1.1	-4.3	
4	-.7	-2.7	-1.1	-4.3	
5	-.5	-1.9	-1.1	-4.3	
6	-.6	-2.3	-.7	-2.7	
7	-1.2	-4.7	-.5	-1.9	
8	-1.4	-5.4	-.7	-2.7	
9	-1.1	-4.3	-.6	-2.3	
10	-.9	-3.5	-.7	-2.7	
11	-.6	-2.3	-1.2	-4.7	
12	-.6	-2.3	-1.4	-5.4	
13	-.5	-1.9	-1.1	-4.3	
14	-.7	-2.7	-.8	-3.1	
15	-1.0	-3.7	-.6	-2.3	
16	-1.3	-5.0	-.6	-2.3	
17	-1.3	-5.0	-.5	-1.9	
18	-1.0	-3.7	-.7	-2.7	
19	-.7	-2.7	-1.0	-3.7	
20	-.8	-3.1	-1.3	-5.0	
21	-.5	-1.9	-1.2	-4.7	
22	-.6	-2.3	-.8	-3.1	
23	-1.0	-3.7	-.7	-2.7	
24	-1.2	-4.6	-.8	-3.1	
25	-1.2	-4.6	-.6	-2.3	
26	-1.0	-3.7	-.7	-2.7	
27	-.9	-3.5	-1.1	-4.3	
28	-.6	-2.3	-1.2	-4.7	
29	-.6	-2.3	-1.1	-4.3	
30	-.8	-3.1	-1.0	-3.7	
31	-.8	-3.1	-1.0	-3.7	
32	-.9	-3.5	-.6	-2.3	
33	-1.4	-5.4	-.4	-1.5	
34	-1.2	-4.7	-.7	-2.7	
35					
36					
37					
38					
39					
40					

Figure 41. Data Sheet Type "V"

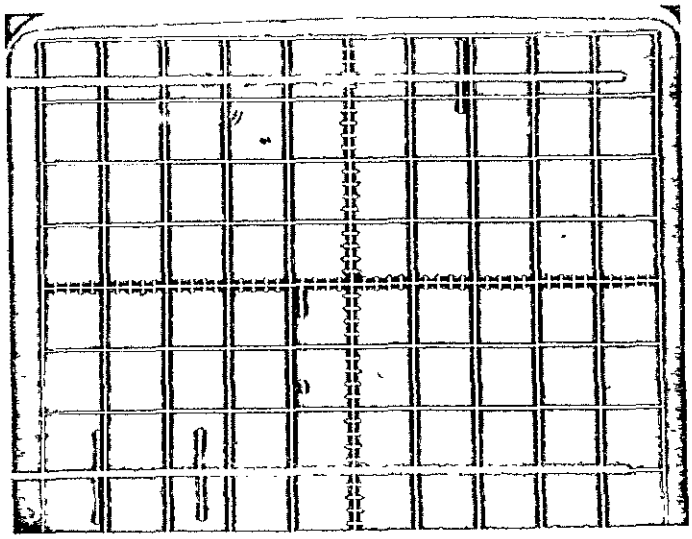

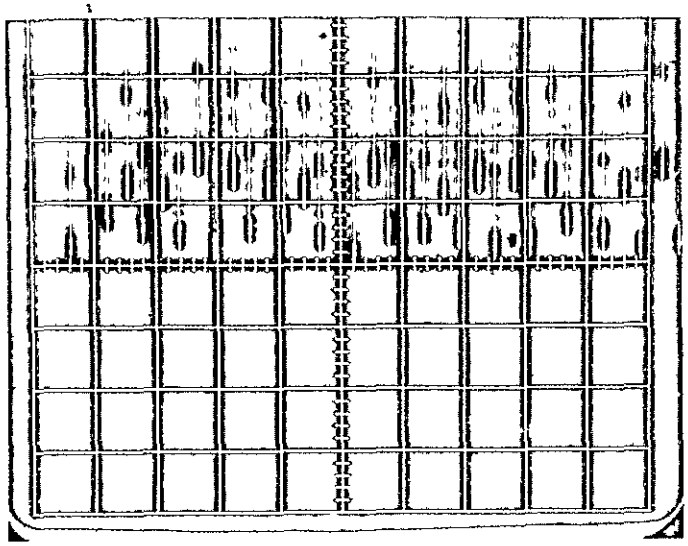

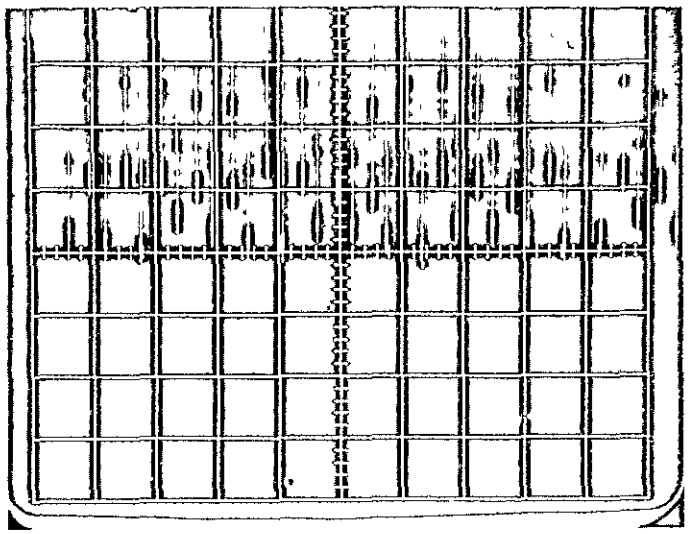

4.2.3.5 Measure angle "ϵ": _____ (mm)

4.2.3.5 Measure angle "α": _____ (mm)

4.2.3.5 Measure distance "ϵ": _____ (inches)

4.2.3.5 Measure distance "α": _____ (inches)

Figure 38. Data Sheet Type "P"

TEST PROCEDURE SCAN MIRROR	BREAD THEMATIC MAPPER	CULVER CITY, CALIF CODE IDENT NO. 82577	SH NO	REV LTR	31891-350 NUMBER

LOCATION #2

No. Turns	div		V
0	4.8 div	@ .2 v/div	.96
1	7.2	@ .1	.72
2	5.1	@ .1	.51
3	3.1	@ .1	.31
4	≈0		≈0
5	≈0		≈0
6	3.6	@ .1	.36
7	4.9	@ .1	.49
8	6.6	@ .1	.66
9	4.3	@ .2	.86
10	5.3	@ .2	1.06
11	6.4	@ .2	1.28

C-6

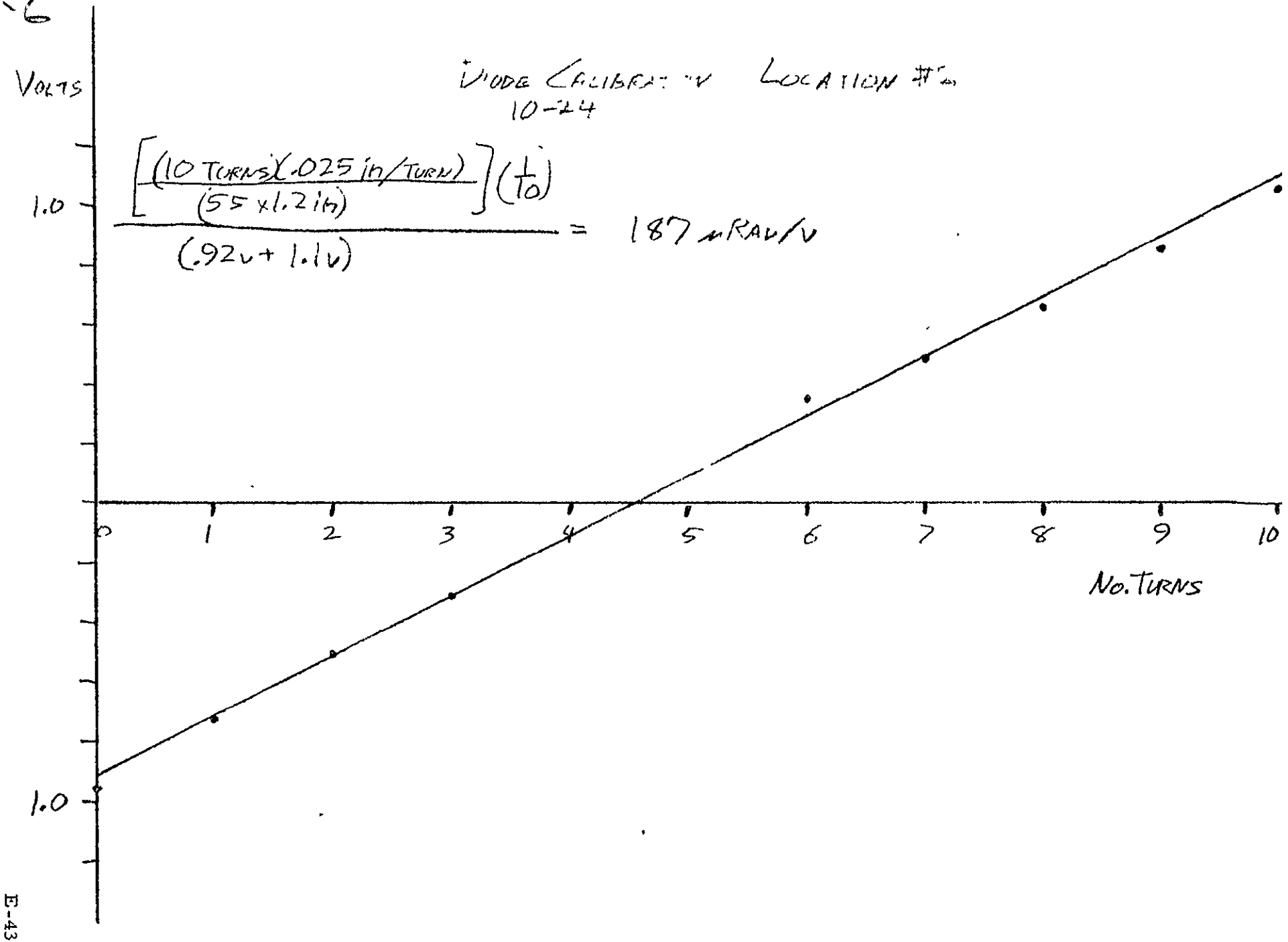

DIODE CALIBRATION LOCATION #5
10-24

$$\frac{\left[\frac{(10\ \text{TURNS} \times .025\ \text{in/TURN})}{(55 \times 1.2\ \text{in})}\right]\left(\frac{1}{10}\right)}{(.92\text{v} + 1.1\text{v})} = 187\ \text{mRAD/V}$$

10-24-75

DATA SET 3 (340 μRAD/V)(.02 V/div) = 6.8 μRAD/div

LOCATION #1

Delta Value	Photo #1 μRAD	Photo #2	Photo #3
1	+.1 div x 6.8 μRad/div = +.7	.0 x 6.8 = .0	
2	+.1 +.7	.0 .0	
3	+.1 +.7	+.2 +1.4	
4	.0 .0	.0 .0	
5	+.1 +.7	.0 .0	
6	+.1 +.7	+.1 +.7	
7	.0 .0	.0 .0	
8	+.1 +.7	+.1 +.7	
9	+.1 +.7	+.1 +.7	
10	+.1 +.7	+.1 +.7	
11	+.1 +.7	+.1 +.7	
12	-.1 -.7	.0 .0	
13	+.1 +.7	+.1 +.7	
14	+.1 +.7	+.1 +.7	
15	+.1 +.7	.0 .0	
16	+.1 +.7	+.1 +.7	
17	+.1 +.7	.0 .0	
18	+.1 +.7	+.1 +.7	
19	.0 .0	+.2 +1.4	
20	.0 .0	.0 .0	
21	+.2 +1.4	+.1 +.7	
22	.0 .0	+.1 +.7	
23	.0 .0	+.1 +.7	
24	+.1 +.7	+.1 +.7	
25	+.1 +.7	+.1 +.7	
26	+.1 +.7	+.1 +.7	
27	+.1 +.7	+.1 +.7	
28	+.1 +.7	.0 .0	
29	+.1 +.7	+.2 +1.4	
30	.0 .0	+.2 +1.4	
31	+.1 +.7	.0 .0	
32	+.1 +.7	+.1 +.7	
33	.0 .0	+.1 +.7	
34	+.1 +.7	.0 .0	
35	.0 .0	+.1 +.7	
36		+.1 +.7	
37			
38			
39			
40			

Figure 40. Data Sheet Type "W"

4.2.3.1 Measure angle "ϵ": _____(mm)

4.2.3.1 Measure angle "α": _____(mm)

4.2.3.1 Measure distance "ϵ": _____(inches)

4.2.3.1 Measure distance "α": _____(inches)

Attach three polaroid photographs to this sheet: _____

Figure 33. Data Sheet Type "R"

LOCATION #1

in		div @.1 v/div	
0		−5.0 @.1 v/div	−.5
1	Turns	−7.3 @.05	−.365
2		−5.1 @.05	−.255
3		−3.0 @.05	−.150
4		≈0	≈0
5		≈0	≈0
6		+4.1 @.05	+.205
7		+6.0 @.05	+.300
8		+7.8 @.05	+.390
9		+5.0 @.1	+.500
~~10~~		~~+7.0 @.1~~	~~+.700~~
~~11~~		~~+6.9 @.1~~	+.690

$$\frac{.25}{600 \times 1} = 4 \times 10^{-4} = 400 \times 10^{-6}$$

$.06 \times 10^{4}$

.04
300
1200

$2 \times 10^{-1} \times 2 \times 10^{2} \times 3.4 \times 10^{1} = 12$

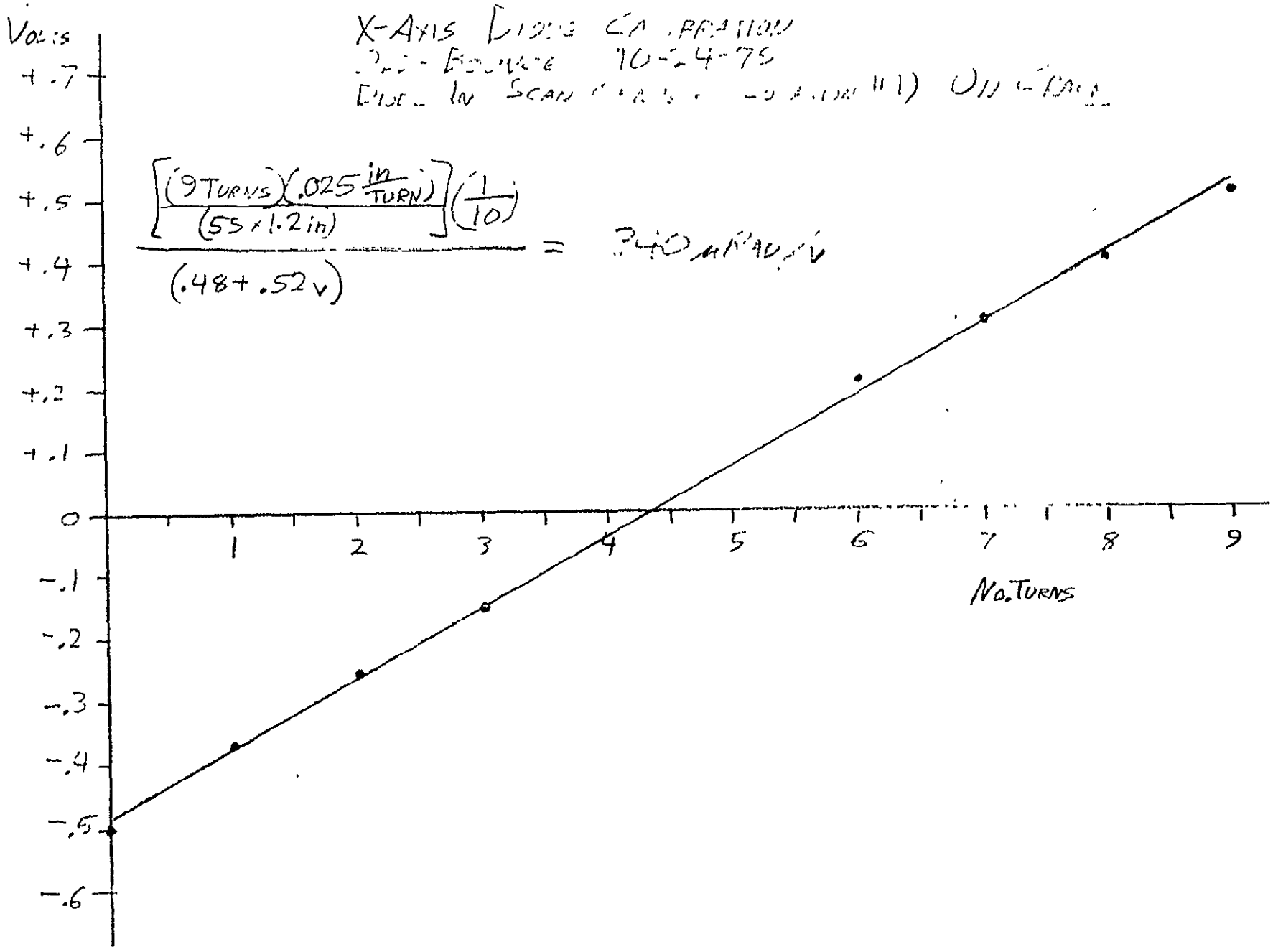
X-AXIS LIDAR CALIBRATION
DATE: 10-24-75
LIDAR IN SCAN MODE (POSITION 1) ON CAL
VOLTS
+.7
+.6
+.5
+.4
+.3
+.2
+.1
0
-.1
-.2
-.3
-.4
-.5
-.6
1
2
3
4
5
6
7
8
9
NO. TURNS
$\frac{\left[\frac{(9\,\text{TURNS})(.025\,\frac{\text{in}}{\text{TURN}})}{(5.5 \times 1.2\,\text{in})}\right]\left(\frac{1}{10}\right)}{(.48 + .52\,\text{V})} = 240\,\text{mV/V}$

10-24-75

DATA SET 4 (187 μRAD/V X .02 V/div) = 3.7 μRAD/div

LOCATION #3

FWD REV

Delta Value	Photo #1	Photo #2	Photo #3
1	4.2 div (3.7 μRAD/div) = +.7 μRAD	+.2 +.7	
2	.0 .0	-.1 -.4	
3	+.4 +1.5	.0 +.0	
4	+.4 +1.5	+.6 +2.2	
5	+.5 +1.9	+.8 +3.0	
6	+.8 +3.0	+.8 +3.0	
7	+.8 +3.0	+.3 +1.1	
8	+.7 +2.6	+.2 +.7	
9	+.5 +1.9	+.3 +1.1	
10	+.3 +1.1	+.2 +.7	
11	+.2 +.7	+.2 +.7	
12	.0 .0	+.4 +1.5	
13	+.2 +.7	+.5 +1.9	
14	+.8 +3.0	+.8 +3.0	
15	+1.0 +3.7	+.6 +2.2	
16	+.9 +3.3	+.4 +1.5	
17	+.2 +.7	+.1 +.4	
18	+.2 +.7	-.1 -.4	
19	+.3 +1.1	+.1 +.4	
20	+.2 +.7	+.2 +.7	
21	+.3 +1.1	+.5 +1.9	
22	+.5 +1.9	+.7 +2.6	
23	+.6 +2.2	+.6 +2.2	
24	+.8 +3.0	+.5 +1.9	
25	+.6 +2.2	+.3 +1.1	
26	+.4 +1.5	+.2 +.7	
27	+.2 +.7	+.2 +.7	
28	.0 .0	0 .0	
29	+.4 +1.5	+.3 +1.1	
30	+.6 +2.2	+.8 +3.0	
31	+.8 +3.0	+.8 +3.0	
32	+.8 +3.0	+.6 +2.2	
33	+.5 +1.9	+2 +.7	
34	+.4 +1.5	+.2 +.7	
35	+.4 +1.5	+.3 +1.1	
36	+.3 +1.1	+.2 +.7	
37	+.3 +1.1		
38			
39			
40			

Figure 42. Data Sheet Type "X"

4.2.3.5 Measure angle "ϵ":_____ (mm)

4.2.3.5 Measure angle "α":_____(mm)

4.2.3.5 Measure distance "ϵ":_____(inches)

4.2.3.5 Measure distance "α":_____(inches)

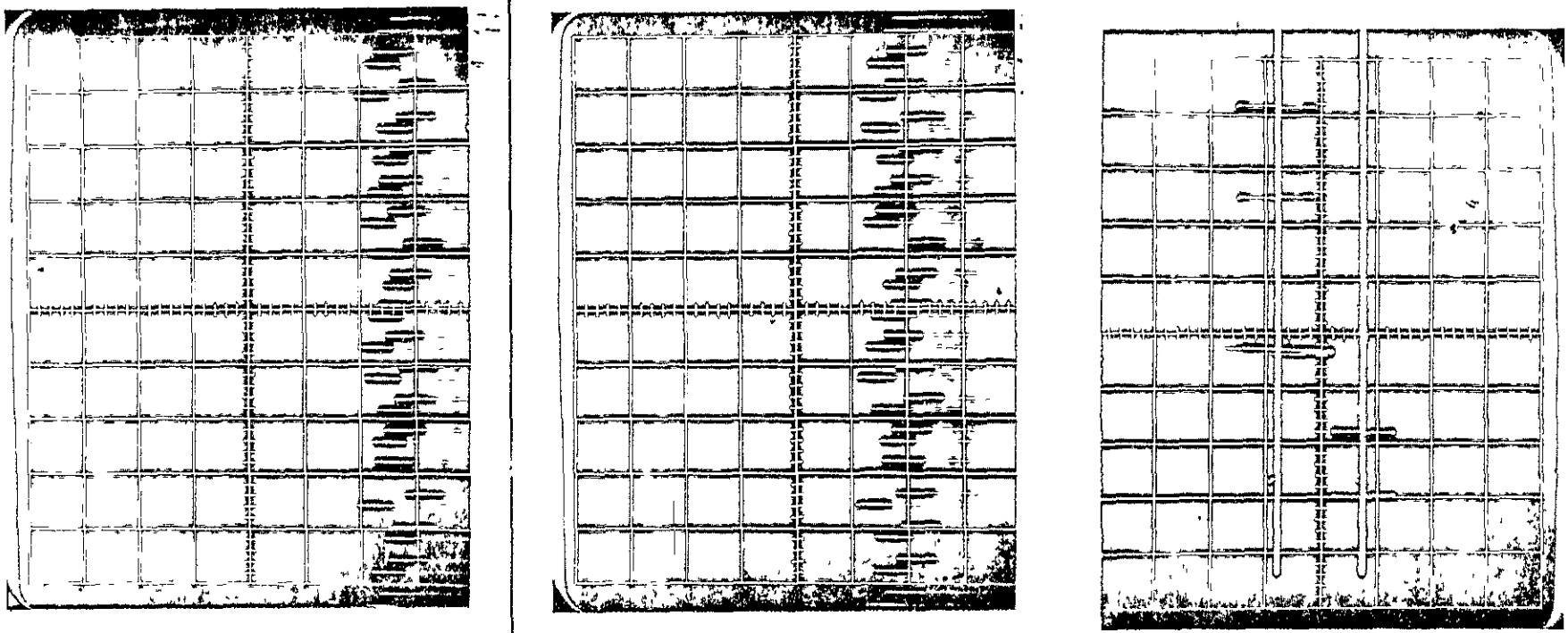

Figure 38. Data Sheet Type "S"

Location #3

No. Turns	div	V
0	4.6 @.2 v/div	.92
3	4.0 @.1	.40
7	4.5 @.1	.45
9	4.5 @.2	.90

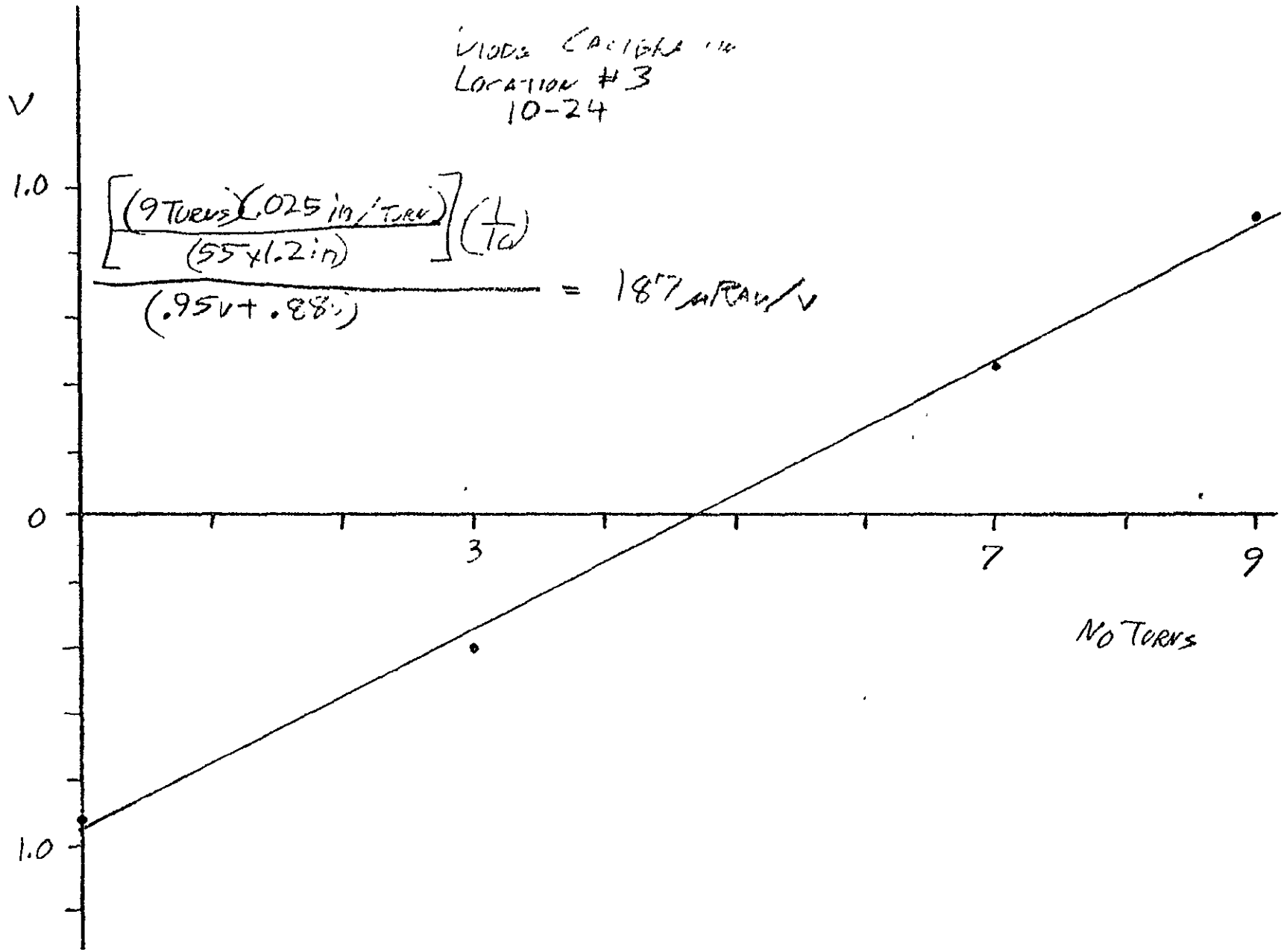
Video Calibration
Location #3
10-24
V
1.0
0
1.0
3
7
9
No Turns
$\frac{\left[\frac{(9\,\text{Turns} \times .025\,\text{in/Turn})}{(55 \times 1.2\,\text{in})}\right]\left(\frac{1}{10}\right)}{(.95V + .85)} = 187\,\mu\text{RAD/V}$

DATA SET 5 (187 μRAD/V)(.02 V/div) = 3.7 μRAD/div 10-24-75

LOCATION #5 FWD REV

Delta Value	Photo #1		Photo #2		Photo #3	
1	(+.1div)(37 μRAD/div) = +.4 μRAD		+.3	+ 1.1	+.7	+ 2.6
2	+.4	+1.5	+.1	+ .4	+.7	+ 2.6
3	+.6	+2.2	.0	.0	+7	+ 2.6
4	+7	+2.6	+2	+ .7	+.5	+ 1.9
5	+.8	+ 3.0	+.4	+ 1.5	+.2	+ .7
6	+.6	+ 2.2	+.6	+ 2.2	.0	.0
7	+.4	+1.5	+.8	+ 3.0	.0	.0
8	+.2	+ .7	+6	+ 2.2	+.6	+ 2.2
9	.0	.0	+.5	+ 1.9	+.8	+ 3.0
10	+.7	+ .7	+.3	+ 1.1	+.6	+ 2.2
11	+.5	+ 1.9	-.1	- .4	+.8	+ 3.0
12	+.6	+2.2	+.1	+ .4	+.6	+ 2.2
13	+.8	+ 3.0	+.3	+ 1.1	+.1	+ .4
14	+.8	+ 3.0	+.6	+ 2.2	.0	.0
15	+.6	+ 2.2	+.8	+ 3.0	+.1	+ .4
16	+.4	+ 1.5	+.7	+ 2.6	+.3	+ 1.1
17	+.2	+ .7	+.6	+ 2.2	+.4	+ 1.5
18						
19						
20						
21						
22						
23						
24						
25						
26						
27						
28						
29						
30						
31						
32						
33						
34						
35						
36						
37						
38						
39						
40						

Figure 42. Data Sheet Type "Y"

4.2.3.5 Measure angle "ϵ": _____ (mm)

4.2.3.5 Measure angle "α": _____ (mm)

4.2.3.5 Measure distance "ϵ": _____ (inche

4.2.3.5 Measure distance "α": _____ (inche

Figure 38. Data Sheet Type "T"

LOCATION #5

No. Turns	div	V
0	+5.0 @.2 v/div	1.0
3	+4.4 @.1	.44
7	-3.7 @.1	.37
10	-5.2 @.2	1.04

Diode Calibration
Location #5
10-24

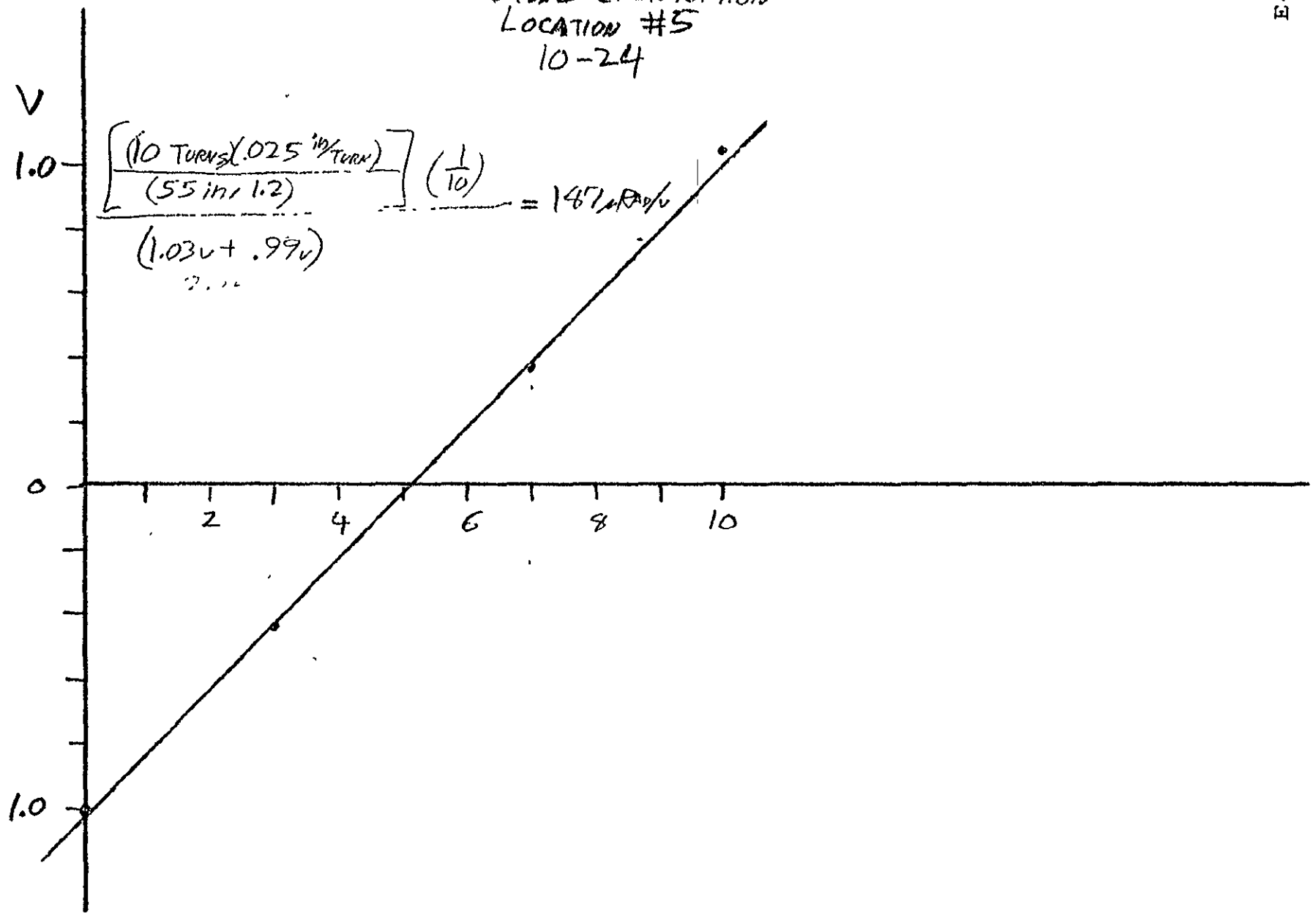

4.2.4.6.1.1	POST-SCAN COMPUTATIONS:
4.2.4.6.1.2	FOR DATA SET 1
4.2.4.6.2.1	RELATIVE DIODE POSITION = 0.169014
4.2.4.6.2.2	MEAN DEVIATION =-2.91333 MICRORADIANS
4.2.4.6.3.1	RMS DEVIATION = 3.09742 MICRORADIANS
4.2.4.6.3.2	FOR DATA SET 2
4.2.4.6.4.1	RELATIVE DIODE POSITION = 0.309859
4.2.4.6.4.2	MEAN DEVIATION =-3.29333 MICRORADIANS
4.2.4.6.5.1	RMS DEVIATION = 3.46833 MICRORADIANS
4.2.4.6.5.2	FOR DATA SET 3
	RELATIVE DIODE POSITION = 0.450704
	MEAN DEVIATION = 0.513333 MICRORADIANS
	RMS DEVIATION = 0.651665 MICRORADIANS
	FOR DATA SET 4
	RELATIVE DIODE POSITION = 0.591549
	MEAN DEVIATION = 1.54 MICRORADIANS
	RMS DEVIATION = 1.85616 MICRORADIANS
	FOR DATA SET 5
	RELATIVE DIODE POSITION = 0.732394
	MEAN DEVIATION = 1.46667 MICRORADIANS
	RMS DEVIATION = 1.79629 MICRORADIANS

DATA SHEET TYPE "2"

Figure 46 Data Sheet Type "AA"

DISTANCE

```
         RMS DEVIATION FORWARD TO REVERSE (MICRORADIANS)
                VS DIODE POSITION (D2-D1),(D3-D1)

                     1                   2                   3
  .........I.........I.........I.........I.........I.........I
.
.
.
.
D  OFF SCALE - (X,Y)=( 0.169014 , 3.09742 )
.
.
.
D  OFF SCALE - (X,Y)=( 0.309859 , 3.46833 )
.
.
-
.
D              +
.
.
D                                       +
.
.
.
D                                     +
```